Transactions of the ASME

Journal of Heat Transfer (ISSN 0022-1481) is edited and published quarterly at the offices of The American Society of Mechanical Engineers, United Engineering Center, 345 E. 47th St., New York, N. Y. 10017. ASME-TWX No. 710-581-5267, New York. Second-class postage paid at New York, N.Y., and at additional mailing offices.
CHANGES OF ADDRESS *must be received at Society* headquarters seven weeks before they are to be effective. Please send old label and new address.
PRICES: To members, $30.00, annually; to nonmembers, $60.00. Single copies, $20.00 each. Add $5.00 for postage to countries outside the United States and Canada.
STATEMENT from By-Laws. The Society shall not be responsible for statements or opinions advanced in papers or . . . printed in its publications (B7.1, para. 3).

INDEXED by the Engineering Index, Inc.

Journal of Heat Transfer

Published Quarterly by The American Society of Mechanical Engineers
VOLUME 104 • NUMBER 2 • MAY 1982

ANNOUNCEMENTS

247 Mandatory excess-page charges

254 Change of address form for subscribers

395 Errata on a previously published Author's Closure by D. W. Pepper and R. E. Copper

396 Information for authors

TECHNICAL PAPERS

223 Buoyancy-Induced Flow Due to Isolated Thermal Sources on a Vertical Surface
Y. Jaluria

228 Natural Convection From a Horizontal Cylinder—Turbulent Regime
B. Farouk and S. I. Güçeri

236 An Experimental Investigation of Merging Buoyant Jets in a Crossflow (80-WA/HT-23)
M. Gregoric, L. R. Davis, and D. J. Bushnell

241 Natural Convection in an Attic-Shaped Space Filled With Porous Material
A. Bejan and D. Poulikakos

248 *Structure of Growing Double-Diffusive Convection Cells*
Y. Suzukawa and U. Narusawa

255 An Application of the Optical Correlation Computer to the Detection of the Malkus Transitions in Free Convection (80-WA/HT-27)
E. F. C. Somerscales and H. B. Parasapour

264 Volumetric Heat-Transfer Coefficients for Direct-Contact Evaporation
R. C. Smith, W. M. Rohsenow, and M. S. Kazimi

271 Hydrodynamics of a Subsonic Vapor Jet in Subcooled Liquid
M. E. Simpson and C. K. Chan

279 *Characteristics of Nucleate Pool Boiling From Porous Metallic Coatings*
A. E. Bergles and M. C. Chyu

286 Effects of Pore Diameters and System Pressure on Saturated Pool Nucleate Boiling Heat Transfer From Porous Surfaces
N. Nakayama, T. Daikoku, and T. Nakajima

292 Pool Boiling Heat Transfer From Enhanced Surfaces to Dielectric Fluids
P. J. Marto and Lt. V. J. Lepere, UNS

300 Critical Heat Flux During Natural Convective Boiling in Vertical Rectangular Channels Submerged in Saturated Liquid
M. Monde, H. Kusuda, and H. Uehara

304 Effects of Mass Flux, Flow Quality, Thermal and Surface Properties of Materials on Rewet of Dispersed Flow Film Boiling
O. C. Iloeje, D. N. Plummer, W. M. Rohsenow, and P. Griffith

309 Inward Melting in a Vertical Tube Which Allows Free Expansion of the Phase-Change Medium
E. M. Sparrow and J. A. Broadbent

316 Transient Freezing of a Liquid in a Convectively Cooled Tube
M. S. Sadeghipour, M. N. Özişik, and J. C. Mulligan

323 Seepage and Heat Flow in Soil Freezing
P. E. Frivik and G. Comini

329 A Theoretical Study on Ignition in the Laminar Mixing Layer
C. K. Law and H. K. Law

338 Transient Conduction With Pyrolysis (Approximate Solutions for Charring of Wood Slabs)
A. M. Kanury and D. J. Holve

344 A Numerical Study of the Response of Building Components to Heating in a Fire
D. J. Holve and A. M. Kanury

351 The Galerkin Method for Solving Radiation Transfer in Plane-Parallel Participating Media
M. N. Ozisik and Y. Yener

355 The Influence of a Laminar Boundary Layer and Laminar Injection on Film Cooling Performance
R. J. Goldstein and T. Yoshida

(Contents Continued on Page 235)

(Contents Continued)

363 Effect of Laminarization and Retransition on Heat Transfer for Low Reynolds Number Flow Through a Converging to Constant Area Duct
H. Tanaka, A. Tateno, S. Hatamiya, and H. Kawamura

372 Flow Induced Vibration in a Heat Exchanger With Seal Strips
J. H. Kissel

TECHNICAL NOTES

379 Corresponding States Correlations of the Spinodal and Homogeneous Nucleation Limits
J. H. Lienhard

381 On the Prediction of Pipe Freeze-Shut in Turbulent Flow
M. Epstein and F. B. Cheung

384 View Factors in Radiation Between Two Parallel Oriented Cylinders of Finite Length
N. H. Juul

388 Heat Transfer by Conduction and Radiation in One-Dimensional Planar Media Using the Differential Approximation
A. C. Ratzel and J. R. Howell

391 Vertical Fin Efficiency With Film Condensation
L. C. Burmeister

Buoyancy-Induced Flow Due to Isolated Thermal Sources on a Vertical Surface

Y. Jaluria
Mechanical and Aerospace Engineering Department,
Rutgers University,
New Brunswick, N.J. 08903
Mem. ASME

The natural convection flow due to multiple isolated heated elements located on a vertical adiabatic surface has been studied analytically. The problem, which is of particular relevance to electronic circuitry cooling and to the question of locating sources in manufacturing systems, is considered for a Prandtl number of 0.7, which applies for air. Of particular interest were the temperature and velocity fields that arise and the dependence of these on the heat input and on the distance between the heated elements. The flow is treated as a boundary layer problem and the governing equations are solved numerically. The results obtained indicate the general nature of the flow and the dependence of the heat-transfer coefficient for an element, located in the wake of another, on the energy input and location. The downstream variation of the surface temperature, the velocity level, and the resulting velocity and temperature profiles are studied in detail. The results obtained are also compared with those for a single source, bringing out several interesting features.

Introduction

The natural convective heat transfer from finite-sized heated elements located on a vertical adiabatic surface is a problem of considerable interest in several technological applications, particularly in electronic circuitry and in some manufacturing systems. Energy dissipating devices and panels act as thermal sources and generate a natural convection flow, which is often of importance in determining the energy input and location that may be employed without overheating the elements and the surface on which they are located. This problem is of particular concern in electrical equipment where the system performance is generally temperature sensitive [1, 2].

The natural convection flow due to a single line thermal source on a vertical adiabatic surface has been studied, employing the similarity method, by Jaluria and Gebhart [3]. Various other investigators have considered the wall plume thus generated, particularly for turbulent flows [4, 5]. In actual practice, finite-sized thermal sources are of interest. Since similarity does not arise for this case, finite difference methods have been employed to determine the temperature and flow fields that result [6]. The flow due to a concentrated thermal source, which is often idealized as a point heat source, on an adiabatic vertical surface has also been studied experimentally to determine the temperature field that arises [7].

The natural convection flow due to multiple thermal sources on a vertical surface is of importance in the design of several systems of practical interest. Of particular interest is the effect of the wake due to a heated element on the heat transfer from, and the flow over, another element located downstream. A problem somewhat similar to the flow considered in the present study has recently been studied by Sparrow and Faghri [8]. They considered two heated isothermal plates separated by a specified distance, so that a free plume arises between the two plates, and numerically determined the heat transfer from the two heated surfaces. The present work considers the natural convection flow due to multiple heated elements, dissipating energy with a uniform surface heat flux. The heat sources are located on a vertical adiabatic surface and are separated by specified distances. Numerical results are obtained for a Prandtl number of 0.7, which applies for air, and for various distances separating the heat sources.

Of particular interest in the problem under consideration are the heat-transfer coefficients for the heated elements located in the wake of others and the downstram variation of the surface temperature and the maximum velocity. The resulting temperature and velocity profiles are obtained and the nature of the flow discussed in terms of the underlying physical processes. The results for a single source are compared with those obtained in earlier studies and a close agreement is obtained.

Analysis

The natural convection flow under consideration is shown in Fig. 1 for three finite-sized heated elements with a uniform thermal energy input flux, q, at the heated surface. The problem is treated as a boundary layer flow, though this assumption is not valid in the immediate vicinity of the ends of the heated elements. However, the nonboundary layer effects decay exponentially downstream and accurate results are expected in regions away from the ends of the heated surfaces [8–12]. For a small separation distance, D, as compared to the height of the heated element, L, these effects may be expected to be significant.

The following dimensionless variables are employed for an analysis of the flow:

$$X=\frac{x}{L}, \quad Y=\frac{y}{L}\,\mathrm{Gr}^{1/5}, \quad \theta=\frac{t-t_\infty}{qL/k\mathrm{Gr}^{1/5}} \tag{1}$$

$$U=u/\left(\frac{\nu}{L}\,\mathrm{Gr}^{2/5}\right), \quad V=v/\left(\frac{\nu}{L}\,\mathrm{Gr}^{1/5}\right), \quad \mathrm{Gr}=\frac{g\beta qL^4}{k\nu^2} \tag{2}$$

These are the variables commonly employed for surfaces dissipating a uniform surface heat flux [5]. The height, L, and flux, q, employed in these definitions is the one pertaining to the lowermost element, since the downstream behavior is determined mainly by this element. The characteristic temperature for the circumstance of isothermal elements is taken as $(t_0 - t_\infty)$, where t_0 is the surface temperature of the element, being qL/k here in the definition of Gr. However, the definition of other variables is also altered for the isothermal case to keep the governing equations unchanged [6]. It must be noted that the validity of the boundary layer assumption depends on the value of Gr. For heated elements

Contributed by the Heat Transfer Division for publication in the JOURNAL OF HEAT TRANSFER. Manuscript received by the Heat Transfer Division April 27, 1981.

typically a few centimeters high, this would be valid for the commonly employed heating rates, as seen later.

The governing boundary layer equations for laminar flow, employing the Boussinesq approximations for the density variation, assuming the remaining properties to be constant and neglecting viscous dissipation and pressure work terms, are:

$$\frac{\partial U}{\partial X}+\frac{\partial V}{\partial Y}=0 \tag{3}$$

$$U\frac{\partial U}{\partial X}+V\frac{\partial U}{\partial Y}=\theta+\frac{\partial^2 U}{\partial Y^2} \tag{4}$$

$$U\frac{\partial \theta}{\partial X}+V\frac{\partial \theta}{\partial Y}=\frac{1}{\mathrm{Pr}}\frac{\partial^2 \theta}{\partial Y^2} \tag{5}$$

Therefore, only the Prandtl number appears as a parameter in the governing equations. However, other variables, such as D/L, L_1/L, q_1/q, etc., appear in the boundary conditions. The relevant boundary conditions for the uniform heat flux condition at the heated elements, or regions, are:

(a) $Y=0$: $U=V=0$,

$$\frac{\partial \theta}{\partial Y}=-1, \text{ for } 0\le X\le 1$$

$$\frac{\partial \theta}{\partial Y}=0, \text{ for } 1<X<(1+D/L)$$

$$\frac{\partial \theta}{\partial Y}=-q_1/q, \text{ for } (1+D/L)\le X\le 1+\frac{D+L_1}{L} \tag{6}$$

$$\frac{\partial \theta}{\partial Y}=0, \text{ for } \left(1+\frac{D+L_1}{L}\right)<X<1+\frac{D+L_1+D_1}{L}$$

and so on for other heated elements.

(b) as $Y\to\infty$, $U=\theta=0$.

Similarly, for the isothermal case, θ is specified as θ_1, θ_2, . . . , at the heated surfaces. Therefore, several additional parameters, such as q_1/q, D/L, etc., arise in the above equations. In most of the results presented here, the heat flux is taken as equal for all the heated surfaces and their heights are also taken as equal, since the general features of the problem may be considered independent of these variables. However, some results are also presented for the case when the heat inputs are different.

The governing equations given above were solved numerically by employing finite difference methods. The time-dependent forms of the equations were considered and the transient solution was obtained by marching explicitly in time until the results converge to the steady-state solution, as indicated by a suitably chosen criterion. This method allows a study of the convergence of the solution to the steady-state circumstance as time elapses and gives better stability characteristics [9, 13]. The initial conditions, the step size ΔX and the convergence criterion were varied to ensure a negligible dependence of the solution on the values chosen. The numerical results were initially obtained for the isolated single source circumstance, and the results compared with those of [3, 6], indicating an agrement within a few percent for the surface temperature distribution. The numerical study was carried out on an IBM 370/168 computer, and the characteristic results obtained are discussed in the next section.

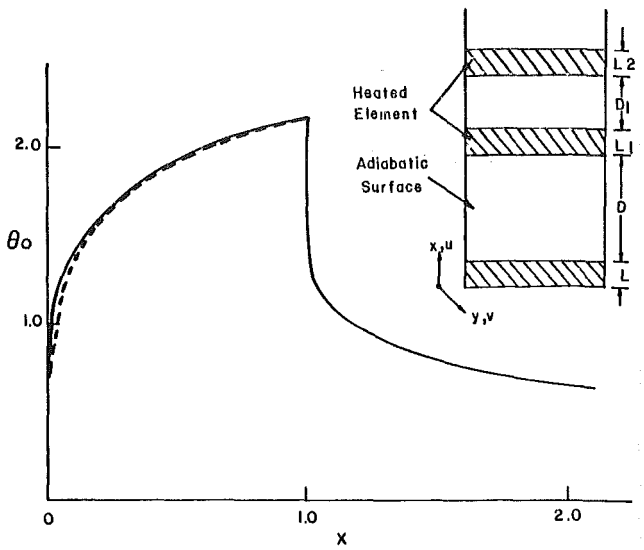

Fig. 1 Coordinate system for the flow under consideration and the surface temperature variation in the neighborhood of an isolated single heated element on a vertical adiabatic surface: ---, theoretical curve for a vertical uniform heat flux surface see [5]

Results and Discussion

The natural convection flow due to a finite-sized heated element, with a uniform convective heat flux input q at its surface, is considered first, and Fig. 1 shows the downstream variation of the surface temperature in the vicinity of the heated element. The temperature rises from the ambient value of zero to a maximum at $X = 1$, and then drops sharply, followed by a gradual decay downstream. The calculated

Nomenclature

D, D_1, D_2 = distance between heated elements, Fig. 1
g = gravitational acceleration
Gr = Grashof number, defined in equation (2)
h = heat-transfer coefficient
k = thermal conductivity of fluid
L, L_1, L_2 = heights of heated elements, Fig. 1
$(\mathrm{Nu})_u$ = Nusselt number for the upper element, $(hL/k)_u$
$(\mathrm{Nu})_l$ = Nusselt number for the lower element, $(hL/k)_l$
Pr = Prandtl number of fluid
q, q_1, q_2 = heat flux input at the heated surfaces
Q = total convective thermal energy input into the flow
t = local temperature in the flow
t_0 = surface temperature
t_∞ = ambient temperature
u = vertical velocity component
U = dimensionless vertical velocity
$U_{\max}$ = maximum dimensionless vertical velocity
v = transverse velocity component
V = dimensionless transverse velocity
x = vertical coordinate
X = dimensionless vertical coordinate
y = transverse coordinate
Y = dimensionless transverse coordinate
β = coefficient of thermal expansion of fluid
ν = kinematic viscosity of fluid
θ = dimensionless temperature, defined in equation (1)
θ_0 = dimensionless surface temperature
δ = boundary layer thickness

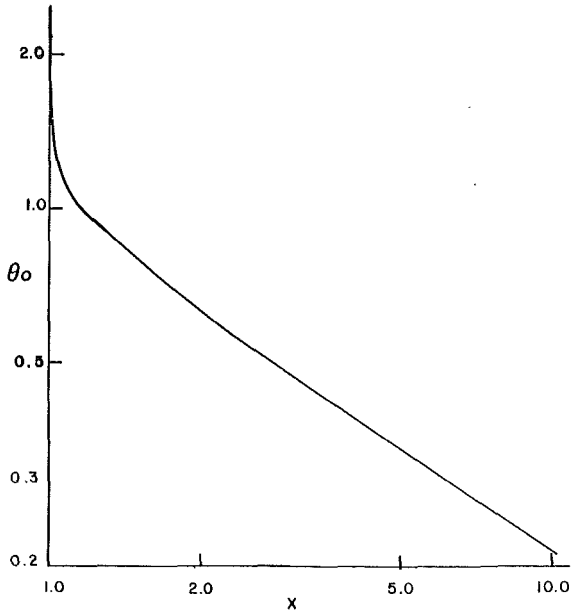

Fig. 2 Downstream decay of the surface temperature for a single heated element

temperature at the surface of the heated element is found to vary as $X^{0.2}$, as predicted by similarity analysis [5], and the values obtained were found to be very close to those obtained in earlier studies as shown. The boundary condition for the temperature gradient changes at $X = 1$ and the adiabatic condition for $X > 1$ brings the surface temperature gradient to zero. This results in a flattening of the temperature profile near the surface, as seen later, and a rapid spreading out of buoyancy away from the surface. This causes the observed sharp temperature drop in the vicinity of the trailing end of the heated surface. However, in actual practice, conduction in the plate would make the drop less steep and the inclusion of nonboundary layer effects would also modify the results in this region. The downstream decay of the surface temperture is shown in Fig. 2 and it is found that for $X \gtrsim 3$, the variation approaches $X^{-0.6}$, which is the variation predicted by similarity analysis for a wall plume [3]. The velocity and temperature profiles obtained were also found to be in good agreement with the earlier work, as seen later.

The surface temperature variation for two heated elements, separated by distance D/L of 2, 4, and 8, is shown in Fig. 3. Since the boundary layer approximation is employed, the upstream results are unaffected by the presence of the second source. However, the calculated results for the downstream element are very much influenced by the presence of the heated element upstream. In the neighborhood of the heated regions, the temperature variation is similar to that observed in Fig. 1. A sharp temperature drop occurs at the trailing end of the heated elements, followed by a gradual decay, as expected for a wall plume. It is interesting to note that in all the three cases shown in Fig.3, the surface temperatures approach the asymptotic behavior expected for a thermal input of $2qL$ far downstream. The starting effects due to the finite size of the elements and their separating distance decay as the flow proceeds downstream, ultimately approaching the expected variation for a wall plume generated by a line source with an input of $2qL$. It is also noted that the temperature of the upper heted surface is higher for $D/L = 2$ and lower for the other two cases. This indicates that the corresponding local heat-transfer coefficient for the upper element is smaller than that for the lower element in the first case and larger in the other two cases. A similar behavior was observed by Sparrow and Faghri [8]. This point is considered in detail later.

The surface temperature variation for three heated

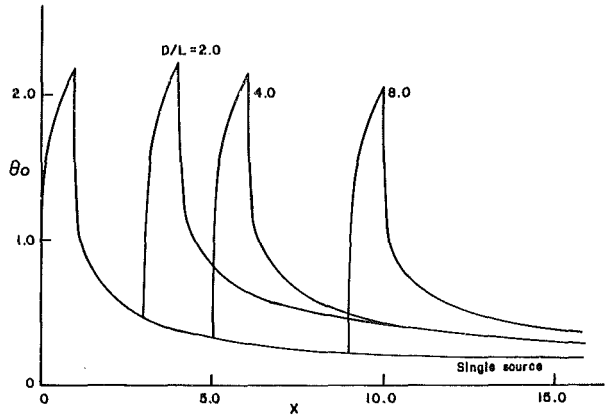

Fig. 3 Surface temperature variation for various distances separating two heated elements

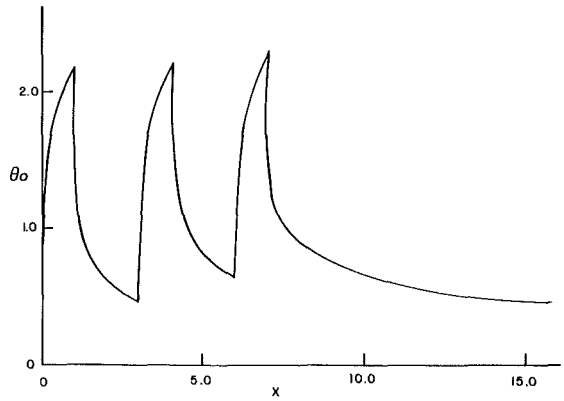

Fig. 4 Surface temperature variation for the flow generated by three heated elements, dissipating a uniform heat flux q at the surface, for $D/L = D_1/L = 2.0$

elements, with $D/L = D_1/L = 2$, is shown in Fig. 4. Again, the results for the two lower elements remain unchanged and the variation changes beyond $X = 6$. The basic trends are similar to those discussed above, but the asymptotic value approached by the surface temperature is higher than that for two elements. This is an expected behavior since the total convective thermal energy input into the flow is $3qL$ in this case. It is interesting to note that the temperature of the uppermost element is the highest, indicating the lowest heat-transfer coefficient for this element. The heat-transfer coefficient for the downstream heated element is obviously a function of the spacing as considered later.

Another physical variable of interest is the maximum local velocity in the flow. Figure 5 shows the downstream variation of U_{max} for various values of D/L. It is seen that the sharp change in temperature observed in the neighborhood of a heated element does not arise in the velocity. The maximum velocity does rise due the buoyancy input at the upper element. But the variation is much more gradual. Buoyancy is a cumulative effect, and the boundary conditions for the velocity field do not change, as they do for the temperature field. The observed behavior is, therefore, an expected one, though a much steeper variation would be expected if the two heated elements were not located on a surface, as considered in [8]. It is also seen in Fig. 5 that the maximum velocity approaches an asymptotic value far downstream. As the starting effects decay downstream, the flow is expected to eventually approach the wall plume circumstance with $2qL$ as the heat input. However, the flow may become turbulent before this occurs and the analysis would not be applicable then. For three elements, the curve shown indicates similar trends, but the asymptotic value approached at large X is

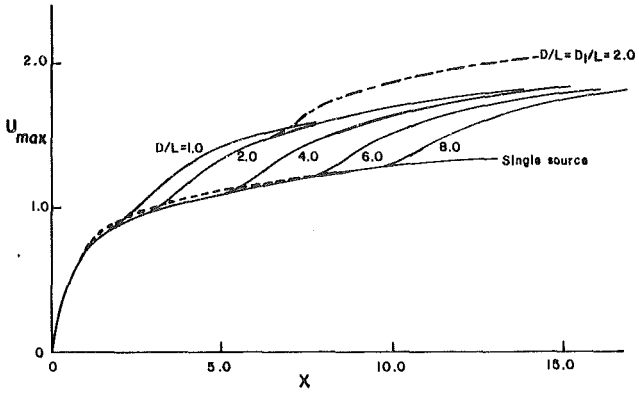

Fig. 5 Downstream variation of the maximum velocity U_{max} for various distances separating two heated elements. Also shown is the curve for three elements with $D/L = D_1/L = 2.0$; ···, theoretical curve for a single isolated line source [3]

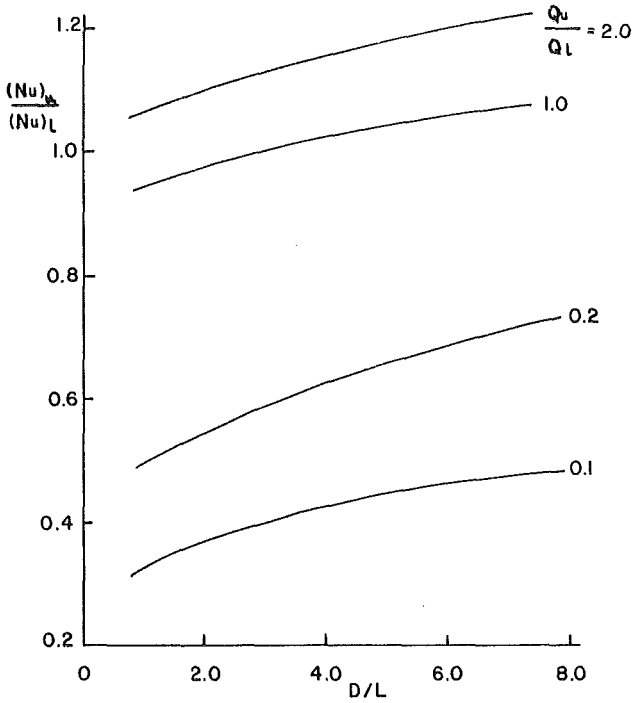

Fig. 6 The variation of $(Nu)_u/(Nu)_l$ with D/L for various values of Q_u/Q_l, the ratio of the heat flux input at the upper element to that at the lower element

higher, as expected. The results upstream of the uppermost element remain unchanged because of the boundary layer assumption employed here. A comparison with the results of [3] shows a close agreement for the single source case.

The dependence of the heat-transfer coefficient for the heated elements on the separation between the two elements is shown in Fig. 6. The average Nusselt number $(Nu)_u$ for the upper element is normalized by the corresponding value $(Nu)_l$ for the lower element and plotted against D/L. If the heat flux input is the same for the two elements, the ratio of the Nusselt numbers is inversely proportional to the ratio of the temperature excess over t_∞. For this case, it is found that this ratio is less than 1.0 for $D/L = 4$, indicating a lower heat-transfer coefficient for the upper element, as compared to that for the lower element. Similarly, if $D/L \gtrsim 4$, the heat-transfer coefficient at the upper element is increased. The axial diffusion terms were added for $D/L = 4$, and it was found that for Gr ranging from around 10^4 to 10^8, which is of practical interest, a difference of less than 2 percent arises in $(Nu)_u/(Nu)_l$, indicating the validity of the present boundary

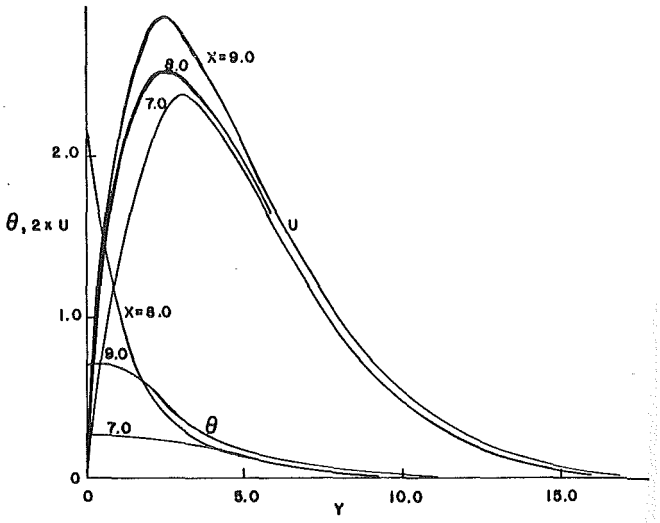

Fig. 7 Temperature and velocity profiles at various downstream locations for $D/L = 6$

layer treatment. The temperature profile in Fig. 3 changed slightly, with the drop at the trailing ends of the elements less severe and the average values of the element temperature affected to a very small extent.

The heat-transfer coefficient for the upper element is affected by the flow generated by the lower element. The fluid coming from below is heated and the upper element is exposed to a moving fluid at a temperature higher than the ambient temperature. It has been seen earlier that the velocity level increases downstream and the temperature level decreases, the former being due to the buoyancy force and the latter being due to entrainment. Therefore, if the upper element were moved downstream, it is exposed to a higher velocity and a lower fluid temperature, resulting in an increased heat-transfer coefficient. It is this behavior that is seen quantitatively in Fig. 6.

The Nusselt number ratio varies from 0.9 to 1.05 for $Q_u/Q_l = 1.0$ as D/L varies from 1.0 to 8.0. The ratio drops sharply as D/L decreases below 1.0. But the full governing equations would need to be considered for low values of D/L. At $D/L = 0$, the problem simply becomes that for an element of twice the height of a single element and the problem may be solved as a boundary layer. The highest surface temperature, at the trailing end of the upper element, would be expected in this case. It is also seen from Fig. 6 that the effect of increasing D/L is quite small beyond a value of around 6.0. Therefore, in the design of such a system, the spacing may be chosen for the given constraints and requirements.

It may also be physically expected that if the heat flux input at the upper element is much larger than that at the lower one, the effect of preheating the fluid due to the lower element would be negligible and the heat-transfer coefficient would be increased due to the velocity effect. Similarly, if the heat input at the upper element is much smaller than that at the lower one, the temperature effect may be expected to dominate, resulting in a lower heat-transfer coefficient. These effects are also shown quantitatively in Fig. 6. It must, however, be noted that the heat-transfer coefficient is defined in terms of the ambient fluid temperature and not the local temperature as seen by the upper element. The sharp increase in the upper element average temperature is reflected as a decrease in the Nusselt number.

The resulting velocity and temperature profiles may also be considered, as shown in Fig 7, for $D/L = 6$. The results are shown at X values of 7.0, 8.0, and 9.0, which correspond to positions at the leading edge, at the trailing end and downstream of the upper element. The form of the temperature

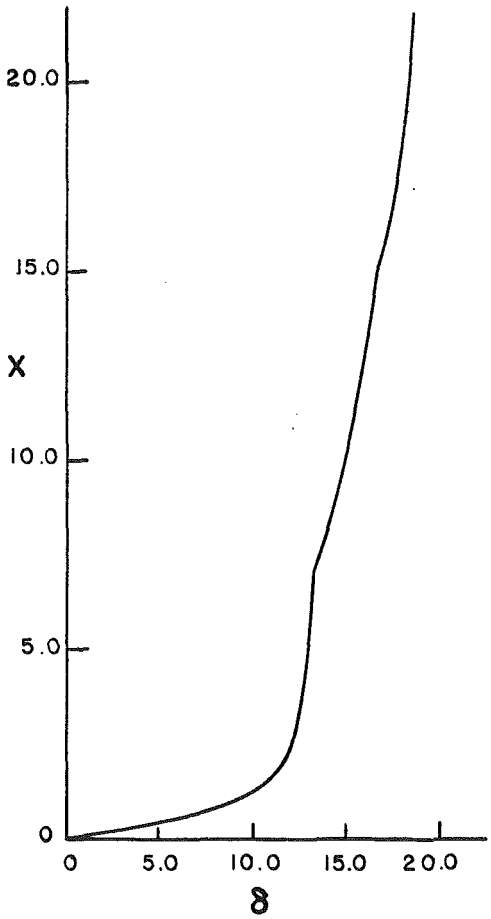

Fig. 8 Downstream variation of the boundary layer thickness for three heated elements

profile is found to undergo a sharp change downstream of the element, as the adiabatic condition arises and the flattened profile typical of a wall plume results. It also causes a sharp drop in the surface temperature. It may be observed here that the velocity level increases from $X = 8.0$ to $X = 9.0$, and the boundary layer thickness increases. Since the total convected energy Q remains unchanged at $2qL$, the temperature level drops sharply to maintain its constancy with the changed form of the profile. The velocity level increases downstream due to buoyancy, the boundary layer thickness increases, and the location of the maximum velocity is seen to shift inwards, particularly from $X = 7.0$ to $X = 8.0$. This may be explained in terms of the increased buoyancy input at the surface as the flow goes over the heated element. This results in increased buoyancy near the surface and, hence, the observed shift in peak velocity towards the surface. The peak does not change appreciably in position further downstream, since the buoyancy input ends at $X = 8.0$.

The growth of the boundary layer thickness in the flow is an interesting feature, and Fig. 8 shows the results for three elements. The edge of the boundary layer is defined as the location where 1.0 percent of the peak velocity is attained as one moves outwards from the peak. The variation is found to be fairly smooth, except for slight changes in gradient at the locations of the leading edges of the heating elements. The lowermost element lies between $X = 0.0$ and 1.0, the second between $X = 8.0$ and 9.0 and the third between $X = 15.0$ and 16.0. The boundary layer thickness rises sharply from zero at $X = 0.0$, and then increases gradually downstream, with the two noticeable variations at the two upper elements. It may also be noted that the boundary layer thickness varies as $Gr^{-1/5}$ (equation(1)). Therefore, for large values of Gr, as determined by the height of the element, L, and the heat input, q, the boundary layer thickness would be much smaller than the downstream distance, x, thus permitting a boundary layer treatment. This circumstance arises for several cases of practical interest, where the heated elements or regions are several centimeters high, and the heat flux input is large enough to allow the present treatment.

Conclusions

An analytical study of the natural convection flow generated by finite sized multiple thermal sources on a vertical adiabatic surface has been carried out. The resulting temperature and velocity fields are determined numerically. Of particular interest were the effect of a heated element on the heat-transfer coefficient for another element located downstream and the variation of the surface temperature and the velocity level downstream. The study initially considers a single heated element, dissipating a uniform heat flux, and the results obtained are compared with earlier studies on wall plumes. A close agreement was obtained. The heat-transfer coefficient for an element located in the wake of an upstream element was studied as a function of the spacing between the two. For two similar elements with the same thermal input, the heat-transfer coefficient for the upper element was lowered due to the upstream element for small spacings and increased for larger ones. Several other interesting features are observed in the results obtained and these are discussed in terms of the underlying physical processes.

The study considers a problem of considerable importance in several practical applications, particularly in those related to electrical equipment and the positioning of heating elements in a manufacturing system. The basic nature of the flow is considered in detail and the relevant aspects with respect to heat transfer from elements located in the wakes of others are outlined.

Acknowledgment

The author acknowledges the financial support of the Department of Mechanical and Aerospace Engineering, Rutgers University, for the computer work.

References

1 Seeley, J. H. and Chu, R. C., *Heat Transfer in Microelectronic Equipment: A Practical Guide*, Marcel Dekker, New York, 1972.

2 Bergles, A. E., Chu, R. C., and Seeley, J. H., "Survey of Heat Transfer Techniques Applied to Electronic Equipment," *ASME Winter Annual Meeting*, New York, Nov. 1972, Paper 72-WA/HT-39.

3 Jaluria, Y. and Gebhart, B., "Buoyancy-Induced Flow Arising From a Line Thermal Source on an Adiabatic Vertical Surface," *International Journal of Heat and Mass Transfer*, Vol. 20, 1977, pp. 153-157.

4 Zimin, V. D. and Lyakhov, Y. N., "Convective Wall Plume," *Journal of Applied Mechanics Tech. Phys.*, Vol. 11, 1970, pp. 159-162.

5 Jaluria, Y., *Natural Convection Heat and Mass Transfer*, Pergamon Press, U.K., 1980.

6 Sparrow, E. M., Patankar, S. V., and Abdel-Wahed, R. M., "Development of Wall and Free Plumes Above a Heated Vertical Plate," ASME JOURNAL OF HEAT TRANSFER, Vol. 100, 1978, pp. 184-190.

7 Carey, V. P. and Mollendorf, J. C., "The Temperature Field Above a Concentrated Heat Source on a Vertical Adiabatic Surface," *International Journal of Heat and Mass Transfer*, Vol. 20, 1977, pp. 1059-1067.

8 Sparrow, E. M. and Faghri, M., "Natural Convection Heat Transfer From the Upper Plate of a Colinear, Separated Pair of Vertical Plates," ASME JOURNAL OF HEAT TRANSFER, Vol. 102, 1980, pp. 623-629.

9 Hardwick, N. E. and Levy, E. K., "Study of the Laminar Free Convection Wake Above an Isothermal Vertical Plate," ASME JOURNAL OF HEAT TRANSFER, Vol. 95, 1973, pp. 289-294.

10 Yang, K. T. and Jerger, E. W., "First-Order Perturbations of Laminar Free-Convection Boundary Layers on a Vertical Plate," ASME JOURNAL OF HEAT TRANSFER, Vol. 86, 1964, pp. 107-115.

11 Kelleher, M., "Free Convection from a Vertical Plate with Discontinuous Wall Temperature," ASME JOURNAL OF HEAT TRANSFER, Vol. 93, 1971, pp. 349-356.

12 Jaluria, Y., "Natural Convection Flow Interaction Above a Heated Body," *Letters Heat Mass Transfer*, Vol. 3, 1976, pp. 457-466.

13 Roache, P. J., *Computational Fluid Dynamics*, Hermosa Pub., 1976.

Natural Convection From a Horizontal Cylinder—Turbulent Regime

B. Farouk
Assistant Professor,
Mechanical Engineering and Mechanics Department,
Drexel University,
Philadelphia, Penn. 19104
Assoc. Mem. ASME

S. I. Güçeri
Associate Professor,
Mechanical and Aerospace Engineering Department,
University of Delaware,
Newark, Del. 19711

A two-equation model has been adopted in obtaining numerical solutions of turbulent natural convection from an isothermal horizontal circular cylinder. The k-ϵ model employed in this study characterizes turbulence through the kinetic energy and its volumetric rate of dissipation. The transport equations for these two variables, along with those for time-averaged stream function, vorticity, and temperature, form a closed set of five coupled partial differential equations. These equations are solved for the entire flow domain, without boundary layer approximations. Buoyancy effects on the turbulence structure are also accounted for. Results are presented for a Rayleigh number range of 5×10^7 to 10^{10} and the average Nusselt numbers are compared with existing correlations and limited available experimental data.

Introduction

Turbulent natural convection from cylindrical surfaces is important in many technological applications. Even though numerous investigations have been made on the laminar case [1, 2, 3], turbulent natural convection from cylindrical surfaces has received relatively less attention in the past. One of the earliest works in turbulent natural convection from a horizontal cylinder was presented by Hermann [4]. However, no heat-transfer results were reported. McAdams [5] presented empirical relations for the Rayleigh number range of 10^9 to 10^{12} and Kutateladze [6] gave experimental data on only average Nusselt number for turbulent free convection from horizontal cylinders.

Heat-transfer correlations that cover both the laminar and turbulent natural convection from a horizontal cylinder have been obtained by Raithby and Hollands [7], Churchill and Chu [8], and Kuehn and Goldstein [9] among others. The correlating equations given in [8] and [9] are based on boundary layer solutions, experimental data, and the correlation model of Churchill and Usagi [10]. The empirical analyses correlate data quite well, but they give no information about the temperature and velocity fields.

Numerical treatment of the external turbulent natural convection problem has been limited to the vertical flat plate problem only. This problem was solved by Cebeci and Khattab [11], Mason and Seban [12], and Noto and Matsumoto [13], who assumed an eddy diffusivity distribution along the flat plate. Plumb and Kennedy [14], and Lin and Churchill [15] have employed a k-ϵ turbulence model for the calculation of the turbulent natural convection from a vertical isothermal flat plate. Recently, Fraikin et al. [16], Farouk and Güçeri [17], and Farouk [18] have applied k-ϵ turbulence models to buoyancy driven recirculating flows.

The objective of the present work is to obtain solutions to the complete Navier-Stokes and energy equations for turbulent natural convection from a horizontal isothermal circular cylinder. A k-ϵ turbulence model is adopted taking into account the influence of the buoyancy on the turbulence length scale and the turbulent kinetic energy. Turbulence is characterized by transport equations for time averaged k, the turbulent kinetic energy and ϵ, its volumetric rate of dissipation. Solutions have been obtained over the Rayleigh number range of 5×10^7 to 10^{10}. Results in this paper include the development of the buoyant turbulent plume which cannot be obtained using boundary layer methods. Heat-transfer results obtained are compared with available experimental data and correlating equations. Detailed contour plots of the turbulent kinetic energy and turbulent viscosity along with plots of time averaged streamlines and isotherms are presented.

Problem Statement

Various authors have proposed closure models for turbulent flows in an attempt to accurately predict the turbulent shear stresses. Due to its demonstrated success in calculating a wide variety of forced flows, the k-ϵ model of Launder and Spalding [19] was chosen for calculating the turbulent natural convection flow around a horizontal cylinder. The turbulent viscosity is proportional to a characteristic velocity of turbulence (e.g., the square root of the turbulent kinetic energy) and a length scale representing the energy containing eddies. In the k-ϵ model under consideration the length scale is taken to be the dissipation length scale

$$l = \frac{k^{3/2}}{\epsilon}$$

Thus the turbulent viscosity can be written as

$$\mu_t = C_\mu \rho \frac{k^2}{\epsilon} \tag{1}$$

where C_μ is a constant of proportionality. In the turbulence model employed, time-averaged values of the temperature, $\bar{T}$, stream function, $\bar{\psi}$ and vorticity, $\bar{\omega}$, are used. The mean motion is considered to be two-dimensional; however, fluctuating components of velocities in all three-dimensions are taken into account. The turbulent heat fluxes are obtained by using the turbulent Prandtl number approach [20]. A transport equation for the turbulent kinetic energy can be derived from the Navier-Stokes equations using Reynolds decomposition. For forced convection flows, turbulence energy is created by the action of the turbulent contribution to the shear stresses on the moving fluid. In natural convection flows, however, there is an additional buoyancy-induced, source of turbulent kinetic energy which is associated with upward movement of light fluid particles and the consequent downward movement of heavy ones [21].

Using the nondimensional variables

$$T^* = \frac{T - T_\infty}{T_w - T_\infty}\ ;\ r^* = \frac{r}{D}\ ;\ v_r^* = \frac{D\bar{v}_r}{\nu}\ ;\ v_\theta^* = \frac{D\bar{v}_\theta}{\nu}\ ;\ \psi^* = \frac{\bar{\psi}}{\mu}$$

Contributed by the Heat Transfer Division for publication in the JOURNAL OF HEAT TRANSFER. Manuscript received by the Heat Transfer Division March 16, 1981.

$$\omega^* = \frac{D^2\bar{\omega}}{\nu};\ k^* = \frac{D^2 k}{\nu^2};\ \epsilon^* = \frac{D^4\epsilon}{\nu^3};\ \mu_t^* = \frac{\mu_t}{\mu} \tag{2}$$

the following closed system of five equations describing turbulent, buoyancy-driven, two-dimensional flow is obtained:

$$\frac{\partial}{\partial r^*}\left[r^*\frac{\partial \psi^*}{\partial r^*}\right] + \frac{\partial}{\partial \theta}\left[\frac{1}{r^*}\frac{\partial \psi^*}{\partial \theta}\right] = -r^*\omega^* \tag{3}$$

$$\frac{\partial}{\partial r^*}\left[\omega^*\frac{\partial \psi^*}{\partial \theta}\right] - \frac{\partial}{\partial \theta}\left[\omega^*\frac{\partial \psi^*}{\partial r^*}\right] - \frac{\partial}{\partial r^*}\left[r^*\frac{\partial[(1+\mu_t^*)\omega^*]}{\partial r^*}\right] - \frac{\partial}{\partial \theta}\left[\frac{1}{r^*}\frac{\partial[(1+\mu_t^*)\omega^*]}{\partial \theta}\right] = \mathrm{Gr}\left[\frac{\partial T^*}{\partial \theta}\cos\theta + \frac{\partial T^*}{\partial r^*}r^*\sin\theta\right] \tag{4}$$

$$\frac{\partial}{\partial r^*}\left[T^*\frac{\partial \psi^*}{\partial \theta}\right] - \frac{\partial}{\partial \theta}\left[T^*\frac{\partial \psi^*}{\partial r^*}\right] - \frac{\partial}{\partial r^*}\left[\left(\frac{1}{\mathrm{Pr}} + \frac{\mu_t^*}{\sigma_T}\right)r^*\frac{\partial T^*}{\partial r^*}\right] - \frac{\partial}{\partial \theta}\left[\left(\frac{1}{\mathrm{Pr}} + \frac{\mu^*{}_t}{\sigma_T}\right)\frac{1}{r^*}\frac{\partial T^*}{\partial \theta}\right] = 0 \tag{5}$$

$$\frac{\partial}{\partial r^*}\left[k^*\frac{\partial \psi^*}{\partial \theta}\right] - \frac{\partial}{\partial \theta}\left[k^*\frac{\partial \psi^*}{\partial r^*}\right] - \frac{\partial}{\partial r^*}\left[\left(1+\frac{\mu_t^*}{\sigma_k}\right)r^*\frac{\partial k^*}{\partial r^*}\right] - \frac{\partial}{\partial \theta}\left[\left(1+\frac{\mu_t^*}{\sigma_k}\right)\frac{1}{r^*}\frac{\partial k^*}{\partial \theta}\right] = r^*\mu_t^*$$

$$\left\{2\left(\frac{\partial v_r}{\partial r^*}\right)^2 + 2\left(\frac{\partial v_\theta^*}{r^*\partial \theta}\right)^2 + 2\left(\frac{v_r^*}{r^*}\right)^2 + \left[r^*\frac{\partial}{\partial r^*}\left(\frac{v_\theta^*}{r^*}\right) + \frac{\partial v_r^*}{r^*\partial \theta}\right]^2\right\} + \mathrm{Gr}\,\frac{\mu_t^*}{\sigma_T}\left[\frac{\partial T^*}{r^*\partial \theta}\sin\theta - \frac{\partial T^*}{\partial r^*}\cos\theta\right] + \epsilon^* \tag{6}$$

and

$$\frac{\partial}{\partial r^*}\left[\epsilon^*\frac{\partial \psi^*}{\partial \theta}\right] - \frac{\partial}{\partial \theta}\left[\epsilon^*\frac{\partial \psi^*}{\partial r^*}\right] - \frac{\partial}{\partial r^*}\left[\left(1+\frac{\mu_t^*}{\sigma_\epsilon}\right)r^*\frac{\partial \epsilon^*}{\partial r^*}\right] - \frac{\partial}{\partial \theta}\left[\left(1+\frac{\mu_t^*}{\sigma_\epsilon}\right)\frac{1}{r^*}\frac{\partial \epsilon^*}{\partial \theta}\right] = C_1 r^*\mu_t^*\frac{\epsilon^*}{k^*}\left\{2\left(\frac{\partial v_r^*}{\partial r^*}\right)^2 + 2\left(\frac{\partial v_\theta^*}{r^*\partial \theta}\right)^2 + 2\left(\frac{v_r^*}{r^*}\right)^2 + \left[r^*\frac{\partial}{\partial r^*}\left(\frac{v_\theta^*}{r^*}\right) + \frac{\partial v_r^*}{r^*\partial \theta}\right]^2\right\} + C_3\mathrm{Gr}\,\frac{\mu_t^*}{\sigma_T}\,\frac{\epsilon^*}{k^*}\left[\frac{1}{r^*}\frac{\partial T^*}{\partial \theta}\sin\theta - \frac{\partial T^*}{\partial r^*}\cos\theta\right] + C_2\frac{\epsilon^{*2}}{k^*} \tag{7}$$

with

$$v_r^* = \frac{1}{r^*}\frac{\partial \psi^*}{\partial \theta};\ v_\theta^* = -\frac{\partial \psi^*}{\partial r^*}$$

The coordinates being r, measured from the center of the cylinder and θ, measured counterclockwise from the downward vertical line. The terms on the right hand side of the k^* equation are the energy production and/or dissipation terms. The sum of these terms in turn determine the description of turbulence. This model contains empirical constants in the preceding expressions. σ_T, σ_k and σ_ϵ are the turbulent Prandtl numbers for T^*, k^* and ϵ^*, respectively. Numerical values for C_μ, C_1, C_2, σ_T, σ_k and σ_ϵ are taken as recommended by Launder and Spalding [19] and are given in Table 1. These values have been optimized against experimental data for forced flows. The constant C_3 does not exist in forced flows, but its value can be chosen to be equal to C_1, implying similar contributions from buoyant and gradient production on the scale and intensity of the turbulence. An improved form for C_3 proposed by Rodi [20] has also been used which considers C_3 as a function of the flux Richardson number. However, this introduces another constant which has been optimized by using experimental data for buoyant jets only. For the present calculations $C_3 \simeq C_1$ has been used.

Table 1 The constants used in the turbulence modeling

C_μ	C_1	C_2	C_3	σ_k	σ_ϵ	σ_T
0.09	1.44	1.92	1.44	1	1.3	1

Of the above constants, C_1, C_2, and C_3 are the more critical ones since they determine the balance between the influence of shear and buoyancy on the turbulent length scale. This balance can be different in forced and natural convection problems.

It should be noted that both the molecular viscosity and the laminar Prandtl number have been taken into account in the turbulent form of the equation. Thus the equations are valid throughout the laminar, semilaminar, and turbulent regions of the field [19]. This is also necessary because of the type of flow considered [7] and the range of Rayleigh number for which solution is obtained.

Nomenclature

C_μ, C_1, C_2, C_3 = empirical turbulence model constants
c_p = specific heat at constant pressure
D = cylinder diameter
g = gravitational acceleration
Gr = $8\rho^2 g\beta R^3(T_w - T_\infty)/\mu^2$
k = turbulent kinetic energy = $\overline{(1/2)(v_r'^2 + v_\theta'^2 + v_z'^2)}$
l = characteristic length scale of turbulence
Pr = Prandtl number
r = radial coordinate
R = radius of circular cylinder
Ra = Rayleigh number (Gr•Pr)
R_∞ = radius of pseudoboundary
T = temperature = $\bar{T} + T'$
T_W = wall temperature
T_∞ = ambient temperature
v_r = radial velocity component = $\bar{v}_r + v_r'$
v_θ = circumferential velocity component = $\bar{v}_\theta + v_\theta'$
v_z = velocity component in the axial direction = $0 + v_z'$

Greek Letters

β = thermal coefficient of volume expansion
ϵ = volumetric dissipation rate of turbulent kinetic energy
θ = circumferential (angle) coordinate
λ = thermal conductivity
μ = molecular viscosity
μ_t = turbulent viscosity
ρ = density
ψ = stream function
ω = vorticity
σ = turbulent Prandtl number

Boundary Conditions

A vertical symmetry plane exists along the center of the cylinder because of the uniform cylinder wall temperatures considered. The problem is thus solved only for the vertical half plane. The two boundary sections considered are the cylindrical wall and a pseudoboundary sufficiently far away from the cylinder.

The time-averaged stream function is constant along the wall as well as along the lines of symmetry. The stream function is set equal to zero on these two boundary sections. The time-averaged vorticity is an odd function about the symmetry lines and equals zero on the symmetry lines, where the angular derivatives of the temperature, the turbulent kinetic energy and its rate of dissipation are assumed to vanish.

An expression for the vorticity boundary conditions on the cylinder wall can be obtained by expanding the stream function near the wall, using a three-term Taylor series and making use of the continuity and the no-slip condition. Thus on the symmetry lines,

$$\psi^* = \omega^* = \frac{\partial T^*}{\partial \theta} = \frac{\partial k^*}{\partial \theta} = \frac{\partial \epsilon^*}{\partial \theta} = 0 \tag{8}$$

On the cylinder surface,

$$\psi^* = 0;\ \omega^* = \frac{-2\psi_p^*}{(\Delta r^*)^2};\ T^* = 1 \tag{9}$$

where ψ_p^* is the value of the stream function at a short distance Δr^* into the fluid.

The near wall region poses some special problems in the numerical computation of turbulent flows. Close to a wall the variations of the flow properties are so steep that a very fine grid is required in the region for accurate calculations. In order to predict the behavior of the flow near the wall, particularly in the viscous sublayer and in the regions downstream; i.e., towards the bottom of the cylinder where the flow is essentially laminar (for the range of Rayleigh numbers considered), the effects of nonisotropic dissipation (if the value of dissipation is set equal to zero at the wall) and molecular viscosity must be taken into account. The latter has been done by the inclusion of the molecular viscosity in the diffusive terms in all of the transport equations. The value of k^* is set equal to zero on the wall. However, the value of ϵ^* is difficult to assign on the walls because $\epsilon \sim k^{3/2}/l$ with k and l being both zero at the wall. The rate of dissipation of turbulent kinetic energy near the wall is fixed by the requirement that the length scale vary linearly with the distance from the wall. Thus on the cylinder surface

$$k^* = 0;\ \epsilon_p^* = \frac{C_\mu^{3/4}}{\kappa} \frac{k_p^{*3/2}}{\Delta r^*} \tag{10}$$

with the subscript p representing the nearest grid point from the wall, and κ is the Von Kármán constant having a value of 0.42. This has been used as the boundary conditions for ϵ^* near the wall and hence the ϵ^* equation is solved in a reduced area excluding the wall.

The necessity to limit the size of the solution domain requires that a pseudoboundary be defined in the far field. A concentric cylindrical pseudoboundary with a radius R_∞ is considered in the far field. Its size is determined such that variations in R_∞ had minimal effect on the flow field solutions. It is assumed that the velocity component in the circumferential direction, along the pseudoboundary is zero implying that in the far field, all flow must be in the radial direction if the domain is properly chosen, making the stream lines normal to the boundary. This boundary condition is an approximation and has been successfully used in predicting laminar natural convection [1, 3, 18]. It is expected that the small inaccuracies in this assumption will not have a major influence on the near-field solutions. Temperature of the fluid drawn into the flow field is the same as the ambient temperature. Turbulent kinetic energy and its rate of dissipation is again negligible for the fluid drawn in to the flow field. However, a generalization along the entire boundary cannot be made since the distributions of the temperature, turbulent kinetic energy, and its rate of dissipation along the section of the boundary where the plume crosses is not known a priori. It is assumed that the T^*, k^*, and ϵ^* gradients normal to the pseudoboundary are zero, indicating that convection is the dominant mode of transport for the above flow variables, i.e., along the pseudoboundary,

$$\frac{\partial \psi^*}{\partial r^*} = \frac{\partial \omega^*}{\partial r^*} = \frac{\partial T^*}{\partial r^*} = \frac{\partial k^*}{\partial r^*} = \frac{\partial \epsilon^*}{\partial r^*} = 0 \tag{11}$$

Solution Procedure

The five governing equations, (3-7), are transformed into finite difference equations by using a finite-difference method in polar coordinates introduced by Gosman et al. [22] and recently applied to a forced flow across tube bundles by Launder and Massey [23] and to natural convection flow by Farouk and Güçeri [1]. Instead of using standard Taylor series expansions, the finite difference equations are obtained by integrating the governing differential equations over arbitrarily small finite cells. A successive substitution technique is employed to solve the finite difference equations. The finite difference procedure adopts an "upwind difference" treatment of the convective terms and the difference equations are solved by a point iteration method.

A grid is established by dividing the region in the r and θ directions. A 41 × 51 grid is considered for the computations. Since the boundary layer tends to become very thin at the high Rayleigh numbers, the grid points have to be closely placed near the cylinder surface. This was ensured by successively reducing the node spacing in the r direction as the wall is approached. The node spacings are reduced by a factor of 2 after every eight divisions. The angular grid lines are spaced every 4.8 deg, except in the region of the plume where a 2.4 deg angular spacing is used.

Due to the relatively large variations of the source terms of k^* and ϵ^* equations during initial iterations, divergence was encountered. This was remedied by using underrelaxation [22].

The ratio of the outer radius to the cylinder radius was limited to 2 for the computations done. Even though for the range of Raleigh numbers considered a thin boundary layer forms close to the cylinder surface, the position of the outer boundary has an effect on the results if it is not set far enough from the surface of the cylinder. Further reduction of the ratio of the outer radius to the cylinder radius to 1.75 caused slight variations of the results in the far field, whereas heat-transfer predictions were essentially unchanged.

The computations were performed on a Burroughs B7700 digital computer. To obtain convergence about 400 interations are needed.

Results and Discussions

All results presented in this section are for air with $\mathrm{Pr} = 0.721$ in Rayleigh number range of 5×10^7 to 10^{10}. The rate of heat transfer, which is most important from a practical viewpoint, is compared with two empirical correlations, which are given as [8]

$$\mathrm{Nu}^{1/2} = 0.60 + 0.387 \left[\frac{\mathrm{Ra}}{[1 + (0.559/\mathrm{Pr})^{9/16}]^{16/9}} \right]^{1/6} \tag{12}$$

and [9]

$$\overline{Nu} = \frac{2}{\ln\left[1 + \frac{2}{\left[\left\{0.518Ra^{1/4}\left[1+\left(\frac{0.559}{Pr}\right)^{3/5}\right]^{-5/12}\right\}^{15} + (0.1\,Ra^{1/3})^{15}\right]^{1/15}}\right]} \quad (13)$$

in Fig. 1 through $\overline{Nu}$ versus Ra plots. Though there are several available correlating equations in the literature with substantial variations in predicting the average Nusselt number in this range of Rayleigh number, the present results fit the correlation of [9] most closely. Figure 2 displays the effect of the Rayleigh number on the angular distribution of the local Nusselt numbers for the isothermal cylinder. For $Ra = 10^8$, where the flow is essentially in the transition zone, the distribution of Nusselt number is found to be similar in shape to that obtained for laminar flows [1, 2] except for a slight hump close to the plume indicating the onset of turbulence. For higher Rayleigh numbers the effect of turbulence is more pronounced, thus causing higher average Nusselt numbers. The peak in the curves shifts to lower values of the angle θ with increasing Rayleigh numbers.

Time-averaged results for temperature, stream function, turbulent kinetic energy, and turbulent viscosity are shown in Figs. 3(*a*), 3(*b*), 4(*a*), and 4(*b*) for $Ra = 10^8$ and in Figs. 5(*a*), 5(*b*), 6(*a*), and 6(*b*) for $Ra = 10^9$. At these large Rayleigh numbers, a thin boundary layer forms around the cylinder which is in agreement with the Schlieren photographs presented by Hermann [3], where he refers to the layer as the "caustic curve". However, the development of the plume makes boundary-layer assumptions invalid and the full Navier-Stokes equations need to be considered. Examining the stream lines, it becomes evident that the majority of the flow approaches the cylinder from the side as opposed to the bottom. Similar behavior was also observed by other investigators [1, 2] even for laminar flow at high Rayleigh numbers. The radial temperature gradients are very high close to the wall, but at larger angles the turning of the flow greatly alters the temperature distribution. The thermal boundary layer thickness is essentially infinite at the center of the plume. The turbulent viscosity is maximum near $\theta \simeq 150$ deg, close to the wall for the range of Rayleigh number considered. Its value is about five times the molecular viscosity at $Ra = 10^8$, about twenty-two times at $Ra = 10^9$ and nearly 115 times at $Ra = 10^{10}$. The turbulent viscosity is also higher along the center of the plume as expected. Towards the bottom of the cylinder and at the far field (except the plume region), the turbulent viscosity becomes negligible in comparison with the molecular viscosity. As the Rayleigh number increases, the value of turbulence viscosity becomes higher as can be seen by observing Figs. 4 and 6. This is consistent with the observations made by Fraikin et al. [15]. The turbulent heat flux is modeled here as being proportional to the vertical temperature gradient. Thus, buoyancy causes dissipation and not production of turbulent kinetic energy in the bottom (upstream) region of the flow domain. Both buoyancy and shear contribute to the production of turbulence in the upper region close to the wall and the plume. This explains why turbulence becomes high at these regions.

The value of k^* is significant near the wall at large values of the angle θ and at the plume as is the case for μ_t^*. The contour plots of ϵ^* are not shown as the value of ϵ^* at any point can readily be found using equation (1).

Time-averaged angular velocity distributions at $Ra = 10^9$ are shown in Fig. 7. The angular velocity distributions for 30 deg $\leq \theta \leq$ 150 deg are similar to those obtained using boundary layer approximations to predict turbulent natural convection about a vertical flat plate [14]. However, for $\theta >$ 150 deg, the plume begins to form and the angular velocity drops to zero at 180 deg. Radial velocities are fairly small and uniform (not shown) around the cylinder but are considerably larger in the outer portion of the boundary layer where the flow is moving away from the cylinder. The angular velocity profiles near the wall also can be used in checking the sufficiency of the grid spacing near the wall. As an example, for $Ra = 10^9$ at $\theta \simeq 150$ deg, there are five points of the grid inside the maximum angular velocity and three points for $Ra = 10^{10}$. The grid used seems sufficient for the Rayleigh number range considered. A more refined grid is needed, however, for higher Rayleigh number predictions.

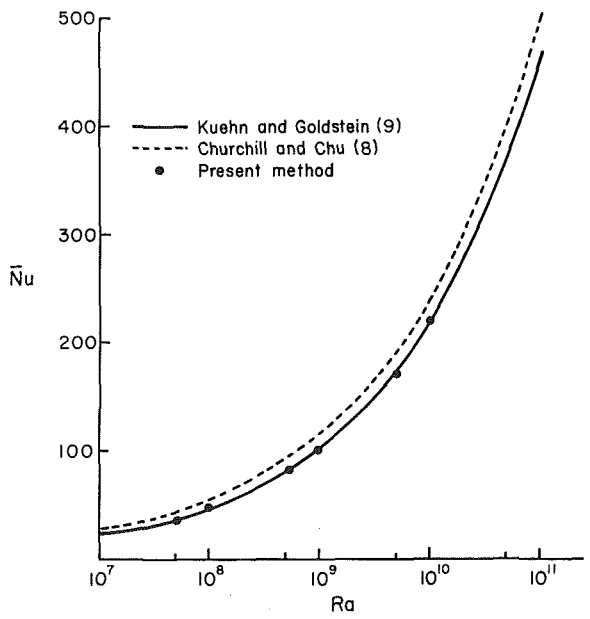

Fig. 1 Average Nusselt number as a function of Rayleigh number for an isothermal cylinder

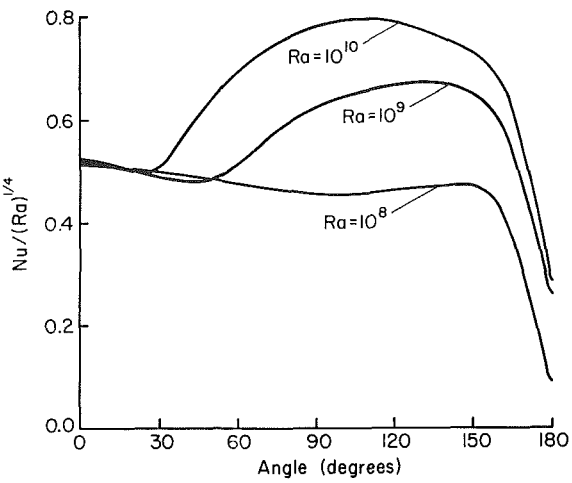

Fig. 2 Influence of Rayleigh number on local heat-transfer coefficients for an isothermal cylinder

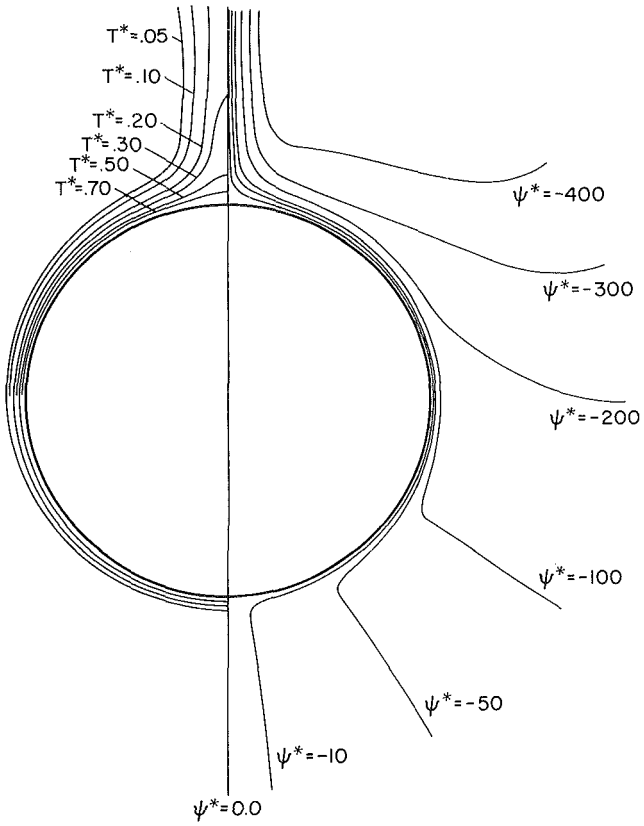

Fig. 3(*a*) Isotherms for turbulent natural convection, $Ra = 10^8$, $Pr = 0.721$

Fig. 3(*b*) Streamlines for turbulent natural convection, $Ra = 10^8$, $Pr = 0.721$

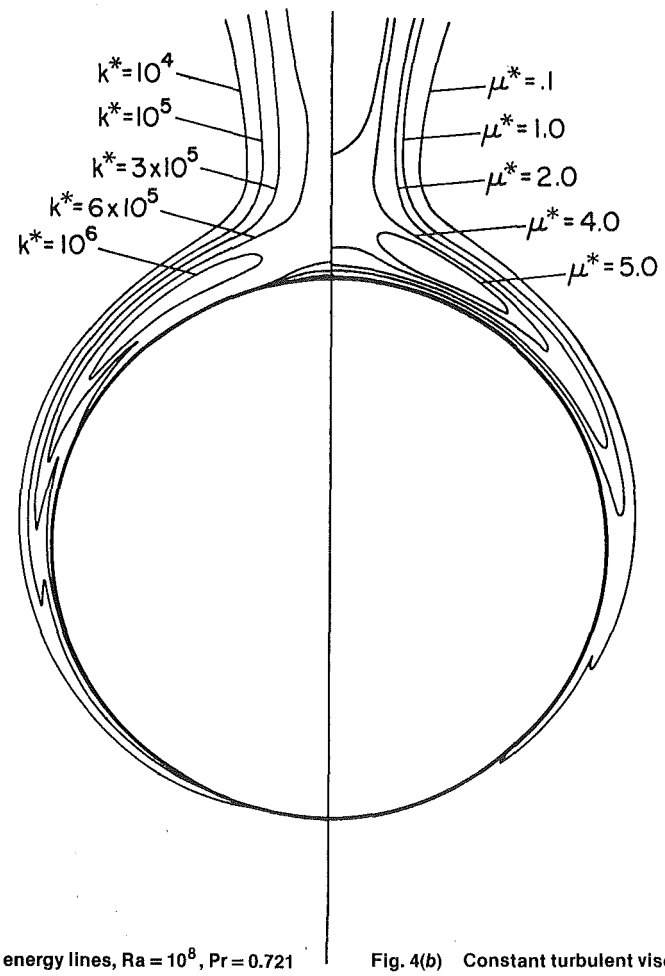

Fig. 4(*a*) Constant turbulent kinetic energy lines, $Ra = 10^8$, $Pr = 0.721$

Fig. 4(*b*) Constant turbulent viscosity lines, $Ra = 10^8$, $Pr = 0.721$

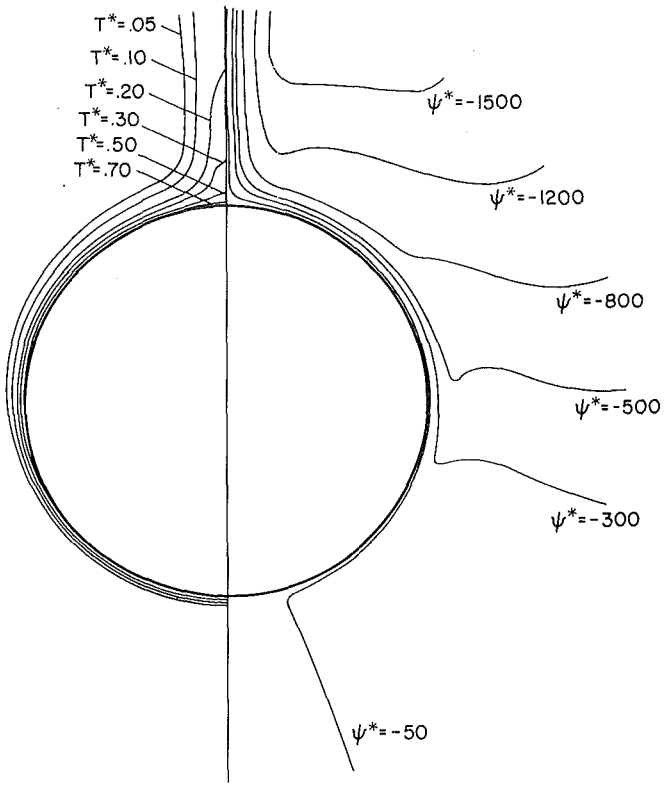

Fig. 5(*a*) Isotherm for turbulent natural convection, $Ra = 10^9$, $Pr = 0.721$

Fig. 5(*b*) Streamline for turbulent natural convection, $Ra = 10^9$, $Pr = 0.721$

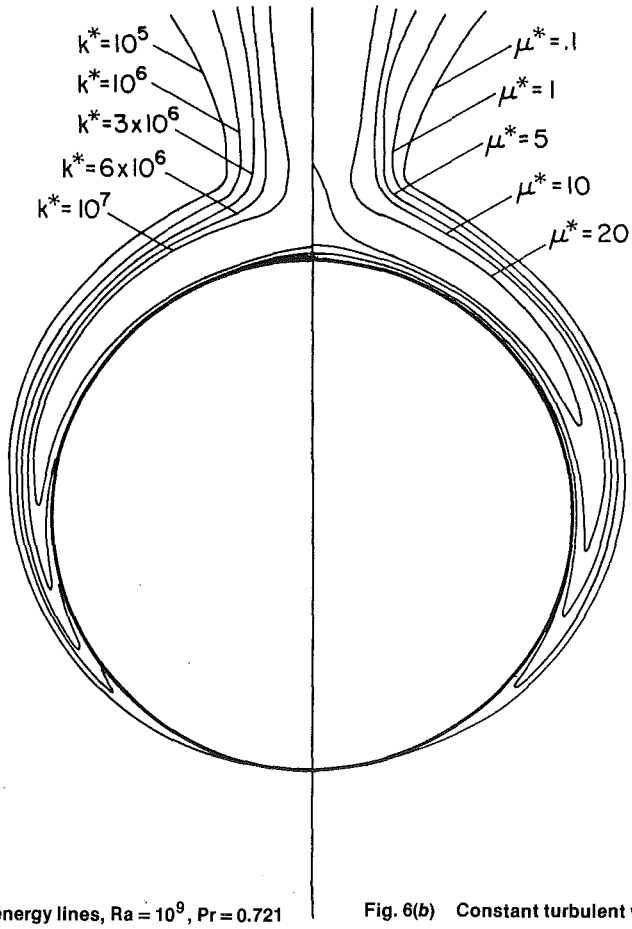

Fig. 6(*a*) Constant turbulent kinetic energy lines, $Ra = 10^9$, $Pr = 0.721$

Fig. 6(*b*) Constant turbulent viscosity lines, $Ra = 10^9$, $Pr = 0.721$

Table 2 Results of sensitivity study for C_3 at Ra = 10^8

C_3	$\bar{Nu}$	ψ^*_{min}	$\mu^*_{t_{max}}$	k^*_{max}	ϵ^*_{max}
1.44†	48.60	−500.1	5.40	1.26×10^6	4.19×10^{10}
C_3 + 20%	+1.9%	+2.8%	−5.92%	−3.93%	−3.84%
C_3 + 10%	+0.85%	+1.6%	−2.86%	−1.78%	−2.17%
C_3 − 10%	−1.5%	−0.64%	+4.1%	2.51%	+2.38%
C_3 − 20%	−2.89%	−1.53%	+5.4%	4.12%	+3.93%

† The reference value for C_3, i.e., $C_3 = C_1$

Turbulent kinetic energy profiles are shown in Fig. 8 for Ra = 10^9. No experimental or numerical data could be found for comparing the above results; however, qualitatively the agreement of these results with the vertical flat plate solutions [12-14] (except at the plume) is good. For the turbulent kinetic energy, no sharp peak was observed within the region where the angular velocity becomes maximum. The peak is found to occur further outward (excluding the plume). This is consistent with the results obtained by Plumb and Kennedy [14] for a vertical flat plate. An energy balance computation showed that the rate of net energy flow along the pseudoboundary was within 5 percent of the energy input from the cylinder to the fluid. Hence the truncation errors caused by the "up-wind" differencing were indeed small,

A sensitivity study was undertaken to determine the sensitivity of the results on the choice of C_3. Table 2 shows the effects of variations in C_3 on the mean Nusselt number, minimum stream function, maximum turbulent viscosity, maximum turbulent energy, and maximum dissipation rate. It is found that the variations on the heat transfer and streamline values are small but the effects on the turbulence quantities are higher; however, they are much smaller when compared to a similar sensitivity study for natural convection in the annulus between horizontal concentric cylinders [17], especially when $C_3 > C_1$. This result is expected as for the concentric cylinder case, at the top of the region the boundary layer becomes close to horizontal.

The shortcoming of this k-ϵ model is that it gives no information about the temperature fluctuations. The turbulent heat fluxes are obtained using the turbulent Prandtl number approach. An additional transport equation for $\bar{T}'^2$ can be used but this would again introduce additional empirical constants which need to be optimized by experimental data. For Rayleigh numbers greater than 10^{10} finer grids become necessary to describe the flow in the region inside the maximum angular velocity, increasing the computation time and storage. This can be avoided if appropriate wall functions are used. Wall function expressions developed for vorticity and temperature for forced flow problems [19] have so far yielded poor results when applied to the present problem.

The application of a $k-\epsilon$ turbulence model to the natural convection from an isothermal horizontal cylinder has been successfully demonstrated. An apparent advantage of the present method is that detailed information on the velocity and temperature fields along with a measurable turbulence quantity, the turbulent kinetic energy are obtained. The effects of the thermophysical properties of the fluid on the heat transfer and flow characteristics can be easily investigated at the turbulent regime. It is observed that measurements of local mean temperature, velocities, and turbulence quantities are needed to further validate the model.

Acknowledgements

The authors wish to thank Professor D. B. Spalding for his helpful suggestions. Support by the University of Delaware Computing Center is greatly appreciated.

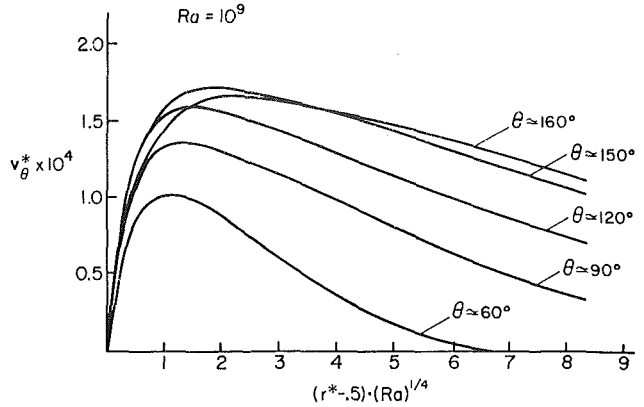

Fig. 7 Angular velocity profiles near cylinder surface, Ra = 10^9, Pr = 0.721.

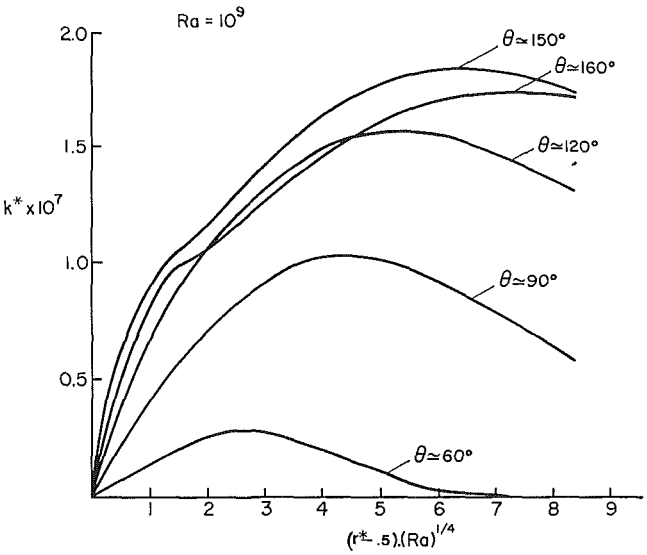

Fig. 8 Turbulent kinetic energy profiles near cylinder surface, Ra = 10^9, Pr = 0.721

References

1 Farouk, B. and Güçeri, S. İ., "Natural Convection from a Horizontal Cylinder-Laminar Regime," ASME JOURNAL OF HEAT TRANSFER, Vol. 103, 1981, pp. 522-527.

2 Kuehn, T. H. and Goldstein, R. J., "Numerical Solution to the Navier-Stokes Equations for Laminar Natural Convection about a Horizontal Isothermal Circular Cylinder," *International Journal of Heat and Mass Transfer*, Vol. 23, 1980, pp. 971-979.

3 Holster, J. L. and Hale, L. A., "Finite Element Simulation of Transient Free Convection from a Horizontal Cylinder," ASME Paper No. 79-HT-49.

4 Hermann, R., "Heat Transfer by Free Convection from Horizontal Cylinders in Diatomic Gases," NACA TM 1366, 1954.

5 McAdams, W. H., *Heat Transmission*, 3d. ed. McGraw-Hill, New York, 1954, pp. 165-183.

6 Kutateladze, S. S., *Fundamentals of Heat Transfer*, Academic Press, New York, 1963, p. 293.

7 Raithby, G. D. and Hollands, K. G. T., "A General Method of Obtaining Approximate Solutions to Laminar and Turbulent Free Convection Problems," *Advances in Heat Transfer*, Vol. 18, 1975, pp. 265-315.

8 Churchill, S. W. and Chu, H. H. S., "Correlating Equations for Laminar and Turbulent Free Convection from a Horizontal Cylinder," *International Journal of Heat and Mass Transfer*, Vol. 18, 1975, pp. 1049-1053.

9 Kuehn, T. H. and Goldstein, R. J., "Correlating Equations for Natural Convection Heat Transfer between Circular Cylinders," *International Journal of Heat and Mass Transfer*, Vol. 19, 1976, pp. 1127-1134.

10 Churchill, S. W. and Usagi, R., "A General Expression for the Correlation of Rates of Transfer and Other Phenomena," *AIChE J.*, Vol. 18, 1972, pp. 1121-1128.

11 Cebeci, T. and Khattab, A., "Prediction of Turbulent Free Convection

Heat Transfer from a Vertical Flat Plate," ASME JOURNAL OF HEAT TRANSFER, Vol. 97, 1975, pp. 469–471.

12 Mason, H. B. and Seban, R. A., "Numerical Predictions for Turbulent Free Convection from Vertical Surfaces," *International Journal of Heat and Mass Transfer*, Vol. 17, 1974, pp. 1239–1336.

13 Noto, K. and Matsumoto, R., "Turbulent Heat Transfer by Natural Convection Along an Isothermal Vertical Flat Surface," ASME JOURNAL OF HEAT TRANSFER, Vol. 97, pp. 621–624.

14 Plumb, O. A. and Kennedy, L. A., "Applications of a k-ϵ Turbulence Model to Natural Convection from a Vertical Isothermal Surface," ASME JOURNAL OF HEAT TRANSFER, Vol. 99, 1977, pp. 70–85.

15 Lin, S. J. and Churchill, S. W., "Turbulent Free Convection from a Vertical, Isothermal Plate," *Numerical Heat Transfer*, Vol. 1, 1978, pp. 129–145.

16 Fraikin, M. P., Portier, J. J., and Fraikin, C. J., "Application of a k-ϵ Turbulence Model to an Enclosed Buoyancy Driven Recirculating Flow," ASME Paper No. 80-HT-68, 1980.

17 Farouk, B. and Güçeri, S. İ., "Laminar and Turbulent Natural Convection in the Annulus Between Horizontal Concentric Cylinder," ASME-AIChE National Heat Transfer Conference, Aug. 1981.

18 Farouk, B., "Laminar and Turbulent Natural Convection Heat Transfer from Horizontal Cylinders," Ph.D. thesis, University of Delaware, 1981.

19 Launder, B. E. and Spalding, D. B., "The Numerical Computation of Turbulent Flows," *Computer Methods in Applied Mechanics and Engineering*, Vol. 3, 1974, pp. 269–289.

20 Rodi, W., "Influence of Buoyancy and Rotation on Equations for the Turbulent Length Scale," 2nd Symposium on Turbulent Shear Flows, Imperial College, London, 1979, pp. 10.37–10.42.

21 Spalding, D. B., "Turbulence Models (2nd Issue)," Heat Transfer Section Report, HT3/76/17, Imperial College, London, 1977.

22 Gosman, A. D., Pun, W. M., Runchal, A. K., Spalding, D. B., and Wolfshtein, M. W., "Heat and Mass Transfer in Recirculating Flows," Academic Press, London, 1969.

23 Launder, B. E. and Massey, T. H., "The Numerical Prediction of Viscous Flow and Heat Transfer in Tube Banks," ASME JOURNAL OF HEAT TRANSFER, Vol. 100, 1978, pp. 565–571.

An Experimental Investigation of Merging Buoyant Jets in a Crossflow

M. Gregoric
Research Engineer,
Institute Jozef Stefan,
Ljubljana, Yugoslavia

L. R. Davis
Professor.

D. J. Bushnell
Associate Professor.

Department of Mechanical Engineering,
Oregon State University,
Corvallis, Ore. 97331

Merging buoyant jets discharged in a crossflow were investigated experimentally using a unique visualization technique. Salt water jets were discharged from a constant head tank while being towed in an inverted position at desired rates through stagnant receiving water. Visualization of the jet cross section was produced by using fluorescent dye and a vertical slit light source. The results were photographed as a sequence of instantaneous cross sections taken by a motor-driven camera. Maximum heights, widths, and the vertical cross sections of the deflected jets were determined for different ratios of crossflow velocity to discharge velocity, number of discharge jets and discharge nozzle line orientation. Horseshoe shaped cross sections were observed in the cases of a single jet and multiple jets where the crossflow velocity was parallel to the line of discharge ports, but the horseshoe pattern was not clear when the cross flow was perpendicular to the line of multiple jets. The wake behind the multiple jets in the crossflow exhibited a distinct trailing vortex sheet.

Introduction

Jets have been the subject of investigation for many years with entire textbooks being written on the subject [1, 2, 3]. A concise state-of-the-art review of thermal plume modeling techiques is presented in [4]. Excellent reviews of single port discharges are found in [5] and [6]. An investigation of submerged multiport diffusers in shallow water is reported in [7]. Analytical models of multiport discharges in deep receiving water and the atmosphere are given in [8, 9]. Multiport buoyant discharge into a crossflow was investigated experimentally in [10], simulating an infinite line of ports. Data for a finite number of ports with buoyant discharges but having no ambient crosscurrents are reported in [11]. In the present investigation an effort was made to determine the characteristics of a finite number of buoyant jets discharging perpendicularly into a uniform crossflow. The influence of the number of discharge ports and the direction of the crossflow was also studied. Unusual visualization techniques were used to show the three-dimensional picture of the merging buoyant jets in a crossflow. The discharge jets were marked with fluorescent dye and illuminated by a thin plane light source as shown in Fig 1. The illuminated cross sections

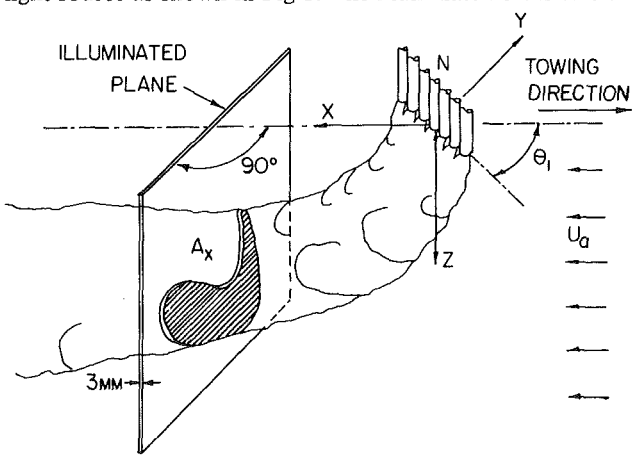

Fig. 1 Definition sketch showing coordinates and angle

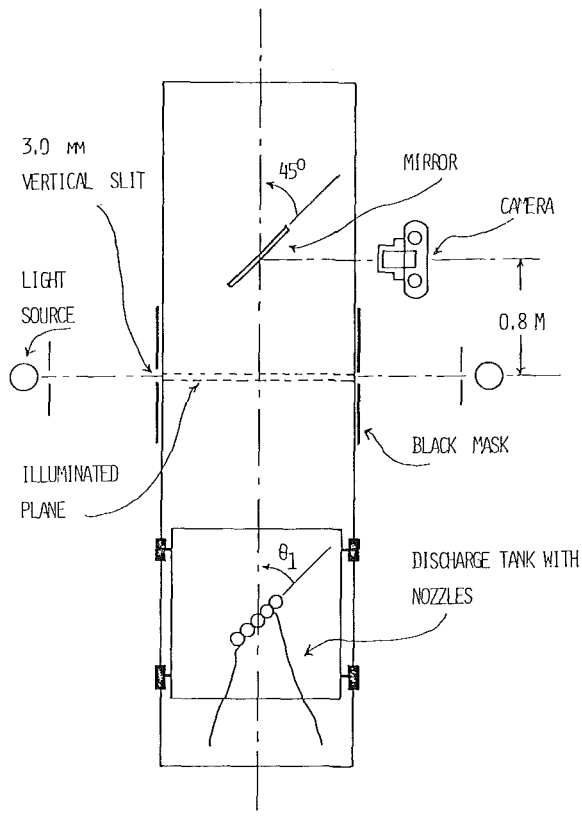

Fig. 2 Visualization and recording technique

were photographed in a timed sequence to provide a complete history of plume growth.

Reviews of different visualization techniques for use in gases and liquids can be found in [12, 13], and in [14, 15] for use in water only. Reference [16] presents abstracts of numerous applications of these techniques.

Experimental Procedure

The experiments were conducted in a towing channel 12.1 m long, 0.61 m wide and 0.91 m high (Fig. 2). A salt water discharge tank was towed on rails above the receiving channel by a cable and adjustable speed motor drive. The discharge

Contributed by the Heat Transfer Division and presented at the ASME Winter Annual Meeting, Chicago, Illinois, November 16–21, 1980. Manuscript received by the Heat Transfer Division January 27, 1981. Paper No. 80-WA/HT-23.

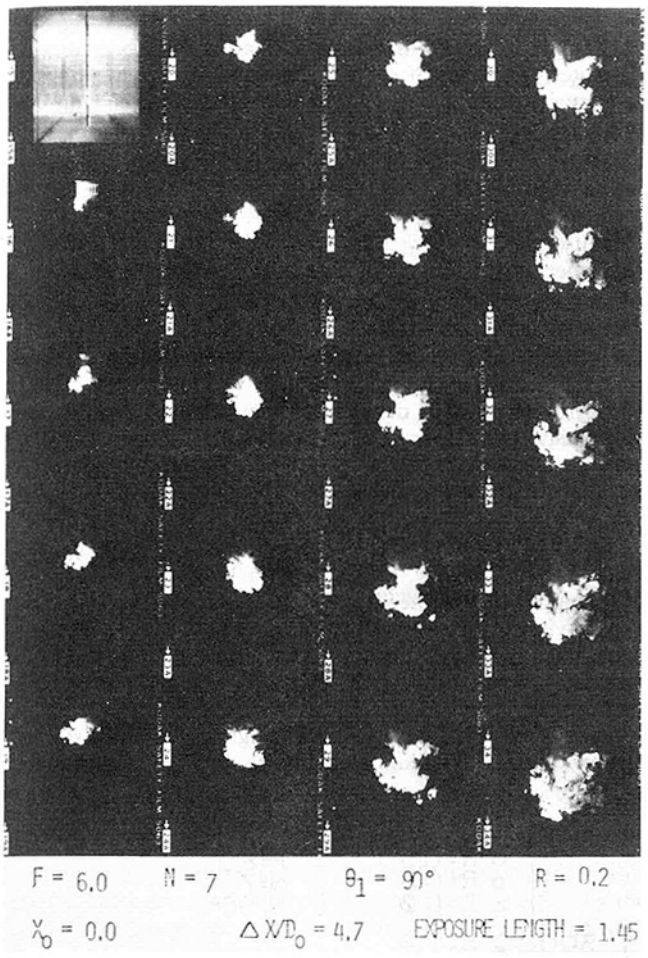

Fig. 3 Photograph sequence of illuminated cross sections: $N = 7$, $R = 0.2$, $\theta_1 = 90$ deg, distance between exposures = 4.7 dia

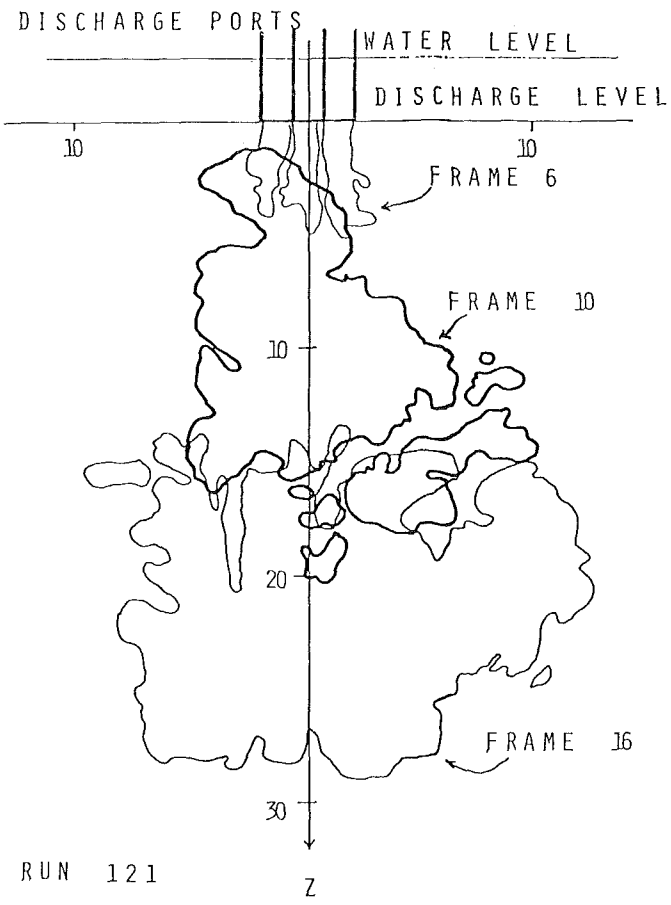

Fig. 4 Selected contours of cross sections: $N = 3$, $R = 0.2$, $\theta_1 = 90$ deg, and $F = 6$

tank was airtight except for breather tubes which maintained a constant velocity head regardless of the liquid level in the tank.

The salt water passed from this tank through a control valve into a plenum chamber with a buffer where it was evenly distributed to each of the discharge tubes. This arrangement was reported in [11]. In this investigation, tubes 9.53 mm i.d. and 12.7 mm o.d. were used. They were placed against each other in a row. This yielded a port spacing to discharge diameter, L/D, of 1.33. The number of discharge ports used were 7, 5, 3, 2 and 1. The length of the tubes was sufficiently long to produce a fully developed turbulent flow at the discharge point. The row of ports were oriented at 90, 45 and 0 deg with respect to the towing direction. The nominal Reynolds number and Froude number for all runs were Re = 2500 and $F = 6.0$. Salt water with a salinity of 30 ppt was used in all experiments.

On each side of the towing channel the walls were masked to form a vertical slit 3 mm wide. The bottom of the channel in the vicinity of the test cross section was blackened to prevent reflections. Light sources were placed on opposite sides of the channel (Fig. 2). The light beams were collimated by slits near each source thus reducing the beam width before reaching the channel slits. In this manner the parallel rays of light were used to form a 3 mm thick vertical illuminated plane in the water perpendicular to the channel walls and perpendicular to the direction of towing.

Salt water jets discharged from the tank were colored with fluorescein dye forming a light yellow-green visible plume. With the laboratory lights off, only the test cross section was illuminated. Clean water was used to fill the channel, so the illuminated section was invisible in the absence of dye. When

Nomenclature

N = number of discharge ports
A_x = area of jet(s) cross section perpendicular to x-axis
D_0 = port discharge diameter
F = densimetric Froude number at outlet, $U_0/(g' D_0)^{1/2}$
g = acceleration due to gravity
g' = reduced gravitational acceleration, $g\frac{\Delta\rho}{\rho_a}$
L = distance between ports
R = velocity ratio = U_a/U_0
S = salinity of the jet
t = time
U_0 = discharge velocity
U_a = crossflow velocity (ambient, towing)
W = plume width
X = rectilinear horizontal coordinate, downstream
Y = rectilinear horizontal coordinate
Z = rectilinear vertical coordinate (*pointed down in channel*)
ρ_a = density of ambient water (in the channel)
ρ_0 = density of discharging water
Δ_ρ = density difference = $\rho_0 - \rho_a$
θ_1 = angle between crossflow and port connection line

Subscripts

a = ambient
o = discharge

the plumes crossed the test section, the light rays were reflected by the dye and made visible. As the tank was towed with constant velocity, the image on this "screen" represented the cross sections of the buoyant jets in a crossflow for particular downstream locations, x/D_0.

To capture the image reflected in the illuminated test section, a vertical mirror was oriented at 45 deg to the symmetry line of the channel, such that the light coming from the image was reflected by 90 deg out through the unmasked portion of the channel to the camera. A camera with motor winder was used to record the sequence of images in the test cross section.

A typical sequence recorded on the film is shown in Fig. 3 for seven discharge ports placed 90 deg to the flow at a velocity ratio, $U_a/U_0 = 0.2$. The negatives were projected on graph paper with millimeter coordinates. A picture of a reference rod was taken in the channel at the beginning of each run and used to adjust the enlargement so that 5 mm on the graph paper equaled one discharge diameter. This scale was then used for data reduction from all frames and all films. The outline contours of each plume cross section were sketched on this graph paper as shown on Fig. 4. The average time between frames was calculated for each run. Using the known towing velocity, the distance between frames was calculated and a downstream distance X/D_0 was assigned to each frame.

The upper edge, Z_{max}, lower edge, Z_{min}, horizontal width, W/D_0, and areas were measured for each frame. Note that the upper edge, Z_{max}, is furthest from the discharge ports.

Results

The main objective of this investigation was to determine characteristic trends of merging buoyant jets when subjected to a crossflow. The independent variables and their nominal values considered in the experiments were:

Variable	Symbol	Nominal values
Number of ports	N	7, 5, 3, 2, 1
Velocity ratio	R	0.2, 0.5, 1.0
Angle between crossflow and line connecting the ports	θ_1	90, 45, 0 deg

The densimetric Froude number was 6.0 for all tests. Not all possible combinations of the above variables were tested. Those investigated in detail were grouped into three cases, with one parameter varying and two fixed. They were:

Case 1	Case 2	Case 3
$N = 7, \theta_1 = 90$ deg	$R = 0.2, \theta_1 = 90$ deg	$R = 0.2, N = 7$
$R = 0.2, 0.5, 1.0$	$N = 1, 2, 3, 5, 7$	$\theta_1 = 0, 45, 90$ deg

The upper edge of the visible plumes were always sharp and clearly visible, hence, easily traced. The lower edges were fuzzy in many cases due to several effects. First, the light reflected from it traveled through a nonhomogeneous medium due to dyed jets which were moving towards the mirror. These jets did not block the light path, but distorted the lower part of the illuminated image slightly. Secondly, the

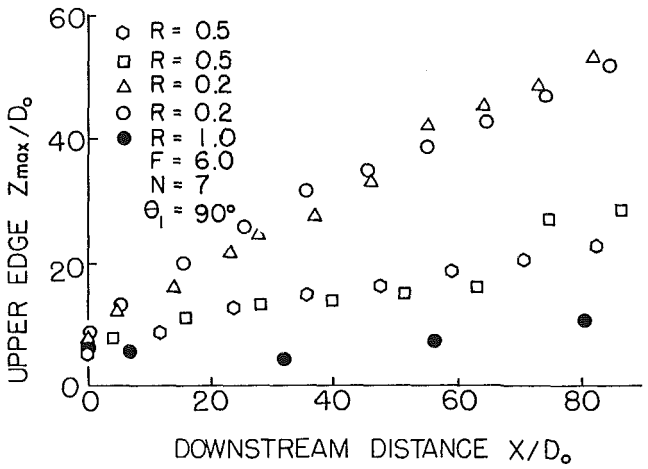

Fig. 5 Effect of R on upper edge trajectory: $N = 7, \theta_1 = 90$ deg, and $F = 6$

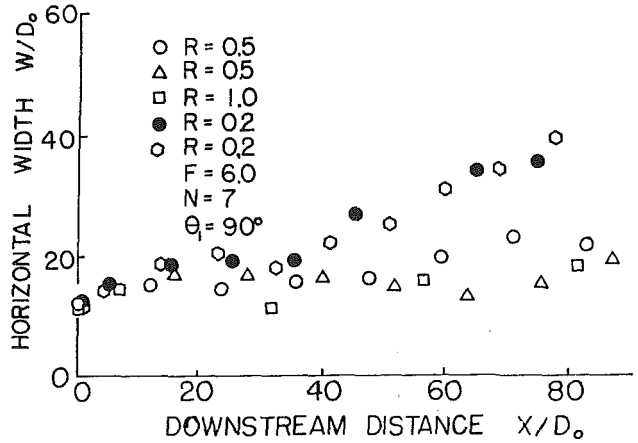

Fig. 6 Effect of R on horizontal width: $N = 7, \theta_1 = 90$ deg, and $F = 6$

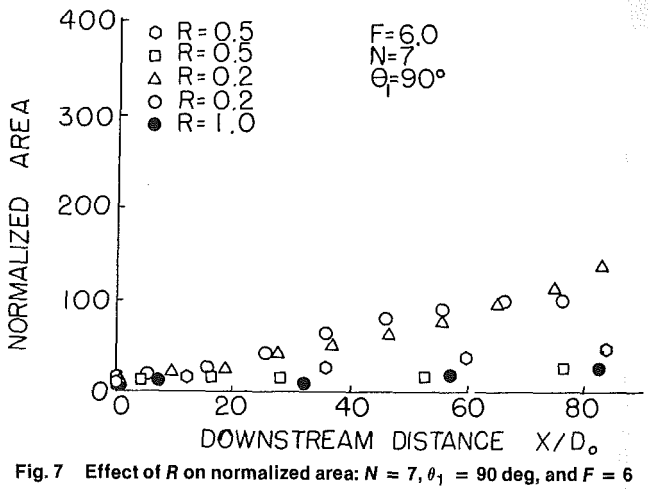

Fig. 7 Effect of R on normalized area: $N = 7, \theta_1 = 90$ deg, and $F = 6$

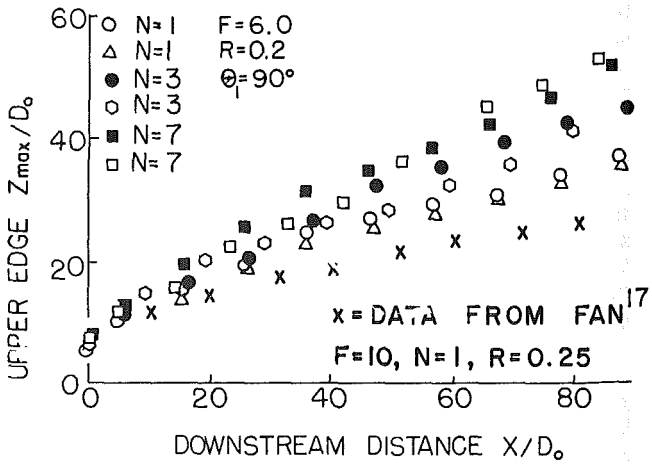

Fig. 8 Effect of number of ports, N, on upper edge trajectory: $R = 0.2$, $\theta_1 = 90$ deg, and $F = 6$

jets acted like a solid body in the flow, producing wake and vortex shedding effects behind the ports. The wake effects of the jets were clearly visible, and one could observe the vortex streets. Again, note should be made that lower means the position closer to the ports, and should not be confused by the fact that the pictures were taken in the channel with the vertical axis pointing downward.

Ambient Velocity Effects (case 1). The upper edge trajectories for case 1 runs are shown in Fig. 5 with $N = 7$, $\theta_1 = 90$ deg, and $L/D = 1.33$, with the jets discharged vertically into the crossflow. The plumes rose to between 5 and 8 dia, depending on the velocity ratio, R, then would deflect with the crossflow. Data points for two separate runs for each case are shown on this and several of the following figures to give an indication of scatter.

The horizontal widths W/D for case 1 runs are shown in Fig. 6. Width data were scattered much more than Z_{max} data. Although scattered, they show larger plumes for lower ambient current.

The normalized area $A_x/(N\pi D_0{}^2/4)$ shown in Fig. 7 for $N = 7$, $\theta_1 = 90$ deg, and $L/D = 1.33$ shows a nearly linear dependence between the area and downstream distance and an increased area with lower velocity ratio.

Effects of Number of Ports (case 2). The upper edge trajectories for a constant velocity ratio $R = 0.2$ and $\theta_1 = 90$ deg, and $L/D = 1.33$ with varying number of ports shows the discharge rapidly bending into a straight line for $N = 7$ and 5 as shown in Fig. 8. The trajectories bend over much more rapidly for a lower number of ports. The data points on Fig. 8 signified by an "X" were extracted from Fan [17] for $F = 10$, $R = 0.25$, and $N = 1$. The slightly lower trajectory is expected with higher values of F and R investigated in this study. The horizontal width W/D_0 showed little effect by the number of ports on plume spreading. The normalized area $A_x/(N\pi D_0{}^2/4)$, shown in Figs. 9 and 10 for case 2 runs, again shows a linear increase with downstream distance with much larger areas for $N = 1$, indicating higher entrainment rates.

The normalized cross-sectional area of a single jet grew from 1 at the port exit to $\simeq 400$ at $X/D_0 = 90$, compared to 130 for $N = 7$. Again, the values marked with an "X" were taken from Fan's data [17] for comparison assuming a circular cross section for $F = 10$, $R = 0.25$, and $N = 1$. If we can, in a first approximation, assume that velocities inside the jet at $X/D_0 = 90$ are only slightly different from ambient velocity and that concentrations inside the instantaneous cross section are uniform, the normalized area gives a measure of dilution.

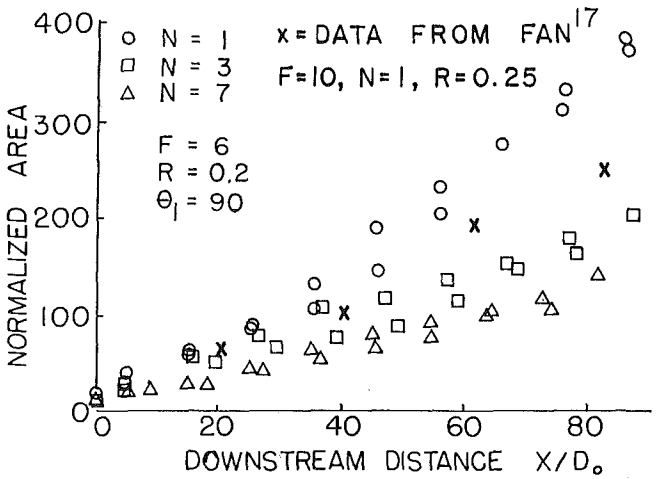

Fig. 9 Effect of N on normalized area: $R = 0.2$, $\theta_1 = 90$ deg, $F = 6$, and $N = 1,3,7$

Effect of Port Orientation (Case 3). The shape of the cross section changes dramatically for different angles of port orientation relative to ambient current. When $\theta_1 = 0$ deg (i.e., crossflow is parallel to nozzle line), a twin vortex structure is rapidly formed as shown in Fig. 11. When $\theta_1 = 45$ deg, the jets were rolled in space along the x-axis. When $\theta_1 = 90$ deg, neither of these effects dominated as seen in Fig. 3. A twin vortex was observed primarily at the lower towing velocities.

The upper edge trajectory (Fig. 12) is the highest for $\theta_1 = 0$ deg, where the jets cut through the ambient fluid. The lowest is for $\theta_1 = 45$ deg, where the jets are rolled. The normalized

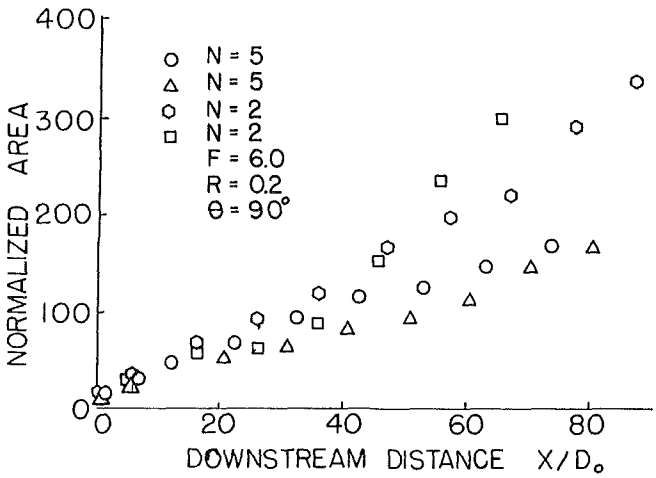

Fig. 10 Effect of N on normalized area: $R = 0.2$, $\theta_1 = 90$ deg, $F = 6$, and $N = 2,5$

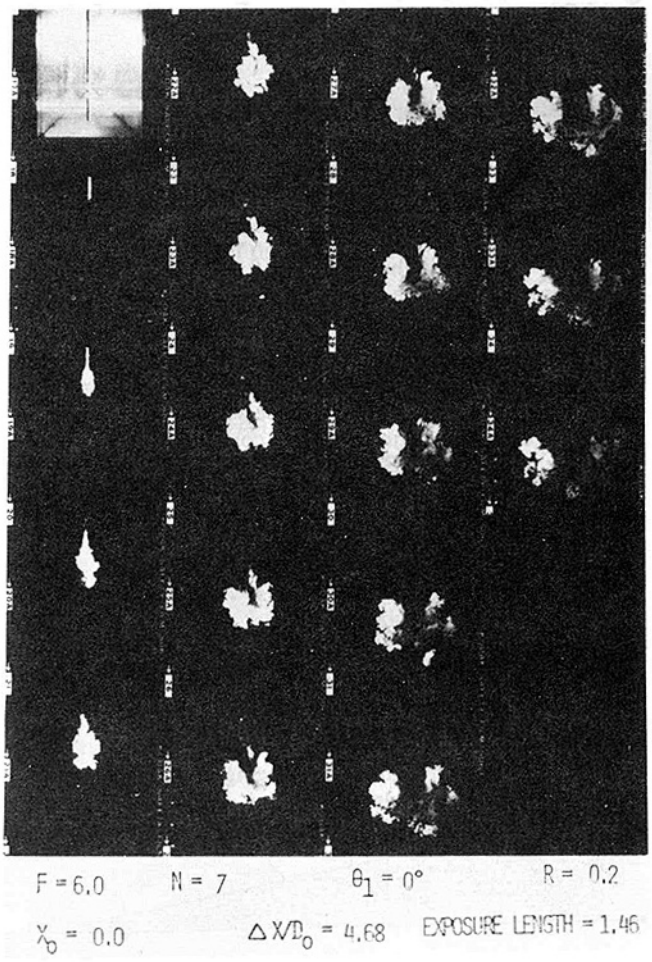

Fig. 11 Photograph sequence of illuminated cross sections: $R = 0.2$, $N = 7$, $\theta_1 = 0.0$, distance between exposures = 4.7 dia

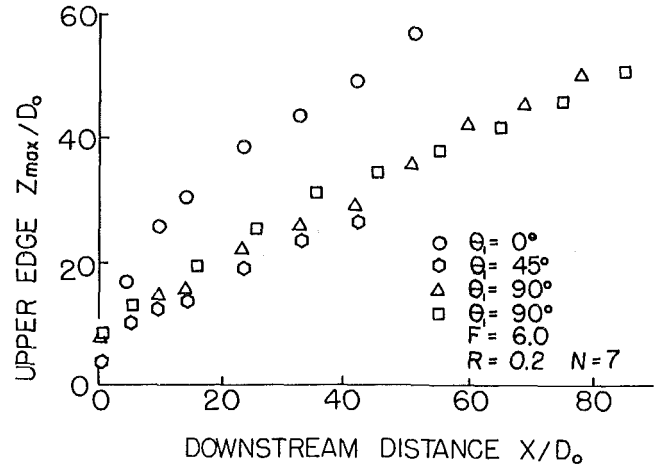

Fig. 12 Effect of discharge port connecting line orientation, θ_1, on upper edge trajectory: $N = 7$, $R = 0.2$, and $F = 6$

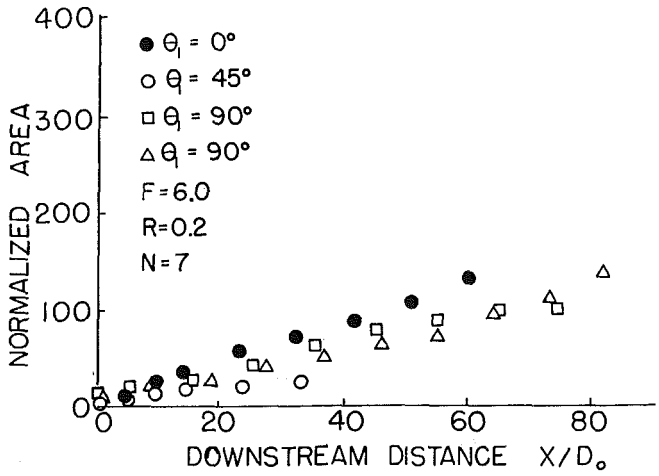

Fig. 13 Effect of discharge port connecting line orientation on normalized area: $N = 7$, $R = 0.2$, and $F = 6$

area (Fig. 13) is the highest for $\theta_1 = 0$ deg, where entrainment is increased by the large vortex pairs and smallest for $\theta_1 = 45$ deg, where the plume is rolled.

Correlation of Data. An attempt was made to correlate the data into empirical dimensionless expressions. It was found that the rolling action that took place with $\theta_1 = 45$ deg caused trends in area and trajectory that could not be correlated. However, good correlations were obtained for trajectory and normalized area for $\theta_1 = 90$ deg. The expression for trajectory is:

$$Z/D_0 = 0.78\,R^{-.93}N^{.17}(X/D_0)^{.52}$$

The expression for normalized area is:

$$A/A_0 = 1.49\,R^{-.71}N^{-.55}X/D_0 + 1$$

These expressions are valid in the range of R from 0.2 to 1.0, N from 1 to 7, and X/D_0 from 0 to 100.

Conclusions

This investigation dealt with merging buoyant jets from a finite number of ports placed in a line, subject to a crossflow from different angles. The visualization technique used was somewhat unusual. A plane light beam and motor-driven camera produced a three-dimensional picture composed of vertical cross sections through the plume in equal intervals downstream. The picture gave the size and position of the instantaneous cross section which was averaged slightly by the finite dimension of the plane light beam and exposure length of the illuminated portion of the plume for a particular ambient velocity. Experimental parameters were chosen so that the effects of the velocity ratio, R, number of ports, N, and angle of crossflow with respect to the nozzle line, θ_1, were investigated.

Correlations for normalized area and trajectory were obtained which showed a strong dependence on velocity ratio. At fixed N and θ_1, upper edge trajectories, plume widths, and normalized areas appeared to increase linearly (from $W = 10$ D on). The normalized areas were larger at lower velocity ratios.

The effect of variable N on trajectory was minor. However, the rate of increase of the normalized area reduced rapidly with increasing N, showing reduced entrainment when two or more jets compete for the same fluid.

With varying θ_1 and fixed N and R, the orientation of the nozzles θ_1 changed the shape of the cross section drastically. At $\theta_1 = 0$ deg, the vortex pair was very strong and aided entrainment of ambient fluid, so the normalized area was the highest. At $\theta = 45$ deg, the jets are rolled in space like a band, and at 90 deg, a vortex pair was formed similar to the single port discharge.

References

1 Pai, S. I., *Fluid Dynamics of Jets*, D. Van Nostrand Co., 1954.

2 Abramovich, G. N., *The Theory of Turbulent Jets*, M.I.T. Press, (translation), Cambridge, Mass., 1963.

3 Rajaratnam, N., *Turbulent Jets*, Elsevier, 1976.

4 Davis, L. R. and Shirazi, M. A., "A Review of Thermal Plume Modeling," Keynote address, *Proceedings of the Sixth International Heat Transfer Conference*, Toronto, Canada, Aug. 1978.

5 Hirst, E. A., "Analysis of Round, Turbulent, Buoyant Jets Discharged to Flowing Stratified Ambients," Oak Ridge National Laboratory, Report ORNL 4685, June 1971.

6 Wright, S. J., "Effects of Ambient Crossflow and Density Stratification on the Characteristics Behavior of Round Turbulent Buoyant Jets," Ph.D. thesis, California Institute of Technology, Pasadena, Calif., 1977.

7 Jirka, G. and Harleman, D. R. F., "The Mechanics of Submerged Multiport Diffusers for Buoyant Discharges in Shallow Water," M.I.T., R. M. Parsons Lab., Report 167, Mar., 1973.

8 Kannberg, L. D. and Davis, L. R., "An Analysis of Deep Submerged Multiple Port Buoyant Discharges," ASME JOURNAL OF HEAT TRANSFER, Vol. 99, Nov. 1977, pp. 698-655.

9 MacDuff, R. B. and Davis, L. R., "Multiple Cell Mechanical Draft Cooling Tower Model," in ASME Symposium Volume *Environmental Effects of Atmosphere Heat/Moisture Releases*, Palo Alto, Calif., May, 1978.

10 Kannberg, L. D., "An Experimental and Analytical Investigation of Deep Submerged Multiple Buoyant Jets," Ph.D. thesis, Oregon State University, Corvallis, Ore., 1976.

11 Davis, L. R., Shirazi, M. A., and Slegel, D. L., "Experimental Simulation of Single and Multiple Cell Cooling Tower Plumes," Corvallis Environmental Research Laboratory, USEPA, Corvallis, Ore., 1976.

12 Bradshaw, P., *Experimental Fluid Mechanics*, Pergamon Press, 2d ed., 1970.

13 Merzkirch, W., *Flow Visualization*, Academic Press, 1974.

14 Werle, H., "Hydrodynamic Flow Visualization," *Annual Review in Fluid Mechanics*, 1973, pp. 361-382.

15 Clayton, B. R., and Massey, B. S., "Flow Visualization in Water: A Review of Techniques," *J. Sci. Instr.*, Vol. 44, 1967, p. 211.

16 Benedict, B. A., Anderson, J. L., and Yandell, E. L., Jr., "Analytical Modeling of Thermal Discharges: A Review of the State-of-the-Art," Argonne National Laboratories, ANL/ES18. Apr. 1974.

17 Fan, L. N., "Turbulent Buoyant Jets into Stratified or Flowing Ambient Fluids," W. M. Keck Laboratory of Hydraulics and Water Resources, California Institute of Technology, Report No. KH-15, June 1967.

Natural Convection in an Attic-Shaped Space Filled With Porous Material

A. Bejan
Assoc. Mem.

D. Poulikakos

Department of Mechanical Engineering,
University of Colorado,
Boulder, Colo. 80309

This article reports an analytical study of natural convection in a wedge-shaped horizontal space filled with a fluid-saturated porous medium. The study focuses on the detrimental effect of natural convection on the insulation value of an attic-shaped porous layer in "winter" conditions (cold roof, warm ceiling). The study reveals the most basic features of the temperature field and flow pattern established in the porous layer. The study addresses two distinct flow regimes: (a) the shallow attic limit ($H/L \to 0$, Ra_H = finite, but fixed) and (b) the boundary layer regime which consists of a boundary layer driven by the sloped (roof) wall plus a core flow moving slowly along the horizontal (ceiling) wall. Heat-transfer results are developed for both flow regimes.

Introduction

The objective of this article is to document the phenomenon of natural convection heat transfer through a fluid-saturated porous medium which occupies an attic- or wedge-shaped space. The "attic" geometry is a generic description for all horizontal porous layers whose upper and lower surfaces are not parallel. Porous layers with perfectly parallel horizontal surfaces have been studied extensively during the past thirty years; as summarized by Cheng [1], the horizontal constant-thickness layer is of fundamental interest in geophysical fluid mechanics, geothermal energy extraction, grain storage, and thermal insulation engineering. The attic or wedge geometry is equally important in all these applications, yet, this geometry remains to be investigated.

The engineering focus of the present study is on the thermal insulation capability of the attic-shaped porous layer. Thus, for a physically more meaningful presentaton, we discuss the phenomenon of natural circulation in the context of an attic filled with porous insulation. In the steady state we identify two basic sets of temperature boundary conditions: (*a*) summer (warm top, cold bottom), when the fluid saturating the porous material is stably stratified, and (*b*) winter (cold top, warm bottom), when the steady circulation of fluid is possible. The present study focuses on the "winter" temperature conditions, and seeks to establish the damaging effect posed by fluid circulation on the thermal insulation potential of the porous layer.

In winter conditions the attic space is heated from below and may experience a thermal instability of the Bénard type [2]. The present study focuses on cases where the porous layer height is small enough so that the thermal instability is inhibited.

Mathematical Formulation

Consider the two-dimensional shallow layer geometry shown in Fig. 1. The two surfaces which are active, i.e., which fuel the circulation of fluid through the cavity, are at different temperatures (T_C, T_H) and form an angle ϵ. In accordance with the "winter attic" description, the warm surface (T_H) was chosen as horizontal; however, since the angle ϵ is small, the heat-transfer results developed in this study apply just as well to the case when the cold surface is horizontal and the warm surface is of slope $-\epsilon$.

The equations governing the steady-state conservation of mass, momentum, and energy at every point in the porous medium are

$$\frac{\partial u_*}{\partial x_*} + \frac{\partial v_*}{\partial y_*} = 0 \tag{1}$$

$$u_* = -\frac{K}{\mu}\frac{\partial P_*}{\partial x_*} \tag{2}$$

$$v_* = -\frac{K}{\mu}\left(\frac{\partial P_*}{\partial y_*} + \rho g\right) \tag{3}$$

$$u_*\frac{\partial T_*}{\partial x_*} + v_*\frac{\partial T_*}{\partial y_*} = \alpha\left(\frac{\partial^2 T_*}{\partial x_*^2} + \frac{\partial^2 T_*}{\partial y_*^2}\right) \tag{4}$$

where u_*, v_*, x_*, y_*, P_*, T_*, are the fluid velocity components, the coordinates of each point, the fluid pressure, and temperature, respectively. Equations (1-4) are based on the "homogeneous porous medium model" [2], in which the fluid is regarded as in thermal equilibrium with the solid porous matrix. Properties μ, ρ, α, and K represent the fluid viscosity, fluid density, aggregate thermal diffusivity based on the thermal conductivity of the fluid/porous matrix composite (k) divided by the "ρc_p" of the fluid, and, finally, the permeability of the porous medium. For moderate temperature differences, as encountered in air-saturated porous insulations and in grain storage facilities, the Boussinesq approximation is appropriate,

$$\rho \cong \rho_0[1 - \beta(T - T_0)] \tag{5}$$

Combining this statement with equations (2, 3), and eliminating the pressure P_*, we obtain a single equation for momentum conservation,

$$\frac{\partial u_*}{\partial y_*} - \frac{\partial v_*}{\partial x_*} = -\frac{Kg\beta}{\nu}\frac{\partial T_*}{\partial x_*} \tag{6}$$

In what follows we rely on equations (1), (4), and (6) to determine analytically the flow pattern and the temperature field inside the attic-shaped cavity. Two distinct regimes of

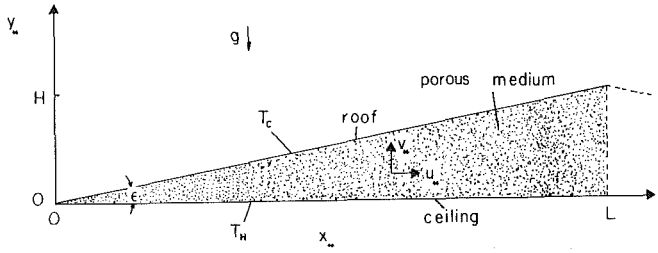

Fig. 1 Schematic of a shallow attic space filled with fluid-saturated porous material

Contributed by the Heat Transfer Division for publication in the JOURNAL OF HEAT TRANSFER. Manuscript received by the Heat Transfer Division September 29, 1981.

operation are investigated: (*a*) the shallow layer limit, and (*b*) the boundary layer regime.

The Shallow Layer Limit

The basic features of the buoyancy-driven circulation can be illustrated by considering the small angle limit ($\epsilon = H/L \to 0$). In this limit, the problem formulated in the preceding section lends itself to a perturbation solution of the type developed by Walker and Homsy [3] for shallow constant-thickness layers heated in the horizontal direction. We note that $0(x_*) = L$ and $0(y_*) = H$, hence, from equation (6), $0(u_*) = \mathrm{E}Kg\beta\Delta T/\nu$, where $\Delta T = T_H - T_C$. Based on this observation, we define the following dimensionless variables

$$x = x_*/L, \quad y = y_*/H,$$

$$\Psi = \frac{\Psi_*}{Kg\beta\Delta TH^2/(\nu L)}, \quad T = \frac{T - T_C}{T_H - T_C} \tag{7}$$

the streamfunction, Ψ_*, being defined in the usual manner by writing $u_* = \partial\Psi_*/\partial y_*$, $v_* = -\partial\Psi_*/\partial x_*$. The dimensionless form of the governing equations is

$$\frac{\partial^2\Psi}{\partial y^2} + \epsilon^2\frac{\partial^2\Psi}{\partial x^2} = -\frac{\partial T}{\partial x} \tag{8}$$

$$\epsilon^2\mathrm{Ra}_H\left(\frac{\partial\Psi}{\partial y}\frac{\partial T}{\partial x} - \frac{\partial\Psi}{\partial x}\frac{\partial T}{\partial y}\right) = \epsilon^2\frac{\partial^2 T}{\partial x^2} + \frac{\partial^2 T}{\partial y^2} \tag{9}$$

where Ra_H is the Rayleigh number based on the maximum vertical dimension of the porous layer,

$$\mathrm{Ra}_H = \frac{Kg\beta\Delta TH}{\alpha\nu} \tag{10}$$

We note that the small parameter appears as ϵ^2 in equations (8, 9), hence, we seek solutions of type

$$\begin{aligned}\Psi(x,y) &= \Psi_0(x,y) + \epsilon^2\Psi_2(x,y) + \epsilon^4\Psi_4(x,y) + \ldots.\\ T(x,y) &= T_0(x,y) + \epsilon^2 T_2(x,y) + \epsilon^4 T_4(x,y) + \ldots.\end{aligned} \tag{11}$$

which satisfy the "isothermal and impermeable walls" conditions

$$T = 1 \quad \text{and} \quad \Psi = 0 \quad \text{at } y = 0$$

$$T = 0 \quad \text{and} \quad \Psi = 0 \quad \text{at } y = f(x) \tag{12}$$

The governing equations (8, 9) and the series solution (11) illustrate the meaning of the shallow layer limit discussed here: the small angle ϵ tends to zero, however, the Rayleigh number is arbitrary and *fixed*.

If, as in Fig. 1, the upper wall (the roof) is flat, then the roof shape function has the simple form

$$f(x) = x \tag{13}$$

It is shown later in this section that the roof shape influences the circulation pattern in the shallow layer.

The successive terms in the series solution (11) are derived systematically by combining expressions (11) with equations (8, 9, 12). For brevity, and since the analytical procedure is described in detail in references [3, 4], we list the final expressions obtained for the $0(\epsilon^0)$, $0(\epsilon^2)$ and $0(\epsilon^4)$ terms:

$$\Psi_0 = \frac{1}{6}\left(y - \frac{y^3}{x^2}\right), \quad T_0 = 1 - \frac{y}{x} \tag{14}$$

$$\begin{aligned}\Psi_2 &= -\frac{1}{18}\left(y - \frac{y^3}{x^2}\right) - \frac{\mathrm{Ra}_H}{2520}\left(5xy - 7\frac{y^5}{x^3} + 2\frac{y^7}{x^5}\right)\\ T_2 &= \frac{1}{3}\left(\frac{y}{x} - \frac{y^3}{x^3}\right) - \frac{\mathrm{Ra}_H}{360}\left(7y - 10\frac{y^3}{x^2} + 3\frac{y^5}{x^4}\right)\end{aligned} \tag{15a}$$

$$\begin{aligned}\Psi_4 &= \frac{-y}{189} - \frac{4y}{45x^2} - \frac{2y^3}{135x^2} - \frac{y^5}{30x^4} + \frac{y^7}{42x^6}\\ &\quad + \mathrm{Ra}_H\left(\frac{xy}{2160} - \frac{y^5}{540x^3} + \frac{y^7}{945x^5} + \frac{y^9}{3024x^7}\right)\\ &\quad - \frac{\mathrm{Ra}_H^2}{360}\left(0.0247x^2y + 0.0358y^3\right.\\ &\quad \left. + \frac{y^5}{84x^2} + \frac{y^7}{280x^4} - \frac{5y^9}{864x^6} + \frac{y^{11}}{720x^8}\right)\\ T_4 &= \frac{4y}{45x} - \frac{y^3}{9x^3} + \frac{y^5}{5x^5} + \mathrm{Ra}_H\left(-\frac{y}{1080} - \frac{y^3}{54x^2} + \frac{7y^5}{360x^4}\right)\\ &\quad - \frac{\mathrm{Ra}_H^2}{360}\left(-0.215xy + \frac{5y^3}{21x} + \frac{y^5}{20x^3} - \frac{2y^7}{21x^5} + \frac{11y^9}{504x^7}\right)\end{aligned} \tag{15b}$$

Figure 2(*a*) shows the patterns of streamlines and isotherms corresponding to the $0(\epsilon^0)$ solution. The slight tilt in the isotherms gives rise in counter-clockwise motion with a time scale of order $L/u_* \sim (L^2/\alpha)/\mathrm{Ra}_H$. The $0(\epsilon^2)$ terms of this limiting solution are shown plotted in Fig. 2(*b*) as stream

Nomenclature

B = auxiliary parameter, equation (38)
c_p = fluid specific heat at constant pressure
f = roof shape, equation (12)
g = gravitational acceleration
H = vertical dimension
k = thermal conductivity of fluid/porous matrix combination
K = permeability
L = horizontal dimension
Nu = Nusselt number, equation (18)
P = pressure
Q = net heat-transfer rate [W/m]
Ra_H = Rayleigh number based on H, equation (10)
Ra_L = Rayleigh number based on L, equation (26)
T = temperature
T_C = roof temperature (cold)
T_H = ceiling temperature (hot)
ΔT = temperature difference, $T_H - T_C$
T_∞ = core temperature
u = longitudinal velocity
U = core velocity
v = transversal velocity
x = longitudinal coordinate
y = transversal coordinate
α = thermal diffusivity, $k/(\rho c_p)$
β = coefficient of thermal expansion
δ = boundary layer thickness, equation (25)
ϵ = small angle (Figs. 1, 4)
λ = top solution parameter
μ = bottom solution parameter (except in equations (2) and(3) where μ = viscosity)
ν = kinematic viscosity
ρ = fluid density
ψ = stream function

Subscripts

$*$ = dimensional quantity
1 = pertaining to the top solution (Fig. 4)
2 = pertaining to the bottom solution (Fig. 4)

function and temperature profiles at $x = 1$. Unlike in the case of infinitely shallow layers heated in the horizontal direction [3], the $0(\epsilon^2)$ correction (ψ_2, T_2) is not proportional to the Rayleigh number Ra_H.

While examining the streamline pattern of Fig. 2(*a*), it is important to keep in mind that this pattern exists only in the limit $\epsilon \to 0$ and that, for the sake of clarity only, the graph shows an exaggerated angle. Not visible on this graph is the end-turn region which is infinitely thin (of order ϵ). The right end region serves to turn the flow by 180 deg and, assuming that the $x_* = L$ plane is adiabatic, has no effect on either the intensity of the counterclockwise cell or on the energy convected by it. Note that equations (14) describe the flow and temperature *only* in the wedge region (where the assumed scale (7) apply, i.e., not in the $x_* = L$ end region).

The pattern in a symmetric (A-shaped) space consists of piecing together end-to-end, two shallow patterns of the type shown in Fig. 2(*a*). Thus, the symmetric attic has two identical cells (the left counterclockwise and the right clockwise) which merge in the middle to form a localized (narrow) updraft right under the peak of the roof. If the roof changes slope from ϵ to $-\epsilon$ *smoothly* (not abruptly, as in an A-shaped space), then the updraft is no longer localized but distributed over a middle region which scales with L. To see this, consider the circulation under a smooth roof, for example

$$f = \sin\left(\frac{\pi}{2}x\right) \tag{16}$$

The corresponding limiting forms of Ψ and T are

$$\Psi_0 = \frac{\pi}{12}\cos\left(\frac{\pi}{2}x\right)\left[y - \frac{y^3}{\sin^2\left(\frac{\pi}{2}x\right)}\right]$$

$$T_0 = 1 - \frac{y}{\sin\left(\frac{\pi}{2}x\right)} \tag{17}$$

Figure 3 shows the cellular flow pattern and the fact that the end-turn regions now occupy half of the attic length. Asymptotic solutions of type (11) can be constructed in the same manner for other roof shapes, $f(x)$.

Regarding the net heat transfer between the two walls, the isotherms of Fig. 2(*a*) indicate that conduction is the dominant mechanism. There is, however, an incipient convective effect which can be calculated from the heat flux along either surface. First, we define the Nusselt number as

$$\mathrm{Nu} = \frac{Q}{kL\Delta T/H} \tag{18}$$

where Q is the overall heat-transfer rate,

$$Q = -\int_0^L k\left(\frac{\partial T_*}{\partial y_*}\right)_{y_*=0} dx_*. \tag{19}$$

combining this definition with expressions (14, 15) for temperature, yields

$$\mathrm{Nu} = \left(1 - \frac{\epsilon^2}{3} + \frac{4\epsilon^4}{45} - \ldots\right)\int_{0^+}^{1}\frac{dx}{x} + \frac{7}{360}\epsilon^2\mathrm{Ra}_H + \frac{\epsilon^4\mathrm{Ra}_H}{1080}\left(1 - \frac{541}{1680}\mathrm{Ra}_H\right) + \ldots \tag{20a}$$

Note that the first term on the right-hand side is the contribution due to pure conduction between floor and ceiling; this term blows up if the two surfaces (T_H, T_C) indeed made direct contact at the tip ($x = 0$). Realistically, the walls near the tip of a very shallow porous wedge will reach an average temperature, between T_H and T_C; hence, the tip region will not contribute to Q. If the length of this inert tip region is l, then the heat-transfer rate is finite in the pure conduction limit,

$$\mathrm{Nu} = \left(1 - \frac{\epsilon^2}{3} + \frac{4\epsilon^4}{45} - \ldots\right)ln\frac{L}{l} + \frac{7}{360}\epsilon^2\mathrm{Ra}_H + \frac{\epsilon^4\mathrm{Ra}_H}{1080}\left(1 - \frac{541}{1680}\mathrm{Ra}_H\right) + \ldots \tag{20b}$$

We learn that the first convective contribution to the heat-transfer rate scales with the group $\epsilon^2\mathrm{Ra}_H$, exactly the same way as in the case of shallow constant-thickness layers heated in the horizontal direction [3].

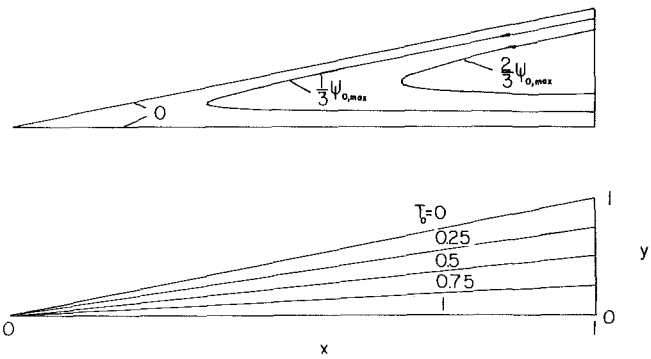

Fig. 2(*a*) Streamlines and isotherms corresponding to the zeroth-order solution

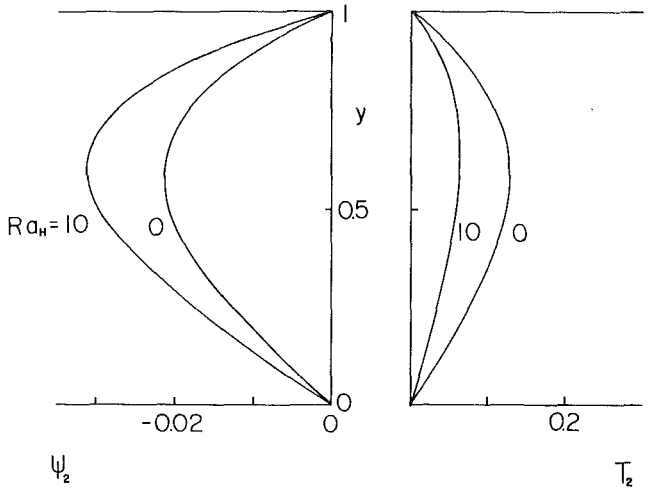

Fig. 2(*b*) Second-order streamfunction and temperature profiles at x = 1

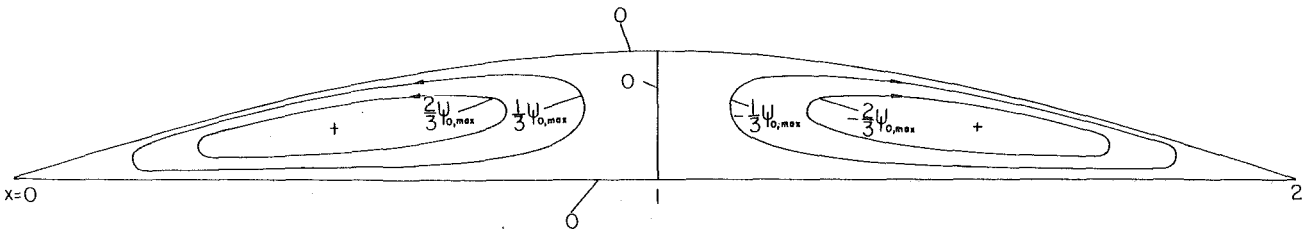

Fig. 3 Zeroth-order flow pattern under a smooth roof, equation (16)

The Boundary Layer Regime

In the preceding section we invoked the ($\epsilon \to 0$, Ra_H fixed) limit to discover the basic features of natural circulation in an attic shaped porous layer heated from below. In the present section, we focus on an attic-shaped layer with ϵ small but *fixed*. We examine the flow of heat-transfer regime when the Rayleigh number is high enough so that a thin boundary layer forms along the driving surface (in this case the top surface, which is not perpendicular to the gravitational acceleration vector).

Figure 4 shows the new formulation of the problem in the boundary layer regime. From the outset, it must be recognized that the successful description of boundary layer circulation in any enclosure depends on how well we guess the conditions which prevail in the core, i.e., far away from both solid walls [5].

At this time, there is no experimental or numerical information we could use to model the core flow. However, the analytical study of natural convection in rectangular enclosures has proven the existence of a *qualitative* parallelism between the pattern of low-Ra laminar flow in an enclosure and the natural circulation through a porous medium filling the same enclosure [6]. This parallelism is illustrated most vividly by a comparison between the laminar flow in a very shallow enclosure [4] and the corresponding flow in a very shallow porous layer [3]. Equipped with this observation, we relied on recent visualizaton experiments of air circulation in a triangular space [7], which showed that the inclined (driving) surface develops a distinct boundary layer, while the core is pushed (displaced) slowly, as a solid body, in the reverse direction.

According to the formulation presented in Fig. 4, the solution is developed in two phases: (*a*) the boundary layer flow along the inclined surface, and (*b*) the matching of this flow to the core which fills the triangular cavity. We begin with the boundary layer equations for mass, momentum, and energy along the top wall; these equations can be put in the following dimensionless form

$$\frac{\partial u_1}{\partial x_1} + \frac{\partial v_1}{\partial y_1} = 0 \tag{21}$$

$$\frac{\partial u_1}{\partial y_1} = -\sin\epsilon \frac{\partial T}{\partial y_1} \tag{22}$$

$$u_1 \frac{\partial T}{\partial x_1} + v_1 \frac{\partial T}{\partial y_1} = \frac{\partial^2 T}{\partial {y_1}^2} \tag{23}$$

by writing

$$x_1 = x_{*_1}/L, \quad y_1 = y_{*_1}/\delta, \quad u_1 = u_{*_1}/(\alpha L/\delta^2) \tag{24}$$

where δ is the boundary layer thickness

$$\delta = L\,\mathrm{Ra}_L^{-1/2} \tag{25}$$

and Ra_L is the Rayleigh number based on L,

$$\mathrm{Ra}_L = \frac{Kg\beta\Delta TL}{\alpha\nu}$$

The symbols appearing in equations (21–23) are defined in Fig. 4 and in the Nomenclature. The dimensionless temperature T is defined as in the preceding section in equation (7).

An exact solution to equations (21–23) is not feasable due to the nonlinear form of the energy equation. This difficulty was dealt with in an approximate way, by employing the Oseen linearization technique pioneered by Ostrach [5] and Gill [8] for natural convection in enclosures. More recently, the same technique has been used with success in problems involving natural convection in enclosures filled with a porous medium [9–11]. According to this technique, we view the energy equation (23) as a linear differential equation in which v_1 and $\partial T/\partial x_1$ are replaced by unknown functions of x_1, $\overline{(v_1)}$ and $\overline{(\partial T/\partial x_1)}$, respectively. Since the geometry is slender and the two surfaces are isothermal, it is reasonable to take $\overline{(\partial T/\partial x_1)}$ as equal to zero. Consequently, the linearized energy equation reduces to

$$\frac{\partial^2 T}{\partial {y_1}^2} - \overline{(v_1)}\frac{\partial T}{\partial y_1} = 0 \tag{27}$$

This form and the two boundary conditions

$$T = 0 \text{ at } y_1 = 0, \text{ and } T \to T_\infty \text{ as } y_1 \to \infty \tag{28}$$

recommend a temperature field which is given by

$$T(x_1, y_1) = -T_\infty e^{-\lambda y_1} + T_\infty \tag{29}$$

In this expression T_∞ is the unknown core temperature, and λ is an unknown function of x_1 (or x_2).

The velocity distribution $u_1(x_1, y_1)$ follows from equations (22) and (29),

$$u_1(x_1, y_1) = -\mathrm{U}\cos\epsilon + T_\infty \sin\epsilon\, e^{-\lambda y_1} \tag{30}$$

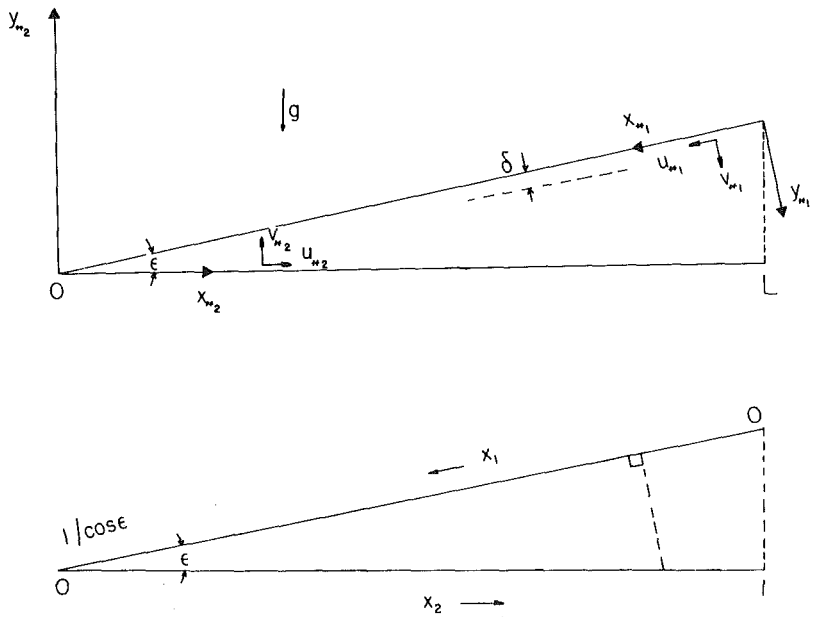

Fig. 4 Coordinate systems for boundary layer analysis

This expression for longitudinal velocity satisfies the core flow condition discussed earlier in this section: the core moves slowly to the right (Fig. 4) at velocity U (unknown function of x_1 or x_2). At this point, we have two approximate expressions for u_1 and T, equations (29, 30), suggested by the linearized version of the energy equation. Expressions (29, 30) do not satisfy the real energy equation (23); however, they can be forced to satisfy equation (23) integrated over the boundary layer thickness (in the y_1 direction). Thus, we obtain the following relationship between $U(x_1)$ and $\lambda(x_1)$,

$$\frac{d}{dx_1}\left(\frac{U\cos\epsilon - \frac{1}{2}T_\infty \sin\epsilon}{\lambda}\right) = -\lambda \tag{31}$$

We obtain a second relationship between U and λ by recognizing that the net mass flowrate through any plane x_1 = constant must be zero. Integrating expression (30) from $y_{*_1} = 0$ to $y_{*_1} = x_{*_2} \sin\epsilon$, yields

$$U\lambda x_2 = \frac{T_\infty}{\cos\epsilon\, \mathrm{Ra}_L^{1/2}} \tag{32}$$

Parameter x_2 indicates the location of the cut made by the x_1 = constant plane on the horizontal surface (see bottom of Fig. 4)

$$x_1 = \frac{1}{\cos\epsilon} - x_2 \cos\epsilon \tag{33}$$

Equations (31, 32) are sufficient for determining U and λ subject to a yet unknown core temperature T_∞. Eliminating λ between equations (31) and (32) we obtain

$$\frac{d}{dx_2}\left[U^2 x_2 - \frac{T_\infty}{2}\tan\epsilon\, U x_2\right] = \frac{T_\infty{}^2}{U x_2\, \mathrm{Ra}_L \cos^2\epsilon} \tag{34}$$

This equation was eventually solved numerically; however, it is more instructive to proceed from the observation that for a sufficiently small angle ϵ the second term on the left-hand side becomes negligible; hence, the core velocity U is given by

$$U \cong \left(\frac{3\, T_\infty{}^2}{x_2\, \mathrm{Ra}_L \cos^2\epsilon}\right)^{1/3} \tag{35}$$

The general solution to equation (34) can be constructed as

$$U = \left(\frac{3\, T_\infty{}^2}{x_2\, \mathrm{Ra}_L \cos^2\epsilon}\right)^{1/3} f_B\,(x_2) \tag{36}$$

where $f_B\ (x_2)$ is the necessary "correction" function. Substituting expression (36) into equation (34), we obtain the differential equation for f_B

$$\frac{df_B}{dx_2} = \frac{1 - f_B{}^3 + 3^{-1/3} B x_2{}^{1/3} f_B{}^2}{6 x_2 f_B{}^2 - \frac{3^{2/3}}{2} B x_2{}^{4/3} f_B} \tag{37}$$

with $f_B(0) = 1$ as boundary condition, and a new dimensionless group

$$B = \left(\frac{T_\infty \mathrm{Ra}_L}{\cos\epsilon}\right)^{1/3} \sin\epsilon \tag{38}$$

The correction function f_B was calculated numerically, and representative results are shown in Fig. 5. In the limit $x_2 \to 0$, function $f_B(x)$ behaves as

$$f_B = 1 + \frac{B}{2}\left(\frac{x_2}{3}\right)^{1/3} - \ldots \tag{39}$$

We conclude that as long as $0(B) \leq 1$, we can safely take $f_B \simeq 1$ and regard equation (35) as a satisfactory solution for the core flow in the boundary layer regime.

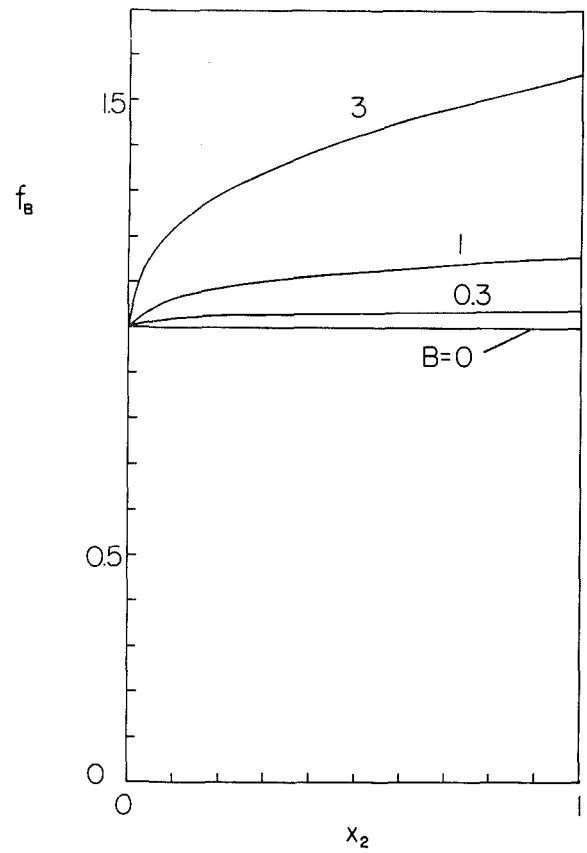

Fig. 5 The correction function f_B, equation (37), as a function of x_2 and B

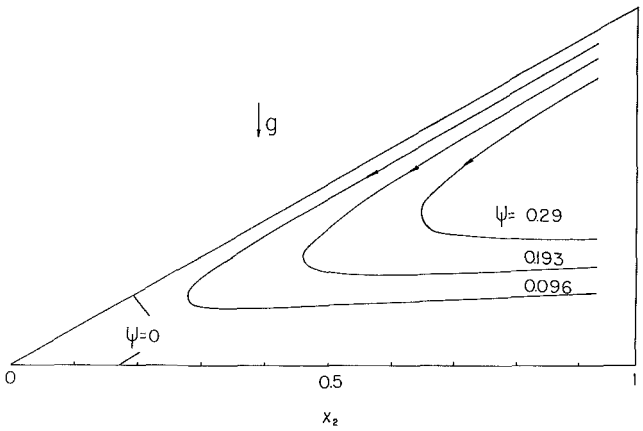

Fig. 6 Illustration of streamline pattern in the boundary layer regime ($\mathrm{Ra}_L = 1000$, $\epsilon = 30$ deg)

Finally, from equations (35) and (32) we deduce that the dimensionless boundary layer thickness (λ^{-1}) varies as $x_2{}^{2/3}$,

$$\frac{1}{\lambda} = \left(\frac{3\, x_2{}^2 \cos\epsilon \sqrt{\mathrm{Ra}_L}}{T_\infty}\right)^{1/3} \tag{40}$$

Physically, this makes sense because the space (including the top wall boundary layer thickness) must vanish at $x_2 = 0$. Representative streamlines of this flow are shown in Fig. 6 where, for visual effect, we set $\epsilon = 30$ deg.

The boundary layer solution developed so far depends on the unknown core temperature T_∞. To determine T_∞, we must consider the heat-transfer rate along the bottom wall and set it equal to the heat-transfer rate through the top wall.

Referring once again to Fig. 4, the governing equations in the vicinity of the bottom wall are

$$\frac{\partial u_2}{\partial x_2} + \frac{\partial v_2}{\partial y_2} = 0 \tag{41}$$

$$\frac{\partial u_2}{\partial y_2} = -\frac{\partial T}{\partial x_2} \tag{42}$$

$$u_2 \frac{\partial T}{\partial x_2} + v_2 \frac{\partial T}{\partial y_2} = \frac{\partial^2 T}{\partial y_2^2} \tag{43}$$

Noting that the velocity scale is imposed by the driving (top) surface, equation (24), equations (41-43) have been undimensionalized by defining

$$x_2 = x_{*_2}/L, \; y_2 = y_{*_2}/\delta, \quad u_2 = u_{*_2}/(\alpha L/\delta^2) \tag{44}$$

where δ is the same as in equation (25). The corresponding Oseen-linearized solution is

$$u_2 = U(x_2) \tag{45}$$

$$T_2 = (1 - T_\infty)\, e^{-\mu y_2} + T_\infty \tag{46}$$

where $1/\mu$ is the dimensionless thickness of the thermal boundary layer developing along the bottom wall as the slow core flow sweeps it counterclockwise. Substituting expressions (45, 46) into the integral of the energy equation (43) [i.e., into the equivalent of equation (31)] we obtain

$$\frac{d}{dx_2}\left(\frac{U}{\mu}\right) = \mu \tag{47}$$

In the range $B \leq 1$, equation (47) yields

$$\frac{1}{\mu} = \left(\frac{3x_2^2 \cos\epsilon \sqrt{\mathrm{Ra}_L}}{T_\infty}\right)^{1/3} \tag{48}$$

The thermal boundary layer along the bottom wall has the same x_2 variation as the boundary layer along the top wall, equation (40).

The continuity of heat transfer between the bottom and top walls requires

$$-\int_0^L k\left(\frac{\partial T_*}{\partial y_{*_2}}\right)_{y_{*_2}=0} dx_{*_2} = \int_0^{L/\cos\epsilon} k\left(\frac{\partial T_*}{\partial y_{*_1}}\right)_{y_{*_1}=0} dx_{*_1} \tag{49}$$

Combining this statement with the temperature solutions developed in this section, equations (29) and (46), yields

$$T_\infty = \frac{\cos^{1/3}\epsilon}{1+\cos^{1/3}\epsilon} \leq \frac{1}{2} \tag{50}$$

Therefore, if the angle ϵ is sufficiently small, the core temperature T_∞ reaches the arithmetic average temperature 1/2.

Finally, we are in a position to evaluate the Nusselt number for net heat-transfer between T_H and T_C, by natural convection in the boundary layer regime. We use definition (18) in combination with

$$Q = -\int_0^L k\left(\frac{\partial T_*}{\partial y_{*_2}}\right)_{y_{*_2}=0} dx_{*_2} \tag{51}$$

and the result is

$$\mathrm{Nu} = 3^{2/3}[1+\cos^{1/3}\epsilon]^{-4/3}\, \mathrm{Ra}_L^{1/3} \tan\epsilon \tag{52}$$

It is worth pointing out that when ϵ is sufficiently small, the net heat-transfer rate Q reaches an asymptotic value which is *independent* of ϵ

$$Q = 0.825\, k\Delta T\, \mathrm{Ra}_L^{1/3} \tag{53}$$

Thus, in the range $B < 1$, the only effect of the small angle ϵ is to maintain a single cell[1] in the wedge-shaped porous space: the actual value of Q does not depend on ϵ.

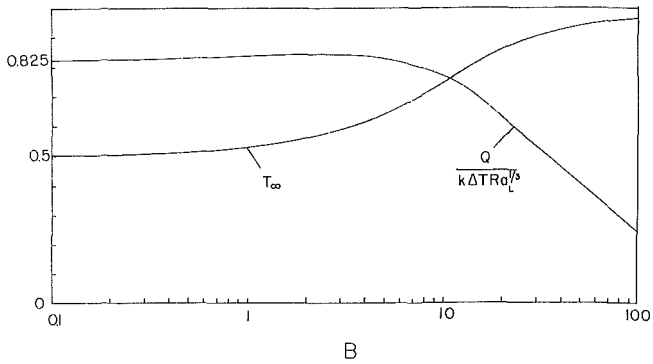

Fig. 7 Numerical solution for core temperature and net heat-transfer rate (range $0.1 < B < 100$)

The present boundary layer analysis was carried out numerically for values of parameter B in the range 1-100. Figure 7 summarizes the key results of this numerical extension. We see that as B increases, the core temperature T_∞ increases steadily from the limiting value of 1/2 (i.e. the core temperature approaches the bottom wall temperature). At the same time the coefficient in the $Q \sim k\,\Delta T\,\mathrm{Ra}_L^{1/3}$ proportionality decreases from its limiting value of 0.825 (equation (53)).

Conclusions

In this article we reported an analytical study of the phenomenon of bouyancy-driven circulation through a porous material filling a wedge-shaped horizontal space. The fundamental objective of this study has been to document the basic features (flow and heat transfer) of the phenomenon. The engineering objective has been to establish the effect of natural convection on the net heat-transfer rate across the porous layer; we examined this effect in the engineering context of an attic-shaped porous insulation which functions in winter-type conditions.

The analytical study was carried out in two parts. In the first part we considered the shallow attic limit ($H/L \to 0$) and showed analytically that the wedge space contains a single cell driven by the development of nonhorizontal isotherms (Fig. 2(*a*)). We showed also that in the shallow attic limit the circulation pattern is influenced greatly by the shape of the roof (Fig. 3). We found that the first convective contribution to the net heat transport between ceiling and roof scales with the group $\mathrm{Ra}_H\,(H/L)^2$.

In the second part of this study we developed a solution for the flow and heat transfer in the boundary layer regime. We based the structure of this solution on flow visualization reports of laminar natural convection in an attic space filled with air [7]: accordingly, we developed a boundary layer solution for the flow descending along the upper (sloped) wall, and matched this solution to the solution for the core fluid displaced slowly along the bottom wall. This analytical path led to the flow scales in the cavity and for the net heat-transfer rate. The heat transfer results are reported in chart form in Fig. 7.

The range of applicability of the present results remains to be established on the basis of future numerical simulations or experiments. Regarding the boundary layer regime, we expect distinct layers to exist when, from equation (29), $\lambda H/\delta > 1$. For small angles ϵ, this condition reads $\epsilon \mathrm{Ra}_L^{1/3} > 1$, which

[1] as opposed to a multitude of Bénard-type cells as in constant-thickness layers [2].

means that boundary layers become more distinct as B exceeds unity (equation (38)). Another limitation is posed by the potential of Bénard instability: local convection cells may form when the Rayleigh number based on height Ra_H exceeds a critical value. This phenomenon remains to be investigated in a future study.

Acknowledgment

This research was supported in part by NSF Grant ENG 78-20957.

References

1 Cheng, P., "Heat Transfer in Geothermal Systems," *Advances in Heat Transfer,* Vol. 14, 1979, pp. 1-105.

2 Elder, J. W., "Steady Free Convection in a Porous Medium Heated from Below," *Journal of Fluid Mechanics,* Vol. 27, 1966, pp. 29-48.

3 Walker, K. L. and Homsy, G. M., "Convection in a Porous Cavity," *Journal of Fluid Mechanics,* Vol. 87, 1978, pp. 449-474.

4 Cormack, D. E., Leal, L. G., and Imberger, J., "Natural Convection in a Shallow Cavity with Differentially Heated End Walls. Part 1. Asymptotic Theory," *Journal of Fluid Mechanics,* Vol. 65, 1974, pp. 209-230.

5 Ostrach, S., "Natural Convection in Enclosures," *Advances in Heat Transfer,* Vol. 8, 1972, pp. 161-227.

6 Bejan, A., "A Synthesis of Analytical Results for Natural Convection Heat Transfer Across Rectangular Enclosures," *International Journal of Heat and Mass Transfer,* Vol. 23, 1980, pp. 723-726.

7 Flack, R. D., Konopnicki, T. T., and Rooke, J. H., "The Measurement of Natural Convective Heat Transfer in Triangular Enclosures," ASME JOURNAL OF HEAT TRANSFER, Vol. 101, 1979, pp. 648-654.

8 Gill, A. E., "The Boundary Layer Regime for Convection in a Rectangular Cavity," *Journal of Fluid Mechanics,* Vol. 26, 1966, pp. 515-536.

9 Bergholz, R. F., "Natural Convection of a Heat Generating Fluid in a Closed Cavity," ASME JOURNAL OF HEAT TRANSFER, Vol. 102, 1980, pp. 242-247.

10 Weber, J. E., "The Boundary Layer Regime for Convection in a Vertical Porous Layer," *International Journal of Heat and Mass Transfer,* Vol. 18, 1975, pp. 569-573.

11 Bejan, A., "On the Boundary Layer Regime in a Vertical Enclosure Filled with a Porous Medium," *Letters in Heat and Mass Transfer,* Vol. 6, 1979, pp. 93-102.

Structure of Growing Double-Diffusive Convection Cells

Y. Suzukawa
Research Engineer.

U. Narusawa[1]
Associate Manager.

Technical Research Center,
Nippon Kokan K.K.,
Kawasaki, Japan

When a fluid with a vertical solute gradient is heated from a sidewall, layers of convection cells form along the wall. For an aqueous solution of common salt (i.e., fixed values of Pr and τ), the convection cells will form along the vertical heated wall for values of $\pi(=\alpha(q/k)/\beta(-dS/dz))$ greater than ~ 0.28. This paper reports the experimental investigation of the structure of the growing convection cells when a uniform heat flux is applied at the vertical wall. A series of tests was conducted using a small tank (23 cm high $\times$ 16 cm deep $\times$ 20 cm wide). Measurements of the vertical temperature distribution in the fluid at five different locations were taken continuously along with shadowgraph pictures to monitor the growth of the convection cells. Based on the set of data thus obtained, the following characteristics of a growing convection cell were found: (a) A convection cell with a vertical height, K, grows laterally into the quiescent fluid at a constant speed, U, and the Reynolds number of a moving front, defined as UH/ν, changes linearly with π on a log-log scale for our experimental range of $\pi = 0.3 - 10$. (b) The vertical averaged temperature inside a growing cell is a linear function of the distance from the heated wall over a major portion of the cell. (c) The lateral temperature gradient inside a cell decreases with time, and is proportional to the inverse of the elasped time.

1 Introduction

Convection in the presence of two opposing buoyancy components is called "double-diffusive convection," and possesses many special characteristics of its own [1]. One of the typical double-diffusive convection phenomena is the formation of convection cells when heat is applied laterally to a fluid with a vertical solute gradient. When the temperature of a vertical wall adjacent to the fluid is raised, the portion of the fluid near the wall starts to rise due to a positive buoyancy induced by the heat, but the height to which it rises is limited to a level where the net density of this portion is closer to the interior fluid. The fluid then starts to flow away from the heated wall to initiate a laterally advancing layer of convection cells.

The criteria for the onset of cellular convection due to lateral heating was investigated by Thorpe, Hutt, and Soulsby [2] for the case of a fluid contained in a narrrow vertical space between two constant temperature walls (one hot, the other cold), and by Chen et al. [3, 4, 5] for the case in which the presence of the opposite wall is not felt by the convecting fluid near the hot, constant-temperature wall. A similar study for the case of an inclined wall has also recently been published by Paliwal and Chen [6, 7].

The stability of cellular convection due to a uniform heat flux at the vertical wall has been studied experimentally by Narusawa and Suzukawa [8], confirming that cellular convection develops if a nondimensional parameter, $\pi(=-\alpha(q/k)/\beta(dS/dz))$, is greater than ~ 0.28 for an aqueous solution of common salt with $\tau = 9 \times 10^{-3}$, and that the critical value of π increases with an increase in τ. Their results also include the size, H, (i.e., vertical height of a roll cell), normalized with respect to a length scale, L $(=[\nu D_T/g\alpha(q/k)]^{1/4})$, as a function of π, indicating an increase of H/L with π. Here, π is the ratio of the Rayleigh number $(=g\alpha(q/k)L^4/\nu D_T)$ to the solute Rayleigh number defined as $g\beta(-dS/dz)L^4/\nu D_T$, and is a measure of the two opposing buoyancy components.

Double-diffusive convection layers have been observed in the ocean [9, 10] as naturally occurring phenomenon, have been utilized in a solar pond [11] as an engineering application, and have also been found to form undesirably in LNG (Liquefied Natural Gas) storage tanks. When an LNG storage tank contains LNG with different densities, vertical density stratification can occur followed by the development of growing convection cells due to heat leak from the surroundings into the tank, resulting in a phenomenon known as "roll-over" in which a sudden and dangerous increase in boil-off gases occurs [12]. The purpose of this study is to investigate the dynamic behavior and structure of growing convection cells when a uniform lateral heat flux is applied to salt-water with an initially-linear solute gradient (i.e., a linear solute concentration change with depth); a study similar in nature of those conducted by Turner [13], and by Huppert and Linden [14] (for layer formation when a fluid with a vertical solute gradient is heated from below), and by Nekrasov et al. [15] (for layer formation when a fluid with a vertical solute gradient is heated laterally).

2 Experimental Method

The test tank, 23-cm high $\times$ 16-cm deep $\times$ 20-cm wide, consisted of two copper (23 cm $\times$ 16 cm) and two acrylic sidewalls with an acrylic bottom (see Fig. 1). The acrylic plates used for both the sidewalls and the bottom were 1.5-cm thick, while the thickness of the copper plates were 1.0 mm. In order to protect the copper plates from corrosion, the side of the plate in contact with the fluid was Teflon-coated (less than 0.1 mm in thickness). A film heater was attached to the back of one of the copper plates. The heater was hooked to an a.c. 100-V supply via a digital wattmeter and a voltage regulator. Since the experiment is aimed at simlating a semiinfinite body of fluid adjacent to a heated wall, the other copper plate was left at room temperature. The back of the copper sidewall as well as the top and bottom of the tank were insulated with pads of calcium silicate, 25-mm thick. Five copper-constantan thermocouples were mounted on a traverse mechanism, motorized in the vertical direction with its horizontal position adjusted manually.

The initial linear solute gradient in the tank was formed using the method described by Oster [16]. The linearity of the initial solute concentration change with depth was checked by a conductivity gauge, confirming that the deviations of salt

Contributed by the Heat Transfer Division for publication in the JOURNAL OF HEAT TRANSFER. Manuscript received by the Heat Transfer Division May 15, 1981.

[1] Present address: Department of Mechanical Engineering, Northeastern University, Boston, Mass.

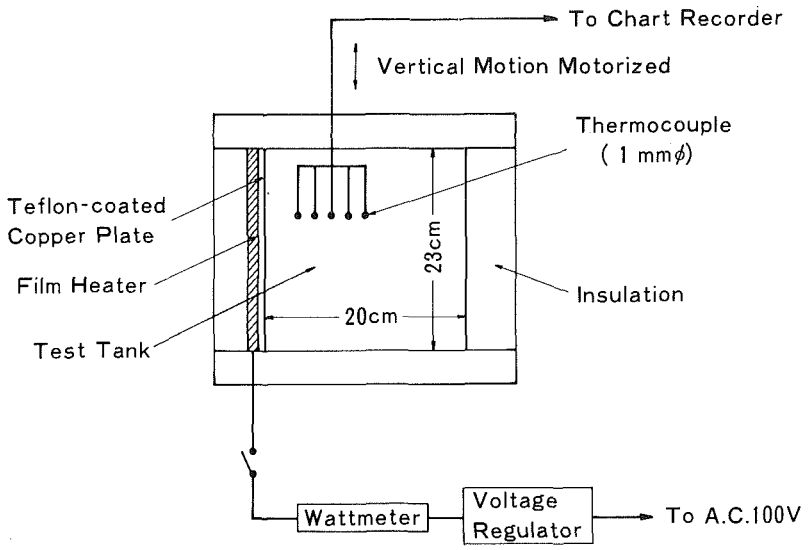

Fig. 1 A schematic drawing of the test apparatus

concentration from linearity were better than ±6 percent for all the data (except near the horizontal boundaries).

The relationship between the applied wattage and the heat flux into the fluid was obtained beforehand by measuring the change of temperature in well-stirred water in the tank with a calibrated mercury thermometer (accuracy ~0.1°C). Based on the results of these calibration tests, it was concluded that the relationship was well represented by a linear equation, q [cal/cm^2 s] = 0.255×10^{-3} W, where W is the applied wattage, with the deviations of q from linearity being smaller than ±2 percent. The combined effect of these deviations in the values of $(-dS/dz)$ and q resulted in an estimated maximum error in the nondimensional parameter, π, of ~8 percent.

When a uniform heat flux is applied at a sidewall so that the value of π is below the critical value (~0.28 for an aqueous solution of common salt), cellular convection does not occur and heat is transferred laterally by conduction. In our previous experiment [8], the time change of temperature at the heated wall under subcritical condition was measured for a given heat flux, and it was confirmed that the measured temperature change agreed well with the theoretical prediction (one-dimensional, transient heat conduction into a semiinfinite body). It was also checked that the uniformity of temperature along the heated copper plate was quite good; the deviation of temperature from the average (of measurements taken at four locations) being less than 0.2°c. Strictly speaking, under supercritical conditions, the heat flux into a stratified fluid is different from the heat flux obtained for a homogeneous fluid; however, since under subcritical conditions the theoretical prediction based on the calibrated values of the heat flux was excellent, we concluded that the use of the heat flux thus obtained was quite satisfactory.

Growth of convection cells was monitored by using the shadowgraph technique coupled with a still camera.

A typical test run began with the formation of a linear solute gradient in the tank. The heater as well as timer were then switched on. By manually adjusting the voltage regulator, fluctuations of the heat flux were limited to within ~2 percent of the average. As convection cells started to grow along the heated wall, the set of thermocouples was traversed vertically through the fluid every ~2–5 min with the chart recorder yielding vertical temperature distributions at five different locations. The traverse speed was ~1–3 [mm/s], slow enough to ensure that the initial solute gradient was not disturbed. The vertical length traversed by the set of thermocouples ranged from 2–6 cm, depending on the vertical size of a cell. The shadowgraph pictures of cell growth were taken every ~ 2 min. Each test run ended when the cells extended across approximately 70–80 percent of the width of the tank.

Nomenclature

A = a function of t defined in equation (4)
C_p = specific heat at constant pressure
D_s = mass diffusivity
D_t = thermal diffusivity
g = gravitational acceleration
H = vertical size of a cell
k = thermal conductivity
L = length scale defined as $\left[\frac{\nu D_T}{g\alpha(q/k)}\right]^{1/4}$
q = heat flux at the wall
Pr = Prandtl number
Re = $\frac{UH}{\nu}$ = Reynolds number of a moving cell front
S = solute concentration
t = elapsed time
T = temperature
T_∞ = temperature of the initial quiescent fluid
ΔT = temperature difference between two walls
U = velocity of a growing cell front
x = horizontal coordinate (distance from the heated wall)
z = vertical coordinate
$\alpha = -\frac{1}{\rho}\left(\frac{\partial \rho}{\partial T}\right)$
$\beta = \frac{1}{\rho}\left(\frac{\partial \rho}{\partial S}\right)$
ν = kinematic viscosity
$\pi = -\alpha\left(\frac{q}{k}\right)\Big/\beta\left(\frac{dS}{dz}\right)$
ρ = density
$\tau = D_s/D_T$ = diffusivity ratio

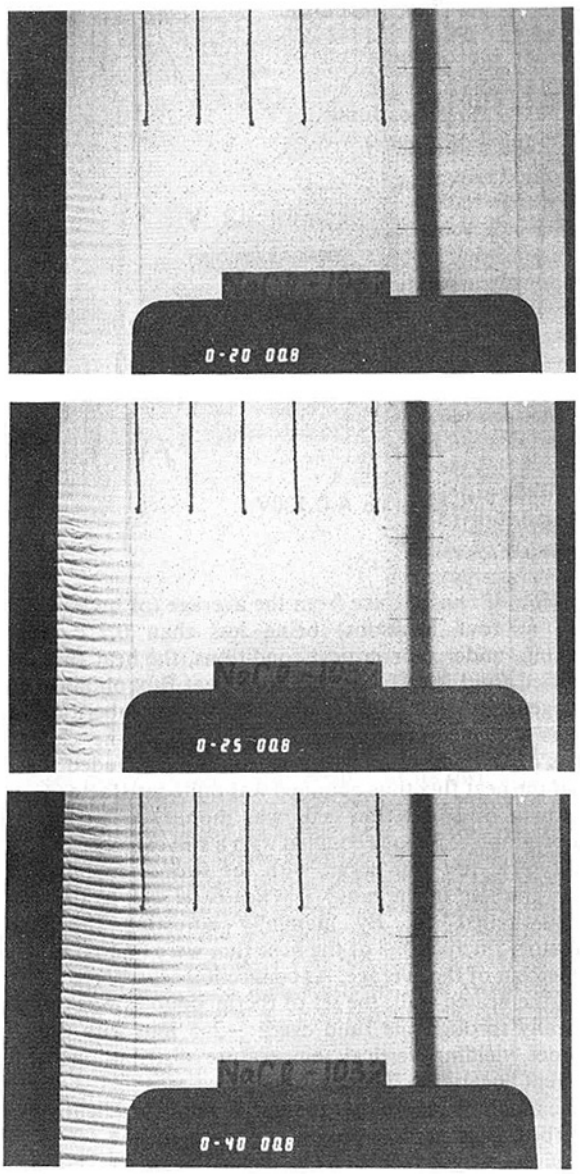

Fig. 2 Development of convection cells (π = 0.32, H/L = 10.1): (*a*) t = 20 min; (*b*) t = 25 min; (*c*) t = 40 min

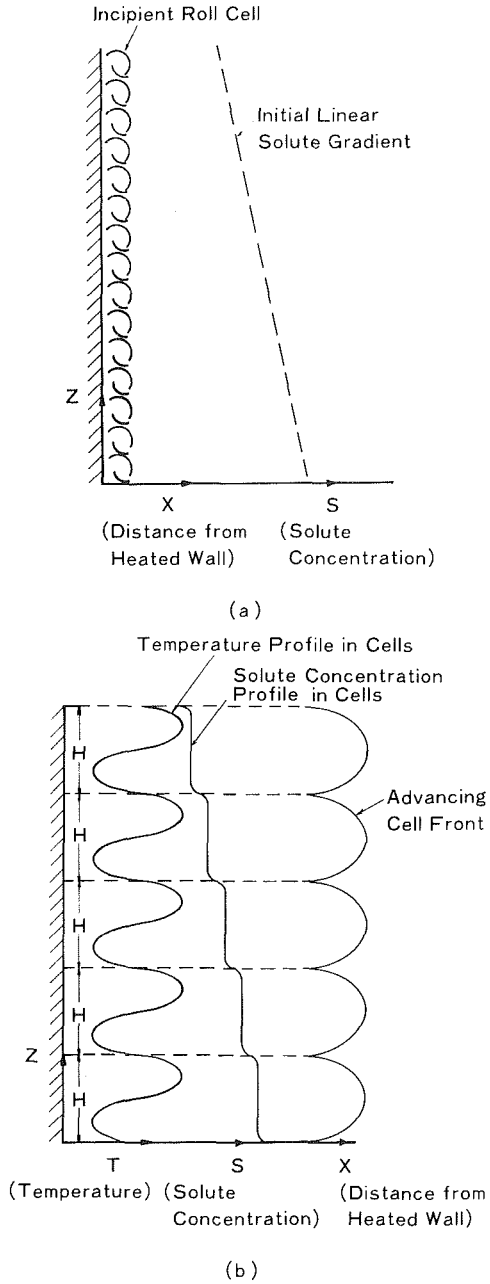

Fig. 3 A sketch of the growing convection cells

Later the height of a cell was determined from the shadowgraph pictures. For small cells, the size was obtained by counting the number of cells present in a known vertical distance, while for cells whose sizes were larger ($\sim$ 1.5 cm or more), the size of each cell was directly measured and averaged. The deviation of each cell size from the average value was less than 10 percent for all the data obtained.

3 Discussion of Results

3.1 General Observation of Growing Convection Cells. Here, based on the results of both the present experiment as well as those of previous investigations, the general characteristics of a growing convection cell will be discussed. Figure 2 shows the development of convection layers for π = 0.32. As can be seen, a series of roll cells starts to form along the heated wall located on the left-hand side of the pictures, growing laterally into the fluid with a linear solute gradient. It should be noted that the vertical height, H, of a cell is maintained as it grows outward, and that cells are slightly tilted downward because of the cooling of the heated fluid as it flows into the outer quiescent body of fluid. Figure 3 shows a sketch of growing convection cells for the case in which the value of π is much larger than the critical. In contrast to the case shown in Fig. 2, initial small roll cells (Fig. 3(*a*)) will quickly merge to form a layer of outer growing convection cells (Fig. 3(*b*)). (See also [8] for photographs of the cell development for the case in which $\pi >> \pi_c$.)

Each cell is bounded both at its top and bottom by a sharp density interface, referred to as a "diffusive interface." The heat amd mass transfer across a diffusive interface has been investigated by Turner [17], Wirtz and Reddy [18], and Takao and Narusawa [19]. It is known that the heat and mass transfer in the vertical direction is considerably reduced by the presence of a diffusive interface. As a consequence, the cells once formed maintain their size for a relatively long time before any merging among cells begins to occur [3, 4, 15].

In order to distinguish the flow pattern within a given cell, a small crystal of dye (potassium permanganate) was dropped into the tank. Figure 4 shows the streak pattern formed after approximately 15 min. The picture clearly shows that in the upper part of a convection cell, the warmer fluid flows away

from the heated wall while in the lower part of the cell the colder fluid flows from the moving front toward the wall. (When this picture was taken, the cell fronts, which are not shown in the picture, have reached a point three quarters of the tank width.)

Figure 5 gives a typical set of raw data on temperature profiles taken simultaneously at four different distances, x, from the heated wall. Based on this figure, the following observations can be made: (*a*) the temperature inside a cell decreases as x increases; (*b*) the vertical temperature distribution varies smoothly; (*c*) the difference between maximum and minimum temperature decreases with an increase in x; and (*d*) the approximate heights of the upper (•) and lower (x) boundaries of the cell decrease as the distance from the heated wall increases, indicating the downward-tilting of the cell as was discussed previously.

3.2 The size, H, and the velocity of the moving front, U, of a growing cell. As might be guessed from Fig. 2, it is difficult to obtain the location of a cell front from shadowgraph pictures. However, similar experimental results were reported by Nekrasov et al. [15]. In their investigation, in addition to the quantities measured in this investigation, they combined a laser-optical system with particle tracers to study the fine structure of motion in the liquid. Their observation shows that a disturbance of the initial solute concentration gradient propagates into the undisturbed, isothermal fluid, and that the propagation speed of this disturbance is higher that the advance speed of the heated-liquid boundary. The temperature at a fixed distance from the heated wall rises when the front of a growing convection cell (or the front of the heated-liquid boundary) reaches that point. Although, prior to the formation of roll cells, heat is transferred laterally by conduction, our data showed that the temperature rise at x = 1 cm (the thermocouple location closest to the heated wall) due to conduction was always less than 0.5° C, with $dT/dt|_x$ much smaller than that due to the arrival of the cell front. A graph of the locations of a cell front (determined from the temperature rise at fixed locations of the thermocouples) versus t (the elapsed time after the heater was turned on) was constructed for each run, and some typical results are shown in Fig. 6. From this figure, it can be concluded that the front of a convection cell grows laterally at a constant velocity, U, whose order of magnitude in this investigation was 0.1–1.0 cm/min.

At this point, the onset of cellular convection will be examined in more detail. When heat is applied at a sidewall, it will be transferred laterally into the fluid by conduction, while the slow vertical motion of the fluid that will be produced near the wall does not contribute to this lateral heat transfer. Also from the analysis by Hart [20], it is known that instability is initiated in a region where the horizontal gradients of temperature and salinity are nearly the same. In other words, before the incipient roll cells start to form, heat has to be transferred into the fluid to produce the horizontal solute gradient. Since we have shown in our previous work [8] that the principal parameter for the case of our interest is π and that for values of π above 0.28 convection cells form along a heated wall, this initial delay of the roll cell formation is expected to become more significant as the value of π approaches its critical value of ~0.28. However, Fig. 6 indicates that this initial delay is negligible for the value of π above 0.32. Similar results are also reported in [15], although direct comparison with our data cannot be made since their data was presented in terms of the temperature difference between the heat wall and the initial isothermal liquid. Figure 7 is the summary of both the size and the velocity of a growing cell, plotted against π. It should be noted that for lower values of π ($< \sim 4.0$) the rate of increase of U with π is more pronounced than the rate of increase of H with π, and that for values of π

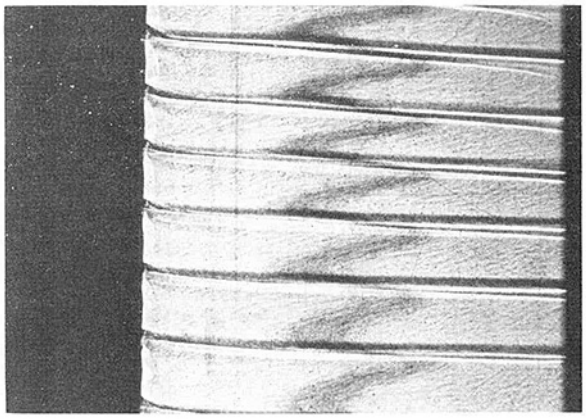

Fig. 4 Flow pattern inside growing convection cells, produced by a dye-marker (π = 5.99, H/L = 52.1)

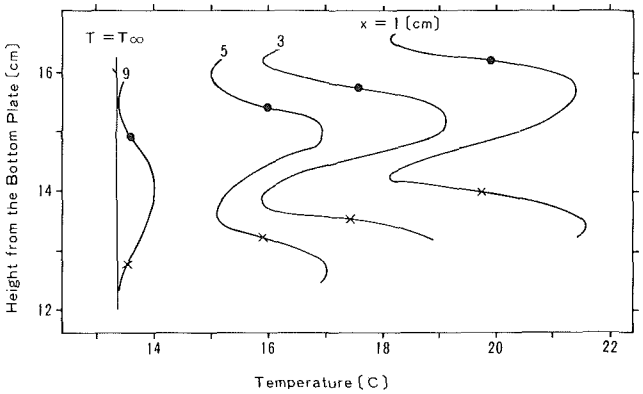

Fig. 5 Measured temperature distribution inside a cell for π = 7.28, t = 10 min. The circles and crosses indicate approximate locations of the upper and lower boundaries of the cell, respectively.

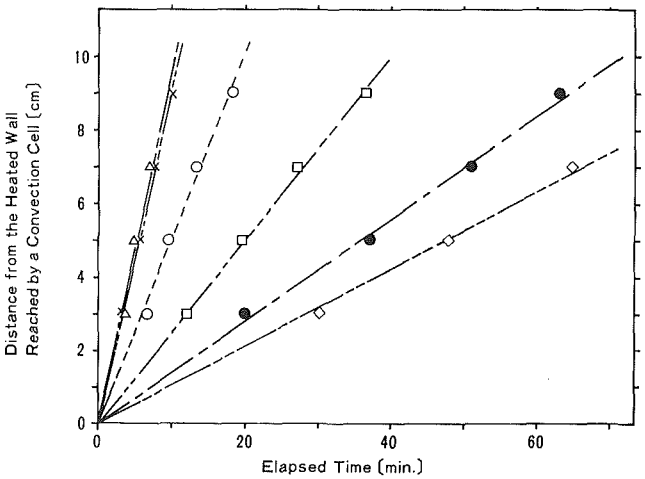

Fig. 6 Measured growth rate of a convection cell: ◇, π = 0.32; ●, π = 0.64; □, π = 1.27, ○, π = 2.45; x, π = 5.15; △, π = 11.40

above ~4.0, U remains more or less constant while H increases rapidly with π. When the value of π was increased to values above ~13, the number of cells produced in the tank was less than five; two of these having the top and bottom of the tank as their boundaries, respectively, and it could not be regarded as a multilayered system, thus imposing the upper limit in this investigation.

The nondimensional representation for the vertical size of a cell, H, has been given in [8] as,

$$H/L = f_1(\pi, \mathrm{Pr}, \tau), \tag{1}$$

where the reference length scale, L, is a length scale associated

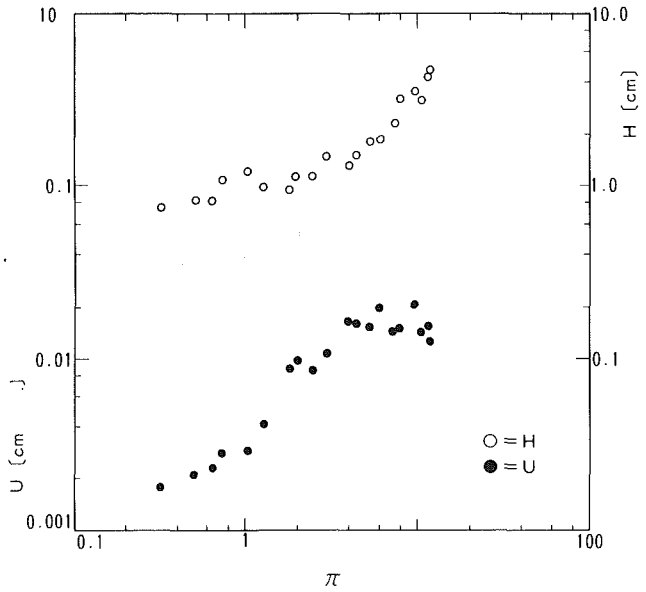

Fig. 7 Summary of the size, H, and the velocity of the moving front, U, of a growing cell, plotted against π

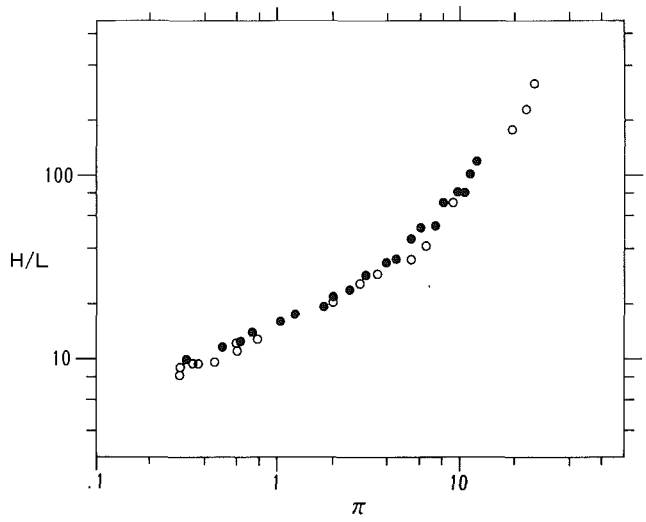

Fig. 8 Summary of experimental results of the cell size in terms of nondimensional parameters, H/L and π

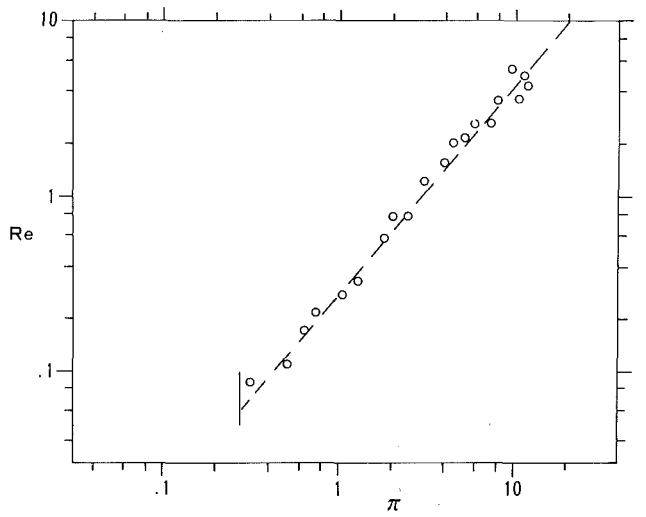

Fig. 9 Summary of experimental results of the velocity of the moving cell front in terms of nondimensional parameters, Re and π

with the thermal boundary layer along the heated wall. Since Pr and τ in our investigation are fixed, H/L then is a function of π. The present results along with the results reported in [8] are shown in Fig. 8, confirming the consistency of our present results with those of our previous investigation. (The test tank used in [8] was different from that used in this investigation, and had a dimension of 23.5 cm high × 16 cm deep × 10 cm wide.) Except near the horizontal boundaries, the measured heights of convection cells for given values of q and $(-dS/dz)$ were uniform and small compared with the height of the test tank. The plotted data in Fig. 8. (which gives consistent results regardless of the tank width), along with the fact that there was no horizontal density gradient in the direction perpendicular to the moving cell front, suggests that the motion was two-dimensional as was assumed a priori.

Similarly, the lateral penetration of a layer of convection cells into a body of quiescent fluid for a fixed value of π, can be described by U, H and three diffusivity quantities of D_T, D_s and ν, which in turn form the following relationship among four nondimensional quantities,

$$\mathrm{Re} = UH/\nu = f_2(\pi, \mathrm{Pr}, \tau). \tag{2}$$

A summary of our experimental results in Fig. 9 shows a linear relationship in a log-log scale between Re and π for an aqueous solution of common salt with a slope of ~ 1.2. (See Table 1 for complete listing of the data.)

3.3 Lateral Temperature Distribution Inside a Cell. Figure 10 is a typical set of data, showing the *average* temperature variation inside a cell as the cell expands laterally from the vertical heated wall. The *average* temperature is defined as the temperature averaged vertically across a single cell at a fixed value of x. Based on the data analysis such as indicated in Fig. 10, the following general observations were made: (i) The cell can be divided into three regions: (*a*) the boundary region near the heated wall (where the cold fluid is heated and flows away from the wall); (*b*) the central (or core) region (where the flow is more or less parallel to the direction of the cell growth, Fig. 4), and (*c*) the region near the moving cell front in which the warmer fluid flowing in the upper part of a cell penetrates into and mixes with the quiescent fluid and is thus cooled to produce a colder fluid moving towards the heated wall. (ii). The temperature of the central region of the cell changes linearly with the distance from the wall with the slope, dT/dx, decreasing with time.

The above observation is consistent with the analysis reported by Bejan and Tien [21]. Although their study differs from the present one in that it deals with steady-state convection between two constant temperature walls, it shows that as the aspect ratio (the ratio of H to the horizontal length of a growing cell) decreases the central region occupies the major portion of the cell, and that the lateral temperature variation in the central region is linear with respect to the distance from the heated wall.

Based on the assumptions that (*a*) there is no net heat leak into a cell through the upper and lower bounds of a cell, and that (*b*) there is a constant solute concentration inside a cell (the validity of these assumptions have been discussed previously), the conservation of energy with a growing cell as a control volume can be written as follows,

$$\frac{\partial}{\partial t}\left[\int_0^{\nu t} \rho c_p (T(t,x) - T_\infty) H dx\right] = qH \tag{3}$$

where $(T(t,x) - T_\infty)$ is the temperature difference between the fluid inside a cell and the quiescent fluid into which the cells are growing. If we further assume that the lateral change of the vertically averaged temperature is linear with respect to the distance from the heated wall, then,

$$T(t,x) = T_\infty = A(t) \cdot (x - Ut) \tag{4}$$

Table 1 Listing of the experimental data

Test No.	q [cal/cm^2•s]	$-dS/dz$ [wt%/cm]	T_∞ [°C]	π	H [cm]	H/L	U [cm/s]	Re
1	0.00765	0.303	6.4	0.32	0.75	10.1	0.0018	0.089
2	0.0117	0.283	6.5	0.51	0.81	12.0	0.0021	0.112
3	0.00612	0.221	18.0	0.64	0.82	12.7	0.0023	0.162
4	0.00765	0.120	9.5	0.73	1.09	14.6	0.0028	0.214
5	0.00561	0.088	14.0	1.03	1.20	16.5	0.0029	0.274
6	0.0122	0.215	17.5	1.27	0.98	18.0	0.0042	0.322
7	0.0331	0.300	9.8	1.80	0.95	19.8	0.0088	0.584
8	0.0311	0.233	9.9	1.99	1.11	22.5	0.0100	0.776
9	0.0255	0.218	16.1	2.45	1.11	24.0	0.0086	0.772
10	0.0245	0.133	13.3	3.00	1.48	29.4	0.0108	1.220
11	0.0688	0.301	11.4	3.99	1.31	33.8	0.0165	1.566
12	0.0408	0.218	18.6	4.40	1.48	37.5	0.0160	2.059
13	0.0612	0.226	14.0	5.15	1.77	45.9	0.0155	2.127
14	0.0969	0.292	11.2	5.99	1.84	52.1	0.0200	2.647
15	0.0510	0.113	13.3	7.28	2.28	54.3	0.0147	2.539
16	0.0510	0.088	11.9	7.88	3.19	72.3	0.0150	3.518
17	0.0535	0.080	12.5	9.54	3.53	82.2	0.0205	5.400
18	0.0663	0.116	15.4	10.50	3.10	82.0	0.0145	3.596
19	0.0663	0.081	12.2	11.40	4.32	105.0	0.0155	4.960
20	0.1000	0.105	10.4	11.70	4.73	122.0	0.0126	4.230

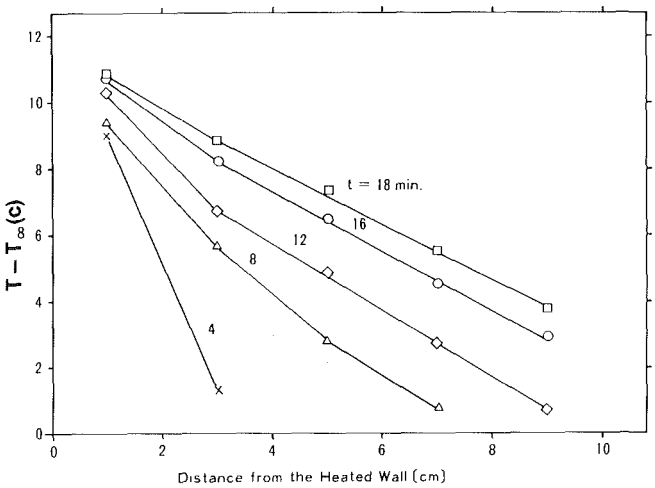

Fig. 10 A typical temperature change inside a growing cell from the measurement at π = 5.15

Substituting equation (4) into equation (3), and then integrating the resulting equation, one obtains,

$$\left(\frac{dT}{dx}\right)\Big/\left(-\frac{2q}{\rho c_p U^2}\right)=1/t \tag{5}$$

Equation (5) indicates that for given values of q and U, the change of the lateral slope of the average temperature inside a cell is proportional to $1/t$. The results of our experimental findings along with equation (5) are plotted in Fig. 11. The values of dT/dx of the data points used in Fig. 11 were obtained from the least square fitting of the data such as that shown in Fig. 10. Examination of Fig. 11 reveals that the data agrees well with equation (5) for relatively small value of $1/t$ (i.e., after a long period of elapsed time), confirming that the assumption of no net heat leak into a cell in the vertical direction is quite adequate to describe the development of cellular convection over a long period of time. However, at the beginning of cell formation (i.e., large $1/t$), the data deviates significantly from the prediction made by equation (5), especially for large values of $\pi(>2)$. This is because the size, H, of a cell increases with π, and at the beginning of cell formation the aspect ratio is still large, making the assumption of linear temperature distribution over a major part of the cell invalid.

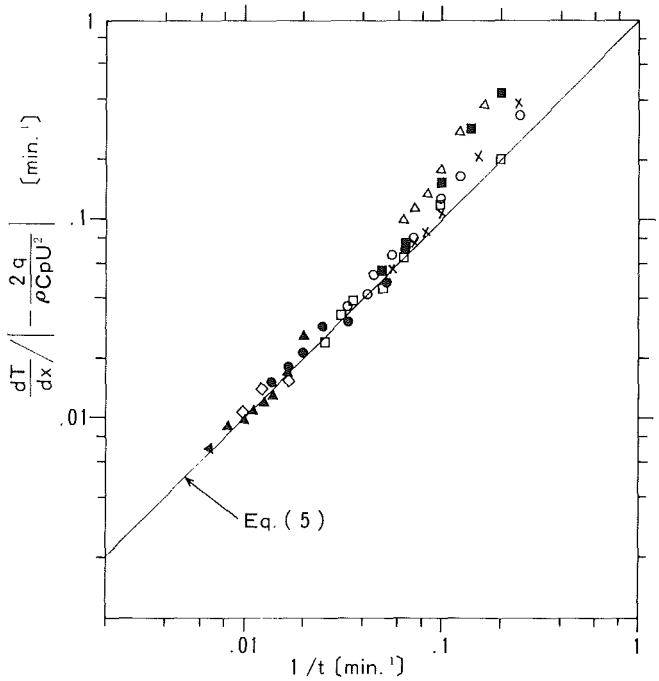

Fig. 11 Measured variation of the horizontal temperature gradient in a growing convection cell: ◇, π = 0.32; ▲, π = 0.51; ●, π = 0.64; □, π = 1.27; ○, π = 2.45; x, π = 5.15; ■, π = 7.28; △, π = 11.40

4 Conclusion

When a uniform heat flux is applied laterally to a fluid with a vertical solute gradient, layers of convection cells grow from the heated wall. The vertical height of a single cell, H, normalized with respect to L is a function of π, Pr and τ. Since the net vertical heat and mass transfer into each cell in this layered structure is nearly zero, the cells once formed maintain their vertical size over a long period of time. These cells grow laterally into the quiescent liquid at a constant speed, U, and the Reynolds number defined as UH/ν changes linearly with π on a log-log scale in our experimental range of π = 0.3–10.0. It was also found that the vertically averaged temperature inside a growing cell is a linear function of the distance from the heated wall over a major portion of the cell, and that the lateral temperature gradient inside a cell changes with time and is proportional to the inverse of the elapsed time.

Although the number of phenomena, which can be explained by double-diffusive convection, is increasing, this study focuses on the "roll-over" phenomenon in LNG storage tanks. (See Huppert and Turner [22] for a more comprehensive survey on applications of double-diffusive convection.) Once double-diffusive layers are formed in an LNG

storage tank, heat energy is accumulated effectively in these layers, giving rise to a sudden overturning or "roll-over." The results of this investigation will help understand the mechanism of these growing convection cells due to lateral heat flux.

Acknowledgment

The authors are grateful to the editor and the reviewers of ASME for their constructive suggestions and comments, particularly for drawing our attention to the reference [15], which was very helpful in the interpretation of our study.

References

1 Turner, J. S., *Buoyancy Effects in Fluids*, Cambridge University Press, 1979.

2 Thorpe, S. A., Hutt, P. K., and Soulsby, R., "The Effect of Horizontal Gradients on Thermohaline Convection, *Journal of Fluid Mechanics*, Vol. 38, 1969, pp. 375–400.

3 Chen, C. F., Briggs, D. G., and Wirtz, R. A., "Stability of Thermal Convection in a Salinity Gradient due to Lateral Heating," *International Journal of Heat and Mass Transfer*, Vol. 14, 1971, pp. 57–66.

4 Wirtz, R. A., Briggs, D. G., and Chen, C. F., "Physical and Numerical Experiments on Layered Convection in a Density-Stratified Fluid," *Geophys. Fluid Dyn.*, Vol. 3, 1972, pp. 265–288.

5 Chen, C. F., "Onset of Cellular Convection in a Salinity Gradient due to a Lateral Temperature Gradient," *Journal of Fluid Mechanics*, Vol. 63, 1974, pp. 563–576.

6 Paliwal, R. C. and Chen, C. F., "Double-Diffusive Instability in an Inclined Fluid Layer—Part 1: Experimental Investigation," *Journal of Fluid Mechanics*, Vol. 98, 1980, pp. 755–768.

7 Paliwal, R. C. and Chen, C. F., "Double-Diffusive Instability in an Inclined Fluid Layer Part 2: Stability Analysis," *Journal of Fluid Mechanics*, Vol. 98, 1980, pp. 769–786.

8 Narusawa, U. and Suzukawa, Y., "Experimental Study of Double-Diffusive Cellular Convection due to a Uniform Lateral Heat Flux," *Journal of Fluid Mechanics*, Vol. 113, 1981, pp. 387–405.

9 Hoare, R. A., "Problems of Heat Transfer in Lake Vanda, a Density Stratified Antarctic Lake," *Nature*, Vol. 210, 1966, pp. 787–789.

10 Neal, V. T., Neshyba, S. and Denner, W., "Thermal Stratification in the Arctic Ocean," *Science*, Vol. 166, pp. 373–374.

11 Tabor, H., "Non-Convecting Solar Ponds," *Phil. Trans. Roy. Soc.*, A295, 1979, pp. 423–433.

12 Sarsten, J. A., "LNG Stratification and Roll-Over," *Pipeline and Gas Journal*, Sept. 1972, pp. 37–39.

13 Turner, J. S., "The Behavior of Stable Salinity Gradient Heated From Below," *Journal of Fluid Mechanics*, Vol. 33, 1968, pp. 183–200.

14 Huppert, H. E. and Linden, P. F., "On Heating a Stable Salinity Gradient From Below," *Journal of Fluid Mechanics*, Vol. 95, 1979, pp. 431–464.

15 Nekrasov, V. N., Popov, V. A., and Chashechkin, Yu D., "Formation of Periodic Convective-Flow Stucture on Lateral Heating of a Stratified Fluid," *Atmospheric and Oceanic Physics*, Vol. 12, 1976, pp. 1191–1200.

16 Oster, G., "Density Gradients," *Science American*, Vol. 212, 1965, pp. 70–76.

17 Turner, J. S., "The Coupled Turbulent Transports of Salt and Heat Across a Sharp Density Interface," *International Journal of Heat and Mass Transfer*, Vol. 8, 1965, pp. 759–767.

18 Wirtz, R. A. and Reddy, C. S., "Heat and Mass Transport Across a Diffusive Interface Bounded by Turbulent Convecting Regions," *International Journal of Heat and Mass Transfer*, Vol. 19, 1976, pp. 471–478.

19 Takao, S. and Narusawa, U., "An Experimental Study of Heat and Mass Transfer Across a Diffusive Interface," *International Journal of Heat and Mass Transfer*, Vol. 23, 1980, pp. 1283–1285.

20 Hart, J. E., "On Sideways Diffusive Instability," *Journal of Fluid Mechanics*, Vol. 49, 1971, pp. 279–288.

21 Bejan, A. and Tien, C. L., "Laminar Natural Convection Heat Transfer in a Horizontal Cavity With Different End Temperatures," ASME JOURNAL OF HEAT TRANSFER, Vol. 100, 1978, pp. 641–647.

22 Huppert, H. E. and Turner, J. S., "Double-Diffusive Convection," *Journal of Fluid Mechanics*, Vol. 106, 1981, pp. 299–399.

An Application of the Optical Correlation Computer to the Detection of the Malkus Transitions in Free Convection

E. F. C. Somerscales
Rensselaer Polytechnic Institute,
Troy, N.Y. 12181
Assoc. Mem. ASME

H. B. Parsapour
IBM Corporation,
Charlotte, N.C. 28257
Mem. ASME

This paper presents the results of an investigation concerned with measurements of the scale-size of the flow patterns near the so-called Malkus transitions. The flow patterns in a heated fluid layer were photographed at various Rayleigh numbers and these photographs subjected to quantitative analysis using an optical correlation computer. The results showed that the method provides a very sensitive technique for locating the transitions. Transitions reported by other investigators have been confirmed for Rayleigh numbers between 5.0×10^3 and 1.0×10^6, and an additional, previously unobserved, transition has been detected. Heat-transfer measurements were also made. This data demonstrated the limitations, compared to the optical method, of this approach to the detection of transitions.

Introduction

The transition points in the heat-transfer curve first reported by Malkus [1] have been related to the development of turbulence in horizontal fluid layers in gravitational fields. Turbulence in such systems is of particular interest because its growth can be much more easily observed and characterized than in the cases of pipe and channel flows.

In spite of numerous investigations to date, the existence of the Malkus transitions is still controversial because the changes in the slope of the heat-transfer data used to find these transitions have been small relative to the precision and accuracy of the measurements, and have therefore been challenged on various grounds.

The present study was designed to independently check the existence of the transitions using an optical correlation technique. This technique has been shown to be quite effective in quantitatively characterizing such diverse systems as solar granulations, free convection, and turbulent two-phase flows. The optical correlation computer used here measured the scale size of the flow patterns in the heated fluid layer. This scale size will be seen to be Rayleigh number dependent, and its characteristic behavior will be used to find the transition points.

Previous Investigations—Theoretical

The essential problem in devising a theory of turbulence is the calculation of such quantities as the distributions of the mean temperature and the mean velocity, and, hence the determination of the shear stress and heat transfer at the boundaries of the system.

It is the usual practice to express the temperatures and velocities as the sum of a mean part and a fluctuating part. However, on introducing these into the governing equations, it is found that there are always more unknowns than equations. In these circumstances assumptions must be made to obtain a solution. One such set of assumptions was proposed by Malkus [1] in 1954. These were based on experimental observations that he had made of the flow in a heated fluid layer.

Malkus's experiments involved the measurement of the relation between the heat transfer through a fluid layer and the temperature difference between the upper and lower surfaces. He found that the relation between the heat transfer and the Rayleigh number (Ra), which is a dimensionless temperature difference, was not smooth but had sharp changes in slope at particular Rayleigh numbers[1] (see Table 1). Malkus associated the slope changes with transitions from one type of fluid flow and temperature distribution to another velocity and temperature field. Specifically, he proposed that at the transition Rayleigh numbers additional solutions of the governing equations became unstable, and in doing so contributed an extra amount of transferred heat. The appropriate solution to the governing equations therefore seemed to depend on a stability criterion.

In the solution the horizontal flow field was assumed to be spatially periodic and to be generated by the solution of the marginal stability of a disturbance on a linear temperature distribution. According to Malkus's calculations [3], as the Rayleigh number increased successive solutions were added to the complete solution. The calculated heat transfer then had the discrete character required by observation and the transitions occurred, within a relatively large uncertainty, at the same Rayleigh numbers as observed in the experiments.

The use by Malkus of linear stability theory to calculate wave numbers in a turbulent flow is not physically very satisfactory. In addition, Malkus also required that the wave numbers correspond to maxima in the heat transfer and that the temperature gradient in the fluid layer nowhere be negative. Both these requirements have been shown to be incorrect on experimental [4, 5] and theoretical grounds [5]. In fact, no criterion for wave number selection has yet been found. On the other hand, the appearance of successive modes in the heat transfer is plausible in view of Malkus's experimental observations. This prompted Howard [6] to investigate the development of turbulence using those elements of Malkus's theory that seem physically realistic. This approach to turbulent flow in a heated fluid layer has been extended by Busse [7] and by Chan [8]. The calculations by Chan, which depend on a limited number of simplifying assumptions, are in quite good agreement with the experimental data on the heat transfer through a heated fluid layer. In these circumstances it seems reasonable to conclude that, even though Malkus's calculations are in many ways

Contributed by the Heat Transfer Division and presented at ASME Winter Annual Meeting, Chicago, Illinois, November 16–21, 1980. Manuscript received by the Heat Transfer Division March 23, 1981. Paper No. 80-WA/HT-27.

[1] Schmidt and Saunders [2] had earlier observed a slope change corresponding to the transition from laminar to turbulent flow.

Table 1 Comparison of the observed transition Rayleigh numbers reported in the literature

Transition No.	Malkus [1]	Catton (Theory) [9]	Willis & Deardorff [10]	Krishnamurti [11, 12]	Carrroll* [13]
1	1.7×10^3	1.708×10^3	1.75×10^3	1.75×10^3	1.7×10^3
2	1.8×10^4	1.761×10^4	2.4×10^4	2.2×10^4	2.3×10^4
3	5.5	7.57	5.6	6.0	5.5
4	1.7×10^5		1.8×10^5	1.79×10^5	1.3×10^5
5	4.25	2.20×10^5	4.1		
6	8.6	5.10	8.3		6.0
Prandtl No.	6.7	∞	0.71	>100	∞
Fluid	Water		Air	Silicone oil	Air (data extrapolated)

*Additional transitions were observed at $2.5 - 3.0 \times 10^3$, 5.0×10^3, 7.7×10^3, 1.3×10^4. These were all obtained from examination of the time variation of the temperature in the fluid layer.

Table 1, continued

Transition No.	Chu & Goldstein** [14]	Krishnamurti [15]	Brown [16]	Threlfall*** [17]	This investigation	
					Computer	Heat transfer
1		1.5×10^3		1.6×10^3		
		5.6	9.6×10^3	9.0		
2			2.6×10^4	2.8×10^4	2.2×10^4	2.3×10^4
3				5.0	6.0	5.4
				6.5		
4					1.5×10^5	
5				3.2×10^5	2.1	2.3×10^5
6	6.1×10^5				5.5	
Prandtl No.	6.7	6.7	0.71	0.8		~450
Fluid	Water	Water	Air	Helium		Silicone oil

**Data at higher Rayleigh numbers not included.
***Threlfall saw slight, unconfirmed transitions at Ra = 1.1, 1.6, 2.3×10^5 and 5×10^6
Note: The following experimental data are not included:
(*a*) Garon and Goldstein [17] (restricted to Rayleigh numbers higher than 5.9×10^7)
(*b*) Krishnamurti [15] (used mercury as the experimental fluid—see the section entitled "Results")

physically unsatisfactory, they have provided the essential features of the very important calculations of Howard [6], Busse [7], and Chan [8].

Although the theories of turbulent free convection and its development that are derived from Malkus's original observations give results that are in general agreement with experiment, there is still an element of uncertainty in this comparison. Malkus's heat-transfer data do not give entirely convincing evidence of the existence of the proposed transitions. The changes in the slope of the experimental curve relating the heat transfer to the Rayleigh number are slight, and, in view of the inherent uncertainty in the measurements, subject to various interpretations. Nevertheless, theoretical approaches to turbulence based on Malkus's work are very attractive, both intuitively and because of their computational advantages. Therefore, because Malkus's theoretical ideas rely strongly on the concept of heat-transfer transitions, it is very important to verify their existence and investigate their character.

Previous Investigations—Experimental

There have been a number of attempts to verify the observations of Malkus's original experiment. However, the existence of the transitions is still not generally accepted, and even where transitions have been shown unambiguously to exist, there is disagreement about their locations (see Table 1 which summarizes the observed transitions[2]). This situation arises from the difficulty of identifying changes in the heat transfer or other indicators of transitions, which would imply that more sensitive, and possibly more accurate techniques are required. The various experimental methods will be briefly examined in this section, and their shortcomings will be reviewed.

The experimental methods used, so far, to study free convection transitions may be classified as: heat-transfer measurements, temperature measurements in the fluid, and flow pattern observations. The use of the latter two methods supposes, as hypothesized by Malkus and supported by independent experimental observation, that heat-transfer transitions are accompanied by other observable changes in the fluid. For clarity and brevity, the various experimental methods are summarized in Table 2.

Of the methods presented in Table 2, the use of helium at cryogenic temperatures, as reported by Threlfall [17] and by Ahlers [20], are among the most interesting. The data are

[2]It should be noted that in reading this table, comparison between the transition points observed by the different experimenters is uncertain, and the relative positions of the various values of the transition Rayleigh numbers depend to some extent on the subjective judgment of the authors when compiling the table.

Nomenclature

C = specific heat
g = acceleration of gravity
k = thermal conductivity
L = fluid layer thickness
Nu = Nusselt number = $gL/(k\Delta T)$
Pr = Prandtl number = ν/α
q = heat-transfer rate per unit area
Ra = Rayleigh number
w = velocity fluctuation
$w\theta$ = horizontal average of the product $w\theta$
α = thermal diffusivity of the fluid
β = coefficient of volume expansion of the fluid
ΔT = temperature difference between lower (hot) and upper (cold) plates
θ = temperature fluctuation
λ = correlation scale size
λ_F = Fitzjarrald's [19] characteristic scale size
ν = kinematic viscosity of the fluid
ρ = density of the fluid

Table 2 Summary of methods used in experimental determinations of transition Rayleigh numbers

Method	Investigations	Measurement technique	Limitations of the technique
Heat transfer measurements	Willis & Deardorff [10]	Temperature gradient in fluid adjacent to upper and lower boundary surfaces measured by long, horizontal resistance thermometer wires	1. Ambiguities in locating heat-transfer transitions 2. Disturbance of flow conditions by resistance thermometer wires 3. Inefficient collection of data due to "line" measurement
	Chu & Goldstein [14]	Interferometric measurement of temperature gradient in fluid	Inefficient collection of data due to "line" measurement
	Brown [16] (see below)	Heat transfer inferred from measured vertical temperature difference across the fluid layer	Ambiguities in locating heat-transfer transitions
	Garon & Goldstein [18]	From power input to test chamber	
	Threlfall [17]	Heat transfer inferred from measured vertical temperature difference across a layer of cryogenic fluid (allows use of very sensitive gas thermometers)	Requires use of cryogenic fluids
	Ahlers [20]		
Temperature measurements in the fluid	Carroll [13]	Time record of temperature at different points in fluid	Qualitative method of identifying transitions
	Brown [16] (see above)	Spectra of θ determined from measurements of θ	1. Disturbance of flow conditions by temperature measurement probe 2. Ambiguities in interpreting spectra of θ in terms of transitions
	Fitzjarrald [19]	Spectra of $w\theta$ determined from measurements of w and θ	1 Disturbance of flow conditions by moving temperature measurement probe 2. Ambiguities in interpreting spectra of $w\theta$ in terms of transitions
Flow pattern	Krishnamurti [11, 12, 15]	Qualitative observation of the flow pattern	Qualitative method of identifying transitions
	Koschmieder & Pallas [21]	Width of rolls measured	Not suitable for random flow patterns

much more accurate and precise than can be obtained at room temperature, so the technique could be a most promising method for detecting Malkus transitions. However, even with this approach, Ahlers [20] did not observe heat-transfer transitions at Rayleigh numbers up to the maximum value (5.4×10^3) used in his experiments. This coincides with the results reported by Koschmieder and Pallas[3] [21] using conventional, noncryogenic techniques in esssentially the same range of Rayleigh numbers. On the other hand, Threlfall [17] did detect several heat-transfer transitions (see Table 1) up to the maximum Rayleigh number (2×10^9) used in his experiments. Although no transitions can be seen in Threlfall's plot of the Nusselt number against the Rayleigh number, transitions are seen when $Nu/Ra^{0.25}$ is plotted against the logarithm of the Rayleigh number. This suggests that even with the superior capabilities of the cryogenic technique, some form of data manipulation must be employed to ensure that transitions are detected.[4]

Both Threlfall and Ahlers noted temporal variations in the heat transfer and found that these underwent characteristic transitions. Threlfall associated this with a Malkus type transition at $Ra = 3.2 \times 10^5$.

It is clear from the experiences of Ahlers, Threlfall, Koschmieder and Pallas, and other investigators (see Table 1), that an ideal experimental system for investigating the Malkus transitions should avoid:

(*a*) the ambiguities associated with attempting to detect transitions using the relatively insensitive indicator provided by measurements of the relation between heat transfer and temperature difference;

(*b*) the insertion of probes into the fluid;

(*c*) the limitations of attempting to interpret temperature and velocity measurements in the fluid layer in terms of spatial spectral data;

(*d*) inefficient averaging of turbulent flow data;

(*e*) qualitative methods.

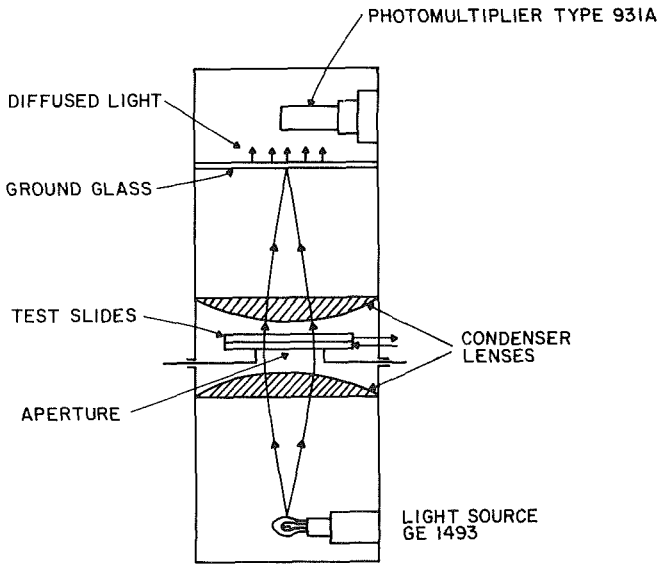

Fig. 1 Schematic diagram of the optical correlation computer (Lens: focal length = 12.7 cm, dia = 10.2 cm, Aperture diameter/maximum flow pattern scale size = 0.7)

A method that appears to have the characteristics of the ideal system involves the use of an optical correlation computer to quantitatively analyze photographs of the flow pattern in the fluid layer. The application of this device to experimental fluid mechanics was originally proposed by Kovasznay [22], and was used in the study of free convection flow by Somerscales [23]. It has also been used by Kretzmer [24] to analyze television pictures, and by Leighton [25] in connection with an investigation of the solar granulation.

[3] The results of these very careful experiments, as well as those of Ahlers, have not been included in Table 1 because of their inability to detect transitions.

[4] It is therefore possible that had Ahlers, and Koschmieder and Pallas plotted their data in the same way as Threlfall, they might have observed heat transfer transitions.

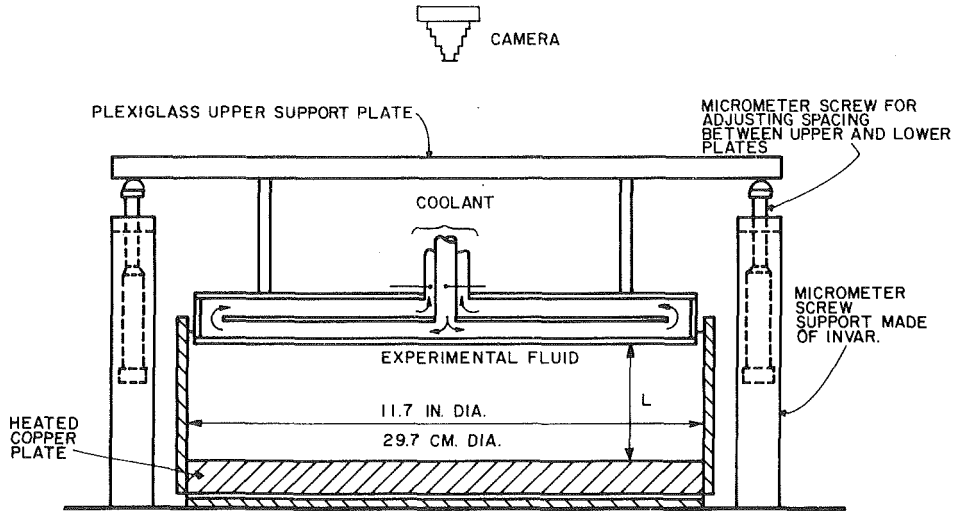

Fig. 2 Schematic diagram of the test chamber

The optical correlation computer measures a characteristic scale size of a photographically recorded flow pattern [22–26]. If the Malkus transitions are related to changes in the flow field, as suggested by Malkus [1] and by the experiments of Krishnamurti [11, 12, 15], then it is hypothesized that this characteristic scale size should exhibit changes at the transition points. A plot of the characteristic scale size as a function of the Rayleigh number would then have features that can be related to the transitions. This paper describes the results of measurements which make use of this technique to study the Malkus transitions. The optical correlation computer used in the experiments, which was based on a design due to Kretzmer [24], is shown schematically in Fig. 1.

Experimental Plan

The experiments in this study were designed to examine the Malkus transition points by means of quantitative measurements of the flow pattern photographs using the optical correlation computer. The particular objectives of the research were: (*a*) to investigate in detail the possibility of detecting transitions by this method, and the nature of, and the repeatability of the data obtained; (*b*) to compare the data on transitions obtained from the optical correlation computer with that obtained from heat-transfer measurements and visual observation of the flow pattern. This second objective was intended to provide supporting evidence for the validity of the optical method and, in the case of the visual observations, to demonstrate the physical basis of the transitions.

In the experiments, the Rayleigh number was maintained constant so as to ensure that conditions in the fluid layer were stationary. Photographs were made of the flow patterns in the fluid layer. These photographs were then analyzed on the optical correlation computer which provided a characteristic scale size for each recorded flow pattern. The scale sizes were then plotted as a function of the Rayleigh number. The resulting graph was examined for changes in the scale size which might indicate transitions in the flow pattern, and, hence, in the rate of heat transfer. The observed transitions were compared with those obtained by Malkus and by other experimenters. The rate of heat transfer through the fluid layer was also measured at the same time as the photographs were taken, and the plot of the rate of heat transfer against the Rayleigh number was examined for evidence of Malkus transitions.

Experimental Apparatus

The test chamber used in the experiments has been designed so that the experimental conditions are as close as possible to the assumptions of the theories. The theoretical assumptions are:

(*a*) The fluid is of infinite horizontal extent.

(*b*) The temperature of the upper and lower bounding surfaces is horizontally uniform.

(*c*) The upper and lower bounding surfaces are perfectly conducting, rigid plates.

The test chamber, which is shown in Fig. 2, consists of a cylindrical container with a heated, copper plate at the bottom, "Plexiglas" side walls, and a transparent upper cooled plate to allow observation of the flow in the chamber. The spacing between the upper and lower plates can be varied to allow the Rayleigh number to be changed. With a maximum spacing between the surfaces of 2.5 cm and an effective chamber horizontal diameter of 29.7 cm, the minimum aspect ratio is 12. This has been shown by Deardorff and Willis [28] to be large enough to ensure that the fluid layer is effectively of infinite lateral extent, as required by the theory. Experiments by Catton and Edwards [29], and by Hollands [30] are in agreement with this conclusion.

The lower copper plate is heated electrically, and measurements of the plate temperature have shown that the horizontal variation of temperature in this plate does not exceed 0.06°C. This corresponds to a horizontal temperature gradient of 0.002°C per cm, which is considered negligible.

The transparent upper surface is made of glass 0.6 cm thick. The ratio of the thermal conductivity of the glass to the thermal conductivity of the experimental fluid (450 centistoke silicone oil) is 7.56. This is not large enough to treat the upper surface as perfect conductor, but the available evidence [31] suggests that the effect of the conductivity ratio is only important under extreme conditions, e.g., when using mercury as an experimental fluid with a glass upper surface.

A "Plexiglas" water box is attached to the glass plate forming the upper surface of the test chamber. This box is divided in two by a horizontal "Plexiglas" baffle (see Fig. 2). The cooling water enters at the center and flows radially outward on the underside of the baffle. It then passes upward through small holes at the outer periphery of the baffle and returns radially inward on the upper side of the baffle. The water leaves by an exit tube concentric with, but outside the inlet tube.

The temperature uniformity of the plate was estimated by measuring the temperature difference between the entering and leaving streams of water which was found to be 1.5°C on the average. Extreme values were 3°C (test 6) and 0.2°C (test 17). This variation could probably be minimized by increasing

Table 3 Relation of flow pattern to Rayleigh number

Ra	Test No.	Classification of flow
5.02×10^3	19	
5.26	17	
6.57	18	Steady two-dimensional flow
7.46	20	
8.86	13	
1.14×10^4	11	
1.64	10	
1.91	12	
2.68×10^4	9	
3.19	8	
3.93	7	
4.10	14	Steady three-dimensional flow
4.65	15	
4.80	3	
5.07	38	
5.82	16	
6.06×10^4	39	
6.53	40	
7.55	21	Time periodic three-dimensional flow
9.85	22	
1.03×10^5	23	
1.05	24	
1.09	25	
1.33	4	
1.57×10^5	26	
1.61	24	
1.79	1r	Unsteady I
1.93	27	
2.04	5	
2.17	1	
2.36×10^5	30	
3.00	31	Unsteady II
3.93	7	
4.56	6	
5.21	32	
6.01	33	
7.23	34	
8.28	35	Turbulent
9.03	36	
9.65	37	

the cooling water flow rate as the heat flux increased, but limitations of the apparatus prevented this. Although the upper surface temperature variation is not as small as that observed on the bottom plate, it is considered satisfactory when the horizontal temperature gradient of 0.06°C per cm is compared with the corresponding average vertical temperature gradient of 20°C per cm. This is supported by the perfectly circular rolls observed by Dougherty [32] and Parsapour [33] in the present test apparatus with a number of different experimental fluids and test chamber aspect ratios at the initiation of flow. Koschmieder [31] has stated that irregularities in the initial flow patterns indicate large temperature nonuniformities in the horizontal boundary surfaces, so that these surfaces cannot be treated as isothermal.

Experimental Procedure

In these experiments the optical correlation measurements were made using photographs obtained with the experimental parameters (Rayleigh number, and, hence, the Nusselt number) fixed during each run. That is, at the beginning of each run the cooling water flow and the bottom plate electric heater were turned on. The power input to the heater was adjusted, on the basis of previous experience, to ensure that the desired final, steady Rayleigh number, with the given fluid and plate spacing, was attained. When steady conditions were achieved, as indicated by the temperatures of the upper and lower plates, and at points in the insulation surrounding the test chamber, the flow pattern was photographed. Forty separate runs were made in order to cover the Rayleigh number range from 5.0×10^3 to 1.0×10^6.

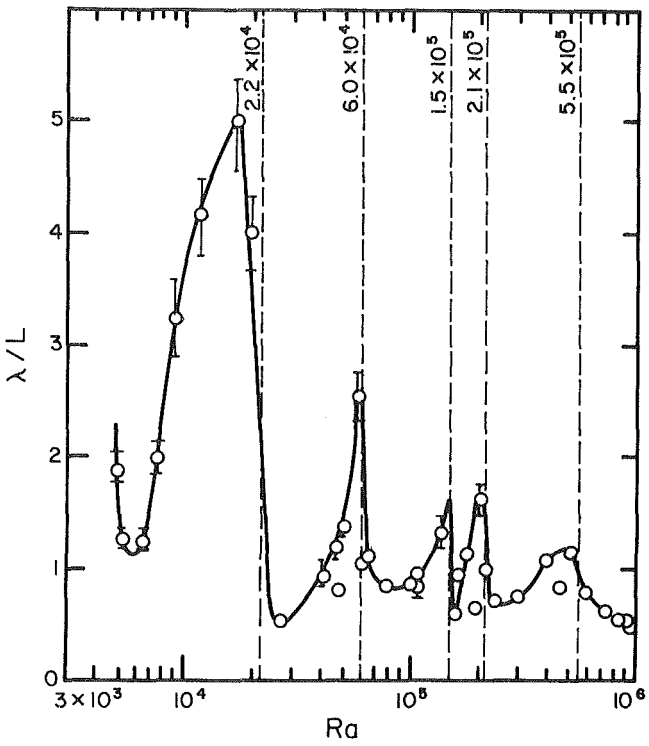

Fig. 3 Scale parameter (λ/L) as a function of the Rayleigh number (Ra) (error bars not shown are within the circle)

The rate of heat transfer (q) through the fluid was obtained from measurements of the power input to the bottom plate electric heater. The heat transfer was obtained by correcting the power input for the heat leakage from the apparatus using a heat loss model for the apparatus devised by Dougherty [32].

The Rayleigh number was evaluated using fluid properties calculated at the average of the upper and lower plate temperatures. The lower plate temperatures were measured by calibrated copper-constantan thermocouples with measuring junctions located to within 0.03 cm of the copper-liquid interface. The temperature of the liquid-glass interface of the upper, glass surface was estimated from a measured relation between the average temperature of the cooling water flowing through the water box and the heat flow through the fluid layer.

The flow pattern was made visible by the addition of a small quantity of aluminum dust to the experimental fluid. Observation of the flow over extended periods and comparison with flow patterns obtained by other techniques, such as the shadowgraph [27], suggested that the flow patterns revealed by the use of aluminum dust could be meaningfully interpreted in terms of the fundamental scale parameters of the flow field.

Results

This section is divided into subsections covering discussions on the measurements with the optical correlation computer, flow pattern observations, and heat-transfer measurements. Each subsection includes a comparison of the results with those of other investigators and a discussion of the significance of the measurements.

Optical correlation computer measurements. The optical correlation computer provides for each photograph a characteristic scale size (λ) for the flow pattern [22-24]. These scale sizes, divided by the fluid layer depth (L), are plotted as a function of the Rayleigh number in Fig. 3. The following three features can be noted from this figure:

(*a*) The scale parameter changes in an irregular oscillatory manner with the Rayleigh number.

(*b*) At particular values of the Rayleigh number the scale parameter undergoes a very sharp drop in value.

(*c*) The overall trend of the scale parameter is to decrease as the Rayleigh number increases.

These observations are interpreted as indicating transitions in the flow pattern occurring at the Rayleigh numbers where a peak in the scale parameter is observed. Five such transitions (peaks) can be detected (see Table 1) within the range of Rayleigh numbers (5×10^3 to 9.7×10^5) covered by the tests, and apart from one (at Ra = 1.5×10^5), these are in good agreement with the observations of other investigators.

It should be remarked that no hysteresis in the wavelength, analogous to the observations of Krishnamurti [15], was detected because the measurements were made under steady state conditions.

On the basis of visual examination of the flow patterns (see the next subsection) and comparison with the optical corrrelation computer measurements, increasing magnitude of the scale parameter was taken to indicate increasing "order" in the flow. So, the transitions were considered to be preceded, as the Rayleigh number increases, by a flow of increasing order that suddenly, at the transition, breaks down into a more disordered flow. The overall decreasing trend in the scale parameter would then indicate that as the Rayleigh number increases, the flow becomes more and more disordered. The limitations imposed by the experimental fluid and the apparatus did not allow the Rayleigh number to exceed 1×10^6. However, it is assumed that the scale parameter would continue its oscillatory, decreasing trend until some minimum value is reached.

The oscillatory, decreasing trend of the scale parameter was also experimentally observed in Fitzjarrald's [19] study of turbulent convection in air. However, the dimensionless spatial scale parameter (λ_F/L, λ_F is defined below) reported by Fitzjarrald in the Rayleigh number range from 1×10^6 to 1×10^7 is about six times as large as the value that would be inferred from the results shown in Fig. 3. This may be a consequence of Fitzjarrald's experimental technique. Fitzjarrald's scale parameter was the median spectral wavelength (λ_F) obtained from a spectral analysis of $w\theta$, where w and θ were measured by a moving probe. The probe could have disturbed the flow. In addition, the observed values of $\overline{w\theta}$ were based on a limited number (100) of line traverses of the fluid layer by the moving probe. Because the area average provided by the optical correlation computer is much more efficient than averaging over a succession of probe tranverses, and because observation of the flow pattern does not disturb the flow, we would prefer to conclude that the horizontal scale of motion at Ra = 1×10^6 is approximately equal to the layer depth, as shown in Fig. 3.

The difference in the Prandtl numbers between air (Pr = 0.7) used by Fitzjarrald and the silicone fluid used here (Pr = 450) could also account for the difference in the spatial scale parameter.

Koschmieder and Pallas [21] made measurements, but not with the optical computer, of the wavelength of the flow patterns for Rayleigh numbers between 3.2×10^3 and 1.2×10^4. Their reported dimensionless wavelengths lay on a straight line with a minimum value of unity and a maximum value of 1.5. This places these results in the vicinity of the first minimum of Fig. 3. The reason for the difference between the results reported here and those presented by Koschmieder and Pallas is not clear but could be, as in the case of Fitzjarrald's measurements, associated with the Prandtl number of experimental fluids (511 and 916).

Comparison cannot be made with other wavelength measurements [11, 12, 15], becasue they refer to lower Rayleigh numbers in which no transitions are to be expected.

The transition points observed in the experiments are compared with those of other investigators in Table 1. There seems to be general agreement on the Rayleigh number for the second transition point. The optical correlation data support the existence of a change in the fluid flow, and hence, a change in the rate of heat transfer at Ra = 2.2×10^4. The next break point in the present study occurs at Ra = 6.0×10^4. There is close agreement among the other reported results, except that Threlfall [17] has points at Ra = 5.0×10^4 and Ra = 6.5×10^4, that is, on either side of the transition observed in the experiments reported here.

The fourth transition point occurs at Ra = 1.5×10^5. Only Carroll's [13] study has a transition point at this Rayleigh number. Malkus [1], Willis and Deardorff [10], and Krishnamurti [11, 12] reported transition points at around Ra = 1.8×10^5. The increasing difficulty in distinguishing slope changes in the heat-flux data at higher Rayleigh numbers must have led to this variation.

The transition detected by the optical correlation computer at Ra = 2.1×10^5 has been predicted theoretically by Catton [9], but it has not been observed by other experimenters.

The last transition point recorded in this study at Ra = 5.5×10^5 was again predicted by Catton [9]. Fitzjarrald [19] also observed in his experiments a sharp change in the predominant scale of the motion at this point. Other experimenters, Threlfall [17] at Ra = 3.2×10^5. Malkus [1] at Ra = 4.25×10^5, Willis and Deardorff [10] at Ra = 4.1×10^5, have observed transitions at slightly lower Rayleigh numbers than 5.5×10^5. There have also been transitions reported at slightly higher Rayleigh numbers, Carroll [13] at Ra = 6.0×10^5, and Chu and Goldstein [14] at Ra = $6.1 \times$

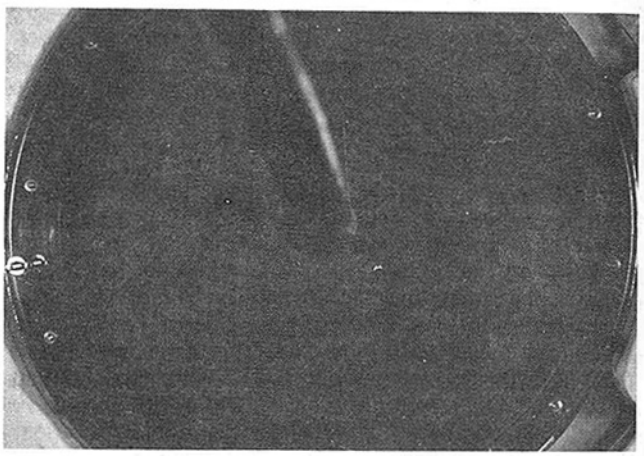

Fig. 4 Test 20 (Ra = 7.46×10^3)

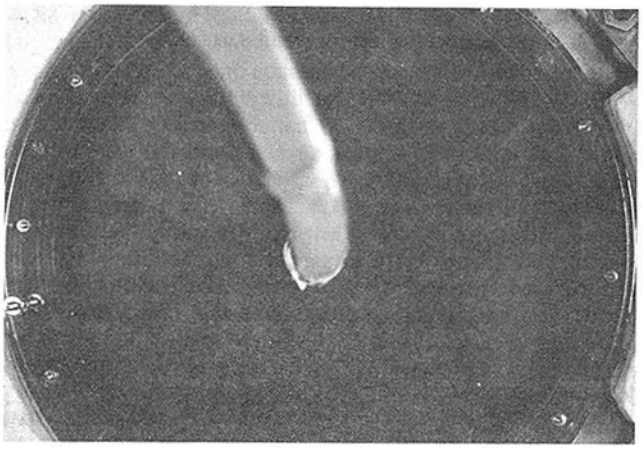

Fig. 5 Test 12 (Ra = 1.91×10^4)

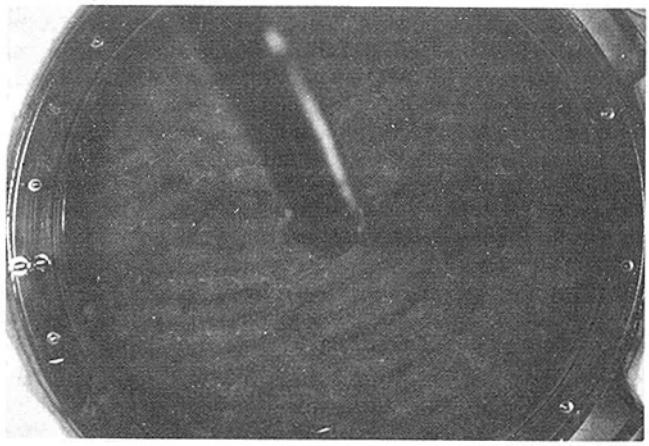

Fig. 6 Test 16 (Ra = 5.82 × 10^4)

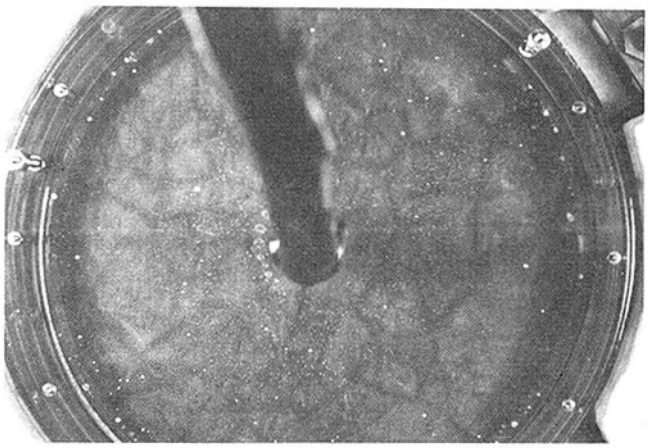

Fig. 7 Test 32 (Ra = 5.21 × 10^5)

10^5. It is clear that experimental difficulties in detecting the transitions as the Rayleigh number increases have contributed to this uncertainty in the reported values. The optical correlation computer also shows a declining sensitivity in its ability to detect transitions as the Rayleigh number increases. However, as can be seen in Fig. 3, the sensitivity of the method is nevertheless much higher than the heat-transfer method at Rayleigh numbers in the range 3×10^3 to 1×10^6.

Flow Patterns. The photographs taken during the experiment were visually examined as well as being subjected to analysis on the optical correlation computer. The observed flow patterns could be broadly classed as steady two-dimensional flow, steady three-dimensional flow, time periodic three-dimensional flow, unsteady flow I, unsteady flow II, and turbulent flow, the division between the classes being determined by combining the results of visual examination with the transition Rayleigh numbers obtained from the optical correlation computer. The flow pattern observations are summarized in Table 3.

In the lowest Rayleigh number range the dominant pattern consisted of two-dimensional rolls. The general alignment of the rolls appeared to be determined by the cylindrical geometry of the test chamber (see Fig. 4, test 20). Except for some minor variations, this two-dimensional flow pattern was maintained up to a Rayleigh number of 1.91×10^4. A count of the number of rolls in the layer showed that this number dropped as the Rayleigh number increased. Koschmieder and Pallas [21] have also reported the loss of three rolls as the Rayleigh number was varied from 1.8×10^3 to 1×10^4. This decrease in the number of rolls is reflected as an increase in the scale parameter measured by the optical computer.

For the Rayleigh numbers above 8.86×10^3 the rolls were no longer circular, but were aligned parallel to each other

Fig. 8 Test 34 (Ra = 7.23 × 10^5)

diagonally across the layer. A closer observation also revealed faint indications of changes in the flow starting at a Rayleigh number of 1.14×10^4. Although the overall character of the rolls remained dominant up to a Rayleigh number of 1.64×10^4, it was quite clear that three-dimensional cells were forming within the rolls. At a Rayleigh number of 1.91×10^4 (see Fig. 5, test 12), cells could be distinguished outside of the roll boundaries in some sections of the layer. The sharp drop in the autocorrelation scale parameter, λ, for this test reflects this change in the character of the flow, and therefore defines the critical Rayleigh number at which the transition to three-dimensional flow takes place.

In the series of tests starting at a Rayleigh number of 2.68×10^4, the three-dimensional flow was found to totally dominate the flow pattern in the layer (see Fig. 6, test 16). Various changes in the size and shape of the cells also took place that could not be characterized by visual observation of the flow patterns. However, the autocorrelation scale parameter showed a definite increase in this range of Rayleigh numbers (Fig. 3).

Krishnamurti [11] has suggested that at a Rayleigh number of 6.0×10^4, the three-dimensional steady flow becomes time periodic. The time dependence was said to be of two forms: (*a*) a slow tilting of the cell boundaries with a time scale of the vertical diffusion time, (*b*) an oscillation with a time scale determined by the orbit time of the fluid around the cell. The method of using the autocorrelation technique in the test reported did not allow the time periodic behavior of the flow to be studied. However, the scale size did indicate a transition at a Rayleigh number of 6.0×10^4.

For the Rayleigh numbers between 6.06×10^4 and 1.33×10^5, the main change in the fluid flow pattern seemed to be towards increasingly larger cells. The cell boundaries were sharply defined, and the flow remained three-dimensional in character. The visual observation of the flow patterns in this Rayleigh number range and the next series of tests starting with a Rayleigh number of 1.57×10^5 did not allow the prediction of a transition point at a Rayleigh number of 1.5×10^5 as shown in Fig. 3. Similarly, the next critical point at a Rayleigh number of 2.1×10^5 could not be predicted from the comparison of the photographs of tests 5 and 1. The sensitivity of the optical autocorrelator, which was able to detect these transitions is, therefore, again demonstrated by these examples.

As higher Rayleigh numbers were reached, the definition of the flow pattern near the side walls progressively decreased. The cells themselves also became less regular in shape and size. Furthermore, the number of such cells decreased until turbulent flow became dominant in the final tests. The outward orientation of the pattern in those tests are similar to Nielsen and Sabersky's [34] observations in their square

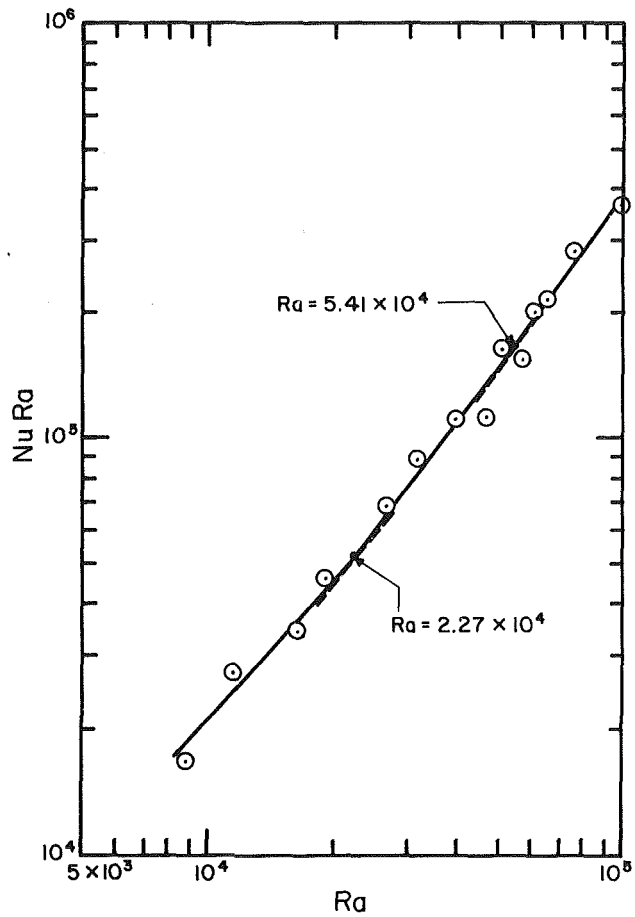

Fig. 9 Dimensionless heat flux (NuRa) plotted against the Rayleigh number (Ra), showing two possible transitions

shaped chamber and must be independent of the geometry of the test chamber.

The last transition point was found by the optical computer to be at Ra = 5.5×10^5. Comparison of the photographs (see Fig. 7, test 32, and Fig. 8, test 34) from tests 32 and 34 on both sides of this Rayleigh number lends visual support for such a transition. The well defined cells present in test 32 are completely gone in test 34. And tests at higher Rayleigh numbers show an increasingly larger degree of turbulence.

Heat Transfer Measurements. Heat-transfer measurements were made for two purposes: (*a*) to compare the conduct of the experiments reported here with other investigations of this type; (*b*) to obtain data which would allow the detection of the transition points by the location of changes in the rate of heat transfer with changing temperature difference between the upper and lower plates, i.e., the conventional technique for detecting transitions.

The heat-transfer measurements were in excellent agreement with those reported by other investigators [9, 11, 12, 14, 21].

To investigate the transitions in the heat-transfer data, it was plotted as the product of the Rayleigh and Nusselt numbers against the Rayleigh number[5] on logarithmic paper. The product does not contain the temperature difference across the fluid layer, and, hence, the error associated with the determination of this quantity is eliminated.

The data were broken into groups bounded by the transition values determined from Fig. 3. Then, using a least-square fit technique, linear equations were determined for each section of the data. The intersection of these lines defined the transition points. A typical plot of the data is shown in Fig. 9. The transition points obtained in this way are shown in Table 1. Agreement with the transition Rayleigh numbers obtained by the optical correlation computer and by other investigators is satisfactory. However, it is clear that without prior knowledge, it would be very difficult to recognize any slope changes in the data.

Summary. The study of the photographs of these tests has shown that some of the critical flow transition points, such as the transition to three-dimensional flow at a Rayleigh number of 2.2×10^4, and transition to turbulent flow at a Rayleigh number of 5.5×10^5, can be visually verified. However, the less pronounced changes in the flow pattern cannot be detected unless the optical computer is employed. The determination of the transitions from heat-transfer measurements agreed with those obtained from the optical computer but prior knowledge of their location was desirable.

Error Considerations

The residual uncertainty of the quantities to be measured in the experiments must be sufficiently small to ensure two things. First, that the anticipated transitions in the characteristic scale size (λ) of the flow pattern can be unambiguously detected. Second, a meaningful comparison with the theoretical results must be possible.

The two main quantities to be measured were the Rayleigh number ($Ra = g\beta\rho CL^3\Delta T/\nu k$), and the dimensionless flow pattern scale size (λ/L). Heat-transfer measurements were also made, and these are presented in terms of the Nusselt number ($Nu = qL/k\Delta T$, where q = rate of heat transfer per unit area).

The following are the estimated residual uncertainties in the measured quantities:

Rayleigh number (Ra): ± 6 percent of measured value
Scale parameter[6] (λ/L): ± 8 percent of measured value
Nusselt number (Nu): ± 9 percent of measured value

The uncertainties in the first two quantities are considered small enough to ensure that significant changes in these parameters, arising from changes in the flow conditions in the fluid layer, could be identified (see error bars in Fig. 3).

The repeatability of the results was assured by the method used to obtain the data. Each data point was obtained, as described in the section "Experimental Procedure", by setting the spacing between the upper and lower plates in the test cell at the desired value, and allowing the apparatus to come to thermal equilibrium at a fixed heat input. In this way, every data point was obtained in a completely separate and independent experiment. In addition, measurements at a number of these settings were repeated at widely separated calendar dates. Many other data points were obtained during the intervening periods. The variation in the measured dimensionless scale parameter (λ/L) among these repeated data points was within the estimated uncertainty of ± 8 percent.

The repeatability of the optical correlation computer was tested by repeated measurement of the autocorrelation scale parameter from the photograph of a single experiment. The results were found to be identical within the uncertainty

[5] The data were also plotted as Nu/Ra^n against log Ra (n = 0.25, following Threlfall [17], and n = 0.33, following Denton and Wood [35]). However, for this approach to provide a satisfactory indication of heat-transfer transitions it is necessary that the Rayleigh number be varied by varying the spacing between the plates [35], but in the experiments reported here the Rayleigh number was changed by adjusting the temperature difference between the upper and lower plates. In consequence, the scatter in the data was too great to allow an unambiguous determination of the heat-transfer transitions.

[6] This estimate is based on the cumulative errors in the various steps of the procedure used to determine the scale parameter in the optical computer. No attempt was made to estimate the uncertainty introduced by the intrinsically random nature of the flow patterns.

established for this apparatus. Therefore, by ascertaining the repeatability of the individual data points in Fig. 3, the repeatability of the whole data set has been assured.

An important consideration in applying the optical correlation method to the photogaphs concerns the effect of extraneous objects, such as the input and output hoses, on the autocorrelation function. Every effort was made to ensure that the obstruction presented by the hoses was as small as possible. However, it was considered advisable to estimate their effect on the autocorrelation function. This was done by painting various shapes on two photographs of the fluid layer. The heights of the nonnormalized autocorrelation curves were found to be related directly to the size of the area covered by the obstruction. This is to be expected since this height is a measure of the mean square fluctuation of the light transmission [26]. However, the measured scale of the flow was unaffected by the shape of the obstruction.

Conclusions

This study has demonstrated the feasibility of applying an optical correlation computer to the detection of the transition points first reported by Malkus [1]. Transitions were detected at Rayleigh numbers of 2.2×10^4, 6.0×10^4, 1.5×10^5, 2.1×10^5, and 5.5×10^5. With the exception of the transition at $Ra = 1.5 \times 10^5$, the other values are in satisfactory agreement with the transition points obtained from heat-transfer measurements by the authors and by other investigators. It is therefore proposed that transitions occur in the flow and these are related to transitions in the heat transfer. However, the determination of the flow transitions, particularly if the optical correlation computer is used, is much easier than detecting the corresponding heat transfer transitions.

In view of the demonstrated effectiveness of the optical correlation computer in detecting transitions, it is believed that the transition reported at $Ra = 1.5 \times 10^5$ is a genuine transition point. The observation of this previously undetected transition is due to the sensitivity of the optical correlation computer method. The sensitivity of the technique was also manifested by the clarity of the changes in the scale parameter as measured by the optical correlation computer, and by the comparative weakness of the corresponding heat transfer transitions.

The experiments have also provided evidence that the transitions correspond to physically observable characteristics of the flow. However, with the possible exception of two points, the visual examination of the photographs of the flow patterns could not have identified the transition points.

Acknowledgments

This paper is based on a thesis for the degree of Doctor of Philosophy presented by one of us [Parsapour [33]] to the Rensselaer Polytechnic Institute in 1977. We would like to acknowledge the support of H. C. Van Ness, F. F. Ling, and G. M. Barthel, in connection with this work.

References

1 Malkus, W. V. R., "Discrete Transitions in Turbulent Convection," *Proceedings of the Royal Society of London*, Vol. 225A, 1954, pp. 185–195.

2 Schmidt, R. J. and Saunders, O. A., "On the Motion of a Fluid Heated from Below," *Proceedings of the Royal Society of London*, Vol. 165, 1938, pp. 216–228.

3 Malkus, W. V. R., "The Heat Transport and Spectrum of Thermal Turbulence," *Proceedings of the Royal Society of London*, Vol. 225A, 1954, pp. 196–212.

4 Somerscales, E. F. C. and Gazda, I. W., "Thermal Convection in High Prandtl Number Liquids at High Rayleigh Numbers," *International Journal of Heat and Mass Transfer*, Vol. 12, 1969, pp. 1491–1511.

5 Suo-Antilla, A. J. and Catton, I., "Large Amplitude Cellular Convection," ASME Paper No. 76-HT-32, 1976.

6 Howard, L. N., "Heat Transport by Turbulent Convection," *Journal of Fluid Mechanics*, Vol. 17, 1963, pp. 405–432.

7 Busse, F. H., "On Howard's Upper Bound for the Heat Transport by Turbulent Convection," ASME *Journal of Fluid Mechanics*, Vol. 37, 1969, pp. 457–477.

8 Chan, S. K., "Infinite Prandtl Number Turbulent Convection," *Studies in Applied Mathematics*, Vol. 50, 1971, pp. 13–49.

9 Catton, I., "Natural Convection in Horizontal Fluid Layers," *The Physics of Fluids*, Vol. 9, 1966, pp. 2521–2522.

10 Willis, G. E. and Deardorff, J. W., "Confirmation and Renumbering of the Discrete Heat Flux Transitions of Malkus," *The Physics of Fluids*, Vol. 10, 1967, pp. 1861–1866.

11 Krishnamurti, R., "On the Transition to Turbulent Convection: Part I—The Transition from Two to Three-Dimensional Flow," *Journal of Fluid Mechanics*, Vol. 42, 1970, pp. 295–307.

12 Krishnamurti, R., "On the Transition to Turbulent Convection: Part II—The Transition to Time-Dependent Flow," *Journal of Fluid Mechanics*, Vol. 42, 1970, pp. 309–320.

13 Carroll, J. J., "The Structure of Turbulent Convection," Ph.D. thesis, University of California, Los Angeles, 1971.

14 Chu, T. Y. and Goldstein, R. J., "Turbulent Convection in a Horizontal Layer of Water," *Journal of Fluid Mechanics*, Vol. 60, 1973, pp. 141–159.

15 Krishnamurti, R., "Some Further Studies on the Transition to Turbulent Convection," *Journal of Fluid Mechanics*, Vol. 60, 1973, pp. 285–303.

16 Brown, W. S., "Heat Flux Transitions at Low Rayleigh Number," *Journal of Fluid Mechanics*, Vol. 60, 1973, pp. 539–559.

17 Threlfall, D. C., "Free Convection in Low-Temperature Gaseous Helium," *Journal of Fluid Mechanics*, Vol. 67, 1975, pp. 17–28.

18 Garon, A. M. and Goldstein, R. J., "Velocity and Heat Transfer Measurements in Thermal Convection," *The Physics of Fluids*, Vol. 16, 1973, pp. 1819–1825.

19 Fitzjarrald, D. E., "An Experimental Study of Turbulent Convection in Air," *Journal of Fluid Mechanics*, Vol. 73, 1976, pp. 693–719.

20 Ahlers, G., "Low-Temperature Studies of the Rayleigh-Bénard Instability and Turbulence," *Physical Review Letters*, Vol. 33, 1974, pp. 1185–1188.

21 Koschmieder, E. L. and Pallas, S. G., "Heat Transfer Through a Shallow Horizontal Convecting Fluid Layer," *International Journal of Heat and Mass Transfer*, Vol. 17, 1974, pp. 991–1002.

22 Kovasznay, L. S. G., "Technique for the Optical Measurement of Turbulence in High-Speed Flow," *Heat Transfer and Fluid Mechanics Institute*, ASME, New York, 1949, pp. 211–222.

23 Somerscales, E. F. C., "Optical Statistical Measurements of Free Convection Flow Patterns," *Turbulence Measurements in Liquids*, edited by G. K. Patterson and J. L. Zakin, University of Missouri, Rolla, Mo., 1971, pp. 25–31.

24 Kretzmer, E. R., "Statistics of Television Signals," Bell System Technical Journal, Vol. 31, 1952, pp. 751–763.

25 Leighton, R. B., "The Solar Granulation," *Annual Reveiw of Astronomy and Astrophysics*, Vol. 1, edited by L. Goldberg, A. J. Deutsch, and D. Layzer, Annual Reviews, Inc., Palo Alto, California, 1963, pp. 19–40.

26 Somerscales, E. F. C. and Parsapour, H. B., "Simplified Theory of the Optical Correlation Computer," submitted to *Journal of Physics*, E, Scientific Instruments.

27 Silverston, P. L., "Warmedurchgang in waagrechten Flussigkeitsschicten," *Forschung auf dem Gebiete des Ingenieurwesens*, Vol. 24, 1958, pp. 59–69.

28 Deardorff, J. W. and Willis, G. E., "The Effect of Two-Dimensionality on the Suppression of Thermal Turbulence," *Journal of Fluid Mechanics*, Vol. 23, 1965, pp. 337–353.

29 Catton, I. and Edwards, D. K., "Effect of Side Walls on Natural Convection between Horizontal Plates Heated from Below," ASME JOURNAL OF HEAT TRANSFER, Vol. 89, 1967, pp. 295–299.

30 Hollands, K. G. T., "Natural Convection in Horizontal Thin-Walled Honeycomb Panels," ASME JOURNAL OF HEAT TRANSFER, Vol. 95, 1973, pp. 439–444.

31 Koschmieder, E. L., "Benard Convection," *Advances in Chemical Physics*, Vol. 26, edited by I. Prigogine and S. A. Rice, John Wiley and Sons, New York, 1974, pp. 177–212.

32 Dougherty, T. S., "Observed Flow Patterns at the Initiation of Convection in a Horizontal Liquid Layer Heated from Below," Ph.D. thesis, Rensselaer Polytechnic Institute, Troy, New York, 1972.

33 Parsapour, H., "A New Approach to the Detection of Malkus Transitions in a Horizontal Layer of Fluid," Ph.D. thesis, Rensselaer Polytechnic Institute, Troy, New York, 1977.

34 Nielsen, R. C. and Sabersky, R. H., "Transient Heat Transfer in Benard Convection," *International Journal of Heat and Mass Transfer*, Vol. 16, 1973, pp. 2407–2420.

35 Denton, R. A. and Wood, I. R., "Turbulent Convection Between Two Horizontal Plates," *International Journal of Heat and Mass Transfer*, Vol. 22, 1979, pp. 1339–1346.

R. C. Smith

W. M. Rohsenow
Fellow ASME

M. S. Kazimi
Mem. ASME

Department of Nuclear Engineering,
Massachusetts Institute of Technology,
Cambridge, Mass. 02139

Volumetric Heat-Transfer Coefficients for Direct-Contact Evaporation

An analytical model has been developed for calculating volumetric heat-transfer coefficients for direct-contact evaporation. Heat transfer is modeled using single droplet correlations for the Nusselt number, while the fluid dynamics are described by a drift-flux model. The analysis is divided into a preagglomerative and a postagglomerative stage on the basis of an assumed maximum value for the dispersed phase volume fraction. The analytical results showed good agreement with data obtained from an experimental direct-contact evaporator using cyclopentane and water.

Introduction

Direct-contact evaporation occurs when immiscible fluids are mixed under conditions resulting in the vaporization of one of the fluids. Because of the absence of solid walls between the fluids, the process has many advantages compared to conventional heat exchangers. Smaller temperature differences are required, and there are none of the problems associated with heat-transfer surfaces, such as corrosion or scaling. Consequently, direct-contact evaporation is an attractive process where driving forces are limited or where surface fouling is intolerable.

Considerable attention has been devoted to studying the phenomena involved when single droplets evaporate as they rise through a denser fluid. Sideman and Taitel [1] developed an analytical expression for the Nusselt number by solving the energy equation, assuming potential flow around a sphere containing vapor partially surrounded by the unevaporated liquid. They ignored heat transfer to the vapor and assumed that the thermal resistance was negligible in the liquid inside the two-phase droplet. Simpson, Nazir, and Beggs [2] postulated that oscillations of the droplet induced sloshing of the liquid inside the droplet, so that a thin film effectively coated the entire interior surface of the droplet. Furthermore, they rejected Sideman's assumption that the resistance of liquid inside the droplet is negligible. Their analysis and data appeared to support the claim that resistance inside the droplet is controlling. However, it is also possible to correlate their butane-water data satisfactorily with an empirical formula derived from neglecting the thermal resistance of the dispersed phase [3], similar to the formula by Klipstein [4], which was based on results from ethyl chloride in a varying mixture of glycerin and water. Letan [5] proposed that in a uniform system of liquid droplets or gas bubbles in a fluid heat transfer by wake shedding may dominate under laminar bulk flow conditions.

In multidroplet systems, direct-contact evaporation can generate two-phase flows with very large vapor velocities. Consequently, the usual problems associated with the analysis of phase transition processes are compounded by the chaotic nature of two-phase flows. Because of the motion of the interfaces between the phases, the process is better described in terms of volumetric heat-transfer coefficients. Sideman and Gat [6] conducted an experiment to investigate the operating characteristics of a spray column utilizing pentane and water. They measured the volumetric heat-transfer coefficient and average void fraction as a function of the pentane and water superficial velocities, the entrance and exit temperatures of the water and the depth of the water through which the pentane rose. Blair, Boehm, and Jacobs [7] conducted a similar study using refrigerant-113 and water. Other experiments have been performed to investigate the feasibility of direct-contact boilers using organic liquids for geothermal heat extraction.

While the experiments mentioned have yielded valuable data and experience concerning the industrial application of direct-contact evaporation, no universal model for volumetric heat transfer was introduced. There is today a growing demand for an analytical model for situations when empirical correlations do not exist. The purpose of this paper is to describe such a model which was also tested experimentally.

Analysis

Assumptions. The fundamental assumption in this mdoel is that multidroplet direct-contact evaporation can be described with single droplet correlations for the heat-transfer rate of individual droplets and a simple drift-flux formulation to describe the two-phase flow. Additionally, it is assumed that there are two stages in the process. In the preagglomeration stage it is assumed that the individual droplets behave independently of one another, while in the postagglomeration stage it is recognized that interference effects occur between the droplets when their volume fraction becomes significant. Accordingly, the analysis is divided into two steps—the preagglomeration stage and the postagglomeration stage.

The model is intended to yield the relationship between the rate of evaporation of droplets and their displacement from their source and site of nucleation, so that the volumetric heat-transfer coefficient may be calculated as a function of this displacement with the following equation (see Fig. 1 and Nomenclature):

$$h_v(z) = \frac{1}{z}\int_0^z A_b(z')n_b(z')h_b(z')dz' \qquad (1)$$

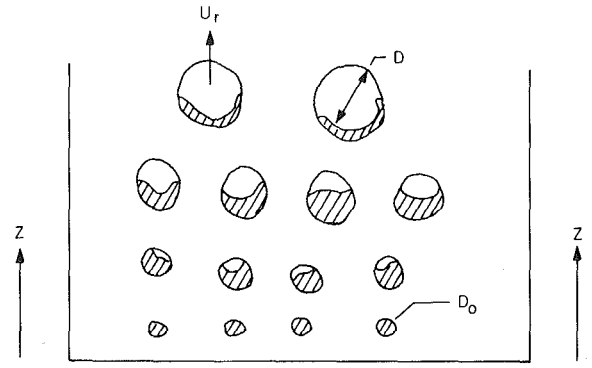

Fig. 1 Illustration of two-phase bubble size dependence on height

Contributed by the Heat Transfer Division for publication in the JOURNAL OF HEAT TRANSFER. Manuscript received by the Heat Transfer Division June 29, 1981.

The droplet surface area, A_b, the droplet number density, n_b and the droplet heat-transfer coefficient, h_b all depend on the instantaneous side of the evaporating droplets. Therefore, it simplifies subsequent calculations to express these quantities in terms of r, which is defined as the ratio of the instantaneous equivalent spherical diameter D to its (initial) value D_0 preceding nucleation. Hence, equation (1) becomes

$$h_v[z(r)] = [z(r)]^{-1} \int_{r_0}^{r} A_b(r') n_b(r') h_b(r') \frac{dz'}{dr} dr' \tag{2}$$

During both the preagglomeration stage and the postagglomeration stage it is assumed that the droplets do not depart from sphericity so significantly that the surface area cannot be approximated by

$$A_b(r) = \pi D_0^2 r^2 \tag{3}$$

Furthermore, during both stages it is assumed that the relative velocity between the droplets and continuous phase can be represented by the drift-flux model [8]

$$U_r = (1-\alpha)^{n-1} U \tag{4}$$

where the single droplet velocity is given by

$$U = U_0 r^y \tag{5}$$

and that the values of n and y during each stage can be selected to simulate the difference in flow characteristics of the preagglomeration and postagglomeration stages. The r dependence in equation (5) accounts for the effect of droplet size on the velocity. Smaller droplets are usually ellipsoidal in shape and their velocity is independent of size ($y=0$), while the larger cap-shaped droplets that result from evaporation have velocities approximately proportional to the square root of their diameter ($y=1/2$).

Further, it is assumed that the single droplet heat-transfer coefficient can be calculated from

$$\mathrm{Nu}_c = \frac{h_b D}{k_c} = \gamma \mathrm{Re}_c^x \mathrm{Pr}_c^{1/3} \tag{6}$$

in terms of the continuous phase properties, which implies that the thermal resistance of the dispersed phase is negligible. Although there is some disagreement concerning the validity of this assumption, which should depend on the relative thermophysical properties of the two components and the flow, equation (6) satisfactorily correlates the data from several experiements with values of x between 0.7 and 1.0 [3]. Furthermore, as evaporation proceeds, the thermal resistance within the droplet will decrease as the liquid film becomes thinner.

Finally, it is assumed that the temperature of the continuous component is spatially uniform and quasi-steady with respect to the evaporation time of an individual droplet.

Preagglomeration Stage. During the preagglomeration stage it is assumed that the droplets are relatively small and do not interfere significantly with one another; therefore, $n=1$ and $y=0$ in equations (4) and (5) during this stage.

The number density of droplets in the preagglomeration stage must be constant since the droplet velocity is constant and droplets neither coalesce nor fragment during this stage. Hence,

$$n_b(r) = n_{b0} \tag{7}$$

during the preagglomeration stage. It simplifies subsequent calculations to define a dispersed phase volume fraction by

$$\alpha(r) = (\pi/6) D_0^3 n_b(r) r^3 \tag{8}$$

The relationship between r and z in equation (2) can be determined by solving for the single droplet evaporation rate

$$\frac{d}{dz}(\rho_{dv} V_{dv}) = \frac{1}{U_0} \frac{\dot{q}}{L_d} \tag{9}$$

The dispersed phase vapor volume per droplet is given by

$$V_{dv} = (\pi/6) \frac{\rho_{dl} D_0^3}{\rho_{dl} - \rho_{dv}} (r^3 - 1) \tag{10}$$

while the heat-transfer rate per droplet is given by

$$\dot{q} = h_b(r) A_b(r) \Delta T \tag{11}$$

Substituting equations (10) and (11) into equation (9) yields

$$(\pi/2) \frac{\rho_{dl}\rho_{dv}}{\rho_{dl} - \rho_{dv}} D_0^3 r^2 \frac{dr}{dz} = \frac{h_b A_b \Delta T}{U_0 L_d} \tag{12}$$

Nomenclature

A = area
A_b = droplet surface area
B = parameter defined by equation (15)
C_p = specific heat
D_0, D = initial and instantaneous equivalent spherical diameter
h_b = individual droplet heat-transfer coefficient
h_v = volumetric heat-transfer coefficient
k = thermal conductivity
K_1, K_2 = constants defined by equations (38) and (39)
L_d = latent heat of vaporization of dispersed phase,
m = $(1-x)(y+1) + 1$
$\dot{m}_v$ = mass flow rate
n = drift-flux model parameter
n_b = droplet number density
Nu = Nusselt number, $\frac{h_b D}{k}$
Pr = Prandtl number, $\frac{\mu C_p}{k}$
r = equivalent spherical diameter ratio D/D_0
Re = Reynolds number, $\frac{\rho U D}{\mu}$
ΔT = temperature difference between continuous and dispersed phases
U_0, U, U_r = initial, instantaneous, and relative droplet velocities, $U_r = (1-\alpha)^{n-1} U$
V = volume
$\dot{W}$ = volumetric flow rate
z = axial displacement
α = void fraction (dispersed phase volume fraction)
γ = constant defined by equation (6)
ρ = density
μ = viscosity

Subscripts

a = value at onset of agglomeration
b = droplet values
c = continuous phase
d = dispersed phase
dl = dispersed phase liquid
dv = dispersed phase vapor
0 = initial value
max = maximum
v = volumetric

Superscripts

x = exponent of Re in equation (6)
y = exponent of r in equation (5)
m = $(1-x)(y+1)+1$

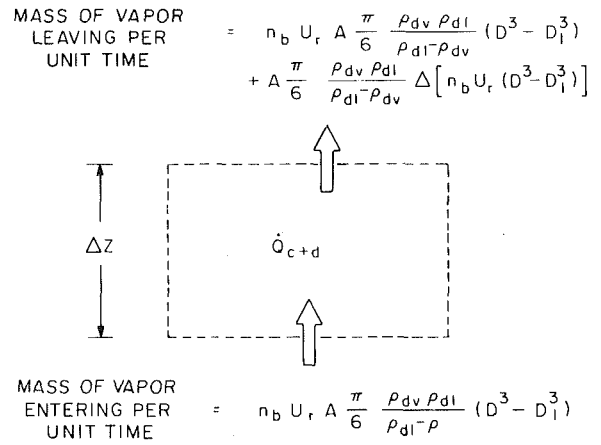

Fig. 2 Diagram of the postagglomeration energy balance calculation

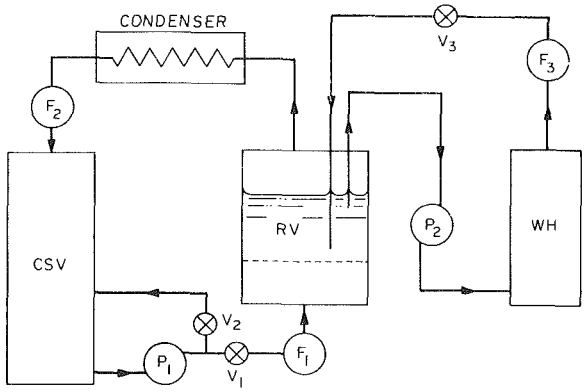

Fig. 3 Schematic of the apparatus used in the cyclopentane-water experiment: P = 0.1 MPa (CSV—cyclopentane storage vessel; RV—reaction vessel; WH—water heater; P—pump; V—valve; F—flow meter)

When equations (7) and (8), and (12) are combined with equation (2), the result is

$$h_v(r) = \frac{\alpha_0}{z(r)} U_0 \frac{L_d}{\Delta T} \frac{\rho_{dl}\rho_{dv}}{\rho_{dl}-\rho_{dv}} (r^3 - 1) \tag{13}$$

The distance z is expressed as a function of r by integrating equation (12). Substituting equations (3) and (6) into equation (12) and integrating the resultant equation yields

$$\frac{r^{2-x}-1}{2-x} = Bz \tag{14}$$

where

$$B = \frac{2h_{b0}\Delta T}{U_0 D_0 L_d} \frac{\rho_{dl}-\rho_{dv}}{\rho_{dl}\rho_{dv}} \tag{15}$$

Hence, equation (13) becomes

$$h_v(r) = 2m\alpha_0 \frac{h_{b0}}{D_0} \frac{r^3 - 1}{r^m - 1}; \quad m = 2 - x \tag{16}$$

In terms of the droplet travel distance:

$$h_v(z) = \frac{\alpha_0 U_0 L_d}{z\Delta T} \frac{\rho_{dl}\rho_{dv}}{\rho_{dl}-\rho_{dv}} [(1+mBz)^{3/m} - 1] \tag{17}$$

which can be also be expressed as

$$h_v(z) = 2m\alpha_0 \frac{h_{b0}}{D_0} \frac{(1+mBz)^{3/m} - 1}{mBz} \tag{18}$$

Postagglomeration Stage. From the preagglomeration analysis it is apparent that the dispersed phase volume fraction α will grow as the droplets evaporate and expand. This situation will almost certainly result in some degree of droplet coalescence. However, in most churn-turbulent, two-phase flows coalescence and fragmentation occur simultaneously, so that the resulting void fraction tends to change slowly with superficial vapor velocity compared to bubbly flow [6, 8, 9]. For this reason and because it greatly simplifies the model, it is assumed that the rate of coalescence in the postagglomeration stage results in a constant value of α. To satisfy this requirement, n_b must decrease (through agglomeration) rapidly enough to constrain $\alpha(r)$ in equation (8). Therefore, following the onset of agglomeration the rate of droplet coalescence is assumed to satisfy

$$n_b(r) = n_{b0}\left(\frac{r_a}{r}\right)^3, \quad r > r_a \tag{19}$$

where the subscript a indicates that the quantity is evaluated at the onset of agglomeration.

Again, the problem reduces to determining how r varies with z. Now, however, it is ncecssary to include the droplet interference effect (agglomeration) in the derivation of the desired relationship. Consider the simple sketch in Fig. 2, where r_l is the equivalent spherical diameter ratio the droplet would have if it were entirely liquid, and where Q_{c-d}, the rate of heat transfer from the continuous phase to the dispersed phase, is given by

$$\dot{Q}_{c-d} = h_b(\pi D_0^2 r^2) n_b \Delta T (A\Delta z) \tag{20}$$

A heat balance yields in the limit:

$$\frac{d}{dz}\left[U_r\left(1 - \left(\frac{r_l}{r}\right)^3\right)\right] = \frac{6h_b\Delta T}{rL_d D_0} \frac{\rho_{dl}-\rho_{dv}}{\rho_{dl}\rho_{dv}} \tag{21}$$

For the churn-turbulent flow of the postagglomeration stage $n = 0$ in equation (4) and $y = 1/2$ in equation (5); hence, equation (4) becomes

$$U_r = (1-\alpha_{\max})^{-1} U_0 \left(\frac{r}{r_a}\right)^{1/2} \tag{22}$$

Because of agglomeration, r_l is a function of z (and, hence, r) in equation (21). The relationship is derived by invoking the principle of conservation of dispersed mass flux which, in conjunction with equation (19), yields:

$$r_l^3 = \frac{U_0}{U_r(r)} \left(\frac{r}{r_a}\right)^3 \tag{23}$$

Substituting equation (23) into equation (21), and combining the result with equations (6) and (22) and integrating, yields:

$$\frac{r_a^{(x-1)/2}}{m_a}(r^{m_a} - r_a^{m_a}) = 12(1-\alpha_{\max})^{1-x} \frac{\rho_{dl}-\rho_{dv}}{\rho_{dl}\rho_{dv}} \frac{h_{b0}\Delta T}{U_0 D_0 L_0}(z - z_a) \tag{24}$$

where

$$m_a = \frac{1}{2}(5 - 3x) \tag{25}$$

During the postagglomeration stage, equation (2) assumes the form

$$h_v = \frac{1}{z_a + (z - z_a)}\left[\int_1^{r_a} A_b n_b h_b \left(\frac{dz}{dr}\right) dr + \int_{r_a}^{r} A_b n_b h_b \left(\frac{dz}{dr}\right) dr\right] \tag{26}$$

The first integral in equation (26) was evaluated in the preagglomeration stage

$$\int_1^{r_a} A_b n_b h_b \left(\frac{dz}{dr}\right) dr = \alpha_0 U_0 \frac{L_d}{\Delta T} \frac{\rho_{dl}\rho_{dv}}{\rho_{dl}-\rho_{dv}} (r_a^3 - 1) \tag{27}$$

The second integral is evaluated using equations (19), (21), and (22)

$$\int_{r_a}^{r} A_b n_b h_b \left(\frac{dz}{dr}\right) dr = \frac{\alpha_{\max} U_0}{1-\alpha_{\max}} \frac{L_d}{\Delta T} \frac{\rho_{dl}\rho_{dv}}{\rho_{dl}-\rho_{dv}} (r^{1/2} - r_a^{1/2}) \tag{28}$$

Finally, substituting equation (14) for z_a and equation (24) for $(z-z_a)$ into equation (26) yields

$$h_v(r) = 2\frac{h_{b0}}{D_0}\frac{\alpha_0(r_a^3-1)+\dfrac{\alpha_{\max}}{1-\alpha_{\max}}(r^{1/2}-r_a^{1/2})}{\dfrac{1}{m_0}(r_a^{m_0}-1)+\dfrac{r_a^{(x-1)/2}}{6m_a}(1-\alpha_{\max})^{x-1}(r^{m_a}-r_a^{m_a})} \tag{29}$$

As a function of z, equation (29) becomes

$$h_v(z) = \frac{2h_{b0}}{D_0 Bz}\left[\alpha_0\{(1+m_0Bz_a)^{3/m_0}-1\}+\frac{\alpha_{\max}}{1-\alpha_{\max}}\times\right.$$
$$\times\{(1+m_aBz_a+6(1-\alpha_{\max})^{1-x}m_aB(z-z_a))^{1/2m_a}$$
$$\left.-(1+m_aBz_a)^{1/2m_a}\}\right] \tag{30}$$

Discussion of the Parameters and Their Effects. Equation (18) reveals that $h_v(z)$ increases with ΔT in the preagglomeration stage, since B is directly proportional to ΔT and $3/m > 3/2$. This temperature difference dependence arises because the volumetric interfacial area increases with evaporation during the preagglomeration stage. Thus, although the basic mechanism is convective in nature, the evaporative expansion results in a positive temperature difference dependence in $h_v(z)$. Conversely, it can be demonstrated with equation (30) that $h_v(z)$ decreases with ΔT in the postagglomeration stage because agglomeration reduces the interfacial area faster than evaporation creates it.

Equations (14) and (24) indicate that the volume required for complete evaporation with a given dispersed phase flow rate, and ΔT increases with D_0^x because the surface to volume ratio decreases as D_0 increases. Consequently, the model predicts more efficient heat transfer as D_0 decreases with $U_0D_0^2$ and ΔT held constant (and a fixed orifice scheme).

The model does not specify a value of $\alpha_{\max}$. This value is determined with consideration of the agglomerative characteristics of the particular system being modeled. Furthermore, the validity of the model is questionable if reasonable values of $\alpha_{\max}$ fail to yield accurate heat-transfer rates. Consequently, it is important to verify that the experimentally observed void function is compatible with the value of $\alpha_{\max}$ that correlates the heat-transfer data.

Experiment

Because most of the previous work on multidroplet, direct-contact evaporation has been done in connection with potential applications to steady-state processes such as geothermal heat extraction and sea water desalination, the systems developed have used either cocurrent or countercurrent flow of the continuous phase relative to the dispersed phase. Unfortunately, such systems are inappropriate for testing the mathematical model developed in this work because both the flow and the temperature profile of the continuous phase are not accounted for in the model.

To achieve a uniform temperature in the stagnant continuous phase, there are basically two choices—the continuous phase can be heated volumetrically, or the experiment can be in the form of a short transient with a spatially uniform but temporally decreasing continuous phase temperature. In this work the second choice was selected.

Description of the Experiment. The experiment, which is depicted schematically in Fig. 3, consisted essentially of a three-phase, direct-contact heat exchanger and condenser in a closed loop arrangement.

Careful consideration was given to the selection of the materials for the experiment. In addition to being immiscible, the fluids were selected on the basis of their relative densities, saturation temperatures, and their price. After an extensive search through tables of thermophysical properties, it was concluded that an organic liquid in water was the best choice. Cyclopentane was selected because its saturation temperature of 49.6 °C precludes boiling at room temperature yet is low enough to allow a wide range for heating temperatures in water. The relevant thermophysical properties of cyclopentane and water are listed in Table 1.

The cycle commenced with pump P_1 drawing cyclopentane from the cyclopentane storage vessel (CSV) and injecting it into the lower cylinder of the reaction vessel (RV). The cyclopentane flow rate was monitored by a Fisher & Porter rotameter F_1 and adjusted with valves V_1 and V_2. Valve V_1 admitted the cyclopentane to the reaction vessel, while V_2 discharged the surplus flow back into the cyclopentane storage vessel. The two ball type valves were required to regulate the flow becasue the Viking rotary gear pump displaced a constant volume of cyclopentane.

The reaction vessel (see Fig. 4) consisted of two glass cylinders separated by a perforated 3/8 in. Lexan distribution plate. The Dow Corning glass cylinders were both 225 mm in dia, but the lower one had a length of 200 mm while the upper one was 300 mm long. The perforated plate was bolted between the flanges holding the cylinders together, and asbestos gaskets were used on both sides of the plate to prevent leakage. 1/4 in. Lexan plates and asbestos gaskets were also used to seal the top and bottom of the vessel. Threaded penetrations were drilled into the Lexan plates so that the copper tubing used could be secured with compression fittings.

Cyclopentane from the lower cylinder percolated through the 0.5 mm dia holes in the distribution plate into hot water in the upper cylinder. Thermal conduction through the distribution plate caused modest surface boiling of the cylopentane in the lower cylinder, so that it can be assumed that the cyclopentane droplets were at their saturation temperature upon contacting the hot water in the upper cylinder. At low flow rates, the cyclopentane tended to nucleate prior to detaching from the holes as discrete two-phase droplets.

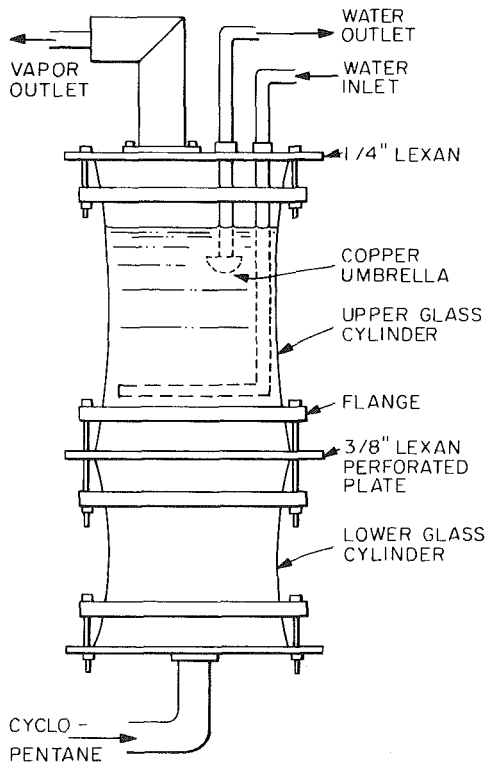

Fig. 4 The reaction vessel

However, at low values of ΔT, less than 7 °C, a significant fraction of the droplets failed to nucleate during their ascent. The size of the droplets at detachment tended to decrease with increasing ΔT, probably because the buoyant force overcame the force of surface tension sooner as the rate of evaporation increased. At higher flow rates the cyclopentane jetted through the holes and nucleated as the jets broke up. In fact, nucleation appeared to be responsible for the breakup of the jets, since the breakup was delayed considerably when the jets failed to nucleate. Cyclopentane vapor left the reaction vessel through a chimney and was consdensed in a shell and tube type heat exchanger cooled by cold tap water.

The water in the upper cylinder was preheated in a separate closed loop consisting of a thermostatically controlled 18-kW Chromalox electric water heater (WH), a Bell & Gossett circulation pump (P_2), a rotameter (F_3), and the reaction vessel. Suction from the pump drew water from the top of the reaction vessel through a 5/8 in. line into the heater. The hot water entered the upper cylinder of the reaction vessel about 4 cm above the distribution plate through a hoop shaped sparger constructed from 1/2 in. copper tubing. A series of sixty-four holes with diameters varying from 0.16 to 0.50 in. were drilled in the bottom of the hoop to ensure a circumferentially uniform flow distribution.

Instrumentation for the experiment consisted of Type E Chromel-Constantan Omega thermocouples in addition to the two rotameters and the graduated cylinder. Preliminary tests with five thermocouples positioned at different axial levels in the upper cylinder indicated there was no significant axial temperature gradient. In subsequent experiments only one thermocouple could be inserted far enough into the vessel to measure the temperature because the water depth had to be decreased to yield the necessary data. However, because the temperature measurements did not change significantly when the experiments were repeated, the measurements are reliable. The output from the thermocouples was monitored by an electronic Kaye Data Logger with an LED display and data printer.

Operation of the Experiment. The experiment was conducted as follows. P_2 and WH were activated to heat the desired volume of water to the desired temperature as monitored by the thermocouples. At the prescribed temperature P_2 and WH were shut off, P_1 was activated and V_1 and V_2 were adjusted to achieve the desired cyclopentane injection rate as measured by F_1. The temperature decline of the water was measured until the appearance of a layer of cylopentane on top of the water indicated that vaporization of the cylopentane was incomplete. The values of the water depth before and after swell, the cyclopentane injection rate and water temperature at the start of incomplete vaporization were finally recorded, and the run was complete. The experiment was repeated for several values of the water depth and the cyclopentane injection rate.

Results of the Experiment. Two series of experiments were conducted. The first series was conducted to establish the proper values of the constants in the formula for the heat-transfer coefficient of single droplets, equation (6). The second series was conducted to examine the effect of large void fraction and bubble agglomeration of the volumetric heat-transfer coefficient.

In the first series of experiments, cyclopentane was injected at a constant flow rate of 6.31 cm^3/s into the hot water through seven 0.5-mm dia holes arranged in a hexagonal array with a 5.0 cm pitch. The minimum water temperature required to vaporize the cyclopentane completely was measured as a function of the water depth. The large pitch was selected intentionally to minimize the influence the bubbles would have on one another, so that this series of experiments could be used to ascertain the proper values of

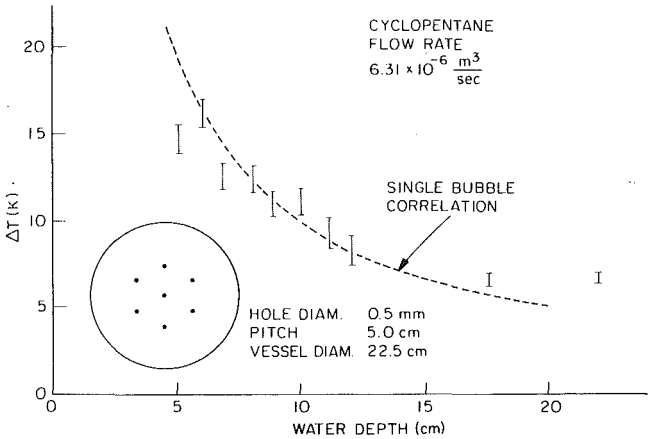

Fig. 5 Minimum water temperature superheat above cyclopentane saturation temperature (49.7 °C at P = 0.1MPa) as a function of water depth without agglomeration

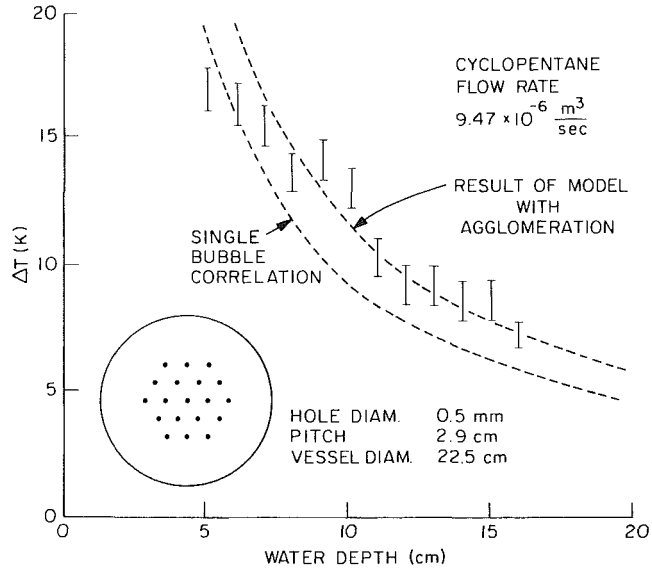

Fig. 6 Minimum water temperature superheat above cyclopentane saturation temperature (49.7 °C at 0.1 MPa) as a function of water depth with agglomeration

the constants in the formula for the heat-transfer coefficient for single bubbles. The measured values of water temperature required for complete evaporation in this series of experiments are presented in Fig. 5. The data and associated error bars bound the results of two independent runs.

In the second series of experiments, cyclopentane was injected into the hot water through nineteen 0.5-mm dia holes arranged in a hexagonal array with a 2.9-cm pitch. Again, the minimum water temperature necessry for complete evaporation was determined as the water depth was varied. The smaller pitch and larger number of holes used in this series of experiments resulted in larger void fractions and substantial agglomeration compared to the first series of experiments. The measured values of water temperature required for complete evaporation in this series of experiments are presented in Fig. 6. The measured values of the average void fraction (determined according to equation (36) in this series of experiments) are presented in Fig. 7. Again, the data and associated error bars bound the results of two independent runs.

The error bars on the data represent the authors' estimation of the error that results for the following reasons. The ΔT measurements are accurate within 10 percent relative error, while the $\bar{\alpha}$ measurements may involve as much as 15 percent relative error. Although the system contained impurities,

Table 1 The thermophysical properties of cyclopentane and water (at 50 °C)

Property	Units	Cyclopentane	Water
ρ_l	kg/m^3	688	1.0×10^3
ρ_v	kg/m^3	3.09	0.08
μ_l	kg/m-s	3.22×10^{-4}	5.17×10^{-4}
k_l	W/m-°C	0.126	0.645
C_{pl}	joules/kg-°C	1.30×10^3	4.19×10^3
L_d	joules/kg	4.19×10^5	2.38×10^6
Pr_l		3.33	3.36

Table 2 Results of the comparison of the model to the heat transfer data

Values of γ inferred from the single droplet data in Fig. 5

D_0 \ x	0.7	0.8	0.9	1.0
0.5	0.0153	0.00587	0.00225	0.000866
1.0	0.0249	0.0102	0.00420	0.00173
2.0	0.0405	0.0178	0.00785	0.00346

Values of α_{max} inferred from the multidroplet data in Fig. 6

D_0 \ x	0.7	0.8	0.9	1.0
0.5	0.0291	0.0289	0.0288	0.0288
1.0	0.105	0.104	0.102	0.102
2.0	0.309	0.302	0.293	0.287

droplet nucleation was delayed or absent in a significant fraction of the droplets as the temperature difference decreased. Below 7 °C, evaporation was incomplete irrespective of water depth; hence, this value of the temperature difference appears to represent the minimum superheat requirement for this system. Therefore, the formation of a layer of liquid cyclopentane above the water resulted from not only incomplete evaporation, but also from the accumulation of droplets that failed to nucleate. Furthermore, stratification of the layer is not immediate but results from the coalescence of tiny liquid droplets that accumulate gradually; consequently, there is a delay between the appearance and identification of incompletely vaporized cyclopentane. Finally, because of water temperature is decreasing steadily as evaporation proceeds, any lag in the thermocouple response or associated electronics will contribute to the error [3].

Comparison of Theory and Experiment

Single Droplet Heat-Transfer Coefficient. For complete evaporation in the absence of agglomeration, equation (14) yields:

$$\left(\frac{\rho_{dl}}{\rho_{dv}}\right)^{m/3} - 1 = \frac{7\pi}{2} \frac{mk_c \gamma \mathrm{Re}_0^x \mathrm{Pr}_c^{1/3}}{\dot{W} L_d \rho_{dv}} z\Delta T \tag{31}$$

where ρ_{dv} has been neglected compared to ρ_{dl} and $\dot{W}$ is the volumetic flow rate of cyclopentane through the seven holes in the distribution plate.

$$\dot{W} = 7\left(\frac{\pi}{4} D_0^2\right) U_0 \tag{32}$$

The Reynolds number is given by

$$\mathrm{Re}_o = \frac{4\rho_c \dot{W}}{7\pi\mu_c D_0} \tag{33}$$

Substituting $\dot{W} = 6.31$ cm^3/s from the first series of experiments and the appropriate thermophysical properties from Table 1 into equation (31) yields

$$m\gamma \mathrm{Re}_0^x z\Delta T = 583 \tag{34}$$

where the product $z\Delta T$ is expressed in units of cm-K. Figure 5 indicates that $z\Delta T$ is approximately 100 cm-K; hence, equation (34) becomes

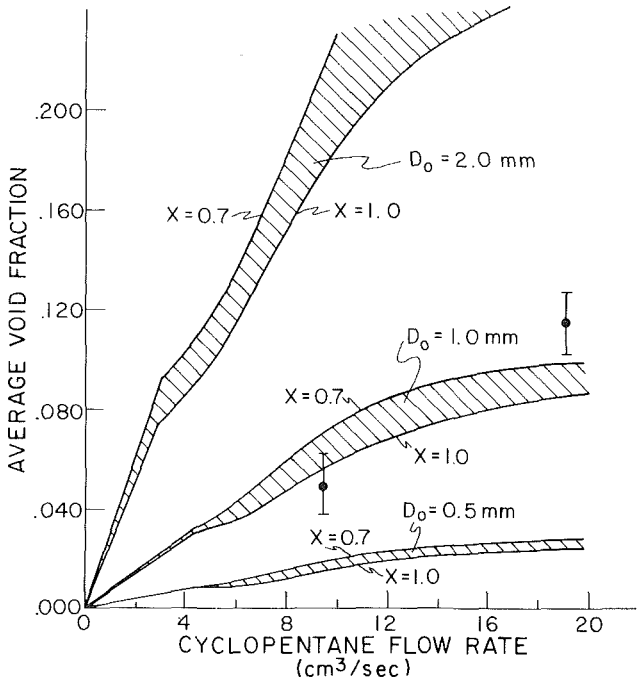

Fig. 7 The experimental and analytical average void fraction versus volumetic flow rate

$$m\gamma \mathrm{Re}_0^x = 5.83 \tag{35}$$

equation (35) contains two unknowns, x and γ (recall $m = 2 - x$ during the preagglomeration stage). In addition, the value of D_0 must be specified to determine Re_0. Photographic observation of droplets that failed to nucleate revealed that D_0 was approximately 1.0 mm irrespective of the volumetric flow rate. Because of the uncertainty in this value, the calculations were performed over a range of D_0(0.5, 1.0, and 2.0 mm). Furthermore, because of the imprecision in the measurements compared to single droplet experiments, no attempt was made to deduce x and γ independently of one another. For particular values of x and D_0 the appropriate value of γ was determined from equation (35).

The Effect of Agglomeration. In the second series of experiments the pitch between holes in the distribution plate was reduced from 5.0 to 2.9 cm, while the number of holes was increased from seven to nineteen in order to promote agglomeration. However, the diameter of the holes was the same as in the first experiment. The modifications induced the desired agglomeration and did not appear to affect the initial size of the droplets. The average cyclopentane void fraction data presented in Fig. 7 was determined according to the following holdup relationship

$$\bar{\alpha} = \frac{z - z_0}{z} \tag{36}$$

where z and z_0 are the water depths measured during the prior to cyclopentane injection, respectively. Because the partial pressure of water at 50°C is less than 2 psi, the correction for water vapor is small and was neglected.

According to the results of the postagglomeration analysis, agglomeration increases the volume required for a given degree of evaporation compared to the single droplet result for the same ΔT. This prediction was verified in this work; the single droplet correlations fall well below the multidroplet data in Figure 6.

Combining equations (14) and (24) yields

$$\Delta T = \frac{K_1 + K_2}{z} \tag{37}$$

Table 3 Comparison of experimental values of h_v

	Sideman and Gat	Blair et al.	Present Expt.
Dispersed phase	n-pentane	refrigerant-113	cyclopentane
Specific gravity	0.63	1.55	0.68
Enthalpy of vaporization (J/kg)	3.57×10^5	1.47×10^5	4.19×10^5
Continuous phase flow Rate (kg/min)	1.295	1.370	0.0
Dispersed phase flow Rate (kg/min)	0.042	0.101	0.257–0.386
h_v watts/m^3 °C	18×10^4	12.2×10^4	$4.52\text{–}6.0\times10^4$

where

$$K_1 = \frac{\rho_{dv} U_0 D_0^2 L_d}{k_c \mathrm{Nu}_0} \frac{r_a^{m_0} - 1}{2m_0} \tag{38}$$

$$K_2 = \frac{\rho_{dv} U_0 D_0^2 L_d}{k_c \mathrm{Nu}_0} \frac{(r^{m_a} - r_a^{m_a}) r_a^{(x-1)/2}}{12 m_a (1-\alpha_{\max})^{1-x}} \tag{39}$$

For complete evaporation

$$r^{m_a} = [(\rho_{dl}/\rho_{dv})\, r_a^{-5/2} (1-\alpha_{\max})]^{2m_a} \tag{40}$$

Substituting equation (40), the appropriate thermophysical properties from Table 1 and

$$\dot{W} = 19\left(\frac{\pi}{4} D_0^2\right) U_0 \tag{41}$$

into equations (38) and (39) yields

$$K_1 = \frac{13.4\dot{W}}{\mathrm{Nu}_0} \frac{r_a^{m_0} - 1}{2m_0} \tag{42}$$

$$K_2 = \frac{13.4\dot{W}}{\mathrm{Nu}_o} \frac{[(\rho_{dl}/\rho_{dv})\, r_a^{-5/2} (1-\alpha_{\max})]^{2m_a} - r_a^{m_a}}{12 m_a (1-\alpha_{\max})^{1-x}} \tag{43}$$

where

$$\alpha_{\max} = \alpha_0 r_a^3 = \frac{\dot{W}}{A U_0} r_a^3 \tag{44}$$

where the flow area A is 138 cm^2. Figure 6 indicates that the product $z\Delta T$ increased to about 120 cm-K as a result of agglomeration. With this result, equations (37) and (41–44) were solved for $\alpha_{\max}$ as a function of x and D_0 for $\dot{W}$ = 9.47 cm^3/s. The results are presented in Table 2.

With the results in Table 2, the average void friction was determined as a function of $\dot{W}$ according to the formula

$$\bar{\alpha} = \left[\frac{1}{z_a}\int_0^{z_a} \alpha\, dz\right] \frac{K_1}{K_1+K_2} + \alpha_{\max} \frac{K_2}{K_1+K_2} \tag{45}$$

The first term on the right side of equation (45) represents the preagglomeration contribution to $\bar{\alpha}$, while the second terms gives the postagglomeration contribution; and $K_1/(K_1+K_2)$ and $K_2/(K_1+K_2)$ are preagglomeration and post-agglomeration volume fractions, respectively. The results are presented in Fig. 7 as a function of $\dot{W}$ for D_0 = 1.5, 1.0 and 2.0 mm for x between 0.7 and 1.0

The results in Fig. 7 suggest that the value of D_0 was indeed close to the observed value of 1.0 mm. Furthermore, the x-dependence does not appear to be very strong in the range 0.7 to 1.0, although the more turbulent values (close to 1.0) consistently yield smaller values of $\bar{\alpha}$. It can be demonstrated that this effect results from an increase in the pre-agglomeration volume fraction as the value of x increases. The postagglomeration volume fraction decreases as x increases, because the Nusselt number increases as Re^x and Re increase continuously with r; hence, the volume required for complete evaporation following agglomeration decreases as x increases. The large effect of D_0 on $\bar{\alpha}_0$ arises because α_0 increases as the square of D_0 according to equations (41) and (44).

The values of $\alpha_{\max}$ determined for D_0 = 1.0 mm are characteristic of systems with relatively few orifice holes and hence large orifice velocities [8]. Such systems promote agglomeration and an early transition to churn-turbulent flow.

It is interesting to note that the volumetric heat-transfer coefficients, h_v, in the present experiments were of the same order as those determined by Sideman and Gat [6], and Blair, Boehm, and Jacobs [7]. Table 3 summarizes the conditions of the three experiments. Sideman's reported parameters (orifice diameter = 0.5 mm, D_0 = 1.4 mm, U_0 = 65–70 cm/s) are very similar to those in the present work, and his qualitative observations (the existence of distinct preagglomeration and postagglomeration zones) are also similar. Therefore, it is suspected that the countercurrent flow in his experiment is primarily responsible for the higher values of the heat-transfer coefficient he reports. Countercurrent flow probably results in both enhanced convection and reduce droplet travel distance per time; both are effects which increase the volumetic heat-transfer rate.

Conclusions

The mathematical model for the volumetric heat-transfer coefficient in direct contact boiling developed in this work (equations 17 and 30) is reasonably successful in predicting the experimental results. The model is based on an integration of single bubble heat-transfer characteristics with the hydrodynamics of two-phase flow. Hence, it would be expected to perform well over a wide range of direct-contact evaporation conditions. Obviously, further confidence can only be gained by comparison of predictions to experiments with a broader range of flow rates than was accomplished here.

References

1 Sideman, S. and Taitel, Y., "Direct-Contact Heat Transfer with Change of Phase: Evaporation of Drops in an Immiscible Liquid Medium," *International Journal of Heat and Mass Transfer*, Vol. 7, 1964, pp. 1273–1288.

2 Simpson, H. C., Beggs, E. C., and Nazir, M., "Evaporation of a Droplet Rising Through a Second Immiscible Liquid: A New Theory of the Heat Transfer Process," *Heat Transfer*, Vol. 5, Paper CT2.3, 1974.

3 Smith, R. C., "Modeling of Fuel-to-Steel Heat Transfer in Core Disruptive Accidents," Ph.D. thesis, M.I.T., Cambridge, Mass., 1980.

4 Klipstein, D. H., "Heat Transfer to a Vaporizing Drop," D.Sc. thesis M.I.T., Cambridge, Mass., 1963.

5 Letan, R., "Design of a Particulate Direct Contact Heat Exchanger: Uniform Countercurrent Flow," 16th National Heat Tranfer Conference, St. Louis, Mo., ASME Paper 76-HT-27, Aug. 9–11, 1976.

6 Sideman, S. and Gat, Y., "Direct Contact Heat Transfer with Change of Phase: Spray-Column Studies of a Three-Phase Heat Exchanger," *American Institute of Chemical Engineers Journal*, Vol. 12, Mar. 1966, pp. 296–303.

7 Blair, C. K., Boehm, R. F., Jacobs, H. R., "Heat Transfer Characteristics of a Direct Contact Volume Type Boiler," ASME 76-HT-23, 1976.

8 Wallis, G. B., *One-Dimensional Two-Phase Flow*, McGraw-Hill, New York, 1969.

9 Kazimi, M. S. and Chen, J. C., "Void Distribution in Boiling Pools with Internal Heat Generation," *Nuclear Science and Engineering*, Vol. 65, 1978, pp. 17–27.

M. E. Simpson
Graduate Student.
Student Mem. ASME

C. K. Chan

Assistant Professor.
Assoc. Mem. ASME

Department of Chemical, Nuclear, and Thermal Engineering,
University of California,
Los Angeles,
Calif. 90024

Hydrodynamics of a Subsonic Vapor Jet in Subcooled Liquid

Small scale experiments were performed to investigate the condensation process and hydrodynamic pressure oscillations when steam was discharged into a subcooled water pool. The dynamic behavior of subsonic jets, differed from that of sonic jets. The interfacial motion of a subsonic jet was periodic, composed by three intervals: bubble growth, bubble translation, and bubble separation (necking). The condensation rate for each interval was governed by different processes. The pressure transient of the subsonic jet was marked by periodic impulses, originated by the necking process. Of the intensive parameters studied, pool subcooling exhibited the largest influence on dynamic behavior. The pulse frequency and intensity were found to be best fit by correlations involving the Jacob number and the Reynolds number.

1 Introduction

Direct vapor condensation in subcooled liquid is a common event encountered in many two-phase systems. Most of the research in vapor jet condensation has been experiment oriented and most researchers have directed their attention towards specific applications and gross geometrical and heat-transfer behavior. Kerney et al. [1] experimentally investigated the parametric effects of vapor mass flux, liquid subcooling, and nozzle configurations on the penetration of vertically injected steam jets at sonic speed. Stanford and Webster [2] examined the steam jet profile of both sonic and subsonic flow. Young and Yang [3] experimented with a horizontal sonic jet in a coaxial, concurrent, parallel stream of subcooled water. Based on a Reynolds flux model, they established a Stanton number correlation for heat transfer at the interface. Bankoff et al. [4] also experimented with co-current, parallel, stratified flows of steam and subcooled water in a channel. They found the heat-transfer rate was strongly affected by the liquid velocity. These observations led to the belief that the interfacial heat transfer was controlled in the liquid region during co-current two phase flow. However, for vapor injection into subcooled liquid, other authors [2, 5, 6] observed that the heat transfer was less affected by the liquid momentum and the heat transfer data were best fit with a kinetic-limited, mass-transfer model in the vapor region.

Several authors [3, 5, 6] observed various hydrodynamical forces associated with the condensation process. Young and Yang [3] qualitatively identified six distinct dynamical regimes, as a function of vapor mass flux. Dynamic characteristics ranged from loud intermittent pops at low mass flux (chugging) to continous rasps at high unchoked velocities, and to piercing shrill sound for highly underexpanded jets. Chan and Lee [7] attempted to classify these different regions by a flow regime map with flow rate and liquid subcooling as governing parameters. At low steam flow rate, the condensation interface became unstable, as water pulsated in and out of the discharge pipe, causing large-magnitude, short-duration pressure spikes. This phenomenon, known as "steam chugging," was examined by Lee and Chan [8], Marks and Andeen [9], Sursock and Duffey [10], and Kowalchuck and Sonin [11]. At high steam flow rates, Cumo et al. [6] observed that sonic jets instabilities became dramatic as pool subcooling became small. He reported the dynamic force of the jet was less affected by the mass flux than by the pool subcooling. Chan [5] examined the details of sonic jet dynamics with a parametric study of pool subcooling, exit mass flux, and exit pipe diameter. He found the pulsation frequency increased with pool subcooling. At low pool temperatures, pulse frequencies decreased with increasing tube diameter, but converged to the eigenfrequency of the liquid pool at temperatures near saturation. Pulse magnitudes increased with jet diameter and increasing pool temperature, but diminished rapidly near saturation temperatures in every case. He found a good correlation between experimental frequencies and those predicted from Rayleigh bubble motion. Greef [12] investigated the effects of pool subcooling and jet diameter on the dynamics of subsonic steam and freon jets. Greef's observed subsonic jet dynamics were characteristically in agreement with Chan's results for sonic jets. The pulse frequency was a positive linear function of pool subcooling.

Some details of the local jet condensation mechanism of a sonic, underexpanded steam jet were examined by Bronnikov et al. [13]. Using a pitot tube to measure the velocity head, Bronnikov discovered three distinct regions of flow in the axial direction. There was a region of expansion nearest to the jet exit where the static pressure decreased to that of the surroundings. This region was steady, unaffected by condensation, and it exhibited a self-similarity in axial velocity distribution. Following the expansion region was a region of extremely high condensation intensity, which was characterized by local condensation centers and large intermittent radial liquid velocity components. No axial velocity similarity profile existed in this region. In the third region, the entrainment of bulk pool water in the flow field caused the jet profile to spread. Once again a similarity in the axial velocity profile prevailed. The minimum velocity head in the jet profile existed at the boundary of the first and the second region, while a relative maximum existed at the boundary of regions two and three.

Bronnikov's observation has raised a related question: does a subsonic vapor jet behave in a similar manner? It is also observed that most of the past works have been related to either vapor jets of high velocity (sonic jet) or vapor injection at low flow rate (steam chugging). The objective of the present work is to examine the basic mechanism of vapor jet condensation at intermediate vapor flow rate (subsonic jet). Owing to the physical complexity of the problem, the present approach is primarily experimental. Specifically, the parametric effects of pool subcooling, exit steam flux, and injection pipe diameter are investigated for the subsonic regime. The condensation characteristics and the governing physics of oscillatory interfacial motion are examined as well.

Apparatus and Procedure

The experimental apparatus is designed to allow controlled

Contributed by the Heat Transfer Division for publication in the JOURNAL OF HEAT TRANSFER. Manuscript received the Heat Transfer Division December 1, 1981.

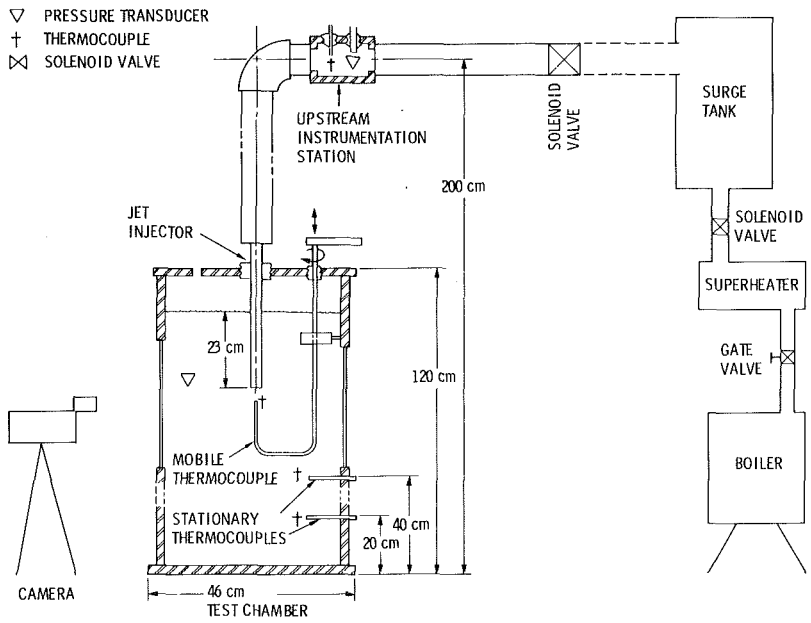

Fig. 1 Experimental apparatus

vertical injection of steam into subcooled water with variable jet exit diameters. The major components of the system consist of the boiler, the surge tank, and the test chamber as shown in Fig. 1.

The central component of the steam supply is the 17-KW, three-phase Chromalox boiler. The boiler has a maximum steam generation rate of 7.56 gm/s. Saturated steam exits from the boiler and flows through a 1.5-kW Chromalox superheater, where its temperature is increased to a maximum of 200 C. After exiting from the superheater, steam flows through a 5.1 cm dia pipe, which contains an isolation solenoid valve. Downstream of the valve, the steam enters into the 0.044 m^3 surge tank. The surge tank is designed to withstand pressures up to 500 kPa. Under control of a second solenoid valve downstream of the surge tank, supply steam flows through a 5.1 cm dia pipe towards the test chamber. The steam supply system is either lined or constructed of 304 stainless steel to mitigate corrosion. The steam pipe is wrapped with electrical heating tapes and insulated with 2.5 cm fiberglass covering to prevent steam condensation. Finally, the channel converges from the 5.1 cm dia pipe to a variable diameter tube of 75 cm in length. The tube is submerged below the water level inside the test chamber.

The test chamber consists of two sections: one stacked on top of the other. The chamber is hexagonal in cross section and symmetric about the vertical jet tube. The distance between flats of the hexagon is 46.0 cm, more than twenty times the largest jet diameter used in experiments. The total depth of the chamber is about 120 cm. The submergence depth of the jet is 23 cm from the surface. The chamber wall is constructed from 0.635 cm (1/4 in.) thick stainless steel plates. The chamber wall effects on the jet behavior is expected to be small. This is based on the theory of incompressible flow, where the liquid velocity at a distance of 20 dia from the interface will be 0.25 percent of the interfacial velocity, and the pressure at that location will be 5 percent of the interfacial value. Open ports in the upper plate of the test chamber maintain atmospheric pressure in the chamber at the water surface. Other ports in the bottom plate and in the side plates of the test chamber allow the insertion of various instrumentation probes. Windows in the side panels of the chamber allow clear visibility and high speed photography of the jet injection phenomenon. High speed movie and digital sampling of instrumentation signals comprise the complimentary techniques of data acquisition used in the experiments. The central piece of photographic equipment is a Red Lake, high-speed 30 m film movie camera with a variable frame rate up to 3000 frames/s. Additional photographic equipment includes 1.0-Kw, high-intensity lighting fixtures, a film speed controller, an internal strobe film timing device, and a signal lamp that is triggered by activating the data acquisition system.

The digital sampling system consists of a sixteen-channel, 1000-gain amplifier bank, sixteen channels of analog-digital (A-D) converters, and a PDP-11 minicomputer which monitors the sampling process with user written software. The maximum sample frequency of the A/D converter is about 10^4 per s. The maximum storage capacity of the computer

Nomenclature

a_1, a_2 = constants
A = area
b_1, b_2 = constants
c = sound speed, constant
C_p = heat capacity
d = jet tube diameter
f = frequency
h = average heat-transfer coefficient
h_{fg} = latent heat
k_1, k_2 = consants
$\dot{m}$ = mass flow rate per unit area (mass flux)
P = pressure
ΔP = pressure difference
r = radius
R = test chamber radius
ΔT = pool subcooling
t = time
u = velocity
Ja = Jacob number $(\rho_l C_{pl} \Delta T)/(\rho_s h_{fg})$
Re = Reynolds number $(u_0 d)/\nu$
St = Strouhal number $(fd\rho_l)/(\rho_s u_0)$
ρ = density
ν = kinematic viscosity

Subscripts

o = jet exit conditions, jet tube
n = necking interval
b = bubble growth interval
s = steam
l = liquid
c = condensation

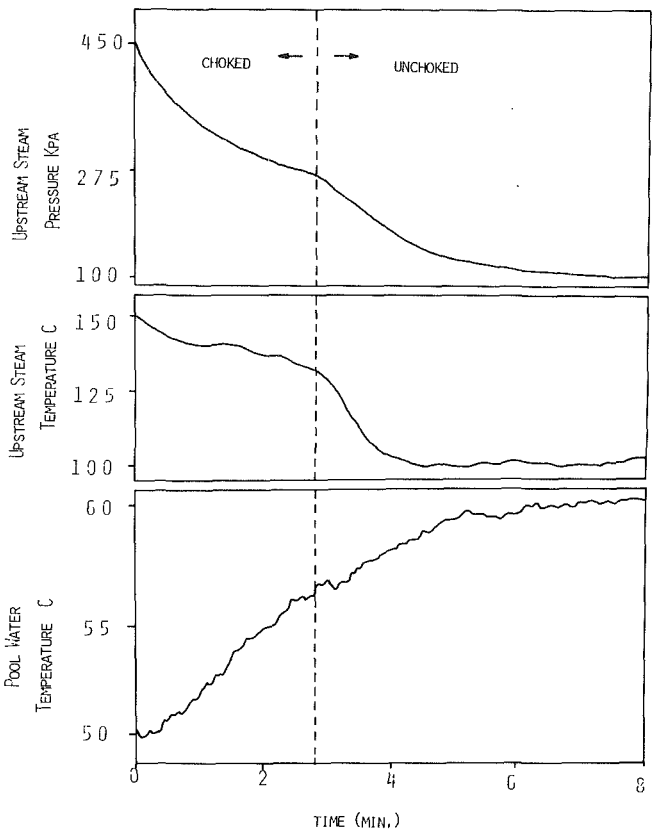

Fig. 2 Blowdown pressure and temperature transients

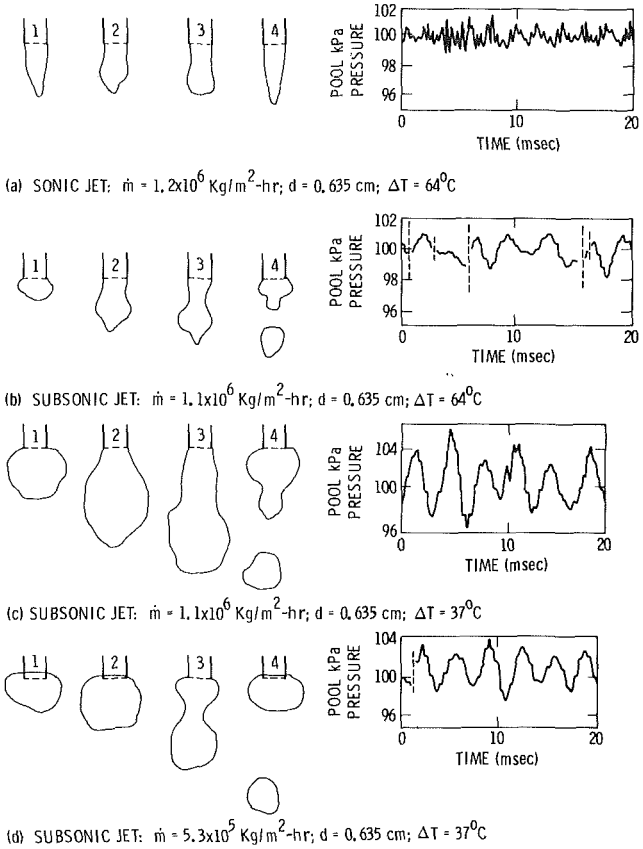

Fig. 3 Sequential steam profile motion and pressure transients for sonic and subsonic jets of different steam flowrates and subcooling

memory is about 9000 independent digital samples divisible between any number of the sixteen signal channels. The signal acceptance criterion of the A-D converter is a ± 10 V range.

Instrumentation consists of iron constantan thermocouples and Statham, flush mounted, strain gage, pressure transducers. In the upstream station, ports are available for insertion of thermocouple and pressure transducer probes into the main steam flow. In the test chamber, dynamics of the injection process are recorded by a pressure transducer mounted on the side wall of the chamber. Bulk pool temperature measurements in the test chamber are made with two thermocouple probes protruding through sealed ports in the walls. The probes are located at heights of 25 cm and 40 cm from chamber bottom and are extended inward about 10 cm from the chamber walls. A special mobile thermocouple, designed to take measurements anywhere in the near region of the jet exit during experiments, is operated manually from outside the test chamber.

Prior to injection of steam, the data acquisition system was calibrated, referenced, and programmed for the upcoming experimental event. A sampling software program was run to specify the sample frequency, number of signal channels, and the total number of discretized data points for the experiment. The sampling system was then put in a standby mode until a manually operated switch was used to actuate the sampling event.

The test chamber and the boiler were filled from the external supply of demineralized water. The jet exit was submerged to a depth of 23 cm in the test chamber. The pool subcooling was set to the desired value by either heating the bottom of the chamber with electrical strip heaters, or by running cooling water through the test chamber cooling coils. Variable power tape heaters were actuated on the main steam line about 30 min before recording, to insure a high steam-line wall temperature during run time. Power was delivered to the boiler while the two solenoid valves in the main steam line remained open. Low pressure steam from the boiler purged the air content in the main line to a minimal fraction. After a few minutes, the downstream valve of the surge tank was then closed; isolating the test chamber from the steam source.

The boiler continued to generate steam causing pressurization of the surge tank. When the surge tank reached the desired pressure level. The solenoid valve downstream of the surge tank was opened and steam quickly accelerated through the jet tube into the liquid pool. At first the flow in the jet reached a sonic speed at the exit. Violent mixing maintained nearly isothermal conditions in the pool while the bulk pool temperature slowly increased. As the pressure in the surge tank slowly dropped, the exit flow became subsonic.

Typical upstream steam pressure and temperature transients and the corresponding test chamber water temperature are shown in Fig. 2. These transients represent an entire blowdown period of the 0.635 cm tube test. The discontinuity in the slope of the pressure and the temperature curves represent the transition from the choked to the unchoked flow. The steam pressure at this transition point is independently verified by the Modified Darcy formula of single phase flow as outlined on pages 4-13 of [14].

The high speed movie camera started upon entry of the subsonic regime. Then, the manually operated control switch simultaneously started the data acqusiition system and the signal lamp. Appearance of the signal lamp on the photo-film marked the onset of data collection by the PDP-11, to relate the data to the movies. The data included the pressure and the temperature in the steam supply line, the pool temperature at three different locations and the pool pressure at the bottom and at the side of the test chamber. A typical value of the data sampling period is 1 s which is small in comparison to the entire blowdown transient of 6 min. Hence, the steam pressure and temperature, the exit mass flux and the pool temperature, can be considered to be constant for the time interval of movie recording.

Table 1 Experimental test parameter

Test node	Tube (cm)	Pool (°C)	Exit steam (flux mass) $Kg/M^2hr.) \times 10^{-6}$
1	0.635	64	1.1
2	0.635	48	1.1
3	0.635	37	1.1
4	0.635	25	1.1
5	1.59	65	1.1
6	1.59	51	1.1
7	1.59	40	1.1
8	1.59	26	1.1
9	2.22	62	1.1
10	2.22	48	1.1
11	2.22	39	1.1
12	2.22	26	1.1
13	0.635	53	0.81
14	0.635	40	0.81
15	0.635	53	0.53
16	0.635	40	0.53
17	0.635	64	1.2

Seventeen tests were performed, each representing a unique set of flow parameters and scaling. The parameter sets are listed in Table 1. Twelve of the test constitute nodes of a parametric matrix, of three jet diameters, and four values of pool subcoolings. Four additional tests, in conjunction with the twelve tests, create a test matrix of three exit mass fluxes and two subcooling temperatures. Pool subcooling temperatures range from 25 to 65 C; jet exit diameters are 0.635, 1.59, and 2.22 cm; and exit mass fluxes are 0.97, 0.71, 0.46 times the critical value. The mass flow rate and the critical mass flow rate are calculated by the Modified Darcy formula [14] for given steam pressure and flow resistance. The calculated flow rates correlate well with the flow rate obtained from calorimetric heat balances of the liquid in the test chamber [15]. In all these tests ambient pressure is atmospheric, and the jet submergence is 23 cm. The last test, node 17, is a sonic jet submerged in a highly subcooled pool. It represents the point of transition from sonic to subsonic exit velocity.

3 Results and Discussions

A cyclic motion of the jet profile is observed from the high-speed film. Figure 3 shows assorted samples of test results at sequential stages during a typical oscillation period. Figure 3(*a*) is a typical result of a sonic jet. Figures 3(*b*),3(*c*), and 3(*d*) are for subsonic jets with different mass fluxes and subcoolings. Each cycle of the steam motion can be classified into four stages. From its smallest configuration (stage 1), the steam region first grows as a bubble, forcing the pool liquid away from the jet exit and shrouding the jet stream from direct contact with the pool liquid. The bubble growth terminates at a maximum radius (stage 2). The impingement of the jet momentum force starts to elongate the steam bubble and enhance bulk convection of the pool liquid in the vertical direction. The elongated bubble appears to translate in the vertical direction until it clears the exit plane of the jet. At this moment, pool liquid encroaches from the radial direction on the cylindrical geometry of the jet core (stage 3). The entrained liquid slug detaches the downstream bubble from the supply, forcing it to quickly collapse. The inertia of the entrained liquid also temporarily retards the vertical motion of the jet stream at the pipe exit (stage 4). The remaining attached steam returns to its minimum dimension, and the cycle repeats itself. In view of these distinct intervals of motion, each cycle can be divided into three periods representing the bubble growth, the bubble translatory motion and the bubble separation (necking). Theses periods are more distinct for subsonic jets than for sonic jets.

The pressure transients for subsonic jets are also quite different. In addition to the sinusoidal wave trains (represented by solid line in Fig. 3), which is a characteristic of the sonic jet, there are periodic impulses (represented by broken lines in Fig. 3) for subsonic jets. These impulses appear to occur more frequently above a threshold value of pool subcooling of 40 C. The amplitude of the dynamic impulse can not be captured in the present experiments because the time interval of the impulse is beyond resolution by the data acquisition system and the response of the pressure transducer. However, by correlating the pressure data with the movie data, the impulse spike is found to occur when the bubble separated (necking) and when the isolated bubble collapsed. In the present experiments the impulses occured mostly during the necking process. On a few occasion, a collapsing bubble produced an impulse in the same order of magnitude as that during necking.

For direct contact condensation, an overall heat-transfer coefficient is used to quantify the condensation rate at the vapor-liquid interface [6]. Assuming a uniform heat flux at the interface area A_c, the heat-transfer coefficient, calculated from an energy balance on the steam with the jet profile, is:

$$h = \frac{\dot{m} h_{fg} A_0}{\Delta T A_c} \tag{1}$$

The interfacial area at a particular time is obtained by tracing the jet profile from the film frame. The elongated jet profile is divided into sectional disks of small thickness. Assuming axial symmetry of the jet profile, the interfacial area is obtained by summing the curved surfaces of all the disks. A_c in equation (1) is the integral average of the interfacial area over a complete cycle. The mass flux $\dot{m}$ is calculated from the upstream steam pressure data [14].

The average heat-transfer coefficients calculated by equation (1) for a complete cycle of subsonic jets, are shown in Fig. 4(*a*). Figure 4(*b*) shows the effect of exit steam velocity on the heat-transfer coefficient. The four data points of lower velocities are obtained from test nodes 13, 14, 15, and 16, while the two data points of Mach number close to 1 at $\Delta T = 40°C$ and 53°C are obtained from interpretation between nodes 2 and 3, and nodes 1 and 2, respectively, as shown in Fig. 4(*a*). For subsonic jets, pool subcooling has a large effect, while exit stream velocity has a small effect. These trends are in good agreement with those reported by Cumo [6] for a sonic jet, although the magnitudes of his heat-transfer coefficients are about five to ten times greater than the present subsonic jet values.

In equation (1), the greatest uncertainty is with the interfacial area. Due to the stripping effect at the boundary, an accurate determination of the area is difficult. With an

estimated 25 percent uncertainty associated with the area, 10 percent uncertainty associated with the mass flux, the heat-transfer coefficient has an uncertainty of 33 percent.

From the movie data, during the growth period, the interface appears to be clear and distinct, indicating no two phase region in-between the vapor and the liquid regions. In accordance to the bubble growth theory [16], the condensation rate is governed by the heat transfer through the liquid phase. On the other hand, during the necking period, the interface appears to be rough and fuzzy, indicating a two phase in-between the vapor and the liquid regions. With the presence of the droplets in the two phase region, the heat

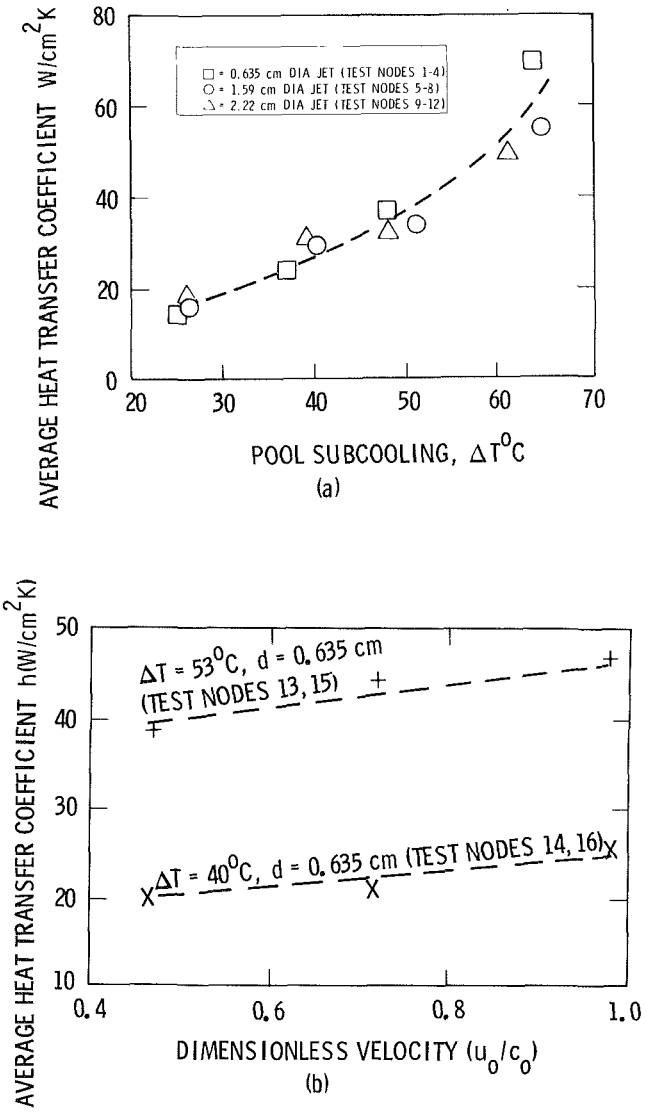

Fig. 4 Experimental average heat-transfer coefficients versus (a) pool subcooling and (b) exit steam velocity

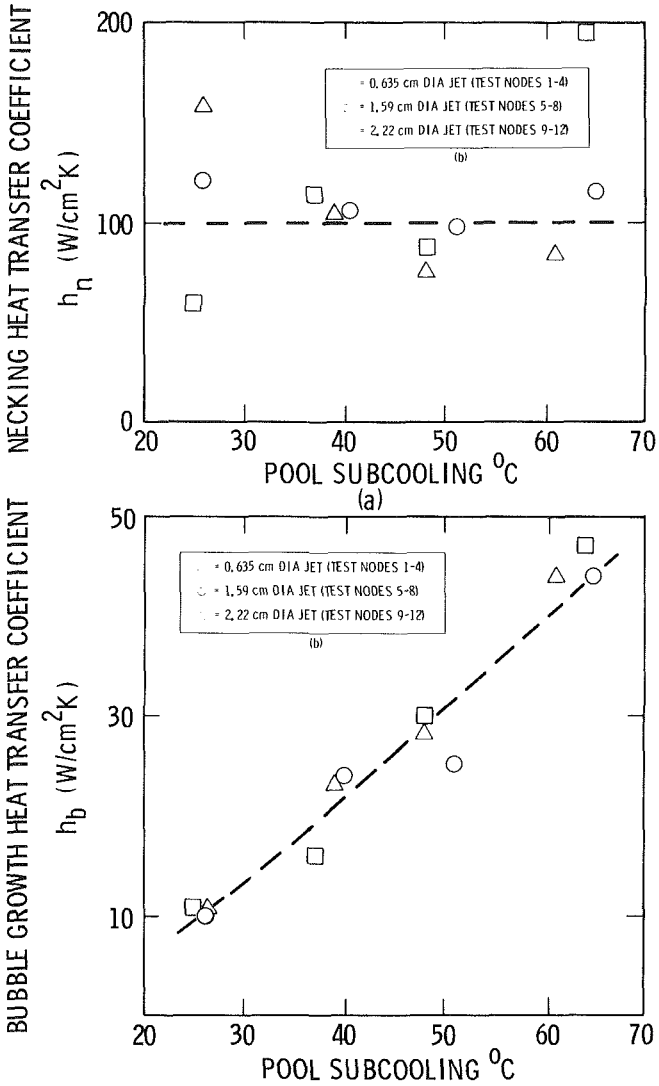

Fig. 5 Average heat-transfer coefficients during (a) necking and (b) bubble growth periods

Table 2 Experimental results

Test node	Heat-transfer coefficients (W/cm^2K^{-1})			Time intervals (milli-s)		Frequency s^{-1}	Dimensionless maximum bubble radius ($r_{b,max.}/r_0$)	Peak to peak pressure oscillation amplitude P (N/m^2)
	h_b	h_n	h	t_b	t_n			
1	47	190	69	1.9	0.3	480	2.2	21.5
2	30	88	36	2.5	0.3	377	3.2	28.7
3	16	114	24	3.7	0.3	284	5.0	29.2
4	11	59	15	7.9	0.5	262	7.4	47.9
5	44	116	55	3.5	0.5	238	2.3	38.3
6	25	97	32	5.8	0.6	222	3.4	52.7
7	24	104	30	7.9	0.6	188	4.0	62.2
8	10	123	16	14.7	0.8	134	7.8	95.7
9	44	84	49	6.0	0.8	175	2.4	43.1
10	28	75	32	10.2	0.9	140	3.3	76.6
13	31	173	46	2.5	0.3	408	2.6	23.9
14	16	91	21	4.2	0.3	246	4.2	31.1
15	26	149	39	2.5	0.3	460	2.3	26.3
16	15	82	20	3.9	0.3	278	3.5	30.1
17	–	–	116	–	–	–	–	–

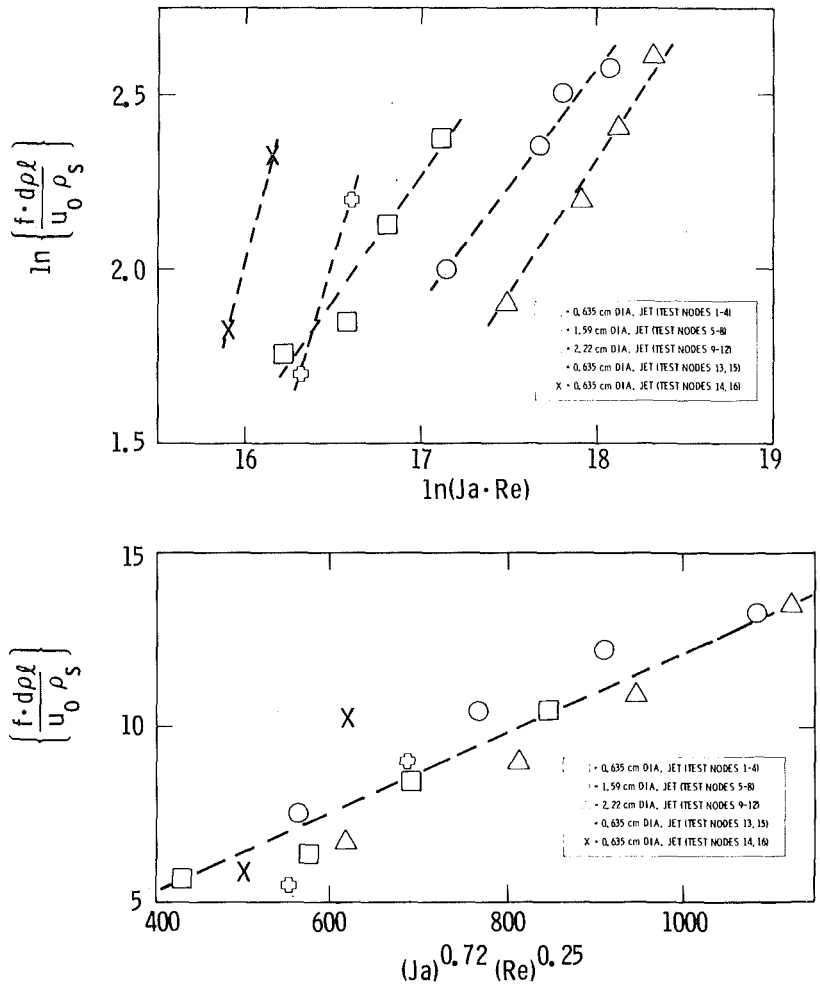

Fig. 6 Correlations of impulse frequencies from experimental data

transfer through the liquid region is no longer important. The condensation rate would be greatly enhanced by the cold droplets.

Because of the different physical processes, the heat-transfer rates in the necking and the bubble growth periods should be identified independently.

Assuming constant heat-transfer coefficients in each of these two periods, the heat-transfer coefficient calculated by equation (1) actually represents the weighted average:

$$h = \frac{h_b t_b + h_n t_n}{t_b + t_n} \tag{2}$$

where:

- h = total average heat transfer coefficient during the cycle;
- h_b = average heat-transfer coefficient during bubble growth interval;
- h_n = average heat-transfer coefficient during necking interval;
- t_b = duration of bubble interval (including growth, translation, separation, and collapse); and
- t_n = duration of necking interval.

The bubble heat-transfer coefficient, h_b, is calculated using equation (1). After calculating h_b, the necking heat transfer, h_n, is calculated from a rearrangement of equation (2).

The results of the h_b and h_n are shown in Fig. 5. The bubble growth heat-transfer coefficient is affected by the subcooling. The necking heat-transfer coefficient shows no definite pool subcooling dependence. Despite spurious scattering in the necking coefficient values, caused by difficulties to obtain accurate values of t_n from the movie data, the mean value of the necking heat-transfer coefficients falls remarkably close to the experimental sonic jet value (node 17). This is consistent with observation that the two-phase droplet region during necking enhances the condensation rate. With an uncertainty of 30 percent associated with t_n, 33 percent associated with h_b, 33 percent associated with h, 4 percent associated with t_b, the h_n calculated from equation (2) has an uncertainty of 65 percent for test node 7.

The values of the heat-transfer coefficients, h, h_b, and h_n, the time intervals, t_b, and t_n, the dynamic impulse frequency, f, the maximum bubble radius, r_b, and the peak to peak pressure oscillation amplitude, ΔP, for all the test runs are tabulated in Table 2.

Examinations of the pressure data indicate the following trends:

(1) Increasing pressure frequency with increasing pool subcooling

(2) Decreasing pressure frequency with increasing jet tube diameter

(3) Increasing pressure amplitude with decreasing pool subcooling

(4) Increasing pressure amplitude with jet tube diameter

(5) Increasing pressure amplitude with increasing exit mass flux

In attempting to correlate the results of the frequency data, physical insight is used to determine the governing parameters. The parameter would be the ratio of the specific energy absorption capabilities of the liquid and the energy density of the steam, i.e., the Jacob number, defined as

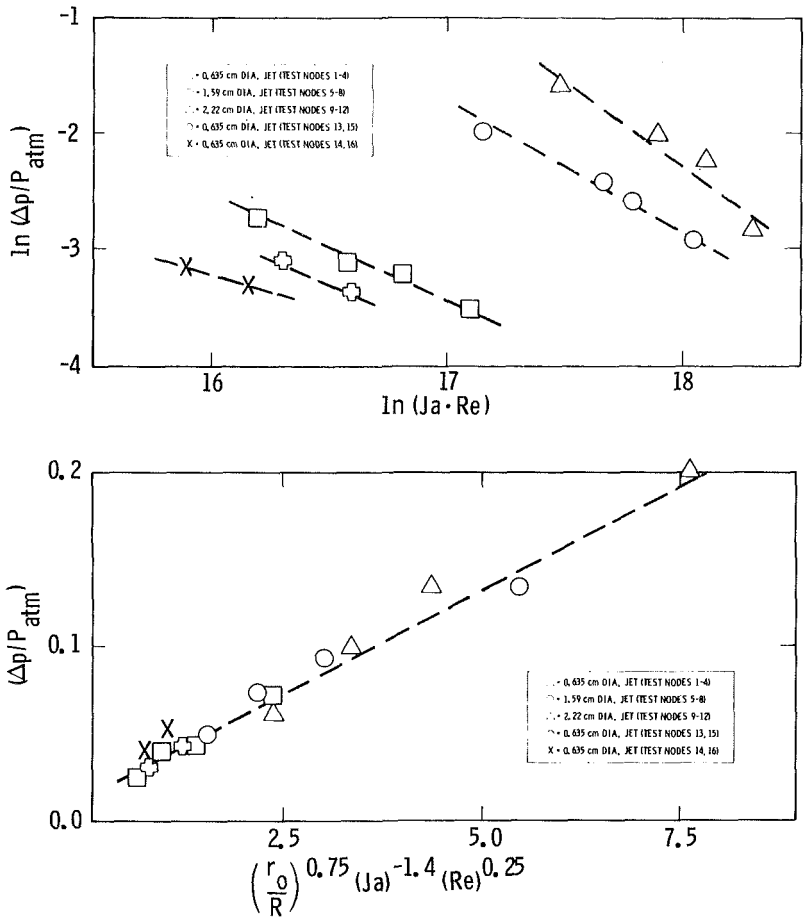

Fig. 7 Correlations of pressure amplitudes from experimental data

$$\mathrm{Ja} = \frac{\rho_l C_{pl} \Delta T}{\rho_s h_{fg}} \tag{3}$$

The droplet stripping rate is governed by another parameter, the Reynolds number defined as $u_0 d/\nu$. Introducing the density weighted Strouhal number for the frequency

$$\mathrm{St} = (f d \rho_l)/(u_0 \rho_s) \tag{4}$$

then a correlation of the following form is sought:

$$\mathrm{St} = k_1 (\mathrm{Ja})^{a_1} (\mathrm{Re})^{b_1} \tag{5}$$

The experimental results of the correlated pulsation frequency are shown in Fig. 6. For the data range in the present study, the values of the constants in equation (5) are $k_1 = 0.011$, $a_1 = 0.72$, and $b_1 = 0.25$ for $77 < \mathrm{Ja} < 260$ and $2.3 \times 10^6 < \mathrm{Re} < 1.7 \times 10^7$.

The wave form of the pressure signal, different from the impulse, reflects the oscillating pressure field inside the steam region of the jet. These fluctuations are generated by the imbalance in the net flow of steam in the jet region. The amplitudes are expected to depend on the same parameters as the dynamic frequency. In addition, the amplitude depends on the relative location of the pressure transducer in relation to the interface. Therefore, a correlation of the following form is anticipated:

$$\Delta P/P = k_2 (r_0/R)^{a_2} (\mathrm{Ja})^{b_2} (\mathrm{Re})^{c} \tag{6}$$

for

$$77 < \mathrm{Ja} < 260$$

$$2.3 \times 10^6 < \mathrm{Re} < 1.7 \times 10^7$$

For $k_2 = 0.024$, $a_2 = 0.75$, $b_2 = 1.4$, and $c = 0.25$, the correlation fits the experimental data best (Fig. 7).

4 Conclusions

By observation the dynamics of subsonic jets are quite different from those of sonic jets. The periodic interfacial motion of subsonic steam jets can be subdivided into three basic intervals: bubble growth, bubble translation, and bubble separation (necking). The condensation rate during the bubble growth and the bubble translation is governed by the heat transfer in the liquid region while the condensation rate during necking is governed by the heat transfer in the steam region. The heat-transfer coefficient is largest in the necking interval and is unaffected by subcooling because of the droplet stripping. The heat-transfer coefficient during bubble growth increases with increasing subcooling. The average heat transfer for subsonic jets is about one-fifth to one-tenth of the sonic jet values.

The subsonic pressure transient is marked by periodic impulses. These impulses originate from the necking of the steam bubble.

Effects of subcooling, jet diameter, and mass flux on the pressure frequency and magnitude are correlated with the Jacob number and the Reynolds number.

Acknowledgment

This work is supported in part by the U.S. Nuclear Regulatory Commission through contract No. AT (48-24)-0342. C. K. Chan is grateful for the manuscript preparation by Jet Propulsion Laboratory.

References

1 Kerney, P. J., Feath, F. M., and Olsen, D. R., "Penetration Characteristics of a Submerged Steam Jet," *A.I.Ch.E. Journal*, Vol. 18, 1972, pp. 548-553.

2 Stanford, L. E. and Webster, C. C., "Energy Suppression and Fission Product Transport in Pressure-Suppression Pools," ORNL-TM-3448, Oak Ridge National Laboratory 1975.

3 Young, R. J., Yang, K. T., and Novotny, J. L., "Vapor-Liquid Interaction in a High Velocity Vapor Jet Condensing in a Coaxial Water Flow," ASME JOURNAL OF HEAT TRANSER 1974, Vol. 3, 1974, pp. 226-230.

4 Lee, L., Bankoff, S. G., Yuen, M. C., and Tankin, R. S., "Local Condensation Rate in Horizontal Co-current Steam-Water Flow," *18th National Heat Transfer Conference*, San Diego, Aug. 1979.

5 Chan, C. K., "Dynamical Pressure Pulse in Steam Jet Condensation," *Sixth International Heat Transfer Conference,* Vol. 2, Toronto, 1978, pp. 395-400.

6 Cumo, M., Farello, G. E., and Ferrari, G., "Direct Heat Transfer in Pressure-Suppression Systems," *Sixth International Heat Transfer Conference*, Vol. 5, Toronto, 1978, pp. 101-106.

7 Chan, C. K., and Lee, C. K. B., "A Condensation Regime Map for Direct Contact Condensation," to appear in *Int. J. of Multi-Phase Flow*.

8 Lee, C. K. B. and Chan, C. K., "An Experimental Study of Low Flow Steam Injection into Subcooled Water," *Basic Mechanisms in Two-Phase Flow and Heat Transfer*, Winter Annual Meeting of the ASME, Chicago, 1980, pp. 73-78.

9 Marks, J. S., and Andeen, G. B., "Chugging and Condensation Oscillation," *ASME Condensation Heat Transfer*, 18 National Heat Transfer Conference, San Diego, 1979, pp. 93-102.

10 Sursock, J. P. and Duffey, R. B., "Condensation of Steam Bubble in a Subcooled Pool," *Topics in Two-Phase Heat Transfer and Flow*, ASME Winter Annual Meeting, San Francisco, 1978, pp. 135-141.

11 Kowalchuck, W. and Sonin, A. A., "A Model for Condensation Oscillations in a Vertical Pipe Discharging Steam Into a Subcooled Water Pool," NUREG/CR 0221, June 1978.

12 Greef, C. P., "A Study of the Condensation of Vapor Jets Injected into Subcooled Liquid Pools," Central Electricity Generating Board, Berkeley Nuclear Laboratories, RD/B/N3262, 1975.

13 Bronnikov, V. K., Mal'tsev, B. K., and Yermolenko, I. P., "The Mechanism of Condensation of a Jet of Steam in A Free Volume of Liquid," NTIS, UDC 536.423.4; 621.039.

14 "Flow of Fluids through Valves, Fittings and Pipe," Technical Paper No. 410, Crane Co. publication, 1969, New York.

15 Simpson, M. E., "Hydrodynamics of a Vapor Jet in Subcooled Liquid," M. S. thesis, UCLA, 1979.

16 Plesset, M. S. and Zwich, S. A., "Growth of Vapor Bubbles in Superheated Liquids," *Journal of Applied Physics,* Vol. 24 No. 4, 1954, pp. 493-500.

Characteristics of Nucleate Pool Boiling From Porous Metallic Coatings

A. E. Bergles
Professor and Chairman.
Fellow ASME

M. C. Chyu
Research Assistant.

Department of Mechanical Engineering,
Iowa State University,
Ames, Iowa 50011

A study of pool boiling from a commercial porous metallic matrix surface is reported. The excellent steady boiling characteristics of this type of surface are confirmed; however, high wall superheats are required in most cases to initiate boiling. The resultant boiling curve hysteresis does not appear to have been previously reported in the literature. This effect is indicated in recent pilot plant tests. The present results generally confirm the speculated mechanism of boiling with these surfaces and suggest reasons whereby single-tube performance may be superior to tube bundle performance.

Introduction

Industrial demands for more efficient boilers and evaporators have spurred the development of methods to increase boiling heat-transfer coefficients or critical heat fluxes. A recent Department of Energy sponsored project led to the documentaiton of 508 papers and reports [1] and 59 U.S. patents [2] related to the enhancement of pool or forced-convection boiling. Of greatest interest are the special surfaces which promote nucleate boiling at low temperature differences. As outlined in reference [3], one of the categories of structured boiling surfaces is coated surfaces, whereby an irregular matrix of potential nucleation sites is produced by such methods as poor welding, sintering or brazing of particles, electrolytic deposition, flame spraying, bonding of particles by plating, galvanizing, plasma spraying of a polymer, or metallic coating of a foam substrate. The general object of these surface treatments is to provide nucleation sites which will be stable, that is, trap vapor so that initial bubble formation can occur at moderate wall superheat. Furthermore, these sites promote high rates of vaporization so that the wall superheat required for developed nucleate boiling is low compared to that required for boiling from surfaces with natural cavities.

Several of these processes for producing a porous metallic matrix have been patented and commercialized. These surfaces achieve the desired objective, but there is still a lack of agreement as to the mechanism of boiling.

Mechanisms. There are several mechanisms which have been postulated for boiling from surfaces with porous artificial coatings or fouling deposits [4]. Consider first, nucleation in the matrix shown in Fig. 1. If the matrix material is poorly wetted, vapor or vapor plus noncondensible gas will be retained in the interstitial space when the temperature is reduced below the saturation temperature. Alternatively, in the more usual wetting situation, re-entrant and doubly re-entrant cavities are required to permit stable dropwise formation so that the cavities are not filled with subcooled liquid. In any event, the matrix increases the probability that nucleation sites are available which will remain active (retain vapor or gas) for repeated cycles of heating and cooling. Furthermore, there is a greater probability that the cavities will have larger effective mouth radii than natural surface cavities, thereby insuring incipient boiling at lower wall superheat.

Turning to established boiling, there are a number of possibilities. If the interior of the matrix becomes dry, there will be bubble formation at the surface – similar to boiling from smooth surfaces with natural cavities, but at lower superheat due to the larger mouth radii. More likely, liquid penetrates the matrix and vapor is generated within the matrix.

O'Neill et al. [5, 6] postulate a vapor bubble formed in an interparticle space. Vapor is generated primarily by evaporation of the thin liquid film segments separating the bubble from the particles. The bubble then grows and squeezes out of a convenient pore. Fresh liquid is supplied to vapor production centers through nonbubbling pores and interconnected channels. The total superheat is assumed to be the sum of the conduction temperature drop across the liquid film and the traditional equilibrium superheat for a curved liquid-vapor interface. When the characteristic pore size or pore size distribution is available, the boiling curve can be obtained by backing-out bubble shape parameters from the experimental data. The latest version of this model yields $q'' \sim \Delta T^{1.1\text{-}7.5}$, depending on the fluid (for a given surface) [7].

In related studies, Cohen [8] and Macbeth [9] have argued

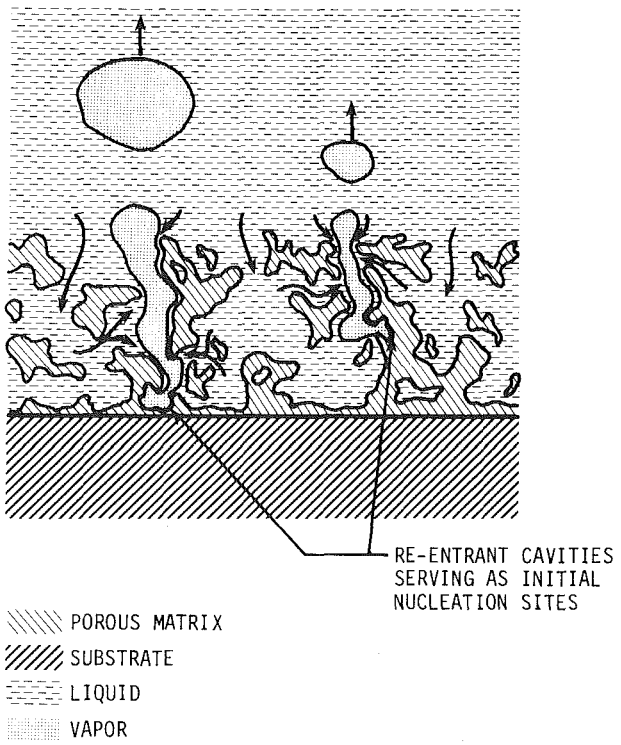

Fig. 1 Conceptual model of boiling in a porous matrix of sintered metallic particles

Contributed by the Heat Transfer Division and presented at the ASME/AIChE 20th National Heat Transfer Conference, Milwaukee, Wisconsin, August 2-5, 1981. Manuscript received by the Heat Transfer Division June 3, 1981.

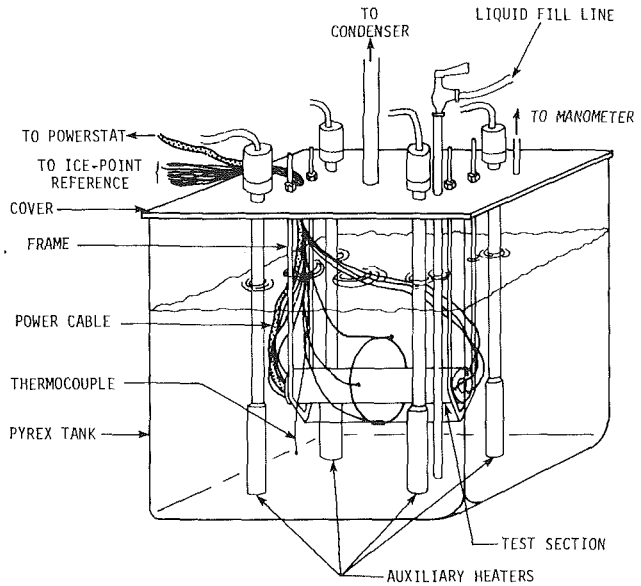

Fig. 2 Pool boiling apparatus

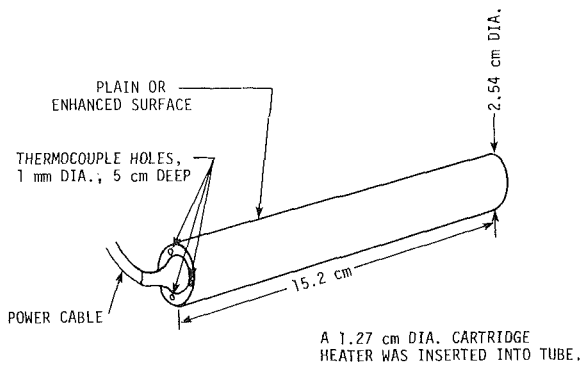

Fig. 3 Test section

that porous corrosion deposits, such as boiler crud, are characterized by "vapor chimneys" at regular intervals. These are fed by surrounding liquid channels with evaporation occurring near the point where these channels meet a chimney. Macbeth assumed that the critical condition is defined by the maximum amount of vapor which can be produced. This, in turn, is limited by the flow rate in the liquid channels. Smirnov [10] has also suggested vapor chimneys, but in a rather dense deposit matrix so that the liquid feed occurs only in reflux fashion on the chimney walls.

A plausible picture that emerges from these brief descriptions, then, is that steady vapor formation in a porous matrix is considered to be primarily internal. There are preferential vapor escape channels; the liquid is supplied primarily through other channels surrounding the vapor channel. Evaporation occurs at the mouths of the liquid channels and on adjacent surfaces wetted by the liquid. A low ΔT is required for evaporation due to the large internal surface area. The vapor which is seen in the pool represents bubbling, as if air were blown into the pool through a perforated plate, rather than the conventional nucleate boiling cycle of nucleation, growth, and departure. This is depicted in Fig. 1.

Unresolved Problems. The most recent work of O'Neill et al. suggests that a semiempirical predictive equation can be generated for developed boiling in porous metallic matrices [7]. The size distribution of the active, vapor-carrying pores is required. Also, two more shape factors determining those pores which generate and carry vapor are needed. As in normal surface cavity boiling, then, experiments are required to establish key parameters. With more refined techniques, perhaps, the model can be simplified to the point where only one adjustable constant is needed, as has been done for nucleate boiling [11].

A question of more urgency seems to be the initial behavior of porous boiling surfaces. Mention of start-up problems or boiling curve hysteresis is conspicuously absent from the rather extensive literature on the subject. Brief mention of such hysteresis is given by Torii et al. [12] when describing the performance of the Hitachi Thermoexcel-E surface; however, that surface is in a quite different category. Although tests have shown that a porous metallic coating can eliminate the pronounced hysteresis of R-113 in forced convection boiling [13], it has not been clearly established that this is the case in pool boiling. The primary object of this study was to obtain detailed information on the nucleate boiling characteristics of a typical coated surface and to relate that information to the behavior of large-scale systems. The parameters studied were surface structure, boiling liquid, surface aging, subcooling, and the way in which heat flux is changed.

Experimental Program

General Apparatus. The pool boiling setup used in this program is shown in Fig. 2. Electrically heated cylindrical test sections were mounted horizontally in a 30-cm cubical Pyrex tank. Working fluids were water or R-113. Insulation was provided on the bottom and sides of the tank; one of the side panels was removable for visual observation. An aluminum plate with a Buna N seal served as the cover. In addition to the test section, provision was made for installation of four auxiliary catridge heaters, pressure tap, fill line, and reflux condenser.

An adjustable-height frame fixed on the cover functioned as a firm support of the test section without noticeable restriction of the liquid flow. As shown in Fig. 2, three thermocouples were attached to a ring of 10-cm dia fixed on the support frame to measure the fluid temperature near the test section.

Test Section. The four test sections studied had the general characteristics shown in Fig. 3. Cartridge heaters were firmly fitted in thick-walled copper cylinders. Three holes of 1-mm dia and 50-mm deep were drilled at each end of the cylinders, at 120 deg intervals with the axis within about 1.6 mm of the surface (uncoated), for insertion of wall temperature thermocouples. The cylinders were provided by Linde Division of Union Carbide Corporation and are designated as test sections 1, 2A, 2B, and 4.

Test section 1 has a plain surface while the other test sections were coated with the Linde High Flux boiling surface. This proprietary process involves brazing of metal powder to the base surface so as to form a porous structure with a void fraction (porosity) of 50 to 65 percent. According to the manufacturer, test sections 2A and 2B have a porous layer thickness of 0.38 mm; about 45 percent of the copper particles constituting the matrix range from 200 (74 μm) to 325 (44 μm) mesh in size, with the remainder being finer. Test section 4 also has a porous layer about 0.38 mm thick; the particle sizes range approximately 75 percent between 200 and 325 mesh,

Nomenclature

p = pressure
q'' = average heat flux for a tube or tube bundle
ΔT = wall superheat: wall temperature minus saturation temperature
U_0 = overall heat-transfer coefficient based on outside tube surface area

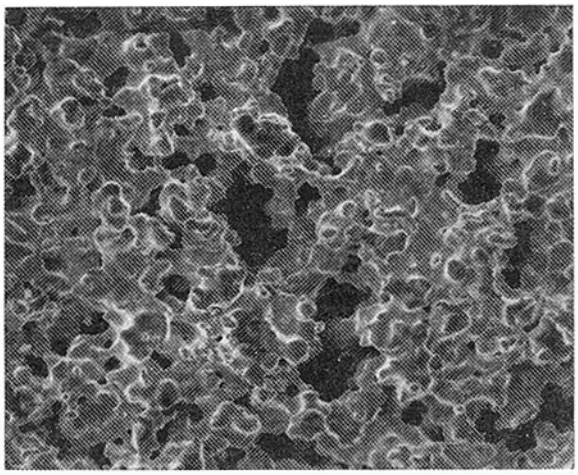

(*a*) 100x

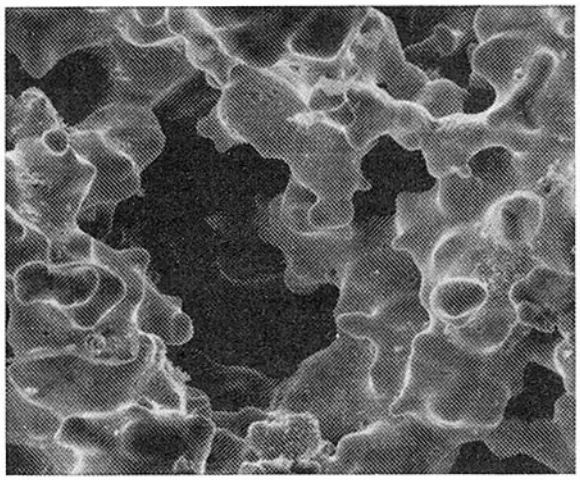

(*b*) 300x, central region of (*a*)

Fig. 4 SEM photographs of test section 2B

with the remainder being finer. As shown in Fig. 4, there are large variations in pore size and shape. The large pore shown in Fig. 4(*b*) probably functions as a vapor escape path or chimney.

Instrumentation. The alternating current power supplied to the heaters of the test sections was adjusted by a powerstat and was monitored by a digital voltmeter and an ammeter. Another powerstat controlled the auxiliary heaters.

Copper-constantan thermocouples were used to measure temperatures. The monitoring of the ten temperature readings was facilitated by use of the Heat Transfer Laboratory Data Acquisition System [14]. The system is basically composed of an ice-point reference, an A/D converter, a scanner, a calculator, and a printer.

A precision mercury barometer was used to measure the atmospheric pressure. The small pressure difference between the atmosphere and tank vapor space was determined by an inclined mercury manometer.

Experimental Procedure. The tank and the test section were cleaned with acetone before each test. The liquid level was maintained at about 8.3 cm above the centerline of the test section by periodic replenishment. It generally took about ten minutes to achieve steady conditions after the power level was changed.

At very low power levels, a compromise was necessary to insure saturated pool conditions. The heat loss, particularly with water, was considerable, so that the pool temperature began to drop when the auxiliary heaters were shut off. On the other hand, these heaters introduced rather strong convection currents in the pool. It was decided to leave the auxiliary heaters on, so as to achieve saturated conditions during boiling, even though this meant that the pool conditions were not truly free convection for nonboiling and very low boiling heat fluxes. The maximum subcooling was 0.3 K.

Effects investigated in this experiment were surface structure, boiling liquid, surface aging, surface subcooling, and the way in which heat flux is changed. The term surface subcooling here means the temperature difference between saturation temperature and temperature of the surface and pool before the test.

Curves of experimental results were coded for convenience and are defined as follows:

- Test section: 1, 2A, 2B, 4
- Fluid: W = distilled water; F = Freon-113
- Surface aging: B = surface was given a moderate heat flux (about 30,000 w/m^2 so as to boil vigorously in a saturated pool for more than 20 min before the run); D = tube was heated by its built-in heater to about 20 K above T_s in air to evaporate the probable entrapped liquid before immersion. Note that the immersed test section was not heated until the pool (and surface) subcooling was removed, as described in the following.
- Surface subcooling: The temperature difference between T_s and the temperature to which the surface was cooled down in the pool before the run, in K. The time required to remove the subcooling ranged from 10 to 30 min. Note that the inevitable subcooling of the pool was 0.3 K for both water and Freon-113.
- Way in which heat flux was changed: C = heat flux was increased continuously and slowly (about 4000 w/m^2-min) to a new operating condition; S = heat flux was increased stepwise, from hundreds to thousands of w/m^2 per step.

For example, 2A-W-B-56-C represents the curve of test section 2A boiling in a pool of distilled water according to the following procedure:

1 The tube was given a heat flux of about 30,000 w/m^2 to boil in a pool of saturated distilled water for more than 20 min.

2 The pool insulation was removed for a few hours until the pool and the immersed test section were cooled down to 56 K lower than T_s.

3 The pool was heated with auxiliary heaters to saturation. No power was supplied to the test section.

4 The power to the test section was increased continuously and very slowly.

The following quantities were then measured: voltage across the test-section heater, heater current, atmospheric pressure, pressure difference between atmosphere and tank, and the pool level above the test section. These quantities were

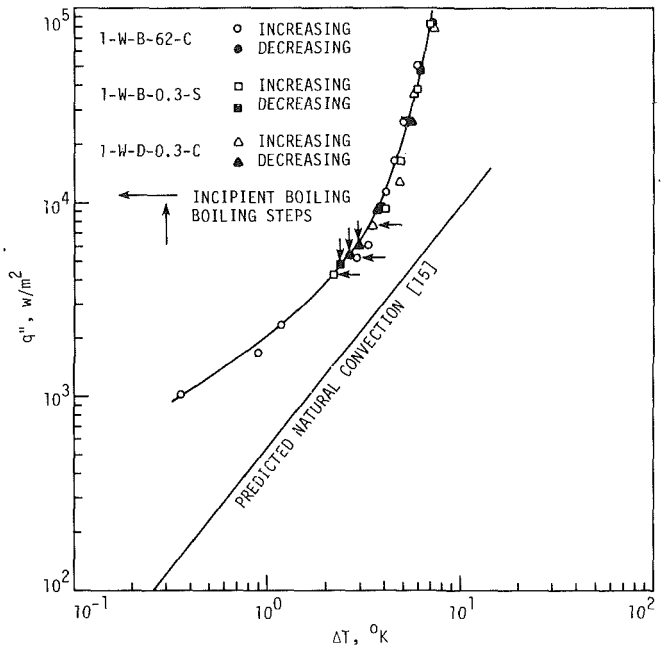

Fig. 5 1-W curves

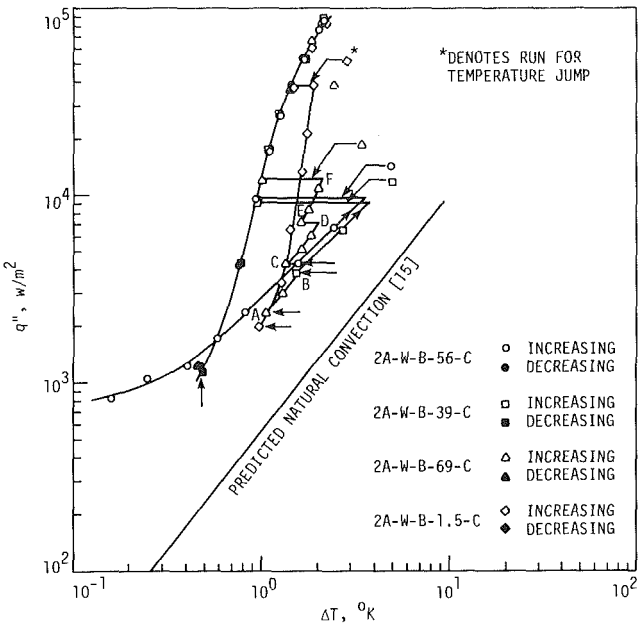

Fig. 6 2A-W-B-C curves

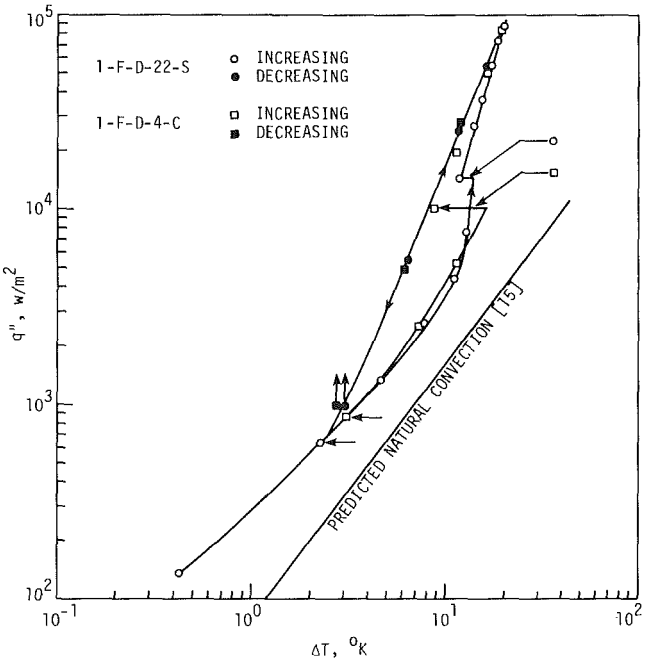

Fig. 7 1-F-D curves

read into the computer, the test section temperatures were sampled (5 to 10 times), and the heat flux and average wall superheat were calculated. The power was increased until the power limit of the heater was reached so as to generate a good portion of the complete boiling curve. Finally, the power was reduced until nucleate boiling ceased.

The heat flux was evaluated assuming uniform heat generation within the heater; the area was based on the radius of the base cylinder. Since the thermocouples were located well away from the ends, end losses could be neglected. Measured temperatures were averaged and corrected for the temperature drop over the distance between the thermocouple bead and the surface of the base cylinder (~ 1.6 mm). The estimated uncertainties in heat flux and wall superheat are 80 w/m^2, 0.1 K and 800 w/m^2, 0.2 K at $q'' = 800$ w/m^2 and $q'' = 80{,}000$ w/m^2, respectively.

Test Results

Water Tests. The plain tube water tests shown in Fig. 5 were very much as expected. The boiling curve for partial and developed boiling was essentially the same for both increasing and decreasing heat fluxes, regardless of surface aging, initial surface subcooling, or rate of heat flux change. The low heat flux nonboiling portion of the curve was higher than the natural convection prediction due to the pool convection induced by the auxiliary heaters.

Typical data for a High Flux surface are shown in Fig. 6. It is evident that a considerable heat flux is required before developed boiling sets in. For example, in the 2A-W-B-69-C test, incipient boiling occurred at A, and there were only several bubbling sites visible before B. At that point a small patch of boiling was evident, and the superheat shifted to C. Another patch broke out at D, and the superheat was reduced to E. Finally, at F the entire surface was boiling, and the superheat dropped to its minimum value at that heat flux. For other subcoolings there was only a single temperature excursion.

The curve marked with dark circles in Fig. 6 was stable for both increasing and decreasing heat flux; that is, once this curve was entered, the heat flux could be changed in any manner, as long as boiling was maintained. The typical traverse then exhibits the characteristic boiling curve hysteresis whereby the increasing flux curve is different from the decreasing flux curve.

The data shown in Fig. 6, as well as other data presented in [4], confirmed that temperature overshoots were generally larger with higher subcooling. The D tests and the S tests yielded increasing flux curves rather close to the stable boiling curve. There was no appreciable difference between stable curves for Test Sections 2A, 2B, and 4.

The most important feature of these data are the dramatic improvements in heat-transfer coefficients with the High Flux surface. If the coefficients are evaluated at constant heat flux, the improvements are about 250 percent. Viewed from the standpoint of a two-fluid heat exchanger, the High Flux surface promotes boiling, with its high heat-transfer coefficients, at superheats below 1 K. The problem is that high superheats or heat fluxes may be required to initiate the effective boiling.

Freon Tests.[1] The smooth surface exhibited modest temperature overshoot and boiling curve hysteresis, as shown by typical data in Fig. 7. Prior to the temperature excursion, patch boiling was evident. There was some indication that the overshoot was greater with higher subcooling and less with step increases in power. The stable curve, defined by the decreasing heat flux data, was unaffected by any of the special procedures.

The data presented in Figs. 8 and 9 indicate that the High Flux surfaces are characterized by large temperature overshoots which lead to dramatic boiling curve hysteresis. The augmented free convection curve was followed typically until about $\Delta T = 8$ K when there was an explosive formation of vapor and a reduction of ΔT to about 0.5 K. With test section 2B (Fig. 9), incipient boiling at isolated points was noted before the excursion. For both 2A and 2B, it was possible to increase the power to a high level, keep it there for some time, and then trigger the excursion by tapping the test section (2A-F-B-0.5-S and 2B-F-B-15-C).

The stable boiling curves for test sections 2A, 2B, and 4, with all procedures, were quite similar and represent a 400 to 800 percent improvement in the boiling heat-transfer coefficient (at constant heat flux). Stability of the curve was confirmed by an 8-hr-long 2B test at 2790 w/m^2, during which time the wall superheat remained constant at 0.5 K.

The stable curves are in excellent agreement with certain of the curves of Nishikawa et al. [17, 18] for pool boiling of R-113 from sintered layers of copper or bronze powder. However, the curves in question were for layers of at least 1 mm thickness and particles of 100 μm.

The temperature overshoot which characterizes the High Flux surface does not have an obvious dependence on subcooling. There is, however, a trend toward initiation at lower ΔT when the power is increased stepwise or when the D treatment is used.

Discussion

Explanation of Hysteresis Characteristics. The present boiling curves for High Flux surfaces are characterized by large-scale boiling curve hysteresis, an effect that does not appear to have been reported previously in the literature. This is due to flooding of the porous matrix with liquid so that only relatively small sites are available for nucleation. By the usual theory of boiling nucleation, these sites must have re-entrant characteristics.

For a given surface, it would be expected that the contact angle would strongly influence the extent of the temperature overshoot. Although such measurements were not made in the present study, previous experience indicates that the contact angle for water-copper is at least 50 deg while the contact angle for R-113 - copper is less than 5 deg [19]. The liquid penetration into the porous matrix in the water tests should be less than in the R-113 tests. The boiling curves, Fig. 6 and Figs. 8 and 9, confirm that there is less temperature overshoot with water, due to the less extensive deactivation of the potential nucleation sites by flooding with liquid. A delay time is expected for liquid penetration, and the number of nucleation sites snuffed out should increase with increasing subcooling. The subcooling effect was indeed evident with water, but with R-113 it appeared that the deactivation was widespread for the smallest subcooling. This effect is related to the high wetting ability of the R-113, and perhaps to the large number of cavities of about the same size. Of course, the rather random nature of the distribution of active sites would show up as patch boiling. Due to the internal generation of vapor, there is less tendency for the vapor to spread over the surface and activate other sites.

[1] The present observations of boiling R-113 from a High Flux surface have been confirmed in recent tests by Marto and Lepere [16].

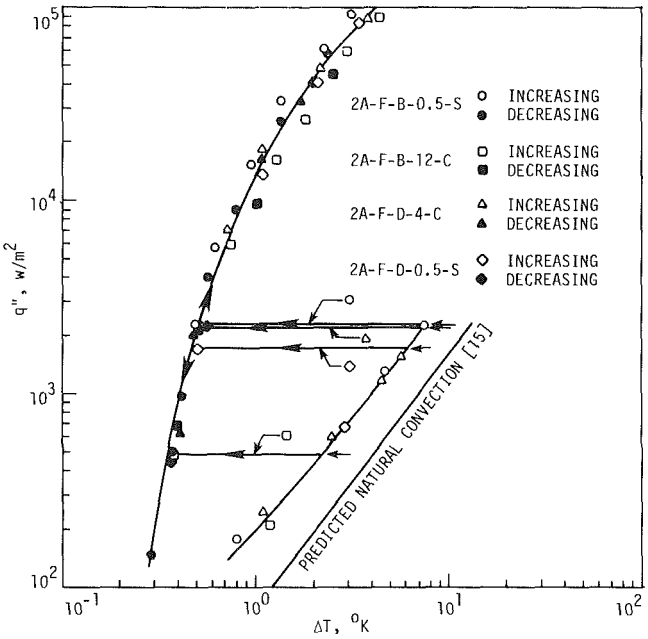

Fig. 8 2A-F curves

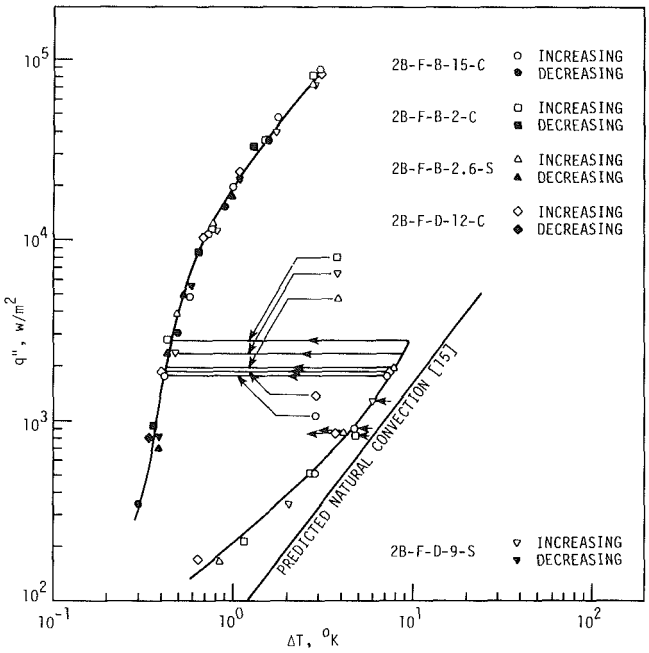

Fig. 9 2B-F curves

Earlier nucleation is promoted by the dry treatment, especially in the case of water, due to the delay time for flooding. The flooding with R-113 progresses rapidly, as indicated by the less pronounced effect of the D treatment. Although the time constant of the test section was rather long, stepwise increase of power should represent a disturbance in that the internal vapor masses are formed more rapidly. The resulting overpressure pushes the vapor out as bubbles rather than the usual situation where the vapor mass spreads along the vapor chimney before bubbling out at the surface. Support for this picture is provided by the effect of tapping the heat section at a high superheat; the bubbles within the matrix are simply shaken loose.

The implications for practical applications of this (and other) porous metallic matrix surfaces would appear to be clear: if established boiling is to be realized in a constant heat flux system, the power must be increased beyond the incipient

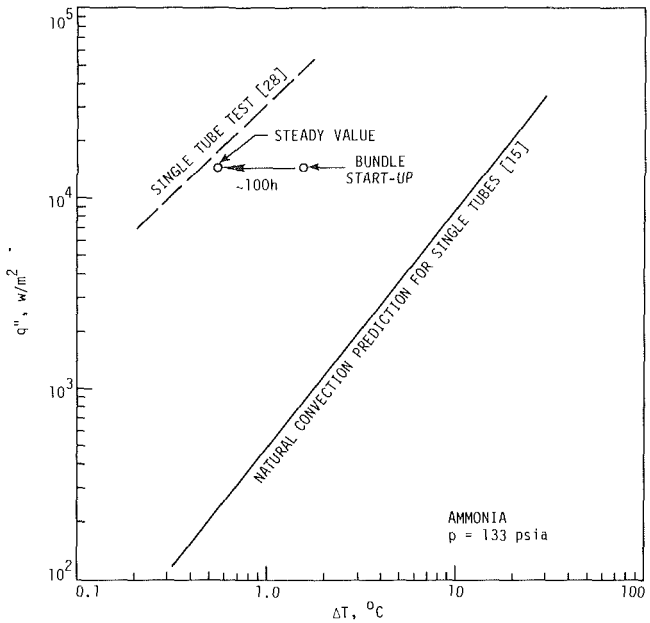

Fig. 10 Average boiling-side performance in Union Carbide flooded-bundle evaporator, as inferred from data in [20]

boiling value. In a constant temperature system, the superheat corresponding to incipient boiling must be exceeded. In either case, the starting condition is not too different from incipient boiling for a smooth surface. The previous history and the disturbance level can be very important. In a forced flow system, for example, it appears that the disturbance level is adequate to completely prevent the temperature overshoot [13].

Industrial Observations

The Argonne National Laboratory (ANL) Tests. As the present study was being concluded, two reports were issued which substantiate the problem of nucleation site deactivation with High Flux surfaces. Lewis and Sather [20, 21] reported erratic heat-transfer behavior in a 279-tube, High Flux flooded evaporator serving as a model for Ocean Thermal Energy Conversion (OTEC) System Applications. This was attributed to deactivation of nucleation sites by the flooding of the sites with liquid ammonia. The lowest value of the overall heat-transfer coefficient, U_0, was estimated at 600 Btu/hr ft^2 °F (3407 w/m^{2}K). The excellent heat-transfer behavior of the High Flux surface was restored by drying out the bundle prior to filling and initiation of heating. After soaking in liquid ammonia for 40 hrs, a five-day run was initiated to determine the reactivation period. The coefficient U_0 increased slowly with time and reached a steady value of 785 Btu/hr ft^2 °F (4450 w/m^{2}K) only after about 100 hrs of operation.

In this system the water-side thermal resistance is relatively large; hence, the initial value of U_0 represents only partial boiling on the shell side, due to deactivation of many nucleation sites. In a large bundle, however, some large active sites will be present and will nucleate with the available superheat. Such sites at the lower tubes will sparge the upper tubes so that nucleate boiling is gradually established throughout the bundle. Figure 10 illustrates the shift in the average boiling-side performance with time. This process is obviously very slow, probably due to the difficulty of activating sites within the matrix. According to the ANL experience, the deactivation takes only about an hour.

This start-up problem might be alleviated by initially having low shell side pressure so that the starting superheat is large or by injecting at the bottom of the bundle.

Subsequent tests at ANL were run with a sprayed bundle (Hillis et al. [22]) and disclosed similar deactivation/activation behavior. However, it was also found that the heat-transfer coefficient may be decreased by dryout if done when the surface is already fully activated. This was attributed to difficulty in rewetting the dry heated surface with the thin falling film of ammonia. An alternate explanation, based upon information given in the report, is that the initially subcooled ammonia film rapidly floods out many cavities, thereby reducing the role of nucleation in enhancing the falling film. In this case also, careful control of the shell side pressure might be used to promote nucleation during start-up.

It should be noted that certain systems appear to be inherently immune from boiling curve hysteresis. In refrigerant chillers, for example, fluid comes from the expansion valve into the pool at a quality of about 10 percent. The sparging and agitation seem to promote nucleation at reasonable superheat. Another factor could be that at start-up the wall superheat is high, since the water is not yet chilled and the refrigerant pressure is simply reduced until vaporization occurs. A similar situation occurs in ethylene plant refrigeration exchangers. In the case of liquefied gas production, there seems to be no problem initiating boiling since there are many heat leaks into the evaporator which result in vapor production.

Comments on Single-Tube vs. Bundle Performance. It is well established that the average boiling characteristics of tube bundles are considerably different than those expected from single-tube tests. As discussed by Palen et al. [23], the boiling curve for a smooth tube bundle lies well to the left (high heat-transfer coefficient) of that for a single smooth tube; however, the peak heat flux is considerably lower for the bundle.

Recent tests by Yilmaz et al. [24] indicate that there is a substantial degradation, relative to single tubes, in the performance of bundles of enhanced tubes with formed re-entrant cavities (Hitachi Thermoexcel-E and Wieland Gewa-T). This contrary behavior is most likely due to disruption of the liquid feed mechanism. The fluid streaming by tubes above the first few rows is not likely to provide the necessary liquid as (*a*) it is a gas-liquid mixture which would have a high pressure drop in the pores, and (*b*) the capillary force is probably not strong enough to overcome the high momentum of the flow streaming by the tubes. The internal vaporization is then replaced by surface vaporizaton similar to nucleate boiling from normal surfaces. It is reasonable to expect that the latter process is less effective; hence, the bundles perform more poorly than the single tube. This same phenomenon is expected with an enhanced surface which depends on internal vaporization; however, the effect would be most pronounced with surfaces with small surface pores. For example, the rolled-over low fins (Trane) [25] or the flattened low fins (Wieland Gewa-T) [26] leave helical channels with relatively large mouth openings ($\sim$0.25 mm). It would be expected that liquid could enter these channels, particularly at the stagnation point, and sustain the normal internal vaporization. The brazed or sintered surfaces and some formed surfaces such as the Hitachi Thermoexcel-E [27] have small individual openings ($\sim$0.07 mm dia) which resist liquid penetration; hence, these should exhibit a larger degradation.

Yilmaz et al. [24] did observe that the decrease in performance for the Thermoexcel-E tube bundle, as compared to the single Thermoexcel-E tube, was more than the difference in performance between the Gewa-T tube bundle and the single Gewa-T tube. All tests were run with clean tubes and R-11. However, the authors noted that the Thermoexcel-E bundle may not have been cleaned properly prior to the test. Thus, their tests do not conclusively confirm the above speculation about the influence of the type of enhanced tube on tube bundle performance.

There is also lack of agreement as to the basic question of single tubes versus tube bundles. As noted in Fig. 10, the Linde OTEC bundle performance is below that of the single tube; however, the difference is within probable experimental error. Czikk et al. [29] found earlier that an R-11 flooded water chiller evaporator performed better than the laboratory test surface; however, the difference was also considered to be within experimental uncertainty. It should also be noted that the laboratory test was performed with a flat disk facing up rather than with a tube. More tests seem to be needed to clarify the bundle behavior of tubes with formed re-entrant cavities and with porous metallic matrix surfaces.

Conclusions

This study of pool boiling of water from a commercial porous metallic matrix surface has established that, in addition to greatly enhanced heat transfer, boiling curve hysteresis is to be expected with both moderately wetting liquids, such as water, and highly wetting liquids, such as R-113. This effect does not appear to have been presented previously in the literature and is somewhat unexpected due to the generally excellent boiling characteristics of these structured surfaces. The surface aging (boiling or drying out), surface subcooling (pool and surface temperature prior to running), and heat flux change (continuously or stepwise to new operating point) affect the extent of the temperature overshoot and resultant boiling curve hysteresis.

Hysteresis has been recorded in tests of flooded and spray evaporators. The simplest way of avoiding the problem is to apply a high heat flux or large temperature difference to initiate boiling. Some systems are not prone to hysteresis due to a high disturbance level or introduction of a gas phase.

These results have generally confirmed the speculated mechanism of boiling with porous metallic matrix surface coatings. Nucleation takes place within the matrix from re-entrant cavities which are not susceptible to flooding by the liquid. In steady boiling, vaporization occurs within the matrix, and the vapor bubbles are forced out. The process depends on adequate liquid feed, and in the case of tube bundles, the two-phase flow may inhibit liquid flow into the matrix. This is a probable explanation for the data which indicate that bundle performance is inferior to single-tube performance. However, since the contrary has also been reported, further tests under carefully controlled conditions should be undertaken.

Acknowledgments

This study was supported in part by the U.S. Department of Energy under Contract EG-78-S-02-4649. Experimental facilities were provided by the Department of Mechanical Engineering and Engineering Research Institute at Iowa State University. Test sections were provided by the Linde Division of Union Carbide Corporation. The technical assistance of Mr. P. S. O'Neill of Linde is gratefully acknowledged.

References

1 Bergles, A. E., Webb, R. L., Junkhan, G. H., and Jensen, M. K., "Bibliography on Augmentation of Convective Heat and Mass Transfer," Heat Transfer Laboratory Report HTL-19, ISU-ERI-Ames-79206, COO-4649-6, Iowa State University, Ames, Iowa, May 1979.

2 Webb, R. L., Junkhan, G. H., and Bergles, A. E., "Bibliography of U.S. Patents on Augmentation of Convective Heat and Mass Transfer," Heat Transfer Laboratory Report HTL-25, ISU-ERI-Ames-81070, COO-4649-14, Iowa State University, Ames, Iowa, Sept. 1980.

3 Bergles, A. E., "Principles of Heat Transfer Augmentation, II: Two-Phase Heat Transfer," *Heat Exchangers, Thermal-Hydraulic Fundamentals and Design*, Hemisphere Publishing Company, Washington, D. C., 1981, pp. 857–881.

4 Chyu, M.-C., "Boiling Heat Transfer from a Structured Surface," M.S., thesis in Mechanical Engineering, Iowa State University, Ames, Iowa, 1979.

5 O'Neill, P. S., Gottzmann, C. F., and Terbot, J. W., "Novel Heat Exchanger Increases Cascade Cycle Efficiency for Natural Gas Liquefaction," *Advances in Cryogenic Engineering*, Vol. 17, 1972, pp. 421–437.

6 Gottzmann, C. F., Wulf, J. B., and O'Neill, P. S., "Theory and Application of High Performance Boiling Surfaces to Components of Absorption Cycle Air Conditioners," *Proceedings of the Conference on Natural Gas Research and Technology*, Paper 3, Chicago, Ill., Feb. 1971.

7 Czikk, A. M., and O'Neill, P. S., "Correlation of Nucleate Boiling from Porous Metal Films," *Advances in Enhanced Heat Transfer*, ASME, New York, 1979, pp. 53–60.

8 Cohen, P., "Heat and Mass Transfer for Boiling in Porous Deposits with Chimneys," *AIChE Symposium Series*, Vol. 70, No. 138, 1974, pp. 71–80.

9 Macbeth, R. V., "Boiling on Surfaces Overlayed with a Porous Deposit: Heat Transfer Rates Obtainable by Capillary Action," Atomic Energy Establishment Winfrith Report, AEEW R-711, June 1971, Winfrith, United Kingdom.

10 Smirnov, G. F., "Approximate Theory of Heat Transfer with Boiling on Surfaces Covered with Capillary-Porous Structures," *Teploenergetika*, Vol. 24, No. 9, 1977, pp. 77–80.

11 Mikic, B. and Rohsenow, W. M., "A New Correlation of Pool Boiling Data Including the Effect of Heating Surface Characteristics," ASME JOURNAL OF HEAT TRANSFER, Vol. 91, 1969, pp. 245–250.

12 Torii, T., Hirasawa, S., Kuwahara, H., Yanagida, T., and Fujie, K., "The Use of Heat Exchangers with THERMOEXCELS's Tubing in Ocean Thermal Energy Power Plants," ASME Paper No. 78-WA/HT-65, 1978.

13 Murphy, R. W. and Bergles, A. E., "Subcooled Flow Boiling of Fluorocarbons—Hysteresis and Dissolved Gas Effects on Heat Transfer," *Proceedings of the 1972 Heat Transfer and Fluid Mechanics Institute*, Stanford University Press, 1972, pp. 400–416.

14 Junkhan, G. H. and Bergles, A. E., "Heat Transfer Laboratory Data Acquisition System," Heat Transfer Laboratory Report HTL-12, ISU-ERI-Ames-77178, Iowa State University, Ames, Iowa, Dec. 1976.

15 McAdams, W. H., *Heat Transmission*, 3rd ed., McGraw-Hill, New York, 1954, p. 176.

16 Marto, P. J. and Lepere, V. J., "Pool Boiling Heat Transfer from Enhanced Surfaces to Dielectric Fluids," *Advances in Advanced Heat Transfer - 1981*, HTD-Vol. 18, ASME, New York, 1981, pp. 93–102.

17 Nishikawa, K., Ito, T., and Tanaka, K., "Enhanced Heat Transfer by Nucleate Boiling on a Sintered Metal Layer," *Heat Transfer - Japanese Research*, Vol. 8, No. 2, 1979, pp. 65–81.

18 Nishikawa, K. and Ito, T., "Augmentation of Nucleate Boiling by Prepared Surfaces," in *Heat Transfer in Energy Problems*, (Proceedings of the Japan-U.S. Joint Seminar 1980, Tokyo) Sept.–Oct. 1980, pp. 111–118.

19 Bergles, A. E., Bakhru, N., and Shires, J. W., Jr., "Cooling of High-Power-Density Computer Components," Engineering Projects Laboratory Report 70712-60, Massachusetts Institute of Technology, Cambridge, Mass., 1968.

20 Lewis, L. G. and Sather, N. F., "OTEC Performance Tests of the Union Carbide Flooded-Bundle Evaporator," ANL-OTEC-PS-1, Argonne National Laboratory, Argonne, Ill., Dec. 1978.

21 Thomas, A., Lorenz, J. J., Hillis, D. L., Yung, D. T., and Sather, N. F., "Performance Tests of the 1MWt Shell-and-Tube Heat Exchangers for OTEC," Presented at the Sixth OTEC Conference, Washington, D.C., June 1979.

22 Hillis, D. L., Lorenz, J. J., Yung, D. T., and Sather, N. F., "OTEC Performance Tests of the Union Carbide Sprayed-Bundle Evaporator," ANL-OTEC-PS-3, Argonne National Laboratory, Argonne, Ill., May 1979.

23 Palen, J. W., Yarden, A., and Taborek, J., "Characteristics of Boiling Outside Large-Scale Horizontal Multitube Bundles," *Chemical Engineering Progress Symposium Series*, Vol. 68, No. 118, 1972, pp. 50–61.

24 Yilmaz, S., Palen, J. W., and Taborek, J., "Enhanced Boiling Surfaces as Single Tubes and Tube Bundles," *Advances in Advanced Heat Transfer - 1981*, HTD-Vol. 18, ASME, New York, 1981, pp. 123–129.

25 Webb, R. L., "Heat Transfer Surface Having a High H. T. Coefficient," U.S. Patent 3,696,861, Oct. 10, 1972.

26 Saier, M., Kästner, H.-W., and Klöckler, R., "Y- and T-Finned Tubes and Methods and Apparatus for their Making," U.S. Patent 4,179,911, Dec. 25, 1979.

27 Fujie, K., Nakayama, W., Kuwahara, H., and Kakizaki, K., "Heat Transfer Wall for Boiling Liquids," U.S. Patent 4,060,125, Nov. 29, 1977.

28 Czikk, A. M., Fricke, H. D., Ganic, E. N., and Sharma, B. I., "Fluid Dynamic and Heat Transfer Studies of OTEC Heat Exchangers," *Proceedings of the Fifth Ocean Thermal Energy Conversion Conference*, Miami Beach, Florida, 1978, pp. VI-181 to VI-236.

29 Czikk, A. M., Gotzmann, C. F., Ragi, E. G., Withers, J. G., and Habdas, E. P., "Performance of Advanced Heat Transfer Tubes in Refrigerant-Flooded Liquid Coolers," *ASHRAE Transactions*, Vol. 1, Part 1, 1970, pp. 96–109.

Effects of Pore Diameters and System Pressure on Saturated Pool Nucleate Boiling Heat Transfer From Porous Surfaces

W. Nakayama
Chief Researcher.
Mem. ASME

T. Daikoku
Researcher.

T. Nakajima
Researcher.

Mechanical Engineering Research Laboratory,
Hitachi, Ltd.,
502 Kandatsu, Tsuchiura,
Ibaraki, Japan

The porous surface structure was manufactured with precision for the experimental study of nucleate boiling heat transfer in R-11. Boiling curves and the data of bubble formation were obtained with a variety of geometrical and operational parameters; the pore diameters were of 50, 100, 150 μm, there was a combination of pores of different sizes; and the system pressures were of 0.04, 0.1, 0.23 MPa. The boiling curves exhibit certain trends effected by the diameter and population density of pores. A combination of high system pressure and pore sizes of 100 or 150 μm dia enables boiling to persist even when the wall superheat is reduced to an extremely low level of 0.1 K. A noteworthy feature of porous surface boiling is that intense bubble formation does not necessarily yield a high heat-transfer performance. Examination of the data indicates that liquid suction and evaporation inside the cavities are a proable mechanism of boiling with small temperature differences.

Introduction

Enhancement of nucleate boiling heat transfer has received ever growing interest in a variety of industries – the refrigeration and air-conditioning, chemical process, and utility industries among others – with the aim of reducing the volume of heat exchangers, improving the plant efficiency or cooling electronic devices.

In recent years, so-called high-performance surfaces have been developed by commercial manufacturers. The surfaces manufactured by either metallurgical or mechanical means can be described as a conglomeration of small re-entrant cavities mutually connected by numerous internal passages. The author's previous papers [1, 2] cited patents and papers published so far on such porous surfaces. Because many parameters of structural geometry and operating conditions are involved, it is difficult to derive from a limited volume of experimental data a heat-transfer correlation which serves as a general guide to the use of high-performance surfaces. In this circumstance, one naturally quests for insights about the heat-transfer mechanism. Working toward this direction, the authors proposed a dynamic model of bubble formation on a relatively simple surface structure composed of parallel tunnels and pores [2]. In the course of this study, however, the authors have become acutely aware of the need to conduct experiments with surfaces prepared with a greater precision than heretofore obtained on commercial surfaces.

The surfaces used in the present experiment have a structure similar to that of the commercial surfaces reported in [1], but have pores of controlled sizes. R-11 was chosen as boiling fluid. Investigation of the influence of the system pressure is important for the design of a broad class of evaporators. The pressure was varied in three steps, 0.04, 0.1 and 0.23 MPa. The present paper reports the boiling curves and the data of bubble formation, and attempts to interpret those data.

Experimental Apparatus

Figure 1 shows enlarged views of a surface. Parallel grooves of rectangular cross section (width 0.25 mm, depth 0.4 mm) were gouged with a pitch of 0.55 mm on the base copper plate (20 mm × 30 mm), then covered by a thin copper plate (0.05 mm thick) having rows of holes. The plate was soldered (the solder's melting point = 200°C) on the flat crests of the grooved surface. Diameter and spacing of holes were brought within ±5 percent of nominal values by a specially made precision boring device.

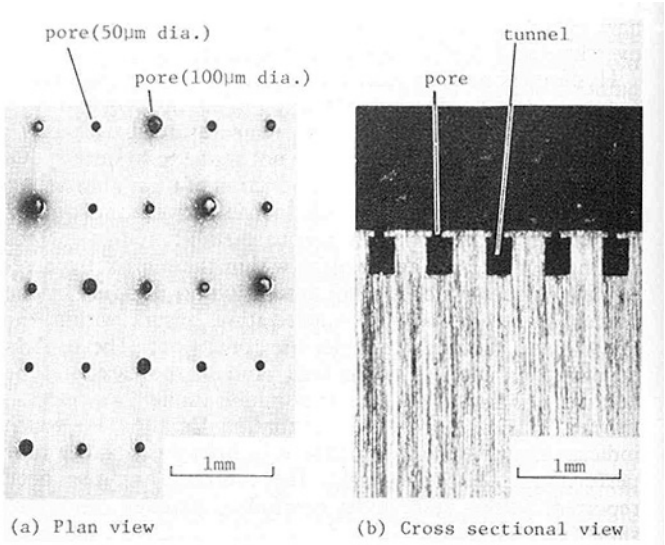

Fig. 1 Enlarged view of structured surface

The hole (pore) diameter was changed systematically as listed in Table 1. Table 1 does not include all the surfaces tested. Among those excluded from the table are a series of surfaces prepared to see the effect of the population density of pores on the heat-transfer performance. On the surfaces having combinations of different pores, large and small pores are arranged with a regularity (see Fig. 1). The relative number densities of large and small pores are given in Table 1 in terms of percentage.

Figure 2 shows the structure of a test block. The copper test surface is mounted on the nickel block by silver-soldering them together at 700°C. (Actually, the soldering of the porous plate to the grooved copper base was made after this operation.) The thickness of the solder was less than 100 μm, so that the thermal contact resistance between the copper and

Contributed by the Heat Transfer Division and presented at the ASME/AIChE 20th National Heat Transfer Conference, Milwaukee, Wisconsin, August 2-5, 1981. Manuscript received by the Heat Transfer Division September 29, 1981.

the nickel was negligible. The entire set was submerged in a pool of R-11, with the test surface facing up and horizontal.

A cylindrical vessel of 140 mm i.d. contains bulk liquid of R-11. The free surface of liquid was maintained 160 mm above the test surface. An auxiliary heater and a reflux condenser set the pressure inside the vessel. The vessel has two sight windows set diametrically opposite each other for visualization of the boiling surface.

Copper-constantan thermocouples of 0.2 mm dia were imbedded in the nickel block at nine locations, three thermocouples along a vertical axis with a spacing of 5 mm; there are three such axes (Fig. 2). Temperatures averaged in three horizontal planes were plotted on a printer chart. After confirming the linearity of the temperature distribution, the heat flux, based on the projected area and denoted by q_w, was determined by Fourier's law. Due to nickel's poor thermal conductivity, determination of heat flux as low as 0.1 W/cm^2 is possible with a sufficient accuracy. The rate of heat flow estimated from temperature distributions differed by no more than 10 percent from the power input to the heater.

The temperature distribution also gave the temperature at the bottom of the tunnel by extrapolation after correcting the change of thermal conductivities from the nickel block to the copper structured surface. This temperature is defined here as the wall temperature T_w. Four copper-constantan thermocouples of 0.2 mm dia were suspended in the bulk liquid above the bakelite frame by the distance of 5 mm and outside the region of bubble columns. The averaged output of the thermocouples was taken as the saturation temperature T_s. The wall superheat is defined as $\Delta T_w = T_w - T_s$.

There was a difference among outputs of the thermocouples in the liquid, the maximum being of the order of 0.2 K at $\Delta T_w = 11$ K, 0.05 K at $\Delta T_w = 0.1$ K. The uncertainties in T_w arise from variations of temperature gradients at three measurement locations in the test block, for example, 0.03 K at $\Delta T_w = 0.1$ K. Estimation of the uncertainty in ΔT_w requires examinations of the data of individual runs, not a mere summation of the maximum uncertainties in T_s and T_w mentioned above. The maximum uncertainty in ΔT_w in all runs is estimated to be 0.06 K at $\Delta T_w = 0.1$ K, 0.62 K at $\Delta T_w = 11$ K. By use of the same thermocouples and the same wirings for the runs where measurements of small ΔT_w were involved, the boiling curves reported herein were found reproducible in the repeated runs.

Data on bubble formation were obtained by scanning the surface with the optical probe. The probe has three prongs, each made of a stainless steel tube with a narrowed end of 0.2 mm i.d. and containing an optical fiber. Figure 3 shows the probe on the surface. From one of the lateral prongs, the laser light (2-mW He-Ne laser) is emitted. The other lateral prong produces signal about the frequency of bubble formation as bubbles scatter the emitted light. As the probe traverses over an active pore at the rate of 0.147 mm/s, those lateral prongs

Table 1 Combination of pore diameters on structured surfaces

Designation	Pore Diameters and Relative Number Densities (μm) (%)	
	Large (RND)	Small (RND)
U5	———	50 (100)
C10-5-1	100 (8.3)	50 (91.7)
C10-5-2	100 (33.3)	50 (66.7)
U10	100 (100)	———
C15-10	150 (8.3)	100 (91.7)
U15	150 (100)	———

Fixed Parameters :
Tunnel cross section = 0.25mm x 0.4mm
Tunnel pitch = 0.55mm
Pore pitch along the tunnel = 0.7mm
The number density of pore locations = 252/cm^2
(RND = Relative Number Densities)

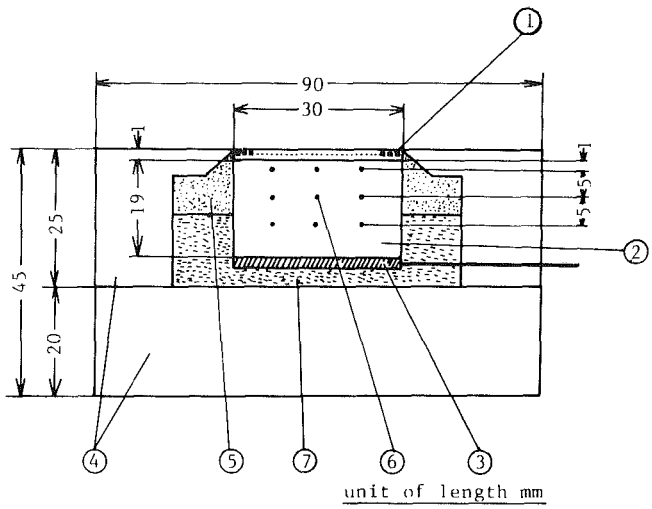

Fig. 2 The structure of a test block: ① structured surface, ② nickel block, ③ heater, ④ bakelite frame, ⑤ resin, ⑥ thermocouple, ⑦ insulation (glass wool)

also yield information about the maximum distance between the one end of bubble boundaries and the other end. This was interpreted as the diameter of the departing bubble at that pore on the assumption that the course of rising bubbles was steady and not deflected by the presence of the probe. Observation of bubbles with a strobe light confirmed that the above assumption was justified in most of the runs. The spacing between the ends of the lateral prongs is 0.9 mm. Most of the observed bubbles were smaller in diameter than this spacing. Even for larger bubbles, the measurement was feasible, because, at the extreme ends of spherical bubbles on the traversing line, the probe ends did not interfere with bubbles.

Data on bubble formation were obtained when heat flux was less than about 1 W/cm^2. For higher fluxes, bubbles were

Nomenclature

A = base heat transfer area, cm^2
A_t = surface area of tunnel walls, cm^2
C_b = constant in equation (1)
d_b = bubble departure diameter, cm
d_0 = diameter of pore, cm
f_b = bubble formation frequency Hz
g = gravity acceleration, cm/s^2
g_c = conversion factor, 10^{-7} J/dyne-cm
h_l = heat-transfer coefficient of evaporation, W/cm^2 K
h_{fg} = latent heat of vaporization, J/g
n = exponent of ΔT_w in equation (2)
N_A = number of active pores
P_s = system pressure, MPa
q_w = heat flux (W/cm^2) based on projected area
q_{ex} = heat flux on the outer surface (W/cm^2) based on projected area
q_L = latent heat flux (W/cm^2) based on projected area
T_s = saturation temperature, deg C
ΔT = temperature difference between the wall and the vapor, K
ΔT_w = wall superheat, K
ρ_l = liquid density, g/cm^3
ρ_v = vapor density, g/cm^3
σ = surface tension, dyne/cm

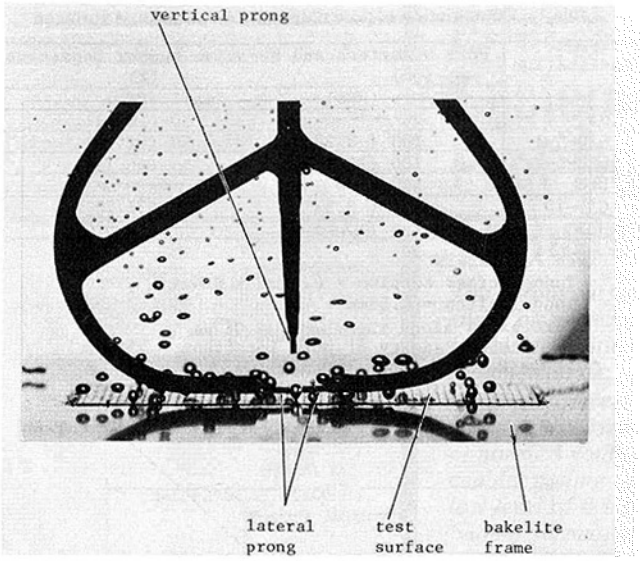

Fig. 3 Optical probe for collection of bubble formation data

too numerous to be subjected to meaningful measurements. The vertical prong receives scattered light, and it is used to detect the location of active pores.

All signals were processed by a computer to produce the departure diameter d_b, the formation frequency f_b at every active pore, the number of active pores N_A, and the latent heat flux q_L estimated by summing up $(\pi d_b^3/6)f_b$ over all active pores and multiplying the sum by $(\rho_v h_{fg}/A)$.

In all runs, the heat flux was initially raised to about 20 W/cm^2, a little less than the critical heat flux located by past experience. This was necessitated by the delayed incipience of boiling in raising heat flux. The temperature overshoots of 10–13°C (at $q_w = 0.6 \sim 0.8$ W/cm^2) were observed with the present surfaces, a roughly comparable magnitude to those observed in boiling fluorocarbon refrigerants on the commercial surfaces reported in [3, 4].

Boiling Curves

The structured surfaces prepared with geometrical precision did produce boiling curves which exhibit the effects of pore diameters in a systematic manner. Many of the interesting results can not be reproduced here due to space limitation, but representative data are shown in Figs. 4 and 5. The curves are drawn by just combining data points. Examples of actual data points are shown on the curves ① and ⑤ in Fig. 4, ② in Fig. 5.

Figure 4 shows the boiling curves at 0.23 MPa (the saturation temperature 50°C). The surface U5 has the poorest performance, although it shows substantial enhancement compared to the boiling curve of a plain surface. Enlargement of one out of twelve pores to 100μm (surface C10-5-1) yields a boiling curve the gradient of which is moderated as the wall superheat is reduced. Heat fluxes greater than 0.1 W/cm^2 are sustained at small superheats lower than 1 K. Quadrupling the number of larger pores (surface C10-5-2) shifts the performance a little higher. The boiling curve of the surface U10 shows a marked enhancement over a broad range of wall superheats. Still larger pores, having the diameter of 150 μm (surface U15), bring about the improvement of heat transfer over that of the surface U10. Surfaces having combinations of 100 μm and 150 μm pores were also tested. They produced boiling curves almost overlapping the curves of U10 or U15. Additional tests were performed with the surface where all pores have the size of 200 μm. At 0.23 MPa deterioration of heat transfer from that of U15 was observed at small

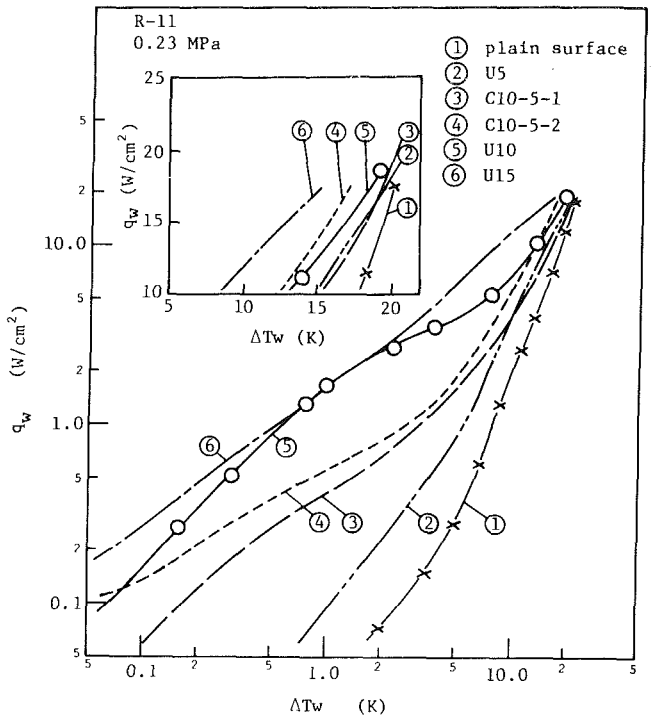

Fig. 4 Boiling curves of different surfaces ($P_S = 0.23$ MPa ($T_S = 50$°C))

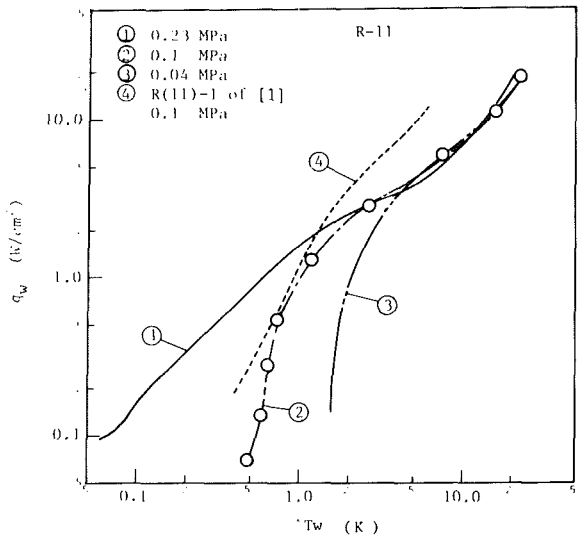

Fig. 5 Boiling curves of U10 under different system pressures

superheats ($\Delta T_w < 2.5$ K), with a drop of heat flux by 1/5 when compared with the heat flux of U15 at a superheat of 0.8 K. Under lower system pressures of 0.1 and 0.04 MPa, similar trends were found.

Figure 5 shows the boiling curves of U10 taken under system pressures of 0.23, 0.1 and 0.04 MPa. At smaller superheats, the boiling curves diverge, the higher the system pressure, the higher heat fluxes are sustained at reduced wall superheats. In case of the system pressure of 0.23 MPa, bubble formation did not cease even when the superheat was reduced to an indeterminable level. The curve (④) of the commercial porous surface R(11)-1 reported in [1] is shown for comparison. The commercial surface has pores of the nominal diameter of 100 μm with the pitch of 0.7 mm along the tunnel, and tunnels of a comparable cross-sectional dimension with the spacing of 0.55 mm. Its surface is microscopically irregular and the pores are of triangular

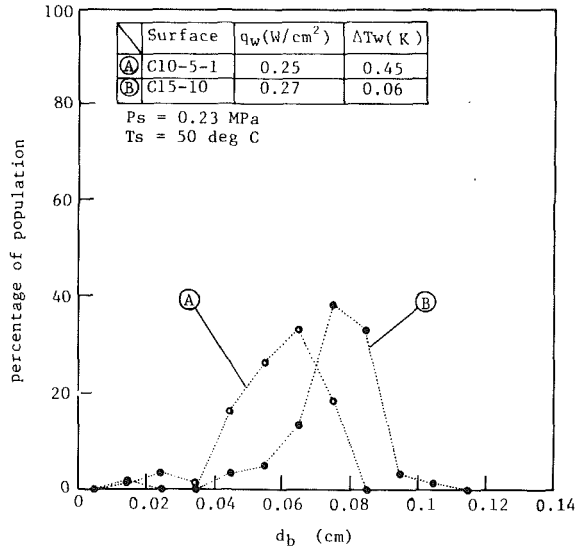

Fig. 6(*a*) Distribution of bubble departure diameter on C10-5-1 and C15-10 at P_s = 0.23 MPa

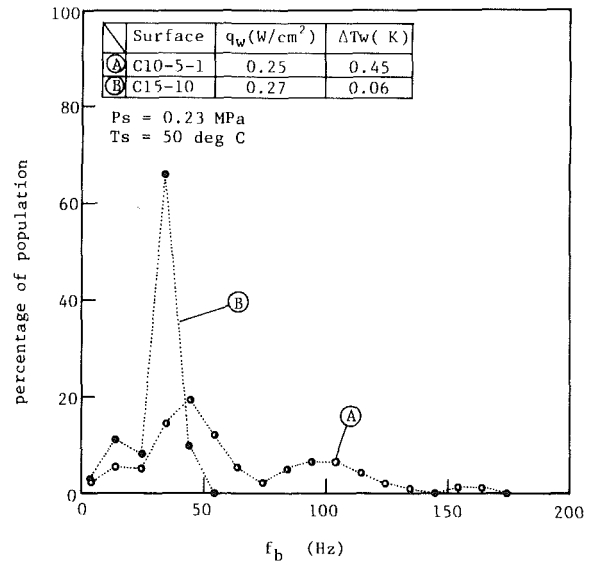

Fig. 6(*b*) Distribution of bubble formation frequency on C10-5-1 and C15-10 at P_s = 0.23 MPa

shape as shown by the photographs of Fig. 2 in [1]. It is probable that those differences cause disagreement between the curves (2) and (4).

Data of Bubble Formation

Figures 6(*a*) and 6(*b*) show the distributions of the departure diameter and the frequency of bubble formation, respectively, on the surfaces C10-5-1 and C15-10. The ordinate is the number of bubbles having a particular value of d_b or f_b divided by the total number of bubbles observed. The boiling curve of C10-5-1 is already shown in Fig. 4, and that of C15-10 almost coincides with the curve of U15 in the range of small superheats less than 2 K.

The total number of pores is 1512 on both surfaces. On C10-5-1, the 100 μm pores number 126, and on C15-10, the 150 μm pores number the same 126. On both surfaces, at those small superheats, bubbles are formed only at larger pores. The number of active pores was 87 on C10-5-1 and 60 on C15-10. The rest of larger pores remained inactive. On C10-5-1, the frequency of bubble formation spreads over a broad range. Site by site inspection of the data revealed no coherent relationship between bubble diameter and

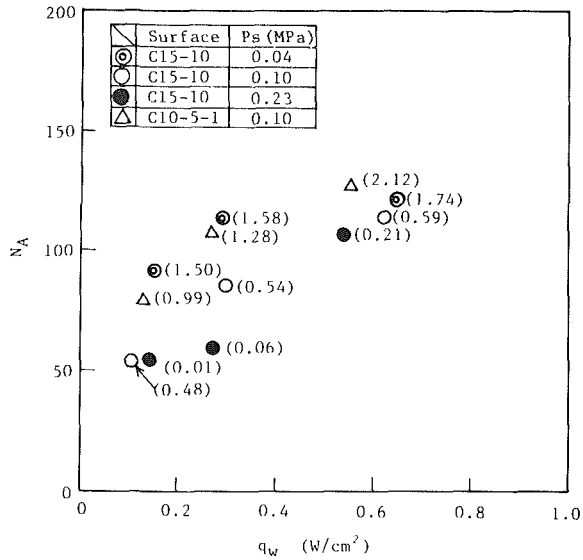

Fig. 7(*a*) Number of active pores versus heat flux. (Total number of pores = 1512. The figure in the bracket is T_w.)

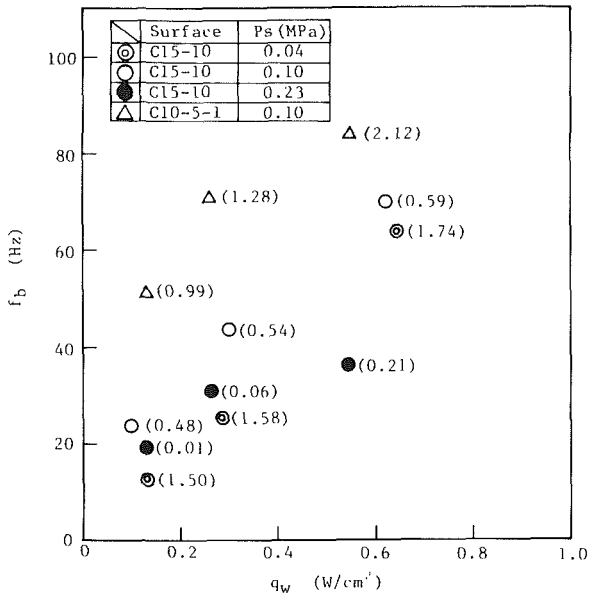

Fig. 7(*b*) Averaged frequency of bubble formation versus heat flux. (The figure in the bracket is T_w.)

frequency. In terms of the averaged values, the frequency on C10-5-1 is apparently greater than that on C15-10.

The data obtained with those surfaces exemplify a noteworthy feature of porous surface boiling. Numerous and active bubble formation does not necessarily guarantee a higher rate of heat transfer. Rather, bubbles emitted with lower frequency and from fewer pores could sustain a higher heat flux with a reduced wall superheat. In order to give a further support to the above finding, the number of active pores and the averaged frequency are plotted in Figs. 7(*a*) and 7(*b*), respectively, with data obtained with different surfaces and under different system pressures. A numeral attached to each data point is the wall superheat. The frequency data at the pressure of 0.04 MPa are somehow exceptional. The frequency drops to a low level reflecting the poor performance at the low system pressure.

The data on bubble departure diameter d_b suggest that the bubble adheres to the surface at the periphery of the pore during growth, called mode A in [5] and departure results when the buoyancy exceeds the surface tension force; hence,

$$d_b = C_b \left[\frac{\sigma d_0}{g(\rho_l - \rho_v)} \right]^{1/2} \quad (1)$$

Figure 8 shows the plot of experimental d_b against the parameter $\sigma d_0/g(\rho_l - \rho_v)$. Each vertical bar (I) shows a band of averaged values of d_b, i.e., it covers the average d_b taken at heat fluxes from 0.1 W/cm^2 to 0.6 W/cm^2. Equation (1) with the constant $C_b = 1.25$ correlates the data within a band of ±30 percent. The data obtained at 0.04 MPa involve relatively large uncertainty due to fluctuating behavior of bubbles.

Discussion

In order to facilitate the following discussion, conceptual sketches of phenomena in tunnels are shown in Fig. 9. In the dried-up mode, the tunnel space is filled with vapor, and vaporization into bubbles takes place outside the tunnels. The heat-transfer mechanism is analogous to that of nucleate boiling on a plain surface, with nucleation sites being located at artificial pores.

The suction-evaporation mode (hereafter abbreviated as the s-e mode) yields the highest heat-transfer performance due to evaporation of liquid on the tunnel walls. Liquid is sucked in the tunnel space through inactive pores by pumping actions of bubbles growing at active pores. It then spreads along the tunnels and evaporates. Vapor thus generated contributes to a next generation of bubbles [1, 2].

In the flooded mode, most of the tunnel space is occupied by liquid, and an active pore operates like an isolated nucleation site.

The following discussion is based on the reasoning that, where any of those modes prevails on the surface, its heat-transfer mechanism produces a characteristic trend of the boiling curve. Transition from one mode to another may also occur as the wall superheat is varied. Hence, if one attempts to correlate the boiling data in a conventional form,

$$q_w = C\Delta T_w{}^n \quad (2)$$

the constant C and the exponent n become functions of ΔT_w (or alternatively q_w), the number density of pores and the pore diameter. The exponent n is defined here on a part of the boiling curve in a log-log diagram approximating it by a straight line.

The dried-up mode is likely to work at high heat fluxes on a surface with small pores. Increased number of active sites and the pressure inside tunnels raised by an order of $4\,\sigma/d_0$ (d_0 = pore diameter) from the system pressure prevent liquid from entering through pores into tunnels. It is plausible that as the dried-up mode comes to prevail, the exponent n approaches to that for the plain surface ($n = 3$ from the curve ① in Fig. 4), as exemplified by the curves ② ③ and ④ in Fig. 4 in the range of high heat fluxes ($q_w > 3 - 4$ W/cm^2). The curves ③ and ④ also demonstrate that the most populous pores (50 μm pore) determine the trend of the boiling curve. It is also remarkable that, in the range of high heat fluxes, the system pressure exerts little or only small influence on the boiling curve as illustrated by Fig. 5. To the authors' knowledge, such behavior has never been reported in the literature in the case of plain surface boiling. An explanation may be given by considering the presence of cavities of various sizes on plain surfaces, the size range of nucleation cavities increasing with pressure [6]. The heat-transfer coefficient of sintered metallic matrix having a distribution of pore size also shows a dependence on pressure [7]. As far as visual observation permitted, no sites of bubble formation other than the drilled pores were observed in the present experiments. Very small effect of the system pressure may be attributed to the uniformity of pore size.

Other notable features of the boiling curves in the range of

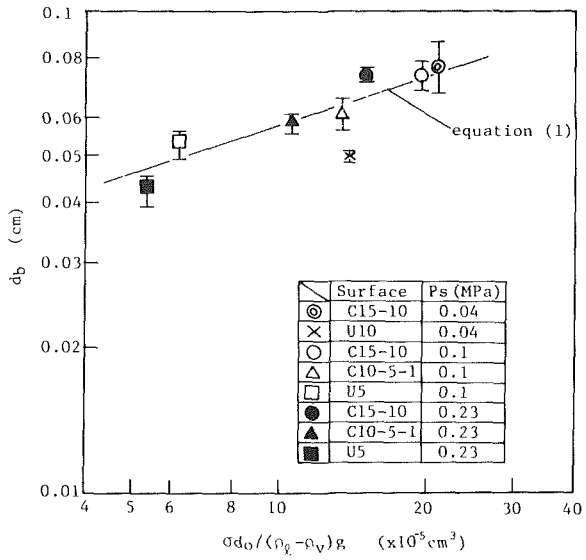

Fig. 8 Correlation of departure diameter. (The line represents equation (1) with $C_b = 1.25$.)

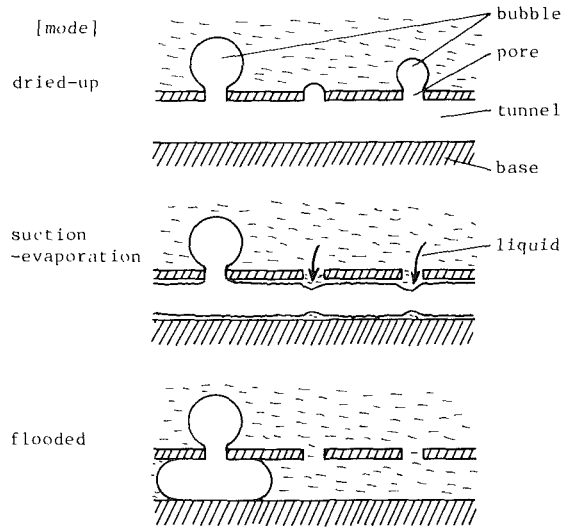

Fig. 9 Possible modes of phenomena in a tunnel

heat fluxes higher than 5 W/cm^2 are; (*i*) as the diameter of the most populous pores increases from 50 μm to 150 μm, the exponent n in equation (2) decreases from 2.2 to 1.0 in the case of the number density of 252/cm^2, and (*ii*) as the number density of pores increases, for example, pores of 100 μm dia from 84/cm^2 to 504/cm^2, n also decreases, from 2.6 to 0.9 at Ps = 0.1 MPa. The higher heat flux is obtained at a given ΔT_w on the surfaces having larger pores or a larger number density of pores. The boiling curves for different number densities tend to converge as heat flux approaches 20 W/cm^2, like those in Fig. 4.

In the range of low heat fluxes ($q_w < 3$W/cm^2), the important parameters are the diameter of largest pores and the system pressure. The number density of largest pores yields almost negligible effect on heat transfer, if it is sufficiently large, for instance, greater than 252/cm^2 on U10. The data of C10-5-1 and C10-5-2 in Fig. 4 (the curves ③ and ④) approach the curve ⑤ as the heat flux is reduced, indicating that the pores of largest size become important for heat transfer. In [2], based on the analytical modeling of the s-e mode, the formula is derived for the latent heat flux to which evaporation on the tunnel walls is a major contributor. Its asymptotic expression for small wall superheats is

$$q_L \sim h_l A_l \Delta T / A \tag{3}$$

where

$$\Delta T \sim \Delta T_w - (g_c T_s / \rho_v h_{fg})(4\sigma / d_0) \tag{4}$$

The internal heat-transfer coefficient h_l is considered almost independent of ΔT, [2]. Moreover, as presently observed, the latent heat flux makes a large contribution to heat transfer when the system pressure is 0.23 MPa, reaching almost 80 percent of the heat flux q_w. Then, for surfaces with relatively large pores where the capillary superheat in equation (4) is small, the exponent n of ΔT_w in equation (2) approaches unity, if the s-e mode is predominant. The curves (5) and (6) in Fig. 4 imply that the s-e mode is operative on those surfaces.

The data shown in Figs. 6(*a*), 6(*b*), 7(*a*), and 7(*b*) provide another implication of the working of the s-e mode on the surfaces which can sustain high heat fluxes with very small temperature differences. Where the dried-up mode works, active bubble formation could yield high heat-transfer performance, as is the case on plain surfaces. In the flooded mode, active bubbling is likewise favorable, as to and from motions of liquid in the tunnels is intensified and contributes to enhancement of heat transfer, a possible mechanism mentioned in the Appendix of [8] which discussed boiling on porous deposits. What Figs. 6(*a*)–7(*b*) exhibit can only be explained in the light of the s-e mode.

At the pressure of 0.1 MPa, the surfaces U10 and U15 also excel in heat-transfer performance compared to other surfaces having larger (200 μm) or smaller (50 μm) pores. The exponent n of ΔT_w in equation (2) in the ranges of low heat fluxes ($q_w < 3 \text{W/cm}^2$), however, is greater than unity. This is likely to be caused by an increased contribution from the heat flux on the outer surface, denoted as q_{ex} in [1, 2]. The contribution from the latent heat flux was found in the range 40–60 percent of q_w, decreased from the high-pressure data due to small vapor density.

All the data at 0.04 MPa show rapid deterioration of heat transfer as ΔT_w is decreased, (see, for example, the curve 3 in Fig. 5). This trend is analogous to the one obtained with an isolated reentrant cavity [9], implying the working of the flooded mode. The flooded mode results when the pumping actions of bubbles are too weak due to small frequency, see the frequency data at 0.04 MPa in Fig. 7(*b*). Too large pores may also invite the flooded mode as evidenced by the data of 200 μm pores (not shown).

Concluding Remarks

1 The present experiment revealed that, on the surface where pores of different sizes are present, the most populous pores govern the rate of heat transfer at heat fluxes above 3-4 W/cm^2. At low levels of heat flux, pores of the largest size play important roles in heat transfer.

2 The surfaces having pores of 100 μm or 150 μm with the number density of 252/cm^2 show excellent heat-transfer performances at the system pressure of 0.23 MPa. The suction-evaporation mode proposed in [2] appears to be operative on such surfaces where high heat fluxes are maintained with reduced levels of bubbling activity.

3 Any attempt to establish a predictive correlation of heat transfer should begin with the identification of the heat transfer mode operating inside cavities (tunnels). What are revealed in the present paper about the effects of operational and geometrical parameters on heat transfer provide the basis for derivation of predictive equations which is now in progress in the authors' laboratory.

4 Spared in order to limit the length of the paper are detailed comparison of performances between the commercial and model surfaces, and discussions on hysteresis and critical heat flux.

References

1 Nakayama, W., Daikoku, T., Kuwahara, H., and Nakajima, T., "Dynamic Model of Enhanced Boiling Heat Transfer on Porous Surfaces—Part I: Experimental Investigation," ASME JOURNAL OF HEAT TRANSFER, Vol. 102, No. 3, 1980, pp. 445–450.

2 Nakayama, W., Daikoku, T., Kuwahara, H., and Nakajima, T., "Dynamic Model of Enhanced Boiling Heat Transfer on Porous Surfaces—Part II: Analytical Modeling," ASME JOURNAL OF HEAT TRANSFER, Vol. 102, No. 3, 1980, pp. 451–456.

3 Bergles, A. E., and Chyu, M.-C., "Characteristics of Nucleate Pool Boiling Water From Porous Metallic Coatings," *Advances in Enhanced Heat Transfer—1981*, ASME HTD-Vol. 18, 1981, pp. 61–71.

4 Marto, P. F., and Lepere, V. J., "Pool Boiling Heat Transfer From Enhanced Surfaces to Dielectric Fluids," *Advances in Enhanced Heat Transfer—1981*, ASME HTD-Vol. 18, 1981, pp. 93–102.

5 Chesters, S. K., "Bubble Sizes in Nucleate Pool Boiling," *BOILING PHENOMENA*, edited by S. J. D. Van Stralen and R. Cole, Vol. 2, Hemisphere, 1979, pp. 879–899.

6 Hatton, A. P. and Hall, I.S., "Photographic Study of Boiling on Prepared Surfaces," *Proceedings of the 3rd International Heat Transfer Conference*, Chicago, Vol. IV, 1966, pp. 24–37.

7 Czikk, A. M., O'Neill, P. S., and Gottzmann, C. F., "Nucleate Boiling From Porous Metal Films: Effect of Primary Variables," *Advances in Enhanced Heat Transfer—1981*, ASME HTD-Vol. 18, 1981, pp. 109–122.

8 Macbeth, R. V., "Boiling on Surfaces Overlayed with a Porous Deposit : Heat Transfer Rates Obtainable by Capillary Action," AEEW-R 711, U.K.A.E.A., 1971.

9 Korner, W. and Photiadis, G. "Pool Boiling Heat Transfer and Bubble Growth on Surfaces with Artificial Cavities for Bubble Generation," *Heat Transfer in Boiling*, edited by E. Hahne and V. Grigull, Hemisphere, 1977, pp. 77–84.

Pool Boiling Heat Transfer From Enhanced Surfaces to Dielectric Fluids

P. J. Marto
Mem. ASME

Lt. V. J. Lepere, USN

Department of Mechanical Engineering,
Naval Postgraduate School,
Monterey, Calif. 93940

Pool boiling heat-transfer measurements were made using a 15.8 mm o.d. plain copper tube and three copper enhanced surfaces: a Union Carbide High Flux surface, a Hitachi Thermoexcel-E surface and a Wieland Gewa-T surface. The dielectric fluids were Freon-113 and Fluorinert FC-72, a perfluorinated organic compound manufactured to cool electronic equipment. Data were taken at atmospheric pressure, and at heat fluxes from 100 W/m^2 to 200,000 W/m^2. Prior to operation, each test surface was subjected to one of three aging procedures to observe the effect of surface past history upon boiling incipience. For Freon-113 the enhanced surfaces showed a two to tenfold increase in the heat-transfer coefficient when compared to a plain tube, whereas for FC-72 an increase of two to five was measured. The High Flux surface gave the best performance over the range of heat fluxes. The Gewa-T surface did not show as much of an enhancement at low fluxes as the other two surfaces, but at high fluxes its performance improved. In fact, it was the only surface tested which delayed the onset of film boiling with FC-72. The degree of superheat required to activate the enhanced surfaces was sensitive to both past history of the surface and to fluid properties.

Introduction

Nucleate pool boiling from enhanced heat-transfer surfaces is being examined in many areas of engineering as a means of attaining high heat fluxes while maintaining low temperature differences between the heated surface and the heat-transfer fluid. One area in which these enhanced surfaces have potential promise is in the field of electronics cooling. Advanced electronic devices can generate large heat fluxes. They are very sensitive to temperature excursions and exhibit a high rate of failure if not adequately cooled. Consequently, in the future these devices may have to be cooled using enhanced nucleate boiling of selected dielectric fluids such as transformer oils, certain refrigerants, and perfluorinated liquids [1-5]. These latter liquids, such as Fluorinert FC-72, are very attractive coolants during nucleate boiling since they are chemically stable and leave no residue during boiling action [6]. Unfortunately, up to now there has been no published information on the nucleate boiling characteristics of FC-72 or other perfluorinated liquids. Some selected properties of FC-72 together with those of Freon-113 [7] are listed in Table 1 for comparison.

Recently, Nishikawa and Ito [8] discussed two methods to augment nucleate boiling. The first method is to treat the surface in a manner that reduces its wettability by the boiling liquid (e.g., using teflon coated pits during boiling of water [9]). However, this method has not been successful with highly wetting liquids (such as Freon-113 [2] and liquid nitrogen [10]), and should therefore be discounted for use with liquids which have very low surface tensions. The alternative therefore is to manufacture a surface with numerous re-entrant cavities which have the ability to trap vapor and keep the nucleation sites active. Several commercially available surfaces have these re-entrant type cavities [11-13], and recent measurements have been made with these surfaces to verify the extent to which this second method is successful [11, 14-18].

Yilmaz, Hwalek, and Westwater [15] compared the nucleate, pool-boiling, heat-transfer performance of a 13 mm o.d. plain copper tube to three commercially available enhanced tubes: a Wieland Gewa-T tube, a Hitachi Thermoexcel-E tube, and a Union Carbide High Flux tube. Their experiments were conducted using a horizontal steam-heated tube in p-xylene at atmospheric pressure. Similar tests were carried out for isopropyl alcohol [16]. All of these tests however were taken in the fully established boiling regime, and no information was provided on the hysteresis behavior of these surfaces or on the unwanted temperature overshoots which can occur at the initiation of bubble nucleation.

Bergles and Chyu [17] compared the nucleate pool boiling heat-transfer characteristics of four different Union Carbide High Flux surface coatings to a 25 mm o.d. plain copper tube in distilled water and R-113. The experiments were conducted with three different aging treatments to the test surface prior to collecting data. Their results showed that both the plain surface and the High Flux surface exhibited significant temperature overshoots prior to the initiation of boiling in R-113, and these overshoots were sensitive to aging, initial subcooling, and power increment changes.

Since semiconductor devices require operation over a fairly narrow temperature range, it is essential that these temperature overshoots be measured, their causes be understood, and their magnitude be reduced before nucleate boiling from enhanced surfaces can be employed as a general electronics cooling scheme. The purpose of this research was therefore to systematically study the performance of commercially available enhanced surfaces during nucleate boiling of both Freon-113 and Fluorinert FC-72 from the incipient point of bubble nucleation up to heat fluxes near, or at, the onset of film boiling. Special attention was placed upon the temperature overshoots which occur during the inception of nucleation to determine to what extent these enhanced surfaces exhibit this property with both Freon-113 and FC-72.

Test Apparatus

Figure 1 is a schematic drawing of the test apparatus, identifying all major components. Boiling occurred from a cylindrical copper test surface heated on the inside by a cartridge heater. The boiler vessel consisted of a thick-walled pyrex glass container with a plexiglass cover fitted with a rubber o-ring. This vessel was placed on an electric hot plate to allow the test liquid to be preboiled for degassing before

Contributed by the Heat Transfer Division for publication in the JOURNAL OF HEAT TRANSFER. Manuscript received by the Heat Transfer Division May 8, 1981.

Table 1 Selected properties of Fluorinert FC-72 and Freon-113

Property	FC-72 [6]	Freon-113 [7]
Normal boiling point, 1atm	56°C	47.57°C
Liquid density, 25°C	1.68 g/cm^3	1.565 g/cm^3
Vapor density, (BP)	0.014 g/cm^3	0.0074 g/cm^3
Specific heat, 25°C	0.25 cal/g°C	0.218 cal/g°C
Heat of vaporization, (BP)	21 cal/g	35.07 cal/g
Thermal conductivity, 25°C	0.057 W/m°C	0.065 W/m°C
Surface tension, 25°C	12 dynes/cm	23 dynes/cm
Dielectric constant, 25°C (1kHZ)	1.76	2.41
Average molecular weight	340	187

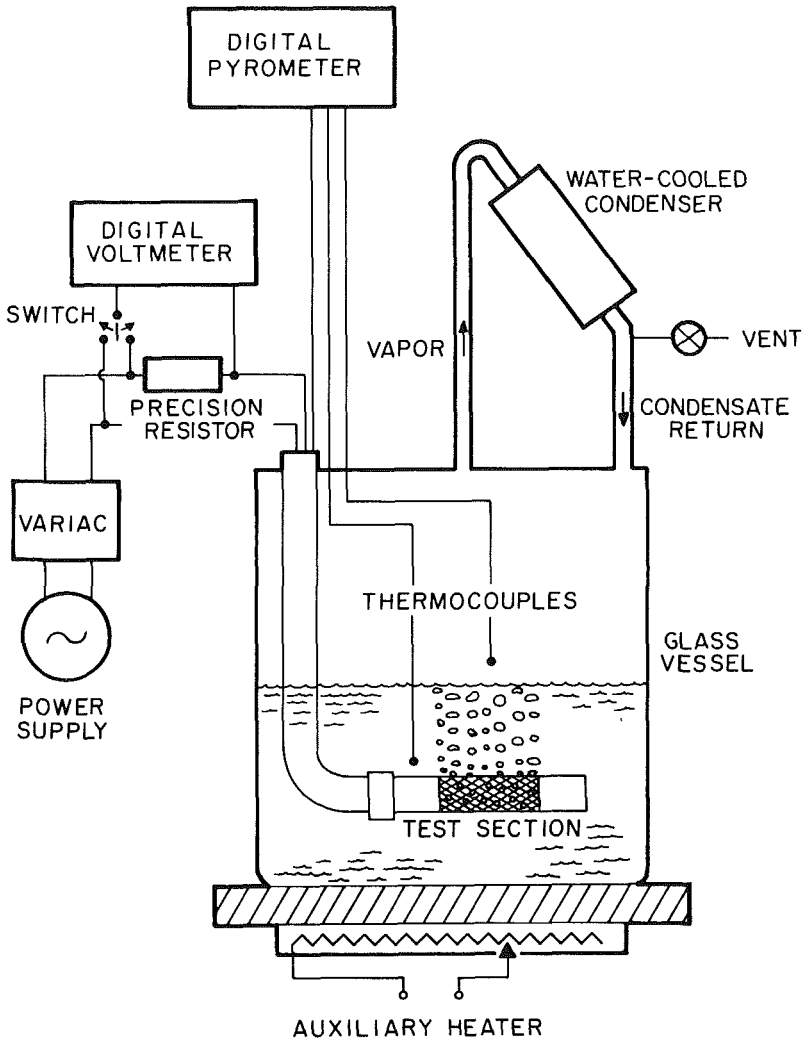

Fig. 1 Schematic drawing of test apparatus

each run, and to maintain the liquid at saturation temperature throughout the run. The vapor was condensed and returned to the boiler by gravity from a pyrex glass condenser using tap water for cooling.

Figure 2 is a cross-sectional representation of the test section. All the wall thicknesses have been exaggerated in this drawing for ease of visualization. Each test section had an overall length of 114 mm with an enhanced surface length of 50 mm. Four thermocouples with an average diameter of 0.76 mm were centered axially around the heater and were soldered into four grooves in the heater sheath spaced 90 deg apart. The heater was centered radially and axially in the test surface, and the void between the heater sheath and the inside tube wall was filled with soft solder under vacuum to avoid the formation of air bubbles between the heater sheath and the inside tube wall. To reduce longitudinal heat losses at each end, the enhancement was machined off, creating a smooth, thin-walled fin. The dimensions and characteristics of the test surfaces are listed in Table 2, and Fig. 3 contains photomicrographs of the enhanced surfaces at various magnifications. The High Flux surface characteristically contains numerous nucleation sites due to the network of

Nomenclature

h_{fg} = latent heat of vaporization, J/kg
N = nucleation parameter, defined by equation (1)
q'' = heat flux, W/m^2
T_w = temperature of the boiling surface, K
T_s = saturation temperature of the liquid, K
ΔT = wall superheat, K
ρ_v = density of vapor, kg/m^3
σ_l = surface tension of liquid, N/m

Table 2 Dimensions and characteristics of test surfaces

Surface	o.d. (mm)	Wall thickness (mm)	Thickness of enhancement (mm)	Other characteristics
Plain	15.8	0.97		used in an "as received" condition
High Flux	18.7	0.86	0.08	46 percent of the copper particles were smaller than 44 μm and the remainder were between 44–74 μm
Thermoexcel-E	16.5	1.32	0.19	average cavity mouth diameter was approximately 0.1 mm.
Gewa-T	17.9	0.70	1.02	centerline to centerline fin spacing was 1.35 mm; surface gap between fins was 0.18 mm

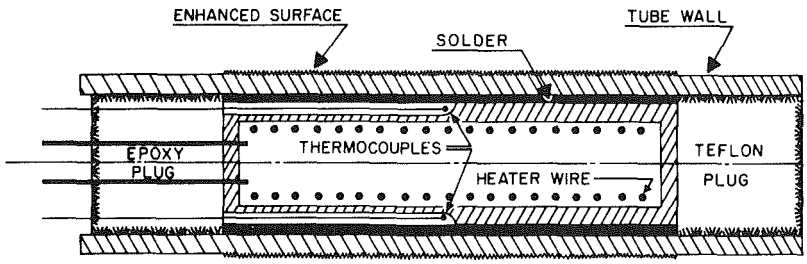

Fig. 2 Cross-sectional representation of the test section

randomly interconnected tunnels throughout the porous coating. The Thermoexcel-E surface has a unique series of circumferential tunnels under the surface skin which are machined on a tight spiral pitch. Numerous triangularly shaped surface openings are available to cause bubble nucleation. The Gewa-T surface contains a series of large tunnels on a tight helical pitch which are separated by "T-shaped" circumferential fins. The surface gap between fins is relatively large in comparison to the cavities on the other enhanced surfaces, and it is reasonable to expect this surface to flood more easily than the other two.

Two additional thermocouples were placed above the boiling fluid to determine fluid vapor temperature, and one thermocouple was immersed in the fluid pool to monitor fluid bulk temperature. All temperatures were measured with calibrated copper-constantan thermocouples. Each thermocouple was read separately through a thermocouple switch and a Newport digital pyrometer which had an accuracy of $\pm 0.06°C$. The test surface heater voltage was measured by a digital voltmeter accurate to 0.01 V. Heater current was determined by measuring the voltage drop across a precision resistor connected in series with the test section heater.

Experimental Procedures

At the start of each run, the plate heater was used to vigorously boil the pool for 1 hr in order to de-gas the test liquid. Power to the plate heater was then reduced to maintain the pool at saturation temperature. The power to the test section was then gradually increased by controlling the test section heater voltage. The voltage was increased in 2 to 4 V increments until the initiation of boiling occurred, at which point 10 V increments were made up to the maximum attainable heat flux. The power was then decreased in the same fashion. At each power setting, the system was permitted to stabilize for five minutes, and the following data were recorded: heater voltage, precision resistor voltage, vapor temperature, liquid pool temperature, and four temperatures around the circumference of the heater sheath.

Surface Aging. The previously mentioned procedure was followed after the test surface had been exposed to one of several different surface aging procedures. These procedures were similar to those of Bergles and Chyu [17] and were designed to investigate how boiling incipience is influenced by the past history of the boiling surface. The first procedure (surface aging A) permitted the surface to cool to ambient temperature while being immersed in the liquid pool overnight. The second procedure (surface aging B) aged the tube by preboiling it at 30 kW/m^2 for 1 hr (while the plate heater was on), and then letting it and the pool cool for 30 min prior to operation. The third procedure (surface aging C) aged the tube by preboiling it at 30 kW/m^2 for 1 hr (while the plate heater was on) followed by immediate operation. The final procedure (surface aging D) was to air dry the tube by heating it to 65°C for 10 min just prior to inserting it into the degassed pool for operation.

Data Reduction. The surface heat flux was determined by calculating the heater power from the measured voltage and current, and subtracting from this power the losses due to conduction of heat longitudinally through each of the thin-walled ends of the test section. These thin walls were assumed to be finite fins with insulated tips. A corrected length was used to account for heat loss through the tip [19]. For the enhanced surfaces, the surface area was based upon the actual length of the enhanced surface and an effective diameter to the base of the enhancement (i.e., a diameter resulting when the enhancement is machined off the surface). The wall temperature calculation was also based upon this same effective diameter. The four measured temperatures in the heater sheath were averaged, and a temperature drop was calculated due to conduction across the solder and the test surface wall up to the base of the enhancement. These calculations caused an estimated uncertainty in the surface heat flux of about ±7 percent, and an estimated uncertainty in wall superheat of $\pm 0.1°C$ at low powers, and $\pm 0.5°C$ at high powers.

(a) Scanning electron micrograph of the High Flux surface (500x)

(b) Optical micrograph of the Thermoexcel-E surface (40x)

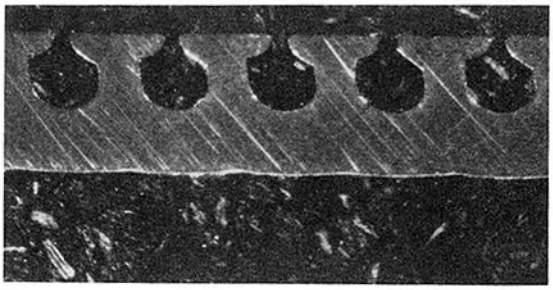

(c) Optical micrograph of a cross section of the Gewa-T surface (20x)

Fig. 3 Photomicrographs of the enhanced surfaces at various magnifications

Results and Discussion

Experimental data were obtained for both test fluids while boiling from the as-received plain tube, and the results obtained after the surface was allowed to cool in the pool overnight are shown in Fig. 4. Notice that a larger incipient boiling superheat is required for Freon-113 than for FC-72, and in each case a hysteresis pattern is evident.

Figure 5 provides a comparison between data obtained during this investigation for Freon-113 and the High Flux surface and data obtained by Bergles and Chyu [17]. Also shown for comparison is the natural convection correlation for a horizontal cylinder [20] which lies slightly below the experimental data. In general, the agreement between the two investigations is excellent, and is somewhat remarkable in that, although the particle size distribution was about the same in each investigation, the coating thickness was very different. Their coating thickness was 0.38 mm compared to a thickness of only 0.08 mm during this investigation. The recent work of Nishikawa and Ito [8] points out that an optimum coating thickness exists for a porous surface manufactured with constant diameter particles. Furthermore, for copper surfaces and particles, they found that this optimum thickness could be represented by four times the diameter of the sintered particle used in the coating. Even though the High Flux surface has a range of particle sizes (see Table 2), an approximate average particle size might be in the neighborhood of 50 μm. This particle size would give an optimum coating thickness of about 0.2 mm, which falls in between the value of 0.38 mm of Bergles and Chyu and the

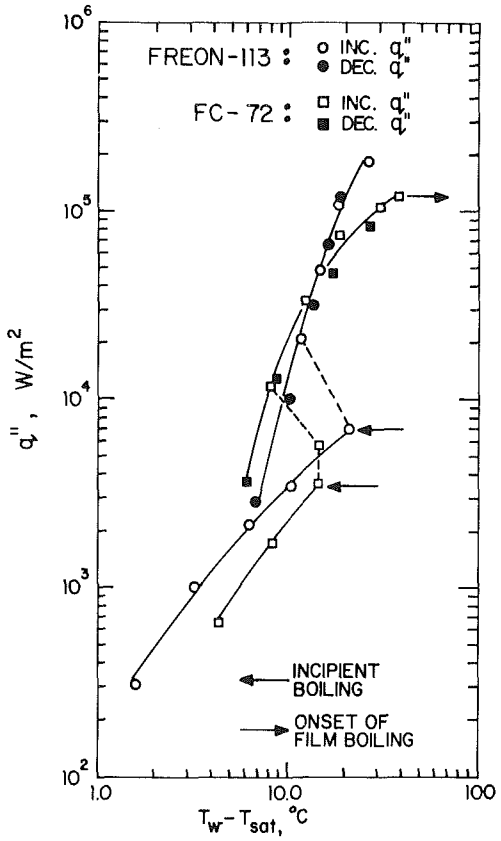

Fig. 4 Pool boiling data from the plain tube

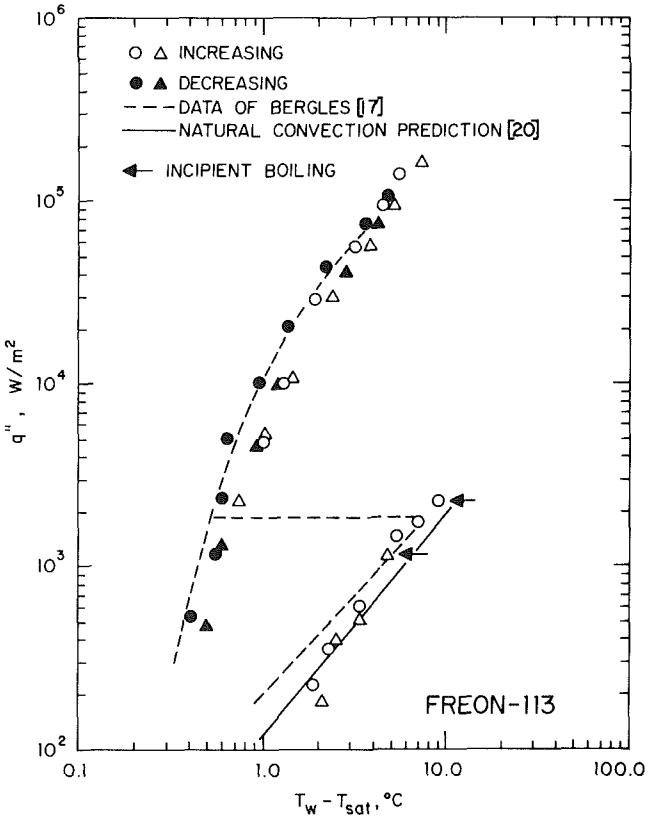

Fig. 5 Comparison of High Flux surface with data of Bergles and Chyu [17]

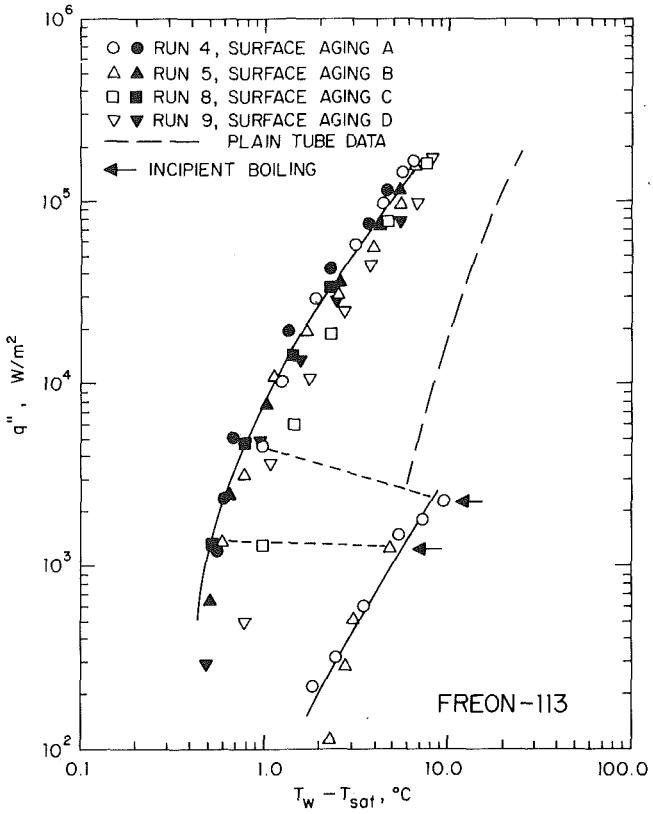

Fig. 6 Comparison of High Flux surface to plain tube for Freon-113

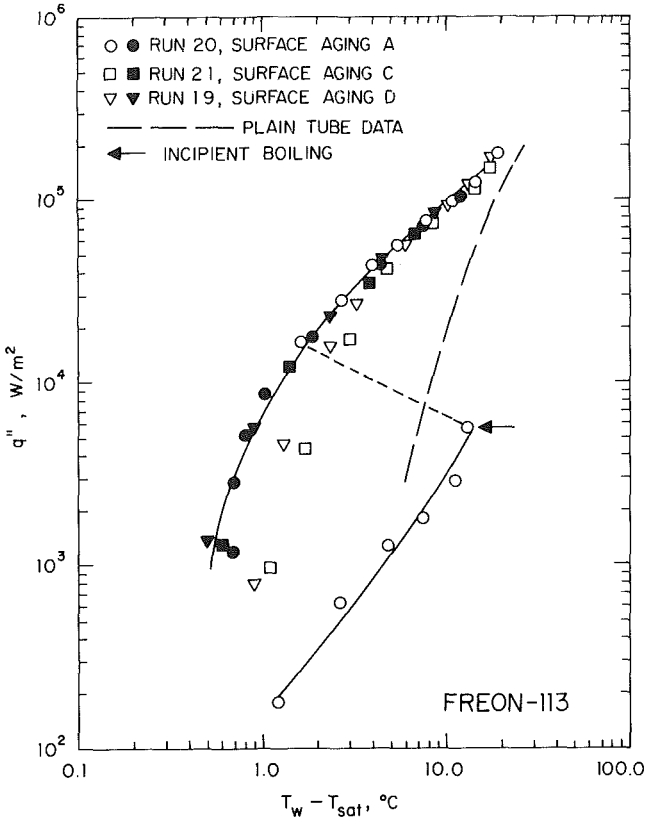

Fig. 7 Comparison of Thermoexcel-E surface to plain tube for Freon-113

value of 0.08 used during this study. Tests should therefore be conducted with varying High Flux coating thicknesses to verify if such an optimum thickness is reasonable.

Figures 6, 7, and 8 compare the results of each of the enhanced surfaces to the plain tube for Freon-113. In the fully established boiling regime, it is evident that the best performance is shown by the High Flux surface. At a low heat flux of 4 kW/m^2, the heat-transfer coefficient with this surface is almost ten times the plain tube value. This enhancement tapers off to a factor slightly above 3 as the heat flux is increased to 100 kW/m^2. The Thermoexcel-E surface demonstrates a similar improvement in the heat-transfer coefficient at low fluxes, but the improvement deteriorates more rapidly with increasing heat flux. The Gewa-T surface shows an improvement of only 2.5 at low heat fluxes, but unlike the other two surfaces, its enhancement actually improves as heat flux increases, giving a heat-transfer coefficient almost three times the plain tube at a flux of 100 kW/m^2. This most likely occurs because at low heat fluxes the large tunnels created within the Gewa-T surface give it the characteristic of a plain tube with fins, rather than a surface with numerous active sites. However, at large heat fluxes, because of the large spacing between the tunnels in relation to the other surfaces, separation of the vapor columns occurs. As a result, neighboring vapor columns do not coalesce as readily, and this surface improves relative to the other surfaces. It should be pointed out, however, that since none of the surfaces tested in this investigation were optimized for the particular liquids used, it is possible that the order of merit described above may be altered if suitably optimized surfaces are tested.

Figures 6, 7, and 8 also show the influence of surface preconditioning or aging upon boiling inception. In every case, the highest measured superheat prior to bubble nucleation occurred for surface aging A, allowing the surface to cool in the pool overnight. During this aging procedure, due to the high wettability of Freon-113 on copper, the large

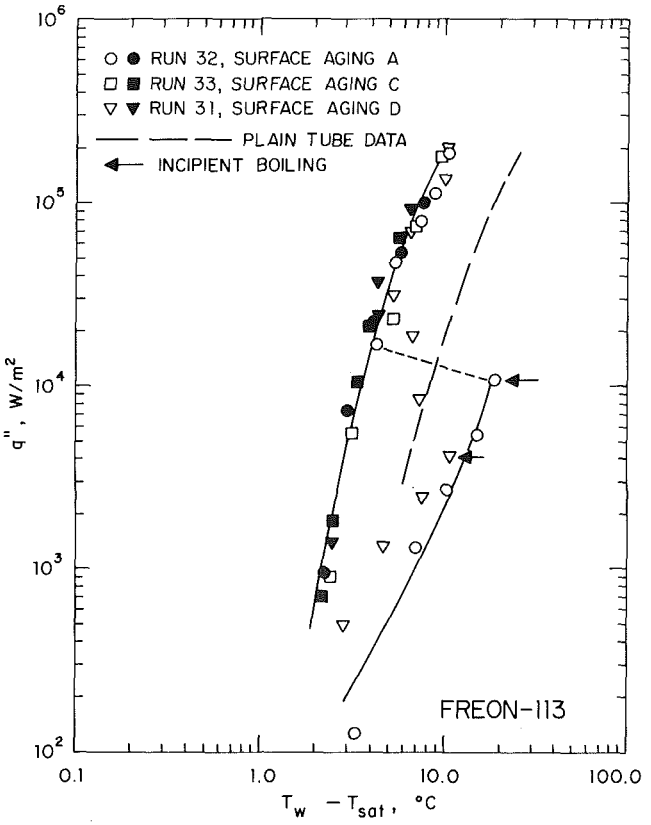

Fig. 8 Comparison of Gewa-T surface to plain tube for Freon-113

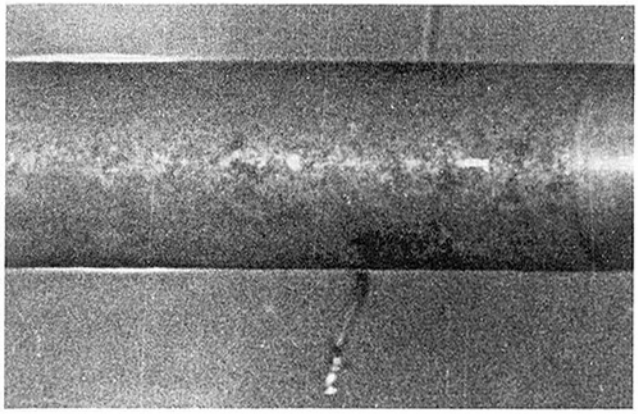

(a) View just prior to boiling initiation, $t = 0$

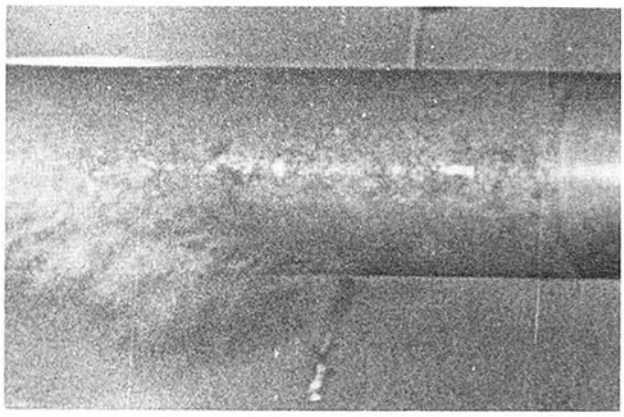

(b) View of explosive nucleation on lower left of surface, t = 0.015 s

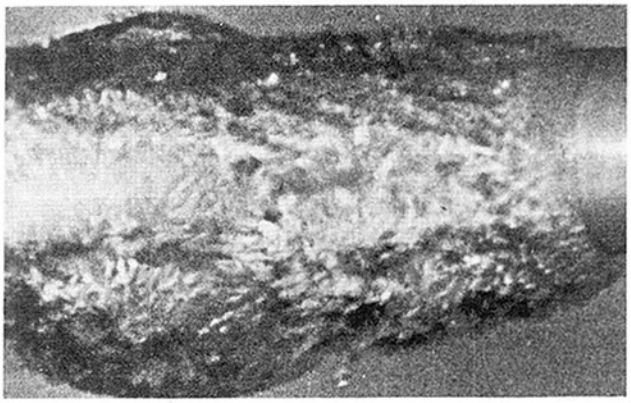

(c) View of vapor eruption following initial nucleation, t = 0.030 s

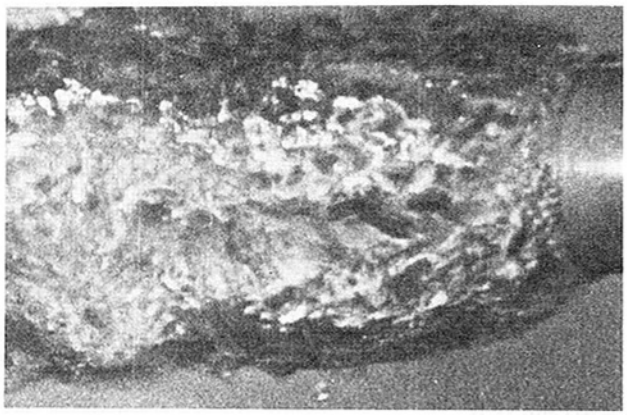

(d) View of vapor blanketing entire enhanced surface, t = 0.045 s

Fig. 9 Sequential movie frames (at 64 FPS) of Freon-113 boiling activation from the High Flux surface

cavities are flooded with liquid and higher superheats are required to nucleate the smaller cavities. Note that in comparing the three enhanced surfaces, the incipient point occurs at the lowest heat flux and superheat for the High Flux surface. The Gewa-T surface requires the largest superheats due to the ease with which the Freon-113 can flood the large tunnels between each fin. Each of the enhanced surfaces requires a lower superheat than the plain tube (Fig. 4). Figure 6 also shows that in surface aging B, preboiling followed by a 30 min subcooling, requires superheats almost as large as the overnight subcooling (surface aging A). It is therefore evident that, upon cooling, the surface cavities become flooded very rapidly. As shown in Figs. 6 and 7, both the High Flux and the Thermoexcel-E surfaces exhibit very little temperature overshoot and hysteresis following surface aging C and D. However, as seen in Fig. 8, (surface aging D) air drying the surface before operation doesn't relieve the hysteresis pattern for the Gewa-T surface. As mentioned above, the large size of the tunnels between the fins on this surface easily flood and deactivate. Notice also that with this surface and aging D, after the incipient point, the superheat does not reduce to the established boiling value in an abrupt fashion, but approaches the fully established boiling superheat only after the heat flux is increased several times.

In general, for most heat-exchange applications, operating heat fluxes are high enough to insure fully established boiling and there is little concern for the temperature overshoot problem. On the other hand, in cooling certain electronic components, the heat fluxes may be low enough for this overshoot problem to be important.

Of all the surfaces tested, the High Flux surface experienced the most rapid and dramatic activation after being submerged in the pool overnight. Once boiling initiated, the entire test section was active in about 0.015 s. Figure 9 shows a sequence of four movie frames showing the initiation of boiling on the High Flux surface in Freon-113 after being submerged in the pool for 3 hrs. The filming was done at 64 frames per s. In Fig. 9(*a*), no boiling is evident. One of the thermocouples immersed in the liquid pool can be seen behind the test surface. In the following frame (Fig. 9(*b*)), the initiation of boiling occurs explosively, as seen in the lower left half of the surface, and in the following two frames, Figs. 9(*c*) and 9(*d*), the entire surface is active and covered with vapor. This rapid initiation of boiling across the surface is probably due to the interconnecting character of the High Flux surface and the high heat capacity of the test section. At high superheats, once one site activates, the rapid expansion of the vapor throughout the porous matrix activates additional nucleation sites over the entire surface. The other surfaces activated gradually with increasing heat flux. With both the Gewa-T and the Thermoexcel-E surfaces, a few sites first became active at some incipient heat flux. As the heat flux increased beyond this value, additional sites became active, subsequently activating a complete ring around the cylinder.

Figures 10, 11, and 12 compare the results of each of the enhanced surfaces to the plain tube for FC-72. In general, the enhanced surfaces behave in much the same way with this fluid as with Freon-113, although the increase in the heat-transfer coefficient in relation to the plain tube is less in FC-72 than in Freon-113 especially at low heat fluxes. This is most

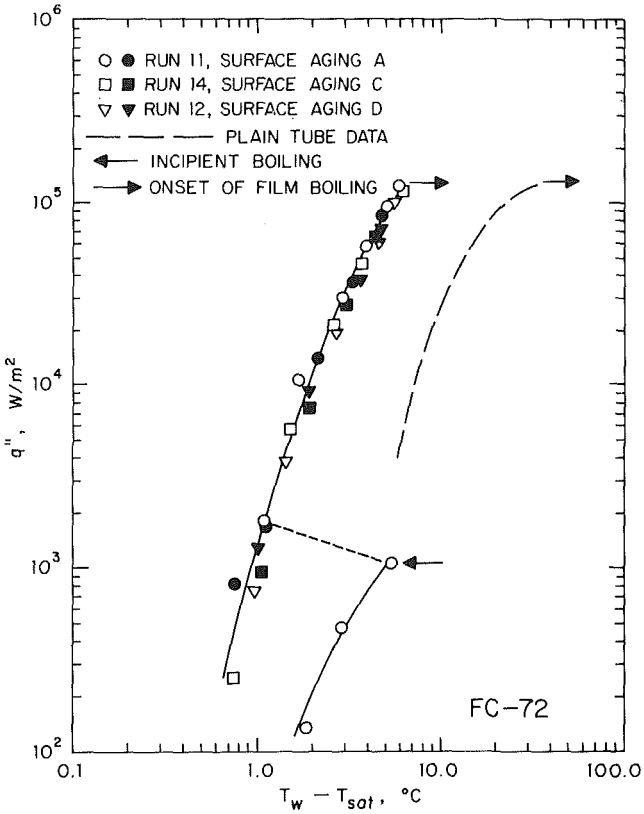

Fig. 10 Comparison of High Flux surface to plain tube for FC-72

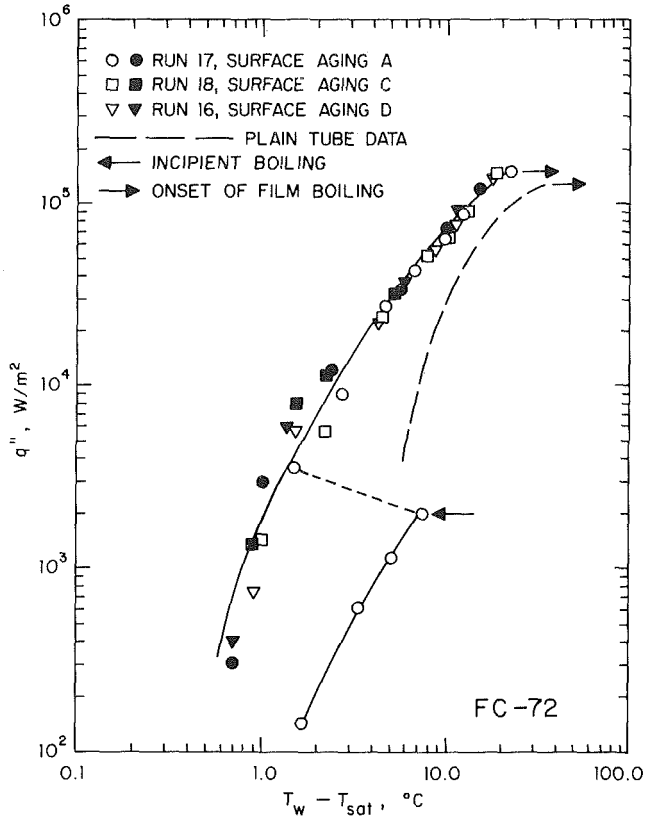

Fig. 11 Comparison of Thermoexcel-E surface to plain tube for FC-72

likely due to the lower heat of vaporization of FC-72 since the performance of each of the enhanced surfaces is markedly influenced by the presence of vapor in their respective interconnected tunnels. The best performance is shown by the High Flux surface which exhibits a heat-transfer coefficient from four to five times the plain tube value as the heat flux is gradually increased. This heat transfer coefficient ratio varies from 4 down to 2 for the Thermoexcel-E surface and remains approximately 3 for the Gewa-T surface.

The effect of surface aging upon boiling inception is also shown in Figs. 10, 11, and 12, and similar trends are observed with FC-72 as with Freon-113. However, the FC-72 requires lower superheats to nucleate than Freon-113. During pool boiling, it is well known that the critical superheat required to nucleate from a vapor-filled cavity is dependent upon a nucleation parameter [21]:

$$N = \frac{\sigma_l T_s}{\rho_v h_{fg}} \tag{1}$$

It is interesting to note that with the properties listed in Table 1, the ratio of this parameter for Freon-113 to FC-72 is 1.85. Upon comparing the incipient boiling superheats (obtained with surface aging A) plotted in Figs. 6, 7, and 8 with those plotted in Figs. 10, 11, and 12, the following superheat ratios for each of the test surfaces result:

Surface	ΔT(R-113)/ΔT(FC-72)
High Flux	1.75
Thermoexcel-E	1.64
Gewa-T	2.4

These experimentally obtained ratios are in close agreement with the theoretical ratio of 1.85 previously mentioned, implying that the nucleation parameter defined in equation (1) may be a reasonable index of incipient boiling superheats from the same surface. It is also of interest to note that in comparing Figs. 6, 7, and 8 for Freon-113 and Figs. 10, 11, and 12 for FC-72, the superheat required at boiling incipience is smallest for the High Flux surface, followed by the

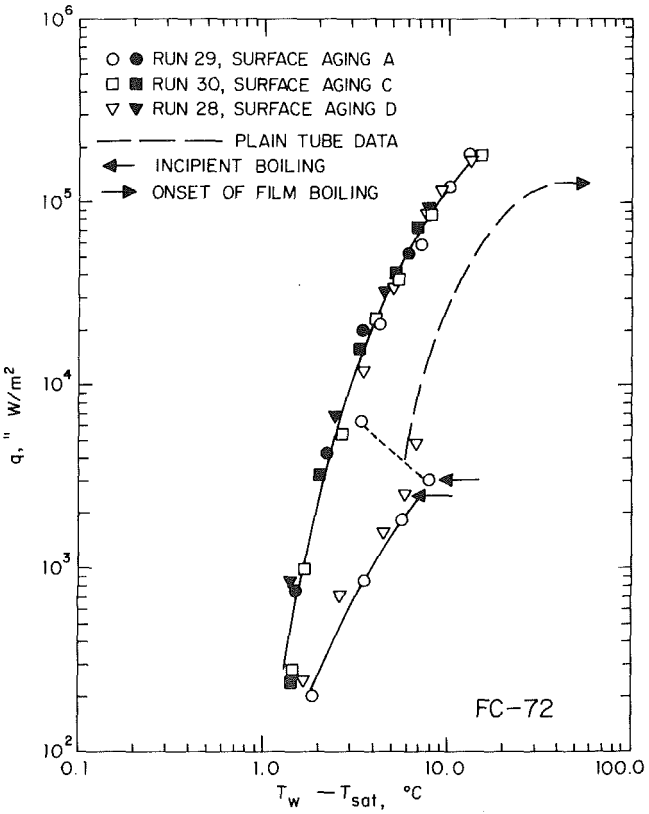

Fig. 12 Comparison of Gewa-T surface to plain tube for FC-72

Thermoexcel-E surface and then the Gewa-T surface. This implies that a larger size effective cavity nucleates for the High Flux surface compared to the other enhanced surfaces.

With FC-72, each of the test surfaces, except the Gewa-T surface, experienced the onset to film boiling when the critical heat flux was reached. A higher critical heat flux was observed for the Hitachi surface compared to the plain tube, whereas the High Flux surface showed no measurable improvement. When this critical heat flux was reached, the wall temperatures increased abruptly. Burnout of the tube wall, however, never occurred since the film boiling superheats with FC-72 are not high enough to cause physical burnout, and sufficient time was available to safely reduce the electrical power to the heater. Using the pool boiling critical heat flux expression developed by Zuber [22], a value of 161 kW/m^2 is obtained for FC-72. This value is in close agreement with the measured values indicated in Figs. 4, 10, and 11. With the Gewa-T surface (Fig. 12), a heat flux of 188 kW/m^2 was achieved with no rapid rise in wall temperature. It is postulated that with the unique design of this surface, the vapor must escape from the surface gaps spaced evenly along the surface. The relatively large spacing of these openings permits a more effective separation of the vapor columns, preventing vapor coalescence which effectively delays the onset of film boiling.

Conclusions

These results lead to the following conclusions:

1 For Freon-113, the enhanced surfaces show a two to tenfold increase in the heat-transfer coefficient when compared to a plain tube, whereas for FC-72, the enhanced surfaces show an increase of only two to five.

2 In general, the High Flux surface gives the best performance over a range of heat fluxes, whereas the Gewa-T surface performs well at high heat fluxes. The order of merit of these surfaces may change, however, if each surface is optimized for the particular liquid being boiled.

3 The degree of superheat required to activate the enhanced surfaces is less than the plain tube, and is sensitive to initial surface conditioning and fluid properties. The superheats required for Freon-113 are approximately twice as large as those required for FC-72, which is in agreement with existing theory. Consequently, the temperature overshoot problem and the resulting nucleate boiling hysteresis pattern is less severe with this liquid than with Freon-113.

4 The peak heat flux was reached with each of the test surfaces in FC-72 except for the Gewa-T surface. It is suspected that the unique design of this surface allows the vapor to escape more rapidly than either the High Flux or the Thermoexcel-E surface, and the onset of film boiling is therefore delayed to higher heat fluxes.

5 In using these enhanced surfaces to cool electronic equipment, care must be exercised at low heat fluxes where temperature overshoots could lead to uncertain semiconductor junction temperatures and lower reliability.

Acknowledgment

The authors would like to thank Mr. Elias Ragi of Union Carbide Corporation, Mr. Fred Weiler of Wieland Corporation, and Dr. Salim Yilmaz of Heat Transfer Research Incorporated for their assistance in obtaining samples of the enhanced surfaces tested during this study.

References

1 Marcellus, M. C., Spilhaus, A. F., and Troeltzsch, L. A., "Heat-Transfer Characteristics of Fluorochemical Inert Liquid FC-75," *Journal of Chemical and Engineering Data*, Vol. 6, No. 3, July 1961, pp. 459-463.

2 Bergles, A. E., Bakhru, N., and Shires, J. W., "Cooling of High-Power-Density Computer Components," Report No. DSR 70712-60, M.I.T., Nov. 1968.

3 Murphy, R. W. and Bergles, A. E., "Subcooled Flow Boiling of Fluorocarbons," Report No. DST 71903-72, M.I.T., Jan. 1971.

4 Powers, J. H., "Better High-Power-Density Circuit Cooling Through Nucleate Boiling," *Electronic Packaging and Production*, May 1970.

5 Fujii, M., Nishiyama, E., and Yamanaka, G., "Nucleate Pool Boiling Heat Transfer from Micro-Porous Heating Surface," *Advances in Enhanced Heat Transfer*, ASME, 1979, pp. 45-51.

6 "Fluorinert Electronic Liquids," 3M Company, Commercial Chemicals Division, 1980 Bulletin.

7 "Freon Technical Bulletin," DuPont de Nemours Company, 1964.

8 Nishikawa, K. and Ito, T., "Augmentation of Nucleate Boiling Heat Transfer by Prepared Surfaces," Japan-United States Heat Transfer Joint Seminar, Tokyo, Sept. 1980.

9 Young, R. K. and Hummel, R. L., *Chemical Engineeirng Progress*, Vol. 60, 1964, pp. 53-58.

10 Marto, P. J., Maynard, M. D., and Moulson, J. A., "Nucleate Pool Boiling of Nitrogen with Different Surface Conditions," ASME JOURNAL OF HEAT TRANSFER, Vol. 90, 1968, pp. 437-444.

11 "High Flux Boiling and Condensation Heat Transfer Tube—Hitachi Thermoexcel," Hitachi Cable, Ltd., Tokyo, 1978.

12 "Gewa-T Tubes, High Performance Tubes for Flooded Evaporators," Wieland-Produkt-Information, Wieland-Werke AG., 1979.

13 Kun, L. C. and Czikk, A. M., "Surface for Boiling Liquids," U.S. Patent No. 3,454,081, July 8, 1969.

14 Gottzmann, C. F., O'Neill, P. S., and Minton, P. E., "Field Experience with High Efficiency Heat Exchangers," AIChE 74th National Meeting, New Orleans, March 1973.

15 Yilmaz, S., Hwalek, J. J., and Westwater, J. W., "Pool Boiling Heat Transfer Performance for Commercial Enhanced Tube Surfaces," ASME paper No. 80-HT-41, Orlando, July 1980.

16 Yilmaz, S. and Westwater, J. W., "Effect of Commercial Enhanced Surfaces on the Boiling Heat Transfer Curve," *Advances in Enhanced Heat Transfer - 1981*, ASME, 1981.

17 Bergles, A. E. and Chyu, M. C., "Characteristics of Nucleate Pool Boiling from Porous Metallic Coatings," *Advances in Enhanced Heat Transfer - 1981*, ASME, 1981.

18 Trepp, C. H. and Hoffman, T. V., "Boiling Heat Transfer from Structured Surfaces to Liquid Nitrogen," Wärme-und Stoffübertragung, Vol. 14, 1980, pp. 15-22.

19 Holman, J. P., *Heat Transfer*, 4th ed., McGraw-Hill, New York, 1976, p. 39.

20 Ibid, p. 245.

21 Bergles, A. E. and Rohsenow, W. M., "The Determination of Forced Convection Surface-Boiling Heat Transfer," ASME JOURNAL OF HEAT TRANSFER, Vol. 86, 1964, pp. 365-372.

22 Zuber, N., "On the Stability of Boiling Heat Transfer," *Transactions* ASME, Vol. 80, 1958, p. 711.

M. Monde
Associate Professor.

H. Kusuda
Professor.

H. Uehara
Associate Professor.

Department of Mechanical Engineering,
Saga University,
Honjo-machi, Saga City,
Saga, Japan 840

Critical Heat Flux During Natural Convective Boiling in Vertical Rectangular Channels Submerged in Saturated Liquid

An experimental study of the critical heat flux has been carried out for natural convective boiling at atmospheric pressure in vertical rectangular channels. Experiments in four kinds of test liquids (water, ethanol, freon 113, and benzene) have been made for the ratio l/s less than 120, in which l is the length of the heated surface and s is the width of the channels. A generalized correlation for the critical heat-flux data in the four test liquids is evolved.

1 Introduction

As is generally known, the critical heat flux [CHF] during ordinary pool boiling on an open heated surface has been studied rather extensively, and generalized correlations, that are applicable to the critical heat flux data for many kinds of fluids, have been derived by Kutateladze [1], Rohsenow and Griffith [2], Zuber [3], Chang and Snyder [4], Zuber et al. [5], and others. Lienhard et al. [6,7], furthermore, developed Zuber's hydrodynamic prediction of critical pool boiling heat flux on an infinite flat plate for predicting the critical heat flux on both large and small heaters, and on finite horizontal flat plates.

On the other hand, research on the critical heat flux during natural convective boiling in confined channels is important as a fundamental study of the CHF phenomenon as well as for its application to industrial problems related to superconducting devices. In this case, owing to the complexity of flow mode, no correlation for the CHF has been evolved that can be applied universally to CHF data for various fluids and conditions.

In the case of horizontal channels in confined channels, Smirnov et al. [8,9], measured the CHF for water (p = 0.5 to 5 bars) and ethanol (p = 1 bar) in horizontal narrow channels and proposed a generalized correlation for the CHF data. But their correlation predicts their CHF data with an accuracy of only - 30 to + 70 percent. Katto and Kosho [10] measured the CHF for four kinds of liquids, two kinds of heated disk surface, and for clearances of more than 0.18 mm between two parallel horizontal disks at atmospheric pressure. Their correlation ([10] see equation(2)) predicts their CHF data with an accuracy of ± 15 percent. It should be noted that their correlation is based upon a generalized correlation given by Katto [11] who deals extensively with the critical heat flux for confined channels.

Most experiments in vertical channels have been made in cryogenic liquids (He, H_2, and N_2) in relation to superconduction devices. Sydoriak and Roberts [12], Lehongre et al. [13], and Vishnev et al. [14] measured q_{cr} in vertical annular channels, and Ogata et al. [15], and Bailey [16] measured q_{cr} in vertical rectangular channels. All of them propose empirical correlations only for their own CHF data. On the other hand, Katto and Kurosaka [17] recently measured the CHF in three liquids (water, ethanol, and R113) except for cryogenic liquids and annular channels. They pointed out that there are three characteristic CHF regimes and developed a generalized correlation for two of the regimes. Katto and Kawamura [18] reported CHF data for water and R12 under high pressures in vertical uniformly heated tubes. They pointed out that the CHF is closely related to the CHF in ordinary pool boiling on an open heated surface.

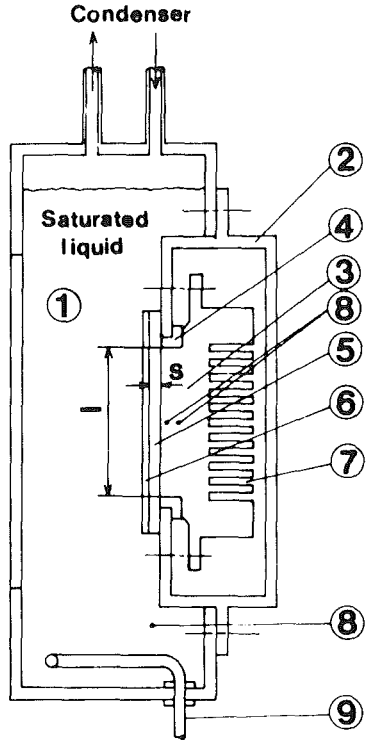

1 Boiling vessel
2 Heating-equipment
3 Copper block
4 Bakelite
5 Glass spacer
6 Glass plate
7 Electric heater
8 C-A thermocouple
9 Auxiliary heater

Fig. 1 Main part of experimental apparatus

In the present study, we measure the CHF in water, ethanol, R113, and benzene in three rectangular heated surface configurations (length l = 20, 35, and 50 mm) and in vertical rectangular channels more than 0.45 mm wide at atmospheric pressure (all combinations of l and s were tested for all fluids except for l = 20 mm, which was tested only for benzene), and we propose a generalized correlation for predicting the CHF data.

2 Experimental Apparatus

A main part of the experimental apparatus is shown

Contributed by the Heat Transfer Division for publication in the JOURNAL OF HEAT TRANSFER. Manuscript received by the Heat Transfer Division May 15, 1981.

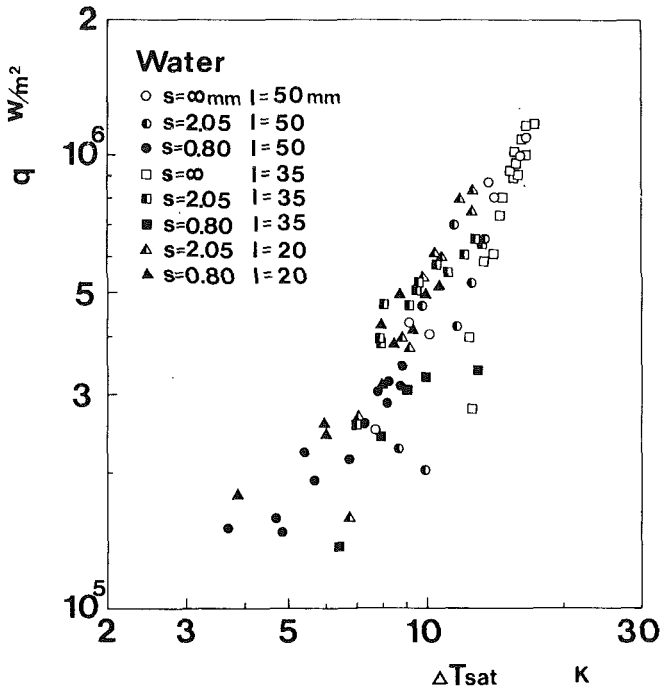

Fig. 2 Nucleate boiling data

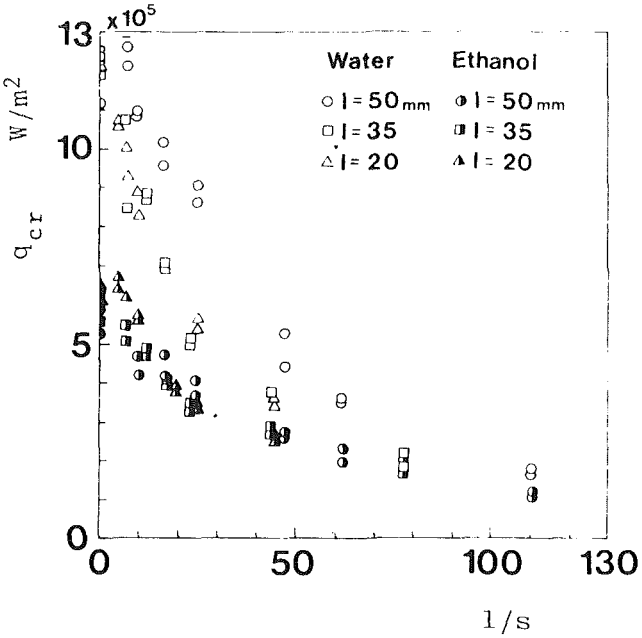

Fig. 3 Experimental measurements of the critical heat flux

schematically in Fig. 1. A test liquid in a boiling vessel (1) designed to stay at atmospheric pressure is heated by an auxiliary heater (9) up to the saturation temperature. The left hand surface of copper block (3), steadily heated by electric heaters (7) mounted in grooves of the copper block, provides a rectangular heated surface. Three different heated surfaces (l = 20, 35, and 50 mm in length and 10 mm in width) are mounted in three heating units (2), respectively. A rectangular space is formed by a glass plate (6) pressing two glass spacers (5) against the boundary of the heated surface. The seven different spacings (s = 0.45, 0.8, 1.05, 2.05, 3.0, 5.0, and 7.0 mm) are formed by changing the two glass spacers. An ordinary pool boiling experiment can be made by removing the glass plate.

The temperature T_w of the heated surface as well as the heat flux q across the heated surface is determined by means of two Chromel-Alumel thermocouples of 0.1-mm dia. located along the axis of the copper block. The thermal conductivity of this copper block, which must be known to calculate the heat flux, has been carefully determined in the preliminary experiment. In this experiment, the vapor that is generated on the heated surface during nucleate pool boiling between 5×10^5 and 10^6 W/m^2 is accumulated in a collector to measure the heat flux across the heated surface and at the same time the temperature gradient along the axis of the copper block is measured by two C-A thermocouples. The rate of heat transfer calculated from the vapor accumulated is from 85 to 90 percent of the electric input to the heaters mounted in the copper block. When the heat flux, thus determined, is compared with the electric input, it is found that the heat loss from the copper block is less than 15 percent of the total input.

The critical heat flux is determined by the following means: we increase the input to the heaters in the copper block in increments that are less than 3 percent of each preceding heat flux, and finally reach the point at which the heated surface temperature runs away. At that point, the CHF is determined with an error of 0 to 3 percent.

3 Experimental Results

3.1 Boiling curve. Figure 2 shows typical data for fully developed nucleate boiling in water obtained in the high heat flux region. It should be noted that the same boiling curve is obtained in the other liquids (ethanol, R113, and benzene).

A week tendency appears, as shown in Fig. 2, for the data to shift to the left and the coefficient of boiling heat transfer becomes higher as the width decreases. This tendency was pointed out by Ishibashi and Nishikawa [19] who studied saturated boiling heat transfer in narrow spaces.

3.2 Critical heat flux. All the CHF data obtained for water and ethanol are represented in Fig. 3: the CHF data are plotted against the ratio of the length, l, of the heated surface to the width s of the spacers. It should be noted that the same tendency for the CHF data is obtained for both R113 and benzene.

Figure 3 shows that the CHF data decrease in a roughly hyperbolic fashion with increasing l/s. This tendency is similar to that presented not only by Ogata et al. [15] and Bailey [16] who obtained the CHF data in Liquid He in long narrow channels at atmospheric pressure, but also by Lehongre et al. [13] who measured the CHF in liquid He in narrow tubes and annuli.

Our observations of fluids in the rectangular channel made with our naked eyes using a spotlight suggest that the CHF

Nomenclature

C = constant depends on physical properties
d = diameter of the heated surface
g = gravitational acceleration
H = vertical dimension of the horizontal ribbon heater
H_{fg} = latent heat of evaporation
K = constant independent of physical properties
l = length of rectangular heated surface
m = power of equation (6)
n = power of equation (6)
q = heat flux
q_{cr} = critical heat flux
s = width of rectangular channel
T_{sat} = saturation temperature
ΔT_{sat} = wall superheat [$= T_w - T_{sat}$]
T_w = temperature of heated surface
ρ_l = density of liquid
ρ_v = density of vapor
σ = surface tension

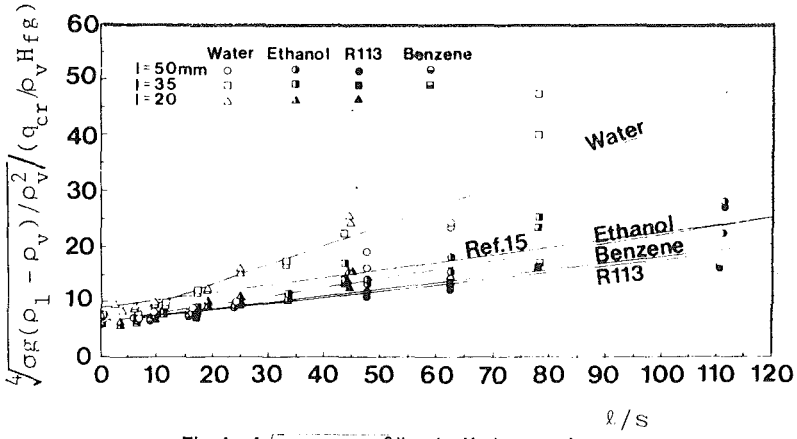

Fig. 4 $4\sqrt{\sigma g(\rho_l - \rho_v)}/\rho_v^2/(q_{cr}/\rho_v H_{fg})$ versus l/s

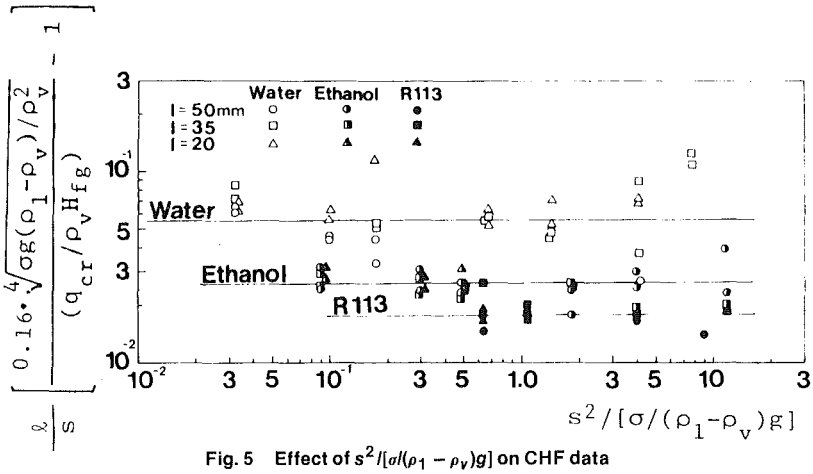

Fig. 5 Effect of $s^2/[\sigma/(\rho_l - \rho_v)g]$ on CHF data

takes place when a dry-patch appears near the exit of the channel, and then this drypatch grows to the entrance of the channel.

4 Correlation of Critical Heat Flux

4.1 Clue for analyzing the CHF data. Katto [11] developed generalized correlation for the CHF during natural convective boiling in confined channels with aid of dimensional analysis as follows:

$$\frac{q_{cr}/\rho_v H_{fg}}{4\sqrt{\sigma g(\rho_l - \rho_v)/\rho_v^2}} = f(\rho_l/\rho_v, g(\rho_l - \rho_v)s^2/\sigma, l/s) \tag{1}$$

Katto and Kosho [10] applied equation (1) to the CHF in saturated natural convective boiling in a space bounded by two horizontal coaxial disks and obtained equation (2) for predicting the measured CHF data with an accuracy of ± 15 percent.

$$\frac{q_{cr}/\rho_v H_{fg}}{4\sqrt{\sigma g(\rho_l - \rho_v)/\rho_v^2}} = \frac{0.18}{1 + 0.00918(\rho_l/\rho_v)^{0.14}[g(\rho_l - \rho_v)d^2/\sigma]^{0.5}(d/s)} \tag{2}$$

Ogata et al. [15] gave a semiempirical correlation (3) for the CHF in liquid He in long narrow vertical channels at atmospheric pressure.

$$q_{cr} = \frac{1}{C_1 + C_2(l/s)} \tag{3}$$

where $C_1 = 1.67 \times 10^{-4}\ Wm^{-2}$ and $C_2 = 2.39 \times 10^{-6}\ Wm^{-2}$

Equation (3), which applies only for He, can be nondimensionalized into the form of equation (1) with the result given by equation (4).

$$\frac{q_{cr}/\rho_v H_{fg}}{4\sqrt{\sigma g(\rho_l - \rho_v)/\rho_v^2}} = 0.105\frac{1}{1 + C_3(l/s)} \tag{4}$$

where C_3 is a constant having a value of 0.0143 for liquid He. The constant C_3, on the other hand, might depend on physical properties.

Kutateladze [1] correlates CHF data for water and some organic liquids in ordinary pool boiling ($l/s \to 0$), using

$$\frac{q_{cr}/\rho_v H_{fg}}{4\sqrt{\sigma g(\rho_l - \rho_v)/\rho_v^2}} = K,\ l/s \to 0 \tag{5}$$

where K is a constant between 0.12 and 0.16 and is independent of physical properties. Lienhard and Dhir [6], moreover, who refine K in equation (5) for many different geometries present K as a function of $H/\sqrt{\sigma/g(\rho_l - \rho_v)}$ and give $K = 0.12$ for the CHF on large horizontal ribbon heaters oriented vertically with one side insulated.

A correlation equation for the present CHF data can be given in the form:

$$\frac{q_{cr}/\rho_v H_{fg}}{4\sqrt{\sigma g(\rho_l - \rho_v)/\rho_v^2}} = \frac{K}{1 + C(\rho_l/\rho_v)^m[g(\rho_l - \rho_v)s^2/\sigma]^n(l/s)} \tag{6}$$

4.2 A generalized correlation of the critical heat flux. Figure 4 shows the dimensionless parameter $4\sqrt{\sigma g(\rho_l - \rho_v)/\rho_v^2}/(q_{cr}/\rho_v H_{fg})$ plotted against l/s. The dot-dash line in Fig. 4 is equation (4).

We conclude from Fig. 4 that

$$4\sqrt{\sigma g(\rho_l - \rho_v)/\rho_v^2}/(q_{cr}/\rho_v H_{fg})$$

is a linear function of l/s for each liquid, and it approaches the nearly same value, K, which is scattered roughly between

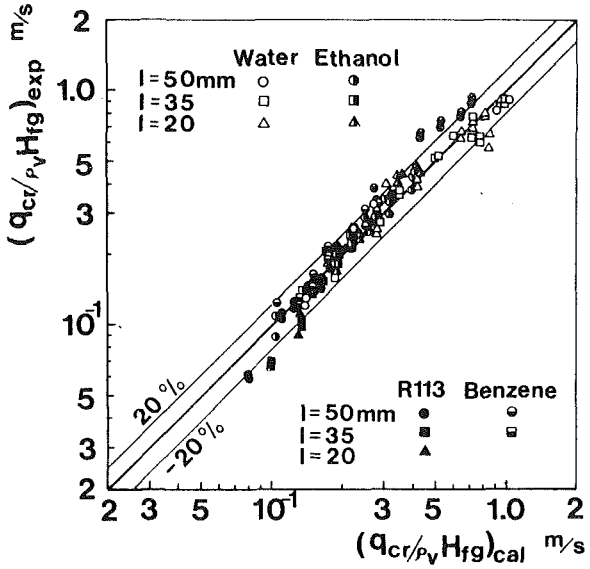

Fig. 6 Nondimensional correlation of CHF

0.12 and 0.17, for all the liquids used in the present experiment as l/s decreases. This value K corresponds to the constant not only predicted by equation (5) and included in Zuber's [3] correlation equation of CHF for ordinary pool boiling but also Lienhard and Dhir [6] correlation equation of CHF for pool boiling in many different geometries. Taking an average, $K = 0.16$. It might be helpful to mention that from Fig. 4, this value is constant when l/s is less than about 10. On the basis of this result, it may be reasonable to divide our description of CHF into two regimes where l/s equals 10, and deal with the CHF for the respective regimes. But, for simplicity, we neglect the regime at small values of l/s.

To determine the exponent n in equation (6), the CHF data are rearranged as shown by the ordinate in Fig. 5 and plotted against $s^2/[\sigma/(\rho_l - \rho_v)g]$ in Fig. 5. Figure 5 shows that the ordinate in Fig. 5 is independent of $s^2/[\sigma/(\rho_l - \rho_v)g]$, so $n = 0$. Next, the constant, C, and the power, m, can be determined, using the least squares method to combine the three groups of CHF data (water, ethanol, and R113) in Fig. 6 into a single group at the same value of l/s. This procedure gives $C = 6.7 \times 10^{-4}$ and $m = 0.6$. When we use these values, the benzene data are superposed into this single group.

The CHF data for natural convective boiling in vertical rectangular channels are thus correlated by

$$\frac{q_{cr}/\rho_v H_{fg}}{4\sqrt{\sigma g(\rho_l - \rho_v)/\rho_v^2}} = \frac{0.16}{1 + 6.7 \times 10^{-4}(\rho_l/\rho_v)^{0.6}(l/s)} \tag{7}$$

Equation (7) is represented by the heavy solid line in Fig. 6. The reason why a part of the CHF data for water as shown by the mark ⊗in Fig. 6 are larger than predicted equation (7) may be that the CHF occurs when a part of the vapor generated on the heated surface overflows from the entrance of the rectangular channels.

Next, applying equation (7) to liquid He ($\rho_l/\rho_v = 8.4$) and comparing it with equation (4), we note that the constant C_3 in equation (4) is six times as large as that of equation (7) and the values predicted by equation (7) are about 50 percent higher than the data for liquid He given by Ogata et al. [15]. The reason why equation (7) can not predict their data of liquid He with an accuracy of ± 20 percent may be that $\sqrt{\sigma/g(\rho_l - \rho_v)}$ and ρ_l/ρ_v in the present study are considerably different from the liquid He data as is shown in Table 1.

5 Conclusions

1 An experimental study of the critical heat flux has been carried out for natural convective boiling in vertical rectangular channels. Experiments in four test liquids have been made for l/s less than 120.

2 A generalized correlation of the CHF data in the present boiling system has been determined as follows:

$$\frac{q_{cr}/\rho_v H_{fg}}{4\sqrt{\sigma g(\rho_l - \rho_v)/\rho_v^2}} = \frac{0.16}{1 + 6.7 \times 10^{-4}(\rho_l/\rho_v)^{0.6}(l/s)}$$

and this correlation agrees with the experimental data within ± 20 percent, but does not predict the CHF data of Helium.

Table 1 Values of dimensionless parameter

	ρ_l/ρ_v	$\sqrt{\sigma/g(\rho_l - \rho_v)}m$
H_2O	1603.0	2.3×10^{-3}
C_2H_5OH	439.0	1.52
R113	204.0	1.01
C_6H_6	288.0	1.60
LHe	8.4	0.302

Acknowledgement

The financial support given by the Ministry of Education, Science, and Culture to the study under Grant in aid of fundamental Scientific Research No. 475160 (1979) is gratefully acknowledged. The authors also express their appreciation to Mr. Y. Hisano for his valuable assistance with the experiment.

References

1 Kutateladze, S. S., "Heat Transfer in Condensation and Boiling," AEC-TR-3770, 1952.

2 Rohsenow, W. H., and Griffith, P., "Correlation of Maximum Heat Transfer Data for Boiling of Saturated Liquids," *Chem. Engng Prog. Symp.*, Ser. 52, 1956, pp. 42-49.

3 Zuber, N., "Hydrodynamic Aspects of Boiling Heat Transfer," USAEC Rept. AECU-4439, 1959.

4 Chang, Y. P. and Snyder, N. W., "Heat Transfer in Saturated Boiling," *Chem. Engng Prog. Symp.*, Ser. 56, 1960, pp. 25-38.

5 Zuber, N., Tribus, M., and Westwater, J. W., "The Hydrodynamic Crisis in Pool Boiling of Saturated and Subcooled Liquids," *International Developments in Heat Transfer*, ASME, New York 1961, p. 230.

6 Lienhard, J. H. and Dhir, V. K., "Hydrodynamic Prediction of Peak Pool-boiling Heat Fluxes from Finite Bodies," ASME JOURNAL OF HEAT TRANSFER, Vol. 95, No. 2, 1973, pp. 152-158.

7 Lienhard, J. H., et al., "Peak Pool Boiling Heat-Flux Measurements on Finite Horizontal Flat Plates," ASME JOURNAL OF HEAT TRANSFER, Vol. 95, No. 4, 1973, pp. 477-482.

8 Smirnov, G. F., et al., "Heat Transfer in Boiling in Narrow Channels; Capillaries and under Other Constraints," *Heat Transfer Soviet Research*, Vol. 8, No. 4, 1976, pp. 88-93.

9 Smirnov, G. F., "Maximum Boiling Heat Fluxes under Some Special Conditions," *Heat Transfer Soviet Research*, Vol. 8, No. 4, 1976, pp. 114-118.

10 Katto, Y. and Kosho, Y., "Critical Heat Flux of Saturated Natural Convection Boiling in a Space Bounded by Two Horizontal Coaxial Disks and Heated from Below," *Int. J. Multiphase Flow*, Vol. 4, 1979, pp. 219-224.

11 Katto, Y., "Generalized Correlation for Critical Heat Flux of Natural Convection Boiling in Confined Channels," *Transactions of JSME* (in Japanese), Vol. 44, No. 387, 1978, pp. 3908-3911.

12 Sydoriak, S. G. and Roberts, T. R., "Study of Boiling in Short Narrow Channels and its application to Design of Magnets Cooled by Liquid H_2 and N_2," *Journal of Applied Physics*, Vol. 28, No. 2, 1957, pp. 143-148.

13 Lehongre, S., et al., "Critical Nucleate Boiling of Liquid Helium in Narrow Tubes and Annuli," *Prog. of the 2nd International Cryogenic Engineering Conference*, 1968, p. 274-275.

14 Vishnev, I. P., et al., "Nucleate Boiling in Crisis of Helium in Vertical Channels with Natural Convection," *Heat Transfer Soviet Research*, Vol. 6, No. 1, 1974, pp. 170-176.

15 Ogata, H., et al., "Boiling Heat Transfer of Liquid Helium in Long Narrow Channels," *Cryogenic Engineering* (in Japanese), Vol. 4, No. 5, 1969, pp. 219-225.

16 Bailey, R. L., "Heat Transfer to Liquid Helium Design Data for Both Cooled Super Conducting Magnets," *Prog. of the 5th International Conference on Magnet Technology*, 1975, pp. 582-589.

17 Katto, Y. and Kurosaka, T., "Critical Heat Flux of Natural Convection Boiling in Vertical Annular Channels," *15th National Heat Transfer Symposium of Japan*, 1979, pp. 280-282.

18 Kawamura, S. and Katto, Y., "Critical Heat Flux of Natural Convection Boiling in Vertical Uniformly Heated Round Tubes," *16th National Heat Transfer Symposium of Japan*, 1980, pp. 280-282.

19 Ishibashi, E. and Nishikawa, K., "Saturated Boiling Heat Transfer in Narrow Space," *International Journal of Heat Mass Transfer*, Vol. 12

Effects of Mass Flux, Flow Quality, Thermal and Surface Properties of Materials on Rewet of Dispersed Flow Film Boiling

O. C. Iloeje
Senior Lecturer,
Department of Mechanical Engineering,
University of Nigeria,
Nsukka

D. N. Plummer
Formerly,
Mechanical Engineering Department.
Assoc. Mem. ASME

W. M. Rohsenow
Professor.
Fellow ASME

P. Griffith
Professor.
Fellow ASME

Mechanical Engineering Department,
Massachusetts Institute of Technology,
Cambridge, Mass. 02139

The effects of mass flux, flow quality, material thermal properties, surface roughness, and surface oxidation on the rewet-wall superheat for dispersed vertical flow were experimentally investigated. The mass fluxes tested were 40.7, 81.4, 169.5 and 271.3 kg/s-m^2. Flow qualities varied from 10–90 percent. The test materials were copper, aluminum, and inconel-600. Overall dimensions of the test pieces were 10.16 mm i.d., 25.4 mm o.d., and 25.4 mm long. A smooth inside surface was prepared for each material, with roughness amplitudes of approximately 0.5 μm. Two inconel test pieces had roughnesses of 15–20 μm and 66 μm, respectively. Another inconel piece was oxidized to a thin oxide layer of approximately 1.3 μm. The test fluid was liquid nitrogen. The results indicated that the rewet wall superheat increased with mass flux. The rewet wall superheat decreased with increasing flow quality, with the rate of decrease being more rapid at higher mass fluxes and higher qualities. Increases in wall roughnesses, and the presence of surface oxidation, increased the rewet superheat. The effect of an oxide layer increased with increasing mass flux and decreasing quality, and was thought to result from the decrease in contact angle between the liquid and the oxidized surface. Differences in wall thermal properties were not very significant up to a mass velocity of 81.4 kg/s-m^2. Above this mass flux, the copper data did not clearly show the increasing T_{min} with increasing mass flux, while the inconel data did. A comparison of T_{min} for several materials with different thermal properties therefore was not made above mass flux of 81.4 kg/s-m^2.

Introduction

Dispersed flow film boiling, in which the liquid phase is dispersed as drops within a continuous vapor phase, can be generated either by "impulse" heating or by gradual "burnout." In the case of impulse heating, dispersed flow is preceded by the inverted annular film boiling regime, as shown in Fig. 1.

In fully developed film boiling, the vapor phase covers the heated wall and the temperatures are generally high. In systems, such as water-cooled nuclear reactors, which are accidentally tripped into film boiling, reattachment of the liquid phase to the wall (i.e., rewetting) must be achieved so as to prevent melting of the fuel cladding. However rewetting should be prevented during transport of cryogenic fluids so as to limit boil-off. Prediction and control of rewet are therefore essential.

Rewet. The rewet point is defined in this paper as the onset of transition or unstable boiling in going from stable film boiling to nucleate boiling. It corresponds to the minimum film boiling heat flux point on the standard boiling curve. This definition implies that all factors which may affect the heat transfer process, and, hence, shift the boiling curve in the transition/film boiling region, will affect the rewet point.

Results and models for ΔT_{min} from previous researchers for forced convection liquid nitrogen are summarized in Table 1. The pool boiling results of reference [3] for water, and the extensive correlation of reference [4] for pool boiling of many fluids on a variety of surfaces are omitted, because it is not clear how they should be compared to a forced convection experiment such as this one. One might expect, however, that any variables such as surface chemistry or thermal properties found important in pool boiling would also have an impact in a forced convection system. This indeed turns out to be the case. References [3] and [5] show the shifts in ΔT_{min} with changing surface chemistry such as noticed here.

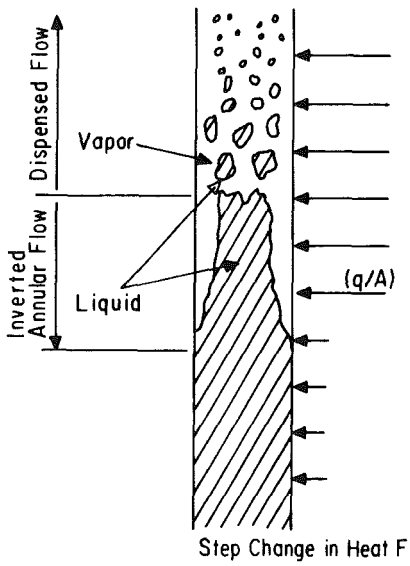

Fig. 1 Generation of dispersed flow by impulse heating

The results of [6] showed that both mass flux and quality affected ΔT_{min} in dispersed flow, and suggested that the data may also have been strongly affected by surface oxidation.

The work leading to this report is an extension of the work of [6], with a controlled study of the effects of roughness, oxidation, material thermal properties, as well as mass flux and quality on ΔT_{min}. From the data reviewed above, it is clear that the definition for rewet used in this report, and first proposed in [6], is more consistent experimental evidence and with the various methods of determining the onset of rewet.

Contributed by the Heat Transfer Division for publication in THE JOURNAL OF HEAT TRANSFER. Manuscript received by the Heat Transfer Division November 14, 1980.

Table 1 ΔT_m for forced convection of N_2 as determined by several investigators

References	Comments	Material; P	ΔT_{min} °C
Spiegler et al. [1]	T_{min} (thermodynamic property) = temperature of limiting superheat of liquid (Vander Waal's equation of state used)	N_2; 1 atm	28.5
Kalinin [2]	ΔT_{min} = function of $(k\rho c)_l / (k\rho c)_w$. Tests for inverted annular flow regime.	N_2/Inconel-600; 1 atm	79 ± 35%
Present work	Dispersed flow, X = 35%, G = 81.4 kg/s-m^2	N_2/smooth, clean Inconel-600; 1 atm	39
" "	" X = 35%, G = 40.7 kg/s-m^2	"	28
" "	" X = 70%, G = 40.7 "	"	22

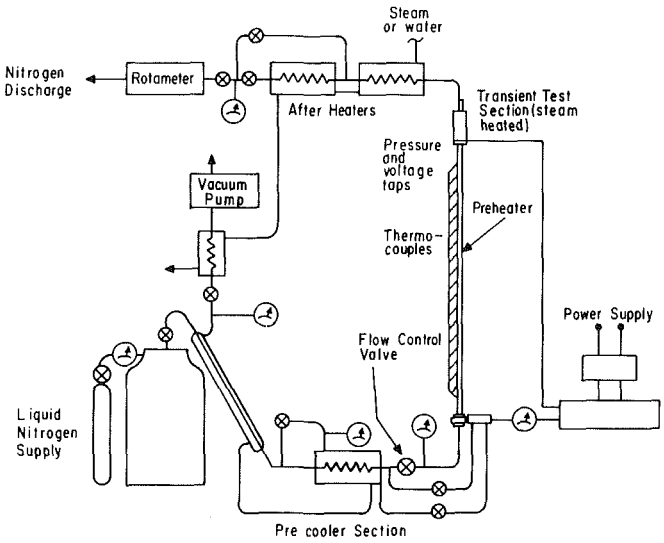

Fig. 2 Nitrogen test loop

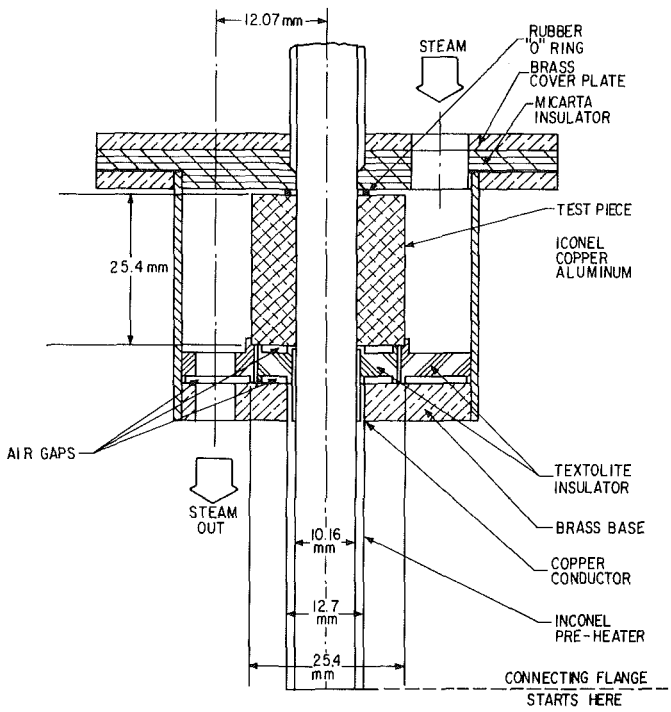

Fig. 3 Test block

Experimental Program

Technique. The mass flow rate and quality were developed in an electrically heated preheater external to the test section. The test piece itself was electrically and thermally insulated from the preheater and its dimensions were such that the Biot number was small enough to permit its treatment as a lumped heat source or sink. By taking each test piece through a transient with the flow held constant, it was made to go from film boiling to nucleate boiling, through rewet and transition boiling. The heat flux from the test piece to the fluid was then given by

$$Q/A = \frac{\rho c V_{mat}}{A} \frac{dT}{dt} \tag{1}$$

The minimum heat flux point, i.e., the unset of rewet, corresponded to the minimum in the magnitude of (dT/dt). The wall superheat corresponding to this point on the temperature-time trace gave the rewet superheat.

The Test Loop. The test loop is illustrated in Fig. 2. Liquid nitrogen was supplied from Dewars and given by prepurified gaseous nitrogen at 6.89 bar held in separate cylinders. The fluid passed through subcooling heat exchangers, and its condition was measured at inlet to the preheater. Power was from a 210-V, a-c supply, through a variac and stepdown transformers.

The preheater was 10.16 mm i.d., 12.7 mm o.d., 2489.2 mm long inconel tube having a low temperature coefficient of resistance. Seven thermocouples were welded at 12.7 mm, 31.75 mm, 50.8 mm, 660.4 mm, and 2489.2 mm from the entrance to the test section. During all but three runs, rewet or transition boiling existed downstream from the third thermocouple location within the preheater. This ensured that the qualities calculated at the entrance to the test section, assuming thermal equilibrium in the flow, was approximately correct.

Nomenclature

A = heat transfer area, m^2
Bi = Biot number
c = specific heat at constant pressure, KJ/kg°C
G = mass flux, kg/s-m^2
H = specific enthalpy, KJ/kg
h = heat transfer coefficient, W/m^2 °C
h_{fg} = enthalpy of evaporation, KJ/kg
k = thermal conductivity, W/m°C
l = length, m
$\dot{m}$ = mass flow rate, kg/s
P = pressure, bar, atm
Q = heat flow rate, W
T = temperature, °C
t = time, hr
V = volume, or voltage, m^3 or V
ΔT_{min} = $(T_w - T_{sat})$ at rewet, °C
ρ = density, kg/m^3

Subscripts

e = electric
ins = insulation
l = liquid
mat = material
sat = at saturation
sub = subcool
w = heat transfer wall surface

Table 2

	Specimen	Finish/Roughness	Preparation technique
1	Inconel-600	Smooth/0.5 μm	Drill, bore and finish
2	Copper	"	with Sonning Products
3	Aluminum	"	honing stone No. K12-J95
4	Inconel-600	Rough/15-20 μm	Drill finish
5	"	Rough/66 μm	Drilled, criss-crossed internally with threads at .051 mm depth and 1.337 mm pitch
6	Inconel-600	Smooth/0.5 μm oxidized, oxide Layer = 1.3 μm	Baked at 538°C for 2 hrs, then at 816°C for 1 hr; oxide thickness determined with electron microscope

The test block containing the test piece, was located at the top of the preheater. Before the flow was exhausted to the atmosphere, it was heated to evaporate all the liquid, and then measured in rotameters.

The Test Block. The test block, sketched in Fig. 3, consisted of a copper steam jacket soldered to a brass base and brass top flange. The base was in turn soldered to the top of the preheater and was well insulated from the test piece by a carefully machined textolite grade 11508 insulating piece (k = 0.346 W/m°C) made by General Electric Co. A copper sleeve, of the same internal diameter as the preheater and test piece, extended from the preheater to within an air gap thickness 0.25 mm from the test piece. The high thermal conductivity of copper ensured that once film boiling existed at the end of the preheater, it would continue to exist right up to the test piece. The test piece and block were electrically and thermally insulated from the exit manifold by a micarta plate. Steam inlet and exit holes were machined into the top and bottom of the test block.

Test Pieces. The test pieces are summarized in Table 2. Each test piece major dimensions in mm were 10.16 i.d., 25.4 o.d., and 25.4 long. Roughness amplitudes were determined from profilometer traces of the surfaces, run at 90 and 120 deg circumferential intervals, parallel to test piece axis. Three thermocouples were inserted at 6.35, 12.7, and 19.05 mm from the end of the test piece. The thermocouple hole was 1.067 mm dia, extending to within 3.175 mm of the boiling surface, and was packed full of silver compound for good thermal contact.

With a film boiling heater-transfer coefficient of about 284 W/m²°C, the Biot numbers for the copper, aluminum, and inconel-600 pieces were 0.01, 0.018, 0.24, respectively. Biot number was defined as

$$B_i = hl/k \tag{2}$$

where the ratio, volume/inside surface area, was taken as the characteristic dimension, l. Other details of the test equipment may be found in [7].

Instrumentation. Data thermocouples and two top thermocouples at the pre-heater exit were measured with a Honeywell Speedomax W Chart Recorder. The recording interval of 1.2 seconds was more than adequate for the transients. Other temperatures were read with a Leeds and Northrop precision potentiometer or with immersion thermocouples. Mass fluxes were measured with rotameters, and the power with voltmeter and ammeter. The preheater power was corrected for heat loss through its insulation, by a previous calibration.

Pressure gauges and mercury manometers were employed in the measurement of pressure. Test section pressures ranged between 1.06 and 1.45 bar.

Experimental Procedure. Test block steam flow, pre-heater nitrogen flow, and preheater power were set to desired values. When steady state was attained, the flow rate, preheater and system temperatures, and the pressures, were read. The chart recorded the outputs of the thermocouples fed to it.

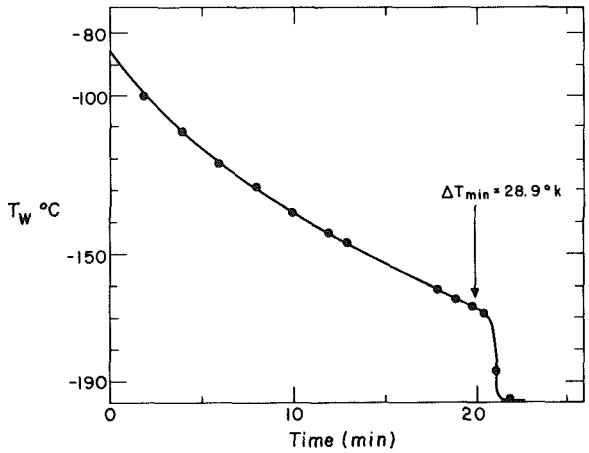

Fig. 4 Typical temperature transient-copper

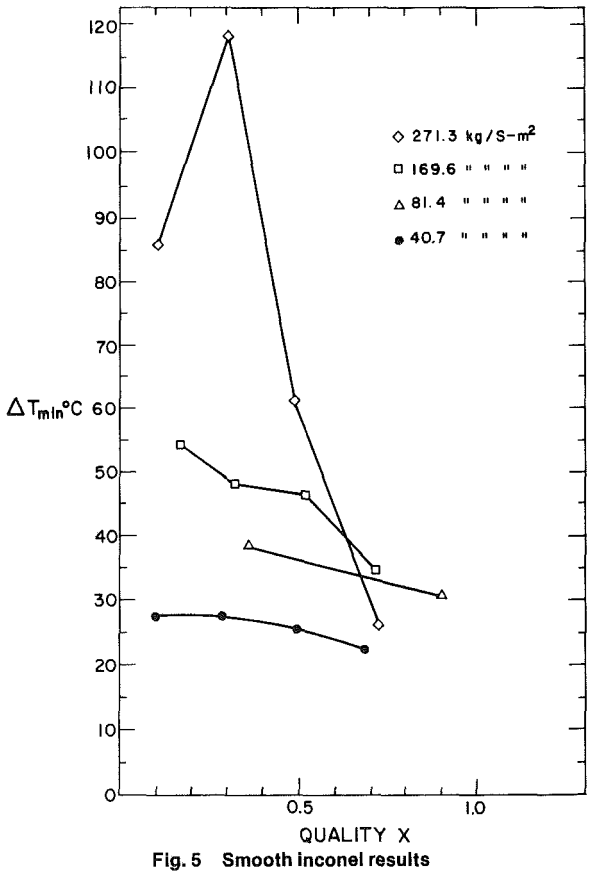

Fig. 5 Smooth inconel results

It was noted that the test piece temperatures, and the wall temperature at the end of the preheater indicated film boiling.

Steam supply was then cut off to start the transient. The test block temperatures fell gradually at first, and then more

rapidly, as the transition boiling region was traversed. A run was terminated after rewet had occurred.

Data Reduction. The flow quality at test section inlet is given by:

$$X = \frac{Q_e + Q_{\text{ins}}}{\dot{m} h_{fg}} - \frac{H_{\text{sat}} - H_{\text{sub}}}{h_{fg}} \tag{3}$$

Figure 4 shows a typical transient for copper. The rewet point corresponded to the point of minimum slope prior to transition boiling. For copper and aluminum, the three thermocouple traces corresponded and showed rewet at essentially the same point. There was thus no axial conduction effect on the rewet wall superheat.

For inconel, the top thermocouple indicated lower temperatures and showed rewet first. There was up to 11°C temperature difference, or less, between the top and bottom thermocouples at rewet. The earlier rewet of the top location may have arisen from the fact that the exit manifold was unheated, causing the liquid to become attached to it. The resulting trajectories of the droplets made the latter closer to the tube at exit than at inlet. Once rewet had occurred at some region of the test piece, rewet at any other region would be axial conduction controlled. Unless allowed for, the apparent rewet point would be higher with axial conduction control. The rewet point of the top thermocouple was chosen as the data point for inconel, as the possible effect of axial conduction was considered to be least for this point. Its estimate in [7] was less than 0.1°C.

Error Estimates on ΔT_{min}. Errors arising from effects of axial conduction, visual technique for determining T_{min} from temperature-time curve, instrument, for chart reading were estimated in reference [7], Appendix A12. The results are summarized below for inconel-600.

X, G(kg/s-m^2)	ΔT_{min} °C	Error °C	% Error
17%, 167	54.4	± 4.5	± 8
10%, 40.7	27.8	± 3.4	± 12

Discussion of Experimental Results

Effect of Quality. The effect of quality on rewet wall superheat is illustrated in Fig. 5. It is seen that ΔT_{min} decreases as quality increases, but that the influence of quality is more significant at high mass fluxes and at higher qualities. These trends are in agreement with the experimental results of reference [6]. The behavior arises from the decrease in heat transferred directly to the liquid component of the flow, which, as derived in reference [7], decreases exponentially with wall superheat, with G, X, and fluid properties held constant. At the time there is a linear increase with wall superheat in the heat transferred to the vapor phase as quality increases. The total heat transferred from the hot wall to the flow is the sum of these two heat transfer components. This heat transfer model, as postulated in [6], and later proved in [7] explains clearly the effect of quality on ΔT_{min}.

Effect of Mass Flux. Figure 5 shows that ΔT_{min} increases with mass flux for the same quality. Increases in mass flux increase the flow Reynolds number, liquid droplet population, and flow turbulence. It decreases the liquid droplet sizes and the nonequilibrium in the fluid. These factors tend to increase both the liquid and vapor components of heat transfer, and make it conceptually more difficult to conclude that ΔT_{min} must increase with mass flux at constant quality. However the experimental results, as well as the computational analysis of [7] indicate that the increase in the liquid component of heat transfer is more significant, thus increasing ΔT_{min} as G increases.

Figure 6, for smooth copper, shows the same trend for 33.9 and 73.2 kg/s-m^2. The data for 162.7 kg/s-m^2 did not fully behave as expected. The data for the two lowest qualities at this mass flux are considered unreliable due to some undetermined error.

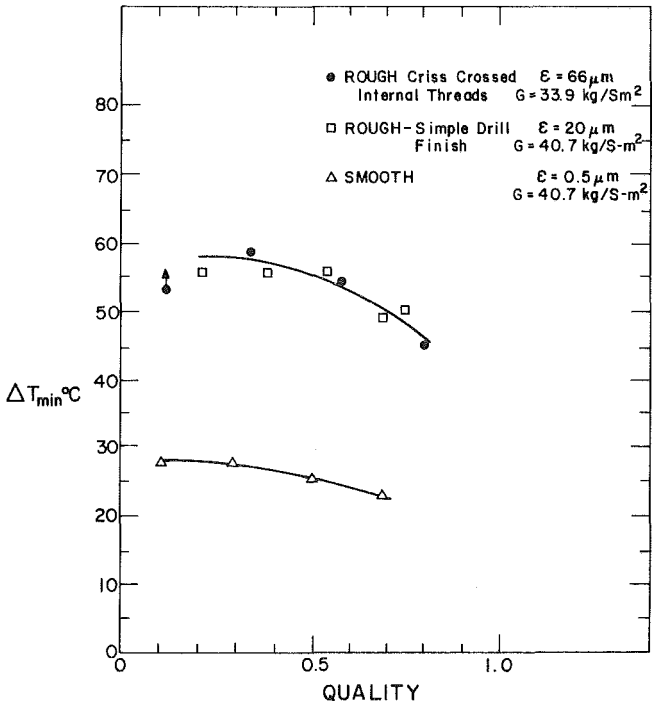

Fig. 7 Effect of wall roughness on ΔT_{min}

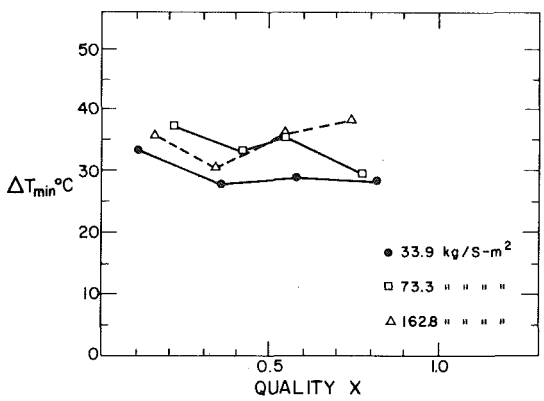

Fig. 6 Smooth copper results

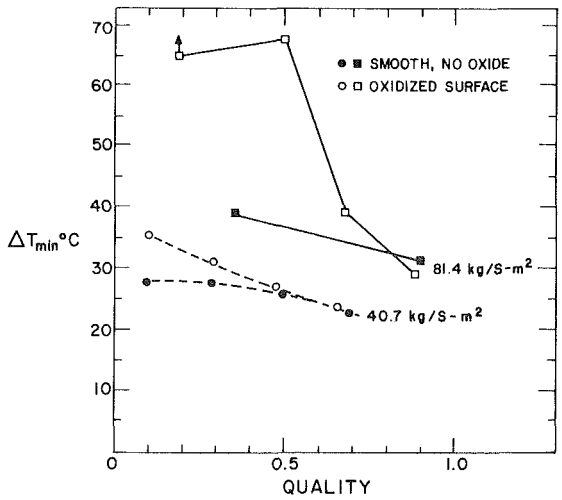

Fig. 8 Effect of oxide film deposit

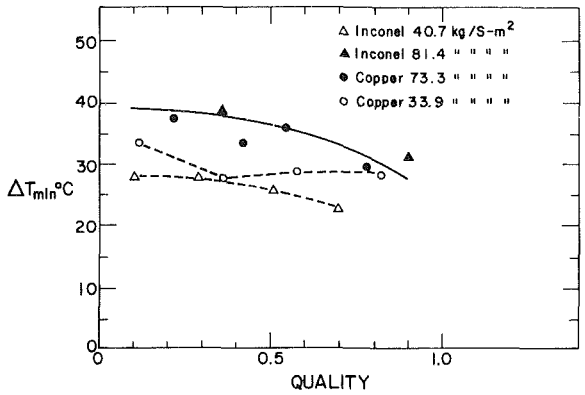

Fig. 9 Comparison of ΔT_{min} versus X: smooth inconel and copper

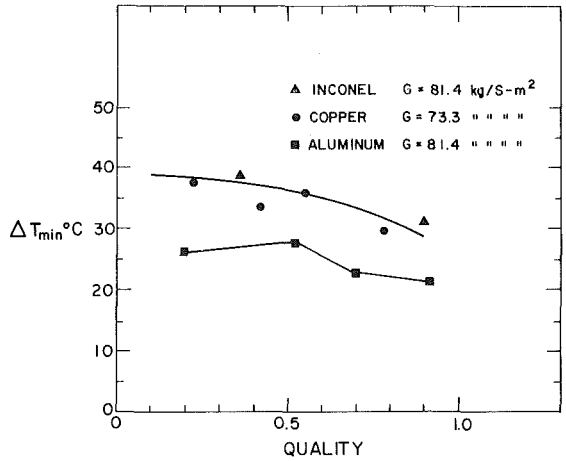

Fig. 10 Effect of material thermal properties

In references [2] and [8], no effect of mass flux on ΔT_{min} were recorded for corresponding pressures and mass flux ranges. However, these data were for the inverted annular regime. The dependence of ΔT_{min} on the heat-transfer process leading to rewet is thus emphasized.

Effect of Roughness. Figure 7 shows the effect of wall roughness. The rough specimen used produced a doubling of ΔT_{min} for the same mass flux and quality, over the values for the smooth specimen. As wall temperature falls from the vapor film boiling levels, the liquid drops get closer to the wall, and if the roughness amplitudes are significant, the liquid drops will begin to contact the roughness peaks more easily. These are cooled, and the cooling effect is propagated to the rest of the heating wall. The contacts lead to an increase in the liquid component heat transfer and hence an increase in the rewet wall superheat.

Effect of Oxide Film or Crud Layer. Figure 8 shows that the presence of an oxide film increases the value of ΔT_{min} in dispersed flow, and this trend agrees with the results of [3] and [9] for pool boiling. The increase is larger at higher mass fluxes. The manner of the influence of oxide film or crud on ΔT_{min} is threefold. First, it provides a high thermal resistance layer on the heat-transfer surface, so that while the oxide film surface temperature is low enough to permit rewet, the tube material inner surface temperature, which is recorded, will still be high. Second, it reduces the contact angle at the surface and causes the liquid to spread over a wider area upon contact with the heat transfer surface. The heat transferred to the liquid subsequently increases, and this increases the value of ΔT_{min}. Third, oxide layers and crud are rough, and as explained above, this fact will lead to an increase in ΔT_{min}.

For Fig. 8, the oxidized specimen was prepared smooth, and the oxide thickness was 1.3 μm. Thus, the surface contact angle was probably the most significant factor.

Effect of Wall Thermal Properties, k, ρ, c. While designing the experiments, it was thought that the thermal conductivity, k, or the property ratio, $R = [(k\rho c)_w/(k\rho c)_l]^{1/2}$ would be an important parameter in determining the values of ΔT_{min}. Subsequently inconel, aluminum, and copper with values of k = 15.57, 205.87, 378.87 W/m°C and R = 16.2, 47.5, and 75.2, respectively, were chosen. Figure 9 shows the data for copper and inconel at mass fluxes from 35.9 to 81.4 kg/s-m^2. These show no effect of material thermal properties, within experimental errors.

Figure 10 shows the data for all three materials at about 81.4 kg/s-m^2. The data for aluminum fell below those for copper and inconel. Since the above mentioned thermal properties for aluminum fall between those for inconel and copper, it would appear that the different result cannot be explained by a thermal property effect. Rather, it is thought that liquid nitrogen wets inconel and copper better than it wets aluminum, and this accounts for the lower values of ΔT_{min} for aluminum.

Conclusion

Data have been presented on the effect of a wide range of thermalhydraulic parameters on ΔT_{min} in yet another flow regime—the dispersed flow regime. The effects of mass flux and quality have confirmed earlier expectations from [6]. However, the effect of mass flux differs from the trend observed for low quality annular vapor flow regime in [2] and [8]. The effects of roughness and surface oxidation are in agreement with the trends observed for pool boiling in [3] and [9]. Contrary to the data of Kalinin for inverted annular flow regime [2], it would appear that the effects of wall thermal properties were not very significant for the dispersed flow regime, at least for the range of parameters for which data were obtained.

References

1 Spiegler et al., "Onset of Stable Film Boiling, and the Foam Limit," *Journal of Heat and Mass Transfer*, Vol. 6, 1963, pp. 987-994.

2 Kalinin, E. K. et al., "Investigation of the Crisis of Film Boiling in Channels," *Proceedings of Two Phase Flow and Heat Transfer in Rod Bundles*, ASME Winter Annual Meeting, Los Angeles, Calif., 1969.

3 Bergles, A. E. and Thompson, W. G., "The Relationship of Quench Data to Steady-State Pool Boiling Data," *International Journal of Heat and Mass Transfer*, Vol. 13, 1970, pp. 55-68.

4 Baumeister, K. J. and Simon, F. F., "Leidenfrost Temperature—Its Correlation for Liquid Metals, Cryogens, Hydrocarbons and Water," ASME JOURNAL OF HEAT TRANSFER, Vol. 95, No. 2, 1973, pp. 166-173.

5 Berenson, P. J., "Transition Boiling Heat Transfer from Horizontal Surfaces," Ph.D. thesis, Mechanical Engineering Dept., M.I.T., 1960.

6 Iloeje, O. C., Plummer, D. N., Griffith, P., and Rohsenow, W. M., "An Investigation of Collapse and Surface Rewet in Film Bokling in Forced Vertical Flow," ASME JOURNAL OF HEAT TRANSFER, May 1975, pp. 166-172.

7 Iloeje, O. C., "A Study of Wall Rewet and Heat Transfer in Dispersed Vertical Flow," Ph.D. thesis, M.I.T., 1974.

8 Iloeje, O. C., Plummer, D. N., and Rohsenow, W. M., "Transition from Film Boiling to Nucleate Boiling in Forced Convection Vertical Flow," M.I.T. Report No. DSR 72718-78, 1972.

9 Bradfield, W. S., "On the Effect of Subcooling on Wall Superheat in Pool Boiling," ASME JOURNAL OF HEAT TRANSFER, Vol. 89, pp. 269-270.

Inward Melting in a Vertical Tube Which Allows Free Expansion of the Phase-Change Medium

E. M. Sparrow
Fellow ASME

J. A. Broadbent

Department of Mechanical Engineering,
University of Minnesota,
Minneapolis, Minn. 55455

Experiments on the melting of a phase-change medium in a vertical tube yielded quantitative results both for the heat transfer and the timewise evolution of the melting front. The upper surface of the phase-change medium was bounded by an insulated air space, which accommodated the volume changes which accompany the melting process. Numerical solutions based on a pure conduction model were also performed for comparison purposes. It was found that the rate of melting and the heat transfer are significantly affected by fluid motions in the liquid melt induced by the volume change and by natural convection, with the former being significant only at early times. For melting initiated with the solid at the phase-change temperature, the experimentally determined values of the energy transfer associated with the melting process were about 50 percent higher than those predicted by the conduction model. Furthermore, the measured values of the energy stored in the liquid melt were about twice the conduction prediction. A compact dimensionless correlation of the experimental results was achieved using the Fourier, Stefan, and Grashof numbers. Initial subcooling of the solid substantially decreased the rate of melting, with corresponding decreases in the energy transfers for melting and sensible heat storage.

Introduction

Interest in the heat transfer aspects of melting and freezing has been heightened in recent years by the proposed use of phase-change processes for the storage of thermal energy. A survey of the recent experimental literature (e.g., [1]) reveals a strong concentration of effort on melting or freezing outside of heated or cooled cylinders embedded either vertically or horizontally in a phase-change medium. There has also been some work on phase change adjacent to plane surfaces. A viable thermal storage arrangement which has not been widely explored in the heat-transfer research literature is the containment of the phase-change medium within a circular tube or cylinder. In such an arrangement, the external surface of the tube is heated by a fluid whose thermal energy is to be stored, giving rise to an inward melting of the medium contained within the tube. For extraction of the thermal energy, the external surface of the tube is cooled, which causes an inward solidification of the contained phase-change medium.

The key processes in the aforementioned storage arrangement are inward melting and solidification in the presence of natural convection in the liquid phase. In considering these processes, it is relevant to distinguish between horizontal and vertical tubes, since the patterns of internal natural convection motion are markedly different for the two orientations. Another issue to be considered for encapsulated storage devices is the procedure for accommodating the density change which accompanies phase change: normally, an expansion upon melting (water being a notable exception).

In the present research, experiments have been performed to investigate the fundamentals of melting of a phase-change medium contained in a vertical cylinder. The upper surface of the medium was bounded by an insulated air gap, the presence of which accommodated the increase of volume due both to melting and to the superheating of the liquid melt. The melting was initiated and maintained by a step-change increase of the surface temperature of the containment tube.

The research encompassed two groups of experiments. In the primary group, the melting was initiated with the solid at its phase-change temperature. A supplementary set of experiments was performed in which the solid phase-change medium was initially subcooled below the melting temperature. In addition to the initial temperature of the solid phase, two other parameters were varied during the course of the research. One of these was the temperature imposed on the surface of the containment tube, while the other was the duration of the melting period. Because of the procedure used to conduct the experiments, a separate data run was carried out for each of the selected melting-period durations. The phase-change medium used in the experiments was 99-percent pure n-eicosane paraffin, with a measured melting temperature of 36.4°C.

The amount of mass melted during each selected melting period was determined by direct weighings, and this yielded the latent heat component of the energy input to the phase-change medium. Also measured was the sensible heat stored in the liquid melt due to its temperature rise above the melting value. The timewise evolution of the position of the solid-liquid interface was determined by direct measurement of the surface contour of the solid which remained unmelted at the conclusion of the respective melting periods.

The foregoing information will be presented in both dimensional and dimensionless forms. Of particular note is the dimensionless correlation of the timewise variation of the energy of melting using both heat conduction and natural convection groups. This correlation serves to generalize the results. Other significant features of the presentation of the experimental results include: (*a*) the quantitative comparison of the energy inputs associated with sensible and latent heat storage, (*b*) the assessment of the effects of initial subcooling, and (*c*) insights into the patterns of natural convection flow as suggested by the timewise evolution of the solid-liquid interface.

To supplement the experiments, numerical solutions were carried out for inward melting in a circular cylinder, with heat conduction being the only transport mechanism. The energies of melting and of sensible heat storage obtained from these solutions were compared with the experimental results in

Contributed by the Heat Transfer Division for publication in the JOURNAL OF HEAT TRANSFER. Manuscript received by the Heat Transfer Division September 4, 1981.

order to assess the relative importance of heat conduction and natural convection.

The available literature which relates to the present research is very sparse. In [2], vertical-cylinder melting data (characterized therein as preliminary) were obtained for a mixture of paraffins which melts over a broad band of temperatures, in contrast to the sharply defined melting temperature of a pure substance. The heat-transfer data were confined to the case of an initially subcooled solid state. They were inferred from measurements of the time-varying temperatures of the hot water which was used as the heat source for the melting and were presented in dimensional, rather than in dimensionless form.

Finite-difference solutions for melting of a phase-change medium contained in a vertical cylinder are presented in [3] for a restricted range of the governing parameters, which does not encompass the conditions of the present experiments. In [4], melting experiments were performed for the annular gap between two vertical cylinders. Although Nusselt numbers are reported, they are of uncertain meaning. This is because one of the temperatures involved in the definition of the heat-transfer coefficient is, from the standpoint of a potential user, altogether unknown.

The Experiments

Experimental apparatus. The containment tube for the phase-change medium was a 39.4-cm-long, hollow copper cylinder, with an internal dia of 5.08 cm and a wall thickness of 0.152 cm. At its lower end, the tube was closed by a removable cylindrical plug whose function was to provide a water-tight seal and to insulate the lower portion of the phase-change medium from extraneous heat transfer. The plug consisted of a short, O-ring-equipped Teflon cylinder to which was bonded a 3.8-cm-long cylinder of closed-pore polystyrene that was wrapped with plastic film in order to present a smooth, impermeable surface to the paraffin. The upper end of the containment tube was closed by a tight-fitting insulating cap, also of plastic-coated polystyrene, which penetrated into the tube. The length of the penetrating portion and the mass of the paraffin charge were selected so that with the paraffin in solid state, there was a 5.3-cm air gap between the upper surface of the paraffin and the lower surface of the cap. This air gap was sufficiently large to accommodate the increase in volume which accompanied the solid-to-liquid phase change and the subsequent superheating of the liquid melt.

At its upper end, the containment tube was fitted with trunions to facilitate its vertical suspension in either of two constant-temperature water baths. One of the baths was used to bring the tube and its charge of solid paraffin to a preselected temperature level (at or below the melting temperature) prior to the start of the data run. The second water bath served as the thermal environment for the containment tube during the melting experiments. Each bath consisted of a specially fabricated containment vessel fitted with a Lauda model B-1 temperature controller-circulator unit and equipped with insulation and a top cover plate to control heat losses. Bath temperature uniformity was better than 0.1°C.

Fittings were affixed to each bath to mate with the trunions of the containment tube. The suspension arrangement was such that the lowermost 35.8 cm of the tube was immersed in the bath, while the upper 3.6 cm protruded above the surface of the water.

The temperature of the wall of the copper containment tube was measured by eight, specially-calibrated thermocouples deployed along the height of the tube. The thermocouples, made from 30-gage, Teflon-coated chromel and alumel wire, were affixed to the outer surface of the wall by copper oxide cement. Additional thermocouples were employed to monitor the temperatures of the water bath, and all thermocouple emfs were read with a 1-μV millivoltmeter. ASTM-certified thermometers, respectively capable of being read to 0.1°F or 0.1°C, were used to stir the liquid melt and to measure its temperature at the end of the data run. All mass measurements were made with an Ohaus triple-beam balance with a smallest scale reading of 0.1 g and a capacity of 2610 g.

Attention will now be turned to equipment involved in the preparation of the solid paraffin specimens used to initiate the melting experiments. The containment tube was filled with liquid, which was then frozen in such a manner as to avoid the formation of internal voids. The freezing procedure yielded a solid specimen with a crater-like upper surface. To obtain a perfectly flat upper surface which was situated at the same elevation for all data runs, a special leveling device was fabricated and employed.

In essence, the device consisted of an aluminum disk, 4.95 cm in dia and 1.95 cm thick, into whose upper surface one end of a threaded rod was embedded. A second disk with a diameter somewhat larger than that of the containment tube was threaded onto the rod and locked in place at a fixed distance above the first disk. The rod passed through the second disk and terminated in a ball-like handle. In use, the device was held vertically, with the ball handle at the top, the second disk in the middle, and the first disk at the bottom.

If the device were to be inserted into the upper end of the containment tube, it would penetrate only until the second disk contacted the upper edge of the tube wall. When the second disk was in contact with the edge of the tube, the lower surface of the first disk was situated 11.05 cm below the upper end of the tube. This distance marked the position of the top of the solid paraffin at the start of the data run. As will be described in the Procedure section, the leveling device fulfilled its function by melting out the excess paraffin.

Experimental procedure. The preparations for a data run always began with the containment tube completely free of paraffin, the cleaning having been performed as the final step of the preceding run. To begin the preparations, a fresh plastic wrap was applied to the insulation layer of the bottom-end plug. Then, a length of 0.018-cm dia monofilament nylon thread was anchored to the center of the exposed face (i.e., the

Nomenclature

c = specific heat of liquid
c_{solid} = specific heat of solid
E = energy transfer, $E_\lambda + E_s$
E_s = energy transfer for sensible heat storage in liquid melt
E_{sub} = energy required to heat subcooled solid to T^*
E_λ = energy transfer for melting
$E_{\lambda,max}$ = energy required to melt total mass in containment tube
Fo = Fourier number, equation (5)
Gr = Grashof number, equation (7)
g = acceleration of gravity
M = melted mass
M_{max} = total mass of phase-change medium in containment tube
R = radius of tube
Ste = Stefan number, equation (6)
T_w = temperature of tube wall
T^* = melting temperature
$\bar{T}$ = bulk temperature of liquid melt
ΔT_{sub} = degree of subcooling of solid
α = thermal diffusivity of liquid
β = expansion coefficient of liquid
λ = latent heat of melting
ν = kinematic viscosity of liquid

upper face) of the insulation by means of a small nail. (As will be explained shortly, the thread facilitates the removal of the unmelted solid at the end of the data run.) The bottom-end plug was then inserted into the containment tube and the nylon thread fixed in position so that it coincided with the axis of the tube.

The tube was then filled with liquid paraffin and placed in an ice bath. Void formation during the freezing period was prevented by irradiating the upper surface of the paraffin with a heat lamp set at a low intensity. Once freezing was completed, the upper surface of the frozen paraffin was leveled using the special device that was described earlier. To use the leveling device, its lower disk was heated on a hot plate and then inserted into the containment tube. The contact of the heated disk with the upper surface of the paraffin caused melting to occur. Successive insertions of the device were continued until no further contact between the heated disk and the solid could be sensed. At this moment, the device was withdrawn and the wand of a vacuum system was inserted to remove the liquid melt. The overall height of the solid resulting from the leveling procedure was 22.22 cm. Upon completion of the leveling, the containment tube and its contents were weighed.

The containment tube was then capped and transferred to the equilibration bath to enable the solid to attain temperature uniformity at a preselected value—either at the melting point (36.4°C) or subcooled by 8.3°C (15°F) below the melting point. In actuality, for the first of these cases, it was found desirable to subcool by a few tenths of a degree below the melting temperature to avoid melting the impurities (the paraffin used in the experiment was 99 percent pure).

Throughout the equilibration period, the test-environment bath was kept in readiness to perform its function of receiving the containment tube and imposing a step change of temperature on the tube wall. The transfer of the containment tube from the equilibration bath to the test-environment bath was accomplished in about 20 s. Once the tube trunions had been seated and the vertical equilibrium position established, the trunions were locked in place. The insulating cap at the top of the tube was kept in position throughout the data run. During the run, the tube-wall and water-bath thermocouples were read at two-min intervals.

Prior to the end of the run, preparations were made for the extraction of the unmelted paraffin and for the measurement of the bulk (i.e., mixed mean) temperature of the liquid melt subsequent to the removal of the solid. A thermometer was employed both for the mixing and the temperature measurement. To minimize the thermal lag of the thermometer, it was placed in the water bath to equilibrate prior to its use in measuring the melt temperature.

At the designated end of the data run, the insulating cap was removed and the unmelted solid extracted from the containment tube by means of the nylon thread; these operations required about five s. Then, the thermometer was taken from the water bath, dried, and immersed into the liquid melt. With well-practiced vigorous stirring, it was found that an equilibrium temperature could be obtained in about ten s.

With the temperature measurement completed, the melt was poured out of the tube. All parts of the tube and the bottom-end plug were immediately washed to remove any residual paraffin and then were thoroughly dried. The plug was then reinserted in the tube, as was the unmelted solid, and a weighing was made.

Subsequently, the surface contour of the unmelted solid was determined. For this purpose, a succession of axial positions along the solid were identified with the aid of a machinist scale. At these stations, the thickness of the solid was measured in two perpendicular directions by means of a dial-gage-equipped caliper. Data runs were made for three different values of the tube wall temperature T_w, respectively corresponding to $(T_w - T^*) = 4.4$, 11.1, and 27.8°C (8, 20, and 50°F), where T^* is the melting temperature. For each fixed value of $(T_w - T^*)$, a succession of data runs were made, each characterized by a progressively longer duration of the melting period. The sequence was terminated when the melted mass was 90–95 percent of the total mass of the paraffin contained in the tube. Data runs for all three of the aforementioned values of $(T_w - T^*)$ were carried out for the initial condition where the solid was at the melting temperature. For the initially subcooled solid, runs were made only for the largest value of $(T_w - T^*)$.

Data reduction. The quantities to be used in the presentation of the results will now be described. The mass melted during a data run will be denoted by M, while $M_{\max}$ will be used to denote the total charge of paraffin in the containment tube. In terms of these quantities, the melted mass will be presented in the dimensionless ratio $M/M_{\max}$.

The energy E_λ transferred inward from the tube wall in order to melt the mass M is

$$E_\lambda = \lambda M \tag{1}$$

and if the entire charge were to be melted

$$E_{\lambda,\max} = \lambda M_{\max} \tag{2}$$

where λ is the latent heat of melting. It then follows that

$$E_\lambda / E_{\lambda,\max} = M/M_{\max} \tag{3}$$

Each element of the mass M, when first liquified, is at the melting temperature T^*. At the end of the data run, the bulk temperature $\bar{T}$ of the melted mass is measured. With these temperatures, the energy E_s transferred inward from the tube wall in order to supply the sensible heat stored in the liquid is

$$E_s = M\int_{T^*}^{\bar{T}} c\,dT \tag{4}$$

where c is the specific heat of the liquid. To compare the sensible-heat and latent-heat components of the energy input to the phase-change medium, the ratio E_s/E_λ will be used in the presentation of the data.

A number of dimensionless groups will be employed both in the presentation of the experimental results and in the comparisons with analytical predictions that are based on a heat-conduction model. The groups relevant to the present work are the Fourier number, Fo, the Stefan number, Ste, and the Grashof number, Gr. These are defined as

$$\mathrm{Fo} = \alpha t/R^2 \tag{5}$$

$$\mathrm{Ste} = c(T_w - T^*)/\lambda \tag{6}$$

$$\mathrm{Gr} = g\beta(T_w - T^*)R^3/\nu^2 \tag{7}$$

in which R denotes the radius of the containment tube. The thermophysical properties α, c, λ, β, and ν of liquid n-eicosane were evaluated from information given in [5]. The temperature used for the properties evaluation will be discussed when the results are presented.

Results and Discussion

The presentation of results will begin with a display of the pattern of inward melting and then goes on to an exposition of the results for the heat transfer and the melted mass.

Pattern of melting. The direct measurement of the surface contour of the unmelted solid at the end of a data run yielded the position and shape of the melting front corresponding to the duration time of the run. The timewise movement of the front was then determined from a succession of runs of different durations. Figures 1–3 have been constructed to illustrate the pattern of inward melting. Each figure corresponds to a given wall-to-melting temperature dif-

ference, respectively $(T_w - T^*) = 4.4$, 27.8, and 27.8°C (8, 50, and 50°F). Figures 2 and 3, which are for the same $(T_w - T^*)$, convey results for different initial temperatures of the solid. For Fig. 2, the solid is initially at the melting temperature, while for Fig. 3, the solid was subcooled by 8.3°C (15°F) below the melting temperature.

Each figure shows the position and shape of the melting front at six instants of time, starting at time = 0 at the left of the figure and proceeding to larger times at the right. At each instant of time, the solid boundary line depicts the melting front, with the unmelted material contained within the boundary and the liquid melt outside. The dashed vertical lines represent the wall of the containment vessel.

Inspection of Figs. 1-3 reveals a melting pattern that is common to all cases. At small values of time (relative to the overall duration of the melting period), the melting front is relatively close to the tube wall and is nearly parallel to it, except for the upper region where a greater displacement of the front from the wall is in evidence. As time passes, the melting front moves inward, but by no means in a uniform manner. Rather, the rate of melting is much higher in the upper region. Furthermore, the height of the unmelted solid shrinks markedly as time passes.

To place these findings in perspective, the behavior of the melting front in the presence of various heat transport mechanisms may be considered. If radial conduction were the sole transport mechanism, the inward movement of the melting front would be uniform along the height of the tube, so that the front would appear to be a vertical line at a given instant of time. At small values of time and in the lower portion of the tube, the melting front is vertical, thereby signaling the dominance of conduction.

There are two factors which contribute to the departure of the actual behavior of the melting front from that for pure conduction. One is the density decrease that accompanies melting. Thus, the liquified solid must seek additional volume into which to expand, and this causes an upflow of liquid from the melt layer into the free space above the solid. The thus-displaced liquid causes melting to occur at the upper surface of the solid as well as at the adjacent side surfaces. It is this volume-change-driven motion which is believed responsible for the initial departures of the melting front from that for pure conduction.

As time passes, natural convection motions develop in the melt layer, with an upflow adjacent to the tube wall and a downflow adjacent to the melting front. This recirculation pattern delivers relatively hot liquid to the upper reaches of the solid, where its presence accelerates the rates of inward and downward melting. Natural convection and the aforementioned volume-change-driven motions are mutually aiding, but natural convection is believed to be the dominant factor during most of the melting period.

Although the patterns of melting displayed in Figs. 1-3 are generally similar, there are important effects in evidence that are related to the operating temperatures. If Figs. 1 and 2 are compared, it is seen that the rate of melting is significantly affected by the wall-to-melting temperature difference $(T_w - T^*)$, which is respectively equal to 4.4 and 27.8°C (8 and 50°F) for the two figures. In particular, the rate of melting is drastically reduced at the lower value of $(T_w - T^*)$.

A comparison of Figs. 2 and 3 shows the effect of an initial subcooling of the solid for a given value of $(T_w - T^*)$. It is evident from these figures that subcooling slows the rate of melting. The reasons for this behavior will be discussed later, when the quantitative results are presented.

Energy of melting and melted mass. The basic results for the energy of melting E_λ and for the melted mass M are presented in Fig. 4 for the case in which the solid is initially at the melting temperature. In the figure, these quantities are

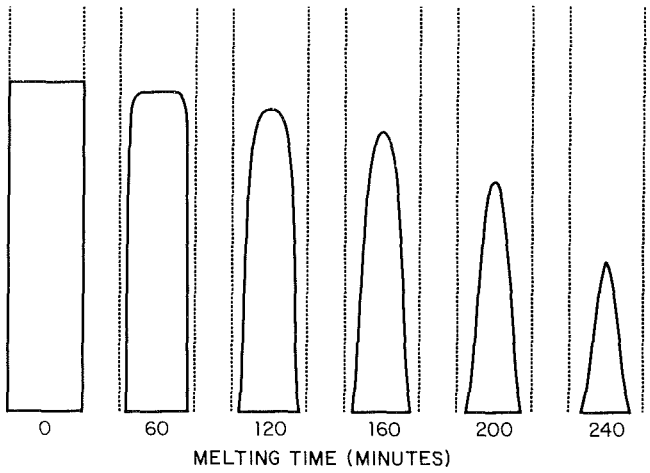

Fig. 1 Timewise movement of the melting front, $(T_w - T^*) = 4.4$°C (8°F), no subcooling

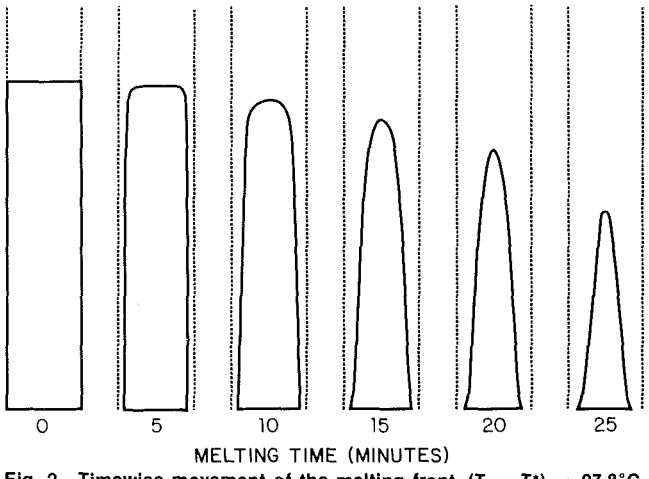

Fig. 2 Timewise movement of the melting front, $(T_w - T^*) = 27.8$°C (50°F), no subcooling

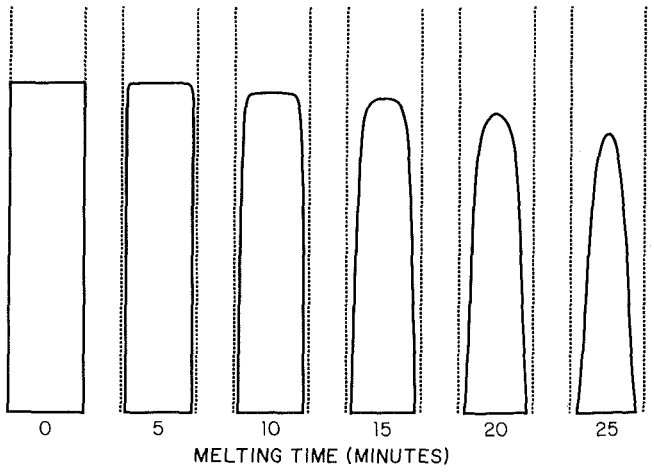

Fig. 3 Timewise movement of the melting front, $(T_w - T^*) = 27.8$°C (50°F), solid initially subcooled by 8.3°C (15°F)

respectively plotted as the dimensionless ratios $E_\lambda/E_{\lambda,max}$ and M/M_{max}. The figure shows how these quantities vary with time as melting proceeds at a given wall-to-melting temperature difference $(T_w - T^*)$, respectively 4.4, 11.1, and 27.8°C (8, 20, and 50°F).

As expected, the melted mass and the corresponding energy of melting increase with time. Furthermore, in concert with Figs. 1-3, the rate of melting is seen to be markedly affected by $(T_w - T^*)$, increasing as $(T_w - T^*)$ increases. Thus, for

example, the half-melted state (i.e., $M/M_{max} = 0.5$) occurs after 8, 25, and 78 minutes of melting, respectively for $(T_w - T^*) = 27.8$, 11.1, and 4.4°C (50, 20, and 8°F). These numerical values indicate that the rate of melting varies nonlinearly with the temperature difference, which is not unexpected when natural convection is present.

If curves are envisioned to be passed through the data for a given $(T_w - T^*)$, it is apparent that the slopes diminish moderately with increasing melting time, which signals a corresponding decrease in the rate of melting. There are several factors which contribute to this decrease, but the main factor is believed to be the decrease in the surface area of the unmelted solid which occurs as melting proceeds (see Figs. 1–3).

Attention will now be turned to the correlation and generalization of the results presented in Fig. 4. As a first rephrasing of the results, dimensionless parameters which emerge from pure heat conduction model of inward melting will be used. The motivations for trying the conduction-related parameters are twofold. First, there is the curiosity about how good (or poor) a correlation will be forthcoming by the use of these parameters. Second, and perhaps of even greater importance, they facilitate a comparison between the data and the results of a pure conduction analysis. Such a comparison will enable identification of the enhancement or degradation of the rate of melting due to nonconduction processes (i.e., natural convection and volume-change-driven motions).

Figure 5 shows the rephrased presentation. The ordinate variable is the same as that of Fig. 4, but the abscissa variable is now the FoSte product. In essence, Fo is a dimensionless time and Ste is a dimensionless form of the temperature difference $(T_w - T^*)$ (see equations (5) and (6)). Furthermore, the data are now parameterized by the Stefan number rather than by $(T_w - T^*)$. The two solid lines shown in the figure represent numerical solutions based on a one-dimensional heat conduction model of radially inward melting. These solutions were performed by the authors using a calculation procedure and associated computer program developed at the Heat Transfer Laboratory of the University of Minnesota [6].

Examination of Fig. 5 indicates that the data have been brought much closer together than they were in Fig. 4, although a noninsignificant spread remains. The incorporation of $(T_w - T^*)$ into the abscissa variable (via Ste) is the factor responsible for the pulling together of the data. However, M depends nonlinearly on $(T_w - T^*)$, so that the FoSte group is not able to bring the data together into a tight band.

The experimental data lie above the predicted results based on the pure conduction model, with the deviation being on the order of 50 percent. This deviation reflects the enhancing effects of fluid motions in the liquid melt.

It is noteworthy that the data are ordered in a regular way with the Stefan number (i.e., with $T_w - T^*$), increasing as $(T_w - T^*)$ increases at a given FoSte. Also, from the comparison of the times required to melt half the solid, made in connection with Fig. 4, it appears that $M \sim (T_w - T^*)^{5/4}$. This type of dependence strongly suggests that natural convection is the primary cause of the fluid motion, although it is probable that the volume change associated with the phase change may play a major role at early times.

The aforementioned considerations suggest the next rephrasing of the data, this time with $FoSteGr^{1/4}$ as the abscissa group. The outcome of the replotting is shown in Fig. 6. Inspection of the figure reveals a remarkably tight correlation of the data, thereby supporting the physical reasoning that led to the structure of the correlating group.

In constructing the preliminary version of Fig. 6, various reference temperatures for the evaluation of the thermophysical properties were examined. The best correlation

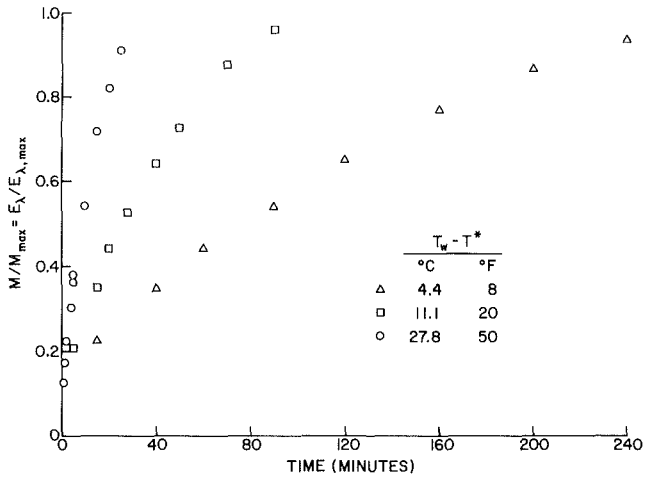

Fig. 4 Timewise variation of the energy of melting and of the melted mass, no subcooling

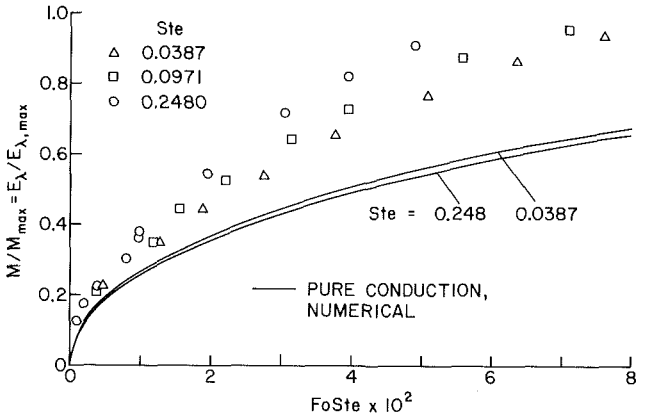

Fig. 5 Rephrasing of the data of Fig. 4 using heat conduction parameters and comparisons with the predicitons from a one-dimensional heat conduction model

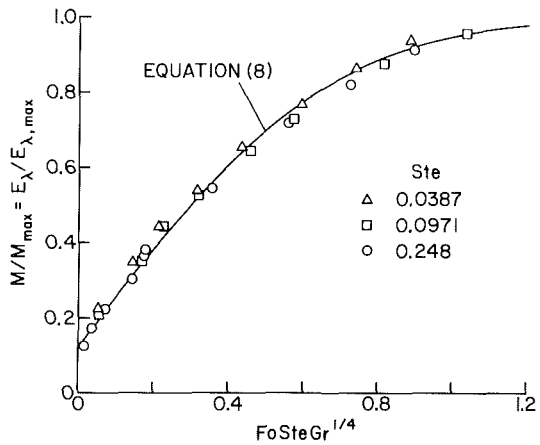

Fig. 6 Global correlation of the experimental results for the energy of melting and for the melted mass, no subcooling

was obtained with the properties evaluated at the melting temperature T^*, and it is those properties that have been used in Fig. 6. This choice may be made plausible by noting that the largest thermal resistance is at the melting surface (temperature T^*), since its area is smaller (in many cases, much smaller) than the surface area of the containment tube. Evaluation of the properties at a mean temperature equal to $\frac{1}{2}(T_w + T^*)$ yielded a correlation only slightly less compact than that of Fig. 6.

The solid line shown in the figure is an algebraic

representation of the correlated data. The equation of the line is

$$M/M_{max} = E_\lambda/E_{\lambda,max} = 0.12 + 0.88 erf(1.34 \text{FoSteGr}^{1/4}) \quad (8)$$

where *erf* denotes the error function. Equation (8) properly yields $M/M_{max} = 1$ at large Fo. However, it does not reduce to $M/M_{max} = 0$ at Fo = 0, nor should it be expected to do so. The hypothesis on which the correlation is based is the dominance of natural convection and, as already noted, other transport processes are dominant at very small times.

Energy stored as sensible heat. The energy E_s that is stored as sensible heat in the liquid melt will now be considered. The sensible heat energy is compared with the energy of melting E_λ in Fig. 7. In the figure, the E_s/E_λ ratio is plotted against the correlating group $\text{FoSteGr}^{1/4}$, and the data points are parameterized by the Stefan number Ste. For the present, attention will be restricted to the open data symbols, which correspond to the case where the solid is initially at the melting temperature.

Inasmuch as the Stefan number is frequently regarded as a measure of sensible heat storage, it is not surprising that E_s/E_λ increases with increasing Stefan number. In particular, it is seen from the figure that

$$E_s/E_\lambda \sim \text{Ste} \quad (9)$$

in the range of higher abscissa values. Since the energy input E to the phase change medium is equal to $(E_\lambda + E_s)$, a convenient representation for E can be written as

$$E = E_{\lambda,max}(1 + \text{Ste})\{rhs\,(8)\} \quad (10)$$

where *rhs* (8) denotes the right-hand side of equation (8).

Further examination of Fig. 7 indicates a tendency for E_s/E_λ to increase with the abscissa variable, i.e., with time. It is believed that this tendency reflects the heating of the liquid situated in the space above the melting solid.

In Fig. 8, the experimental data for E_s/E_λ are compared with numerical predictions based on a pure conduction model. Correspondingly, conduction variables are used on the abscissa. The comparison shows that the experimentally determined E_s/E_λ values are larger (on the order of 50 percent larger) than those from the conduction model. Furthermore, according to Fig. 5, the E_λ for the experiments are larger than the E_λ for the conduction model (also by about 50 percent). Therefore, the E_s values for the experimental data are about twice the conduction values.

There are two factors which contribute to this outcome. First, the fluid motions associated with natural convection give rise to a more uniform fluid temperature distribution than that for pure conduction. Second, the heating of the liquid melt situated in the upper reaches of the tube, above the melting solid, enhances the sensible heat storage.

Initial subcooling of the solid. The effect of initial subcooling of the solid on the energy of melting E_λ and on the melted mass M is shown in Fig. 9. Both sets of data that are plotted in the figure are for $(T_w - T^*) = 27.8°\text{C}$ (50°F). The open symbols correspond to no subcooling, while the black symbols are for subcooling of 8.3°C (15°F) below the melting temperature.

It is apparent that subcooling significantly retards the melting process, and there are two main causes of this behavior. First, in the presence of subcooling, all of the energy delivered to the melting front is not solely utilized for melting; rather, a portion penetrates the solid and is used to raise its temperature. Second, because the melt region is relatively narrow in the presence of subcooling (compare Figs. 2 and 3), the natural convection motions are inhibited. This latter effect is believed to be the main cause of the reduction in the energy of melting in evidence in Fig. 9.

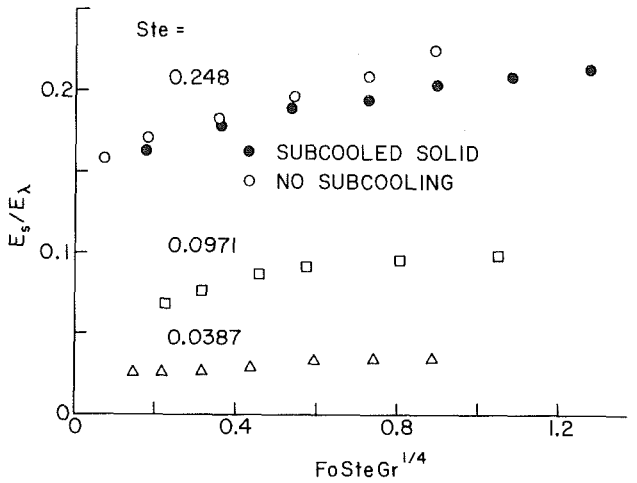

Fig. 7 Comparison of the energy stored as sensible heat in the liquid melt with the energy of melting

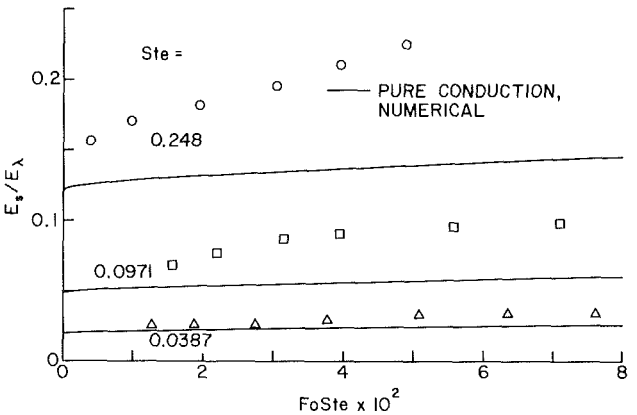

Fig. 8 Comparison of the experimental data for the energy stored as sensible heat in the liquid melt with the predictions of a pure conduction model

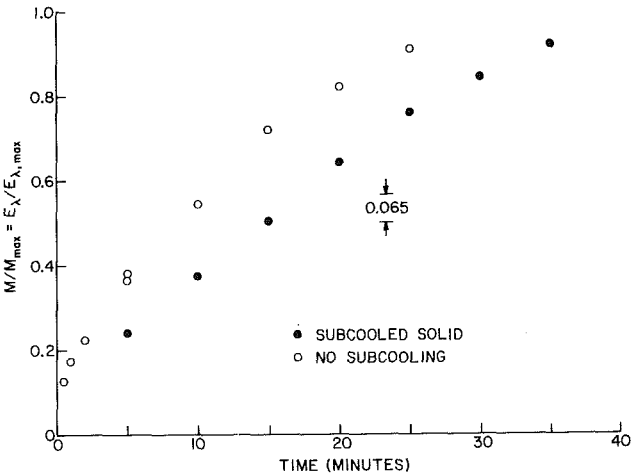

Fig. 9 Effect of initial subcooling of the solid on the energy of melting and on the melted mass

It is interesting to inquire whether the energy added to the phase change medium in order to overcome the initial subcooling of the solid is large enough to compensate for the reduction in E_λ. The energy E_{sub} required to bring the subcooled solid from its initial temperature to T^* is readily shown to be

$$E_{sub}/E_{\lambda,max} = c_{solid}\Delta T_{sub}/\lambda \quad (11)$$

which is equal to 0.065 in the present instance. By inspection

of Fig. 9, it is evident that the difference between the $E_\lambda/E_{\lambda,max}$ with and without subcooling, is greater than 0.065.

The effect of subcooling on the energy stored as sensible heat in the liquid melt can be observed in Fig. 7 by comparing the open and blackened data symbols for Ste = 0.248. The E_s/E_λ values are not very different for the two cases but, since E_λ is diminished in the presence of subcooling, so is E_s.

Thus, from the foregoing paragraphs, it follows that subcooling decreases the energy transfer to the phase change medium. This outcome is believed due to the diminished vigor of the natural convection motions.

Concluding Remarks

Inward melting of a phase change medium contained in a vertical tube is significantly affected by fluid motions in the liquid melt. At early times in the melting period, the motions are believed to be induced by the volume change that accompanies phase change. However, for most of the melting period, the primary cause of the fluid motions is natural convection.

Experimental data for melting initiated with the solid at its phase-change temperature (i.e., no subcooling) displayed melting-related energy transfers that were about 50 percent larger than those predicted by a model based on pure conduction. These data were very compactly correlated using a dimensionless group that involves the Fourier, Stefan, and Grashof numbers. Measurements of the energy stored as sensible heat in the liquid melt yielded results that also exceeded (by about a factor of two) those predicted by the conduction model. In general, the energy transfer associated with melting was substantially larger than that for sensible heat storage. The latter was nearly proportional to the Stefan number, and this relationship was incorporated into the dimensionless energy-transfer correlation.

Initial subcooling of the solid decreases the rate of melting and, correspondingly, the energy transfers for melting and sensible heat storage are decreased. The energy transfer required to raise the temperature of the subcooled solid to the phase-change value does not compensate for the reductions of the melting and sensible-heat energies.

Acknowledgment

This research was performed under the auspices of the U.S. Department of Energy, Office of Basic Energy Sciences.

References

1 Viskanta, R., Bathelt, A. G., and Hale, N. W., Jr., "Latent Heat-of-Fusion Energy Storage: Experiments on Heat Transfer During Solid-Liquid Phase Change," *Proceedings, Third Miami Conference on Alternative Energy Sources*, Dec., 1980.

2 Mujumdar, A. S., Ashraf, F. A., Menon, A. S., and Weber, M. E., "PCM Thermal Energy Storage in Cylindrical Containers of Various Configurations," *Proceedings, Second International Conference on Alternative Energy Sources*, Miami, Dec., 1979.

3 Pannu, J., Joglekar, G., and Rice, P. A., "Natural Convection Heat Transfer to Cylinders of Phase Change Material Used for Thermal Storage," *AIChE Symposium Series*, Vol. 76, No. 198, 1980, pp. 47–55.

4 Bareiss, M. and Beer, H., "Influence of Natural Convection on the Melting Process in a Vertical Cylindrical Enclosure," *Letters in Heat and Mass Transfer*, Vol. 7, 1980, pp. 329–338.

5 Griggs, E. I. and Humphries, W. R., "A Design Handbook for Phase Change Thermal Control and Energy Storage Devices," NASA Technical Paper 1074, 1977.

6 Chuck, Winston, personal communication, Department of Mechanical Engineering, University of Minnesota, May, 1981.

M. S. Sadeghipour

M. N. Özişik
Mem. ASME

J. C. Mulligan
Mem. ASME

Department of Mechanical and Aerospace Engineering,
North Carolina State University,
Raleigh, N. C. 27650

Transient Freezing of a Liquid in a Convectively Cooled Tube

The transient freezing of a liquid in laminar flow inside a circular tube subjected to convection heat transfer on the external surface is investigated analytically. The effects of Biot number, fluid inlet temperature, and the external ambient temperature on the length of this freeze-free zone are illustrated. The variation of the thickness of the freeze layer as a function of time and position along the tube is determined.

Introduction

Freezing problems are being addressed in relation to applications in such diverse areas as cryogenics, cold region geophysics, and liquid metal cooling. The freezing process is, in fact, one of the promising processes now under development for sea-water desalination and waste-water treatment.

As a class, these problems are physically difficult to categorize because of the myriad of complex mechanisms which are oftentimes involved. Mathematically, they are difficult to solve because of the nonlinearities and fluid-flow couplings. Even in cases involving pure liquids, generalizations and models of the physical mechanisms are oftentimes in disagreement with experiments. Nonequilibrium thermodynamic effects on crystallization, such as supercooling and nucleation, have been shown [1] to be important, and, under certain conditions, dendritic growth has been shown to occur. In some freezing work which displayed a smooth, nondendritic, solid formation, it was found [2] that under certain internal flow conditions the solid formation is actually unstable and exhibits a wavy structure due to hydrodynamic phenomena. It has also been shown [3, 4] that under the proper combination of conditions natural convection becomes an important phenomenon, especially in the freezing of superheated liquids at low Reynolds numbers. Simultaneous melting and freezing has even been demonstrated [5]. Good surveys of these and other related papers have been presented recently [2, 6].

In addition to these mechanisms, the work involving internal freezing [3, 7] has suggested that the thermal boundary conditions themselves are extremely important in determining the type of transient growth pattern as well as the degree of final, steady-state occlusion.

The work presented in this paper is related exclusively to the determination of the influence of convective boundary conditions on the transient growth of an internal frozen layer. The problem under steady-state conditions has been addressed analytically [8], but experimentally oriented studies of tube flows have suggested a strong and complex influence on the transient growth patterns.

Analysis

Consider an imcompressible, constant property fluid at a uniform temperature, T_0, flowing with a fully developed laminar velocity profile inside a circular tube of inner radius, r_w, while the ambient external to the tube is also at temperature T_0. At the origin of the time coordinate, $t = 0$, the temperature of the ambient in the region $z \geq 0$ in the downstream direction is suddenly lowered from T_0 to a temperature T_∞, which is lower than the freezing temperature, T_f, of the liquid. The heat dissipation from the tube wall to the external environment is by convection, with a heat-transfer coefficient, h.

The warm liquid entering the chilled tube at $z = 0$ is first cooled without freezing up to the location z_f, where the tube wall temperature is finally lowered to the freezing temperature, T_f. Then, in the region $z \geq z_f$, a smooth and regular freeze layer is assumed to form on the inside tube surface. The thickness of this freeze layer increases with both time and the axial position along the tube.

The problem, essentially, is that of determining the length of the freeze-free zone, that is, the cooling zone, as well as the thickness of the freeze layer within the freezing zone as a function of time and position along the tube, as illustrated in Fig. 1. In developing a tractable mathematical model for the analysis, the usual assumptions are employed. These are:

(*a*) The physical properties are constant and the densities are equal.

(*b*) The natural convection is negligible and the problem possesses axial symmetry.

(*c*) There is no supercooling, and the solid-liquid interface is at the freezing temperature.

(*d*) The axial heat conduction is negligible.

(*e*) The tube L/D is large enough to neglect second order effects in the interface heat transfer.

(*f*) The tube wall is sufficiently thin to neglect its thermal resistance.

(*g*) The variation of the thickness of the freeze layer with both time and position along the tube axis is small, consistent with small Stefan number assumption.

(*h*) The flow rate is constant.

Such assumptions have also been considered previously [9, 10] for the analysis of transient freezing inside a tube subjected to constant wall temperature. To solve this heat-transfer problem, the region of the tube $z \geq 0$ is divided into two zones. These are (i) the "freeze-free" or "cooling" zone ($0 < z \leq z_f$), where z_f is the location where the wall temperature is equal to the freezing temperature, and (ii) the "freezing" zone ($z > z_f$), wherein the wall temperature is below the freezing temperature and a frozen layer has formed at the inside tube surface. Analyses are developed for each of these zones and coupled at z_f as now described.

The Cooling Zone ($0 < z \leq z_f$). The energy equation for the parabolic flow of liquid in the thermal entrance region of a tube is given, in dimensionless form, as

$$\frac{\partial\theta(r,z,\tau)}{\partial\tau} + 2(1-r^2)\frac{\partial\theta}{\partial z} = \frac{\partial^2\theta}{\partial r^2} + \frac{1}{r}\frac{\partial\theta}{\partial r} \qquad (1a)$$

in $0 < r < 1$, $0 < z < z_f$, $\tau > 0$, and the boundary and initial conditions as

Contributed by the Heat Transfer Division for publication in the JOURNAL OF HEAT TRANSFER. Manuscript received by the Heat Transfer Division June 8, 1981.

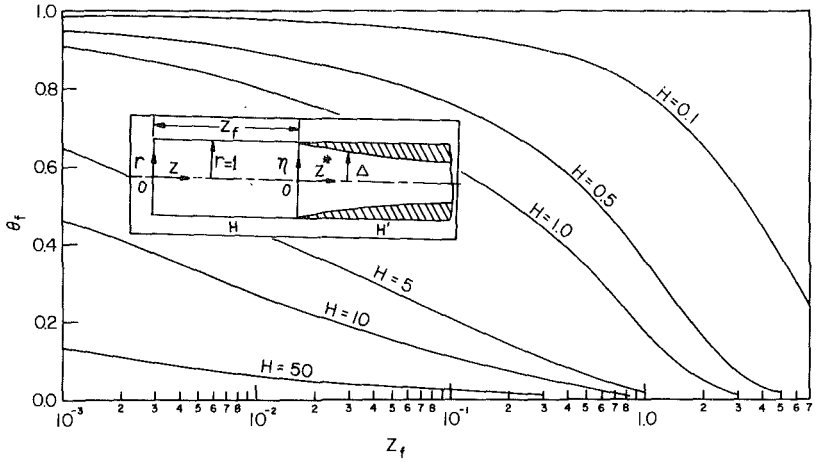

Fig. 1 The geometry and coordinates and variation of ice fuel zone, z_f, with dimensionless freezing temperature, θ_f, for different Biot numbers

$$\frac{\partial\theta(0,z,\tau)}{\partial r}=0, \tag{1b}$$

$$\frac{\partial\theta(1,z,\tau)}{\partial r}+H\theta(1,z,\tau)=0 \tag{1c}$$

$$\theta(r,0,\tau)=1 \tag{1d}$$

$$\theta(r,z,0)=1 \tag{1e}$$

By following a procedure described in reference [11], the finite integral transform pair in the r variable is defined as

$$\bar{\theta}(\beta_m,z,\tau)=\int_0^1 r'(1-r'^2)G(\beta_m,r')\theta(r',z,\tau)dr' \tag{2a}$$

$$\theta(r,z,\tau)=\sum_{m=0}^{\infty}\frac{G(\beta_m,r)}{N(\beta_m)}\bar{\theta}(\beta_m,z,\tau) \tag{2b}$$

where the normalization integral, $N(\beta_m)$, is defined as

$$N(\beta_m)=\int_0^1 r'(1-r'^2)G^2(\beta_m,r')dr' \tag{2c}$$

and $G(\beta_m, r)$ and β_m are the eigenfunctions and eigenvalues, respectively, of the eigenvalue problem

$$\frac{d^2G(r)}{dr^2}+\frac{1}{r}\frac{dG}{dr}+\beta^2(1-r^2)G=0 \text{ in } 0<r<1 \tag{3a}$$

$$\frac{dG(0)}{dr}=0 \tag{3b}$$

$$\frac{dG(1)}{dr}+HG(1)=0 \tag{3c}$$

The integral transform of the system (1) by the application of the transform (2a) yields

$$\int_0^1 rG_n\frac{\partial\theta}{\partial\tau}dr+2\frac{\partial\bar{\theta}_n}{\partial z}=-\beta_n^2\bar{\theta}_n, \text{ in } 0<z<z_f,\tau>0 \tag{4a}$$

$$\bar{\theta}_n=\bar{1} \tag{4b}$$

$$\text{at } z=0 \text{ and } \tau=0 \tag{4c}$$

where the bar denotes the integral transform according to the definition given by equation (2a). The function θ appearing under the integral sign in equation (4a) can be expressed in terms of $\bar{\theta}$ by utilizing the inversion formula (2b). Then the system (4) becomes

$$\sum_{m=0}^{\infty}\frac{\int_0^1 rG_nG_m\,dr}{N_m}\frac{\partial\bar{\theta}_m}{\partial\tau}+2\frac{\partial\bar{\theta}_n}{\partial z}=-\beta_n^2\bar{\theta}_n \tag{5a}$$

Nomenclature

$B = \dfrac{k_s}{k_l} = \dfrac{K_s}{K_l} = \dfrac{H}{H'}$

h = heat-transfer coefficient at the outer surface of the tube

$H = \dfrac{hr_w}{k_l}$ = Biot number based on liquid thermal conductivity

$H' = \dfrac{hr_w}{k_s}$ = Biot number based on solid thermal conductivity

$K_l = \dfrac{k_l(T_0-T_\infty)}{\alpha_l\rho\lambda}$

$K_s = \dfrac{k_s(T_0-T_\infty)}{\alpha_l\rho\lambda}$

k = thermal conductivity

$\text{Pr} = \dfrac{\nu}{\alpha_l}$ = Prandtl number

r' = radial variable

$r = \dfrac{r'}{r_w}$ = dimensionless radial variable

r_w = inside radius of the tube

$\text{Re} = \dfrac{2r_wU_m}{\nu}$ = Reynolds number

s = Laplace transform variable

$\text{Ste} = C_l(T_0-T_f)/\lambda = K_l(1-\theta_f)$, Stefan number based on liquid phase

t = time variable

t_f = time at which first freezing takes place on the tube surface

T = temperature

T_0 = inlet temperature

T_f = freezing temperature

T_∞ = temperature of the external environment

U_m = mean velocity

$U(\tau-z)$ = unit step function defined by equation (9c)

u_z' = axial velocity

u_r' = radial velocity

z' = axial variable

$$\bar{\theta}_n = \bar{1} \tag{5b}$$

$$\text{at } z=0 \text{ and } \tau=0 \tag{5c}$$

The Laplace transform of the system (5) with respect to the τ variable yields

$$\sum_{m=0}^{\infty} b_{mn}\,(s\tilde{\bar{\theta}}_m - \bar{1}) + 2\frac{d\tilde{\bar{\theta}}_n}{dz} = -\beta_n^2\,\tilde{\bar{\theta}}_n, \tag{6a}$$

$$\tilde{\bar{\theta}}_n = \frac{\bar{1}}{s} \quad \text{at } z=0 \tag{6b}$$

where

$$b_{nm} = \frac{\int_0^1 rG_nG_m\,dr}{\int_0^1 r(1-r^2)G_m^2\,dr} \tag{6c}$$

Here s is the Laplace transform variable, and the tilde denotes the Laplace transform of the function.

Equations (6*a*)–(6*c*), with $n = 1, 2, 3, \ldots$, provide an infinite set of coupled ordinary differential equations for the functions $\bar{\theta}_n$, $n = 1, 2, 3, \ldots$. They are similar to those studied in the reference [12], where it was shown that the trace solution obtained by taking those terms in the series where $m = n$, was sufficiently accurate. Therefore, a similar procedure is utilized here and only the diagonal elements of the system of equations (6) are considered; then the system (6) reduces to

$$b(s\tilde{\bar{\theta}}_m - \bar{1}) + 2\frac{d\tilde{\bar{\theta}}_m}{dz} = -\beta_m^2\,\tilde{\bar{\theta}}_m, \quad z>0 \tag{7a}$$

$$\tilde{\bar{\theta}}_m = \frac{\bar{1}}{s} \qquad \text{at } z=0 \tag{7b}$$

where

$$b \equiv b_{mm} = \frac{\int_0^1 rG_m^2\,dr}{\int_0^1 r(1-r^2)G_m^2\,dr} \tag{7c}$$

Clearly, the coefficient b depends on the eigenvalue β_m and is less than or equal to 2. However, to match the solution for the freeze-free region to that in the region where freezing begins we need to take $b = 2$; then the solution of the equation (7) for the double transform $\tilde{\bar{\theta}}(\beta_m, z, s)$ becomes

$$\tilde{\bar{\theta}}(\beta_m,z,s) = \bar{1}\left[\frac{1}{s} - \frac{1}{s+\frac{1}{2}\beta_m^2}\right]e^{-\left(s+\frac{1}{2}\beta_m^2\right)z} + \frac{1}{s+\frac{1}{2}\beta_m^2} \tag{8}$$

The temperature $\theta(r,z,\tau)$ for the cooling zone is recovered by successive inversion of this double transform

$$\theta(r,z,\tau) = \sum_{m=0}^{\infty} A_m\left\{\left[e^{-\frac{\beta_m^2}{2}z} - e^{-\frac{\beta_m^2}{2}\tau}\right]U(\tau-z) + e^{-\frac{\beta_m^2}{2}\tau}\right\}G(\beta_m,r), \tag{9a}$$

for $0 < z < z_f$ and where

$$A_m = \frac{\int_0^1 r(1-r^2)G_m\,dr}{\int_0^1 r(1-r^2)G_m^2\,dr} \tag{9b}$$

and the step function, $U(\tau-z)$, is defined as

$$U(\tau-z) = \begin{cases} 0 & \text{for } \tau<z \\ 1 & \text{for } \tau\geq z \end{cases} \tag{9c}$$

To determine the location $z = z_f$ along the tube at which the tube surface temperature becomes equal to the freezing temperature for the liquid, it is only necessary to set $r = 1$, $\tau = z \equiv z_f$ and $\theta = \theta_f$ in equation (9*a*). We note that, numerically, the dimensionless instant of time at which ice begins to form is equal to the dimensionless location at which it initiates, namely $\tau_f = z_f$. Then the following implicit equation is obtained for the determination of z_f.

$$\theta_f = \sum_{m=0}^{\infty} A_m\,G(\beta_m,1)e^{-\frac{1}{2}\beta_m^2 z_f} \tag{10}$$

For times $\tau > \tau_f$, the liquid temperature in the cooling zone, $0 < z \leq z_f$, is determined from equation (9*a*) by setting in that equation $U(\tau-z) = 1$; we obtain

Nomenclature (cont.)

$z = \dfrac{2z'}{\text{Re Pr } r_w}$ = dimensionless axial variable

$z_f = \dfrac{2z_f'}{\text{Re Pr } r_w}$ = dimensionless length of the freeze-free or cooling zone

$z^* = z - z_f$

Greek Letters

α = thermal diffusivity

β_m = eigenvalues of the eigenvalue problem (3)

δ = radius of solid-liquid interface

$\Delta = \dfrac{\delta}{r_w}$ = dimensionless radius of solid-liquid interface

$\phi = \theta_l - \theta_f$

$\eta = \dfrac{r}{\Delta}$ = normalized radial coordinate

$\theta_j = \dfrac{T_j - T_\infty}{T_0 - T_\infty}$ = dimensionless temperature, $j \equiv f$, l or s

λ = latent heat of phase change

γ_n = eigenvalues of the eigenvalue problem (16)

ν = kinematic viscosity

ρ = density of liquid

$\tau = \dfrac{\alpha_l t}{r_w^2}$ = dimensionless time variable or the Fourier number

$\tau_f = \dfrac{\alpha_l t_f}{r_w^2} = Z_f$ = dimensionless time at which solid begins to form

$\tau^* = \tau - \tau_f$

Subscripts

f = refers to freezing condition

l = refers to liquid-phase

0 = refers to tube inlet

s = refers to solid-phase

w = refers to inside surface of the tube

Superscripts

$-$ = integral transform

$\sim$ = Laplace transform

$$\theta(r,z) = \sum_{m=0}^{\infty} A_m G(\beta_m, r) e^{-\frac{1}{2}\beta_m^2 z} \tag{11}$$

The Freezing Zone ($z > z_f$). In writing the energy equation for the liquid phase, the new variables η, z^*, τ^* and ϕ are defined as

$$\eta = \frac{r}{\Delta} \tag{12a}$$

$$z^* = z - z_f \tag{12b}$$

$$\tau^* = \tau - \tau_f \equiv \tau - z_f \tag{12c}$$

$$\phi = \theta_l - \theta_f \tag{12d}$$

where θ_l and θ_f are the dimensionless, liquid-phase temperature and the freezing temperature, respectively. As assumed in reference [4], the axial velocity profile can be represented as $u_{z'} = 2\,U_m\,(r_w/\delta)^2\,(1-\eta^2)$ and the radial velocity profile as $u_{r'} = u_{z'}\,\eta\,d\delta/dz'$. Also, because of the assumption (7), that the Stefan number is small, the contribution of the term $\partial\Delta/\partial\tau^*$, which occurs in the energy equation because of the coordinates η, z^*, τ^*, is negligible, as pointed out in connection with equation (15*a*). The energy equation, then, for the liquid-phase in the freezing zone is given by

$$\Delta^2 \frac{\partial\phi(\eta,z^*,\tau^*)}{\partial\tau^*} + 2(1-\eta^2)\frac{\partial\phi}{\partial z^*} = \frac{\partial^2\phi}{\partial\eta^2} + \frac{1}{\eta}\frac{\partial\phi}{\partial\eta} \tag{13a}$$

in $0 < \eta < 1$, $z^* > 0$ and $\tau^* > 0$, subject to the boundary and initial conditions

$$\frac{\partial\phi(0,z^*,\tau^*)}{\partial\eta} = 0, \tag{13b}$$

$$\phi(1,z^*,\tau^*) = 0 \tag{13c}$$

$$\phi(\eta,0,\tau^*) = F(\eta) - \theta_f \tag{13d}$$

$$\phi(\eta,z^*,0) = F(\eta) - \theta_f \tag{13e}$$

where $F(\eta)$ is obtained from equation (11) by setting in that equation $z = z_f$ and $r = \eta$. That is,

$$F(\eta) = \begin{cases} \displaystyle\sum_{m=0}^{\infty} A_m G(\beta_m,\eta) e^{-\frac{1}{2}\beta_m^2 z_f} & \text{for } H \neq \infty \quad (13f) \\ 1 \text{ (i.e., no cooling zone)} & \text{for } H = \infty \quad (13g) \end{cases}$$

The energy equation and the boundary conditions for the solid phase, for the case of Large L/D and, therefore, negligible axial conductive effects and the quasi-steady growth condition described in assumption (7), are given by

$$\frac{d}{dr}\left(r\frac{d\theta_s}{dr}\right) = 0 \quad \text{in} \Delta < r < 1 \tag{14a}$$

$$\theta_s(\Delta) = \theta_f, \tag{14b}$$

$$\frac{d\theta_s(1)}{dr} + H'\theta_s(1) = 0 \tag{14c}$$

Finally, the energy-balance equation for the liquid-solid interface is written as

$$\left[K_s\frac{\partial\theta_s}{\partial r} - K_l\frac{\partial\theta_l}{\partial r}\right]_{r=\Delta} = \frac{\partial\Delta(z^*,\tau^*)}{\partial\tau^*}, \tau^* > 0 \tag{15a}$$

$$\Delta(z^*,0) = 1 \tag{15b}$$

where θ_l is related to ϕ by equation (12*d*). In this expression it can be seen that $\partial\Delta/\partial\tau^*$ is approximately proportional to the liquid phase Stefan number, and contributes little in the energy equation (13*a*).

The problems defined by equations (13), (14), and (15) are solved by first addressing the liquid-phase energy equation, then the solid-phase conduction equation, and finally the interface coupling equation, in order.

Solution for the Liquid-Phase. To solve equations (13) we consider the following eigenvalue problem

$$\frac{d^2R(\eta)}{d\eta^2} + \frac{1}{\eta}\frac{dR}{d\eta} + \gamma^2(1-\eta^2)R = 0 \quad \text{in } 0 < \eta < 1 \tag{16a}$$

$$\frac{dR(0)}{d\eta} = 0, \tag{16b}$$

$$R(1) = 0 \tag{16c}$$

This eigenvalue problem is similar to that given by equations (3), except the boundary condition at $\eta = 1$ of the first kind. It should be noted that this is specifically the eigenvalue problem associated with the Graetz solution.

The integral transform pair applicable to the η variable is constructed from the eigenfunctions of the eigenvalue problem (16) and the resulting transform is applied to the system (13) to remove the partial derivatives with respect to the η variable following the procedure described previously. If the dependence of Δ on τ^* is assumed to be of second order significance with assumption (7), the Laplace transform of the resulting system with respect to the τ^* variable yields

$$\Delta^2 \sum_{m=0}^{\infty} d_{mn}(s\tilde{\phi}_n - a_m) + 2\frac{d\tilde{\phi}_m}{dz^*} = -\gamma_m^2\tilde{\phi}_m, \text{ for } z^* > 0 \tag{17a}$$

$$\tilde{\phi}_m^{(0)} = \frac{a_m}{s} \tag{17b}$$

where s is the Laplace transform variable, tilde denotes the Laplace transform of the function, and d_{mn} is defined as

$$d_{mn} = \frac{\displaystyle\int_0^1 \eta R_m R_n\,d\eta}{\displaystyle\int_0^1 \eta(1-\eta^2)R_n^2\,d\eta} \tag{17c}$$

The system (17) is an infinite set of coupled ordinary differential equations for the functions $\tilde{\phi}_m$, $m = 0, 1, 2, \ldots$ As discussed previously we consider only the terms in the series for which $m = n$. Then the following differential equation is obtained for the determination of the functions $\tilde{\phi}(\gamma_n, z^*, s)$

$$\Delta^2(s\tilde{\phi}_n - a_n)d + 2\frac{d\tilde{\phi}_n}{dz^*} = -\gamma_n^2\tilde{\phi}_n, \quad z^* > 0 \tag{18a}$$

$$\tilde{\phi}(0) = \frac{a_n}{s} \tag{18b}$$

where

$$d_{mn} \equiv d \equiv \frac{\displaystyle\int_0^1 \eta R_n^2\,d\eta}{\displaystyle\int_0^1 \eta(1-\eta^2)R_n^2\,d\eta} \tag{18c}$$

Here, the parameter, d, depends on the eigenvalue γ_n, and its value lies between 1 and 2; but the results are found to be rather insensitive to the variation of d. To match the solutions for the solid and liquid phases at the solid-liquid interface, the same value of d should be used for all eigenvalues in the solution for the liquid phase. With this physical requirement, we used a constant value of $d = 1.584$, determined by averaging it over the first ten eigenvalues.

Equation (18) is solved and the resulting double transform is inverted as

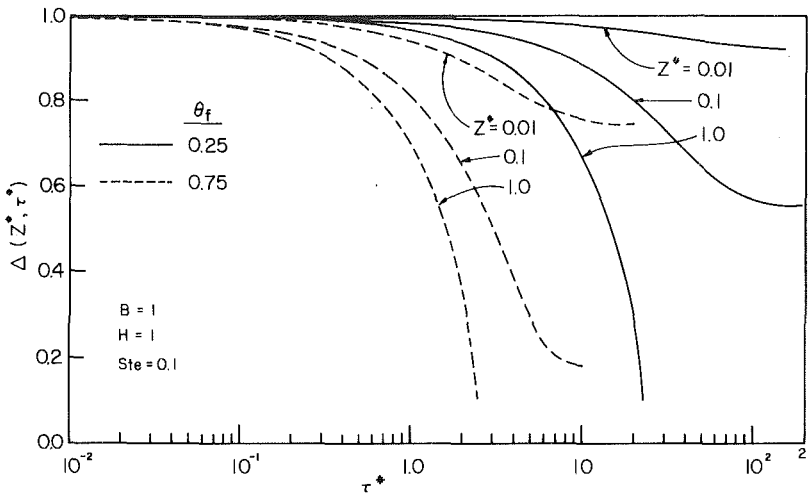

Fig. 2 Variation of freeze layer thickness, $1-\Delta$, with time, τ^*, and axial position, z^*, for $B = 1$, $H = 1$, Ste = 0.1

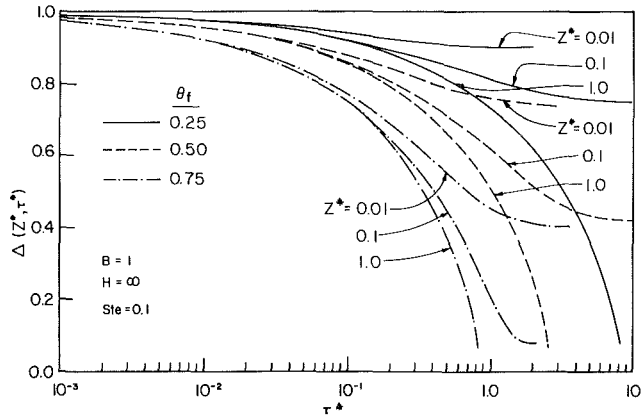

Fig. 3 Variation of freeze layer thickness, $1-\Delta$, with time, τ^*, and axial position, z^*, for $B = 1$, $H = \infty$, and Ste = 0.1

$$\phi(\eta,z^*,\tau^*)=\sum_{n=0}^{\infty} D_n\left\{\left[e^{-\frac{\gamma_n^2}{2}z^*}-e^{-\frac{\gamma_n^2}{\Delta^2 d}\tau^*}\right]U\left(\tau^*-\frac{z^*\Delta^2 d}{2}\right)+e^{-\frac{\gamma_n^2}{\Delta^2 d}\tau^*}\right\}R(\gamma_n,\eta), \tag{19a}$$

where

$$D_n=\begin{cases}-C_n\left[\theta_f+\sum_{m=0}^{\infty}\dfrac{A_m G(1)}{\left(\frac{\beta_m}{\gamma_n}\right)^2-1}e^{-\beta_m^2 z_f/2}\right] & \text{for } H\neq\infty \quad (19b)\\ C_n(1-\theta_f) & \text{for } H=\infty \quad (19c)\end{cases}$$

and the eigenvalues γ_n and the coefficients $[-C_n\ R'\ (1)/2]$ that are needed for the determination of the thickness of the solid layer are tabulated in reference [13]. In the present work, more accurate values of these eigenvalues and eigenconstants were calculated.

Knowing the function $\phi(\eta,\ z^*,\ \tau^*)$, the temperature distribution, $\theta_l\ (\eta,\ z^*,\ \tau^*)$, in the liquid phase for the freezing zone is given by

$$\theta_l(\eta,z^*,\tau^*)=\theta_f+\phi(\eta,z^*,\tau^*) \tag{20}$$

Solution for the Solid-Phase. The solution of equations (14) for the solid-phase temperature, θ_s, is

$$\theta_s(r,\Delta)=\theta_f\frac{1-H'\ln r}{1-H'\ln\Delta} \tag{21}$$

The Coupling Condition. Taking derivatives of equations (20) and (21) and introducing the resulting expressions into the interface energy balance equation (15*a*) yields the differential equation for the dimensionless radius, $\Delta(z^*,\ \tau^*)$, as

$$\frac{B\theta_f}{\ln\Delta-\frac{1}{H'}}-\sum_{n=0}^{\infty}D_n e^{-\frac{\gamma_n^2}{\Delta^2 d}\tau^*}R'(1)=\frac{\Delta}{K_l}\frac{\partial\Delta(z^*,\tau^*)}{\partial\tau^*} \tag{22}$$

for $\tau^* < z^*\Delta^2 d/2$, and

$$\frac{B\theta_f}{\ln\Delta-\frac{1}{H'}}-\sum_{n=0}^{\infty}D_n e^{-\frac{\gamma_n^2 z^*}{2}}R'(1)=\frac{\Delta}{K_l}\frac{\partial\Delta(z^*,\tau^*)}{\partial\tau^*} \tag{23}$$

for $\tau^* \geq z^*\Delta^2 d/2$, where $B = K_s/K_l = k_s/k_l = H/H'$ and D_n is defined by equation (19*b*).

For the steady state, $\Delta(z^*,\ \infty)$, equation (23) is immediately solved by setting the right-hand side equal to zero. Thus,

$$\Delta(z^*,\infty)=\exp\left[\frac{B\theta_f}{A(z^*)}+\frac{1}{H'}\right] \tag{24a}$$

where

$$A(z^*)=\sum_{n=0}^{\infty}D_n R'(1)e^{-\frac{1}{2}\gamma_n^2 z^*} \tag{24b}$$

For the general time dependent case, equations (22) and (23) can be solved numerically and the values of $\Delta(z^*,\ \tau^*)$ determined as a function of time and the axial position for given values of the parameters B, θ_f, and H.

Results and Discussion

The length of the freeze-free zone, z_f, defined by equation (10) is a function of the dimensionless freezing temperature, θ_f, and the Biot number, H. The calculations were carried out for parametric values of H and are shown plotted in Fig. 1. For a liquid with a given freezing temperature, the value of θ_f clearly increases when the inlet temperature T_0 is reduced.

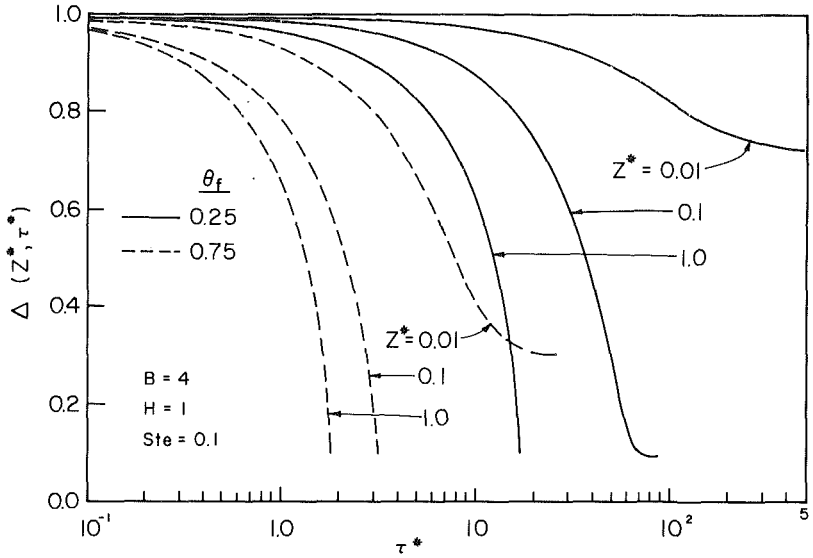

Fig. 4 Variation of freeze layer thickness, $1-\Delta$, with time, τ^*, and axial position, z^*, for $B = 4$, $H = 1$, and Ste = 0.1

Accordingly, if the external heat-transfer coefficient (Biot number) and T_∞, are fixed, an increase in θ_f indicates a reduction in the length of freeze-free entrance region, z_f. For values of $H > 1$ (all θ_f) and $H < 1$ ($\theta_f > 0.8$) the dependence of z_f on θ_f can be extremely sensitive.

Equations (22) and (23) were solved numerically, by iteration, using the values of z_f already computed. The equations were cast in integral form and integrated in Δ increments of 0.005 for $\Delta < 0.8$, and in increments of 0.001 for $0.8 < \Delta < 1.0$, because the variation of τ^* increased rapidly as $\Delta \to 1.0$. The solution of equation (22) served to provide the initial and boundary conditions for equation (23), and the calculations were carried out for a range of values of θ_f, B, Ste, and H. The effects of these parameters on Δ at different times and locations along the tube are illustrated in Figs. 2–5. It can be seen that the interface $\Delta(z^*, \tau^*)$ is displayed in terms of z^* and τ^*, the first of which represents the distance measured only in the freezing zone ($z - z_f$), and the second of which represents the time measured from the instant ice begins to form ($\tau - \tau_f$). It can be seen from these figures that some of the variations of Δ seem to approach a steady-state condition, but Δ does not reach zero, since, the flow rate is specified as a constant greater than zero. Therefore, very small values of Δ are not plotted. Practically, very small values of Δ represent freeze blockage conditions since in an actual situation the pressure drop required to maintain such a constant flow would be extremely large.

The values of z^*, B, H, and Ste chosen for the plots are representative of those conditions most commonly found in actual situations. In Figs. 3 and 5, results are plotted for $H = \infty$ which represents the behavior to be expected when the wall temperature is uniform and constant and equal to T_∞.

The curves presented in Figs. 2 and 4 are intended to illustrate the effects of the ratio of the solid-phase to liquid-phase thermal conductivity, $B = k_s/k_l$, on the freezing process for $H = 1$. It is clearly seen that a pronounced effect does not exist. The curves presented in Figs. 3 and 5 illustrate that for large H, a fluid with a large B will freeze more rapidly. With smaller H, the relative thermal conductivities of the solid and liquid phases becomes less important. Conversely, with large H, the relative thermal conductivities of the phases can introduce significant effects. Most fluids of interest in heat transfer will have a value of B in the range of 1 to 4.

The effect of the fluid latent heat, as expressed in the Stefan

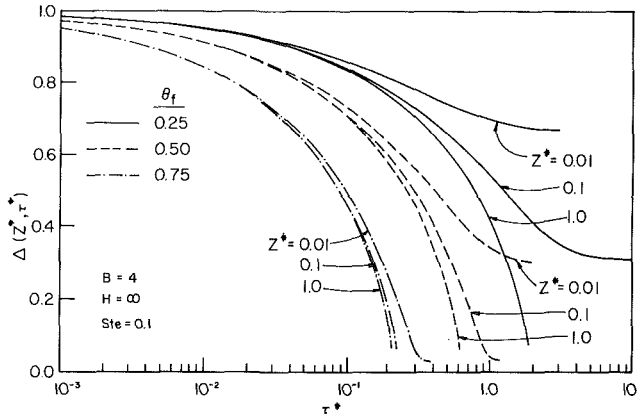

Fig. 5 Variation of freeze layer thickness, $1-\Delta$, with time τ^*, and axial position, z^*, for $B = 4$, $H = \infty$, and Ste = 0.1

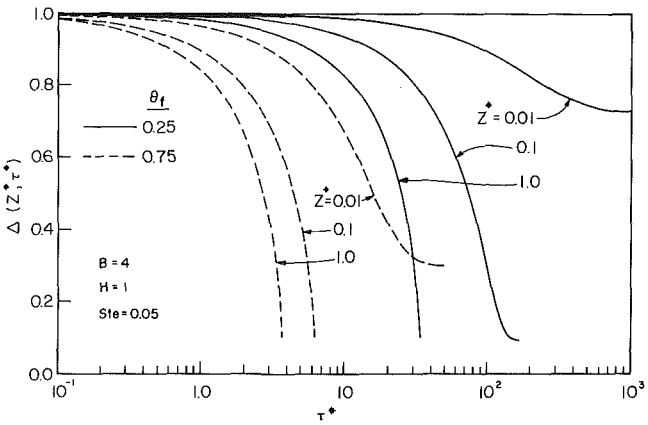

Fig. 6 Variation of freeze layer thickness, $1-\Delta$, with time, τ^*, and axial position, z^*, for $B = 4$, $H = 1$, and Ste = 0.05

number, Ste, is illustrated in Fig. 6. By comparing the results in Figs. 4 and 6, it can be seen that an increase of λ (decrease of Ste) results in a thinner layer of solid at any given time and location, a result to be expected. It would also be expected, although not shown here, that this effect would become less pronounced as H increased. The Stefan number range of 0.05 to 0.1 is representative of applications involving water and many other common fluids of engineering interest.

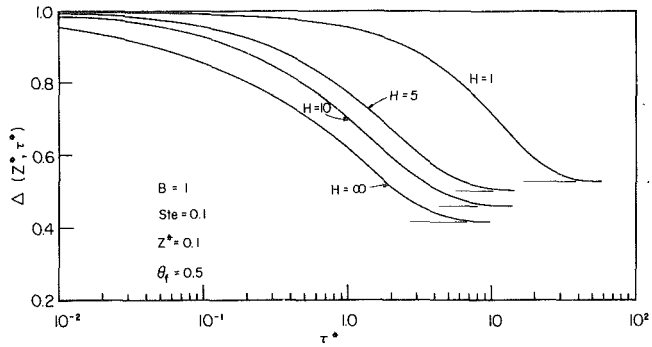

Fig. 7 Effect of Biot number, H, on the variation of freeze layer thickness, $1 - \Delta$, with time, τ^*, for $B = 1$, Ste = 0.1, and $Z^* = 0.1$

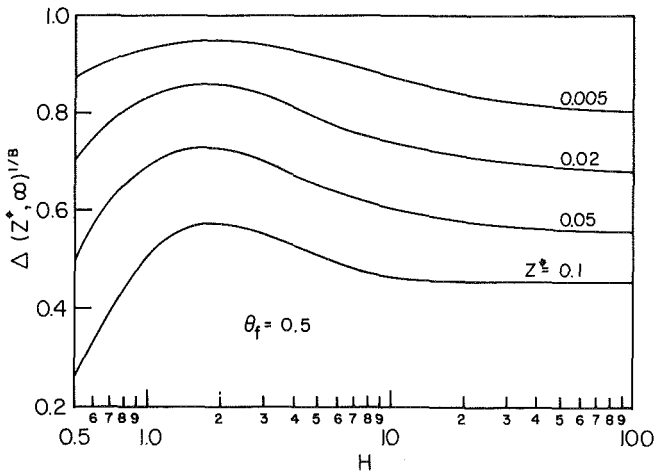

Fig. 8 Variation of the steady-state freeze layer thickness, $1 - \Delta(z^*, \infty)$, with the Biot number, H, at different locations for $\theta_f = 0.5$

To clearly depict the influence of H, a plot of Δ versus τ^* is presented in Fig. 7 for parametric values of H. A single set of representative values of B, Ste, and z^* were chosen for the display. The time required to achieve steady state increased with $(1/H)$ as expected. However, as H decreased from infinity, the steady-state thickness surprisingly first decreases and then increases as illustrated in Fig. 8, in which the steady-state radius Δ (F^*, ∞) raised to the $1/B$ power is plotted against H. The inclusion of B in the exponent effectively eliminates B as a parameter, thus requiring only a specification of θ_f in the figure. The maximum is clearly seen and remains about constant at $H \simeq 1.5$ for all z^* with a $\theta_f = 0.5$. The explanation is simply that Δ at a given distance from the beginning of the freezing zone, $z^* = z - z_f$, and $\tau = \infty$, should decrease when H is increased. However, as shown in Fig. 1, z_f will decrease and thus alter the temperature profile of the liquid entering the freezing section of z_f. In this illustration, it will be warmer as an average because of the shorter length z_f, and thus will tend to increase Δ. It turns out that for $\theta_f = 0.5$ this latter effect is dominant for $H < 1.5$, and the former expected behavior occurs for $H > 1.5$. Very little effect of H is noted above $H = 100$.

Acknowledgment

This work was supported in part by the National Science Foundation through the research grant Engr. 77-12949, and was carried out in concert with related work performed under Contract No. 14-34-0001-9530, OWRT, U. S. Department of the Interior.

References

1 Gilpin, R. R., "The Effects of Dendritic Ice Formation in Water Pipes," *International Journal of Heat and Mass Transfer*, Vol. 20, 1977, pp. 693-699.

2 Gilpin, R. R., "The Morphology of Ice Structure in a Pipe at or Near Transition Reynolds Numbers," AIChE Symposium Series No. 189, Vol. 75, 1979, pp. 89-94.

3 Mulligan, J. C. and Jones, D. D., "Experiments on Heat Transfer and Pressure Drop in a Horizontal Tube with Internal Solidification," *International Journal of Heat and Mass Transfer*, Vol. 19, 1976, pp. 213-219.

4 Zerkle, R. D. and Sunderland, J. E., "The Effect of Liquid Solidification in a Tube Upon Laminar-Flow Heat Transfer and Pressure Drop," ASME JOURNAL OF HEAT TRANSFER, Vol. 90, 1968, pp. 183-190.

5 Yim, A., Epstein, M., Bankoff, S. G., Lambert, G. A., and Hauser, G. M., "Freezing-Melting Heat Transfer in a Tube Flow," *International Journal of Heat and Mass Transfer*, Vol. 21, 1978, pp. 1185-1196.

6 Kuzay, T. M. and Epstein, M., "Penetration of a Freezing Liquid into an Annular Channel," AIChE Symposium Series No. 189, Vol. 75, 1979, pp. 95-102.

7 Depew, C. A. and Zenter, R. C., "Laminar Flow Heat Transfer and Pressure Drop with Freezing at the Wall," *International Journal of Heat and Mass Transfer*, Vol. 12, 1969, pp. 1710-1714.

8 Zerkle, R. D., "The Effect of External Thermal Insulation on Liquid Solidification in a Tube," Sixth Southeastern Seminar on Thermal Sciences, Apr. 13-14, 1970, pp. 1-19.

9 Özişik, M. N. and Mulligan, J. C., "Transient Freezing of Liquids in Forced Flow Inside Circular Tubes," ASME JOURNAL OF HEAT TRANSFER, Vol. 91, 1969, 385-390.

10 Bilenas, J. A. and Jiji, L. M., "Axisymmetric Fluid Flow in Tubes with Solidification," *J. Franklin Inst.*, Vol. 289, 1970, 265-279.

11 Özişik, M. N., *Heat Conduction*, John Wiley and Sons, Inc., New York, 1980.

12 Vick, B., Özişik, M. N., and Bayazitoğlu, Y., "A Method of Analysis of Low Peclet Number Thermal Entry Region Problems with Axial Conduction," *Letters in Heat Mass Transfer*, Vol. 7, No. 4, 1980, pp. 235-248.

13 Sellers, J. R., Tribus, M., and Klein, J. S., "Heat Transfer in Laminar Flow in a Round Tube or Flat Conduit—The Graetz Problem Extended," Trans. ASME, Vol. 78, 1956, pp. 441-448.

P. E. Frivik
Division of Refrigeration Engineering,
The Norwegian Institute of Technology,
Trondheim, Norway

G. Comini
Istituto di Fisica Tecnica e di
Tecnologie Industriali,
Università degli Studi di Udine,
Udine, Italy

Seepage and Heat Flow in Soil Freezing

In this paper we describe a system of computer programs based on the finite element method, which can be used for the calculation of coupled velocity and temperature fields during freezing and thawing of soils in the presence of seepage flow. In the programs, the mass and energy conservation equations are solved simultaneously, without the use of too limiting assumptions. The results of the computations are compared with experimental measurements made on a laboratory model of a soil freezing system, and the agreement between measured and computed values is good.

Introduction

Artificial soil freezing for mining and construction applications has been in use for many years, but only recently the method has gained widespread attention in civil engineering practice. Currently, artificial soil freezing is used extensively both as a structural support system and as a water barrier for large scale open excavations and for tunnel and shaft constructions (see, for example, [1, 2]). Seepage flow must be accounted for in most of these projects, since the neglect of seepage in planning the freezing process often leads to serious difficulties and even to the disruption of the working schedule ([1], p. 87).

In northern climates, freezing and thawing of soils in the presence of seepage flow, must also be considered in several thermal and permafrost engineering applications, such as the realization of ground based heat pump systems and the construction of earth dams, roads and pipelines in permafrost areas [3].

Quantitative evaluation of the effects of ground-water flow on freezing and thawing of soils requires simultaneous solution of the equations for the ground-water velocity and the temperature distributions.

Due to the complexity of the problem, it has not been possible, as yet, to develop a satisfactory analytical solution. However, in connection with artificial freezing investigations, Khakimov ([1], p. 109) and Takashi [4], developed approximate methods for predicting sufficient conditions for the joining of the ice-soil cylinders around a row of freeze-pipes in the presence of a seepage stream.

Following Takashi's approach, a semianalytical solution, based on the finite-difference method, has also been produced to compute transient temperature profiles and ground-water seepage rates around a row of equally spaced freeze-pipes, assuming perfectly circular frozen zones and uniform seepage flow in the unfrozen zones [5].

These approximate methods can probably yield predictions of the overall performance of a freezing system which are good enough for many practical purposes. On the other hand, they cannot produce computations of temperature and velocity fields as accurate as those needed in critical applications such as, for example, the estimation of the long-term bearing capability of frozen soil barriers [6].

In this paper, we describe a system of computer programs, based on the finite element method, which can be used for the calculation of coupled velocity and temperature fields during freezing and thawing of soils in the presence of a seepage stream. In the program, the mass and energy conservation equations are solved simultaneously without the use of simplifying assumptions as limiting as those employed in previous studies.

The results of the computations are compared with experimental measurements made on a laboratory model of a soil freezing system, expressly built for this research at the Division of Refrigeration Engineering of the Norwegian Institute of Technology.

This way, the accuracy of the finite element calculations and the reliability of the mathematical model are demonstrated experimentally.

Mathematical Model

The problem is to analyze energy transport in a porous medium, in the presence of bulk flow of an incompressible fluid. The flow is governed by the momentum and continuity equations. The momentum equations, for seepage flow of ground water in soils, reduce to Darcy's equations [7] and, using Cartesian coordinates, can be written, for a two dimensional region A, as:

$$\left.\begin{aligned} u &= -k_p \frac{\partial p}{\partial x} \\ v &= -k_p \frac{\partial p}{\partial y} \end{aligned}\right\} \tag{1}$$

where k_p is the coefficient of permeability and

$$p = p^1 + \rho g z \tag{2}$$

is the driving pressure, p' and z being, respectively, the total fluid pressure and the vertical distance from a horizontal plane, taken as positive in the upwards direction.

From equation (1) it follows that the continuity equation can be expressed as:

$$\frac{\partial}{\partial x}\left(k_p \frac{\partial p}{\partial x}\right) + \frac{\partial}{\partial y}\left(k_p \frac{\partial p}{\partial y}\right) = 0 \tag{3}$$

by neglecting the soil capacity for water accumulation and the influence of temperature gradients on seepage flow.

In the presence of a bulk flow of ground-water, the energy equation for the medium under consideration, can be written, in two-dimensional Cartesian coordinates, as:

$$C_s \frac{\partial t}{\partial \tau} = \frac{\partial}{\partial x}\left(k_t \frac{\partial t}{\partial x}\right) + \frac{\partial}{\partial y}\left(k_t \frac{\partial t}{\partial y}\right) - C_l\left(u \frac{\partial t}{\partial x} + v \frac{\partial t}{\partial y}\right) \tag{4}$$

assuming that latent heat effects during freezing and thawing of soils can be accounted for by using a temperature dependent volumetric heat capacity C_s over a suitable range of temperatures [8].

In the above, k_p, k_t and C_s are functions of temperature to be evaluated, for the soil under investigation, from experimental measurements or from suitable semiempirical correlations.

Contributed by the Heat Transfer Division for publication in the JOURNAL OF HEAT TRANSFER. Manuscript received by the Heat Transfer Division May 28, 1981.

The essential features of the process investigated are well-reproduced by the mathematical model. In fact, equations (1-4) are valid for the entire region of interest, regardless of the state of the ground-water contained in the pores of the soil. Thus, a very low value of permeability at below freezing temperatures automatically yields, through equations (1), very low rates of seepage flow. This way proper convection contributions to total energy transfer are taken into account by equation (4), both at above and below freezing temperatures.

Boundary conditions of practical interest for equations (1-4) may be taken as:

$$p = p_w \text{ on part of the boundary } P_1; \tag{5}$$

$$k_p \frac{\partial p}{\partial x} l_x + k_p \frac{\partial p}{\partial y} l_y + q_p = 0 \quad \text{on part of the boundary } P_2; \tag{6}$$

$$t = t_w \text{ on part of the boundary } P_3; \tag{7}$$

$$k_t \frac{\partial t}{\partial x} l_x + k_t \frac{\partial t}{\partial y} l_y + q_t = 0 \quad \text{on part of the boundary } P_4; \tag{8}$$

In the above, l_x, l_y are direction cosines of the outside normal to the boundary surface P, q_p is the density of volumetric flow while q_t is the heat flow density through the boundary. The variables p_w, t_w, q_p and q_t are assumed to be known functions of positions and/or time and P_1, P_2, P_3, P_4 are such that both P_1, P_2 and P_3, P_4 include the entire boundary P.

Finite Element Formulation

The spacewise discretization of equations (3) and (4), subjected to boundary conditions (5-8), has been accomplished by means of the Galerkin method [9].

The unknown functions p and t are approximate throughout the solution domain, A, at any time, τ, by the relationships:

$$\left.\begin{aligned} p &= \sum_{j=1}^{m} N_j(x,y)\, p_j(\tau) = \mathbf{N}\bullet\mathbf{P} \\ t &= \sum_{j=1}^{m} N_j(x,y)\, t_j(\tau) = \mathbf{N}\bullet\mathbf{T} \end{aligned}\right\} \tag{9}$$

where N_j are the usual shape functions, defined piecewise element by element, with p_j or $\mathbf{P}$ and t_j or $\mathbf{T}$ being the nodal parameters. The simultaneous equations allowing the solution for m values of p_j and m values of t_j are obtained typically, for point j, by equating to zero the integral, over the domain A, of the product of the weighting function N_j by the residual resulting from substitution into equations (3) and (4) of equations (9). After making use of Green's theorem, in order to avoid second derivatives in the integrals imposing unneccessary continuity conditions between elements, the 2m equations can be written down in matrix form as:

$$\left.\begin{aligned} \mathbf{V}\bullet\mathbf{P} + \mathbf{R} &= 0 \\ \mathbf{K}\bullet\mathbf{T} + \mathbf{C}\,\dot{\mathbf{T}} + \mathbf{Q} &= 0 \end{aligned}\right\} \tag{10}$$

where

$$\dot{\mathbf{T}} = \partial\mathbf{T}/\partial\tau \tag{11}$$

Typical matrix element are [9]:

$$V_{jk} = \sum \int_{A^e} \left(k_p \frac{\partial N_j}{\partial x} \frac{\partial N_k}{\partial x} + k_p \frac{\partial N_j}{\partial y} \frac{\partial N_k}{\partial y} \right) dA \tag{12}$$

$$K_{jk} = \sum \int_{A^e} \left(k_t \frac{\partial N_j}{\partial x} \frac{\partial N_k}{\partial x} + k_t \frac{\partial N_j}{\partial y} \frac{\partial N_k}{\partial y} \right) dA + \sum \int_{A^e} C_l N_j \left(u \frac{\partial N_k}{\partial x} + v \frac{\partial N_k}{\partial y} \right) dA \tag{13}$$

$$C_{jk} = \sum \int_{A^e} C_s N_j N_k \, dA \tag{14}$$

$$R_j = \sum \int_{P^e} N_j q_p \, dP \tag{15}$$

$$Q_j = \sum \int_{P^e} N_j q_t \, dP \tag{16}$$

where $j, k = 1,\text{m}$. In the above, velocities u, v are computed from equation (1) by the program shape function routines.

Equation (10) can be written in a more compact form using partitioned matrices:

$$\begin{bmatrix} \mathbf{V} & 0 \\ 0 & \mathbf{K} \end{bmatrix} \begin{Bmatrix} \mathbf{P} \\ \mathbf{T} \end{Bmatrix} + \begin{bmatrix} 0 & 0 \\ 0 & \mathbf{C} \end{bmatrix} \begin{Bmatrix} 0 \\ \dot{\mathbf{T}} \end{Bmatrix} + \begin{Bmatrix} \mathbf{R} \\ \mathbf{Q} \end{Bmatrix} = 0 \tag{17}$$

or

$$\mathbf{S}\bullet\boldsymbol{\phi} + \mathbf{M}\bullet\dot{\boldsymbol{\phi}} + \mathbf{F} = 0 \tag{18}$$

where

$$\mathbf{S} = \begin{bmatrix} \mathbf{V} & 0 \\ 0 & \mathbf{K} \end{bmatrix} \tag{19}$$

$$\mathbf{M} = \begin{bmatrix} 0 & 0 \\ 0 & \mathbf{C} \end{bmatrix} \tag{20}$$

Nomenclature

A = domain of definition
C = heat capacity per unit volume
$\mathbf{C}$ = heat capacity matrix, equation (14)
$\mathbf{F}$ = reaction vector, equation (22)
g = acceleration of gravity
k_p = permeability
k_t = thermal conductivity
$\mathbf{K}$ = conductivity matrix, equation (13)
l_x, l_y = direction cosines of the outward normal
$\mathbf{M}$ = mass matrix, equation (20)
$\mathbf{N}$ = shape function vector, equation (9)
p = driving pressure, equation (2)
p' = total fluid pressure
$\mathbf{P}$ = vector of node pressures, equation (9)
P = external boundary
q_p = mass flow density
q_t = heat flow density
$\mathbf{Q}$ = heat flow density matrix, equation (16)
$\mathbf{R}$ = mass flow density matrix, equation (15)
$\mathbf{S}$ = stiffness matrix, equation (19)
t = temperature
$\mathbf{T}$ = vector of node temperatures, equation (9)
u,v = velocity components in the x, y directions
$\mathbf{V}$ = permeability matrix, equation (12)
x,y = Cartesian coordinates
z = vertical coordinate
ρ = density
τ = time
ϕ = potential vector, equation (21)

Subscripts

i = initial value
l = liquid
p = connected with the seepage flow
s = soil
t = connected with the heat flow
w = at the external surface
x,y = in the x, y directions

Superscripts

e = element
n = at the time level n

$$\phi = [\mathbf{P},\mathbf{T}]^T \quad ; \quad \dot{\phi} = \partial\phi/\partial\tau \qquad (21)$$

$$\mathbf{F} = [\mathbf{R},\mathbf{Q}]^T \qquad (22)$$

The system of equation (18) is nonlinear, since physical properties k_p, k_l and C_s are dependent on temperature. Values of potentials ϕ, at three consecutive levels, are then used to march in time, which results in the following recurrence scheme:

$$\phi^{n+1} = -[\mathbf{S}^n/3 + \mathbf{M}^n/(2\Delta\tau)]^{-1} \cdot [\mathbf{S}^n\phi^n/3 + \mathbf{S}^n\phi^{n-1}/3 - \mathbf{M}^n \cdot \phi^{n-1}/(2\Delta\tau) + \mathbf{F}^n] \qquad (23)$$

where the subscript n refers to the time value and $\Delta\tau$ is the time step.

It can be seen that central values of the matrices **S**, **M**, **F** are used in equation (23), which circumvents the necessity for iteration within each time step.

The scheme requires two starting values of ϕ for initiation, but this presents no difficulties as known stationary values can be easily assumed.

The scheme is unconditionally stable. Oscillations arising from sudden variations in boundary conditions can be kept under control by adopting an automatic time step adjustment feature based on prescribed maximum and minimum values for the norm. Undulations arising from the "numerical noise" inherent in the approximations made are reduced by redefining vector ϕ^{n-1} at each time step after the first one, as [8]:

$$\phi^{n-1} = (\phi^{n+1} + \phi^n + \phi^{n-1})/3 \qquad (24)$$

The program implementing algorithm (23) follows the usual pattern [9]. However matrices **K** (and **S**) are now nonsymmetrical and thus a nonsymmetric solver must be utilized. Besides matrices **V**, **K**, **C**, **Q** (and **S**, **M**, **F**) are time-dependent through the variations of coefficients with temperature and/or time and a completely new solution has to be obtained at each stage.

The evaluation of temperature-dependent material properties in equations (12–14) is carried on as suggested in [10], with reference to the derivatives, and with respect to temperature, of the property integrals. This averaging process gives representative values of material properties even in the phase change zone. Obviously, in zones of constant temperature, recourse is made to direct evaluation.

In the program, eight-node isoparametric elements are used with 3 × 3 integration points.

To perform the necessary matrix inversion at each time step, a Gaussian elimination technique is used which takes full advantage of the limited bandwidth of the resulting system of algebraic equations.

Physical Properties

From equations (3) and (4) it follows that physical properties of interest for the finite element simulations are:

- volumetric heat capacity of the ground-water C_l;
- volumetric heat capacity, C_s, thermal conductivity, k_t, and permeability k_p of the soil.

A constant value $C_l = 4.18$ MJ/m^{3}K has been used in the calculations for the volumetric heat capacity of the ground-water. Variations with temperature have not been considered because of the vanishing influence of the convective term at below freezing temperatures.

Extensive information on physical properties of the soil used in the laboratory model of the freezing system has been collected before starting the freezing tests.

The soil considered is an average texture "Hokksundsand" sand whose solid fraction is characterized by a 35 percent mass quartz content and by a density of 2700 kg/m^3 [11]. Dry density values for this sand are, approximately, 1600 kg/m^3, corresponding to a 41 percent porosity. Thus, the total mass water content for the saturated sand is of the order of 20 percent. In the experimental runs, care was always taken to ensure conditions of complete saturation.

Table 1 Physical properties of the "Hokksundsand" sand referred to in the finite element simulation.

t(°C)	C_s(MJ/m^{3}K)	k_t(W/mK)	k_p(m^{2}s/Pa)
15.0	2.48	2.0	3.16×10^{-8}
−0.04	2.44	2.0	2.46×10^{-8}
−0.045	1871	2.0	0.
−0.06	1079	2.41	0.
−0.1	262	2.72	0.
−0.3	36.5	2.99	0.
−1.0	5.30	3.15	0.
−5.0	2.00	3.25	0.
−15.0	1.80	3.26	0.
−40.0	1.60	3.27	0.

The volumetric heat capacity of a soil, defined as the derivative of enthalpy with respect to temperature in order to account for latent heat effects, depends on the sensible heat capacity of the individual components-solids, water, ice, and on the contribution of latent heat due to the change in unfrozen water content. The volumetric heat capacity versus temperature curve for the sand used in the experimental section has been determined experimentally in an adiabatic calorimeter, in accordance with the procedure proposed in [12]. This way the unfrozen water content versus temperature curve has also been determined.

The thermal conductivity versus temperature curve has been estimated from the knowledge of soil texture, density of dry sand, degree of saturation, quartz and unfrozen water contents. A detailed description of the semiempirical method used for prediction of thermal conductivity values is reported in [12].

Finally, permeability of the unfrozen sand has been evaluated "in situ" by means of a linear regression procedure, and from measured values of flow rates and corresponding pressure gradients in the test section under steady-state isothermal conditions [11]. Zero permeability values have been assumed at below freezing temperatures and the assumption has been confirmed experimentally, at least for completely frozen soils. Values of physical properties of the "Hokksundsand" sand referred to in the computations are reported in Table 1.

Physical properties related to cryosuction, temperature induced water migration, ice segregation, and frost heave have not been considered and the influence of these phenomena on heat and moisture transport is not taken into account by the mathematical model. On the other hand, the granulometric distribution of the "Hokksundsand" sand, characterized by a 94 percent mass fraction of particles with equivalent diameters larger than 0.2 mm [11], seems to rule out any form of moisture migration not related to hydraulic pressure gradients [8]. This assumption too has been confirmed by visual observation made during the freezing tests.

Experimental Apparatus

The experimental apparatus built for this research is described in detail in [11]. Therefore, only essential information on the test section, represented in Fig. 1, is reported here.

Brine, at suitably chosen flow rates and temperatures, is supplied by a high-capacity refrigeration system to a row of three, 38-mm, outside diameter freeze pipes placed vertically in the test section, with a 450-mm spacing between their axes. The coolant distribution system, the brine temperature versus time curves, the diameter and the relative spacing of the refrigeration pipes are all chosen on the base of the criteria followed in the design of ground freezing plants [2].

Large flow rates of the coolant and heavy thermal insulation at the top and at the bottom of the test section are used in order to ensure two-dimensional temperature fields in correspondence with the horizontal measuring plane. As an additional protection against vertical temperature gradients, an auxiliary fluid can be circulated, at suitable temperatures and flow rates, through the interspace at the bottom of the test section.

Heavy thermal insulation, shown in Fig. 2, is also employed at the sides of the test section in order to reduce lateral heat flow.

Water is supplied to the test section, at a constant pressure, by means of a feeding bottle which can be suspended at different heights. A homogeneous bulk flow through the test soil is ensured by a circulation system made up by perforated feeding and draining pipes, immersed in expanded clay, and by two perforated aluminium plates with a 35 percent net flow area.

Flow rates through the test section are easily evaluated by weighting the amount of water drained during a fixed interval of time.

A total of 23 measuring and 13 control copper-constantan thermocouple locations are accurately selected and, as it can be seen from Fig. 2, much care is taken to allow for a direct comparison of measured and computed temperature values.

During the runs, temperature readings are taken automatically, at predetermined time intervals, by means of a data logger.

Temperatures of the coolant as low as $-40°C$ were reached during the experimental measurements. Flow rates in the freeze-pipes were such that differences between supply and return temperatures of the brine never exceeded 4 K with cooling capacities as high as 500 W/m.

Vertical temperature gradients were always kept lower than 3 K/m, even during the initial stages of the freezing processes. Thus, we believe that the temperature fields realized can be considered two-dimensional within the general limits of accuracy of the proposed model.

Hydraulic pressure gradients, up to 1000 Pa/m, were easily obtained and maintained in the test section, while pressure gradients for building drainage ducts in sands are assumed to be between 60 and 200 Pa/m ([1], p. 86).

Results

The programming system used in the present investigation has been checked against the results of finite element solutions available for the continuity equation (3), and for the energy equation (4), in the case of velocity u, v arbitrarily set equal to zero. The capabilty of the program for dealing correctly with the convection term has also been checked by assuming known, constant, linear, and parabolic velocity profiles, and then comparing the results obtained with available analytical and numerical solutions. Agreement with previous analytical solutions was of the order of 1 percent, while the same results, to the 4th decimal place, were obtained from different finite element programs when the same problems were solved [13, 14].

Finally, comparisons have been made with approximate analytical [1, 4] and finite difference solutions [5] for the artificial freezing problem and agreement, within a few percent, was found in the estimation of the maximum mass flow density at which joining of frozen soil zones around the freezing pipes can still occur [13].

In this paper the results of comparisons with the experimental measurements are presented for the first time.

The artificial freezing problem. Several soil freezing tests in the presence of seepage flow have been carried out, in the experimental apparatus described in the previous section, at various coolant temperatures and for different values of the hydraulic pressure gradient [11]. The large amount of comparison data produced would make a detailed description of all the results obtained very time consuming. Thus only one typical test will be described here.

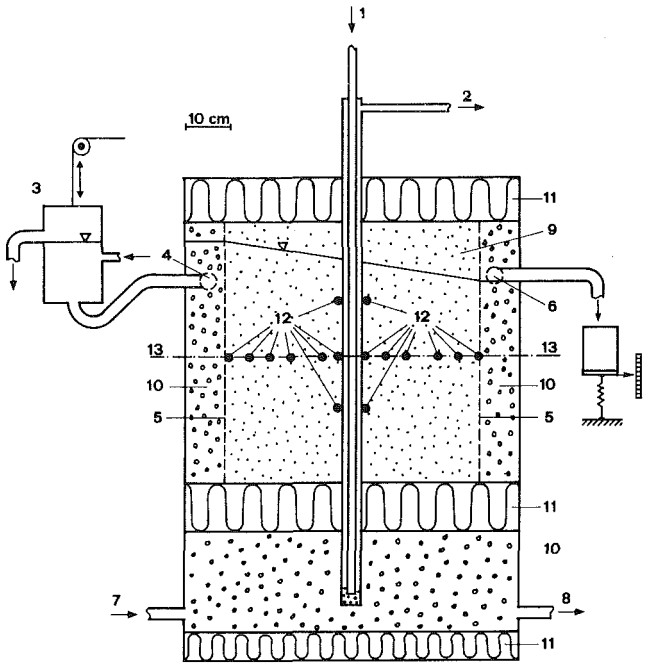

Fig. 1 Experimental test section: (1) brine inlet, (2) brine outlet, (3) constant pressure water feeding system, (4) perforated water feeding tube, (5) perforated aluminium plates, (6) perforated water draining tube, (7), (8) auxiliary brine circulation system for the control of vertical temperature gradients, (9) test soil, (10) expanded clay, (11) extruded polystyrene, (12) indicative locations of copper-constantan thermocouples, (13) measuring plane location

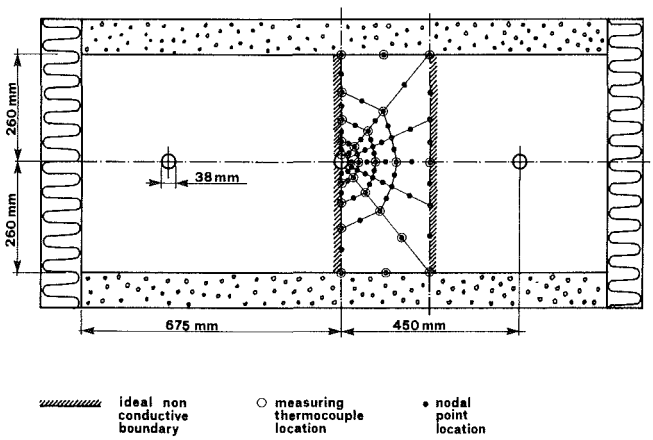

Fig. 2 Cross section of the experimental apparatus, in correspondence with the measuring plane, showing locations of the measuring thermocouples and the mesh used in the finite element simulations

The geometry considered is illustrated in Fig. 2. The amount of geometrical data necessary to define the problem is greatly reduced by the use of eight-nodes, parabolic, isoparametric elements. Thus only 24 element and 93 nodes are employed in the present simulation.

Boundary conditions for the test considered were as follows:

- Boundary conditions of the first kind did exist in correspondence with upstream and downstream external surfaces. A constant pressure difference of 206 Pa was maintained between the upstream and downstream surfaces

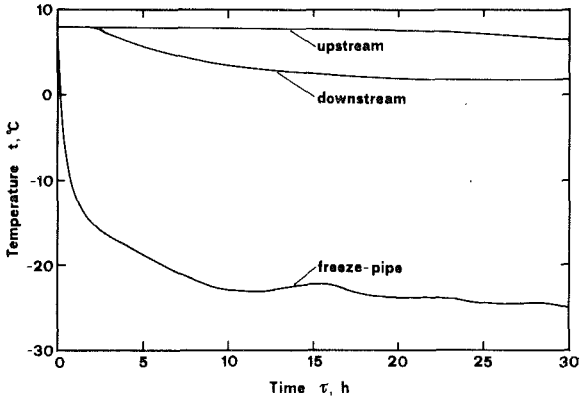

Fig. 3 Temperature boundary conditions of the first kind referred to in the finite element calculations

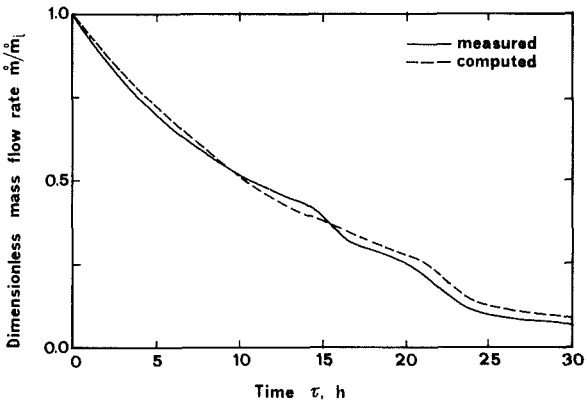

Fig. 4 Measured and computed values of mass flow rates through the test section expressed as a ratio with respect to the initial mass flow rate

during the test considered. Measured values of temperatures in correspondence with the same surfaces were used as time-dependent boundary condition of the first kind in the finite element calculations. These temperature versus time curves are illustrated in Fig. 3.

- Temperature boundary conditions of the first kind did exist in correspondence with the external surface of the freeze-pipe. Again the measured values of temperature, reported in Fig. 3, were used as time-dependent boundary conditions.
- The freeze-pipe represented a nonconductive boundary, as far as pressure boundary conditions were concerned.
- The ideal boundaries, in correspondence with symmetry planes, represented nonconductive boundaries both for the pressure and the temperature field.

Before starting the freezing run, care was taken to saturate the test section with water and uniform initial conditions, with a temperature $t_i = 8°C$, were maintained in the test section.

Computing time for this problem was of the order of 12 s per time step on a UNIVAC 1108 computer and a total number of 50 time steps was required to complete a 30 hr simulation.

Measured and computed values of mass flow rates, are compared in Fig. 4. The sum of "reactions" at nodes on P_1, where pressure values are restrained, is used in the calculation of mass flow rates at step n (see, for example, [15], p. 37). Dimensionless units are used in the comparison since nonlinear regression was utilized in the estimation of permeability values at above freezing temperatures and, therefore, error-free estimates of initial mass flow rates m_i are to be expected.

As it can be seen from Fig. 4, agreement between measured and computed values of mass flow rates is satisfactory. Mass

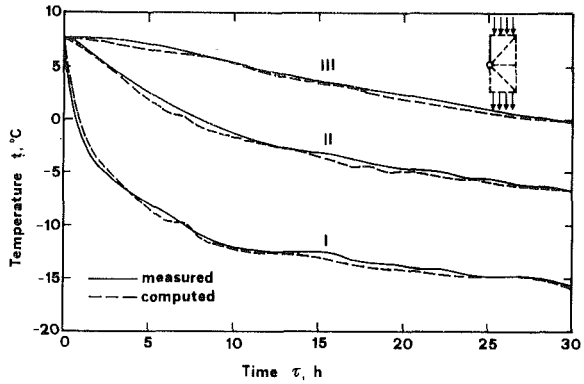

Fig. 5 Measured and computed time-temperature curves along the upstream axis of symmetry in the test section. Distance of reference points from the axis of the freeze-pipe are as follows: I:44.0 mm; II:94.0 mm; III:159 mm.

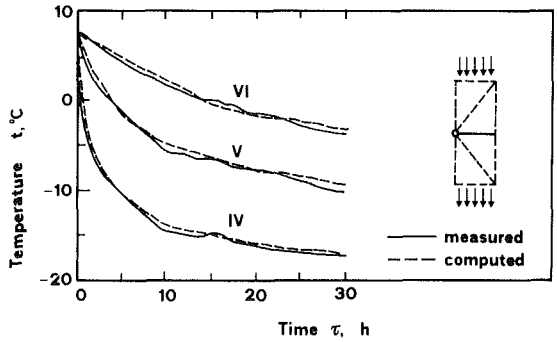

Fig. 6 Measured and computed time-temperature curves along the centerline of the test section. Distance of reference points from the axis of the freeze-pipe are as follows: IV:39 mm, V:80.0 mm, VI:139 mm.

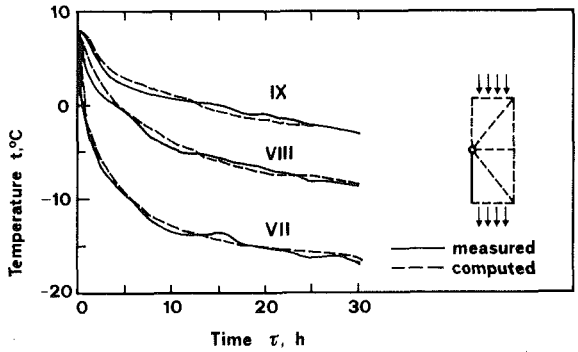

Fig. 7 Measured and computed time-temperature curves along the downstream axis of symmetry in the test section. Distance of reference points from the axis of the freeze-pipe are as follows: VII:44 mm, VIII:94 mm, IX:159 mm.

flow rates tend to be slightly overestimated by the finite element simulation at the end of the freezing process. This effect may be due to a number of reasons, among which errors in the estimation of thermal properties that yield errors in the evaluation of the frozen zone. On the other hand, convective contributions to heat transfer tend to become negligibly small towards the end of the freezing process. Thus no attempt has been made to further improve predictions of mass flow rate versus time curves.

Measured and computed temperatures at various locations are compared in Figs. 5, 6, and 7. As it can be seen, agreement is quite good.

In Fig. 8, locations of the "end of freezing" $-1°C$ isotherms are shown at different values of time. Agreement between measured and calculated locations is quite good with calculations tending to underestimate the extension of the

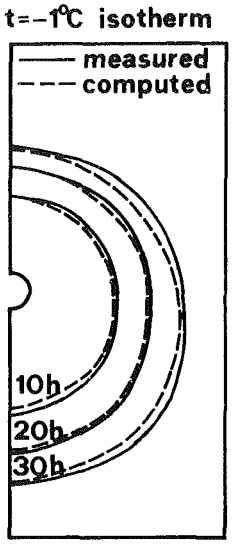

Fig. 8 Measured and computed locations of the "end of freezing" −1°C isotherm at different times

frozen zone. This may be an advantage in practical applications since it leads to a slight overestimation of the time required for the joining of the ice-soil cylinders around a row of freeze-pipes.

Finally, in Figs. 9 and 10, computed velocity and temperature fields are shown at different values of time.

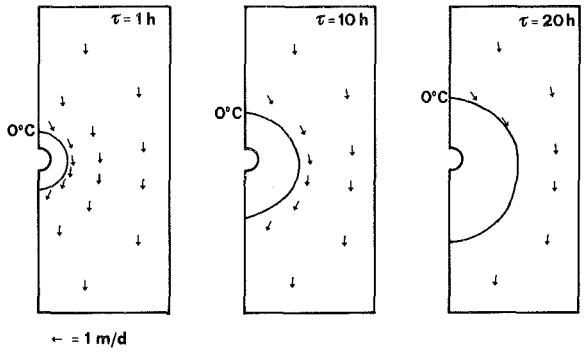

Fig. 9 Computed velocity fields at different times

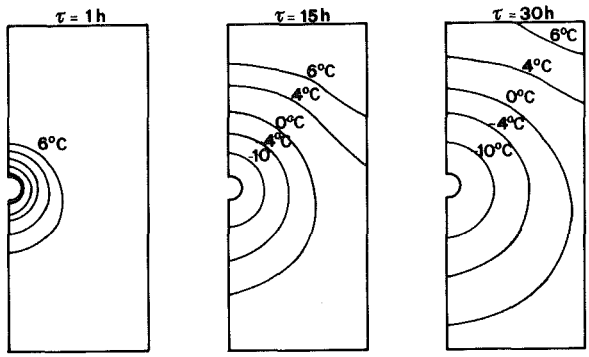

Fig. 10 Computed temperature fields at different times

Conclusions

A system of computer programs, based on the finite element method, has been presented for the calculation of coupled velocity and temperature fields during freezing and thawing of soils in the presence of seepage streams.

A laboratory model of a soil freezing plant has been built in order to check the results of computations against experimental measurements. This way good agreement has been found between computed and measured temperature fields.

Future improvements of the programming system might include consideration of moisture migration in frost susceptible soils under the influence of temperature gradients, in order to compute acceptable amounts of frost heave.

Acknowledgment

A large part of the programming system used in this research was developed by G. Comini, at the Division of Refrigeration Engineering, NTH, Trondheim, under a post-doctorate fellowship from the Royal Norwegian Council for Scientific and Industrial Research.

References

1 Khakimov, K. R., *Artificial Freezing of Soils: Theory and Practice*, Israel Program for Scientific Translations, Jerusalem, Israel, 1966.

2 Jones, J. S., "Engineering Practice in Artificial Ground Freezing: the State of Art," *Proceedings of the 2nd International Symposium on Ground Freezing*, NTH, Trondheim, Norway, 1980, pp. 837–856.

3 ISGF 80, "Engineering Design and Case Histories: Session D," *Proceedings of the 2nd International Symposium on Ground Freezing*, NTH, Trondheim, Norway, 1980.

4 Takashi, T., "Influence of Seepage Stream on the Joining of Frozen Soil Zones in Artificial Soil Freezing," Special Report 103, Highway Research Board, 1969, pp. 273–286.

5 Hashemi, H. T. and Shepcevich, C. M., "Effect of Seepage Stream on Artificial Soil Freezing," *Journal of the Soil Mechanics and Foundation Division*, ASCE, Vol. 99, No. SM3, 1973, pp. 267–289.

6 Jessberger, H. L., "State of the Art Report on Ground Freezing: Mechanical Properties, Processes and Design," *Proceedings of the 2nd International Symposium on Ground Freezing*, NTH, Trondheim, Norway, 1980.

7 Harr, M. E., *Groundwater and Seepage*, McGraw-Hill, New York, N.Y., 1962.

8 Frivik, P. E., et al., "Thermal Design of Pavement Structures in Seasonal Frost Areas," ASME JOURNAL OF HEAT TRANSFER, Vol. 99, 1977, pp. 533–540.

9 Comini, G. and Lewis, R. W., "A Numerical Solution of Two-Dimensional Problems Involving Heat and Mass Transfer," *International Journal of Heat and Mass Transfer*, Vol. 19, 1976, pp. 1387–1392.

10 Comini, G. and Del Giudice, S., "Thermal Aspects of Cryosurgery," ASME JOURNAL OF HEAT TRANSFER, Vol. 98, 1976, pp. 543–549.

11 Berggren, A., *"Artificial Freezing of Seepage Flow* (in Norwegian), B.Sc. thesis, Division of Refrigeration Engineering, NTH, Trondheim, Norway, 1979.

12 Johansen, O. and Frivik, P. E., "Thermal Properties of Soils and Rock Materials," *Proceedings of the 2nd International Symposium on Ground Freezing*, NTH, Trondheim, Norway, 1980.

13 Frivik, P. E. and Thorbergsen, E., "Thermal Design of Artificial Soil Freezing Systems," *Proceedings of the 2nd International Symposium on Ground Freezing*, NTH, Trondheim, Norway, 1980.

14 Comini, G., 1979, unpublished results.

15 Hinton, E. and Owen, D. R. J., *Finite Element Programming*, Academic Press, London, 1977.

C. K. Law
Professor.
Mem. ASME

H. K. Law
Senior Research Engineer.

Department of Mechanical and Nuclear Engineering, Northwestern University, Evanston, Ill. 60201

A Theoretical Study of Ignition in the Laminar Mixing Layer

The structure of the weakly reactive states leading to ignition in the laminar mixing layer flow is studied both analytically and numerically. It is shown that the flow consists of a reactive region and a self-similar frozen region separated by a transitional, nonsimilar frozen region, that the reactive region is intrinsically nonsimilar because of its excessively slow diffusion rate, and that the ignition characteristics are primarily governed by the velocity of the hot stream and therefore minimally dependent on the velocity distribution. Fundamental functional groups are identified, and an explicit prescription is presented, for large activation energy reactions, for the evaluation of the minimum streamwise distance to achieved ignition.

1 Introduction

A classical problem in combustion research is that of Marble and Adamson [1] in which the ignition of a semi-infinite stream of cold combustible by a parallel semi-infinite stream of hot inert is investigated. The problem is of fundamental interest in that it is representative of the broad class of problems involving chemically reacting boundary layer flows, that because of the premixed nature of the reactants, finite-rate chemistry is manifested in an essential way, and that the continuous streamwise variation of the reaction rate renders the flow intrinsically nonsimilar and thereby mathematically challenging.

The problem also commends technological relevance for such practical devices as flame stabilization by bluff bodies and torch ignition of lean mixtures when ignition occurs close to the injection nozzle. The relevant information to be sought in these studies is the minimum distance at which ignition can be achieved as function of such parameters as mixture concentrations, the temperature of the hot inert, and the velocities of the two streams.

Previous theoretical techniques on the study of mixing layer ignition can be classified into three categories, namely, series expansion using the streamwise distance, s, as the small expansion parameter [1], iterative substitution [2] by approximating the reactive and streamwise convection terms with the lower order solutions, and numerical integration [3]. The scopes of these worthwhile studies, however, are sometimes limited either because of the substantial assumptions required to arrive at analytical expressions, or because of the multiparameter nature of the problem, rendering exhaustive numerical investigation difficult.

In the present study, we shall first discuss some interesting features of the flow by an examination of the structure of the governing equations and, also, through complete numerical solutions. In particular the ignition characteristics and the question of nonsimilarity will be discussed. The equations governing the weakly reactive states leading to ignition are then solved numerically. It is further shown that these numerical results can be systematically correlated to yield a final, explicit expression, giving the minimum distance to achieve ignition as a function of all the flow and kinetic parameters of the system. The analogous problem of ignition in the nonpremixed system is treated in Appendix C.

2 Governing Equations

The problem of interest is shown in Fig. 1. Here a fast, hot, inert gas stream with velocity, u_∞, and temperature, T_∞, meets a parallel, slow, cold, combustible gas stream with

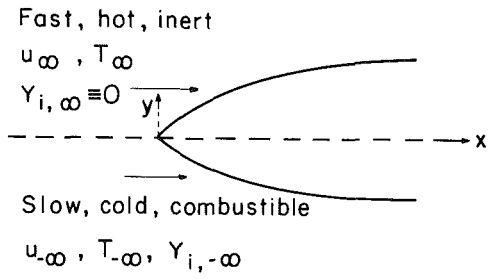

Fig. 1 Schematic of the mixing layer flow

velocity, $u_{-\infty}$, temperature, $T_{-\infty}$, and reactant mass fractions, $Y_{i,-\infty}$ at $x=0$. A mixing layer is subsequently developed through which thermal energy is transferred from the hot to the cold stream while the reactants from the cold to the hot stream. Chemical reaction will be initiated within the mixing layer; its intensity depends on the local temperature and species concentrations. Eventually intense chemical reaction is achieved at a certain location (x_I, y_I), hence initiating the development and propagation of a laminar, premixed flame into the cold combustible. The mixture is said to be ignited. We are interested in the weakly reactive states leading to ignition.

Assuming that the reaction between the fuel F and oxidizer 0 leading to the formation of the product P can be represented by a one-step overall irreversible reaction,

$$\nu_0[0] + \nu_F[F] \rightarrow \nu_P[P] \tag{1}$$

with a reaction rate proportional to

$$c_0{}^{a_0} c_F{}^{a_F} T^{a_T} \exp(-E/R^\circ T) \tag{2}$$

the conservation equations of momentum and energy, with the conventional property assumptions such as unity Lewis number, constant $\rho^2 D$ and specific heats, are respectively described by [4, 5]

$$f''' + ff'' = 0 \tag{3}$$

$$\frac{\partial^2 \tilde{T}}{\partial \eta^2} + f\frac{\partial \tilde{T}}{\partial \eta} - 2sf'\frac{\partial \tilde{T}}{\partial s} = -s\omega \tag{4}$$

where $\omega = (1/2)\, Y_0{}^{a_0} Y_F{}^{a_F} \tilde{T}^n \exp(-\tilde{T}_a/\tilde{T})$, where s and η are the Howarth-Dorodnitsyn variables related to the physical coordinates x,y through

$$s = x\left(\frac{4B\sigma^{a_0}}{u_\infty}\right)\left(\frac{\nu_F W_F}{W_0 a_{0_{W_F}} a_F}\right)\left(\frac{p\bar{W}}{R^\circ}\right)^{(a_0+a_F-1)}\left(\frac{Q}{c_p}\right)^n \tag{5}$$

$$\eta = \left(\frac{u_\infty}{2x\rho_\infty \mu_\infty}\right)^{1/2} \int_0^y \rho(x,y')dy'$$

Contributed by the Heat Transfer Division and presented at the 20th ASME/AIChE National Heat Transfer Conference, Milwaukee, Wisconsin, August 2-5, 1981. Manuscript received by the Heat Transfer Division July 16, 1981. Paper No. 81-HT-20.

where $f(\eta)$ is related to the stream function $\psi(x,y)$ through

$$f(\eta) = \frac{\psi(x,y)}{(2x\rho_\infty \mu_\infty u_\infty)^{1/2}}$$

where a prime designates total differentiation with respect to η, where the species mass fraction $\tilde{Y}_i$ are [4]

$$\tilde{Y}_i = \tilde{T}_\infty + (\tilde{Y}_{i,-\infty} - \beta)\xi - \tilde{T} \tag{6}$$

and where $\lambda = u_{-\infty}/u_\infty$ is the velocity ratio, $\beta = \tilde{T}_\infty - \tilde{T}_{-\infty}$ a heat-transfer parameter, and

$$\xi = \frac{(1-f')}{(1-\lambda)} \tag{7}$$

Equations (3) and (4) are to be solved subject to the boundary conditions

$$f'(-\infty) = \lambda, f(0) = 0, f'(\infty) = 1 \tag{8}$$

$$\tilde{T}(s,-\infty) = \tilde{T}_{-\infty}, \tilde{T}(s,\infty) = \tilde{T}_\infty \tag{9}$$

and a similar initial profile

$$\tilde{T}(0,\eta) = \tilde{T}_\infty - \beta\xi \tag{10}$$

It is important to emphasize that we have assumed that similar velocity and temperature profiles are established immediately upon contact of the streams. This neglects the formation of boundary layers along the splitter plate initially separating the flows. The presence of the splitter plate can significantly change the ignition distance [6], especially if it is heated [7, 8].

The problem is well-defined at this stage. Furthermore, since the momentum equation, equation (3), does not depend on $\tilde{T}$, f can be solved independently for given λ. Thus the primary task here is to seek solution of the energy equation, equation (4). It may also be noted that whereas the velocity profile is similar, the presence of s in the reaction term in equation (4) implies that the effect of reaction is perpetually being manifested in the streamwise direction. Hence the temperature and species profiles, and thereby the ignition characteristics, are intrinsically nonsimilar. The coupling function, $(\tilde{Y}_i + \tilde{T})$, however, remains similar as shown in equation (6).

In the above formulation we have introduced a variable ξ. In later developments it will be found useful to use ξ instead of η as the independent "transverse" variable. Thus in ξ-space, equations (4) and (9) become

$$\left\{\frac{f''}{(1-\lambda)}\right\}^2 \frac{\partial^2 \tilde{T}}{\partial \xi^2} - 2s\{1-(1-\lambda)\xi\}\frac{\partial \tilde{T}}{\partial s} = -s\omega \tag{11}$$

$$\tilde{T}(s,\xi=1) = \tilde{T}_{-\infty}, \tilde{T}(s,\xi=0) = \tilde{T}_\infty \tag{12}$$

The advantages of using ξ are immediately clear. First it eliminates the nonessential transverse convection term so that equation (11) is characterized by the three essential processes representing "transverse" diffusion, streamwise convection, and reaction. Furthermore, in the absence of chemical reaction, $\partial/\partial s \equiv 0$ such that $\tilde{T}$, and therefore $\tilde{Y}_i$, vary linearly in ξ-space. Thus the presence of chemical reactions can be easily identified by observing deviations of $\tilde{T}$ from linearity. Finally, the ξ-space is bounded in the finite domain [0, 1], with the hot boundary located at the origin, $\xi = 0$; these properties facilitate analysis and interpretation, as will be demonstrated subsequently.

3 Qualitative Dynamics

Since chemical reaction, and therefore ignition, are facilitated with increasing temperature and reactant concentration, ignition is favored to occur near the hot boundary because of the high temperature, and near the cold boundary because of the high concentrations. However, except for systems with very large reaction orders which are probably quite unrealistic, chemical reaction varies most sensitively with the Arrhenius factor. Thus it is reasonable to expect that ignition occurs *near* the hot boundary. It cannot occur *at* the hot boundary because of the absence of reactants. It may also be noted that the temperature of the hot stream is less than the adiabatic flame temperature of the combustible. Figure 2 shows the development of the temperature and concentration profiles for a flow with $\tilde{T}_\infty = 5\times10^{-2}$, $\tilde{T}_{-\infty} = 7.5\times10^{-3}$, $\tilde{Y}_{0,-\infty} = \tilde{Y}_{F,-\infty} = 0.1$, $\tilde{T}_a = 1$, $n = 0$, $a_0 = a_F = 1$, and $\lambda = 0$, which correspond to the physical values of $T_\infty = 2\times10^3$ K, $T_{-\infty} = 300$ K, $T_a = 4\times10^4$ K, $c_p = 0.25$ cal/gm-K, and $Q = 10^4$ cal/gm. The solutions were obtained with a second-order-accurate implicit numerical scheme with $-10 \le \eta \le 8$ and $\Delta\eta = 0.05$.

Figure 2 shows that in the absence of reaction ($s = 0$), $\tilde{T}$ decreases monotonically from the hot to the cold boundary. However, with increasing chemical activity as the mixture

Nomenclature

a_i = reaction order
a_T = temperature exponent in equation (2)
$\tilde{a}$ = overall reaction order, $(a_0 + a_F)$
B = frequency factor
c = concentration
c_p = specific heat
E_a = activation energy
f = Blasius function
F = defined in equation (31)
k = defined in equation (24)
m = defined in equation (24)
n = $a_T - a_0 - a_F + 1$
p = pressure
P = concentration parameter set, $(a_0, a_F, \alpha_0, \alpha_F)$
Q = specific heat of combustion
R° = universal gas constant
R = defined in equation (29)
s = streamwise coordinate, defined in equation (5)
T = temperature
T_a = E_a/R°
T_c = $T - T_f$
$\tilde{T}$ = $c_p T/Q$
u = x-velocity
W_i = molecular weight
$\bar{W}$ = average molecular weight
Y_i = mass fraction
$\tilde{Y}_i$ = $(\nu_F W_F/\nu_i W_i)Y_i$
α_i = $\epsilon/\tilde{Y}_{i,-\infty}$
$\tilde{\alpha}$ = $(a_0\alpha_0 + a_F\alpha_F)$
β = $(\tilde{T}_\infty - \tilde{T}_{-\infty})$
$\tilde{\beta}$ = β/ϵ
D = binary diffusion coefficient
ϵ = $\tilde{T}_\infty^2/\tilde{T}_a$
ζ = streamwise coordinate, equation (26)
η = boundary layer transverse variable
θ = perturbed temperature
λ = velocity ratio, $u_{-\infty}/u_\infty$
μ = viscosity coefficient
ν_i = stoichiometric coefficient
ξ = equation (7) and equation (A 20)
$\tilde{\xi}$ = $\tilde{\beta}\xi$
ρ = density
σ = stoichiometric oxidizer to fuel mass ratio
ω = reaction rate

Subscripts

c = unignitable system
f = chemically frozen state
F = fuel
i = index for species
I = ignition state
0 = oxidizer
P = Product
NC = no reactant consumption
RC = with reactant consumption
$\infty, -\infty$ = locations of the freestreams

flows downstream, a temperature bulge eventually develops ($s \simeq 7\times10^{11}$) and propagates toward the cold stream with rapidly increasing intensity. Thus, an adiabaticity ignition criterion and a thermal runaway ignition criterion can be defined, in the following.

The adiabaticity criterion states that at the location (s_I,η_I) there is so much chemical heat release that, rather than receiving heat from the hot boundary, heat is actually being transferred to the hot boundary. Thus chemical reaction has become self-sustaining. This location would then be characterized by the first appearance of the temperature bulge [1] or

$$\left(\frac{\partial \tilde{T}}{\partial \eta}\right)_{s_I,\eta_I} = 0 \tag{13}$$

$$\left(\frac{\partial^2 \tilde{T}}{\partial \eta^2}\right)_{s_I,\eta_I} < 0 \tag{14}$$

The thermal runaway criterion indicates the establishment of a steadily propagating flame. In analogy with the thermal explosion theory, one expects that with increasing s, the maximum temperature, $\tilde{T}_{\max}$, initially increases slowly, then rises rapidly around the ignition region, and finally levels off as a steady flame is established. Thus the flame can be considered to be established, at (s_I^*,η_I^*), when the temperature increase starts to slow down, or

$$\left[\frac{d^2 \tilde{T}_{\max}(s,\eta_I^*)}{ds^2}\right]_{s_I^*} = 0 \tag{15}$$

It is obvious that $s_I^* > s_I$.

In the present study, we shall use the adiabaticity criterion because it is easier to obtain numerically and because the ignition location from the two criteria are quite close anyway. Furthermore, it is also important to recognize that the present boundary layer formulation, which neglects streamwise diffusion, becomes increasingly inadequate with the intensification of the streamwise gradients as (s_I^*,η_I^*) is approached.

Further insight on the structure of the flow field can be gained by comparing the relative magnitudes of the four component processes representing transverse-diffusion, transverse-convection, streamwise-convection, and reaction. The comparison can best be carried out by examining the variations of

$$\tilde{T}_c = \tilde{T} - \tilde{T}_f$$

which is the increase in the local temperature as a result of chemical reaction, where $\tilde{T}_f = \tilde{T}(0,\eta)$ is the temperature profile in the absence of reaction. Hence substituting $\tilde{T}_c$ into equation (4) yields

$$\frac{\partial^2 \tilde{T}_c}{\partial \eta^2} + f\frac{\partial \tilde{T}_c}{\partial \eta} - 2sf'\frac{\partial \tilde{T}_c}{\partial s} = -s\omega \tag{16}$$

The various terms in equation (16) are plotted in Fig. 3 for $s = 2\times10^{11}$ for the same case studied in Fig. 2. Since the temperature bulge is not developed until $s \simeq 6\times10^{11}$, the present location can be considered to be quite weakly reactive.

Figure 3 shows that there exist three types of flow regions, namely (*a*) A reaction region in which chemical reaction and rapid variations of $\tilde{T}_c$ take place; (*b*) *Frozen, self-similar* regions as $\eta \to \pm\infty$, in which convection and diffusion balance in the transverse direction; and (*c*) Transitional, *frozen, nonsimilar* regions separating the reaction and self-similar regions. In these transitional regions, transverse-diffusion and convection, and streamwise-convection, are all important. The fact that self-similarity does not exist here, even though chemical reaction is negligible, is because of the streamwise variation at their boundaries with the nonsimilar reaction region.

Figure 3 also demonstrates the interesting result that in the

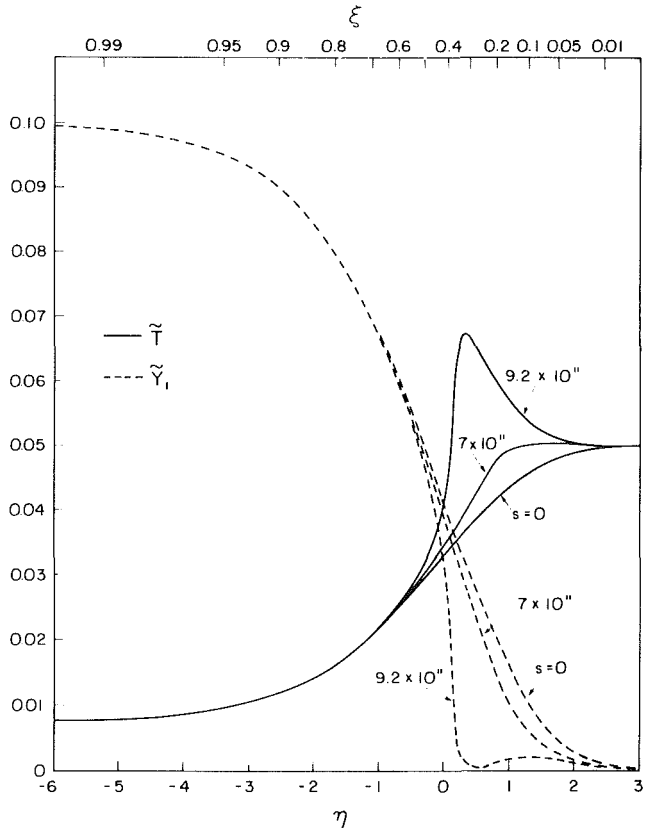

Fig. 2 Development of the temperature and species concentration profiles as mixing progresses

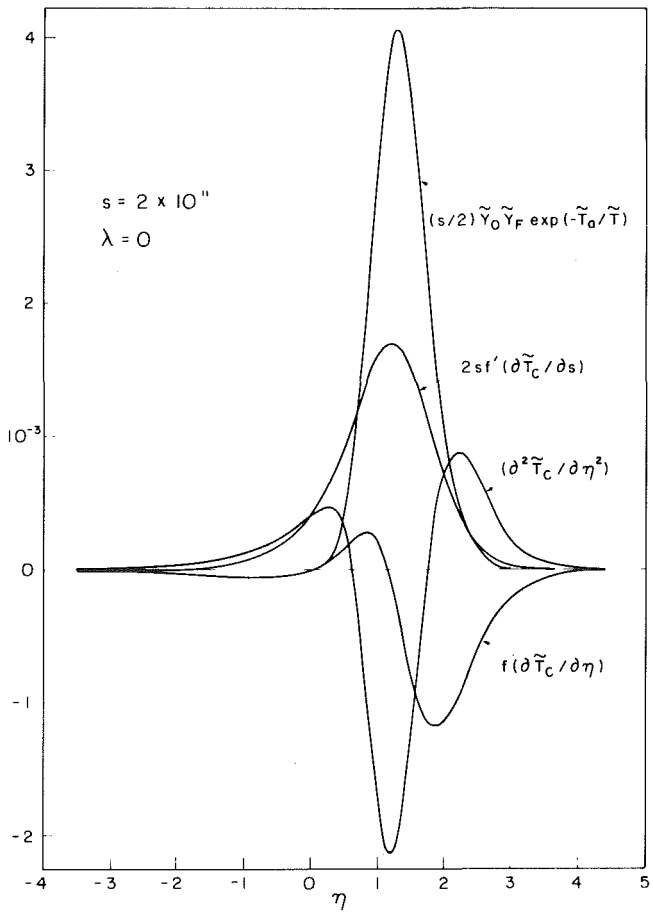

Fig. 3 Comparison of the magnitudes of terms representing transverse-diffusion, transverse-convection, streamwise-convection, and reaction, for a representative weakly-reactive state

reaction region the streamwise-convection term is of the same order of magnitude as other terms. This is contrary to the findings from other ignition studies—say the ignition of a cold combustible by a hot flat plate [5]—in which it is shown that because of the steep variations within the reaction region, the convective terms are at least one order smaller than the diffusive and reactive terms. This results in significant mathematical simplification, in that by neglecting the streamwise-convective term, or in other words by making the local-similarity assumption, the governing equation becomes an ordinary differential equation whose solution is much simpler. Streamwise variation is then manifested parametrically, through the presence of s in the reactive term, rather than differentially.

Such a simplification, however, does not exist for the present mixing-layer flow. The difference here is the excessively long characteristic diffusion length in the reaction region which is close to the hot boundary located at $\eta=\infty$. This point can be further demonstrated by examining equation (11) in the reaction region, as $\xi\to 0$. In Appendix A it is shown that as $\xi\to 0$,

$$\frac{f''}{(1-\lambda)} \sim \xi \tag{17}$$

Substituting equation (17) into equation (11), we have

$$\xi^2 \frac{\partial^2 \tilde{T}}{\partial \xi^2} - 2s\{1-(1-\lambda)\xi\}\frac{\partial \tilde{T}}{\partial s} = -s\omega \tag{18}$$

Equation (18) demonstrates clearly that even though the second-order gradient, $\partial^2 \tilde{T}/\partial \xi^2$, may assume large values in the narrow reaction region (in ξ-space), it is balanced by the excessively small coefficient, ξ^2, such that $\xi^2 \partial^2 \tilde{T}/\partial \xi^2$ is of the same order as the convective and reactive terms in equation (18). Thus the flow in the reaction region is intrinsically nonsimilar. Streamwise diffusion, however, is still negligible based on boundary-layer considerations, until the ignition point is approached.

Equation (18) can be further simplified by noting that in the reaction region $(1-\lambda)\xi << 1$; thus it becomes

$$\xi^2 \frac{\partial^2 \tilde{T}}{\partial \xi^2} - 2s\frac{\partial \tilde{T}}{\partial s} = -s\omega \tag{19}$$

Equation (19) does not exhibit any explicit dependence on λ. Furthermore, since the external, nonreactive, self-similar region is governed by $d^2\tilde{T}/d\xi^2 = 0$ in which λ is also absent, therefore the ignition characteristics are not expected to depend too sensitively on λ. Since $s \sim u_\infty^{-1}$, we have therefore arrived at the interesting conclusion that ignition primarily depends on u_∞, but not on $u_{-\infty}$. This is physically reasonable because ignition occurs close to the hot boundary which moves with u_∞. This result was first observed by Marble and Adamson [1], although the present demonstration is somewhat clearer and simpler.

The analogous problem when the hot inert stream has the slower velocity is treated in Appendix B, in which it is shown that ignition primarily depends on $u_{-\infty}$, except when $u_{-\infty}=0$. Then ignition again depends on u_∞.

4 Determination of Ignition Distance

In the present section we aim to obtain an explicit description of the ignition distance, x_I, which will be useful for quantitative estimation and also assessment of the functional dependence of x_I on the various parameters of the flow. Since it is obviously difficult to obtain an analytical solution for either equation (4) or equation (11), because the problem is intrinsically nonsimilar, the solution will be sought numerically. It is, however, also recognized that the usefulness of a numerical solution is frequently quite limited in that the solution is generally problem-specific and depends on the values of the system parameters used. This is particularly true for the present flow in which even the nondimensional ignition distance s_I is a function of eight parameters, namely λ, $\tilde{T}_{-\infty}$, $\tilde{T}_\infty$, $\tilde{T}_a$, $\tilde{Y}_{0,-\infty}$, $\tilde{Y}_{F,-\infty}$, a_0 and a_F, if we assume $n=0$ without loss of generality. Thus our first task is to further reduce the number of system parameters through systematic grouping.

First, from our previous discussions, the ignition characteristics are minimally dependent on λ. Thus all the subsequent numerical results were obtained with $\lambda=0$, with the understanding that they are approximately applicable to all λ's.

Next we note that for the weakly reactive states leading to ignition, the temperature is expected to be perturbed from its frozen value by a small amount. Hence we can write

$$\tilde{T} = \tilde{T}_f + \epsilon\theta(s,\eta) \tag{20}$$

where $\epsilon = \tilde{T}_\infty^2/\tilde{T}_a$ is the appropriate small parameter of expansion for reactions with large activation energies. Using equation (10), equation (20) can be written as

$$\tilde{T} = \tilde{T}_\infty + \epsilon(\theta - \tilde{\beta}\xi) \tag{21}$$

where $\tilde{\beta} = \beta/\epsilon$. Substituting equation (21) into equation (4), using equation (6), and expanding, we have

$$\frac{\partial^2\theta}{\partial\eta^2} + f\frac{\partial\theta}{\partial\eta} - 2sf'\frac{\partial\theta}{\partial s} = -\left\{\left(\frac{s}{2\epsilon}\right)\tilde{Y}_{0,-\infty}^{a_0}\tilde{Y}_{F,-\infty}^{a_F}\exp(-\tilde{T}_a/\tilde{T}_\infty)\right\}\times \{(\xi-\alpha_0\theta)^{a_0}(\xi-\alpha_F\theta)^{a_F}\exp(\theta-\tilde{\beta}\xi)\} \tag{22}$$

with the boundary and initial conditions

$$\theta(s,-\infty) = \theta(s,\infty) = \theta(0,\eta) = 0 \tag{23}$$

where $\alpha_i = \epsilon/\tilde{Y}_{i,-\infty}$.

Equation (22) shows that chemical reaction is important only for $\xi \le 0(\tilde{\beta}^{-1})$. Since $\tilde{\beta} >> 1$, therefore $\xi << 1$ as expected. It may also be noted that although we have assumed $\xi << 1$ in expanding the exponential term whereas our numerical solution will be sought over the entire ξ-domain, the accuracy of expansion for $\xi = 0(1)$ is unimportant because the reaction term is exponentially small there anyway.

The problem has now been reduced to that of five parameters, namely $\tilde{\beta}$, α_0, α_F, a_0 and a_F; the first bracketed term on the RHS of equation (22) is a constant and is proportional to the ignition distance. Equation (22) is the final form of the governing equation whose numerical solution will be presented in the following. Before doing so, however, we shall identify some further approximate groupings of the above five parameters in order to facilitate correlation of the numerical results.

Since the reaction region is expected to be very narrow in ξ-space, occurring close to $\xi=0$, we first define a stretched variable $\tilde{\xi} = \tilde{\beta}\xi$ such that $\tilde{\xi} = 0(1)$. Next, we note from Fig. 9 in the Appendix that for small ξ we can write

$$\frac{f''}{(1-\lambda)} = k\xi^m \tag{24}$$

in which $m \simeq 1$ and $m \to 1$ as $\xi \to 0$. Equation (24) takes into account of the approximate range in ξ within which ignition occurs and therefore provides a more refined correlation than equation (17).

Thus by expressing equation (22) in $\tilde{\xi}$-space, using equation (24), we obtain

$$k^2\tilde{\xi}^{2m}\frac{\partial^2\theta}{\partial\tilde{\xi}^2} - \frac{2\zeta}{\tilde{\beta}^{2(1-m)}}\left[1-(1-\lambda)\frac{\tilde{\xi}}{\tilde{\beta}}\right]\frac{\partial\theta}{\partial\zeta} = -\zeta\tilde{\xi}^{\tilde{a}}(1-\alpha_0\tilde{\beta}\theta/\tilde{\xi})^{a_0}(1-\alpha_F\tilde{\beta}\theta/\tilde{\xi})^{a_F}\exp(\theta-\tilde{\xi}) \tag{25}$$

where

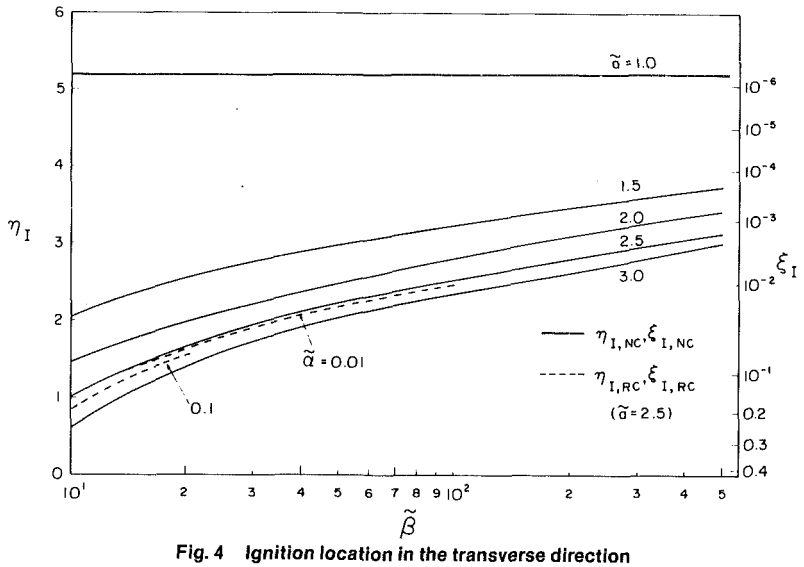

Fig. 4 Ignition location in the transverse direction

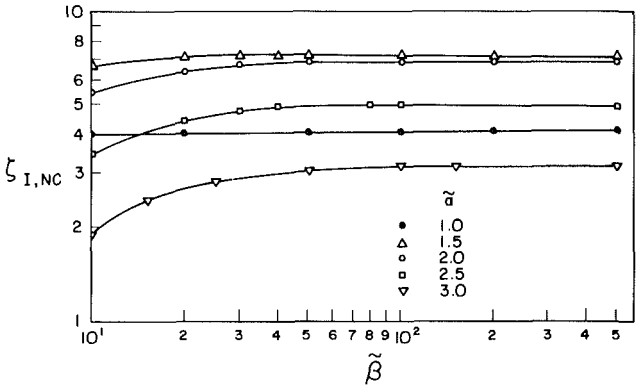

Fig. 5 Streamwise ignition location without reactant consumption

$$\zeta = \frac{s Y_{0,-\infty}^{a_0} Y_{F,-\infty}^{a_F} \exp(-T_u/T_\infty)}{2\epsilon\, \tilde{\beta}^{\tilde{a}+2(1-m)}} \tag{26}$$

and $\tilde{a} = a_0 + a_F$ is the overall reaction order. Equation (25) shows that when the nondimensional ignition distance is expressed in terms of ζ instead of s, the explicit dependence of the problem on $\tilde{\beta}$ is minimal. This is because $\tilde{\beta}^{2(1-m)} \simeq 1$, $\tilde{\xi}/\tilde{\beta} << 1$, and $\alpha_i \tilde{\beta}$ can be grouped as a new parameter. It is also of interest to note that, by comparing the diffusive and reactive terms in equation (25), we expect the system will behave somewhat differently for $\tilde{a} \gtrless 2m \simeq 2$, that is, for the overall reaction order being greater or smaller than two.

Finally, we expect that for ignition to be reasonably efficient, the reactant concentrations cannot be too low, implying that in the reaction term $\alpha_i \tilde{\beta}\theta/\tilde{\xi} << 1$. Thus the concentration term can be approximated as

$$(1 - \alpha_0 \tilde{\beta}\theta/\tilde{\xi})^{a_0}(1 - \alpha_F \tilde{\beta}\theta/\tilde{\xi})^{a_F} \simeq 1 - \tilde{\alpha}\tilde{\beta}\theta/\tilde{\xi} \tag{27}$$

where $\tilde{\alpha} = a_0\alpha_0 + a_F\alpha_F$ can be called a reactant consumption factor.

Combining the above discussions, we can expect that the ignition distance ζ_I primarily depends on only two parameters, namely $\tilde{a}$ and $\tilde{\alpha}\tilde{\beta}$. In the limit of $\epsilon \to 0$, or $\alpha_i \to 0$, the amount of reactant depletion prior to ignition is negligible and ignition is then just governed by $\tilde{a}$.

Thus the methodology of the solution is as follows. Equation (22) is first solved by assuming there is no reactant consumption, viz. $\alpha_i = 0$. From this the ignition distance with no consumption, $\zeta_{I,NC}$, can be determined as functions of $\tilde{a}$ and to a weaker extent $\tilde{\beta}$. Then reactant consumption is allowed and the ignition distance, $\zeta_{I,RC}$, is determined for $\tilde{\beta}$ and also the set of parameters representing concentration effects, $P = (a_0, a_F, \alpha_0, \alpha_F)$. Subsequently $\zeta_{I,RC}$ is systematically correlated with $\zeta_{I,NC}$, $\tilde{\alpha}$ and $\tilde{\beta}$.

It may also be noted that whereas much of our previous discussion have been conveniently carried out in ξ-space, we have found it necessary to carry out the numerical computations in the original η-space. This is because ignition generally occurs for $\eta > 1$ and therefore excessively small ξ. Consequently, with the adoption of equal grid size for numerical integration, the flow structure can be adequately resolved in η-space but not in ξ-space. On the other hand it can also be anticipated that analytical solutions should best be sought in ξ-space because the reactive region is now properly confined to a thin layer at the origin.

In Fig. 4, η_I and the corresponding ξ_I are plotted versus $\tilde{\beta}$ for values of $\tilde{a}$ of practical interest. It is seen that η_I increases with increasing $\tilde{\beta}$, decreasing $\tilde{a}$, and decreasing $\tilde{\alpha}$, as would be expected. This is because increasing $\tilde{\beta}$ implies increasing temperature of the hot stream whereas decreasing $\tilde{a}$ and $\tilde{\alpha}$ both imply reduced concentration dependence; all these cause ignition to take place closer to the hot boundary.

It is also seen that in general ξ_I is a small number. In particular for $\tilde{a} = 1$, the concentration dependence is extremely weak such that ξ_I assumes a very small, almost constant value of about 10^{-6}. This behavior is also evident from equation (22) which shows that for $\xi << 1$ the sensitive Arrhenius factor, which largely determines the reaction intensity, becomes approximately $\exp(\theta)$ and therefore does not depend on $\tilde{\beta}$.

Finally, Fig. 4 shows that η_I is not affected much with substantial reactant consumption, even if the ignition distance ζ_I is significantly lengthened, as will be shown later.

In Fig. 5, we show the ignition distance without reactant consumption, $\zeta_{I,NC}$, as function of $\tilde{\beta}$ and $\tilde{a}$. In the discussions leading to equation (25), it is clear that by using the proper m as defined in equation (24), $\zeta_{I,NC}$ can be made to be very insensitive to $\tilde{\beta}$ for large values of $\tilde{\beta}$. The values of m can be easily assessed from the solution of the stream function (Fig. 9) and also from knowing the approximate range of ξ_I over which ignition takes place. It is thus found that $m \simeq 0.96$ for $\tilde{a} = 1$, and $m = 0.91$ for $\tilde{a} = 1.5$, 2.0, 2.5, and 3.0. These values of m are close to unity as should be (Appendix A), and provide fine adjustments for the correlation. Using these m, Fig. 5 demonstrates the near-independence of $\zeta_{I,NC}$ on $\tilde{\beta}$ for large $\tilde{\beta}$.

Figure 5 also shows that with decreasing $\tilde{a}$, $\zeta_{I,NC}$ first increases, then decreases. The slowdown starts around $\tilde{a}=2$, which is anticipated from our previous discussions on the significance of $\tilde{a} \gtrsim 2m$. The $\tilde{\beta}$-independent ignition distance $s_{I,NC}$, however, monotonically increases with increasing $\tilde{a}$ as should be.

Since it is obviously difficult to obtain a general correlation for $\zeta_{I,NC}$, we shall simply treat Fig. 5 as the graphical solution of $\zeta_{I,NC}$. For $\tilde{a}=2.0$, 2.5, and 3.0, it is found that the asymptotic values of $\zeta_{I,NC}$, for large $\tilde{\beta}$ approximately follow a linear relation

$$\zeta_{I,NC} = 14.1 - 3.65\tilde{a} \tag{28}$$

Finally, in our previous discussions it is anticipated that the ignition aspects of the problem are primarily governed by the velocity of the hot stream and therefore minimally dependent on λ. In Fig. 6, $\zeta_{I,NC}$ is plotted versus $\tilde{\beta}$, with $\tilde{a}=2$, for $\lambda=0$, 0.5, and 0.99, which (almost) cover the complete range of λ possible. It is seen that whereas increasing λ delays the occurrence of ignition, the variations are very small and are almost negligible for large values of $\tilde{\beta}$. Variations of $\eta_{I,NC}$ with λ are also very small.

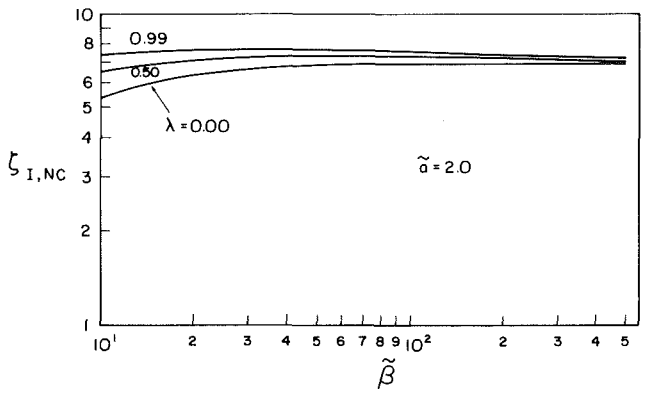

Fig. 6 Effect of the velocity of the cold stream on the streamwise ignition location

To investigate effects of reactant consumption, and recognizing that chemical reactivity now differs from the case with no consumption by the approximate factor shown in equation (27), an ignition distance correction factor

$$R = 1 - \zeta_{I,NC}/\zeta_{I,RC} \tag{29}$$

is defined and is plotted versus $\tilde{\beta}$ for some representative cases in Fig. 7. It is found that for the diverse values investigated for the concentration parameter set P, R only depends on $\tilde{a}$ and $\tilde{\alpha}$, in accordance with our previous discussions. Figure 7 also shows that R varies with $\tilde{\beta}$ in a power-law fashion,

$$R \sim \tilde{\beta}^{1.07} \tag{30}$$

regardless of $\tilde{a}$ and $\tilde{\alpha}$. This behavior has also been found to exist with ignition along a flat plate allowing for reactant consumption [9].

Figure 7 illustrates the importance of allowing for reactant consumption in estimating ζ_I. Neglecting this process will result in, say, an underestimate by a factor of two for $\tilde{\alpha}$ as low as 0.05, with $\tilde{a}=2$ and $\tilde{\beta}=24$. Furthermore, since R increases with increasing $\tilde{\beta}$, attempts to facilitate ignition by increasing the temperature of the hot stream will at the same time aggravate the effect of reactant consumption.

Anticipating from equation (27) that $\tilde{\alpha}\tilde{\beta}$ appears as a group, R can be fitted according to

$$R = F(\tilde{\alpha};\tilde{a})\beta^{\gamma} \tag{31}$$

where $\gamma = 1.07$ as just determined. Figure 8 shows that $F(\tilde{\alpha};\tilde{a})$ indeed varies linearly with $\tilde{\alpha}$. Furthermore, it is also found that the slopes of the straight lines in Fig. 8 are approximately linear functions of $\tilde{a}$. Thus $F(\tilde{\alpha};\tilde{a})$ can be simply expressed, to within ± 4 percent, as

$$F(\tilde{\alpha};\tilde{a}) = 0.1(4.9 - \tilde{a})\tilde{\alpha} \tag{32}$$

for $1 \le \tilde{a} \le 3$ and $\tilde{\alpha} \le 0.1$.

Combining equations (29-32), we finally obtain an ex-

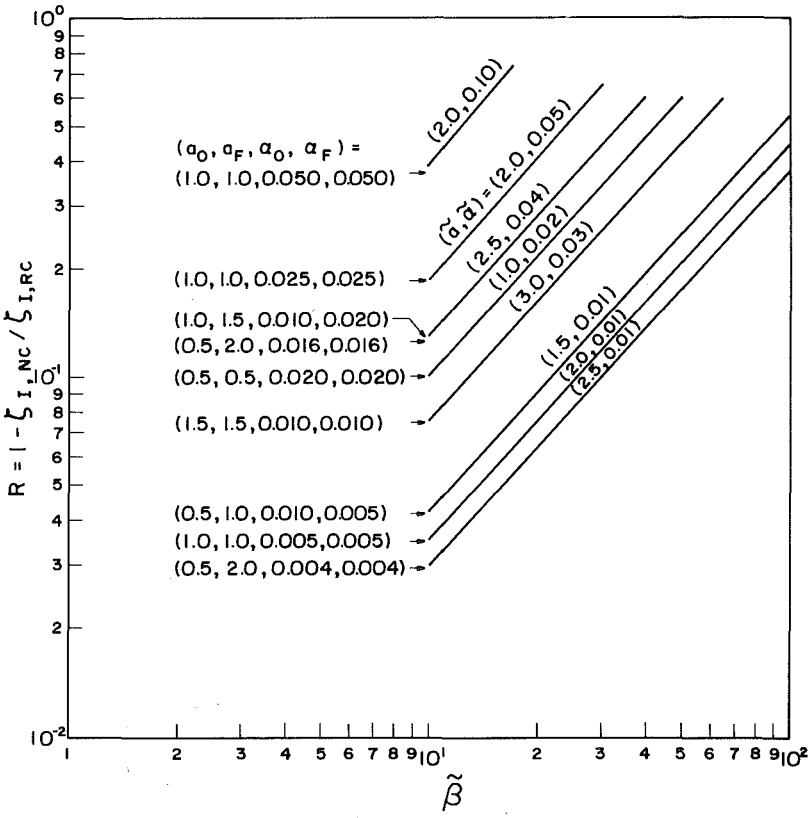

Fig. 7 Correction factor to account for reactant consumption

pression for the ignition distance allowing for reactant consumption

$$\zeta_{I,RC} = \zeta_{I,NC}/[1 - 0.1(4.9 - \tilde{a})\tilde{\alpha}\tilde{\beta}^{1.07}] \tag{33}$$

with $\zeta_{I,NC}$ given by Fig. 5 or equation (28).

It may be noted here that because of numerical difficulties we were not able to trace R to $R \to 1$. However, if we can extrapolate the linear behavior shown in Fig. 7 to $R \to 1$, then equation (33) shows that there exists a lower limit in the concentration,

$$\tilde{\alpha}_c = [0.1(4.9 - \tilde{a})\tilde{\beta}_c^{1.07}]^{-1} \tag{34}$$

for which $\zeta_{I,RC} \to \infty$; that is, ignition is not possible. Physically it may be anticipated that since the chemical heat release needed to initiate ignition is produced at the expense of the reactant concentrations, for mixtures with very low concentrations the depletion can be so severe that ignition can be significantly prolonged, if not entirely inhibited.

It is also of interest to note that if we assume a unity power for $\tilde{\beta}$ in equation (34), then equation (34) can be expressed as

$$\left(\frac{a_0}{Y_{0,-\infty,c}} + \frac{a_F}{Y_{F,-\infty,c}}\right) = \frac{10}{(4.9 - a)\beta_c} \tag{35}$$

which does not depend on ϵ.

Finally, using equations (5) and (26), the ignition distance in the physical coordinate x is

$$x_{I,RC} = \left(\frac{u_\infty}{2}\right)\left(\frac{W_0^{a_0} W_F^{a_F}}{\nu_F W_F \sigma^{a_0}}\right)\left(\frac{R^0}{p\bar{W}}\right)^{(\bar{a}-1)}\left(\frac{c_p}{Q}\right)^n$$

$$\times \left\{\frac{\epsilon\beta^{\bar{a}+2(1-m)}\exp(\tilde{T}_a/\tilde{T}_\infty)}{B\tilde{Y}_{0,-\infty}^{a_0}\tilde{Y}_{F,-\infty}^{a_F}}\right\}\zeta_{I,RC} \tag{36}$$

with $\zeta_{I,RC}$ given by equation (33).

5 Concluding Remarks

While the general purpose of the present study is to understand the structure of mixing layer ignition, we also tried to achieve two specific goals which are essential for a numerical study of the present nature. That is we would like to identify special features of the flow useful for further analytical studies, and also to obtain some concrete results for quantitative applications.

For the first goal we have shown that for $\tilde{\beta} \to \infty$, or $\epsilon \to 0$, the ignition characteristics are essentially governed by only two parameters, namely, the overall reaction order $\tilde{a} = a_0 + a_F$ and $\tilde{\alpha}\tilde{\beta} = (a_0 \tilde{Y}_{0,-\infty}^{-1} + a_F \tilde{Y}_{F,-\infty}^{-1})\beta$. The approximation introduced in equation (27) to take into account of reactant consumption with arbitrary reaction orders can be quite useful, especially for only moderate amount of consumption. The identification that ignition is only minimally dependent on the velocity of the cold stream is interesting and allows us to use the simplest velocity distribution, for example the isovelocity case with $f(\eta) = \eta$, to carry out the analytical work. In fact, our discussions of the structure of the governing equation in ξ-space show that the ignition location can be approximately determined without even using any $f(\eta)$-related functions; that is, the solution of the Blasius equation is not necessary. Thus there is definite advantage in working in ξ- rather than η-space for analysis.

Despite the above simplifications, the present study also shows that the reactive region is intrinsically nonsimilar in that streamwise-convection is of the same order as transverse-diffusion. This inadmissibility to make the local similarity assumption probably poses the greatest analytical difficulty because partial, rather than ordinary, differential equations have to be solved.

For the second goal we have obtained an explicit relation for the minimum ignition distance and through it the proper functional dependence of the various system parameters. In particular it is shown that the ignition distance increases linearly with u_∞, varies in an Arrhenius manner with T_∞, and can also be significantly lengthened for lean mixtures when reactant consumption is allowed. The functional form of equation (36) for $x_{I,RC}$ also permits simple experimental comparison.

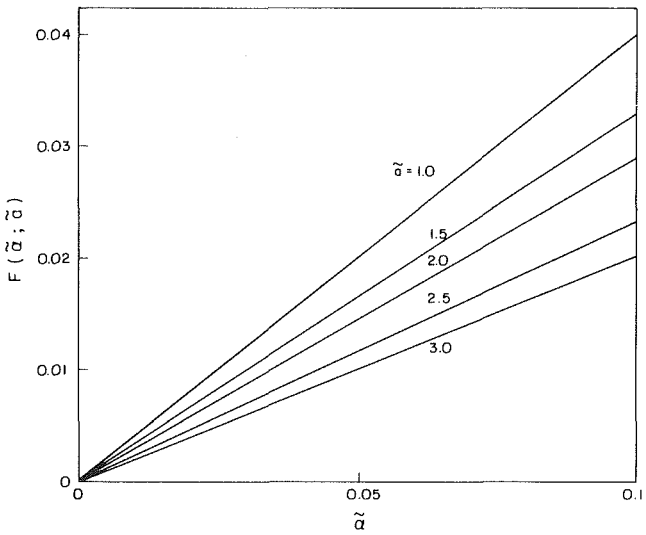

Fig. 8 Variations of F with $\tilde{\alpha}$ and $\tilde{a}$

Acknowledgment

C. K. and H. K. Law were respectively supported by the Division of Basic Energy Science, Department of Energy under Contract No. DE-AC02-77ER-04433 and by the Heat Transfer Program of the National Science Foundation under Grant CME-7820013.

References

1 Marble, F. E. and Adamson, T. C., "Ignition and Combustion in a Laminar Mixing Zone," *Jet Propulsion*, Vol. 24, 1954, pp. 85-94.

2 Dooley, D. A., "Ignition in the Laminar Boundary Layer of a Heated Plate," *Heat Transfer Fluid Mech. Inst.*, Stanford Univ., 1957, pp. 321-342.

3 Sharma, O. P. and Sirignano, W. A., "On the Ignition of a Pre-Mixed Fuel by a Hot Projectile," *Combust. Sci. Tech.*, Vol. 1, 1970, pp. 481-494.

4 Williams, F. A., *Combustion Theory*, Addison-Wesley, ch. 1, 1965.

5 Law, C. K. and Law, H. K., "Thermal Ignition Analysis in Boundary Layer Flows," *Journal of Fluid Mechanics*, Vol. 92, 1979, pp. 97-108.

6 Cheng, S. I. and Kovitz, A. A., "Ignition in the Laminar Wake of a Flat Plate," *Sixth Symposium (International) on Combustion*, The Combustion Institute, Pittsburgh, Pa., 1957, pp. 418-427.

7 Chen, L.-D. and Faeth, G. M., "Ignition of a Combustible Gas near Heated Vertical Surfaces," *Combust. Flame*, Vol. 42, 1981, pp. 77-92.

8 Chen, L.-D. and Faeth, G. M., "Ignition of Gases during Flow near a Heated Surface," *First International Specialist Meeting of the Combustion Institute*, Bordeaux (France), July 20-25, 1981.

9 Law, C. K. and Law, H. K., "Flat-Plate Ignition with Reactant Consumption," *Combust. Sci. Tech.*, Vol. 25, 1981, pp. 1-8.

10 Lock, R. C., "The Velocity Distribution in the Laminar Boundary Layer Between Parallel Streams," *Quart. J. Mech. and Applied Math.*, Vol. IV, 1951, pp. 42-57.

APPENDIX A

Asymptotic Solution of $f(\eta)$

We aim to obtain the asymptotic behavior of $f''/(1-\lambda)$ as $\eta \to \pm\infty$ for the Blasius equation

$$f''' + ff'' = 0 \tag{A1}$$

with

$$f'(\infty) = 1, f'(-\infty) = \lambda \tag{A2}$$

The methodology follows and extends that of Lock [10].

First we study the limit of $\eta \to \infty$. Integrating $f'(\infty) = 1$, we obtain

$$f \sim \eta + C_\infty \tag{A3}$$

where C_∞ is a constant. Substituting equation (A3) into equation (A1), integrating, and noting that $f''(\infty) = 0$, we have

$$f'' \sim D_\infty e^{-z^2} \tag{A4}$$

where $z = (\eta + C_\infty)/\sqrt{2}$ and D_∞ is another constant.

Integrating equation (A4) yields

$$f' \sim 1 - \sqrt{2} D_\infty \operatorname{erf}(z) \tag{A5}$$

with $$\operatorname{erf}(z) = \int_z^\infty e^{-t^2} dt \tag{A6}$$

But $$\operatorname{erf}(z) \sim \frac{e^{-z^2}}{2z} \text{ as } z \to \infty \tag{A7}$$

therefore $$f' \sim 1 - \frac{D_\infty}{\sqrt{2}} \frac{e^{-z^2}}{z} \tag{A8}$$

Combining equations (A4) and (A8), we have

$$\frac{f''}{(1-\lambda)} \frac{(1-\lambda)}{(1-f')} \sim \sqrt{2} z \sim f \tag{A9}$$

Hence if we define

$$\xi = \frac{1 - f'}{(1-\lambda)} \tag{A10}$$

then

$$\frac{f''}{(1-\lambda)} \sim f\xi \tag{A11}$$

A direct evaluation of equation (A11) for $\eta \to \infty$ yields an indeterminant form for $f\xi$. Hence using L'Hospital's Rule we have

$$\left[\frac{f''}{(1-\lambda)}\right]_{\eta\to\infty} \sim \left[\frac{f}{\xi^{-1}}\right]_{\eta\to\infty} \sim \frac{f'(\infty)}{[-\xi^{-2} d\xi/d\eta]_{\eta\to\infty}}$$

$$\sim \frac{f'(\infty)}{(-\xi^{-2})_{\xi\to 0}[-f''/(1-\lambda)]_{\eta\to\infty}} \tag{A12}$$

Rearranging equation (A12), and using $f'(\infty) \sim 1$, we finally obtain

$$\left[\frac{f''(\eta)}{(1-\lambda)}\right]_{\eta\to\infty} \sim (\xi)_{\xi\to 0} \tag{A13}$$

Equation (A13) can be alternately expressed as

$$[f''(\eta) + f'(\eta)]_{\eta\to\infty} \sim 1$$

In Fig. 9, the numerical solution of the complete equation, equations (3) and (8), are plotted. It is seen that for $\xi << 1$ equation (A13) indeed approximately holds in that $f''/(1-\lambda)$ depends only weakly on λ and varies nearly linearly with ξ.

In the limit $\eta \to -\infty$, we follow the same procedure except the expansion has to be kept to a higher order to allow for the case of $\lambda = 0$. Hence integrating $f'(-\infty) = \lambda$, we have

$$f \sim \lambda\eta + C_{-\infty} \tag{A14}$$

from which and the Blasius equation, we obtain

$$f'' \sim D_{-\infty} e^{-z^2} \tag{A15}$$

where $z = -(\lambda\eta + C_{-\infty})/(2\lambda)^{1/2}$. Integrating equation (A15) twice results

$$f' \sim \lambda + \frac{D_{-\infty}}{(2\lambda)^{1/2}} \frac{e^{-z^2}}{z} \tag{A16}$$

$$f \sim \lambda\eta + C_{-\infty} + \frac{D_{-\infty}}{2\lambda} \frac{e^{-z^2}}{z^2} \tag{A17}$$

Substituting equation (A17) into equation (A1) and integrating again, we obtain a higher order approximation for f'',

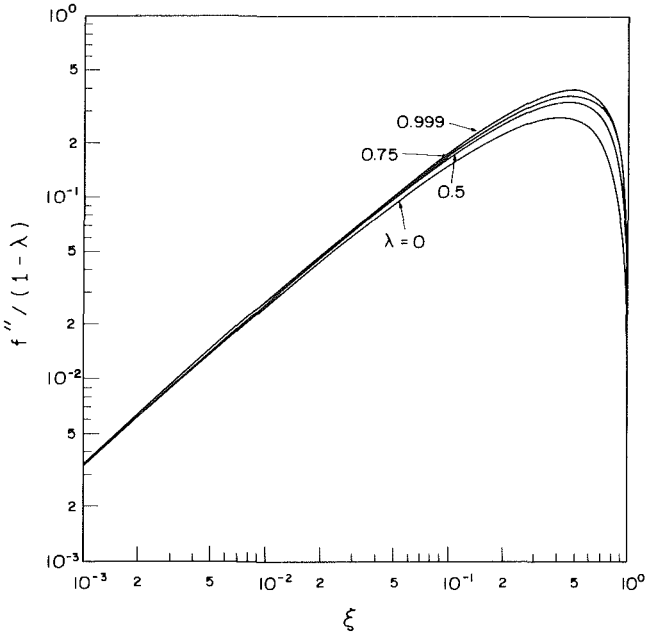

Fig. 9 Plot demonstrating the relation $f''/(1-\lambda) \sim \xi$ for $\xi \to 0$

$$f'' \sim D_{-\infty} e^{-z^2} - \frac{D_{-\infty}^2 e^{-2z^2}}{(2\lambda)^{3/2} z^3} \tag{A18}$$

Hence from equations (A16) and (A17), we have

$$\frac{f''}{(1-\lambda)} \frac{1}{\xi} \sim (2\lambda)^{1/2} z - \frac{D_{-\infty}}{2\lambda} \frac{e^{-z^2}}{z^2} \tag{A19}$$

where $$\xi = \frac{(f' - \lambda)}{(1-\lambda)} \tag{A20}$$

For $\lambda \neq 0$, we need to keep only the first order expansion, hence

$$\frac{f''}{(1-\lambda)} \sim (2\lambda)^{1/2} z\xi \sim -(\lambda\eta + C_{-\infty})\xi \sim -f\xi \tag{A21}$$

Taking the limit $\eta \to -\infty$, we finally have

$$\left[\frac{f''}{(1-\lambda)}\right]_{\eta\to-\infty} \sim \lambda^{1/2} (\xi)_{\xi\to 0} \tag{A22}$$

For $\lambda = 0$, equations (A17) and (A19) show

$$f'' \sim -(f - C_{-\infty})\xi$$

Taking the limit of $\eta \to -\infty$,

$$(f'')^2 \sim f' \xi^2 \sim \xi^3$$

Therefore $$(f'')_{\eta\to-\infty} \sim (\xi^{3/2})_{\xi\to 0} \tag{A23}$$

APPENDIX B

Ignition at Slow Boundary

The case studied in the text has the hot inert having the faster velocity. We shall now study the analogous case when it has the slower velocity. Thus we now place the cold combustible in the upper half plane and the hot inert in the lower half plane. The only major change necessary is to redefine ξ as

$$\xi = \frac{(f' - \lambda)}{(1-\lambda)} \tag{B1}$$

such that ignition again occurs close to $\xi = 0$.

The general correlations obtained in the text can also be used by redefining certain parameters. The governing equation in (s, ξ) space can now be written as

$$\left[\frac{f''}{(1-\lambda)}\right]^2 \frac{\partial^2 \tilde{T}}{\partial \xi^2} - 2s\{\lambda + (1-\lambda)\xi\}\frac{\partial \tilde{T}}{\partial s} = -s\omega \qquad \text{(B2)}$$

For $\lambda \neq 0$, using equation (A22) and assuming $(1-\lambda)\xi << \lambda$, equation (B2) becomes

$$\xi^2 \frac{\partial^2 \tilde{T}}{\partial \xi^2} - 2s\frac{\partial \tilde{T}}{\partial s} = -(s/\lambda)\omega \qquad \text{(B3)}$$

Comparing equation (B3) with equation (19), we see that the two problems are asymptotically analogous if we substitute s (or ζ) by s/λ (or ζ/λ) for the present problem. This is physically reasonable because now ignition occurs closer to the slower boundary as implied by the result that the ignition distance $x_I \sim u_\infty \lambda = u_{-\infty}$.

For $\lambda = 0$, using equation (A23), equation (B2) becomes

$$\xi^3 \frac{\partial^2 \tilde{T}}{\partial \xi^2} - 2s\,\xi\frac{\partial \tilde{T}}{\partial s} = -s\omega \qquad \text{(B4)}$$

By further applying the perturbation equation (20), equation (B4) becomes

$$\tilde{\xi}^2 \frac{\partial^2 \theta}{\partial \tilde{\xi}^2} - 2\zeta\frac{\partial \theta}{\partial \zeta} = -\left(\frac{\zeta}{\tilde{\beta}}\right)\tilde{\xi}^{(\tilde{a}-1)}(1-\alpha_0\tilde{\beta}\,\theta/\tilde{\xi})^{q_0} \times (1-\alpha_F\tilde{\beta}\,\theta/\tilde{\xi})^{q_F}\exp(\theta-\tilde{\xi}) \qquad \text{(B5)}$$

Comparing equation (B5) with equation (25) (for $k=m=1$), it is seen that the present problem is again asymptotically analogous to the one treated in the text if ζ is replaced by $\zeta/\tilde{\beta}$ and if the overall reaction order, $\tilde{a}$, used in computing $\zeta_{I,NC}$, is reduced by one when calculating the present $\zeta_{I,NC}$.

APPENDIX C

Ignition for the Nonpremixed Flow

Let us assume the hot, fast stream consists of the oxidizer whereas the cold, slow stream consists of the fuel (Fig. 1). Then the species concentrations, equation (6), are now replaced by

$$\tilde{Y}_0 + \tilde{T} = (\tilde{Y}_{0\infty} + \tilde{T}_\infty) - (\tilde{Y}_{0\infty} + \beta)\xi \qquad \text{(C1)}$$

$$\tilde{Y}_F + \tilde{T} = \tilde{T}_\infty + (Y_{F,-\infty} - \beta)\xi \qquad \text{(C2)}$$

Ignition is still expected to occur at $\xi \to 0$, except now oxidizer depletion is negligible because of its abundance at the reaction region. Thus by following the same procedure in deriving equations (25) and (26), it can be easily shown that ignition of the present nonpremixed system is analogous to the premixed system treated in the text by setting $\tilde{a} = a_F$ and $\alpha_0 = 0$.

Transient Conduction With Pyrolysis (Approximate Solutions for Charring of Wood Slabs)

A. M. Kanury
Department of Aerospace and Mechanical Engineering, University of Notre Dame, Notre Dame, Ind. 46556
Mem. ASME

D. J. Holve
Sandia National Laboratories, Livermore, Calif. 94550

The rate of charring of a heated one-dimensional, wood-like solid slab is predicted by solving the transient conduction equation with a phase-change energy sink term. This solution procedure uses an integral method with spatially-linear-temperature profiles. Two types of front-face boundary conditions are considered—prescribed temperature and prescribed heat flux. The backface is insulated. The prescribed temperature condition leads to the conclusion that for all reasonable exposure temperatures, the slab would only partially char. The maximum char depth is most sensitive to the char conductivity and exposure temperature and less sensitive to the char specific heat and charring endothermicity. Results of the constant flux are in reasonable agreement with the available experimental data both qualitatively and quantitatively.

1 Introduction

In an earlier paper [1] the standard fire test ASTM E-119 of the American Society for Testing and Materials [2] is introduced for a theoretical analysis. Generalization and extrapolation of the experimental results beyond the circumstances of a particular test are not feasible to date. The present theoretical analysis is intended to make progress in this generalization.

Briefly stated, the E-119 test seeks to measure the resistance of various building construction components to a structural fire. The resistance to penetration of fire through the barrier is expressed in terms of a time rating. A "two-hour-door," for example, can successfully contain a standard fire for 2 hrs. The fire resistance time is defined as either (*i*) the time taken by the pyrolysis layer to reach the backface, or (*ii*) the time taken to attain at the backface a specified critical temperature. The first definition indicates the endurance of the wall to destruction by charring and degeneration of its load-bearing strength. The second definition indicates the resistance of the wall to fire penetration which may cause new ignitions. The description of the test is presented in [1] and [2]. The physical problem of fire resistance of a wall entails transient heat conduction with decomposition reactions and internal convection [1].

In this paper, approximate solutions are developed for the rate of charring of a slab of wood exposed on one side to a simulated fire and insulated on the other side. Although the development primarily addresses the issue of wood-charring, the methodology is directly useful in drying of porous solids [3], combustion of coal fuel beds [4], in situ phase-change in coal seams, and storage of energy in the latent heat storage reservoirs where moving boundary problems [5–7] are involved.

2 The Physical Problem

Consider a slab of a pyrolyzable solid of thickness, l, initially at a uniform temperature, T_i. The solid is assumed to be homogeneous with regionally constant properties. The front face $x = 0$ is exposed to a fire for time $t \geq 0$. As shown in Fig. 1, this exposure may be expressed [8] in terms of: (*i*) a prescribed, uniform, constant surface temperature, T_s, (i.e., Dirichlet type boundary condition); (*ii*) a prescribed, constant, uniform surface energy flux, $\dot{q}_s''$, (i.e., Neumann type b.c.); or (*iii*) a convective heating from an ambient temperature, T_∞, with a heat-transfer coefficient, h, (i.e., Robin or Cauchy type b.c.). (Only the Dirichlet and Neumann problems are solved in this paper.) Based on previous estimates [1], the backface $x = l$ is assumed to be insulated. The transient thermochemical response of the slab involves the following three phases [9].

Preheat Phase. As heating proceeds by the Neumann or Robin exposure, a temperature profile, assumed here to be linear in space, evolves as shown in Fig. 1(*c*). The thermal perturbation is penetrated to a depth x_T. In $x_T \leq x \leq l$, the solid is in the initial state so that the finite thickness of the body is irrelevant.

An instant would soon ensue when the surface temperature T_s is high enough for the solid to pyrolyze, marking the end of the preheat phase, i.e., at time t equals t_0, T_s equals T_c, a characteristic temperature at which the solid abruptly degrades. In the case of Dirichlet exposure with $T_s \geq T_c$, the surface starts to char at $t = 0$, so that the preheat phase is absent altogether.

Early-Charring Phase. As heating continues for $t > t_0$, a continuously thickening char layer exists near the exposed surface. In the char region $0 \leq x \leq x_c$, as shown in Figs. 1(*a*) and 1(*d*), the properties are denoted by the subscript c. At $x = x_c$, the temperature is T_c, and there exists an energy sink of strength L (equal to energy per unit mass of pyrolysis gases released). As the char front $x = x_c$ propagates into the solid at the same rate as the isotherm $T = T_c$ does, the thermal wave $x = x_T$ precedes it. The finiteness of the slab is still irrelevant.

An instant $t = t_s$ would soon arrive when the thermal wave penetrates through the entire body, i.e., $x_T = l$. In time $t \geq t_s$, the backface temperature increases with time and the finiteness of the body becomes crucial.

Late-Charring Phase. for $t > t_s$, as shown in Figs. 1(*b*) and 1(*e*), continued heating will propagate the char front into the solid and the insulated backface warms up.

Comments. (*a*) The problem at hand is to determine the transience of x_T and T_s (or $\dot{q}_s''$) in the preheat phase, x_c, x_T,

Table 1 Representative property values

		Wood	Char
Conductivity	W/m°C	0.17	0.03
Specific Heat	J/kg°C	2500	2000
Density	kg/m^3	600	200
Diffusivity	m^2/s	11.3×10^{-8}	7.5×10^{-8}

Latent heat of Pyrolysis J/kg 300,000
Pyrolysis temperature °C 325
$\kappa \approx 0.176$ $\lambda \approx 0.267$ $\sigma \approx 0.267$

Contributed by the Heat Transfer Division for publication in the JOURNAL OF HEAT TRANSFER. Manuscript received by the Heat Transfer Division May 5, 1981.

and T_s (or $\dot{q}_s''$) in the early-charring phase, and x_c, T_b, and T_s (or $\dot{q}_s''$) in the late-charring phase. In some applications, the post-charring phase heating of the inert porous char body may be important.

(*b*) The pyrolysis reaction kinetics are simplifed in the present work by assuming that once the solid is heated to a threshold temperature, T_c, it is abruptly converted to char and combustible gases endothermically. This assumption defers from the fact that all chemical reactions generally depend upon temperature according to the Arrhenius law. The idealization chosen here corresponds to an infinite activation energy of pyrolysis kinetics.

(*c*) Flow of the pyrolysis gases from $x = x_c$ to the exposed surface $x = 0$ results in a convective heat transfer [10] opposing the inward conduction. This convection effect is not considered here explicitly.

(*d*) The thermophysical properties are assumed to be independent of temperature but dependent on density. Some representative property values for wood and char are presented in Table 1.

(*e*) The spatial distributions of temperature within various regions of the slab are assumed to be linear in order to amplify conceptual clarity of the analysis.

(*f*) The analysis is easily adaptable to cylindrical and spherical coordinates for application in other problem areas.

3 The Mathematical Model

With the above assumptions and simplifications, the one-dimensional transient conduction equation with pyrolysis energy sink is

$$K\frac{\partial^2(T-T_i)}{\partial x^2} - L\dot{W}''' = \rho C\frac{\partial(T-T_i)}{\partial t} \tag{1}$$

Integrating equation (1) once with respect to x,

$$K\frac{\partial(T-T_i)}{\partial x} - L\int \dot{W}'''\,dx = \frac{\partial}{\partial t}\int \rho C(T-T_i)\,dx \tag{2}$$

Abrupt kinetics imply

$$\int \dot{W}'''\,dx = -\int \frac{\partial \rho}{\partial t}\,dx = -\Delta\rho\frac{dx_c}{dt} = (\rho_0-\rho_c)\frac{dx_c}{dt} \tag{3}$$

where dx_c/dt is the propagation rate of the pyrolysis front into the solid. The assumed linear temperature profiles are:

Preheat Phase:

$$\begin{aligned} T &= T_s - (T_s-T_i)(x/x_T) && : 0\le x\le x_T \\ T &= T_i && : x_T\le x\le l \end{aligned} \tag{4}$$

Early-Charring Phase:

$$\begin{aligned} T &= T_s - (T_s-T_c)(x/x_c) && : 0\le x\le x_c \\ T &= T_c - (T_c-T_i)(x-x_c)/(x_T-x_c) && : x_c\le x\le x_T \\ T &= T_i && : x_T\le x\le l \end{aligned} \tag{5}$$

Late-Charring Phase:

$$\begin{aligned} T &= T_s - (T_s-T_c)(x/x_c) && : 0\le x\le x_c \\ T &= T_c - (T_c-T_b)(x-x_c)/(l-x_c) && : x_c\le x\le l \end{aligned} \tag{6}$$

In addition to x_c, x_T, and the insulated backface temperature, T_b, the unknown functions of time are the heat flux $\dot{q}_s''$ at $x = 0$ in the Dirichlet and Robin problems and the surface temperature T_s at $x = 0$ in the Neumann and Robin problems.

The following four integrals signify the energy content respectively in the preheat layer, char layer, virgin solid in the early-charring phase, and virgin solid in the late charring phase.

$$I_1 \equiv \int_0^{x_T} \rho_0 C_0[T_s - (T_s-T_i)(x/x_T) - T_i]dx$$

$$I_2 \equiv \int_0^{x_c} \rho_c C_c[T_s - (T_s-T_c)(x/x_c) - T_i]dx$$

$$I_3 \equiv \int_{x_c}^{x_T} \rho_0 C_0[T_c - (T_c-T_i)(x-x_c)/(x_T-x_c) - T_i]dx$$

$$I_4 \equiv \int_{x_c}^{l} \rho_0 C_0[T_c - (T_c-T_b)(x-x_c)/(l-x_c) - T_i]dx$$

Application of equations (2) and (3) for the preheat phase gives, for Neumann and Robin problems

$$\dot{q}_s'' = \frac{K_0(T_s-T_i)}{x_T} = \frac{dI_1}{dt} \tag{7}$$

Application of equations (2) and (3) for the char and for the virgin solid zones in the early-charring phase gives

$$\dot{q}_s'' = \frac{K_c(T_s-T_c)}{x_c} = \frac{dI_2}{dt} + L(\rho_0-\rho_c)\frac{dx_c}{dt} + \frac{K_0(T_c-T_i)}{(x_T-x_c)} \tag{8}$$

$$\frac{K_0(T_c-T_i)}{(x_T-x_c)} = \frac{dI_3}{dt} \tag{9}$$

Finally, for the late-charring phase,

$$\dot{q}_s'' = \frac{K_c(T_s-T_c)}{x_c} = \frac{dI_2}{dt} + L(\rho_0-\rho_c)\frac{dx_c}{dt} + \frac{K_0(T_c-T_b)}{(l-x_c)} \tag{10}$$

Nomenclature

a = empirical constant
b = empirical constant
C = specific heat
E = pyrolysis activation energy
F = function of τ defined at equation (22)
h = convective heat-transfer coefficient
$I_1 \ldots I_4$ = energy integrals
K = thermal conductivity
l = slab thickness
L = latent heat of pyrolysis
n = an index near 1.6.
$\dot{q}''$ = heat flux
$\bar{q}$ = nondimensional surface heat flux; nondimensional slab thickness; modified Biot number.
R = universal gas constant
t = time
T = temperature
$\dot{W}'''$ = pyrolysis rate
x = depth coordinate
α = thermal diffusivity
β = a function of κ, θ_s, λ and σ defined in equation (13)
θ = nondimensional temperature
κ = char to wood thermal conductivity ratio
λ = nondimensional latent heat of pyrolysis
ξ = nondimensional depth
$\bar{\xi}$ = an averaged nondimensional depth
ρ = density
σ = char to wood volumetric heat capacity ratio
τ = nondimensional time

Subscripts

b = insulated backface
c = charring; char; char wave
e = endurance
i = initial
max = maximum
0 = end of preheat phase
0 = virgin solid
r = resistance
s = exposed surface; end of early-charring phase
T = thermal wave
∞ = ambient gas

$$\frac{K_0(T_c-T_b)}{(l-x_c)}=\frac{dI_4}{dt} \tag{11}$$

Define the following nondimensional quantities:

$$\theta\equiv\frac{T-T_i}{T_c-T_i}\quad;\quad \xi\equiv\frac{x}{l}\quad;\quad \tau\equiv\frac{\alpha_0 t}{l^2}\quad;\quad \kappa\equiv\frac{K_c}{K_0}\quad;$$

$$\lambda\equiv\frac{L(\rho_0-\rho_c)}{\rho_0 C_0(T_c-T_i)}\quad;\quad \sigma\equiv\frac{\rho_c C_c}{\rho_0 C_0}\quad;\quad \tilde{q}\equiv\frac{\dot{q}_s'' l}{K_0(T_c-T_i)}$$

Equations (7–11) then reduce to the following form:

$$\tilde{q}=\frac{\theta_s}{\xi_T}=\frac{1}{2}\frac{d}{d\tau}(\xi_T\theta_s) \tag{7a}$$

$$\tilde{q}=\frac{\kappa(\theta_s-1)}{\xi_c}=\lambda\frac{d\xi_c}{d\tau}+\frac{\sigma}{2}\frac{d}{d\tau}[\xi_c(\theta_s-1)]+\frac{1}{(\xi_T-\xi_c)} \tag{8a}$$

$$\frac{1}{(\xi_T-\xi_c)}=\frac{1}{2}\frac{d}{d\tau}(\xi_T-\xi_c) \tag{9a}$$

$$\tilde{q}=\frac{\kappa(\theta_s-1)}{\xi_c}=\lambda\frac{d\xi_c}{d\tau}+\frac{\sigma}{2}\frac{d}{d\tau}[\xi_c(\theta_s-1)]+\frac{(1-\theta_b)}{(1-\xi_c)} \tag{10a}$$

$$\frac{(1-\theta_b)}{(1-\xi_c)}=\frac{1}{2}\frac{d}{d\tau}[(1-\xi_c)(1+\theta_b)] \tag{11a}$$

4 The Dirichlet Problem

Equation (7) is irrelevant. The surface temperature θ_s is a prescribed constant to simplify the differentials in equations (8*a*) and (10*a*).

Early-Charring Phase. Equation (9*a*) with initial condition $\xi_T=\xi_c=0$ at $\tau=0$ gives

$$(\xi_T-\xi_c)=2\sqrt{\tau} \tag{12}$$

Equation (8*a*) then becomes

$$\frac{\kappa(\theta_s-1)}{\xi_c}=\left\{\lambda+\frac{\sigma}{2}(\theta_s-1)\right\}\frac{d\xi_c}{d\tau}+\frac{1}{2\sqrt{\tau}}$$

the solution of which is

$$\xi_c=\beta\sqrt{\tau} \tag{13}$$

where

$$\beta\equiv\frac{(1+8\,\kappa'\lambda')^{1/2}-1}{2\lambda'}$$

with $\kappa'\equiv\kappa(\theta_s-1)$ and $\lambda'\equiv\lambda+\sigma(\theta_s-1)/2$. The surface heat flux is

$$\tilde{q}=\kappa'/\beta\sqrt{\tau} \tag{14}$$

Equations (12–14) hold until time $\tau=\tau_s$ when the thermal wave penetrates to the insulated backface, i.e., $\xi_T=1$. The pyrolysis wave location at this time is denoted by ξ_{cs}.

$$\tau_s=1/(\beta+2)^2$$
$$\xi_{cs}=\beta/(\beta+2) \tag{15}$$

Late-Charring Phase. Equations (10*a*) and (11*a*) take control over for $\tau\geq\tau_s$ with the backface temperature θ_b as the second unknown. Elimination of θ_b leads to a second order nonlinear differential equation for $\xi_c=\xi_c(\tau)$ which can be solved only numerically. As ξ_c increases from ξ_{cs} to unity note that θ_b increases from zero to unity so that the quantity $(1-\theta_b)/(1-\xi_c)$ varies between $1/(1-\xi_{cs})$ and unity. For wood-like solids exposed to a $\theta_s\approx 4$, $\xi_{cs}\approx 0.264$ so that the term in question varies between about 1.36 and unity.

Note also that in this problem, the energy inflow rate decreases as the char layer thickens, leading to a situation in which the energy demand for continued pyrolysis is not met. The char layer, as a result, is bounded. From equation (10*a*) when $d\xi_c/d\tau=0$, the maximum permitted ξ_c can be found.

$$\xi_c\leq\frac{2\kappa(\theta_s-1)}{\beta+2} \tag{16}$$

For wood exposed to $T_s\approx 1225°C$ (i.e., $\theta_s=4$) with $\kappa\approx 0.176$, $\lambda\approx 0.276$ and $\sigma\approx 0.276$, $\xi_{cmax}\approx 0.45$. ξ_{cmax} is most sensitive to char conductivity κ and quite insensitive to λ and σ. It is almost lineraly proportional to the surface temperature.

Within the limits of reasonably expected practical conditions, therefore, the last term of equation (10*a*) may safely be replaced by a constant of approximate value $1/(1-\xi_{cs})$. The solution with the time condition $\tau=\tau_s$, $\xi_c=\xi_{cs}$, is then obtained as

$$(\xi_c-\xi_{cs})+\kappa(\theta_s-1)(1-\xi_{cs})\,ln\left\{\frac{\kappa(\theta_s-1)(1-\xi_{cs})-\xi_c}{\kappa(\theta_s-1)(1-\xi_{cs})-\xi_{cs}}\right\}$$
$$=-\frac{(\tau-\tau_s)}{\left[\lambda+\frac{\sigma}{2}(\theta_s-1)\right](1-\xi_{cs})} \tag{17}$$

Equation (11*a*) may be solved for θ_b (with $\theta_b=0$ at $\tau=\tau_s$) with the approximation $\xi_c\approx\bar{\xi}_c\approx(\xi_{cs}+\xi_{cmax})/2$.

$$\theta_b\approx 1-\exp\{-2(\tau-\tau_s)/(1-\bar{\xi}_c)^2\} \tag{18}$$

Substituting equations (17) and (18) into equations (10*a*) and (11*a*), the error involved in the approximation can be estimated. The worst error occurs at large θ_s and small $\tau-\tau_s$. For the $\theta_s=4$ case, this is found to be between 15 and 25 percent. Inasmuch as the Dirichlet problem does not yield complete charring for surface temperatures of practical consequence, the endurance time τ_e is infinity. However, the resistance time τ_r based on any specified backface temperature θ_{br} can be estimated from equation (18), with equations (15) and (16).

$$\tau_r\approx\frac{1}{(\beta+2)^2}\left\{1+2\,ln\left[\frac{1}{1-\theta_{br}}\right][1-\kappa(\theta_s-1)]^2\right\} \tag{19}$$

Equation (19) indicates that the resistance time is proportional to the square of the slab thickness. In Figs. 2 and 3, the Dirichlet solution is depicted graphically for a later discussion.

5 The Neumann Problem

Preheat Phase. Solving equation (7*a*) with $\xi_T=\theta_s=0$ at $\tau=0$,

$$\xi_T=\sqrt{2\tau} \tag{20}$$
$$\theta_s=\tilde{q}\sqrt{2\tau} \tag{21}$$

The exact solution according to Carslaw and Jaeger [8] is $\theta_s=(2\tilde{q}/\sqrt{\pi})\sqrt{\tau}$. Linear temperature profiles thus cause an error of the order 25 percent. Equations (20) and (21) are operational until time τ_0 when $\theta_s=1$ at which the surface begins to pyrolyze.

$$\tau_0=\frac{1}{2\tilde{q}^2}$$

$$\xi_{TO}=\frac{1}{\tilde{q}}$$

Early-Charring Phase. Solution of equation (9*a*) with $\tau=\tau_0$, $\xi_T=\xi_{TO}$, $\xi_c=0$, and $\theta_s=1$, is

$$\xi_T-\xi_c=\left\{4\left[\tau-\frac{1}{2\tilde{q}^2}\right]+\frac{1}{\tilde{q}^2}\right\}^{1/2}\equiv F(\tau) \tag{22}$$

Equations (8*a*) and (22) lead to

$$\lambda\xi_c+\frac{\sigma\tilde{q}}{2\kappa}\xi_c^2=\tilde{q}\tau-\frac{1}{2}F(\tau) \tag{23}$$

$$\theta_s = \frac{\bar{q}\xi_c}{\kappa} + 1 \tag{24}$$

Equation (23) is quadratic in both ξ_c and τ. The physically permissible positive char layer thickness is thus

$$\xi_c = \left\{\left[1 + \frac{2\sigma\bar{q}}{\kappa\lambda^2}\left[\bar{q}\tau - \frac{1}{2}F(\tau)\right]\right]^{1/2} - 1\right\} \Big/ \frac{\sigma\bar{q}}{\kappa\lambda} \tag{23a}$$

ξ_c, ξ_T, and θ_s are thus known functions of τ in the early-charring phase. These solutions hold until $\xi_T = 1$ at $\tau = \tau_s$. The finiteness of the body is now relevant. $\xi_c(\tau_s) \equiv \xi_{cs}$ and $\theta_s(\tau_s) \equiv \theta_{ss}$.

Late-Charring Phase. Equations (10*a*) and (11*a*) have to be solved for θ_s, θ_b, and ξ_c, functions of time τ, with the time-condition: $\tau = \tau_s$, $\xi_c = \xi_{cs}$, $\theta_s = \theta_{ss}$ and $\theta_b = 0$. The same approximation employed in the Dirichlet problem is made here; that is, $\theta_b \approx 0.5$, $\xi_c \approx (\xi_{cs} + 1)/2$, so that the last term of equation (10*a*) is about $1/(1-\xi_{cs})$. The corresponding solution is

$$\lambda(\xi_c - \xi_{cs}) + \frac{\sigma\bar{q}}{2\kappa}(\xi_c^2 - \xi_{cs}^2) \approx \left(\bar{q} - \frac{1}{1-\xi_{cs}}\right)(\tau - \tau_s) \tag{25}$$

$$\theta_s = \frac{\bar{q}\xi_c}{\kappa} + 1 \tag{26}$$

and

$$\theta_b \approx 1 - \exp[-2(\tau - \tau_s)/(1-\xi_{cs})^2] \tag{27}$$

Substituting equations (25) and (27) in equations (10*a*) and (11*a*), the error involved in the approximation is found to be about 8 to 15 percent. The quadratic equation (25), is typical of constant flux problems. The positive ξ_c root is obtained as

$$\xi_c = \left[\left(1 + \frac{2\sigma\bar{q}}{\kappa\lambda^2}\left\{\left[\bar{q} - \frac{1}{(1-\xi_{cs})}\right](\tau - \tau_s) + \lambda\xi_{cs} + \frac{\sigma\bar{q}}{2\kappa}\xi_{cs}^2\right\}\right)^{1/2} - 1\right] \Big/ \frac{\sigma\bar{q}}{\kappa\lambda} \tag{25a}$$

As $\xi_c \to 1$, the surface temperature continues to increase according to equation (26) in an unbounded manner within the context of the physics employed here.

The endurance time τ_e is deduced from equation (25*a*) by setting $\xi_c = 1$; and the resistance time τ_r (for any prescribed backface temperature θ_{br}) from equation (27).

$$\tau_e = \tau_s + \left[\bar{q} - \frac{1}{(1-\xi_{cs})}\right]^{-1}\left\{\left[\left(\frac{\sigma\bar{q}}{\kappa\lambda} + 1\right)^2 - 1\right]\frac{\kappa\lambda^2}{2\sigma\bar{q}} - \lambda\xi_{cs} - \frac{\sigma\bar{q}}{2\kappa}\xi_c^2\right\} \tag{28}$$

$$\tau_r = \tau_s + \frac{(1-\xi_{cs})^2}{2}\ln\left[\frac{1}{1-\theta_{br}}\right] \tag{29}$$

Figures 4 and 5 display the Neumann solution graphically.

6 Discussion

The probable thermochemical properties of wood-like solids are listed in Table 1. The ratio of char conductivity to wood conductivity κ is about 0.176. The latent heat of pyrolysis, λ, and the ratio, σ, of volumetric heat capacity of char to that of wood are both about 0.267. These parameters are expected to be different for different species of wood although little or no quantitative data is available in the literature.

The Dirichlet Problem. With κ, λ, and σ at these standard values, Fig. 2 shows, for three different values of exposure temperature θ_s, the temporal history of the thermal and pyrolysis waves, the surface heat flux, and the backface temperature. As the char layer thickens, the surface heat flux falls. No sooner the thermal wave reaches the insulated backface of the slab, the backface begins to warm up. The higher the exposure temperature, the sooner this event occurs.

More importantly, even for the highest shown exposure temperature ($\theta_s = 4$) only partial charring is possible due to the efficient thermal insulation of the char. A higher κ would lead to a thicker ultimate char layer. This simple prediction may indeed be an artifact of the mathematical model. However, it is an artifact apparently consistent with the view of designers engaged in the century-old practice of building with wood for an assured structural integrity in a fire.

Whether or not the prescribed surface temperature boundary condition is realistic at all for wood burning in fires is itself a matter of concern. Nevertheless, two relevant questions arise: first, upon attaining the maximum char layer thickness, what is expected to happen to the solid with continued exposure? Second, what sort of a behavior is expected when the exposure temperature θ_s is quite close to but only infinitesimally larger than unity? The answer to the second

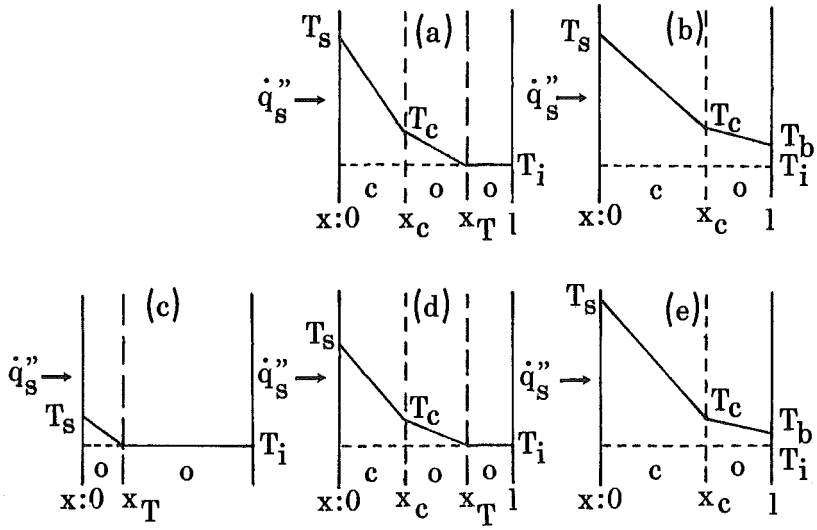

Fig. 1 Schematic of a charring slab (C-char; O-virgin solid; Dirichlet b.c. (*a*) early-charring phase, (*b*) late-charring phase; Neumann b.c. (*c*) preheat phase, (*d*) early-charring phase, (*e*) late-charring phase)

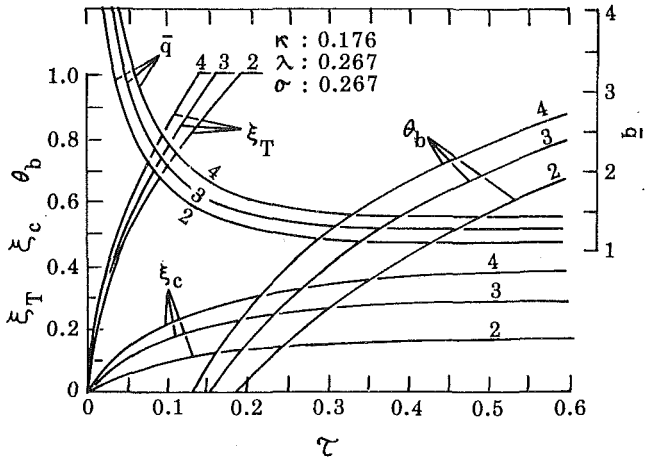

Fig. 2 Constant surface temperature solution (numbers on curves refer to the exposure temperature θ_s)

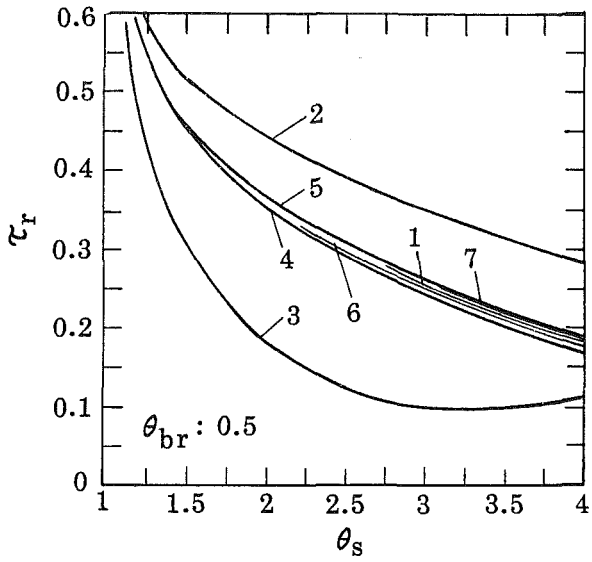

	κ	λ	σ
1.	0.176	0.267	0.267
2.	0.100	"	"
3.	0.500	"	"
4.	0.176	"	0.100
5.	"	"	0.500
6.	"	0.100	0.267
7.	"	0.500	"

Fig. 3 Resistance time as predicted by the Dirichlet solution

question includes that to the first. With low intensity exposures (i.e., θ_s is marginally larger than unity), a distinct char front boundary may not exist between the regions of char and virgin solid. Transient conduction would continue to occur even at low exposure but the temperature gradients in the solid would perhaps be less severe; the local rates of heating will probably be so low as to result in a spatially distributed slow pyrolysis process in which the pyrolysis kinetic detail cannot be simplified. The mechanism of this slow, uniform pyrolysis process warrants an altogether different model displacing that of this paper. Such a model dealing with uniform heating of thermally thin solids is expected to hold even in situations involving moderate θ_s values after the limiting char layer thickness is attained (i.e., in answer to the first question).

Inasmuch as only partial charring is possible with the Dirichlet heating condition, concern about loss of structural integrity of the wall is unnecessary. One needs only to obtain fire resistance time from the history of the backface temperature θ_b. Given a critical temperature θ_{br}, one can obtain, from equation (19) or Fig. 2, the resistance time τ_r.

Figure 3 shows this τ_r for a θ_{br} of 0.5. In general, τ_r is smaller for a higher exposure temperature θ_s. Even more importantly, τ_r is relatively independent of both the char heat capacity σ, and the pyrolysis endothermicity λ. It is, however, strongly influenced by the char conductivity κ. This finding is in excellent agreement with White and Schaffer [11].

Due to difficulties of experimentally maintaining constant temperature at the surface, there are no data available in the literature to tally with our predictions. However, the predictions are substantially consistent with intuitive expectations and detailed numerical results which are to be published in a subsequent paper.

The Neumann Problem. With the standard value of κ, λ, and σ, Fig. 4 shows the temporal development of the thermal and pyrolysis waves and of the exposed surface and backface temperatures for two exposure heat fluxes $\bar{q}$. The exposed surface temperature rapidly increases and the thermal wave penetrates into the solid. The higher the heat flux the sooner the surface starts to char. The rate of charring, once initiated, appears to be insensitive to the heating intensity. As the thermal wave reaches the backface, θ_b begins to rise.

Continued heating would result in continued charring and backface warming. An anamoly, however, exists in the fact that the surface temperature θ_s is unbounded. The physics underlying the present analysis does not account for convective and radiative losses from the hot surface. These two mechanisms will, in actuality, come into play to modulate the surface temperature. In order to take this into account, numerical solutions are required [12]. Not withstanding this difficulty, the histories of the char thickness and backface temperature appear to be reasonable.

Figure 5 shows the predictions (for $\kappa = 0.176$, $\lambda = 0.276$, and $\sigma = 0.276$ with $\theta_{br} = 0.5$), along with some data. In this figure, the x-axis is the nondimensional heat flux $\bar{q}$ which can also be viewed as the nondimensional thickness of the slab. The slab thickness is eliminated from time τ by multiplying it by $\bar{q}^2$ so that the y-axis is $\bar{q}^2\tau = \dot{q}''^2\,\alpha_0 t/[K_0(T_c - T_i)]^2$.

The pattern of dependency of $\bar{q}^2\tau$ on $\bar{q}$ is similar between the endurance and resistance times, consistent with the view in fire-safety practice. The general shape of these curves is also consistent with the literature of charring [9], drying [14], and cement slab heating [16]. It is well-known [15] that fire resistance and endurance times depend on slab thickness l, either as $t \propto l^n$ (with n near 1.6) or as $t \propto (al + bl^2)$ (a is a function of L and $\dot{q}_s''$, and b is a function only of α_0 [13].) At small values of $\bar{q}$, the slope of either of the curves in Fig. 5 is about unity while at large values of $\bar{q}$, the slope is about 2, in good agreement with the well-known trends. The endothermicity plays a dominant role at small values of $\bar{q}$.

Some measurements of char depth as a function of exposure are available in the literature [11–13, 15, 17]. However, lack of precise exposure conditions in terms of the surface condition renders these data relatively difficult to be translated to our theoretical coordinates. Bamford's data [12] are derived from three different wood species exposed either to gas flames ($l = 0.01$ m) or a radiant source ($l = 0.012$ to 0.030 m). While the radiant heat fluxes are all stated in the description of the experiment in [12], the heat flux from flames is estimated by us to be about 2.37×10^4 W/m^2. Thermal properties are found both in [12] and various handbooks. Bryan and Doman [17] exposed 1/2-in. thick slabs of assorted species of wood to furnace gas flames until

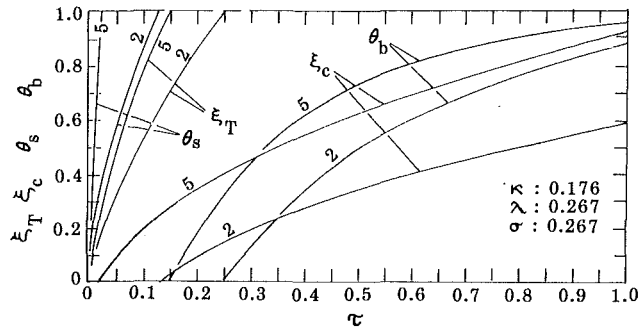

Fig. 4 Constant surface heat flux solution (numbers on curves refer to the exposure heat flux $\bar{q}$)

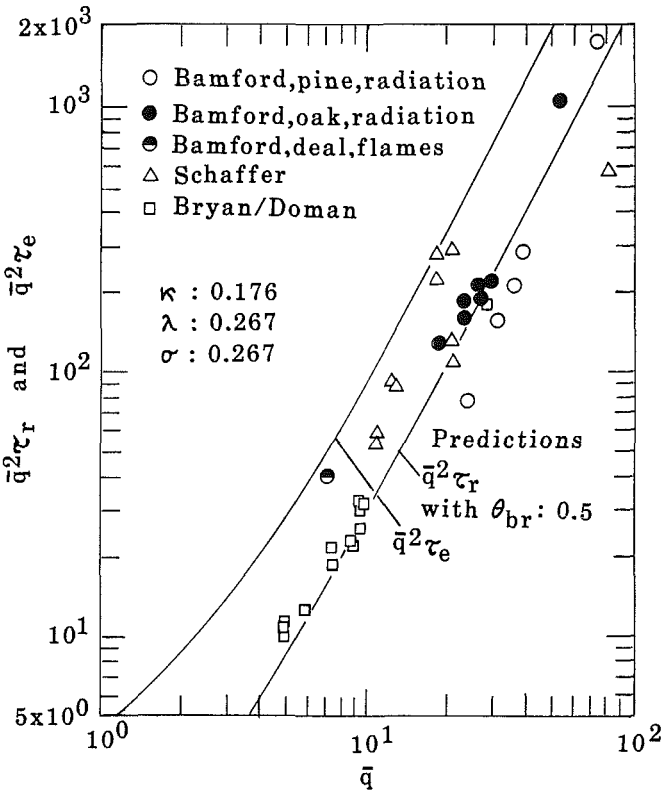

Fig. 5 Time of endurance and of resistance (Neumann solution compared with data from literature)

burnthrough occurred. Schaffer [15] reports the burnthrough times of 1-in. thick plates of various woods exposed on one side to the ASTM E-119 furnace. The heat flux to the surface from the intensely mixed furnace flames is estimated by us to be about 2.73×10^6 W/m^2 for the data of both [15] and [17].

Noteworthy in Fig. 5 is the reasonably good agreement, especially in the trends, between these various data and the present predictions of the endurance time τ. The theory consistently overestimates τ. The estimation of $\dot{q}_s''$, discount of the differences in λ, σ, and κ between different wood species, and variable moisture content are among the factors responsible both for the departure of experiments from the present theory, and for the scatter among the data points.

The heating function $\bar{q}$ may be viewed as a ratio of the physical thickness of the slab l to the thermal thickness $K_0(T_c - T_i)/\dot{q}_s''$ expressing the slab thickness in a physically meaningful nondimensional way. $\bar{q}$ also can be viewed as a Biot number. When $\bar{q}$ is small, it is obvious that one has a situation of low-intensity heating of physically thin slabs of a highly conductive material with high pyrolysis temperature. One then encounters a situation in which the thermal wave would penetrate to the backface well before the surface begins to pyrolyze, i.e., $\tau_s < \tau_0$. The body may even be heated with ignorable internal temperature gradients. While the present theory is fully capable of handling this thermally thin body situation, it may be even easier to tackle this situation by the well-known [18] lumped capacity technique of conduction analysis.

7 Concluding Remarks

Even with the severe approximations made in the present theory, the essential physics of charring of wood appears to have been captured and to predict the correct trends of dependency. The present approximate analytical results for the dependency of endurance time on slab thickness are consistent with previous results obtained by dimensional analysis and by experiment, i.e., $t_e = al + bl^2$. Consideration of the fully nonlinear exposure boundary condition of the Robin-type with additionally included radiant loss from the surface will improve the predictions. Heating of moist porous solids such as gypsum board and charring of composite walls with and without interstitial air gap are among the other problems of this family which need attention.

8 Acknowledgments

This problem was conceived when the authors were in the employ of Stanford Research Institute working on a project sponsored by the National Bureau of Standards with Dan Gross as technical monitor. Our thanks to Stan Martin for his help with the pyrolysis chemistry.

References

1 Kanury, A. M. and Holve, D. J., "Response of Building Components to Heating in a Fire," ASME Journal of Heat Transfer, Vol. 101, No. 2, May 1979, pp. 365-370.

2 *1977 Annual Book of ASTM Standards, Part 18*, American Society for Testing and Materials, 1916 Race Street, Philadelphia, Pa, 1977, pp. 739-759.

3 Luikov, A. V., *Heat and Mass Transfer in Capillary Porous Bodies*, Pergamon Press, Oxford, U.K., 1966.

4 Singer, J. G., ed., *Combustion*, 3rd ed., Combustion Engineering, Inc., New York, 1981.

5 Jacob, M., *Heat Transfer, Vol. I*, 6th Printing, John Wiley, New York, N.Y., 1958, pp. 343-349.

6 Landau, H. G., "Heat Conduction in a Melting Solid," *Quarterly of Applied Mathematics*, Vol. 8, 1950, pp. 81-94.

7 Ashton, G. D., "River Ice," *American Scientist*, Vol. 67, No. 1, Jan.-Feb. 1979, pp. 38-45.

8 Carslaw, H. S. and Jaeger, J. C., *Conduction of Heat in Solids*, Oxford University Press, London, 1959.

9 Kanury, A. M., "Rate of Charring of Wood (A Simple Thermal Model)," *Combustion Science and Technology*, Vol. 5, 1972, pp. 135-146.

10 Kanury, A. M. and Blackshear, Jr. P. L., "On the Combustion of Wood: II. The Influence of Internal Convection on the Transient Pyrolysis of Cellulose," *Combustion Science and Technology*, Vol. 2, 1970, pp. 5-9.

11 White, R. H. and Schaffer, E. L., "Application of CMA Program to Wood Charring," *Fire Technology*, Vol. 14, No. 4, Nov. 1978, pp. 279-291.

12 Bamford, C. H., Crank, J., and Malan, D. H., "The Combustion of Wood. Part I," *Proceedings of Cambridge Philosophical Society*, Vol. 42, 1946, pp. 166-182.

13 Kanury, A. M., "Rate of Charring Combustion in a Fire," *Fourteenth Symposium (International) on Combustion*. The Combustion Institute, Pittsburgh, Pa. 1973, pp. 1131-1142.

14 Kawagoe, K., "Calculation of Temperature in Double-Layer Walls Heated From One Side," *Bulletin of Fire Prevention Society of Japan*, Vol. 13, No. 2, Aug. 1965, pp. 29-35.

15 Schaffer, E. L., "Review of Information Related to the Charring Rate of Wood," U.S. Forest Service Research Note No. FPL-0145, Forest Products Laboratory, Madison, Wis., Nov. 1966.

16 Harmathy, T. Z., "Design to Cope with Fully Developed Fires," in *Design of Buildings for Fire Safety*, Special Technical Publication No. 685, American Society for Testing and Materials, Philadelphia, Pa. 1979, pp. 198-276.

17 Bryan, J. and Doman, L. S., "Fire Resistance—the Comparative Resistance to Fire of Various Species of Timber," *Wood*, Vol. 5, No. 1, 1940, pp. 19-23.

18 Lienhard, J. H., *A Heat Transfer Text Book*, Prentice-Hall Inc. Englewood Cliffs, N.J., 1981.

A Numerical Study of the Response of Building Components to Heating in a Fire

D. J. Holve
Sandia National Laboratories,
Livermore, Calif. 94550

A. M. Kanury
Department of Aerospace and
Mechanical Engineering,
University of Notre Dame,
Notre Dame, Ind. 46556
Mem. ASME

This paper addresses the problem of fire resistance of building systems. A numerical parametric study is performed to find the influence of various physical and chemical parameters on the thermochemical response of wood, gypsum, and wood-under-gypsum walls subjected to a simulated fire on the front face. It is found that: (i) the thermal radiation terms are important in the exposure boundary condition; (ii) the pyrolysis kinetic detail required to design fire-resistive walls is minimal; and (iii) the earlier dimensional and approximate analyses are in agreement with the present numerical results. These results suggest use of a simple analytical relationship to describe and correlate the ASTM E-119 fire endurance test data.

Introduction

This paper is concerned with a mathematical analysis of the ASTM E-119 fire test [1] which measures the ability of construction components to withstand a structural fire. In an earlier paper [2] the physics of this test has been described and adapted to mathematics. Dimensional and order-of-magnitude analyses have been carried out to arrive at qualitative dependencies of the fire resistance of walls on various properties of the wall and of the fire. In a subsequent paper [3], approximate closed-form solutions are obtained to the linearized problem of transient conduction in pyrolyzing wood slabs. Although the trends predicted by these order-of-magnitude and approximate analyses are in reasonable accord with empirical building design rules, three simplifying assumptions made in these studies remain to be justified. These assumptions are related to: (*a*) the exposure boundary condition, (*b*) the role of internal convection due to flow of pyrolysis products out of the body [4], and (*c*) the pyrolysis chemistry.

The primary intent of the present paper is to evaluate these assumptions by numerically solving the complete problem, and thus to justify the correlative relationship of [3] to describe the ASTM test data.

The Problem

Consider a pyrolyzable solid slab of thickness, l, the frontface of which is exposed to a simulated fire, and the backface which is insulated. As this slab is transiently heated, it will progressively char. The equations governing the thermochemical response history of this wall are formulated and discussed in [2].

The assumptions underlying the present model are: (*i*) the physical properties of the solid are independent of temperature, but vary linearly between their respective values for the original wood and the final char; (*ii*) a single first-order Arrhenius expression describes the pyrolysis kinetics; (*iii*) fuel volatiles flow out of the solid immediately after their generation and are in thermal equilibrium with the residual char; (*iv*) the char remains intact (no fissuring or mechanical cracking would occur); and (*v*) the process is one-dimensional. The energy equation expresses a balance between the transient energy accumulation rate, with the sum of the rates of conduction, pyrolysate convection, and energy sink due to pyrolysis.

$$\rho C\frac{\partial T}{\partial t}=\frac{\partial}{\partial x}\left(K\frac{\partial T}{\partial x}\right)+m_g''C_g\frac{\partial T}{\partial x}+L\frac{\partial \rho}{\partial t} \tag{1}$$

x is depth in the solid measured from the exposed surface; $\dot{m}_g''$ is the pyrolysate mass flux; C_g is the specific heat of the pyrolysates; L is the heat of pyrolysis. The pyrolysis rate $\partial\rho/\partial t$, rate of change of local solid density with time, is assumed to be related [2] to local instantaneous temperature and density according to

$$\frac{\partial \rho}{\partial t}=-a\left(\frac{\rho-\rho_c}{\rho_w-\rho_c}\right)\exp\left(-E/RT\right) \tag{2}$$

where ρ_w is the original wood density, ρ_c is final char density, a is the preexponential rate factor, E is activation energy, and R is the universal gas constant. Both a and E are chemical kinetic characteristics of the decomposition reaction along with the assumed reaction order of unity.

Continuity of mass states that the spatial rate of increase in local mass flux is equal to the temporal rate of local production of pyrolysates.

$$\frac{\partial \dot{m}_g''}{\partial x}=\frac{\partial \rho}{\partial t} \tag{3}$$

The boundary condition for equation (1) at the exposed surface ($x=0$, subscript s) states that the net heat flux $\dot{q}_n''$ conducted into the solid wall is equal to the sum of the radiative (subscript r) and convective (subscript c) fluxes from the flame (subscript f) less the reradiative (subscript rr) loss from the surface.

$$\dot{q}_n''=-K\frac{\partial T}{\partial x}\bigg|_s=\dot{q}_r''+\dot{q}_c''-\dot{q}_{rr}''=\sigma\epsilon_f T_f^4$$

$$+h^*(T_f-T_s)-\sigma\epsilon_s T_s^4 \tag{4}$$

σ, ϵ and h^* are the Stefan-Boltzman constant, emissivity, and the heat-transfer coefficient, respectively. In [2], it has been shown that for modest backface (subscript b) temperature rise above the ambient temperature, the backface heat loss is insignificant so that

$$\dot{q}_b''=-K\frac{\partial T}{\partial x}\bigg|_b\approx 0 \tag{5}$$

The initial conditions are

$$T(x,0)=T_\infty;\ \rho(x,0)=\rho_w;\ \text{and}\ \dot{m}_g''(x,0)=0 \tag{6}$$

The variation of the flame temperature T_f with time is meant to imitate the transient nature of an actual com-

Contributed by the Heat Transfer Division for publication in the JOURNAL OF HEAT TRANSFER. Manuscript received by the Heat Transfer Division June 22, 1981.

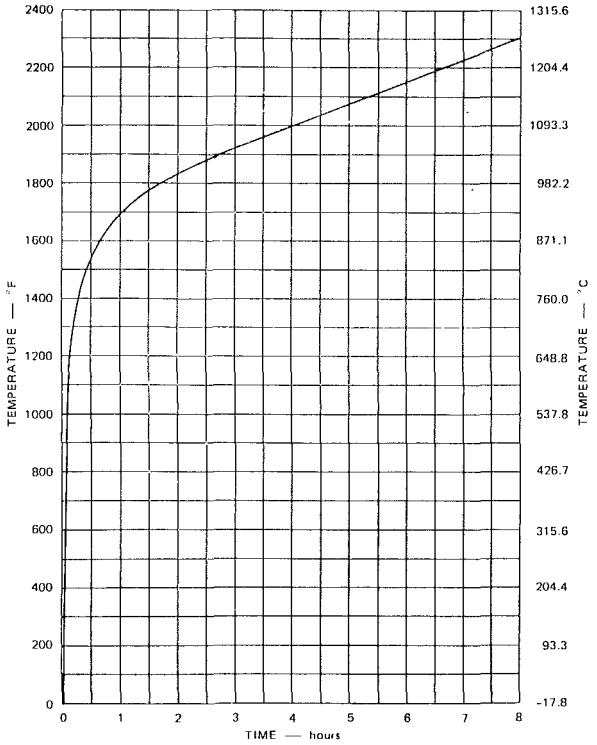

Fig. 1 ASTM E-119 standard temperature curve

partment fire. A number of $T_f(t)$ relations are available in the literature as reviewed in [5]. Two particular patterns of $T_f(t)$ are considered here. The first is the standard ASTM/ISO temperature-time history shown in Fig. 1 and described by the following formula.

$$T_f - T_\infty = 345 \log_{10}(1 + 8t) \quad [T \text{ in } °C,\ t \text{ in min}] \tag{7}$$

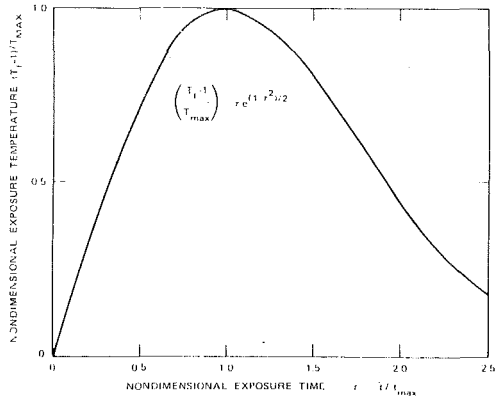

Fig. 2 Two parameter peaked fire exposure curve

where T_∞ is the ambient temperature. In a typical compartment fire, however, the temperature rises relatively rapidly, reaches a maximum, and then decays. Butcher, Chitty, and Ashton [6], and Robertson and Gross [7] have presented experimentally measured $T_f(t)$ profiles for a variety of enclosure fires. Figure 2 shows the nondimensional plot of a two-parameter formula which correlates the data of these experiments. The two parameters T_{max}, the maximum flame temperature, and t_{max}, the time at which T_{max} is attained depend on the variables of the enclosure, such as the fuel loading and ventilation. A satisfactory version of this formula is

$$\frac{T_f - T_\infty}{T_{max}} = \left(\frac{t}{t_{max}}\right) \exp\{[1 - (t/t_{max})^2]/2\} \tag{8}$$

Based on the data of [7], the following three values of T_{max} and the corresponding t_{max} are chosen to represent a range of fires.

T_{max}(K)	900	1100	1350
t_{max}(min)	10	20	30

Nomenclature

a = constant; also pyrolysis preexponential factor
b = constant
C = specific heat
$\bar{C}$ = nondimensional specific heat $\equiv C/C_w$
E = activation energy $\equiv RT_e$
h = enthalpy
h^* = convective heat-transfer coefficient
K = thermal conductivity
$\bar{K}$ = nondimensional conductivity $\equiv K/K_w$
l = slab thickness
L = latent heat of pyrolysis $\equiv Q_p + h_g + (\rho_c h_c - \rho_w h_a)/(\rho_w - \rho_c)$
$\dot{m}_g''$ = pyrolysate mass flux $\equiv \int_x^l (\partial\rho/\partial t)dx$
$\bar{M}_g$ = nondimensional mass flux $\equiv \dot{m}'' C_w l/K_w$
$\bar{M}_L$ = nondimensional mass loss $\equiv \int_0^{\bar{t}}\int_0^1 (\partial\bar{\rho}/\partial\bar{t})d\bar{x}d\bar{t}$
$\dot{q}''$ = heat flux
Q_p = pyrolysis endothermicity referred to T_∞
$\bar{Q}$ = nondimensional enthalpy accumulated in the solid $\equiv \int_0^{\bar{t}}\int_0^1 \bar{\rho}\bar{C}(\partial\bar{T}/\partial\bar{t})d\bar{x}d\bar{t}$
R = universal gas constant
t = time
$\bar{t}$ = nondimensional time $= \alpha_w t/l^2$
T = temperature
$\bar{T}$ = nondimensional temperature $= T/T_\infty = T/300°K$
T_e = activation temperature $= E/R$
x = depth in the solid measured from the exposed surface
$\bar{x}$ = nondimensional depth $= x/l$
α = thermal diffusivity
ϵ = emissivity
ρ = density
$\bar{\rho}$ = nondimensional density $= \rho/\rho_w$
σ = Stefan-Boltzman constant

Subscripts

∞ = ambient
max = maximum
end = endurance
1.5 = when $\bar{T}_b = 1.5$
b = backface
c = final char, convective
e = activation
f = furnace flame
g = pyrolysate
i = interface, ith node in space
n = net
p = pyrolysis
r = radiant
rr = reradiant
s = exposed surface
w = original wood

Past Work

The most serious of the assumptions made in [3] relate to the time dependence of the exposure heat flux and to the simplification of pyrolysis kinetics. The nonlinearities arising in the general problem warrant the use of numerical solution techniques. Sensitivity analyses are possible to identify the properties that influence the fire endurance time of the wall. The approximate analytical results of [3] can complement the numerical work of the present paper, providing guidance in deriving general working formulae.

Kung [8] solved equations (1-6) numerically for the transient temperature, density, and gas flow rate in the interior of a single wall, but with equation (4) simplified to a prescribed constant heat flux. Bamford, Crank, and Malan [9] solved the problem numerically with a constant flame temperature, T_f. These simplifications are shown in [3] to lead to reasonable closed-form solutions. In the present work, however, the full transience of the problem is maintained by equation (4) with the $T_f(t)$ given by either equation (7) or equation (8). The calculations of [8] resulted in unrealistically high solid temperatures which, in turn, invoked extremely rapid pyrolysis rates. Retention of the transience in the boundary condition generates realistic temperatures and reveals the net effects of the exposure conditions and of the relative importance of radiative, reradiative, and convective heat fluxes.

The present work additionally deals with composite walls, i.e., walls composed of two intimately held layers of two different materials such as wood protected by a gypsum board. The equations are then adapted for each of the two materials with appropriate properties for each material. The interface is assumed to present a perfect thermal contact.

$$K_a \left.\frac{\partial T}{\partial x}\right|_{i^-} = K_b \left.\frac{\partial T}{\partial x}\right|_{i^+} ; \; T_{i^-} = T_{i^+} \tag{9}$$

The present composite wall calculations are restricted to materials having the same gas phase specific heat, and to situations where the material decomposing at lower temperatures is used on the exposed face.

Finally, the mass flux at the sealed backface is zero

$$\dot{m}_g''(l,t) = 0 \tag{10}$$

Method of Solution and Stability Requirements

The governing equations are nondimensionalized and reduced to a set of finite difference equations in [5]. Following Kung's [8] analysis, Crank-Nicholson method is used to solve the finite difference equations. This method is satisfactory for fixed boundary conditions but is rather time consuming if the boundary conditions nonlinearly depend on the current time-step solution. This difficulty is overcome by using the variable secant form (regula falsi) of the Newton-Raphson method, which provides a satisfactory iterative procedure for each unknown. Although numerical stability requirements are satisfied by the Crank-Nicholson method with no restrictions on time and spatial step sizes, it was discovered that the Arrhenius rate term imposes the dominant condition for both accuracy and stability. Instabilities in the convective term arise for materials with high activation energy because of sudden release of pyrolysates. For sufficient accuracy, the time and space step size should be chosen to satisfy

$$\left| \frac{\partial \bar{\rho}}{\partial \bar{t}} \cdot \frac{\bar{T}_e}{\bar{T}_p} \cdot \frac{\Delta \bar{T}/\Delta \bar{x}}{\bar{T}_p} \right| \leq \left| \frac{\Delta(\partial \bar{\rho}/\partial \bar{t})}{\Delta \bar{x}} \right| \tag{11}$$

where $\Delta \bar{x}$ is the space step size, $\bar{T}_p$ is nondimensional average decomposition temperature, $\bar{T}_e$ is nondimensional pyrolysis activation temperature E/RT_∞, and $\Delta \bar{T}$ is nondimensional spatial temperature increment. A change in rate of density change $|\Delta(\partial \bar{\rho}/\partial \bar{t})| \leq 0.1$ was found to give sufficient accuracy implying that

$$\frac{|\Delta \bar{T}|}{\bar{T}_p} \leq \frac{0.1}{\partial \bar{\rho}/\partial \bar{t}} \cdot \frac{\bar{T}_p}{\bar{T}_e} \tag{12}$$

$\Delta \bar{T}$ is required to be small only in the region where the pyrolysis activity is vigorous, i.e., where $\partial \bar{\rho}/\partial \bar{t}$ is large, of the order of unity. Equation (12) reduces, in the pyrolysis zone, to

$$|\Delta \bar{T}|/\bar{T}_p \leq 0.1 \; \bar{T}_p/\bar{T}_e \tag{13}$$

A low value of $\bar{T}_p$ and a high value of $\bar{T}_e$ require a small value of $\Delta \bar{T}$ to give the needed accuracy. This can be achieved by reducing the spatial step size for high activation energy materials. Step size in the pyrolysis region should be chosen small enough to permit convergence. Outside the pyrolysis region it may be chosen large under the normal constraints of accuracy.

Table 1 Fixed parameters

Thermal properties	Wood	Gypsum board
C_w(cal/g°C)	0.5	0.36
C_g(cal/g°C)	0.25	1.0
C_c(cal/g°C)	0.25	0.2
ρ_w(g/cm^3)	0.6	0.6
ρ_c(g/cm^3)	0.125	0.48
K_c/K_w	–	2.22
ϵ_s	0.8	0.8
a,(1/s)	–	3.93×10^{12}
E(kcal/mole)	–	24.0
Q_p(cal/g)	–	540
K(cal/cm s°C)	–	0.00109
T_∞(K)	300	300

Table 2 Variable parameters for wood

Parameters	Standard values	Other values
l(cm)	2	0.5, 1, 4, 8
Q_p(cal/g)	100	200
K_w(cal/cm s°C)	4.5×10^{-4}	8×10^{-4}, 2×10^{-4}
K_c/K_w	0.5	0.25, 1
ϵ_f	0.45	0.2, 0.6
[a:E][s^{-1}:(kcal/mole)]	[5.25×10^7:30]	[1.72×10^4:18][1.52×10^{11}:42]

Results and Discussion

Endurance time t_{end} is defined in this study as the time at which significant pyrolysis occurs at the backface. It is an indicator of the structural integrity of the wall exposed to fire. Resistance time $t_{1.5}$, on the other hand, is defined as the time the backface takes to attain an absolute temperature of one-and-a-half times the initial ambient absolute temperature. $t_{1.5}$ is an indicator of the wall's ability to resist fire penetration. Most of the computations discussed below are made with the ASTM/ISO standard $T_f(t)$ exposure (Fig. 1) on walls of wood, gypsum board, and gypsum board backed by wood. In the study of wood walls attention is focused on the sensitivity of endurance time to a variety of exposure and material properties; studies of gypsum, with and without wood-backing, are intended to obtain a comparative measure of fire performance. In the same vein, the peaked $T_f(t)$ exposure (Fig. 2) is used only in a few cases on wood walls to establish the role played by the exposure history.

Representative [4,5,9,10] fixed values of the thermophysical and chemical properties of wood and of gypsum board are given in Table 1. Table 2 gives the properties which are chosen for parametric variation. The first column gives a set of property values which characterize a "standard wood slab." The second column gives other considered values of each parameter. In a typical calculation, one parameter of the standard set is varied over the values shown in the second column, holding the other five parameters fixed at their standard values.

(a) General Nature. The general nature of the numerical solutions is shown in Fig. 3, which depicts the transient

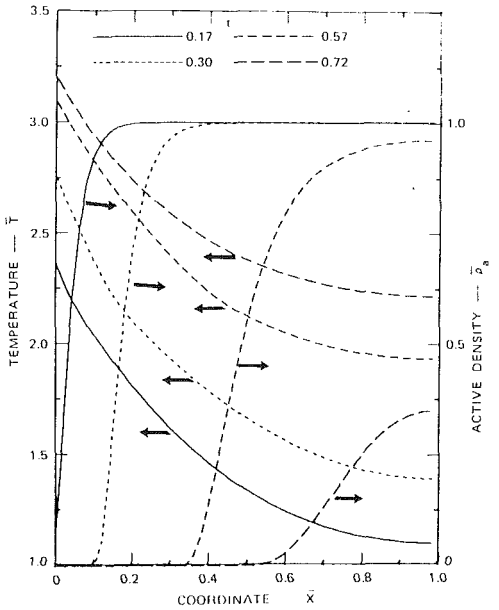

Fig. 3 Temperature and density profiles in standard wood exposed to standard $T_f(t)$

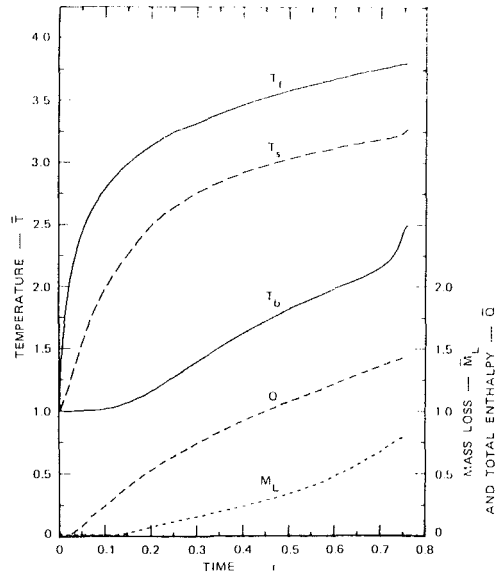

Fig. 4a Temperatures, mass loss and accumulated energy in standard wood exposed to standard $T_f(t)$

temperature and density profiles in the standard wood slab for the standard exposure. It is clear from this figure that the thickness in the solid over which pyrolysis occurs actively is finite and increases with time. This is in contrast with the assumption of zero-thickness pyrolysis front made in [3]. This departure makes the approximation that the temperature profile is linear in space, questionable. Not withstanding this difference the integrated behavior of slab charring is found to be remarkably close to the approximate predictions of [3].

(b) **Overall Characteristics.** The temporal history of the prescribed furnace temperature, $\bar{T}_f(\bar{t})$, the computed exposed surface temperature, $\bar{T}_s(\bar{t})$, and the computed backface temperature, $\bar{T}_b(\bar{t})$, are shown explicitly for the standard wood slab in Fig. 4. The internal temperature profiles when integrated spatially yield the total energy accumulation $\bar{Q}$ in the solid as a function of time. Similarly, integration of the density profiles across the entire slab thickness will result in the total mass lost $\bar{M}_L$ as a function of time. Both these quantities are additionally presented in Fig. 4.

It is evident that the exposed surface temperature $\bar{T}_s$ faithfully exhibits the exposure pattern. The accumulated heat $\bar{Q}$ and the total mass lost $\bar{M}_L$ are relatively insensitive to the exposure furnace temperature-time history. The backface temperature $\bar{T}_b$ is also relatively invariant with the time-dependent thermal driving forces which are distinctly different between the two types of exposures. This is probably due to the compensation mechanism provided by surface reradiation as discussed in section (c) below. The specific shape of the temperature-time exposure curve therefore exerts only a minor effect on the net heat flux and hence, on the endurance time of a reradiating wall. This finding justifies the exposure-flux-related approximation of [3].

(c) **Surface Heat-Flux Partition.** Shown in Fig. 5 are typical components of the exposed surface flux. The convective flux is comparable in magnitude to the radiative flux for only a short initial duration irrespective of the exposure pattern. At longer times (i.e., $\bar{t} \geq 0.2$) it can be neglected to justify the approximation of [3]. The radiative and reradiative components are nearly linearly related to one another in both the standard and peaked exposures.

The net flux exhibits a maximum near 0.2 cal/cm^2 s independent of the slab thickness, and the exposure ($T_f(t)$) history. The net flux at longer times reaches, even if briefly, a

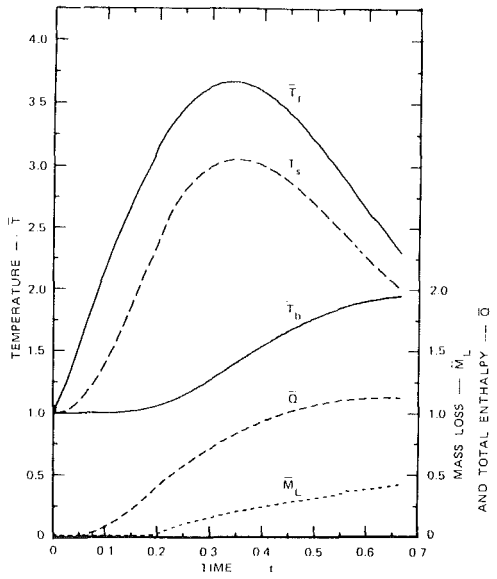

Fig. 4b Temperatures, mass loss and accumulated energy in standard wood exposed to peaked $T_f(t)$: T_{max} = 1100°C, t_{max} = 30 min

nearly constant value for the ASTM/ISO exposure—this effect being more pronounced for thicker slabs. The numerical value of this net flux constant is near 0.1 cal/cm^2 s for thinner samples and near 0.05 cal/cm^2 s for thicker ones. Even though this net flux seems to be lower for thicker samples, the incoming radiative exposure heat flux reaches, for 8-cm thick slab, as high as 3 cal/cm^2 s. However, the reradiative flux also being high, the net flux is reduced. Thick slabs, thus, offer a two-fold advantage to enhance fire endurance time: they are in the diffusivity-controlled asymptotic regime of $\bar{t}_{1.5}$ = constant (see *(d)* below); and their surface heat balance results in high surface temperatures to reradiate most of the incoming radiation flux.

Although the maximum net flux for the $T_f(t)$ exposure of Fig. 2 is same in magnitude as for the ASTM/ISO $T_f(t)$ exposure, this maximum is somewhat delayed in time. The heat flux drops to zero as the fuel in the compartment is consumed.

(d) **Variation of Endurance and Resistance Time with Slab Thickness.** Figure 6 shows the variation of endurance and resistance times with the slab thickness and solid conductivity.

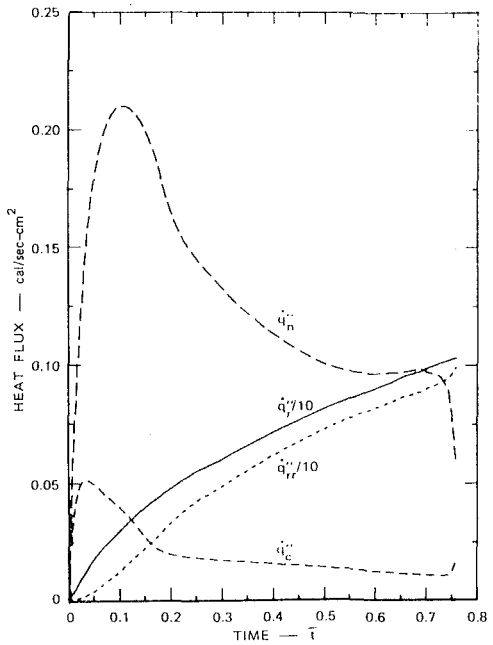

Fig. 5a Heat flux inventory of a standard wood exposed to standard $T_f(t)$

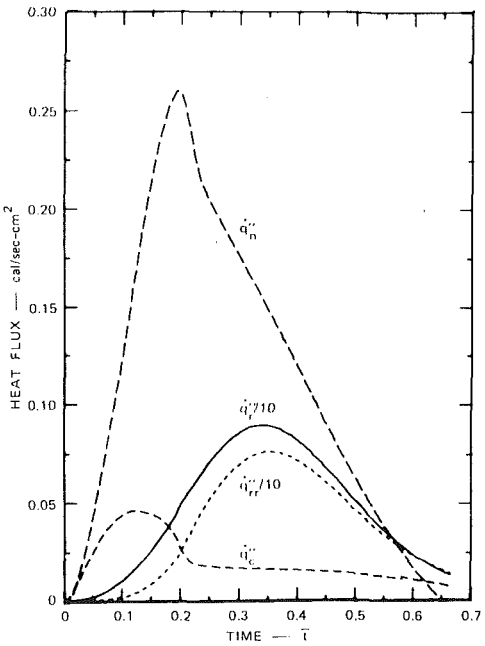

Fig. 5b Heat flux inventory of a standard wood exposed to a peaked $T_f(t)$: T_{max} = 1100°C, t_{max} = 30 min

The thickness-dependence may be expressed in the form $t_{1.5} \propto l^n$, with $n = 1$ for slabs of thickness ≤ 1 cm and $n = 2$ for slabs of thickness ≥ 4 cm. The endurance time of thick walls thus depends weakly on the thermochemical properties of the wall material and strongly on thermal transport properties such as diffusivity. This finding is in excellent accord with the results of both [2] and [3] indicating that the thermal penetration into the interior of the wall is not overly sensitive to the transience of the exposure heat flux; rather, the thermal fluence, i.e., time integrated heat flux, is of primary importance.

Figure 6 also indicates that the dependence of t_{end} on l is closely parallel to that of $t_{1.5}$. This parallelism, firmly demonstrated by the approximate analyses and corroborated by several available experimental data [3], not only relates the char-front-arrival criterion with the prescribed temperature-rise criterion, but also points out how faithfully the pyrolysis

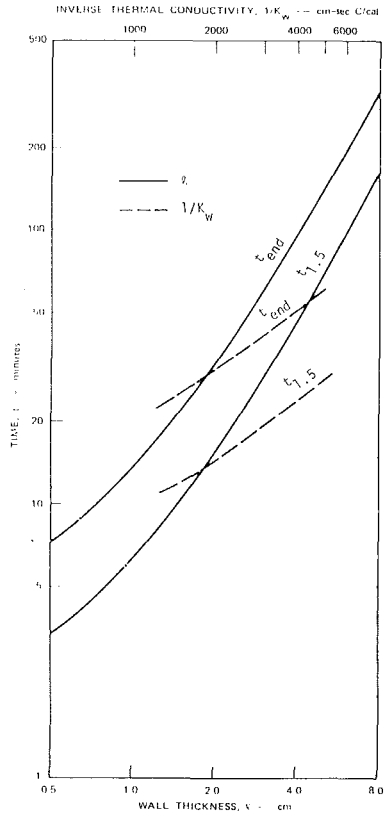

Fig. 6 Effect of slab thickness and wood conductivity on endurance and resistance times

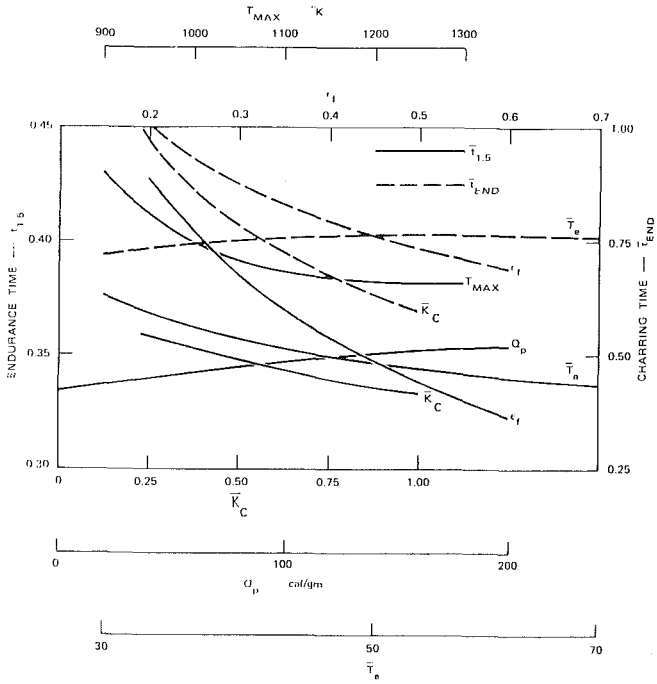

Fig. 7 Sensitivity of t_{end} and $t_{1.5}$ to variations in latent heat Q_p, activation temperature $\bar{T}_e$, furnace flame emissivity ϵ_f, maximum temperature of peaked $T_f(t)$, and char conductivity $\bar{K}_c$

wave follows the thermal wave suggesting that the complex pyrolysis process may be represented by a simplified vaporization and phase change process as done in [3].

***(e)* Effect of Heat of Pyrolysis.** As evident from Fig. 7, the endurance time of wood slabs is relatively insensitive to the heat of pyrolysis. This appears to be in minor disagreement

with the approximate solutions of [3] where the pyrolysis endothermicity is noted to contribute an appreciable energy sink. However, apparently the benefit of these sinks is not realizable unless the active pyrolysis temperature range (determined by the pyrolysis activation energy) is in the vicinity of, if not below, the temperature chosen for the endurance criterion. The predicted $\bar{T}_b(t)$ profile of Fig. 4 appears to indicate the role of pyrolysis heat sink which manifests itself in an apparent plateau at about $\bar{T}_b \approx 1.7$. Nonetheless, a higher value of heat of pyrolysis does exert a noticeable effect on the total charring time, t_{end}.

(*f*) Effect of Wood Conductivity, K_w. The virgin wood conductivity exerts a strong effect on the endurance time. The results shown in Fig. 6 indicate a nearly inverse linear relation between the endurance and resistance times and K_w. This finding is consistent with one's expectation that a higher conductivity facilitates energy transport, leading to faster charring in agreement with the approximate solutions of [3].

Thermal conductivity plays a dual role in determining the endurance time: first, it directly controls the transfer of heat to the backface and thus its temperature rise; second, a lower thermal conductivity causes the exposed surface temperature to be higher, which in turn increases the reradiative loss of heat to reduce the net flux into the solid. A fourfold decrease in conductivity is found to nearly double the reradiative loss.

(*g*) Effect of the Char Conductivity, K_c. Figure 7 indicates that the char thermal conductivity affects the endurance time only weakly if the critical endurance temperature is lower than the decomposition (or charring) temperature. Only 20 percent of the wall has been found to char when the backface reaches the critical temperature. K_c becomes an important factor in determining the endurance time only if appreciable char information occurs before the backface attains the critical temperature.

(*h*) Effect of the Furnace Flame Emissivity, ϵ_f. The furnace emissivity as shown in Fig. 7 exerts an effect on the surface energy flux. A three-fold increase in ϵ_f produces only a 30 percent decrease in the endurance time. Thus, although the furnace emissivity intuitively seems to be important, its effect is not as strong as one might suspect. The underlying reason appears to be that as a three-fold increase in ϵ_f would cause an 80 percent increase in the peak net heat flux, the resultant higher surface temperature would also increase the reradiative flux. Consequently, the endurance or resistance time is affected rather weakly.

(*i*) Effect of T_{max} in Peaked $T_f(t)$ Exposure. With the peaked $T_f(t)$ exposure, Fig. 7 indicates that the endurance time is decreased by about a mere 12.5 percent over the three considered values of T_{max} and only 1.5 percent between T_{max} = 1000 and 1350 K. The endurance time under these conditions is only 10.5 percent greater than under the standard $T_f(t)$ exposure conditions.

(*j*) Effects of the Pyrolysis Constants. The decomposition temperature for wood is known [10, 11] to be about 350°C. The activation energy, however, is not as well characterized. In [5], values for the activation energy and preexponential factor are adjusted in pairs to give essentially the same average decomposition temperature (350°C). As the pair [a, T_e] increases, decomposition becomes more abrupt approaching the average value of T_p ($\approx$350°C).

Figure 7 shows that doubling the activation energy gives only an 8 percent decrease in endurance time, demonstrating that knowledge of the decomposition temperature is more important than the exact kinetics. This is in accord with the point made in item (*d*) above and with the assumption of a unique decomposition temperature T_p made in [3]. It may be important to know if several pyrolysis steps occur in different temperature ranges, especially if some of these steps are exothermic and others endothermic, and if they occur at temperatures below and above the critical temperature.

(*k*) Gypsum Board Exposed to Standard $T_f(t)$ Fire. The desorption of the water of hydration of gypsum board occurs rather abruptly at the normal boiling point of water, that is, the desorption process has an apparent activation energy approaching infinity. Difficulties associated with numerical instabilities due to this high activation energy may be overcome by choosing a finer spatial grid in the decomposition region. However, since our numerical code is not set up to handle a varying mesh size we resort to a grid fine enough to yield reasonable convergence and yet not so fine as to be unreasonable in terms of CPU time. Further, since the endurance time is not particularly sensitive to the activation energy, the activation energy for the water desorption process is lowered until reasonable ($\approx +15$ percent error) accuracy is obtained.

The evaporating water suppresses the temperatures of both the exposed surface and the backface until all the water is nearly gone. Although the suppressed surface temperature increases the net heat flux, the high latent heat of vaporization of water strongly compensates. Note here that decomposition occurs at a temperature *below* the usual critical temperature. The resultant endurance time is about 3 percent lower than that of an equivalent standard wood wall, an insignificant difference. Even though gypsum board has a higher thermal diffusivity than wood, the energy sink due to moisture overshadows the diffusional effects.

(*l*) Gypsum Board with Wood Backing. In this case, a 1-cm thick slab of gypsum board backed by a 1-cm thick wood slab is considered. The standard $T_f(t)$ exposure is taken. Water in the gypsum board evaporates quickly, suppressing the surface temperature and giving a high net heat flux as in the case of gypsum board alone. As soon as all the water is lost, the surface temperature and reradiation increase rapidly. In addition, the backface temperature rises rapidly whereas the total heat absorption, $\bar{Q}$, rises less rapidly with time. The result is an endurance time of about 20 percent less than that offered by wood or gypsum board alone. ($t_{1.5} \approx 15.4$ min for wood alone, 14.9 min for gypsum alone and 12.5 min for the composite.) This nonlinear result is surprising and not predictable from approximate solutions [3].

A plausible explanation of this nonlinear result requires a comparison of pure gypsum board with the composite wall. Calculations show that the composite wall requires the same length of time to evaporate water as does the pure gypsum board for the same amount of water. However, after the water is gone from the composite solid, there remains a front slab of dry gypsum board of relatively high thermal diffusivity backed by wood of lower thermal diffusivity and essentially little latent heat absorption capabilities. Because the thermal diffusivity of gypsum is much larger than that of wood, heat transfer will be controlled primarily by the wood section of the slab. The wood section being only half as thick, the endurance time is more dependent on the slab thickness than on the thermal diffusivity. Heat transfer to the backface then occurs more rapidly than for a high thermal diffusivity, high latent heat backing such as gypsum board.

Conclusions and Recommendations

The exact solutions of this paper considerably improve the existing insight into the factors affecting the fire endurance time of wood walls with and without gypsum board protection. They also lead to validation of a number of approximations used in [3] in obtaining simpler closed-form solutions. Specifically, the following conclusions were reached:

(*i*) Heat transfer from the furnace to the specimen surface is predominantly radiative. The reradiative heat losses from the exposed surface are as important as the furnace exposure conditions, the balance of the two determining the net thermal loading of the specimen.

(*ii*) The pyrolysis process is confined to a thin spatial zone except at long times when the front nears the backface. The approximation that pyrolysis occurs abruptly at a given temperature seems fairly reasonable.

(*iii*) The precise time-wise pattern of the exposure furnace appears to be irrelevant in determining the charring rate and fire endurance of slabs under normal fire loading conditions.

(*iv*) The dimensional analysis, approximate solutions, exact solutions, and experimental data are all consistent in giving a relationship for the dependence of endurance time on the slab thickness: $t_{end} = al + bl^2$ where a is a function of enthalpy terms and as an approximation can be characterized [12] by a lumped mass transfer number B', $a \propto (B')^{-1}$, and b is a function of thermal diffusivity α, $b \propto (\alpha)^{-1}$. Current and future experimental results should be correlated accordingly, developing more precisely the dependence of a and b on the wall thermal properties and exposure heat flux.

Acknowledgments

The work reported here is initiated under partial support from the National Bureau of Standards, Center for Fire Research under Contract (No. 4-36105) with SRI International. The authors thank Mr. D. Gross of NBS for his advice in this work, Dr. H. C. Kung of Factory Mutual for his help in adapting his pyrolysis code to our problem, Lynn Cohen for suggesting rapid numerical convergence techniques, and Mr. Stanley B. Martin for all the encouragement given to us.

References

1 *1977 Annual Book of ASTM Standards, Part 18,* American Society for Testing and Materials, 1916 Race Street, Philadelphia, Pennsylvania, 1977, pp. 739-759.

2 Kanury, A. M., and Holve, D. J., "Response of Building Components to Heating in a Fire," ASME JOURNAL OF HEAT TRANSFER, Vol. 101, No. 2, May 1979, pp. 365-370.

3 Kanury, A. M., and Holve, D. J., "Transient Conduction with Pyrolysis (Approximate Solutions for Charring of Wood Slabs)," Submitted to ASME JOURNAL OF HEAT TRANSFER, Apr. 1981.

4 Kanury, A. M., and Blackshear, P. L. Jr., "On the Combustion of Wood: II: The Influence of Internal Convection on the Transient Pyrolysis of Cellulose," *Combustion Science and Technology*, Vol. 2, 1970, pp. 5-9.

5 Kanury, A. M., and Holve, D. J., "A Theoretical Analysis of the ASTM E-119 Standard Fire Test of Building Construction and Materials," Final Report of National Bureau of Standards Contract No. 4-36105, Stanford Research Institute, Menlo Park, California, 94025, 1975.

6 Butcher, E. G., Chitty, T. B., and Ashton, L. A., "The Temperature Attained by Steel in Building Fires," Fire Research Technical Paper No. 15, Fire Research Station, Borehamwood, Herts, England, 1966.

7 Robertson, A. F., and Gross, D., "Fire Load, Fire Severity, and Fire Endurance," *ASTM STP 464,* American Society for Testing and Materials, Washington, D.C., 1969, pp. 3-29.

8 Kung, H. C., "A Mathematical Model of Wood Pyrolysis," *Combustion and Flame*, Vol. 18, 1972, pp. 185-195.

9 Bamford, C. H., Crank, J., and Malan, D. H., "The Combustion of Wood," *Proceedings of Comb. Phil. Soc.,* Vol. 46, 1946, pp. 166-182.

10 Kanury, A. M., and Blackshear, P. L. Jr., "Some Considerations Pertaining to the Problem of Wood-Burning," *Combustion Science and Technology*, Vol. 1, 1970, pp. 339-355.

11 Kanury, A. M., "Thermal Decomposition Kinetics of Wood Pyrolysis," *Combustion and Flame*, Vol. 18, 1972, pp. 75-83.

12 Kanury, A. M., "Rate of Charring Combustion in a Fire," *14th Symposium (International) on Combustion*, The Combustion Institute, Pittsburgh, Pennsylvania, 1973, pp. 1131-1142.

M. N. Özisik
Mechanical and Aerospace Engineering Department,
North Carolina State University,
Raleigh, N.C. 27650
Mem. ASME

Y. Yener[1]
Mechanical and Aerospace Engineering Department,
University of Delaware,
Newark, Del. 19711

The Galerkin Method for Solving Radiation Transfer in Plane-Parallel Participating Media

The Galerkin method is applied to solve radiative heat transfer in an isotropically scattering, absorbing, and emitting plane-parallel medium with diffusely reflecting boundaries. In this approach, the integral form of the equation of radiative transfer is transformed into a set of algebraic equations for the determination of the expansion coefficients associated with the representation of the incident radiation in a power series in the space variable. The method is easy and straightforward to apply and requires relatively little computer time for the computations, since explicit analytical expressions are obtainable for the expansion coefficients.

Introduction

Various methods utilizing an expansion in the space variable have been reported in the literature for the solution of the neutron transport equation and the equation of radiative transfer [1–8]. In all these methods a suitable expansion, usually the Legendre polynomial expansion in the space variable, is applied to reduce the problem to the solution of a set of algebraic equations for the expansion coefficients associated with the representation of the source function. The advantage of an expansion in the space variable lies in the fact that the convergence of the solution is fast. When the Legendre polynomial expansion is used it becomes very cumbersome to obtain analytical expressions for the higher order coefficients; as a result, the coefficients for the higher order solutions should be calculated numerically. The use of the Galerkin method, however, leads to a power series expansion in the space variable, which makes it possible to determine explicit analytical expressions for the expansion coefficients of any order.

Formulation of the Problem

We consider the problem of radiative heat transfer in an absorbing, emitting, isotropically scattering, plane-parallel, and gray medium of optical thickness, a, between two diffusely reflecting, diffusely emitting, opaque, and gray bounding surfaces given in the form [9]

$$\mu\frac{\partial I(x,\mu)}{\partial x}+I(x,\mu)=(1-\omega)H(x)+\frac{\omega}{2}\int_{-1}^{1}I(x,\mu')\,d\mu' \quad (1a)$$

$$\text{in } 0\le x\le a \quad , \quad -1\le\mu\le 1$$

$$I(0,\mu)=A_1+2\rho_1\int_0^1 I(0,-\mu')\,\mu'\,d\mu' \quad , \quad \mu>0 \quad (1b)$$

$$I(a,-\mu)=A_2+2\rho_2\int_0^1 I(a,\mu')\,\mu'\,d\mu' \quad , \quad \mu>0 \quad (1c)$$

where

$$H(x)=\frac{n^2\bar{\sigma}T^4(x)}{\pi} \quad (2a)$$

$$A_k=\epsilon_k\frac{n^2\bar{\sigma}T_k{}^4}{\pi} \quad , \quad k=1,2 \quad (2b)$$

Here, x is the optical variable, μ is the cosine of the angle between the positive x-axis and the direction of radiation intensity $I(x,\mu)$, ϵ_1 and ϵ_2 are the emissivities, ρ_1 and ρ_2 are the diffuse reflectivities, and T_1 and T_2 are the temperatures of the bounding surfaces, and $T(x)$ is the temperature distribution in the medium. Furthermore, n is the refractive index, ω is the single scattering albedo of the medium and $\bar{\sigma}$ is the Stefan-Boltzmann constant.

The problem defined by equations (1) is now split up into simpler problems by following the approach discussed in reference [7] as

$$I(x,\mu)=I_1(x,\mu)+(A_1+2\rho_1K_1)I_2(x,\mu)+(A_2+2\rho_2K_2)I_2(a-x,-\mu) \quad (3)$$

where

$$K_1=\int_0^1 I(0,-\mu')\,\mu'\,d\mu' \quad (4a)$$

and

$$K_2=\int_0^1 I(a,\mu')\,\mu'\,d\mu' \quad (4b)$$

and the intensity functions $I_i(x,\mu)$, $i=1,2$, are the solutions of the following two simpler problems:

$$\mu\frac{\partial I_i(x,\mu)}{\partial x}+I_i(x,\mu)=\delta_{i1}(1-\omega)H(x)+\frac{\omega}{4\pi}G_i(x) \quad (5a)$$

$$\text{in } 0\le x\le a \quad , \quad -1\le\mu\le 1$$

$$I_i(0,\mu)=\delta_{i2} \quad , \quad \mu>0 \quad (5b)$$

$$I_i(a,-\mu)=0 \quad , \quad \mu>0 \quad (5c)$$

where δ_{ij} is the Kronecker delta and

$$G_i(x)=2\pi\int_{-1}^{1}I_i(x,\mu')\,d\mu' \quad , \quad i=1,2 \quad (6)$$

It is easier to solve the problems for $I_i(x,\mu)$ defined by equations (5) than the more general problem for $I(x,\mu)$ defined by equations (1); but to determine $I(x,\mu)$ from equation (3), we need to know the coefficients K_1 and K_2. To establish the relations for the calculation of K_1 and K_2, equation (3) is evaluated first at $x=0$ and at $x=a$, and then the resulting expressions for $I(0,-\mu)$ and $I(a,\mu)$ determined in this manner are introduced into equations (4*a*) and (4*b*). Thus, we obtain the following two equations for the determination of K_1 and K_2:

$$K_1=Q_1(0)+(A_1+2\rho_1K_1)Q_2(0)+(A_2+2\rho_2K_2)Q_2(a) \quad (7a)$$

$$K_2=Q_1(a)+(A_1+2\rho_1K_1)Q_2(a)+(A_2+2\rho_2K_2)Q_2(0) \quad (7b)$$

where

$$Q_i(0)=\int_0^1 I_i(0,-\mu')\,\mu'\,d\mu' \quad , \quad i=1,2 \quad (8a)$$

$$Q_i(a)=\int_0^1 I_i(a,\mu')\,\mu'\,d\mu' \quad , \quad i=1,2 \quad (8b)$$

[1] Permanent address, Mechanical Engineering Department, Middle East Technical University, Ankara, Turkey.

Contributed by the Heat Transfer Division for publication in the JOURNAL OF HEAT TRANSFER. Manuscript received by the Heat Transfer Division August 20, 1981.

Here, $Q_i(0)$ and $Q_i(a)$ are considered known quantities when the intensities I_i $(0, -\mu)$ and I_i (a, μ), $\mu > 0$, are available from the solution of the simpler problems (5). Equations (8*a*) and (8*b*) provide two independent relations for the determination of the coefficients K_1 and K_2. Knowing K_1 and K_2, the intensity $I(x, \mu)$ is determined from equation (3). Then, the net radiative heat flux $q^r(x)$ anywhere in the medium is evaluated from

$$q^r(x) = q^+(x) - q^-(x) \tag{9a}$$

with the forward and backward radiative heat flux components expressed as

$$q^+(x) = q_1^+(x) + (A_1 + 2\rho_1 K_1) q_2^+(x) + (A_2 + 2\rho_2 K_2) q_2^-(a-x) \tag{9b}$$

$$q^-(x) = q_1^-(x) + (A_1 + 2\rho_1 K_1) q_2^-(x) + (A_2 + 2\rho_2 K_2) q_2^+(a-x) \tag{9c}$$

where

$$q_i^+(x) = 2\pi \int_0^1 I_i(x, \mu')\mu' d\mu' \quad , \quad i = 1,2 \tag{10a}$$

$$q_i^-(x) = 2\pi \int_0^1 I_i(x, -\mu')\mu' d\mu' \quad , \quad i = 1,2 \tag{10b}$$

which can be determined once the intensities $I_i(x, \mu)$ are available. The Galerkin method can now be applied to solve these problems as described next.

Solution by the Galerkin Method

Galerkin [10], in 1915, proposed an approximate method of analysis for boundary-value problems. A discussion of the theory and application of this method is given in several references [11-15]. In order to apply the Galerkin method, we focus our attention to the integral form of equation (5*a*) for the incident radiation $G_i(x)$, written as [9]

$$\mathcal{L}\{G_i(x)\} \equiv G_i(x) - F_i(x) - \omega \int_0^a K(x,x') G_i(x') dx' = 0 \tag{11a}$$

with

$$K(x,x') = \frac{1}{2} E_1(|x - x'|) \tag{11b}$$

$$F_i(x) = 2\pi \left\{ \delta_{i2} E_2(x) + \delta_{i1}(1-\omega) \int_0^a E_1(|x-x'|) H(x') dx' \right\} \tag{11c}$$

where $E_n(x)$ are the exponential integral functions.

We now consider a power series representation in the space variable x of the functions $G_i(x)$ as

$$G_i(x) = \sum_{n=0}^{N} C_{i,n} x^n \quad , \quad i = 1,2 \tag{12}$$

where $C_{i,n}$ are the unknown expansion coefficients which are yet to be determined. The Galerkin method can now be applied to the integral equation (11*a*) as

$$\int_0^a \mathcal{L}\left\{ \sum_{n=0}^{N} C_{i,n} x^n \right\} x^m dx = 0, \quad m = 0,1,2, \ldots, N \tag{13}$$

which yields $N + 1$ algebraic equations for the determination of the expansion coefficients for each i. The results given by equation (13) are written more compactly as

$$\sum_{n=0}^{N} B_{mn} C_{i,n} = A_{i,m} \quad , \quad m = 0,1,2, \ldots, N; \quad i = 1,2 \tag{14}$$

where

$$A_{i,m} = 2\pi \left\{ \delta_{i2} \int_0^a E_2(x) x^m dx + \delta_{i1}(1-\omega) \int_0^a \int_0^a E_1(|x-x'|) H(x') x^m dx dx' \right\} \tag{15a}$$

$$B_{mn} = \frac{a^{m+n+1}}{m+n+1} - \frac{\omega}{2} \int_0^a \int_0^a E_1(|x-x'|) x^m x'^n dx dx' \tag{15b}$$

The analytical expressions for various integrals appearing in the above equations are listed in the Appendix.

Once the expansion coefficients are determined from equation (14) and, hence the functions $G_i(x)$ are available, then the forward and backward radiation intensities and the radiative heat flux components are readily obtained in terms of the functions $G_i(x)$ as described in [9].

Nomenclature

A_1, A_2 = radiation intensities emitted by the boundaries at $x = 0$ and $x = a$, as defined by equation (2*b*)
a = optical thickness
$A_{i,m}, B_{mn}$ = constants defined by equations (15*a*) and (15*b*), respectively
$C_{i,n}$ = expansion coefficients defined by equation (14)
$E_n(x)$ = exponential integral function
$G_i(x)$ = incident radiation defined by equation (6)
$H(x)$ = radiation intensity emitted by the medium, defined by equation (2*a*)
$I(x,\mu)$ = radiation intensity
K_1, K_2 = constants defined by equations (4*a*) and (4*b*)
$K(x,x')$ = kernel
N = order of solution
n = refractive index
$Q_i(0), Q_i(a)$ = constants defined by equations (8)
$q^r(x)$ = net radiative heat flux
$q^+(x), q^-(x)$ = forward and backward half-range fluxes
R = hemispherical reflectivity defined by equation (16*a*)
$T(x)$ = temperature distribution in the slab
T_1, T_2 = temperatures at the bounadries $x = 0$ and $x = a$
x = optical variable
ϵ_1, ϵ_2 = emissivities of the boundaries $x = 0$ and $x = a$
μ = direction cosine
ρ_1, ρ_2 = reflectivities of the boundaries $x = 0$ and $x = a$
$\bar{\sigma}$ = Stefan-Boltzmann constant
Γ = transmissivity as defined by equation (16*b*)
ω = single scattering albedo

Table 1 The hemispherical reflectivity and transmissivity of a slab with a reflecting boundary at $x = a$ and a transparent boundary at $x = 0$ (radiation is incident at $x = 0$)

ω	Wall reflectivity at $x=a$	$a=0.5$			$a=1.0$			$a=2.0$		
	ρ_2	R	Γ	N†	R	Γ	N	R	Γ	N
0.0	0.0	0.0	0.4432	1	0.0	0.2194	1	0.0	0.0603	1
	0.5	0.0982	0.2216	1	0.0241	0.1097	1	0.0018	0.0301	1
	1.0	0.1964	0.0	1	0.0481	0.0	1	0.0036	0.0	1
0.5	0.0	0.1077	0.5350	4	0.1342	0.3067	5	0.1451	0.1071	6
	0.5	0.2589	0.2827	3	0.1846	0.1644	5	0.1513	0.0577	6
	1.0	0.4284	0.0	3	0.2428	0.0	5	0.1585	0.0	6
1.0	0.0	0.2958	0.7042	2	0.4466	0.5534	2	0.6099	0.3901	2
	0.5	0.5868	0.4132	2	0.6437	0.3563	2	0.7193	0.2807	2
	1.0	1.0	0.0	1	1.0	0.0	1	1.0	0.0	1

†N is the order of solution.

Applications

As a first illustration of the accuracy of the present method of analysis, we consider the radiation problem for a slab with $A_1 = 1$, $\rho_1 = A_2 = H(x) = 0$. Clearly, this particular case corresponds to a physical situation in which the boundary at $x = 0$ of the slab is transparent and irradiated by an isotropic radiation of unit intensity, the boundary at $x = a$ has a diffuse reflectivity ρ_2, while the contributions of the emission terms $H(x)$ and A_2 from the medium and the wall at $x = a$ are considered negligible. For this particular case, we list in Table 1 the hemispherical reflectivity and transmissivity of the slab as determined from

$$R = \frac{q^-(0)}{\pi} \tag{16a}$$

and

$$\Gamma = (1-\rho_2)\frac{q^+(a)}{\pi} \tag{16b}$$

for various values of the optical thickness a, the diffuse reflectivity ρ_2 and the single scattering albedo ω. In obtaining the results given in Table 1, the order of the approximation (i.e., the value of N) was so selected that absolute values of the differences between the values of R and Γ corresponding to $N-1$ and N were less than 10^{-5}. The value of N selected for each case is also indicated in Table 1. In Table 2, we list the hemispherical reflectivity R for various orders of solution, together with the exact results for optical thicknesses $a = 0.5$, 1, 2 and for various values of ω when the diffuse reflectivity of the boundary at $x = a$ is $\rho_2 = 1.0$. The exact results in Table 2 are the ones calculated by using the singular eigenfunction expansion technique and have been taken from reference [9].

As a second example, we consider the radiation problem for a slab with $H(x) = 1, A_1 = A_2 = \rho_1 = \rho_2 = 0$. This particular case is chosen, because exact results are available in the literature for certain cases. We list in Table 3 the values of the exit flux $q^+(a)$ for an optical thickness $a = 1$, determined from its definition

$$q^+(a) = 2\pi\int_0^1 I(a,\mu')\mu' d\mu' \tag{17}$$

together with the exact results taken from reference [7]. Also included in this Table is the order of solution, N, used for the Galerkin method. In addition, because of symmetry, we have $q^+(a) = q^-(0)$.

Conclusions

The present method provides a very simple and straightforward approach for the solution of radiation transfer in absorbing, emitting and isotropically scattering media compared to the singular eigenfunction expansion technique and various other approximate methods of solution. Over the range of parameters considered in this paper, the convergence of the solution is found to be extremely fast; even the lowest

Table 2 The accuracy of the Galerkin method in determining the hemispherical reflectivity of a slab with a reflecting boundary at $x = a$ and a transparent boundary at $x = 0$ for $\rho_2 = 1.0$ (radiation is incident at $x = 0$)

ω	Order of the approximation N	Hemispherical reflectivity $a=0.5$	$a=1.0$	$a=2.0$
0.1	0	0.23077	0.07265	0.01723
	1	0.23120	0.07503	0.02394
	3	0.23134	0.07563	0.02599
	4		0.07564	0.02604
	5			0.02605
	Exact	0.2312	0.0756	0.0261
0.5	0	0.42675	0.23110	0.11398
	1	0.42802	0.24062	0.14962
	3	0.42843	0.24278	0.15831
	5		0.24281	0.15848
	6			0.15849
	Exact	0.4284	0.2428	0.1585
0.9	0	0.82592	0.69702	0.53022
	1	0.82615	0.70025	0.55756
	3	0.82622	0.70090	0.56242
	5			0.56246
	Exact	0.8262	0.7009	0.5626
0.95	0	0.90693	0.82760	0.70402
	1	0.90700	0.82874	0.71652
	3	0.90702	0.82897	0.71868
	5			0.71870
	Exact	0.9070	0.8290	0.7187
0.995	0	0.99007	0.98032	0.96136
	1		0.98033	0.96161
	2			0.96165
	Exact	0.9901	0.9803	0.9617

Table 3 The exit flux $q^+(a)$ for a slab of optical thickness $a = 1$ with $H(x) = 1, A_1 = A_2 = \rho_1 = \rho_2 = 0$

ω	Galerkin method	Order of the solution N	Exact result
0.0	2.4524	0	2.4523
0.1	2.3480	4	2.3472
0.2	2.2299	4	2.2290
0.3	2.0949	4	2.0955
0.4	1.9391	2	1.9391
0.5	1.7565	8	1.7565
0.6	1.5399	2	1.5399
0.7	1.2778	2	1.2778
0.8	0.9538	2	0.9538
0.9	0.5421	2	0.5421
0.950	0.2910	2	
0.995	0.0312	0	

order solutions yield results which are sufficiently close to the exact values that are computed with the singular eigenfunction expansion technique. By carrying out the computations to higher order terms, the exact results are obtainable with the present method. In the present method, the numerical computations required very little computer time, because all the integrals appearing in the expansion coefficients could be performed analytically. With significant reduction achieved in the computation time, this method can be attractive for use in the analysis of the problems of interaction of radiation with convection and conduction in participating media. It can also be extended to solve the problems of radiation in composite media consisting of parallel layers of slabs, to problems with anisotropic scattering and to other geometries.

Acknowledgments

One of the authors, Y. Yener, acknowledges the hospitality extended to him by the Mechanical and Aerospace Engineering Department of the University of Delaware, Newark, Delaware, during his stay.

This work was supported in part through a grant by the National Science Foundation, No. MEA 8110705.

References

1 Asaoka, T., "Space-Angle Energy-Time Dependent Neutron Transport in a Homogeneous Slab by the J_N Method," *Nuclear Science and Engineering*, Vol. 34, 1968, pp. 122–133.

2 Kschwendt, H., "Application of the J_N Method in Neutron Transport in Slabs and Spheres," *Nuclear Science and Engineering*, Vol. 36, 1969, pp. 447–450.

3 Kschwendt, H., "Legendre Expansion and Integral Equations of Displacement Type," *Journal of Computational Physics*, Vol. 5, 1970, pp. 84–102.

4 Boffi, V. C., Santarelli, F., and Stramigioli, C., "Integral Transform Method in Radiative Transfer," *Journal of Quantitative Spectroscopy and Radiative Transfer*, Vol. 18, 1977, pp. 189–203.

5 Boffi, V. C., and Spiga, G., "Integral Theory of Radiative Transfer with Anisotropic Scattering and General Boundary Conditions," *Journal of Mathematical Physics*, Vol. 18, 1977, pp. 2443–2455.

6 Sutton, W. H., and Özişik, M. N., "A Fourier Transform Solution for Radiative Transfer in a Slab with Isotropic Scattering and Boundary Reflection," *Journal of Quantitative Spectroscopy and Radiative Transfer*, Vol. 22, 1979, pp. 55–64.

7 Özişik, M. N., and Sutton, W. H., "A Source Function Expansion in Radiative Transfer," ASME JOURNAL OF HEAT TRANSFER, Vol. 102, Nov. 1980, pp. 715–718.

8 Özişik, M. N., and Shouman, S. M., "Source Function Expansion Method for Radiative Transfer in a Two-layer Slab," *Journal of Quantitative Spectroscopy and Radiative Transfer*, Vol. 24, 1980, pp. 441–449.

9 Özişik, M. N., *Radiative Transfer*, John Wiley and Sons, New York, 1973.

10 Galerkin, G. B., *Vestnik Inzhenerov Tecknikov*, 1915, pp. 897–908.

11 Özisik, M. N., *Heat Conduction*, John Wiley and Sons, New York, 1980.

12 Kantorovich, L. V., and Krylov, V. I., *Approximate Methods of Higher Analysis*, John Wiley and Sons, New York, 1964.

13 Collatz, L., *The Numerical Treatment of Differential Equations*, (English translation), Springer-Verlag, Heidelberg, 1960.

14 Crandal, S. H., *Engineering Analysis*, McGraw-Hill, New York, 1956.

15 Courant, R., and Hilbert, D., *Methods of Mathematical Physics*, 1st English edition, Vol. 1, Interscience Publishers, New York, 1953.

16 Le Caine, J., "A Table of Integrals Involving the Functions $E_n(x)$," *National Research Council of Canada*, Report No. MT-131, 1948.

APPENDIX

Analytical expressions for the integrals in equations (15):

$$\int_0^a x^m E_2(x)\,dx = \frac{m!}{m+2} - \sum_{j=0}^{m} \frac{m!}{(m-j)!}\, a^{m-j} E_{j+3}(a) \quad \text{(A1)}$$

$$\int_0^a \int_0^a x^m E_1(|x-x'|) H(x')\,dx\,dx'$$

$$= (-1)^{m+1} m! \int_0^a E_{m+2}(x') H(x')\,dx'$$

$$+ \sum_{j=0}^{m} \frac{m!}{(m-j)!} \left\{ \frac{[1+(-1)^j]}{1+j} \int_0^a (x')^{m-j} H(x')\,dx' \right.$$

$$\left. - a^{m-j} \int_0^a E_{j+2}(a-x') H(x')\,dx' \right\} \quad \text{(A2)}$$

$$\int_0^a \int_0^a E_1(|x-x'|) x^m x'^n\,dx\,dx' = (-1)^{n+1} \frac{m!n!}{m+n+2}$$

$$+ m!n! \left[(-1)^n \sum_{i=0}^{m} \frac{a^{m-i}}{(m-i)!} E_{n+i+3}(a) \right.$$

$$\left. + (-1)^m \sum_{i=0}^{n} \frac{a^{n-i}}{(n-i)!} E_{m+i+3}(a) \right]$$

$$+ \sum_{i=0}^{n} \frac{n!}{(n-i)!} \frac{[1+(-1)^i]}{1+i} \frac{a^{m+n-i+1}}{m+n-i+1}$$

$$- \sum_{i=0}^{n} \sum_{j=0}^{m} \frac{m!n!}{(n-i)!\,(m-j)!} \frac{(-1)^j}{i+j+2} a^{m+n-i-j} \quad \text{(A3)}$$

The expressions (A1–A3) have been obtained by the manipulation of the relations given in reference [16].

The Influence of a Laminar Boundary Layer and Laminar Injection on Film Cooling Performance

R. J. Goldstein
Department of Mechanical Engineering,
University of Minnesota,
Minneapolis, Minn. 55455
Fellow ASME

T. Yoshida
National Aerospace Laboratory,
Tokyo, Japan
Assoc. Mem. ASME

Measurements are reported of the film cooling effectiveness and heat transfer following injection of air into a mainstream of air. A single row of circular injection holes inclined at an angle of 35 deg is used with a lateral spacing between the holes of 3 dia. Low Reynolds number mainstream and injection flow permit studying the influence of a laminar approaching boundary layer and laminar film coolant flow. Measurements of the surface heat transfer taken with no injection indicate that the hole openings can effectively trip the laminar boundary layer into a turbulent flow. The type of the approaching boundary layer has relatively little influence on either the adiabatic effectiveness or the heat transfer with film cooling. The importance of the nature of the injected flow on film cooling performance can at least be qualitatively explained by the differences in the transport mechanisms and in the penetration of the injected air into the mainstream.

Introduction

Film cooling has been used in many systems to protect solid surfaces exposed to high-temperature gas streams. The coolant injected into the boundary layer acts as a heat sink, reducing the gas temperature near the surface. Applications have been widespread, particularly in gas turbine systems where combustion chamber liners, turbine blades, and other hot parts of the engine have used air, usually taken from the exit of the engine compressor, for the film coolant.

In the leading edge region of turbine blades there is often a very high surface heat transfer. In this region, film cooling and the associated convection cooling in the coolant-injection holes have found widespread use in maintaining suitable skin temperatures. In most experiments done on film cooling, both the wall boundary layer and the flow through the injection holes have been turbulent. However, in the leading edge region and for some distance downstream, the boundary layer flow along the blade may be laminar. In addition, at low injection rates, the flow in the injection holes may be laminar.

Several investigators have considered film cooling with a laminar boundary layer along a flat surface [1–4]. In addition, experimental studies on leading edge injection have been reported using a cylindrical model [5, 6] and a flat-plate model with a circular nose [7]. There are also data on the characteristics of film-cooled turbine blades with injection holes in the leading edge region [8–13] and on full-coverage film cooling [14–17]. There has been little attention paid to a direct comparison between the film cooling results with a laminar boundary layer and with a turbulent boundary layer on the surface as well as for laminar versus turbulent flow in the injection holes. In the present work, local measurements of the adiabatic wall effectiveness and heat transfer with film cooling on a flat plate are described. By inserting or removing trips along the wall and/or in the injection tubes, laminar or turbulent flow can be obtained at approximately the same wall or tube Reynolds numbers.

Experimental Apparatus and Test Conditions

The present study has been conducted in a low-speed, open-circuit, induced-flow wind tunnel at the University of Minnesota. A sketch of the wind tunnel is shown in Fig. 1. A detailed description of the wind tunnel is given elsewhere [18, 19]. The test section has been changed from previous studies by decreasing its length and by removing trips when a laminar approaching boundary layer is desired.

The test section floor is of low thermal conductivity material with stainless steel heater foils stretched across it. Five circular injection tubes are located at three-diameter spacing in the lateral direction and inclined at 35 deg to the mainstream flow. When a turbulent boundary layer is desired, a trip is placed on the wall as shown in Fig. 1. A thin tape may be placed across the injection holes to reduce their influence on the mainstream flow when studying the boundary layer in the absence of injection. The cross-sectional area of the test section is essentially constant and the streamwise pressure gradient is close to zero.

The freestream velocity is kept constant at 4.5 m/s. With this velocity the Reynolds number, Re_D, is of the order of magnitude of that which exists in the leading edge region of a gas turbine blade (3000 to 10,000).

The flow through the injection tubes can be changed to obtain different blowing rates. At the lowest blowing rates, the flow in the absence of any trip in the tubes is laminar. To obtain a turbulent boundary condition at low Reynolds numbers, trips 10 dia upstream of the tube exits are used. No trips are used at the high Reynolds number for which turbulent tube flow occurs naturally. In both the boundary layer and the injection tubes, velocity and turbulence measurements are obtained with a hot-film anemometer having a 0.051 mm dia by 1.0 mm long sensor.

The experiments are conducted under steady-state conditions. When measuring adiabatic wall temperature, heated air is injected to simplify the flow and measurement system. Assuming constant properties, the dimensionless adiabatic wall temperature should be the same with film "heating" as with film cooling. For the heat-transfer experiments, an approximately constant heat flux boundary condition is obtained from the foil heaters and the injected air is not heated so that it is essentially at the same temperature as the free stream (and $T_{aw} = T_\infty$).

Wall temperatures are measured by thermocouples embedded in the tunnel floor beneath the foil heaters. A correction is made for radiation from the heater and for conduction through the tunnel floor. However, no correction is made for conduction in the lateral, Z, direction; such

Contributed by the Heat Transfer Division for publication in the JOURNAL OF HEAT TRANSFER. Manuscript received by the Heat Transfer Division March 16, 1981.

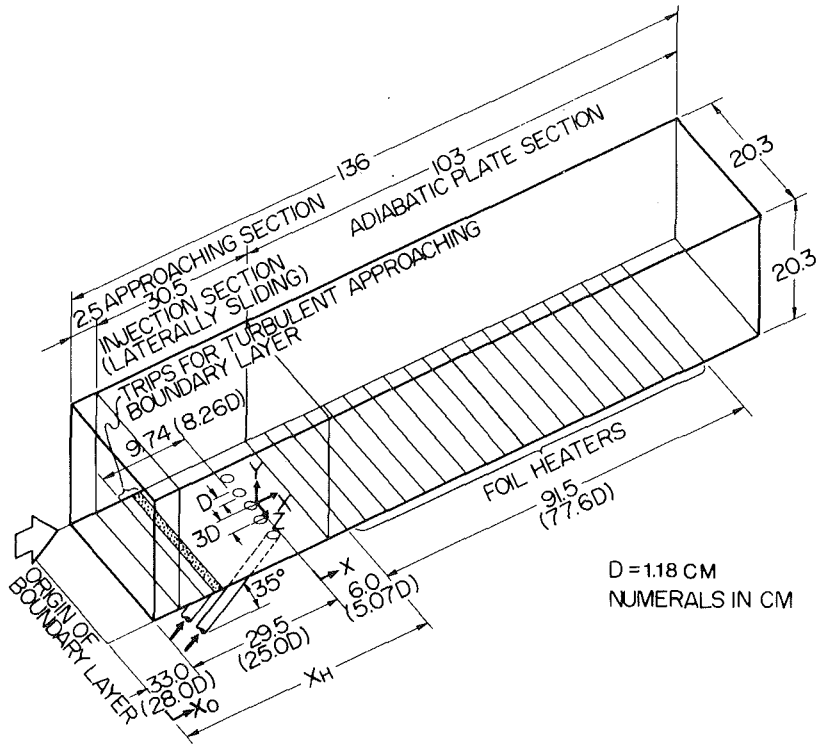

Fig. 1 Schematic drawing of test section

conduction would tend to smooth out the measurements of effectiveness and heat transfer from their true distribution. Thus the lateral distribution should only be used for qualitative discussion. The laterally averaged values should not be significantly changed by this conduction.

The adiabatic-wall film cooling effectiveness and heat-transfer coefficients are defined by the following equations:

$$\eta = \frac{T_{aw} - T_r}{T_2 - T_r} \approx \frac{T_{aw} - T_\infty}{T_2 - T_\infty} \tag{1}$$

$$h = \frac{q}{T_w - T_{aw}} \tag{2}$$

Nomenclature

D = inner diameter of injection tube
h = heat-transfer coefficient with injection (see equation 2)
h_0 = heat-transfer coefficient without injection
I = momentum flux ratio ($\rho_2 \bar{U}_2^2 / \rho_\infty U_\infty^2$)
k = thermal conductivity
K = acceleration parameter ($\mu_\infty / \rho_\infty U_{\infty x}^2$) ($dU_{\infty x}/dX$)
L = abbreviation for "laminar flow"
M = blowing rate ($\rho_2 \bar{U}_2 / \rho_\infty U_\infty$)
M_0 = fictitious blowing rate when $U_\infty = 0$, calculated from $\rho_2 \bar{U}_2$ and the normal value of $\rho_\infty U_\infty$
Pr = Prandtl number
q = wall heat flux
Re = Reynolds number ($\mathrm{Re}_D = \rho_\infty U_\infty D/\mu_\infty$, $\mathrm{Re}_j = \rho_2 \bar{U}_2 D/\mu_2$, $\mathrm{Re}_{x_0} = \rho_\infty U_\infty X_0/\mu_\infty$)
T = abbreviation for "turbulent flow"
T = temperature
T_{aw} = adiabatic wall temperature with film cooling
T_r = freestream recovery temperature
T_w = wall temperature
Tu = turbulence intensity
U = fluid velocity
U' = rms turbulence fluctuation from mean velocity
$\bar{U}_2$ = mean velocity of injected flow
$U_{2\max}$ = maximum velocity in injection tube
X = distance downstream of downstream edge of injection hole; see Fig. 1
X_H = distance from origin of boundary layer to first foil heater
X_0 = distance downstream of effective origin of boundary layer
U_∞ = freestream velocity immediately upstream of injection holes
$U_{\infty x}$ = freestream velocity
Y = height above test surface
Z = lateral distance from centerline of injection hole
β = angle of injection tube from streamwise direction
δ = boundary layer thickness (Y where $u/u_\infty \sim 0.95$)
δ^* = boundary layer displacement thickness
δ_0^* = boundary layer displacement thickness near injection location (2mm upstream of injection hole leading edge in present experiment)
η = adiabatic film cooling effectiveness (see equation 1)
η_{c_L} = effectiveness directly downstream of center line of injection hole (i.e., $Z = 0$)
θ = boundary layer momentum thickness
μ = viscosity
ρ = density

Subscripts

L = laminar
max = maximum value
o = without injection
T = turbulent
2 = injected flow at tube exit
∞ = freestream condition immediately upstream of injection holes

Superscripts

$-$ = average in spanwise (Z) direction or across injection tube exit

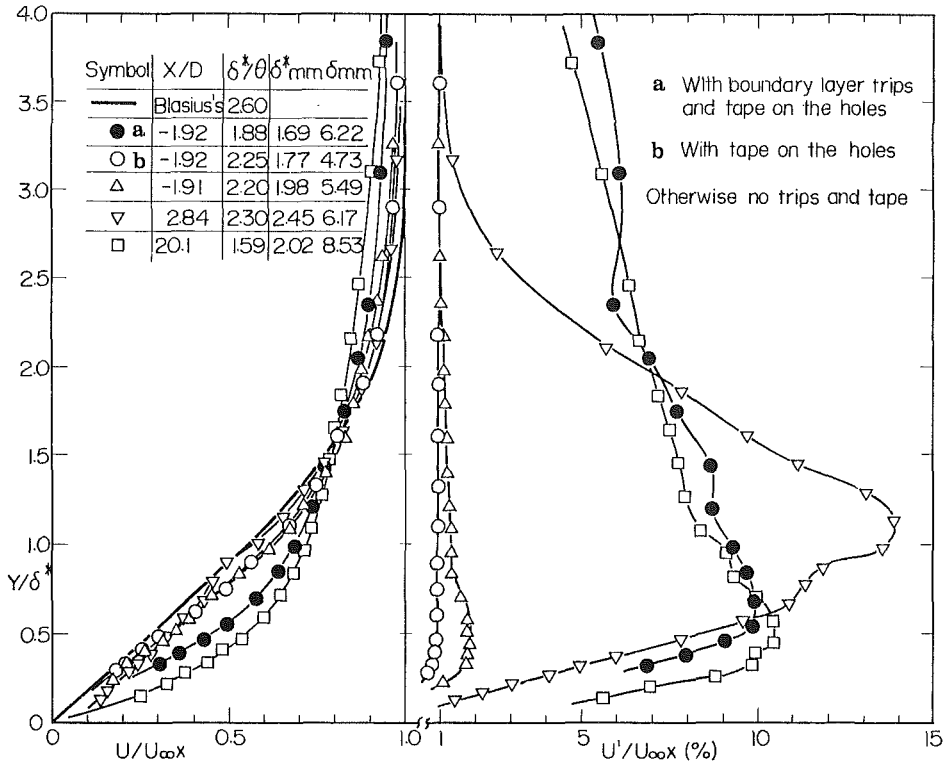

Fig. 2 Boundary layer profiles without injection

In the present study, local wall temperature measurements are made and then average values calculated.

Table 1 shows the range of test conditions in the present study.

Table 1 Experimental range in the present study

Freestream mean velocity, U_∞	4.5 m/s
Freestream turbulence intensity, Tu_∞	$\simeq 1\%$
Blowing rate, M	0.2, 0.35, 0.5 1.0, 1.50, 2.0
Momentum flux ratio, I	0.060 – 5.1
Density ratio, ρ_2/ρ_∞	0.85, 1
Reynolds number, $Re_D (=\rho_\infty U_\infty D/\mu_\infty)$	3.4×10^3
Reynolds number, $Re_j (=\rho_2 U_2 D/\mu_2)$	$6.0 \times 10^2 - 6.7 \times 10^3$
Normalized displacement thickness 2mm upstream of leading edge injection hole, δ_0/D	0.16—laminar 0.14—turbulent
Acceleration parameter, K	1.2×10^{-7}

Boundary Layer Flow Without Injection

Figure 2 shows dimensionless velocity and turbulence intensity profiles above the wall at different positions along the flow. The Blasius profile for a laminar boundary layer is indicated as a reference. The location, $X/D = -1.9$ and $Z/D = 0$, corresponds to a position 2mm upstream of the central injection hole upstream edge. At this location, in the absence of a trip, the measured profile is very close to the Blasius curve. This is true whether or not tape is used on the injection holes. The slight deviation from the theoretical curve may be due to the near-constant, cross-sectional area of the test section which produces a slight acceleration of the mainstream (see Table 1). When a trip (wire plus sandpaper roughness) is attached to the wall, the boundary layer becomes turbulent. The trips have been placed at a location to obtain approximately the same displacement thicknesses at the injection holes for the turbulent boundary layer as for the laminar boundary layer.

Somewhat downstream of injection ($X/D=2.84$), the boundary layer is still apparently laminar with open holes in the absence of trips, although some distortion in the velocity profile is evident. Further downstream, at $X/D=20.1$, the boundary layer appears to be turbulent with the open holes even in the absence of a trip. Although not shown in this figure, the boundary layer at this location is still laminar in the absence of a trip when tape is placed over the holes.

Injection Flow in the Absence of Mainstream

Figure 3 shows dimensionless velocity and turbulence intensity profiles of the flow exiting from the central injection hole ($Z/D=0$ and $Y/D=0.02$) in the absence of the mainstream. The flow is not heated. M_0 indicates a fictitious blowing rate for a density ratio of unity if the mainstream had a velocity of 4.5 m/s.

At low Reynolds number ($Re_j \sim 1.5 \times 10^3$), the velocity profile, in the absence of a trip, is close to that of a fully developed laminar pipe flow. The turbulence intensity is less than 0.4 percent everywhere across the flow. At the same Reynolds number, when the trip ring is attached on the inner surface of the tube, 10 dia upstream of the tube exit, the profile is similar to that for fully developed turbulent tube flow [20]. At larger Reynolds numbers no trip ring is used, and the velocity profile is close to that of a fully developed turbulent flow.

Film Cooling Effectiveness

The variation of the laterally averaged, film-cooling effectiveness with downstream position is shown in Fig. 4 for two different blowing rates. Curves representing results of some previous studies are shown for comparison. The key to the upper case letters, indicating the source of the earlier data for this and later figures, is contained in Table 2.

The most notable variation among the results from the present experiment occurs for a blowing rate of 0.5. The average effectiveness with laminar injection is considerably lower than with turbulent injection. This is true for either the laminar or turbulent boundary layer along the wall. It is known [18] that the film cooling effectiveness with $\beta=35$ deg reaches a maximum with variation in blowing rate near

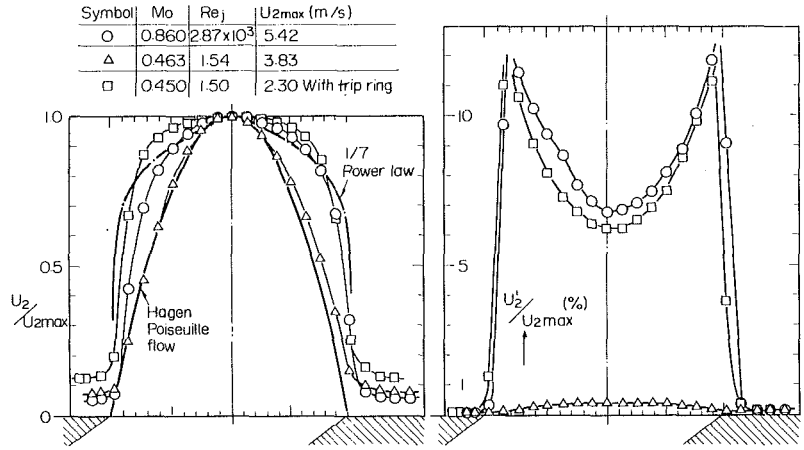

Fig. 3 Injection flow without mainstream

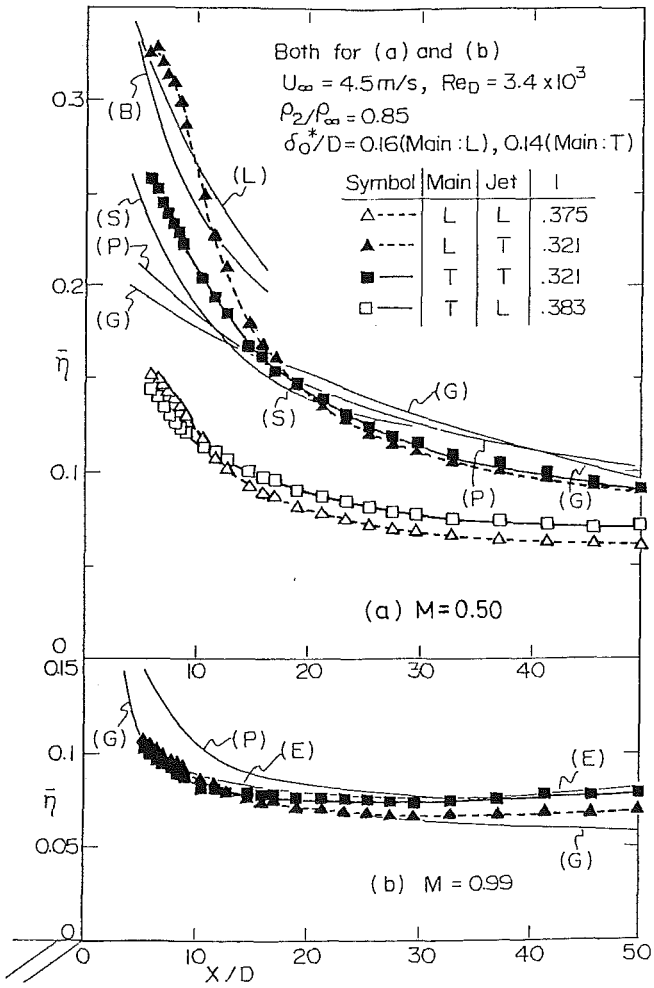

Fig. 4 Laterally averaged film-cooling effectiveness (see Table 2 for key to letters designating results from other studies)

$M=0.5$ for a density ratio close to unity. It is at this blowing rate that there is the greatest sensitivity to potential lift-off of a jet flowing from a film-cooling hole. When the jet penetrates into the mainstream its "cooling" influence on the wall is reduced; the enthalpy deficit it provides is no longer near the surface but rather is dissipated in the core of the primary flow.

In many of the earlier studies, done with turbulent injection or with a very short injection tube, the coolant entering the mainstream has a relatively blunt profile so that the maximum velocity is close to the mean velocity. With developed laminar tube flow, the peak velocity is considerably greater than the average velocity. Thus, the mean momentum flux at the exit plane for laminar tube flow would be greater than the mean momentum flux at the same blowing rate, M, for a turbulent or plug-type flow.

At the same mean velocity, or M, the value of the mean square velocity for fully developed laminar tube flow is about 30 percent greater than the mean square velocity for 1/7 power law turbulent flow. Actually, the measured values of the momentum flux ratio, I, for the laminar jet were only about 18 percent greater than for the turbulent jet. A greater value of I at a given value of M could lead to greater penetration of the jet into the mainstream. The film-cooling effectiveness would be particularly sensitive to this effect at injection rates close to those yielding the maximum effectiveness.

With turbulent injection, the influence of the nature of the boundary layer approaching the injection holes is most pronounced close to the injection holes. The effectiveness is higher with a laminar boundary layer at $M=0.5$. The flow in the turbulent boundary layer with its greater fluctuations tends to dilute the influence of the injected fluid. Further downstream the curves cross and a slightly higher effectiveness occurs with a turbulent boundary layer, particularly with the laminar jets. This may be due to the turbulence causing the jet to mix more and diffuse back towards the wall.

The trends of most of the other investigations are close to the present ones for turbulent jets entering a turbulent boundary layer. The differences that occur may be due to uncertainty in experimental measurements and differences in the Reynolds number. Other influences may be the very blunt injection profile in reference [1] and the slightly smaller inclined angle and closer spacing in reference [2].

At a blowing rate close to unity there is a relatively good agreement with earlier studies that were performed in this laboratory, though not always with the same apparatus. The results of [21] indicate somewhat higher effectiveness, but in those tests the density ratio (ρ_2/ρ_∞) was somewhat higher than in the other studies.

Lateral distributions of the film cooling effectiveness at different downstream locations are presented in Fig. 5. When the approaching mainstream boundary layer is turbulent, a relative maximum appears near the region $Z/D=1$. This may be due to a pair of vortex flows and the resulting high turbulence which have been observed there. The adjacent minimum has been described [2] as due to the pumping effect

Table 2 Earlier works for film cooling effectiveness used for comparison

Worker	M	$Re_D \times 10^4$	ρ_2/ρ_∞	δ_0^*/D	Research
(B) Bergeles [2]	0.5	3.3	1.0	0.095	Spacing = 2.67D β = 30 deg mass transfer
(E) Eriksen, V. L. [19]	0.493 0.976	4.4	0.842 0.848	0.149	For heat transfer M = .496 $\rho_2 = \rho_\infty$
(G) Goldstein, Eckert, Eriksen, and Ramsey. [22]	0.5 1.0	2.2	0.85	0.124	
(K) Kadotani and Goldstein [23]	0.5	1.1 4.4	0.85	0.245 0.175	(K1) (K2)
(L) Liess, C. [1]	0.57	1.5	0.79	0.087	Main: L Jet: E[+]
(P) Pedersen, Eckert and Goldstein [21]	0.513	1.1	0.960	0.162	Mass transfer
(S) Sasaki, Takahara, Kumagai and Hamano [24]	0.537	1.5	0.94	0.10	β = 45 deg Jet: E

[+] Jet: E means not fully developed turbulent but entrance region at the exit of injection holes.

Unless specified:
spacing = $3D$
β = 35 deg
main: T and Jet: T
smooth surface, free stream turbulence intensity $\leq$ 1.5%
η from wall temperature measurements

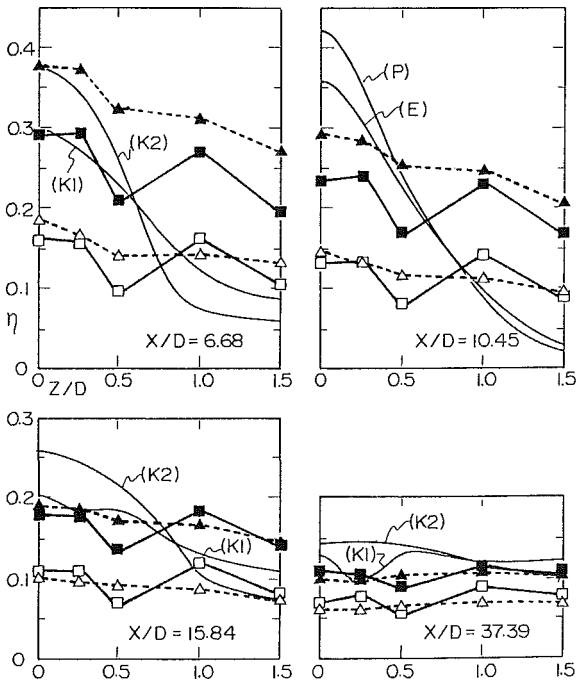

Fig. 5 Lateral distributions of effectiveness at M = 0.5 (see Table 2 for key to letters designating results for other studies; symbols for flow conditions are the same as in Fig. 4)

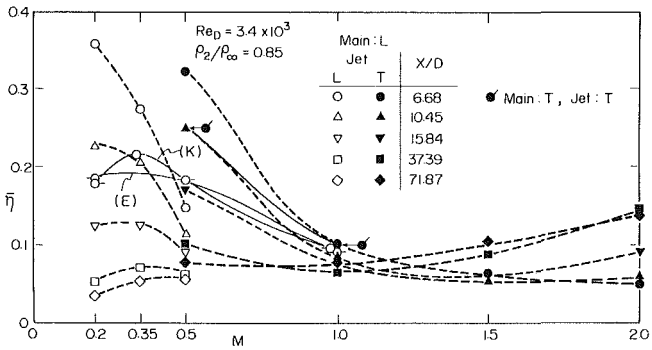

Fig. 6 Laterally averaged effectiveness versus blowing rate (see Table 2 for key to letters designating results from other studies)

of the pair of rotating vortices. There is considerable difference in the lateral variation in the present study compared to the earlier ones shown in the figure. The present results indicate more uniform effectiveness in the Z direction. This may be partially due to the smoothing out of the results by conduction in the wall in the present work, but perhaps of more importance is the large difference in Reynolds number. The present results were taken at Reynolds number $\rho_\infty U_\infty D/\mu_\infty$, about one-tenth of those used in the earlier studies for the turbulent boundary layer and turbulent jet flow. This is also borne out by comparison of curve K1 to K2. These results are obtained on the same apparatus but the data for curve K1 are at lower Re than for K2.

Figure 6 shows the variation of the average effectiveness with blowing parameter at different downstream locations. At blowing rates greater than 0.5, the injected flow is turbulent and the curves show the familiar decline of effectiveness with increasing M. As M is increased still further, above 1.0 or 1.5, the jets merge together and their influence is felt down on the wall, especially at large X.

At low blowing rates ($M < 0.5$), the flow in the injection holes is laminar. The maximum of $\bar{\eta}$ occurs at considerably lower values of M with laminar injection than with turbulent injection. It is also noteworthy that $\bar{\eta}$ for the laminar jet at low values of M can be higher than the peak $\bar{\eta}$ for turbulent injection. This is probably due to the relatively small amount of mixing (with the mainstream) of the laminar jet; at low M, when the jet does not leave the wall, this can result in high effectiveness. It should be noted, too, that the present results

for turbulent boundary layer and turbulent injection indicate a higher mean effectiveness than was found in [19] and [23] at $M=0.5$. This may be due to the higher (~three times) mainstream and jet Reynolds numbers in those earlier works.

The variation of centerline effectiveness, η_{c_L}, with M is shown in Fig. 7. As observed in the previous figures, the effectiveness at a given M is considerably lower with the laminar injection. At moderate values of M, the centerline effectiveness for turbulent injection is somewhat higher with the laminar mainstream. The centerline effectiveness measured in the present study is less than that observed in [19], [22], and [23] for similar conditions of turbulent injection and turbulent boundary layer. This difference is apparently due to the lower Reynolds numbers during the present tests.

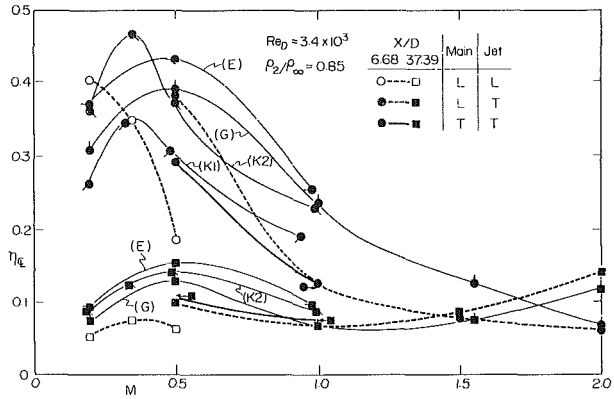

Fig. 7 Centerline effectiveness versus blowing rate (see Table 2 for key to letters designating results from other studies)

Heat-Transfer Coefficient

Figure 8 shows the spanwise-average, heat-transfer coefficient at various downstream locations in the absence of injection. A linear average of the local values measured at $Z/D=0$, 0.75, and 1.5 is used. Two sets of data were obtained with the holes covered by a thin layer of tape to prevent them from introducing a cavity-type roughness which could disturb the flow. In the other two runs the holes were open, as would occur when injection takes place, although there is no net throughflow of gas. For both the open- and closed-hole conditions there is a set of data when the boundary layer trips were placed on the wall and another set when there were no trips.

When the holes are closed, there is little variation (approximately 3 percent) of the heat-transfer coefficient in the lateral direction. With open holes in the presence of trips this variation is approximately 5 percent. With no trip, the open holes can initiate transition and this leads to a significant variation of h_0 across the span; the maximum value of h_0 occurs at $Z/D=0$, except very close to the downstream edge of the holes. The variation of the heat-transfer coefficient from the mid-point of the holes to the region half-way between the holes ($Z/D=1.5$) averages about 10 percent for these open holes without trips and has a maximum of 17 percent.

Note in Fig. 8, with taped-over holes in the absence of trips the heat transfer closely follows the equation (1) which represents heat transfer along a flat plate with a laminar boundary layer. Far downstream, the measured points rise somewhat above the predicted curve, perhaps due to transition. The other three sets of data appear to be represented, at least some distance downstream, by the heat-transfer correlation (equation (2)) for a turbulent boundary layer on a flat plate. When the trips are present there is virtually no difference between the measured results for the closed and open holes. In the absence of trips with the holes open, there is a transition region downstream from the start of heating. This is indicated by the somewhat lower heat transfer results for this flow condition till approximately 20 dia downstream of the injection hole location. Further downstream there appears to be little difference between this and the data obtained with a boundary layer trip.

Figure 9 shows the variation of the average heat-transfer coefficient with downstream position for a blowing rate of 0.5 and different conditions of mainstream and injected flow. At this blowing rate with the turbulent boundary layer there is very good agreement with an earlier study [19]. The average heat-transfer coefficient is increased little over that without injection.

When the boundary layer is initially laminar, the injection has a bigger effect on the heat transfer. With the laminar boundary layer, for both laminar injection and turbulent injection, two curves are plotted on Fig. 9. In one, the reference heat-transfer coefficient is the same as for the

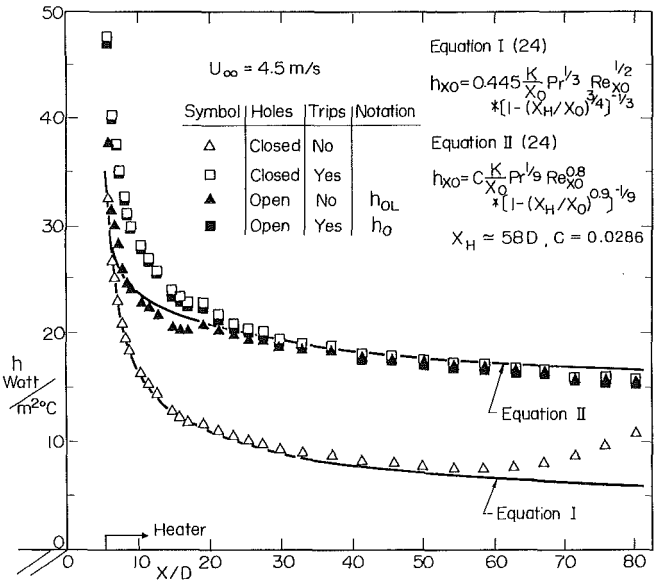

Fig. 8 Laterally averaged heat-transfer coefficient without injection

turbulent boundary layer studied and is taken from the data in the present experiment with the trip, as was true for the plots with the turbulent boundary layer in the top portion of Fig. 9. It should be noted that this is a somewhat arbitrary reference state—used only for comparison with the other data—as the boundary layer flow for these runs was laminar upstream of injection. With this reference value (in the denominator of the ratio), we see that there is not a great variation from the heat-transfer coefficient for a turbulent boundary layer without injection other than close to the holes. There, laminar flow injection results in lower heat-transfer coefficients (smaller transport coefficients); with turbulent injection, the eddies along the wall give an increase in the heat-transfer coefficient.

The other two curves for the initially laminar boundary layer case refer to the data (h_{0L}) from Fig. 8 for open holes in the absence of a trip. Compared to this case, which had a somewhat lower heat-transfer coefficient than when the trip was present, the injection increases the heat transfer to a maximum of 20–30 percent over that without injection. In the absence of injection there are still essentially laminar patches along the wall with relatively small heat transport. Injection results in eddies which make the heat-transport coefficient greater than that with the laminar patches. Far downstream at this blowing rate, the heat-transfer coefficient is little altered by the injection and, of course, is little different from the heat transfer with the turbulent boundary layer in the absence of injection.

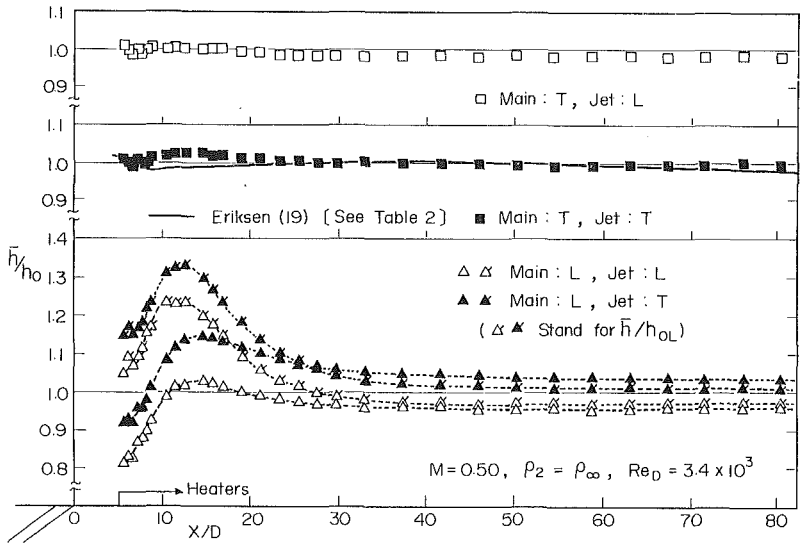

Fig. 9 Laterally averaged heat-transfer coefficient

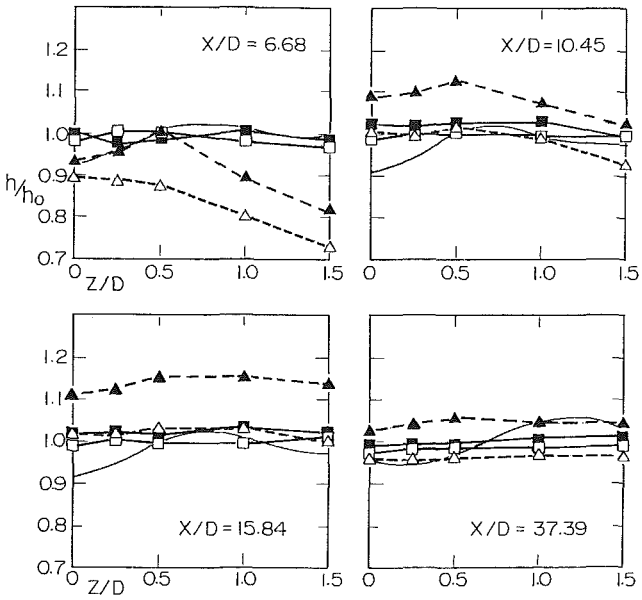

Fig. 10 Lateral distributions of heat-transfer coefficient (symbols and experimental conditions are the same as those described in Fig. 9)

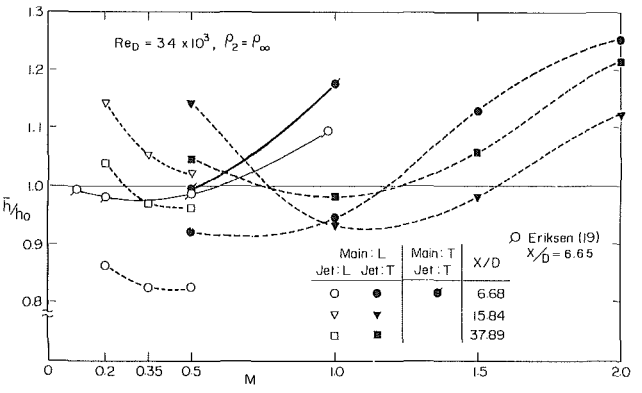

Fig. 11 Laterally averaged heat-transfer coefficients versus blowing rate

Figure 10 shows the spanwise variation of the heat-transfer coefficient—in all cases compared to the heat-transfer coefficient for the turbulent boundary layer with the trip in the absence of injected flow. There is little variation with Z other than close to injection. With an initially laminar boundary layer, h is relatively small between the holes at $X/D = 6.68$, where one might expect incomplete transition to turbulence. Relatively low h also occurs in a laminar boundary layer in this region when there is no injection yet open holes.

Figure 11 shows the variation of the average heat-transfer coefficient with blowing rate at three different downstream locations. Some results from [19] are included for comparison. The results for laminar injection and a laminar boundary layer should be noted. The ratio, $\bar{h}/h_0$, is less than unity at small X/D over the range of M for which experiments could be run. If the denominator of this ratio were the heat transfer with a laminar boundary layer and no injection (even with the holes open), the three points would be close to or above unity. Further downstream, the ratio is near or above unity. With laminar injection the heat-transfer coefficient decreases with increasing M in the range studied. The turbulent jets are still attached to the wall at $M = 0.5$ and lead to a somewhat higher heat transfer than do the laminar jets.

There is a decrease in $\bar{h}/h$ as M increases for the case of the turbulent jet in an initially laminar boundary layer due to jet penetration. At higher blowing rates the heat transfer coefficient increases with M, as had been shown in an earlier study [19] for the turbulent boundary layer and turbulent jet combination. Under those conditions, the turbulent jet flow tends to dominate the transport characteristics in the mainstream.

Conclusions

The major influence of the character of the boundary layer and of the injection jets for film cooling in the geometry studied is in the differing results for laminar jet flow versus turbulent jet flow. With laminar jets the maximum in film cooling effectiveness occurs at relatively small values of the blowing parameter M. This is due to the greater penetration of the laminar jets at a given value of M as compared to turbulent jets. The fuller the velocity profile of the jet, the greater is the blowing rate before the jet tends to lift off the surface. In this regard, it should be noted that flow through a short entrance section occurs in many applications and will often result in a blunt velocity profile.

The nature of the boundary layer seems to play a bigger role when the jet is turbulent, at least in terms of the film-cooling effectiveness. Thus, there is a higher effectiveness with the laminar boundary layer and turbulent jets, at least close to injection, as compared to the turbulent boundary layer with

the turbulent jet. With the laminar jet, the nature of the boundary layer does not greatly influence the effectiveness.

In terms of heat transfer with the turbulent boundary layer, both the turbulent and laminar jets appear to have similar influences. For the initially laminar boundary layer the most important effect of injection is its influence on transition to turbulence.

Acknowledgment

The support of the U.S Army Office of Research under Grant DAA29-79-C-0117 is gratefully acknowledged. Early portions of the study were supported by the Power Branch of the Office of Naval Research.

References

1 Liess, C., "Experimental Investigation of Film Cooling with Ejection From a Row of Holes for the Application to Gas Turbine Blade," ASME *Journal of Engineering for Power*, Vol. 97, 1975, pp. 21-27.

2 Bergeles, G., "Three-Dimensional Discrete-Hole Cooling Processes. An Experimental and Theoretical Study," *Ph.D. thesis*, Imperial College, University of London, 1976.

3 Pavri, R. and Tabakoff, W., "An Analytical Solution of Wall-Temperature Distribution for Transpiration and Local Mass Injection Over a Flat Plate," ASME Paper No. 72-HT-57, 1972.

4 Nilson, R. H. and Tsuei, Y. G., "Film Cooling by Oblique Slot Injection in High-Speed Laminar Flow," *AIAA Journal*, Vol. 13, 1975, pp. 1199-1202.

5 Luckey, D. W., Winstanley, D. K., Hanus, G. J., and L'Ecuyer, M. R., "Stagnation Region Gas Film Cooling for Turbine Blade Leading-Edge Applications," *J. Aircraft*, Vol. 14, 1977, pp. 494-501.

6 Russell, L. M., "Flow Visualization of Discrete-Hole Film Cooling with Spanwise Injection Over a Cylinder," NASA TP 1491, 1979.

7 Sasaki, M., Takahara, K., Sakata, K., and Kumagai, T., "Study on Film Cooling of Turbine Blades," *Bulletin of the JSME*, Vol. 19, 1976, pp. 1344-1352.

8 Hiroki, T. and Katsumata, I., "Design and Experimental Studies of Turbine Cooling," ASME Paper No. 74-GT-30, 1974.

9 Muska, J. F., Fish, R. W., and Suo, M., "The Additive Nature of Film Cooling from Rows of Holes," ASME *Journal of Engineering for Power*, Vol. 98, 1976, pp. 457-464.

10 Yoshida, T., Minoda, M., Sakata, K., Nouse, H., Takahara, K., and Matsuki, M., "Low- and High-Speed Cascade Tests of Air-Cooled Turbine Blades," ASME Paper No. 76-GT-40, 1976.

11 Hanus, G. J. and L'Ecuyer, M. R., "Leading-Edge Injection for Film Cooling of Turbine Vanes," *Journal of Energy*, Vol. 1, 1977, pp. 44-49.

12 Nouse, H., Takahara, K., Yoshida, T., Yamamoto, A., Sakata, K., Inoue, S., Mimura, F., and Usui, H., "Aerodynamic and Cooling Performances of a Film-Cooled Turbine," *Proceedings of the 1977 Tokyo Joint Gas Turbine Congress*, 1977, pp. 206-214.

13 Sakata, K., Usui, H., and Takahara, K., "Cooling Characteristics of Film Cooled Turbine Vane Having Multi-Row of Ejection Holes," ASME Paper No. 78-GT-21, 1978.

14 Metzger, D. E., Takeuchi, D. I., and Kuenstler, P. A., "Effectiveness and Heat Transfer with Full-Coverage Film Cooling," ASME *Journal of Engineering for Power*, Vol. 95, 1973, pp. 180-184.

15 Mayle, R. E. and Camarata, F. J., "Multi-Hole Cooling Film Effectiveness and Heat Transfer," ASME Paper No. 74-HT-9, 1974.

16 Crawford, M. E., Kays, W. M., and Moffat, R. J., "Full Coverage Film Cooling on Flat, Isothermal Surfaces: A Summary Report on Data and Predictions," NASA CR-3219, 1980.

17 Launder, B. E. and York, J., "Discrete-Hole Cooling in the Presence of Free Stream Turbulence and Strong Favourable Pressure Gradient," *International Journal of Heat and Mass Transfer*, Vol. 17, 1974, pp. 1403-1409.

18 Goldstein, R. J., Eckert, E. R. G., and Ramsey, J. W., "Film Cooling with Injection Through a Circular Hole," NASA CR-54604, University of Minnesota HTL TR No. 82, 1968.

19 Eriksen, V. L., "Film Cooling Effectiveness and Heat Transfer with Injection Through Holes," NASA CR-72991, University of Minnesota HTL TR No. 102, 1971.

20 Laufer, J., "The Structure of Turbulence in Fully-Developed Pipe Flow," NACA TR-1174, 1954.

21 Pedersen, D. R., Eckert, E. R. G., and Goldstein, R. J., "Film Cooling with Large Density Differences Between the Mainstream and the Secondary Fluid Measured by the Heat-Mass Transfer Analogy," ASME JOURNAL OF HEAT TRANSFER, Vol. 99, 1977, pp. 620-627.

22 Goldstein, R. J., Eckert, E. R. G., Eriksen, V. L., and Ramsey, J. W., "Film Cooling Following Injection Through Inclined Circular Tubes," *Israel Journal of Technology*, Vol. 8, 1970, pp. 145-154.

23 Kadotani, K. and Goldstein, R. J., "On the Nature of Jets Entering a Turbulent Flow, Part B: Film Cooling Performance," ASME *Journal of Engineering for Power*, Vol. 101, 1979, pp. 466-470.

24 Sasaki, M., Takahara, K., Kumagai, T., and Hamano, M., "Film Cooling Effectiveness for Injection from Multirow Holes," ASME *Journal of Engineering for Power*, Vol. 101, 1979, pp. 101-108.

25 Hartnett, J. P., Eckert, E. R. G., Birkebak, R., and Sampson, R. L., "Simplifed Procedures for the Calculation of Heat Transfer to Surfaces with Non-Uniform Temperatures," University of Minnesota HTL TR No. 10, 1956.

Effect of Laminarization and Retransition on Heat Transfer for Low Reynolds Number Flow Through a Converging to Constant Area Duct

H. Tanaka
Associate Professor,
Department of Mechanical Engineering,
University of Tokyo,
Bunkyo-ku, Tokyo, 113 Japan

H. Kawamura
Senior Scientist,
Japan Atomic Energy Research Institute,
Tokai-mura, Ibaraki-ken,
319-11 Japan

A. Tateno
Graduate Student.

S. Hatamiya
Research Assistant.

Department of Mechanical Engineering,
University of Tokyo,
Bunkyo-ku, Tokyo, 113 Japan

A fully developed turbulent air flow between two parallel plates with the spacing of 15 mm was accelerated through a linearly converging passage of 200 mm in length, from which it flowed into a parallel-plate channel again. A foil heater was fastened on one wall surface over the entire channel, and local heat-transfer coefficient distribution was measured over the channel Reynolds number range of 5000 to 14,000 and also the slope of the accelerating section between 2/200 mm/mm and 10/200 mm/mm. (The acceleration parameter K ranged between 1.4×10^{-6} and 2×10^{-5}.) The Nusselt number at the outlet of the accelerating section was considerably lower than in the initial fully turbulent state, suggesting laminarization of the flow. The measured Nusselt number continued to decrease in the first part of the downstream parallel-plate section to a minimum and then began to increase sharply, suggesting reversion to turbulent flow. Heat transfer along the parallel-converging-parallel plate system was reproduced fairly satisfactorily by applying a k-kL model of turbulence.

Introduction

The phenomenon of laminarization of internal turbulent flow subjected to strong heating is of current interest because of the requirement for accurate design criteria for high-temperature, gas-cooled nuclear reactors. The second author of the present investigation has applied the so-called two-equation models of turbulence to this problem [1]. He modified the *k-kL* model originally proposed by Rotta [2, 3] so as to be applicable to turbulent flows at low Reynolds numbers. The modified model was fairly successful in predicting the complex variation of the heat-transfer coefficient determined experimentally [4–6].

The phenomenon of laminarization in a strongly heated internal flow is, however, complicated because of great variation of the physical properties imposed by large wall-to-bulk temperature ratios. In order to investigate the physical phenomena involved in the laminarization of internal flow essentially under a constant property condition, the first author of this investigation has performed an experimental study [7], in which a fully developed turbulent flow between two parallel plates was accelerated through a passage between two converging flat plates. Following the accelerating section a parallel-plate section was placed again, and the subsequent reversion of the laminarized flow to turbulence was examined. It was found that the process of reversion was significantly affected by the channel Reynolds number as well as by the extent of diminution of the Nusselt number at the outlet of the accelerating section as compared with the fully developed turbulent value at the inlet.

The main purpose of the present study is to investigate in detail the physics of the foregoing process of reversion from the laminarized flow to turbulence, by performing new carefully arranged systematic experiments as well as by making use of the *k-kL* model in [1] to gain further insight into the physical mechanisms of the process. From the viewpoint of improvement of a turbulence model, application of the model to the process of reversion to turbulence is considered to provide a critical test of its soundness in turbulent flows at low Reynolds numbers. While there exist a number of studies of laminarization that assume external boundary layer flow [8–12], this investigation may be characterized by dealing with laminarization and retransition of complete internal flow, essentially under a constant property condition, at relatively low-channel Reynolds numbers such as are relevant to laminarization in strongly heated internal flow [4–6].

As introduction, a brief explanation of the basic mechanism of laminarization will be given here along the lines of [13, 14]. It seems to be generally suspected that laminarization in a heated internal gas flow is brought about essentially by the same mechanism as for the case of an external turbulent boundary layer whose free stream velocity is accelerated strongly [5, 6]. In the former case, the acceleration of the mean flow velocity is also caused by thermal expansion of the gas. When the free/mean stream velocity, u_m, increases considerably in the flow direction, x, the shear stress, τ, in the neighborhood of the wall where inertial effects are negligible can be expressed approximately by equation (1), in which τ_w is the shear stress at the wall, y is the distance from the wall and ρ is the fluid density [14, 15].

$$\tau-\tau_w \simeq \frac{dp}{dx}y \simeq -\rho u_m \frac{du_m}{dx}y \tag{1}$$

This can be transformed to

$$\tau/\tau_w = 1-(c_f/2)^{-3/2}Ky^+ \tag{2}$$

where K is the acceleration parameter $(\nu/u_m^2)(du_m/dx)$ (ν is the kinematic viscosity), c_f is the friction coefficient, and y^+ is the usual nondimensional distance from the wall. If $K_c=3\times10^{-6}$ is taken as a threshold value of the acceleration parameter for turbulent flow to be sustained, and if $c_f=0.005$ is tentatively assumed, then by extrapolating expression (2)

Contributed by the Heat Transfer Division for publication in the JOURNAL OF HEAT TRANSFER. Manuscript received by the Heat Transfer Division January 13, 1981.

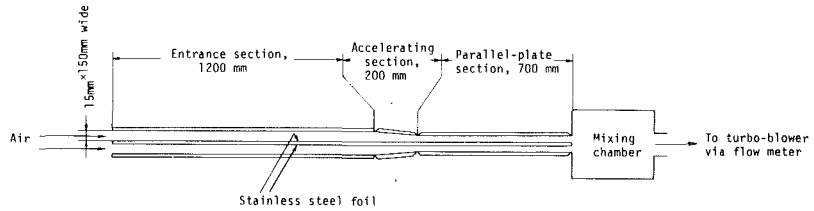

Fig. 1 Test section

(even beyond the range of its validity) we find that the shear stress would vanish at $y^+ = 42$. Therefore, when the acceleration parameter exceeds K_c, the shear stress will reach a low value in the part of the wall layer where turbulence production, $-\rho\overline{u'v'}(\partial\bar{u}/\partial y) = \mu_t(\partial\bar{u}/\partial y)^2$, is usually very high, and the turbulence production will be reduced, leading to laminarization.

Experiment

Figure 1 shows the test section. From the reason described later the test section was made up of two channels which were arranged symmetrically with respect to the center plate. Local heat transfer was measured for air flow in a horizontal, rectangular channel which was 2100 mm in length and 150 mm in width. The height of the channel over the first 1200 mm length was kept constant at $h_0 = 15$ mm so that the flow attained the fully developed turbulent state in this entrance section. The flow was tripped to turbulence at the inlet by a wire. In the succeeding section of $l = 200$ mm in length, the height of the channel, h, was converged linearly. In the last 700 mm section the height of the channel was again kept constant at the value at the outlet of the converging section, h_1.

From the condition of continuity, the linearly converging geometry permitted the flow to be accelerated at a constant value of K according to the relation:

$$K = 2\beta/\mathrm{Re} \tag{3}$$

where β is the inclination of the roof plate: $-dh/dx = (h_0 - h_1)/l$. The Reynolds number is defined by introducing a hydrodynamic equivalent diameter d_e on the assumption of two-dimensional flow as:

$$\mathrm{Re} = d_e u_m/\nu = 2hu_m/\nu \tag{4}$$

Since hu_m is constant in the two-dimensional flow, the Reynolds number defined in this way becomes constant along the entire channel when the flow rate of air is given. The air flow rate was measured by means of an orifice at the exit and a manometer.

The test section was made of 10-mm thick bakelite plate ($\lambda \simeq 0.23$ W/(mK)). A pair of stainless steel foils, 30-μm thick, 150-mm wide and 2100-mm long, were fastened on both sides of the center plate over the entire channel length. By passing an alternating current through them in series, both flows in the upper and lower channels were heated. The electrical input was regulated so that the difference between the heating surface temperature, T_w, and the bulk fluid temperature, T_b, was within 5 °C. This small heating rate justified the flow in being free from buoyancy effect [16] (for experimental conditions, $\mathrm{Ri} = 4\mathrm{Gr}/\mathrm{Re}^2 < 4\times10^{-4}$) as well as from the effect of thermal expansion [6] ($q^+ < 1\times10^{-4}$). Since heating started from the inlet of the test channel, the flow was fully developed thermally as well as hydrodynamically before it was subjected to acceleration. The heating surface temperature, T_w, was measured along the center line at intervals of 30 mm by copper-constantan thermocouples which were placed directly under the upper side foil. The temperature of the lower heating surface was also measured at four positions, and it agreed well with the upper surface temperature. The bulk fluid temperature, T_b, was linearly interpolated between the inlet room-air temperature and the outlet fluid tem-

Nomenclature

c_f = friction coefficient, $2\tau_w/(\rho u_m^2)$
g = acceleration of gravity
Gr = Grashof number, $h^3 g(T_w - T_b)/(T_b \nu^2)$
h = height of the channel
h_0 = channel height in the entrance section
h_1 = channel height in the downstream parallel-plate section
K = acceleration parameter, $(\nu/u_m^2)(du_m/dx) = 2\beta/\mathrm{Re}$
k = turbulent kinetic energy, $(\overline{u'^2} + \overline{v'^2} + \overline{w'^2})/2$
L = characteristic length scale of turbulence
l = length of the accelerating section
l_m = mixing length
Nu = Nusselt number, $2h\alpha/\lambda$
p = pressure
Pr = molecular Prandtl number
q = heat flux from wall to gas
q^+ = heat flux parameter, $q/(\rho c_p u_m T_b)$
Re = Reynolds number, $2hu_m/\nu$
Ri = bulk Richardson number, $(gh/T_b)(T_w - T_b)/u_m^2$
R_t = turbulent Reynolds number, $\sqrt{k}\,L/\nu$
T_b = bulk fluid temperature
T_w = heating surface temperature
u_m = mean flow velocity
$\bar{u}$ = time-mean velocity in x direction
$\bar{v}$ = time-mean velocity in y direction
$\overline{u'^2}, \overline{v'^2}, \overline{w'^2}$ = mean-square fluctuating components of velocity in Cartesian coordinates, x, y, z
x = distance in the flow direction, measured from the inlet of the accelerating section
x_r = location of minimum Nusselt number
y = distance from the wall
y^+ = nondimensional distance, $y\sqrt{(\tau_w/\rho)}/\nu$
α = heat-transfer coefficient, $q/(T_w - T_b)$
β = inclination of the roof plate of the accelerating section, $(h_0 - h_1)/l$
κ = von Kármán constant
λ = thermal conductivity
μ = molecular viscosity
μ_t = turbulent viscosity, defined in equation (8)
ν = kinematic viscosity
σ_k = turbulent Prandtl number for diffusion of k
σ_L = turbulent Prandtl number for diffusion of kL
ρ = density
τ = shear stress
τ_w = shear stress at the wall

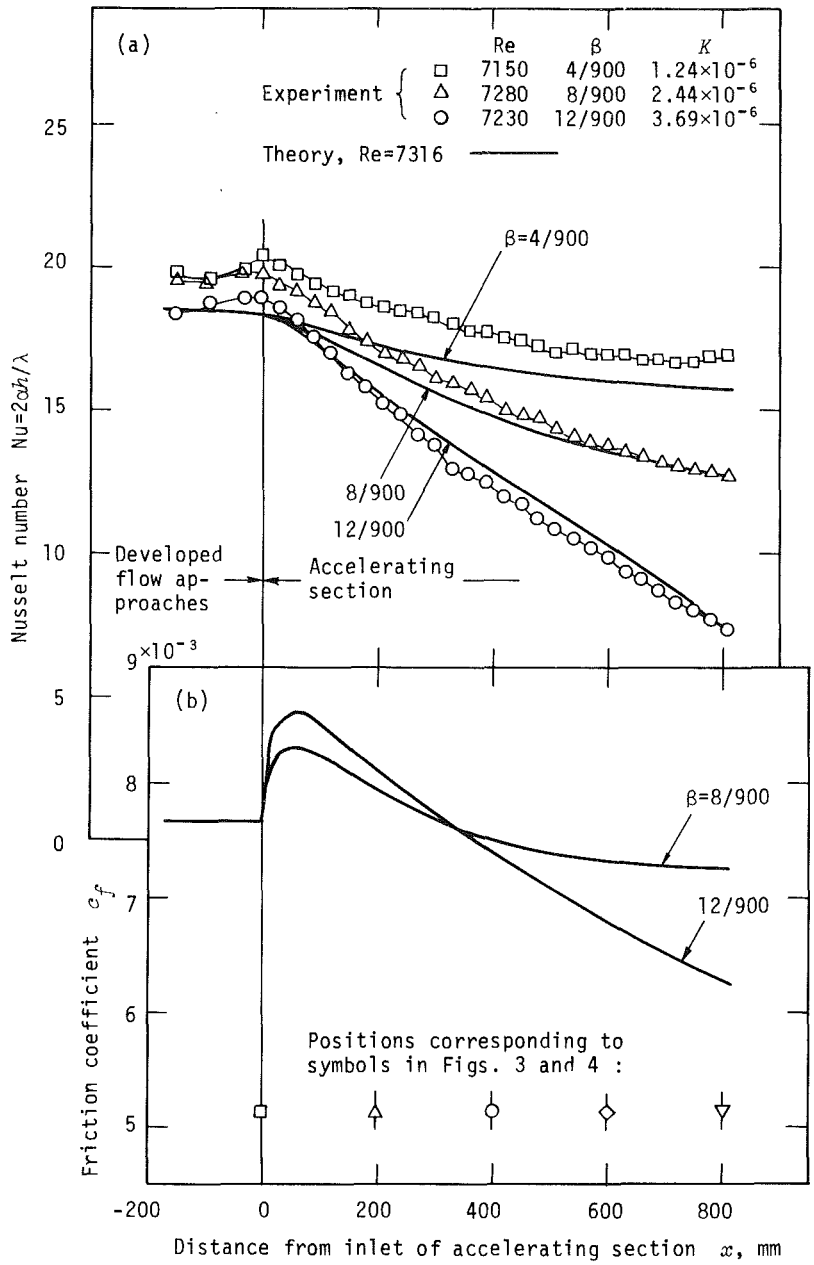

Fig. 2 Results for flows at Re = 7300, laminarizing in 900 mm long accelerating section: (*a*) comparison between experimental and theoretical Nusselt numbers, (*b*) predicted friction coefficient

perature, which was measured in the mixing chamber, shown in Fig. 1. The local heat-transfer coefficient α was determined by

$$\alpha = q/(T_w - T_b) \tag{5}$$

Here, the heat flux q from heating surface to gas was calculated from the electrical input with the compensation for radiation. The symmetrical arrangement about the center plate permitted the heat loss to the backside of the heating foil to be ignored except the neighborhood of the edges. The compensation for radiation, however, amounted to as much as 30 percent at the lowest Reynolds number. Then, for the purpose of better estimation of this value, the whole inside surfaces of the channels, including the stainless steel foils, were coated with the paint whose emissivity was known as 0.95 ± 0.02, and the temperature of the roof plate was also measured. The outside of the test section was covered with insulating material ($\lambda \simeq 0.04$ W/(mK), 50-mm thick).

The uncertainty in the Reynolds number, which arised chiefly from uncertainties in the coefficient of flow rate of the orifice and in reading the manometer, ranges from ± 1.5 percent (odds of 20 to 1) at high Reynolds numbers to ± 2.5 percent at the lowest Reynolds number. The uncertainty in setting local height, h, of the channel, which was performed by applying specially-designed spacer blocks, was ± 0.2 mm. The uncertainty in the heat flux, q, which was influenced by uncertainty in estimating the radiation as well as by uncertainty in measuring the electrical input, ranges from ± 2 percent at the highest Reynolds number to ± 4 percent at the lowest Reynolds number. The uncertainty in temperature measurement was ± 0.1°C. In this experiment the temperature difference $(T_w - T_b)$ at the outlet of the entrance section was between 3 and 5°C. If we assume for $(T_w - T_b)$ its lower bound of 3°C, the uncertainty in the heat-transfer coefficient α at that location together with the uncertainty in the Nusselt number (defined in equation (10)) range from ± 5 percent at the highest Reynolds number to ± 6 percent at the lowest Reynolds number. In the accelerating section as well as

in the downstream parallel-plate section, the channel height h was smaller than h_0, and the uncertainty of the channel height increases to influence appreciably the uncertainty in the Nusselt number. Further, when the flow reverted to the fully developed turbulent state in the downstream parallel-plate section, the temperature difference $(T_w - T_b)$ became smaller than in the entrance section, resulting in the increase in the uncertainty of $(T_w - T_b)$. In the case of $h_1 = 5$ mm ($\beta = 10/200$) and Re = 5000, the uncertainties of α and Nu at the end of the downstream parallel-plate section are estimated to be ± 10 percent and ± 11 percent, respectively. Except this extreme case, the uncertainty of the Nusselt number is less than ± 9 percent.

Turbulence Model

The mathematical model of turbulence employed in this work is explained in detail elsewhere [1]. It is based on the k-kL model proposed by Rotta [2, 3]. In this model the turbulent kinetic energy of the fluid, k, and a characteristic length scale of turbulence, L, are calculated from transport equations, in which k and kL are chosen as the dependent variables. In [1], a modification has been made to include the influence of the molecular viscosity. The modified version is expressed for the case of two-dimensional boundary-layer type flow as

$$\rho\bar{u}\frac{\partial k}{\partial x} + \rho\bar{v}\frac{\partial k}{\partial y} = \frac{\partial}{\partial y}\left\{\left(\frac{\mu_t}{\sigma_k} + \mu\right)\frac{\partial k}{\partial y}\right\} + \mu_t\left(\frac{\partial \bar{u}}{\partial y}\right)^2 - c_D\rho\frac{k^{3/2}}{L} - \frac{\mu}{y}\left(\frac{\partial k}{\partial y}\right) \tag{6}$$

$$\rho\bar{u}\frac{\partial (kL)}{\partial x} + \rho\bar{v}\frac{\partial (kL)}{\partial y} = \frac{\partial}{\partial y}\left\{\left(\frac{\mu_t}{\sigma_L} + \mu\right)\frac{\partial (kL)}{\partial y}\right\} + c_1\mu_t L\left(\frac{\partial \bar{u}}{\partial y}\right)^2 - c_2 c_D \rho k^{3/2} - c_3\mu_t\frac{2L^3}{y^2}\left(\frac{\partial \bar{u}}{\partial y}\right)^2 - c_4\mu\frac{L}{y}\left(\frac{\partial k}{\partial y}\right) \tag{7}$$

where the turbulent viscosity μ_t is given by

$$\mu_t = c_\mu f_\mu \rho\sqrt{k}L \tag{8}$$

The various constants in the foregoing equations were assigned the following values.

$$\begin{aligned}
\sigma_k &= 1.0 \\
\sigma_L &= 1.5 \\
c_D &= 0.15 \\
c_1 &= 1.3[1 - 0.55\exp\{-(R_t/8.35)^4\}] \\
c_2 &= 0.7[1 + 0.57\exp\{-(R_t/3)^2\}] \\
c_3 &= 3.1 \\
c_4 &= 6 \\
c_\mu &= 0.6 \\
f_\mu &= 1 - 0.7\exp\{-(R_t/20)^2\}
\end{aligned}$$

where the turbulent Reynolds number R_t is defined as

$$R_t = \sqrt{k}L/\nu \tag{9}$$

These constants were already tested in [1] and found to give good results for a heated gas flow in a circular tube. Since the last term of equation (6) and also that of equation (7) have a physical significance only near a wall, they are set to zero when $\partial k/\partial y < 0$. The boundary conditions for equations (6) and (7) are given on the wall surface as

$$k = L = 0, \quad \text{at } y = 0$$

Equations (6) and (7) were integrated together with the equations for momentum and energy for the actual experimental conditions by means of a modified version of the finite difference procedure developed by Patankar and Spalding [15]. A 600 mm long pre-entrance section that preceded the actual entrance section was introduced in the calculation, partly because the influence of the tripping wire was not clear. The initial conditions at the inlet of this pre-entrance section were assumed as follows:

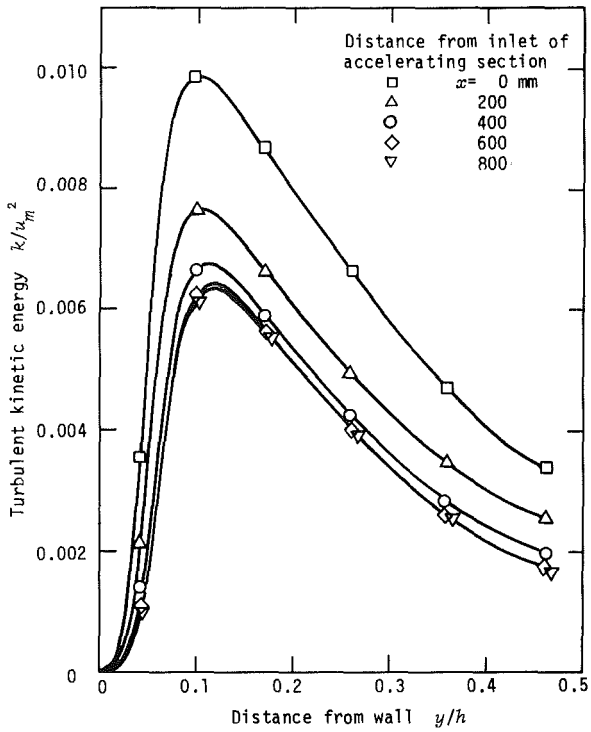

Fig. 3 Predicted development of asymptotic distribution of turbulent kinetic energy for Re = 7316, β = 8/900 and $K = 2.43 \times 10^{-6}$ (for symbols, see the bottom of Fig. 2)

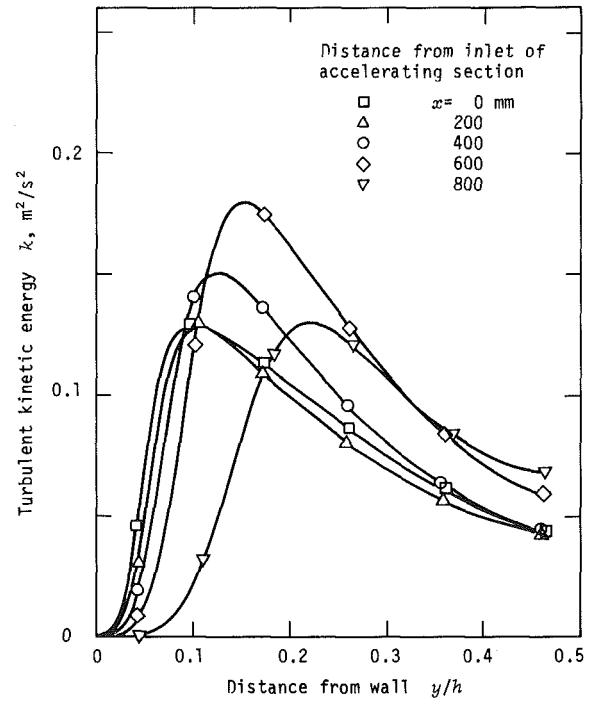

Fig. 4 Predicted change of turbulent kinetic energy distribution for Re = 7316, β = 12/900, and $K = 3.64 \times 10^{-6}$ (for symbols, see the bottom of Fig. 2)

$$u \propto y,\ k \propto y^2 \text{ and } L = \kappa y \text{ for } 0 < y \leqq h_0/4;$$

$$u = \text{const},\ k = C_k = \text{const and } L = \text{const for } h_0/4 \leqq y \leqq h_0/2$$

The constant C_k was assigned a value of $6\tau_{w0}/\rho$ where τ_{w0} was the wall shear stress for the fully developed turbulent state. In the y direction, the channel height was divided into 100 uneven intervals so that ten grid-points were included within the region: $y^+ < 20$ for the fully developed flow at Re = 10000. The step-width in the streamwise direction was set to one-twentieth of local channel height. A special manipulation was necessary to avoid a numerical instability. An outline of this technique is described in the Appendix. In integrating the energy equation, a uniform temperature distribution was assumed at the inlet of the pre-entrance section, and the condition of a heated wall started from the inlet of the actual entrance section. The turbulent Prandtl number for heat transfer was taken as 0.9.

Results and Discussions

Sink Flow. As a preliminary experiment, the so-called sink flow was investigated. It is generally admitted that, when flow is accelerated between converging flat plates, a self-preserving state is eventually reached, with the boundary-layer parameters such as friction coefficient and shape factor becoming all invariant with x. This asymptotic flow is usually referred to as a sink flow. There exist a number of experimental and theoretical works on the sink flow (see [17, 18]). The present work, however, differs from previous work in that (*i*) both hydrodynamic and thermal conditions at the inlet to the accelerating section are well defined, and (*ii*) the inclination of the roof plate β is very small, having an order of one-hundredth. It should be noted that even a small inclination of $\beta = 0.015$ is sufficient to yield $K = 3 \times 10^{-6}$ when Re = 10000, as is easily understood from equation (3).

At this experimental stage, a 900 mm long roof plate was employed. The latter half of the test channel of 900 mm in length (indicated as the accelerating and parallel-plate sections in Fig. 1) was used as an accelerating section without a downstream parallel-plate section. Measurements were performed for four Reynolds numbers: Re = 5000, 7300, 10,000, and 14,000. For each Reynolds number, the inclination of the roof plate was varied from β = 4/900 mm/mm to 12/900 mm/mm at intervals of 2/900 mm/mm. Tabulated data for all runs of the preliminary experiment and also those of the main experiment, described in the following section, are available in [19].

In Fig. 2 (*a*), experimental Nusselt numbers are plotted against the distance from the inlet of the accelerating section, x, for three typical runs taken at three different β's with a constant Reynolds number of about 7300. Here, the Nusselt number is defined by using the local height of the channel h as

$$\text{Nu} = \frac{2h\alpha}{\lambda} \tag{10}$$

where λ is the thermal conductivity of the fluid. Theoretical predictions from the foregoing turbulence model are also plotted as solid lines in Fig. 2. The Nusselt number for a developed turbulent flow between parallel plates, with one wall heated and the other wall insulated, is reported to be correlated by the following empirical equation [20].

$$\text{Nu} = 0.018\ \text{Re}^{0.8}\,\text{Pr}^{0.4} \tag{11}$$

Both experimental and theoretical Nusselt numbers just before the accelerating section agreed fairly well with equation (11), especially around Re = 10,000. As for the behavior in the accelerating section, agreement between the experimental and theoretical Nusselt numbers was again good, as is seen for the three typical runs in Fig. 2. It is noteworthy that, in the first two cases of $K < 3 \times 10^{-6}$ in Fig. 2 (*a*), the Nusselt number decreases more gradually with distance downstream, whereas in the last case where $K > 3 \times 10^{-6}$, the Nusselt number continues to decrease sharply. The distinction is more clearly demonstrated by the predicted variations of the friction coefficient c_f with x plotted in Fig. 2 (*b*).

The predicted changes of the turbulent kinetic energy distribution along the channel are shown in Figs. 3 and 4, which correspond to the cases of $\beta = 8/900$ and 12/900 in Fig. 2, respectively. In the coordinates of Fig. 3, a fully developed, unaccelerated turbulent state is expressed by a fixed distribution peculiar to the Reynolds number, i.e., the distribution at $x = 0$. In the case of $K = 2.4 \times 10^{-6}$ (Fig. 3), the asymptotic sink flow seems to have developed hydrodynamically at $x = 600$ mm, with the $k/u_m{}^2$-distribution merging to a single curve from that location forward. In the case of $K = 3.6 \times 10^{-6}$ (Fig. 4), on the other hand, the $k/u_m{}^2$-distribution, if plotted, lowers monotonically with x without limits, and the flow seems to converge eventually to the completely laminar state, with the relative turbulence intensity $(2k/3)^{1/2}/u_m$ tending to zero. Figure 4 shows subtle change of the absolute value of k in the accelerating section. Namely, the peak value of the k-distribution first increases with x, but then it does decrease from $x = 600$ mm.

From the results presented in this section, we may conclude that a turbulent flow can no longer be sustained beyond $K = 3 \times 10^{-6}$, as has been generally accepted [9, 17]. Further, the turbulence model employed in this work seems to be capable of predicting the development of the asymptotic sink flow as well as the process leading to the complete laminarization.

Reversion to Turbulence. The main experiment was carried out for four Reynolds numbers: Re = 5000, 7300, 10,000, and 14,000. For each Reynolds number, the inclination of the roof plate of the accelerating section was varied from β = 2/200 mm/mm to 10/200 mm/mm at intervals of 2/200 mm/mm. From equation (3), the acceleration parameter K exceeded 3×10^{-6} with the exception of the following cases: Re = 14,000 and $\beta \leqq 4/200$; Re = 10,000 and $\beta = 2/200$; and Re = 7300 and β = 2/200. Thus, the flow in the most cases would have tended to the completely laminar state if it had been subjected to acceleration beyond the finite length of l = 200 mm.

The experimental results for Re = 10000 and 7300, respectively, are presented in Figs. 5 and 6, together with the predictions from the turbulence model described previously. Figure 5 (*a*) shows the variations of the experimental local heat-transfer coefficient. Despite the great acceleration of the mean stream velocity, the heat-transfer coefficient increases only slightly in the accelerating section, due to the effect of laminarization. The heat-transfer coefficient tends to decrease in the first part of the parallel-plate section, reaches a minimum, and then it increases and approaches a new level that corresponds to the fully-developed turbulent state in the downstream parallel-plate section. In Fig. 5 (*b*) and Fig. 6, the results are plotted in the form of the variations of the Nusselt number. In these figures the Nusselt number should finally recover and converge to the initial value that it had before being subjected to acceleration, since the Reynolds number remains constant over the entire channel length.

The behavior of the Nusselt number in the downstream parallel-plate section has a resemblance to that observed in the thermal entrance region of a circular tube which starts after a bellmouth entrance in a laminar state and experiences the laminar-turbulent transition [21]. The decrease of the Nusselt number in the first part of the downstream parallel-plate section is considered to be essentially an entrance effect attributable to an increase of the thermal boundary layer. The fact that the Nusselt number reaches a minimum (at a point

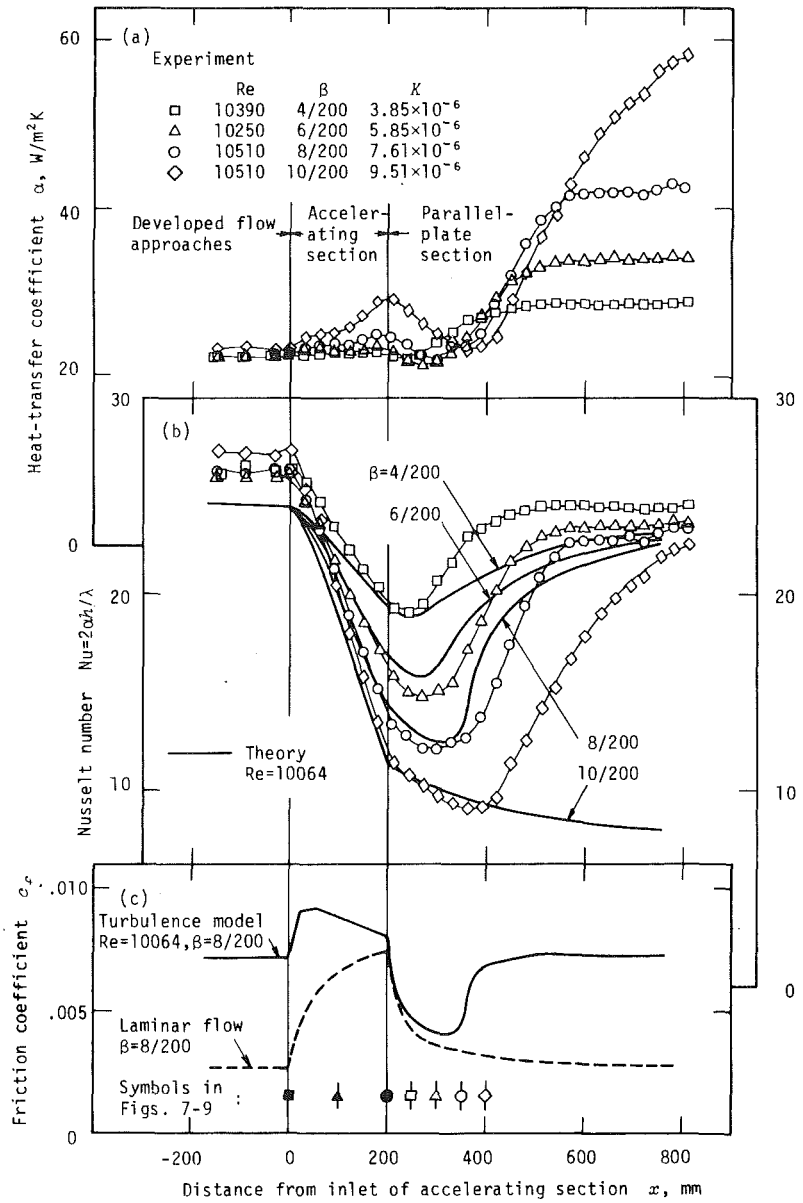

Fig. 5 Results for flows at Re = 10,000, laminarizing in 200 mm accelerating section and then reverting to turbulence in succeeding parallel-plate section: (*a*) variations of experimental local heat-transfer coefficient, (*b*) comparison between experimental and theoretical Nusselt numbers, (*c*) comparison of the friction coefficient predicted from the turbulence model to that assuming laminar flow

defined by $x=x_r$) and then increases suggests that the flow starts to become more turbulent from $x=x_r$. This hypothesis seems to be consistent with the fact that x_r increases according as the extent of laminarization at the inlet of the parallel-plate section (which may be quantitized by the ratio of Nu at that location to Nu_0 of the fully developed flow) becomes stronger, and also as the channel Reynolds number decreases (note the resemblance to the case with a bellmouth entrance in [21]). These tendencies are clearly demonstated in Figs. 5 and 6.

The theoretical predictions which are plotted by solid lines in the figures reproduce the complicated behavior of the experimental local Nusselt numbers fairly successfully, except for the cases of $\beta = 10/200$ in Fig. 5 and $\beta=8/200$ in Fig. 6. In these two cases a nondimensional distance $(x_r - l)/h_1$ reaches to 32 and 40, respectively, with a Reynolds number defined by $(x_r - l)u_m/\nu$ coming to 1.7×10^5 and 1.5×10^5. From [21], a flow in a circular tube with a bellmouth entrance undergoes transition to turbulence at a distance from the inlet x_{cr} that satisfies $x_{cr}u_m/\nu = 1.6\times10^5$. So it is not surprising that the theory fails in predicting the reversion to turbulence in the foregoing two cases, because it is likely that the transition in these cases may depend on wave type instabilities, which are not accounted for by the turbulence model employed in this work.

As for the case of Re = 10000 and $\beta = 8/200$, predicted changes along the channel of distributions of the normalized turbulent kinetic energy $k/u_m{}^2$, the turbulence length scale, L, and the total shear stress, τ, are presented in Figs. 7-9, respectively. The behavior in the accelerating section which extends from $x=0$ to 200 mm has been discussed previously, but Figs. 8 and 9 supply further information. In fact, the sharp decrease of τ near the wall, which was mentioned in the Introduction concerning the basic mechanism of laminarization, is clearly observed in Fig. 9. Comparison between the τ-distributions at $x=200$ mm (the outlet of the accelerating section) and $x=400$ mm is very demonstrative. The channel height is the same at the both locations, and at

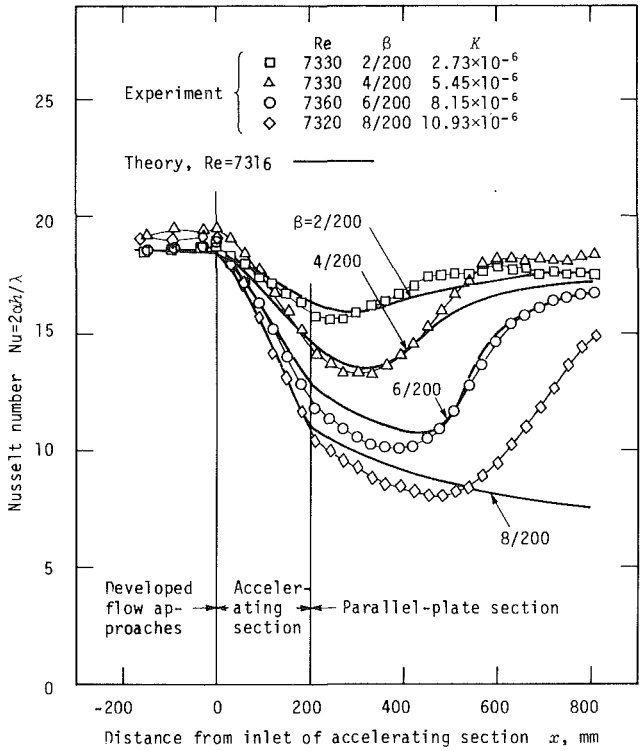

Fig. 6 Comparison between experimental and theoretical Nusselt numbers for flows at Re = 7300, laminarizing in 200 mm accelerating section and then reverting to turbulence in succeeding parallel-plate section

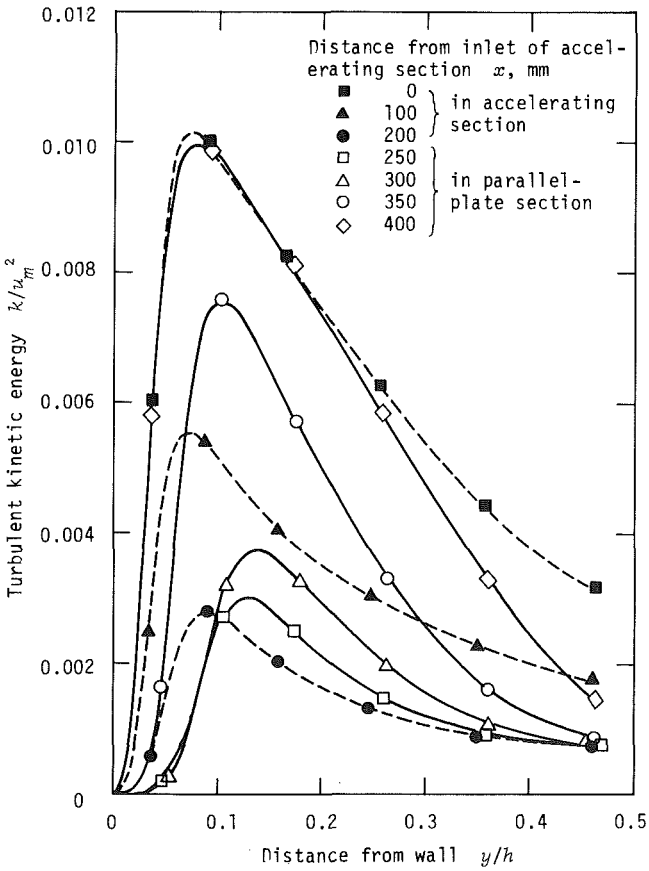

Fig. 7 Predicted change of turbulent kinetic energy distribution for Re = 10, 064 and β = 8/200 (for symbols, see the bottom of Fig. 5)

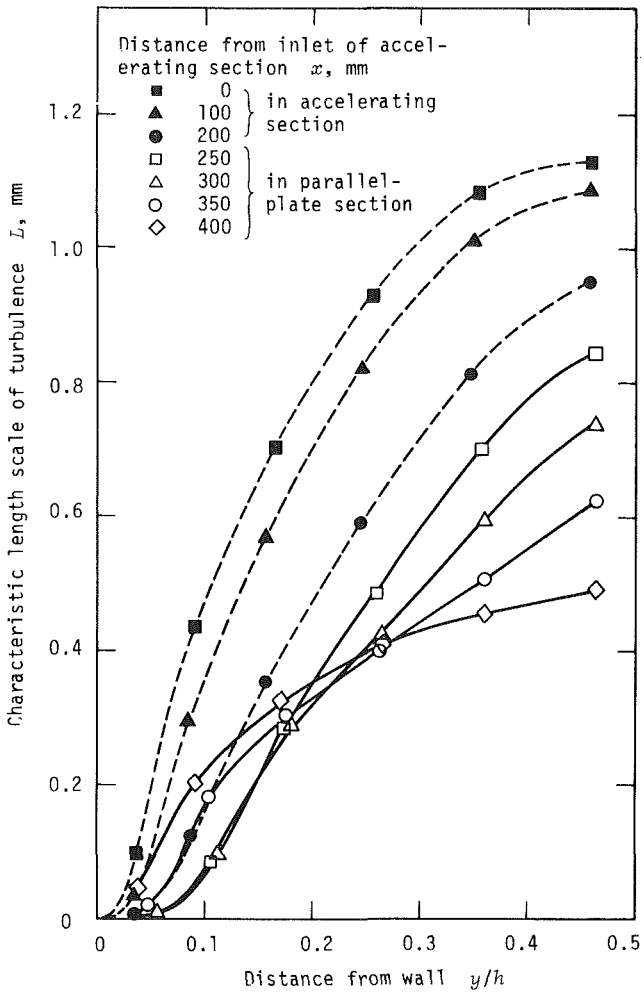

Fig. 8 Predicted change of turbulence length scale distribution for Re = 10,064 and β = 8/200 (for symbols, see the bottom of Fig. 5)

$x=400$ mm the flow has almost reverted to the fully developed turbulent state, as described later. For the fully developed turbulent flow at Re = 10000, $y/h=0.1$ is almost equivalent to $y^+=30$. In Fig. 8, the turbulence length scale L decreases monotonically in the accelerating section, but the relative rate of decrease is higher in the near-wall region than in the core region.

After the flow enters the parallel-plate section, the turbulent kinetic energy k shown in Fig. 7 continues to decrease in the neighborhood of the wall up to $x=300$ mm. At $x=350$ mm, it begins suddenly to increase having a peak at about $y/h=0.1$, and it almost reaches the fully developed turbulent distribution at $x=400$ mm. The turbulence length scale L as well continues to decrease up to $x=300$ mm (see Fig. 8). The rate is again rapid near the wall. It begins to increase together with k from $x=350$ mm in the near-wall region. At $x=400$ mm, the L-distribution has almost developed and agrees with that at $x=0$ when normalized by the local channel height. The shear stress τ_w at the wall sharply decreases immediately after the inlet of the parallel-plate section (see Fig. 9). It remains at a low value to $x=350$ mm. At this location the τ-distribution has a strange profile with a peak at $y/h=0.1$ in accordance with the newly generated maximum of the k-distribution. Here, it is noted that the Reynolds stress is nearly proportional to k except in the vicinity of the central plane of the passage. At $x=400$ mm, τ follows an almost linear distribution as for a fully developed flow.

In order to understand the behavior in the first part of the

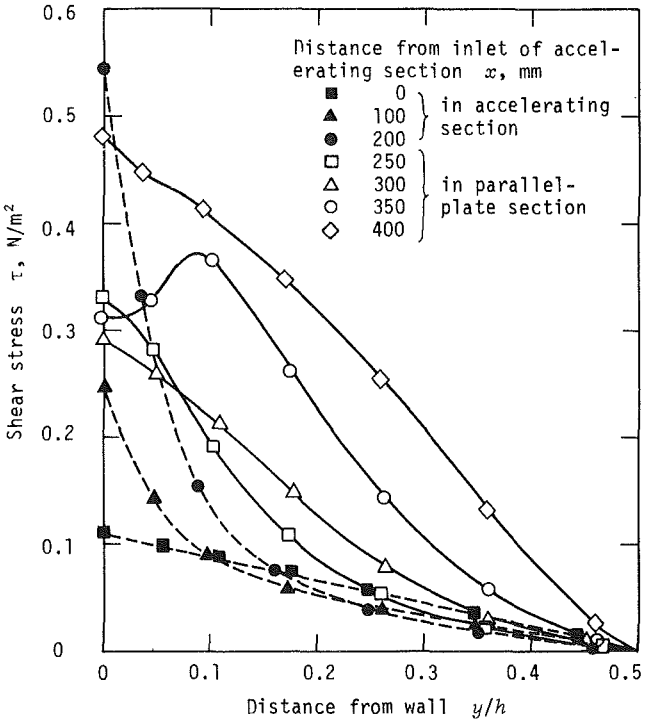

Fig. 9 Predicted change of shear stress distribution for Re = 10,064 and β = 8/200 (for symbols, see the bottom of Fig. 5)

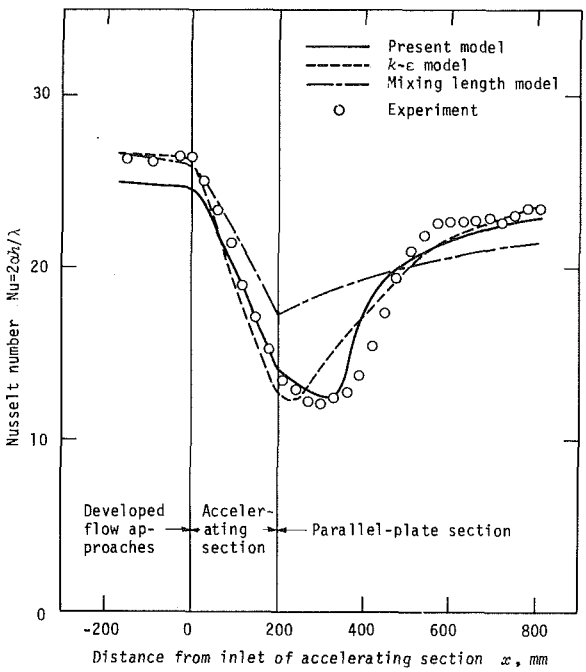

Fig. 10 Comparison between various turbulence models for the case of Re = 10,000 and β = 8/200

parallel-plate section, a solution assuming a completely laminar state was calculated for Re = 10000 and $\beta = 8/200$. In Fig. 5 (*c*), the friction coefficient c_f obtained in this solution is compared with that from the turbulence model. It can be seen that the variations of c_f from the two solutions behave quite similarly from $x = 200$ mm to $x = 320$ mm. At the same time, as for velocity and shear stress distributions, the turbulent solution has a strong resemblance to the laminar solution. Thus, it can be said that as a first approximation the apparent hydrodynamic features in the first part of the parallel-plate section can be explained by assuming a laminar state, when the flow is decisively laminarized in the near-wall region. A certain degree of turbulent motion, however, remains with a maximum at a considerable distance from the wall. It recovers its strength gradually. This is directly linked with an increase in the Reynolds stress. Finally, the turbulence level increases sharply and the flow is progressively restored to the fully turbulent state. It seems from Fig. 5 that, although the flow is hydrodynamically in an almost developed state at $x = 400$ mm, a longer distance is needed for the flow to develop thermally. This seems to be partly attributable to the fact that thermal disturbance has to penetrate to the unheated side of the channel beyond the shear-stress-equal-zero plane.

In Fig. 10, predictions from various turbulence models are compared with the experimental results for the case of Re = 10000 and β = 8/200. Jones and Launder's k-ϵ model [18] and a usual mixing length model were chosen. In these two models again, the turbulent Prandtl number for heat transfer was taken as 0.9. In the mixing length model, van Driest's formula was assumed near the wall:

$$l_{m1} = \kappa y\{1 - \exp(-y^+/A)\}$$

with $\kappa = 0.41$ and $A = 26.0$. Far from the wall it was assumed that

$$l_{m2} = \lambda(h/2)$$

with $\lambda = 0.09$. The foregoing two expressions were smoothly interpolated by

$$\frac{1}{l_m^2} = \frac{1}{l_{m1}^2} + \frac{1}{l_{m2}^2}$$

It can be seen from Fig. 10 that the mixing-length model fails in predicting the measured results. Especially, the minimum of the Nusselt number appears just at the end of the accelerating section, contrary to the experimental results. In such a simple mixing-length theory as above, a local equilibrium between generation and dissipation of the turbulent energy is implicitly assumed. So it is likely that such a model cannot deal with an inequilibrium flow such as the laminarizing flow successfully. A more refined mixing-length model, however, might be able to predict the laminarizing flow, but such a model will require more experimental knowledge and ad hoc empirical input. The present model, on the other hand, was already found to be successful also for a strongly heated gas flow in a circular tube with the same set of constants as employed here. The k-ϵ model gives a good agreement in the accelerating section, but the predicted dip of the Nusselt number in the entrance part of the downstream parallel-plate section is too small. It is generally admitted, however, that the k-ϵ model has a broad applicability as well as predictive capabilities. It seems possible that the k-ϵ model will give better predictions than present if the constants in the model are optimized.

Conclusions

When a low Reynolds number turbulent flow between parallel plates is laminarized through a passage between converging flat plates and then flows into a parallel-plate channel, the Nusselt number decreases at first in the downstream parallel-plate section together with the friction coefficient. Reversion to turbulence proceeds gradually. It manifests itself as a sharp increase in the Nusselt number as well as in the friction coefficient. Finally, the flow approaches a fully developed turbulent state. The flow and heat transfer in the converging and parallel sections are predicted acceptably well by the k-kL model in [1], provided that the extent of laminarization at the inlet of the parallel-plate section is not very high, i.e., unless the Nusselt number at that location falls below 12, within the scope of the present investigation.

Acknowledgment

This paper was completed during the first author's visit to the University of California at Davis. He would like to express his sincere gratitude to Professor W. H. Giedt, who kindly reviewed the manuscript and made constructive comments. He also acknowledges various conveniences offered by the Department of Mechanical Engineering of UCD.

References

1 Kawamura, H., "Analysis on Laminarization of Heated Turbulent Gas Using a Two-Equation Model of Turbulence," *Proceedings of the 2nd Symposium on Turbulent Shear Flows*, London, 1979, pp. 18.16-18.21; also, Kawamura, H., "Prediction of Heated Gas with Large Property Variations Using a Two-Equation Model of Turbulence," *Transactions of the Japan Society of Mechanical Engineers*, Series B, Vol. 45, No. 395, 1979, pp. 1038-1046.

2 Rotta, J. C., "Statistische Theorie nichthomogener Turbulenz," *Zeitschrift für Physik*, Bd. 129, 1951, s. 547-572.

3 Rotta, J. C., *Turbulente Strömungen*, Teubner, Stuttgart, 1972.

4 Perkins, H. C. and Worsoe-Schmidt, P., "Turbulent Heat and Momentum Transfer for Gases in a Circular Tube at Wall to Bulk Temperature Ratios to Seven," *U.S. Atomic Energy Commission Technical Report*, SU247-7, 1964; also, *International Journal of Heat and Mass Transfer*, Vol. 8, 1965, pp. 1011-1031.

5 Coon, C. W., "Transition from the Turbulent to the Laminar Regime for Internal Convective Flow with Large Property Variations," PhD dissertation, The University of Arizona, 1968; also, Coon, C. W., and Perkins, H. C., ASME JOURNAL OF HEAT TRANSFER, Vol. 92, 1970, pp. 506-512.

6 Bankston, C. A., "The Transition from Turbulent to Laminar Gas Flow in a Heated Pipe," ASME JOURNAL OF HEAT TRANSFER, Vol. 92, 1970, pp. 569-579.

7 Tanaka, H. and Shimizu, J., "Laminarization in Low Reynolds Number Turbulent Duct Flows," ASME JOURNAL OF HEAT TRANSFER, Vol. 99, 1977, pp. 682-684.

8 Launder, B. E., "Laminarization of the Turbulent Boundary Layer in a Severe Acceleration," ASME *Journal of Applied Mechanics*, Vol. 31, 1964, pp. 707-708.

9 Moretti, P. M. and Kays, W. M., "Heat Transfer to a Turbulent Boundary Layer with Varying Free-Stream Velocity and Varying Surface Temperature," *International Journal of Heat and Mass Transfer*, Vol. 8, 1965, pp. 1187-1202.

10 Back, L. H. and Seban, R. A., "Flow and Heat Transfer in a Turbulent Boundary Layer with Large Acceleration Parameter," *Proceedings of the 1967 Heat Transfer and Fluid Mechanics Institute*, edited by P. A. Libby et al., pp. 410-426.

11 Patel, V. C. and Head, M. R., "Reversion of Turbulent to Laminar Flow," *Journal of Fluid Mechanics*, Vol. 34, Part 2, 1968, pp. 371-392.

12 Badri Narayanan, M. A. and Ramjee, V., "On the Criteria for Reverse Transition in a Two-Dimensional Boundary Layer Flow," *Journal of Fluid Mechanics*, Vol. 35, Part 2, 1969, pp. 225-241.

13 Hall, W. B. and Jackson, J. D., "Laminarization of a Turbulent Pipe Flow by Buoyancy Forces," ASME Paper, No. 69-HT-55, presented at the ASME-AIChE Heat Transfer Conference, Minneapolis, Minn., Aug. 1969.

14 Tanaka, H., Tsuge, A., Hirata, M., and Nishiwaki, N., "Effects of Buoyancy and of Acceleration Owing to Thermal Expansion on Forced Turbulent Convection in Vertical Circular Tubes," *International Journal of Heat and Mass Transfer*, Vol. 16, 1973, pp. 1267-1288.

15 Patankar, S. V. and Spalding, D. B., *Heat and Mass Transfer in Boundary Layers*, 2nd ed., Intertext Books, London, 1970.

16 Arya, S. P. S., "Buoyancy Effects in a Horizontal Flat-Plate Boundary Layer," *Journal of Fluid Mechanics*, Vol. 68, Part 2, 1975, pp. 321-343.

17 Jones, W. P. and Launder, B. E., "Some Properties of Sink-Flow Turbulent Boundary Layers," *Journal of Fluid Mechanics*, Vol. 56, Part 2, 1972, pp. 337-351.

Part 2, 1972, pp. 337-351.

18 Jones, W. P. and Launder, B. E., "The Prediction of Laminarization with a Two-Equation Model of Turbulence," *International Journal of Heat and Mass Transfer*, Vol. 15, 1972, pp. 301-314.

19 Tateno, A., "Laminarization of Low Reynolds Number Turbulent Duct Flow and its Subsequent Reversion to Turbulence," Master thesis, Department of Mechanical Engineering, University of Tokyo, 1980 (in Japanese).

20 Dalle Donne, M. and Meerwald, E., "Heat Transfer and Friction Coefficients for Turbulent Flow of Air in Smooth Annuli at High Temperatures," *International Journal of Heat and Mass Transfer*, Vol. 16, 1973, pp. 787-809.

21 Mills, A. F., "Experimental Investigation of Turbulent Heat Transfer in the Entrance Region of a Circular Conduit," *Journal of Mechanical Engineering Science*, Vol. 4, No. 1, 1962, pp. 63-77.

APPENDIX

In the numerical integration of equations (6) and (7), the solution often becomes unstable, giving a negative value of k and L. A reason and a technique to avoid it are described here.

Assuming a fully developed flow for simplicity, one can rewrite equation (6) as

$$-\frac{\partial}{\partial y}\left\{\left(\frac{\mu_t}{\sigma_k}+\mu\right)\frac{\partial k}{\partial y}\right\}=\mu_t\left(\frac{\partial \bar{u}}{\partial y}\right)^2 - c_D\rho\frac{k^{3/2}}{L}-\frac{\mu}{y}\left(\frac{\partial k}{\partial y}\right) \tag{6a}$$

A finite difference formula for equation (6a) is

$$-Ak_{i-1}+Bk_i-Ck_{i+1}=\mu_t\left(\frac{\partial \bar{u}}{\partial y}\right)_i^2-c_D\rho\frac{k_i^{3/2}}{L_i} -\frac{\mu}{y_i}\left(\frac{\partial k}{\partial y}\right)_i \tag{6b}$$

where i is the suffix for the mesh in the direction perpendicular to the flow, and A, B, and C are the coefficients relevant to the diffusion term.

This type of equation with three unknowns can be solved easily by a successive substitution (see [15] for example). However, the direct application of equation (6b) often gives a negative k_i. This is because the generation and dissipation terms are very large in their magnitude and their difference is balancing with the diffusion term. So, only a small change in the generation and/or dissipation term results in a rather large change in their difference giving even a negative k_i sometimes.

This difficulty was already recognized in the study of [1]. After many trials, the following manipulation of equation (6b) was found to be effective.

$$-Ak_{i-1}+\left[B+c_D\rho\frac{k_i^{1/2}}{L_i}+\frac{\mu}{y_i}\left(\frac{\partial k}{\partial y}\right)_i/k_i\right]k_i-Ck_{i+1} =\mu_t\left(\frac{\partial \bar{u}}{\partial y}\right)_i^2 \tag{6c}$$

a similar manipulation is made for equation (7). These equations together with the momentum equation can be solved iteratively (or, in the case where the convective terms are included, with a very small mesh in the flow direction), without giving a negative k or L.

Flow Induced Vibration in a Heat Exchanger With Seal Strips

J. H. Kissel
American Standard, Heat Transfer Division,
Buffalo, N.Y. 14240
Mem. ASME

Flow induced vibration tests using water as the shell side medium were conducted on a shell and tube exchanger with single segmental baffles and various tube layouts. The heat exchanger was of the externally packed floating head type with seal strips that directed the water flow into the bundle to prevent by-passing of the fluid between the bundle and the shell. High localized velocities exist in the vicinity of the seal strips and contributed directly to the vibration problem. The tube natural frequency for various baffle spacings was measured at the vibration point and a gap velocity at the critical section of the bundle was estimated. A correlation was then made with these parameters and the fluidelastic excitation theory. A discussion of the velocity profile through the heat exchanger is included.

1 Introduction

Shell and tube heat exchangers are often fabricated where the tube bundle is allowed to expand axially and independently of the shell to allow for differential thermal expansion or to provide a removable bundle for cleaning purposes. For a particular design, the floating tube sheet is secured by external packing rings, and the waterbox is attached directly to the tube sheet. The tube bundle diameter in this type of construction is generally much smaller than the shell diameter and seal strips are employed to prevent by-passing of shell side fluid. These seal strips improve heat transfer but create high localized velocities which encourage flow induced vibration at low flow rates.

Tests were conducted on a small diameter heat exchanger employing seal strips with water on the shell side. The tube bundle diameter and baffle spacing were varied and vibration results were compared to those predicted by existing theory and to full bundle results.

Prediction of flow induced vibration involves an analysis of the gap velocities in the critical areas of the heat exchanger. These velocities are extremely difficult to measure so it is necessary to calculate velocities based on available flow area and effective fluid flow rate. Another parameter of equal importance and equally difficult to predict is the logarithmic decrement which is the sum of the system mechanical,

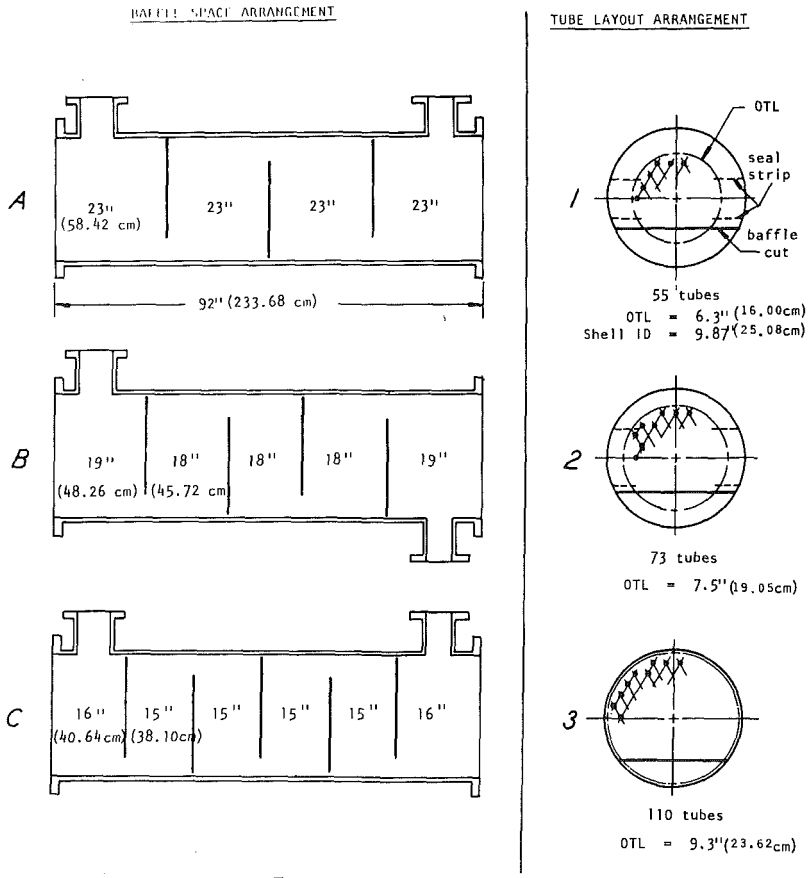

Fig. 1 Baffle and tube layout

Contributed by the Heat Transfer Division for publication in the JOURNAL OF HEAT TRANSFER. Manuscript received by the Heat Transfer Division December 20, 1980.

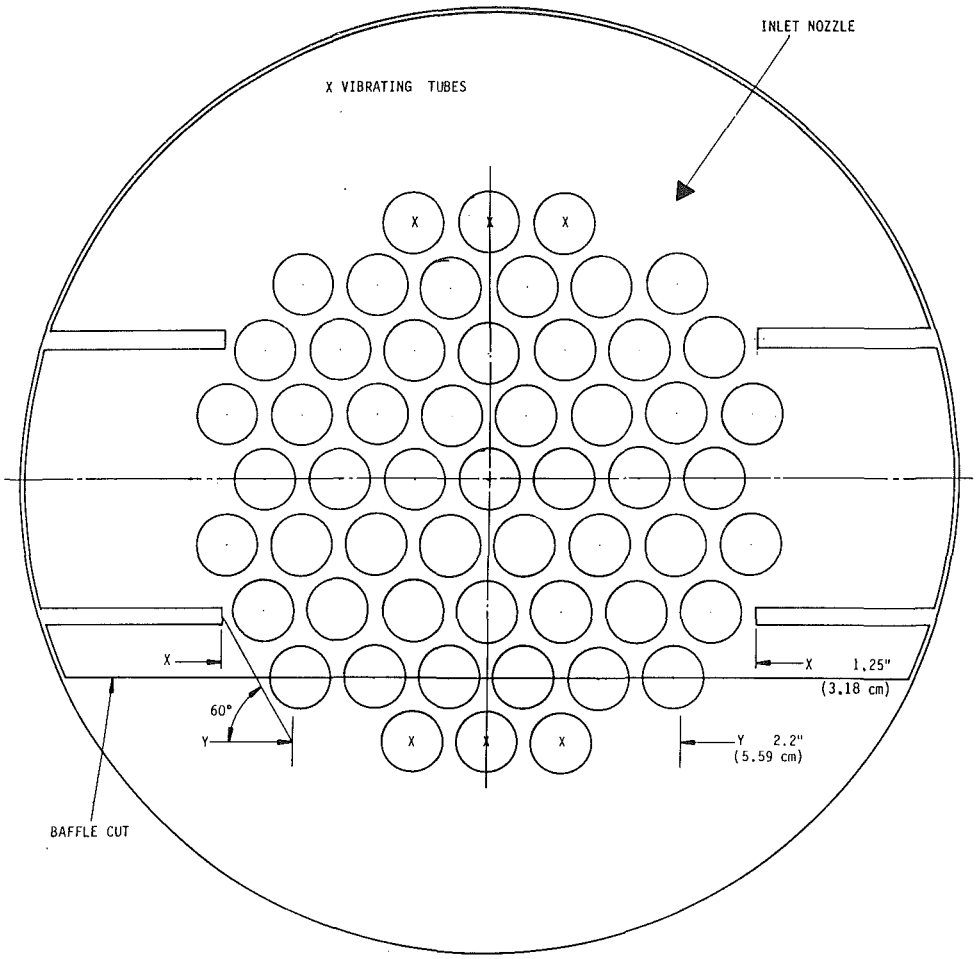

TEST	BFL. SPG. in. (cm)	VIBR. FLOW GPM (m^3/s)	VELOCITY ft/sec (m/s) X - X	Y - Y	WINDOW	NOZZLE	LOCATION OF VIBR.
A1	23" (58.42)	550 (0.35)	5.4 (1.65)	3.1 (0.94)	8.7 (2.65)	6.2 (1.89)	Away from Nozzle
B1	18" (45.72)	725 (0.46)	9.1 (2.77)	5.2 (1.58)	11.4 (3.47)	8.2 (2.50)	Under Nozzle
B1.1	18" (45.72)	900 (0.57)	11.3 (3.44)	6.4 (1.95)	14.0 (4.27)	10.2 (3.11)	Away from Nozzle
C1	15" (38.10)	910 (0.57)	13.7 (4.18)	7.9 (2.41)	14.2 (4.33)	10.3 (3.14)	Away from Nozzle

Fig. 2 Estimated bundle velocities (55 tubes)

hysteretic, and hydrodynamic damping. Viscous damping by definition increases with natural frequency and depending on tube amplitude and initial tube constraint conditions could be nonlinear. The logarithmic decrement is used for correlating test data and determining the threshold instability constant in the fluidelastic excitation mechanism.

A certain amount of scatter in the test results is apparent because of the difficulty in estimating the velocity and damping. However, the results are consistent enough to allow a substantial reduction in degree of safety factor previously thought necessary for this type of design.

2 Heat-Exchanger Data and Test Procedure

Figure 1 describes the baffle and tube layout in the test heat exchangers. Each of the three tube layouts with the various outer tube limits (OTL) was tested with each of the three baffle spacings. The shell dia was 10 in. (25.40 cm) nominal with 6 in. (15.24 cm) nominal inlet and outlet nozzles. The tubes were 5/8 in. (1.59 cm) dia, admiralty brass, 18 BWG on 25/32 in. (1.98 cm) triangular pitch and 92 in. (234 cm) long. The test heat exchanger could be readily assembled and disassembled to accommodate the various bundle and baffle

Nomenclature

d = tube diameter, ft (m)
f_n = natural frequency in the n^{th} mode of vibration, Hz
OTL = outer tube limit, diameter of a circle circumscribed around the outermost tubes, ft (m)
U = flow velocity in the gap between adjacent tubes in the same transverse row, ft/s (m/s)
U_{en} = effective flow velocity for the n^{th} mode of vibration, ft/s (m/s)
W_e = tube weight per unit length, lb/ft (Kg/m)
x = vibration amplitude, ft (m)
z = position along the length of the tube measured from one end, ft (m)
L = span length, ft (m)
β = threshold instability constant, dimensionless
δ_η = logarithmic decrement for a tube vibrating in the n^{th} mode of vibration, dimensionless
ρ = fluid density, lb/ft^3 (Kg/m^3)

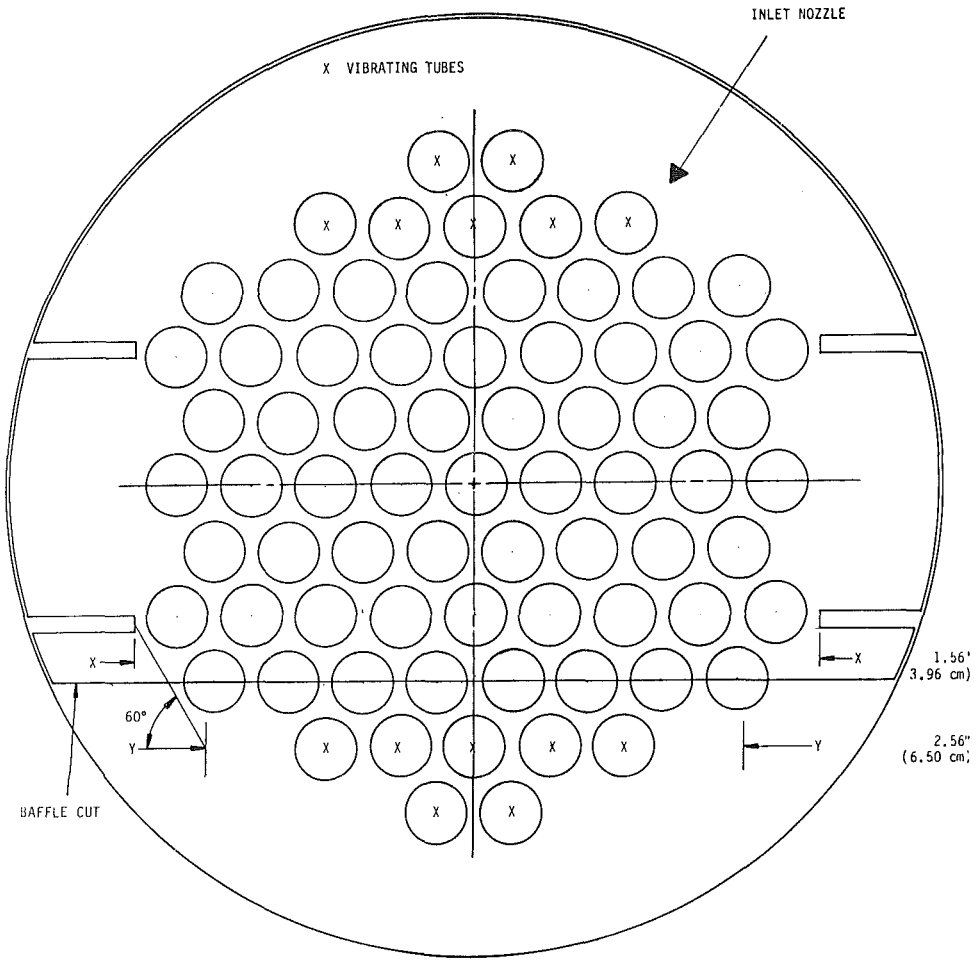

TEST	BFL. SPG. in. (cm)	VIBR. FLOW GPM (m^3/s)	VELOCITY ft/sec (m/s) X - X	Y - Y	WINDOW	NOZZLE	LOCATION OF VIBR.
A2	23" (58.42)	720 (0.45)	5.6 (1.71)	3.4 (1.04)	14.5 (4.42)	8.1 (2.47)	Away from Nozzle
B2	18" (45.72)	870 (0.55)	8.7 (2.65)	5.3 (1.62)	17.5 (5.33)	9.8 (2.99)	Under Nozzle
C2	15" (38.10)	1230 (0.78)	14.8 (4.51)	9.0 (2.74)	24.7 (7.53)	13.9 (4.24)	Away from Nozzle

Fig. 3 Estimated bundle velocities (73 tubes)

arrangements. The tubes were sealed with individual O-rings compressed between tube sheets at each end of the test unit.

Water at room temperature was circulated through the shell side with flow rate increasing until the onset of vibration was detected. The resulting natural frequency of tube vibration was measured with an accelerometer mounted on the inside of the tube. The accelerometer was mounted in an adapter with O-rings and could conveniently be moved axially along the tube and from tube to tube. Flow rates and pressure drops were measured for all tests.

Figures 2, 3, and 4 show the tube pattern and location of the sealing strips, baffle cut, and shell nozzle inlet. The shell side fluid flow fractions across the tubed section and between outer tube limit and shell inside diameter were calculated using the HTRI [1] stream analysis method. It was found that, for the first two groups of tests (55 tubes and 73 tubes), approximately 88 percent of the total flow follows these paths, with 12 percent leakage through the tube to baffle tube holes and between baffle outside diameter and shell inside diameter. For the full bundle (110 tubes) the effective flow fraction across the bundle is 80 percent with 20 percent leakage.

The crossflow velocity was then calculated at two sections of the bundle as shown in Figs. 2, 3, and 4.

The values of X-X are shown for reference only, since the most severe tube vibration occurs at plane Y-Y which is the first row past the baffle cut.

The velocity at Y-Y is predicted by assuming a 60 deg angle from the critical first tube row past the baffle cut to the seal strip edge. The dimensions at X-X and Y-Y in the figures represent the length at those points minus tube diameters. This length times the baffle spacing will determine the free flow area which in combination with the effective flow rate will yield the gap velocity. The window velocity is based on the free window area and effective flow rate, while the nozzle velocity is predicted on the total flow.

3 Test Results

Table 1 lists the pertinent data for the heat exchanger and compares some constants as predicted by the fluidelastic excitation theory.

The measured tube natural frequency correlates within ±7 percent of the calculated frequency, assuming fixed end supports, simply supported intermediate supports, and a hydrodynamic inertia coefficient of 1.8 for 1.25 triangular pitch to tube diameter ratio. This hydrodynamic inertia coefficient was used to determine the effective tube weight per unit length (W_e) in the Connors [2] fluidelastic excitation prediction:

$$\frac{U}{f_n d} = \beta\left(\frac{W_e \delta_n}{\rho d^2}\right)^{1/2}$$

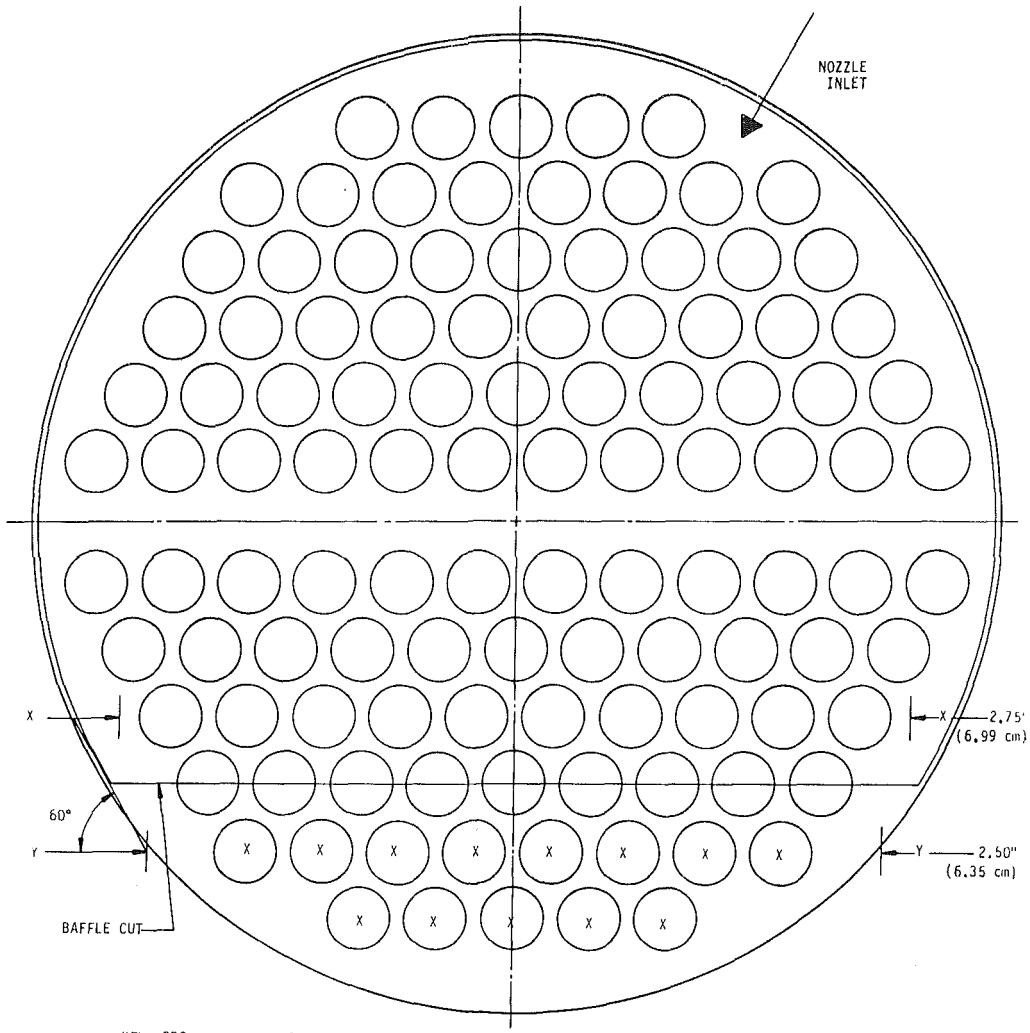

TEST	BFL. SPG. in. (cm)	VIBR FLOW GPM (m^3/s)	VELOCITY ft/sec (m/s) X - X	Y - Y	WINDOW	NOZZLE	LOCATION OF VIBR.
A3	23" (58.42)	700 (0.44)	2.8 (0.85)	3.2 (0.98)	17.6 (5.36)	7.9 (2.41)	Away from Nozzle
B3	18" (45.72)	1000 (0.63)	NO VIBRATION				

Fig. 4 Estimated bundle velocities (110 tubes)

In this relationship, U is the gap velocity, f_n is the tube natural frequency, d is the tube diameter, ρ is the fluid density and δ_n is the log decrement.

Connor's tests [3] indicate that an instability constant $\beta = 4.0$ should be used for the triangular (30 deg) tube pattern, with a tube pitch to tube diameter ratio of 1.25 as we have here. Table 1 lists the values of the calculated log decrement using $\beta = 4.0$ at both the X-X and Y-Y locations in the bundle.

4 Discussion

Several interesting items are noted in Table 1. The crossflow velocity at the Y-Y section for the 23 in. (58.42 cm) baffle spacing tests (A1, A2, A3) ranges from 3.1 ft/s (0.94 m/s) to 3.4 ft/s (1.04 m/s), which is fairly consistent. The same velocity consistency exists for the 18 in. (45.72 cm) baffle spacing tests (B1, B2) where the Y-Y velocity is 5.2 ft/s (1.58 m/s). This velocity at Y-Y is the important parameter because this is the critical first tube row past the baffle cut where the maximum tube vibration was observed.

This consistency is not inherent in either the window or nozzle velocities. In test A1, the window velocity is 8.7 ft/s (2.65 m/s), while for test A2, it is considerably greater at 14.5 ft/s (4.42 m/s). If window velocity were a major contributing factor to vibration, the critical flow rate in test A2 would be closer to that of test A1. Since this was not the case, it can be concluded that window velocity is of lesser significance than cross flow velocity. This observation has been reported by others in the literature and is undoubtedly due to the flow being parallel to the tube axis in the window.

For the tests with the 23 in. (58.42 cm) and 15 in. (38.10 cm) baffle spacing, both inlet and outlet nozzles are located at the top of the heat exchanger, and the tubes diametrically opposed or away from the nozzles were the first to vibrate. The natural frequency for the baffle window tubes directly under the nozzle is 7 to 10 percent greater than the window tubes away from the nozzle. This slightly higher natural frequency should make these tubes less susceptible to vibration than those away from the nozzle. However, tubes in close proximity to the nozzle are subjected to high bundle entrance velocity which should negate the effects of a slightly higher natural frequency. For test A3, 23 in. (58.42 cm) baffle spacing, the bundle entrance velocity as calculated by the TEMA method [4] is in excess of 25 ft/s (7.62 m/s). Even with this extremely high velocity, the tubes did not vibrate as readily as those at the bottom of the heat exchanger.

Table I Test results

NO. TUBES	TEST NO.	BAFFLE SPACING (in.)	MEAS. FREQ. (HZ)	VIBR. FLOW (GPM)	VELOCITY (FT/SEC) X-X	Y-Y	WINDOW	NOZZ.	LOG DECREMENT β=4.0 X-X	Y-Y
55	A1	23	24	550	5.4	3.1	8.7	6.2	.35	.11
	B1	18	38	725	9.1	5.2	11.4	8.2	.39	.13
	C1	15	48	910	13.7	7.9	14.2	10.3	.55	.18
73	A2	23	24	720	5.6	3.4	14.5	8.1	.37	.14
	B2	18	37	870	8.7	5.3	17.5	9.8	.36	.13
	C2	15	47	1230	14.8	9.0	24.7	13.9	.69	.24
110	A3	23	27	700	2.8	3.2	17.6	7.9	.07	.11
	B3	18	37	No Vibr 1000 +	-	-	-	-	-	-

NO. TUBES	TEST NO.	BAFFLE SPACING (cm)	MEAS. FREQ. (HZ)	VIBR. FLOW (m^3/s)	VELOCITY (m/s) X-X	Y-Y	WINDOW	NOZZ.	LOG DECREMENT β=4.0 X-X	Y-Y
55	A1	58.42	24	0.35	1.65	0.94	2.65	1.89	.35	.11
	B1	45.72	38	0.46	2.77	1.58	3.47	2.50	.39	.13
	C1	38.10	48	0.57	4.18	2.41	4.33	3.14	.55	.18
73	A2	58.42	24	0.45	1.71	1.04	4.42	2.47	.37	.14
	B2	45.72	37	0.55	2.65	1.62	5.33	2.99	.36	.13
	C2	38.10	47	0.78	4.51	2.74	7.53	4.24	.69	.24
110	A3	58.42	27	0.44	0.85	0.98	5.36	2.41	.07	.11
	B3	45.72	37	No Vibr 0.63 +	-	-	-	-	-	-

This behavior is typical of many industrial heat exchangers. Examination of the mode shapes is appropriate and may help explain why certain tubes are more susceptible to vibration than others. Figure 5 shows the calculated first four mode shapes for test A3 for the window tubes underneath the nozzles, and Fig. 6 shows those 180 deg away. Since the fluid at the inlet nozzle impinges on the short span underneath the nozzle, it is particularly evident for the first mode that the effect of velocity is much less pronounced than it is in the adjacent axial long span. The mode shape for the tubes 180 deg away or at the bottom of the heat exchanger indicate high susceptibility of these tubes to vibration and they are in fact the first to vibrate.

Another fact that may explain why the tubes underneath the inlet nozzle did not vibrate as readily as those 180 deg away is the location of the inlet nozzle in relation to the first baffle. Figure 7 illustrates this relationship. For the 23 in. (58.42 cm) baffle case, the flow through the 6 in. (15.24 cm) inlet nozzle will impinge on approximately a fourth of the span with one end of the span fixed at the tube sheet providing additional support.

An illustration of this effect can be seen by applying the effective velocity rationale presented in Connors [3] for an array of tubes comprised of a single span with constant fluid density and tube mass per unit length.

For the case where an end is fixed and the other end simply supported, the fundamental mode shape is

$$x = \sinh\frac{\pi Z}{L} - \sin\frac{\pi Z}{L} + \gamma\left(\cosh\frac{\pi Z}{L} - \cos\frac{\pi Z}{L}\right)$$

where

$$\gamma = \left[\frac{\sinh\alpha - \sin\alpha}{\cos\alpha - \cosh\alpha}\right]$$

where α is the eigenvalue corresponding to the first mode of a clamped simple beam.

Assume a flow velocity distribution

$$U = U_{(z)}$$

The integral equivalent of Connors [3] equation (10) is

$$U_{en} = \frac{\int_0^L \left[U_{(z)}^2\right]\left[\sinh\frac{\pi Z}{L} - \sin\frac{\pi Z}{L} + \gamma\left(\cosh\frac{\pi Z}{L} - \cos\frac{\pi Z}{L}\right)\right]^2 dz}{\int_0^L \left[\sinh\frac{\pi Z}{L} - \sin\frac{\pi Z}{L} + \gamma\left(\cosh\frac{\pi Z}{L} - \cos\frac{\pi Z}{L}\right)\right]^2 dz}$$

If the flow impinges on a fourth of the span nearest the next support, and after considerable integration we obtain:

$$U_{en} = 0.123\, U_0$$

If it is assumed that the flow only impinges on the center of the span where:

$$U_{(z)} = U_0 \text{ for } \frac{3L}{8} \le z \le \frac{5L}{8}$$

$$U_{en} = 0.691\, U_0$$

A ratio of these two effective velocities shows that the flow

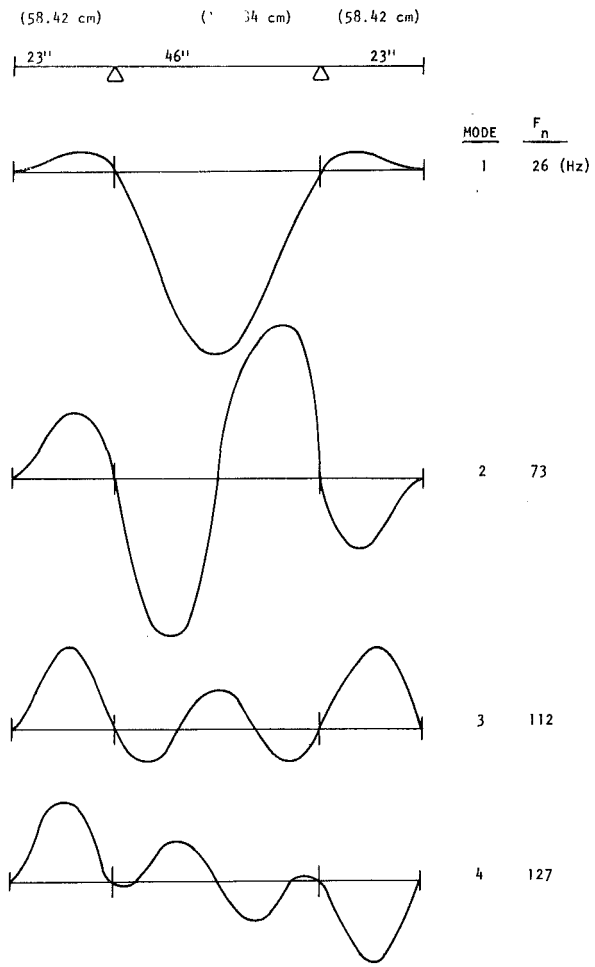

Fig. 5 Mode shapes and frequencies for test A3—tubes underneath the nozzles

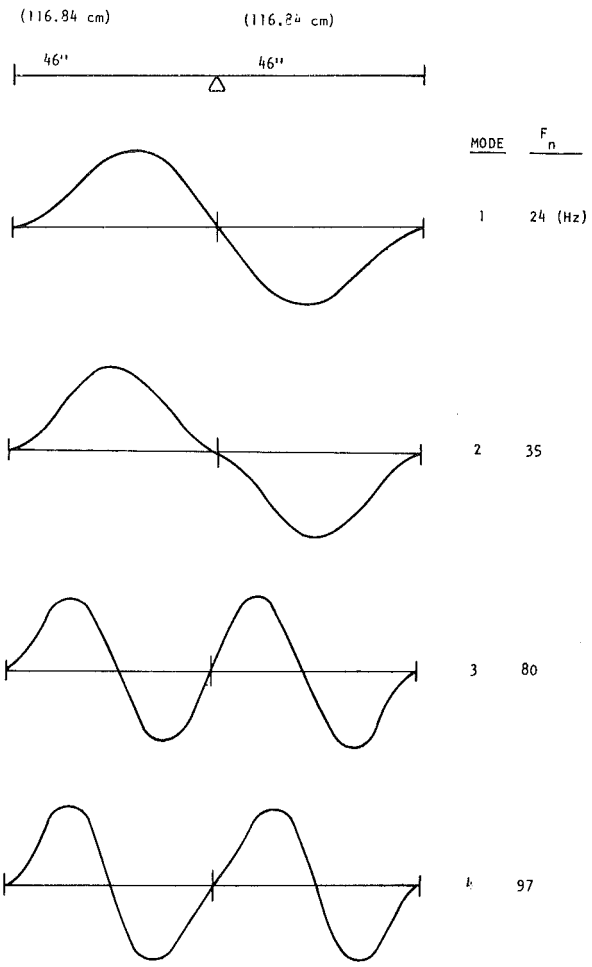

Fig. 6 Mode shapes and frequencies for test A3—tubes away from nozzles

in the quarter span nearest the fixed support would have to be 0.691/0.123 = 5.62 times greater than in the central quarter span to have the same effect.

This analysis clearly illustrates the support given to the tubes by the fixed condition at the tube sheets and the effect of nozzle to baffle location. It would be interesting and informative to conduct tests where the location of the inlet nozzle is moved axially along the shell without changing any of the other parameters to determine the optimum position of nozzle inlet in regard to first baffle.

In the B1 and B2 tests, the nozzles were 180 deg apart with 18 in. (45.72 cm) baffle spacing. The window tubes at the top and bottom of the heat exchanger have the same natural frequency, and a comparison of tests B1 and B1.1 in Fig. 2 show the inlet nozzle tubes were the first to vibrate.

Figure 8 shows the mode shapes of the top window tubes. This indicates that a high flow velocity over the 37 in. (93.98 cm) span should easily excite mode 2. It is not entirely clear why the top tubes vibrated sooner than the bottom, since the mode shapes and natural frequencies are identical. Spanwise variation in velocity could be responsible since this has been shown to be a significant parameter.

The test results in Table 1 list calculated log decrements based on a constant instability factor of 4.0. For both the first and second series of tests with 55 and 73 tubes, respectively, there is an increase of log decrement (or conversely in the instability constant) with a decrease in baffle spacing.

Damping is obviously a variable and could depend on natural frequency and amplitude of vibration. It is interesting

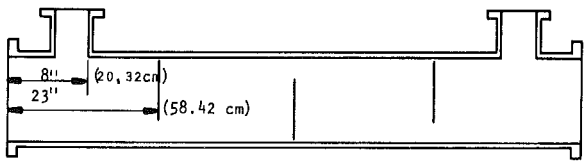

Fig. 7 Nozzle and first baffle position for test A3

to note that the log decrement is directly proportional to the window velocity and increases with increasing natural frequencies.

The damping in the system is difficult to predict and testing generally is accomplished by summing the mechanical, hysteretic, and hydrodynamic damping in still fluid. The damping for tube arrays in a flowing fluid can be quite different from still fluid, and testing indicates that the tubes continue to vibrate well after the flow has been decreased below the critical. In test A3, the tubes started to vibrate at 700 gpm (0.44 m^3/s) and stopped at 630 gpm (0.40 m^3/s). It may be possible by further test to relate this difference in flow as a function of time to the system damping in the flowing fluid. This dynamic system damping may be relatively constant for one heat exchanger to another because of similarity in heat exchanger design and manufacturing tolerances.

A review of the test results in Table 1 indicate that a log decrement of 0.11, and an instability constant of 4.0 may be reasonable design factors for water flowing over closely spaced tubes on triangular (30 deg) pitch. The maximum log

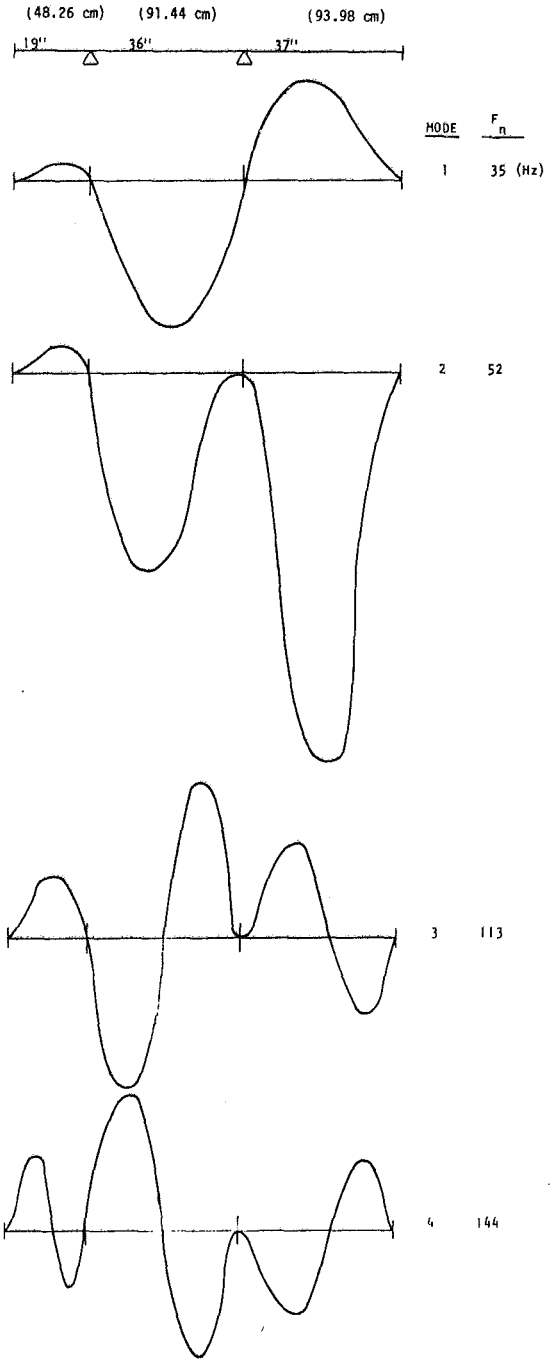

Fig. 8 Mode shapes and frequencies for test B1—tubes underneath the nozzles

decrement occurs for Test C2 with a value of 0.24. Since the critical vibration velocity varies as the square root of the damping, the deviation is $(0.24)^{1/2} - (0.11)^{1/2}/(0.11)^{1/2} = 0.48$. This deviation is still substantial but suggests that much lower safety factors for vibration analysis can be used than previously thought.

Analysis of tube vibration has made significant progress in the last ten years, but present prediction methods still result in conservative designs which are costly. A good evaluation of the state-of-the-art is contained in a report published by Chenoweth [5], summarizing the discussions and research recommendations of an international panel of vibration experts.

5 Conclusions

(*a*) Flow-induced vibration analysis of a heat exchanger with water on the shell side with flow obstructions such as seal strips involves an analysis of the velocity profile through the exchanger and the dynamic system damping. Prediction of these parameters still requires good engineering judgment because of difficulty in measuring these items.

(*b*) Tests reported in this paper indicate flow induced vibration for this type of heat exchanger with water on the shell side can be predicted with good results by the fluidelastic excitation method if an instability factor of 4 is used with a log decrement of 0.11 for closely spaced tubes on 30 deg triangular pitch.

(*c*) A thorough vibration analysis should include a study of mode shapes and of spanwise variation in flow velocity.

References

1 Palen, J. W., and Taborek, J., "Solution of Shell Side Flow Pressure Drop and Heat Transfer by Stream Analysis Method," *CEP Symposium Series*, Vol. 65, No. 92, 1969.

2 Connors, H. J., Jr., "Fluidelastic Vibration of Tube Arrays Excited by Cross Flow," presented at the ASME Winter Annual Meeting, New York, 1970.

3 Connors, H. J., Jr., "Fluidelastic Vibration of Heat Exchanger Tube Arrays," ASME Paper No. 77-DET-90, presented at the ASME Design Engineering Technical Conference, Chicago, Sept. 1977.

4 Standards of Tubular Exchanger Manufacturers Association, Sixth ed., 1978.

5 Chenoweth, J. M., "Flow-Induced Vibrations In Shell and Tube Heat Exchangers," ERDA Reports SAN/1273-1, Feb. 1977.

Journal of Heat Transfer

Technical Notes

This section contains shorter technical papers. These shorter papers will be subjected to the same review process as that for full papers.

Corresponding States Correlations of the Spinodal and Homogeneous Nucleation Limits

J. H. Lienhard[1]

Nomenclature

$f_1, f_2 \ldots$ = arbitrary functions of ω
j = number of nucleation events for each molecular collison
k = Boltzmann's constant, $1.3805(10)^{-23}$ J/°K
p = absolute pressure
Δp = $p_{sp} - p_{\text{sat}}$
T = absolute temperature
T_n = temperature between T_{sat} and T_{sp}, but close to T_{sp} where pure homogeneous nucleation occurs
ΔT = $T_{sp} - T_{\text{sat}}$
v, v_f, v_g = specific volume (v for saturated liquid and vapor)
σ = surface tension
ω = the Pitzer factor, see equation (2)

Subscripts

c = denotes a critical property
r = denotes a reduced property—one divided by its critical value
sat = denotes states defined in Fig. 1
sp = denotes states defined in Fig. 1

Introduction

Lienhard and Karimi [1, 2] have shown that the limit of homogeneous nucleation lies very close to the spinodal line in a liquid, but not in a vapor. The spinodal line is clearly subject to the law of corresponding states, thus the liquid limit of homogeneous nucleation must also obey it. Corresponding states correlations of the highest temperatures observed in liquids are familiar to us (see e.g., [3]). Lienhard [4] made an effective correlation of measurements made by Skripov et al. [5, 6] of extreme nucleation temperatures, T_n:

$$\frac{T_n - T_{\text{sat}}}{T_c} \simeq \frac{T_{sp} - T_{\text{sat}}}{T_c} \equiv \Delta T_r = 0.905 - T_{r_{\text{sat}}} - 0.095 T^8_{r_{\text{sat}}} \quad (1)$$

In such correlations the limit should depend on two physical variables:

1 $T_{\text{sat}}, T_{sp}, p_{\text{sat}}$, or p_{sp} (see Fig. 1)
2 a molecular coordinate such as the critical compressibility factor, the Riedel factor, or the Pitzer factor, ω [7]. The Pitzer factor is defined as:

$$\omega = -1 - \log_{10} p_{r_{\text{sat}}} (T_{r_{\text{sat}}} = 0.7) \quad (2)$$

None of the previous correlations have involved a molecular parameter. Equation (1) represented the available data within about ± 5 percent, and this scatter showed little consistent trend in ω, or in any other molecular parameter. This suggests that the data-scatter of the available measurements exceeded the influence of ω.

Homogeneous nucleation theories normally take the form:

$$j \frac{\text{nucleation events}}{\text{molecule-collison}} = \exp\left[- \frac{\text{critical work needed to trigger nucleation}}{kT} \right]$$

In [2], the argument was made that T should be replaced with the critical temperature, T_c. The resulting implicit equation for either the spinodal pressure or the homogeneous nucleation pressure was[2]

$$j = 10^{-5} = \exp\left[- \frac{16\pi\sigma^3}{3kT_c(1 - v_f/v_g)^2 (p_{sp} - p_{\text{sat}})^2} \right] \quad (3)$$

Although equation (3) was developed for water, there is nothing in its development that restricts it to water. Therefore, we invert it to get the general spinodal equation:

$$p_{\text{sat}} = p_{sp} - 1.2064 \left. \frac{\sigma^{1.5}}{\sqrt{kT_c}(1 - v_f/v_g)} \right|_{\text{at } T_{sp}} \quad (4)$$

Equation (4) gives the maximum isothermal depressurization that can be achieved from a saturated initial state as p_{sp}.

We can use equation (4) to calculate p_{sat} and from it, the corresponding value of T_{sat}. The resulting ΔT_r is compared with equation (1) in Fig. (2) using the physical properties of water. The empirical homogeneous nucleation correlation falls about 9°C below the water spinodal line except at high temperature where the difference diminishes to zero. Of course, the data upon which equation (1) is based are for nucleation with $j \simeq 10^{-13}$ instead of the limit of 10^{-5}, and thus do not represent the limit of pure homogeneous nucleation. An empirical equation, similar to equation (2), is fitted to the limiting points, in Fig. 2.

The properties v_f, v_g, and σ can be annoyingly hard to locate for use in equation (4). Our aim is, therefore, to use the Law of Corresponding States to recast equation (4) into a convenient correlation for p_{sp} in terms of T_{sat}.

The Correlation

We first get around the lack of v_f and v_g data, for many fluids for which $\sigma(T)$ is known, by correlating v_f/v_g as a function of T_r. If we plot the limited available v_f/v_g data

[1] Professor, Heat Transfer and Phase Change Laboratory, Mechanical Engineering Department, University of Houston, Houston, Texas 77004. Fellow ASME

Contributed by the Heat Transfer Division for publication in the JOURNAL OF HEAT TRANSFER. Manuscript received by the Heat Transfer Division August 10, 1981.

[2] *Caveat lector*: The subscripts sp and sat defined here are reversed in [2]. (Both that paper and this are internally consistent.)

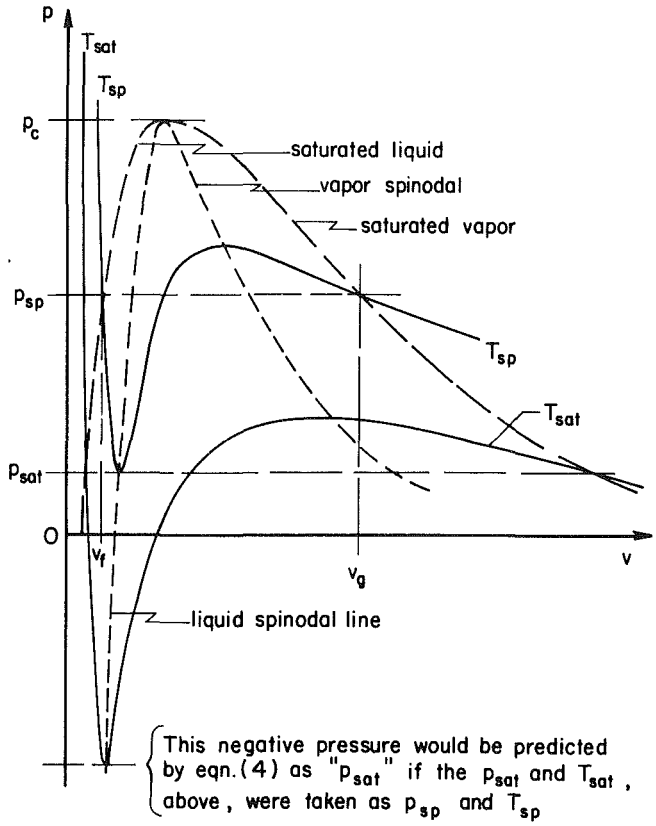

Fig. 1 Definition of terms on a p-v state diagram

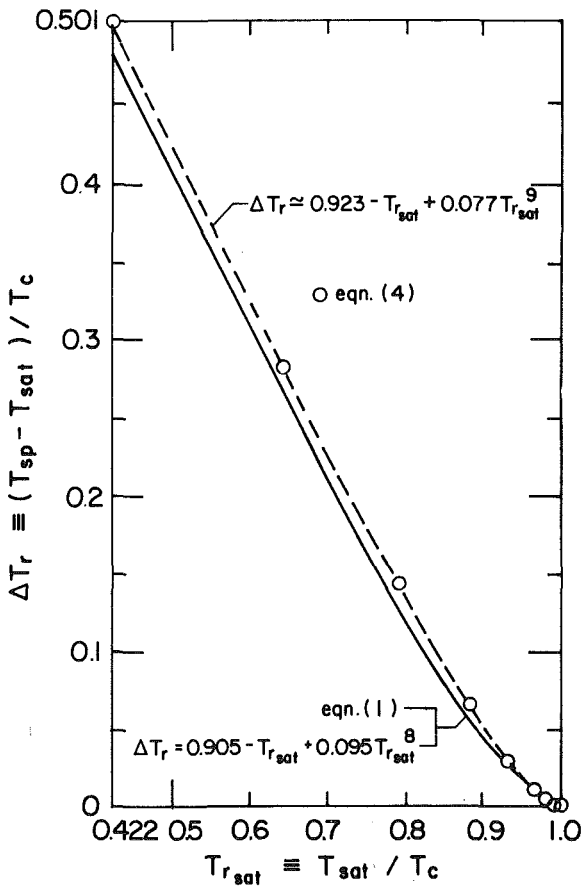

Fig. 2 Comparison of the spinodal prediction for water (equation (4)) with the correlation of homogeneous nucleation data (equation (2))

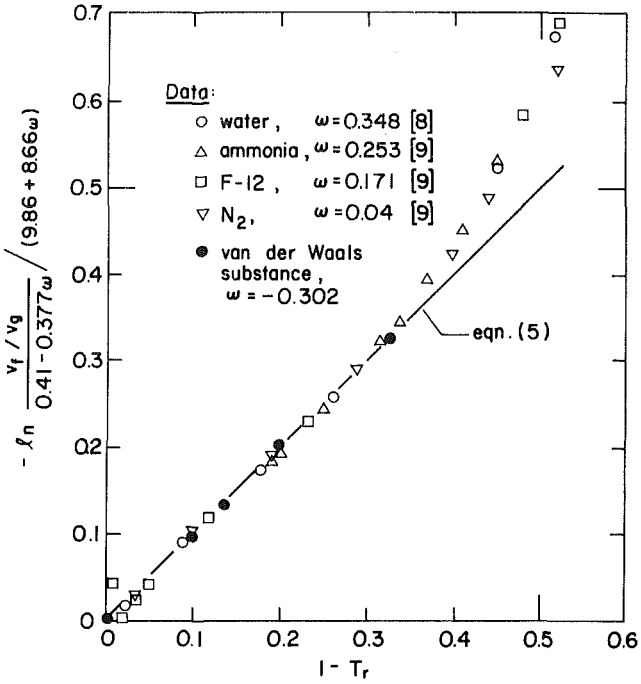

Fig. 3 Corresponding states correlation of v_f / v_g

against $1 - T_r$, we obtain a set of almost straight lines of the form, $\ln v_f/v_g = f_1(\omega) - f_2(\omega) \cdot [1 - T_r]$. Crossplotting to obtain f_1 and f_2, we obtain the correlation in Fig. 3. In the range $0.02 \leqslant 1 - T_r \leqslant 0.30$, this correlation takes the form:

$$1 - v_f/v_g = 1 - (0.41 - 0.377\omega)\, e^{-(9.86 + 8.66\omega)(1 - T_r)} \qquad (5)$$

Since v_f/v_g is $<< 1$ in the range of the correlation, the small error in v_f/v_g leads to a tiny error in $1 - v_f/v_g$. Notice that data for the van der Waals substance are included. The properties of a van der Waals substance, and its membership in the family of real substances, are developed and explained by Lienhard [10] and Peck [11]. The Pitzer factor for van der Waals' fluid is -0.302.

We should also like to obtain a direct corresponding states correlation for σ; however, previous attempts to make such σ correlations have not yielded good accuracy [12]. We shall instead correlate Δp_r directly, using equation (5) to calculate $1 - v_f/v_g$ when measured values are not available. Jasper's [13] σ data are used for all substances except water. Surface tension data for water are given in [14]. Values of Δp_r calculated from equation (4) in this way take the form:

$$\Delta p_r \simeq f_3(\omega)[1 - T_{r_{sp}}]^{1.83} \qquad (6)$$

when Δp_r is plotted against $(1 - T_{r_{sp}})$ on log-log coordinates.

The exponent, 1.83, is the slope that fits all of the data best on plots; however, we note in retrospect that the $T_{r_{sp}}$ dependence of Δp is almost entirely carried in $\sigma^{1.5}$. It is well-known (see e.g., [12]) that $\sigma \sim (1 - T_{r_{sp}})^{11/9}$. Thus, the exponent $1.5(11/9) = 1.83$ might have been anticipated. Crossplotting from these curves, we obtain f_3 such that:

$$\Delta p_r = (33.25 + 66.14\omega)(1 - T_{r_{sp}})^{1.83} \qquad (7a)$$

Figure 4 shows available data in comparison with equation (7a). The equation represents all but one or two of them within a pencil-width in the crucial range: $0.98 \leqslant T_{r_{sp}} \leqslant 0.90$. And it yields a good approximation down to $T_{r_{sp}} = 0.70$.

Finally, if we were to replace $j = 10^{-5}$ with a general value of j in equation (3), and then carry through the same development, we would obtain a slightly different form of equation (7a):

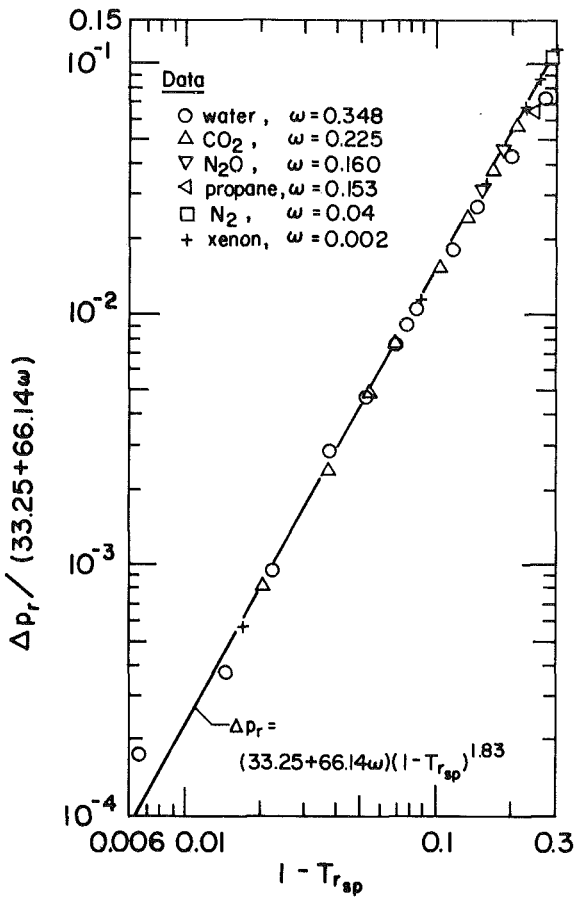

Fig. 4 Corresponding states correlation of the spinodal pressure undershoot

$$\Delta p_r = \frac{112.82 + 224.42\omega}{\sqrt{-ln(j)}}(1 - T_{r_{sp}})^{1.83} \qquad (7b)$$

which can be used to obtain Δp in real systems if j can be estimated.

Summary and Conclusions

The scarcity of high-pressure v_f, v_g, and σ data that appear in predictions of homogeneous nucleation (or of the spinodal limit) in liquids, often makes their evaluation difficult or impossible. We have shown how these predicted limits can easily be developed from corresponding states correlations. In particular we find that:

1 Equation (4) predicts spinodal points that are only slightly beyond the correlation of the highest homogeneous nucleation that has been achieved.

2 Equation (5) provides, *en passent*, a useful correlation of $1 - v_f/v_g$ in the range $0.98 \geqslant T_r \geqslant 0.7$. For lower temperatures, Fig. 3 should be used directly in place of equation (5), although in this range $1 - v_f/v_g \simeq 1$.

3 Equation (6) allows us to estimate the isothermal spinodal pressure depression with very limited physical data.

4 Equation (7) should be used in practical systems where $j << 10^{-5}$.

5 $\Delta T_r = 0.923 - T_{r_{sat}} + 0.077\ T_{r_{sat}}$ represents $T_{sp_{water}}$ better than equation (1) does. It also gives a better estimate of T_{sp} for other liquids, but it fails to include the role of ω, which *is* given by equation (4).

References

1 Lienhard, J. H. and Karimi, A., "Corresponding States Correlations of the Extreme Liquid Superheat and Vapor Subcooling," ASME JOURNAL OF HEAT TRANSFER, Vol. 100, No. 3, 1978, pp. 492–495.

2 Lienhard, J. H. and Karimi, A., "Homogeneous Nucleation and the Spinodal Line," ASME JOURNAL OF HEAT TRANSFER, Vol. 103, No. 1, 1981, pp. 61–64.

3 Blander, M. and Katz, J. L., "Bubble Nucleation in Liquids," *AICh.E Journal*, Vol. 21, No. 5, 1975, pp. 833–848.

4 Lienhard, J. H., "Correlation for the Limiting Liquid Superheat," *Chem. Engr. Sci.*, Vol. 31, 1976, pp. 847–849.

5 Skripov, V. P. and Paplov, P. A., "Explosive Boiling of Liquids and Fluctuation Nucleus Formation," *Teplofizika Vysokih Temp.*, Vol. 8, No. 4, 1970, pp. 833–839.

6 Pavlov, P. A. and Skripov, V. P., "Kinetics of Spontaneous Nucleation in Strongly Heated Liquids," *Teplofizika Vysokih Temp.*, Vol. 8, No. 3, 1970, pp. 579–585.

7 Pitzer, K. S., Lippman, D. Z., Curl, R. F., Huggins, C. M., Peterson, D. E., *Journal of the American Chemical Society*, Vol. 77, 1955, p. 3433.

8 Irvine, J. F. Jr., and Hamett, J. P., eds., *Steam and Air Tables in S.I. Units*, Hemisphere Pub. Co., Washington, D.C., 1976.

9 van Wylen, G. J. and Sonntag, R. E., *Fundamentals of Classical Thermodynamics 2nd ed.*, John Wiley and Sons, Inc., New York, 1973.

10 Lienhard, J. H., "Relation Between van der Waals' Fluid and Real Substances," *Iranian J. Sci. and Tech.*, Vol. 5, No. 3b, 1976, pp. 111–116.

11 Peck, R. E., "The Assimilation of van der Waals' Fluid in an Extended Law of Corresponding States," *Canadian Journal of Chemical Engineering*, (in press).

12 Brock, J. R. and Bird, R. B., "Surface Tension and the Principle of Corresponding States," *A.I.Ch.E. Jour.*, Vol. 1, No. 2, 1955, pp. 174–177.

13 Jasper, J. J., "The Surface Tension of Pure Liquid Compounds," *J. Phys. and Chem. Ref. Data.*, Vol. 1, No. 4, 1972, pp. 841–1010.

14 "Release of Surface Tension of Water Substance," The International Association for the Properties of Steam, Available from the Exec. Sec., IAPS, Office of Std. Ref. Data, Nat'l. Bur. of Stds., Dec. 1976.

15 Hijikata, K., Mori, Y., and Nagatan, T., "Experimental Study on Bubble Nucleation in the Oscillating Pressure Field," ASME Preprint 77-HT-22, ASME-AICHE Heat Transfer Conf., Salt Lake City, Utah, August 15–17, 1977.

On the Prediction of Pipe Freeze-Shut in Turbulent Flow

M. Epstein[1] and F. B. Cheung[2]

Introduction

Solidification in steady, turbulent pipe flow with a constant, uniform wall temperature has been analyzed as an entrance region problem both by Shibani and Ozisik [1] and by Thomason, Mulligan, and Everhart [2]. By ignoring the thermal entrance region, known to be short for highly turbulent flow and Prandtl numbers above ~ 0.5, we obtain a simple, asymptotic closed-form solution for the problem and use it to predict the conditions for the onset of freeze-shut in a pipe containing turbulent water flow. The observations of Gilpin [3] of the development of ice waves in internal solidification are used to fix the limitations on our results.

Analysis

Our model for internal solidification is identical with that of reference [2], viz. we consider a steady turbulent flow of a liquid with constant physical properties through a cold pipe of inside radius R_0. The flow is assumed to be axisymmetric, incompressible, hydrodynamically fully developed, and of uniform temperature T_0 greater than the freezing temperature T_f at the entrance $z = 0$ to the freeze section of the pipe. In the freeze section, the wall temperature T_w is taken to be uniform and below the freezing temperature of the liquid. We consider a small length, dz, of the freeze section of the pipe. The heat leaving through the frozen layer is equal to the decrease in enthalpy of the flowing liquid. Thus

$$\frac{1}{2}\rho C_p \left(\frac{R_0}{R}\right)^2 UR\frac{dT}{dz} = -h(T - T_f) \qquad (1)$$

[1]Fauske and Associates, Inc., Willowbrook, Ill. 60521. Mem. ASME

[2]Reactor Analysis and Safety Division, Argonne National Laboratory, Argonne, Ill. 60439. Mem. ASME

Contributed by the Heat Transfer Division for publication in the JOURNAL OF HEAT TRANSFER. Manuscript received by the Heat Transfer Division August 13, 1981.

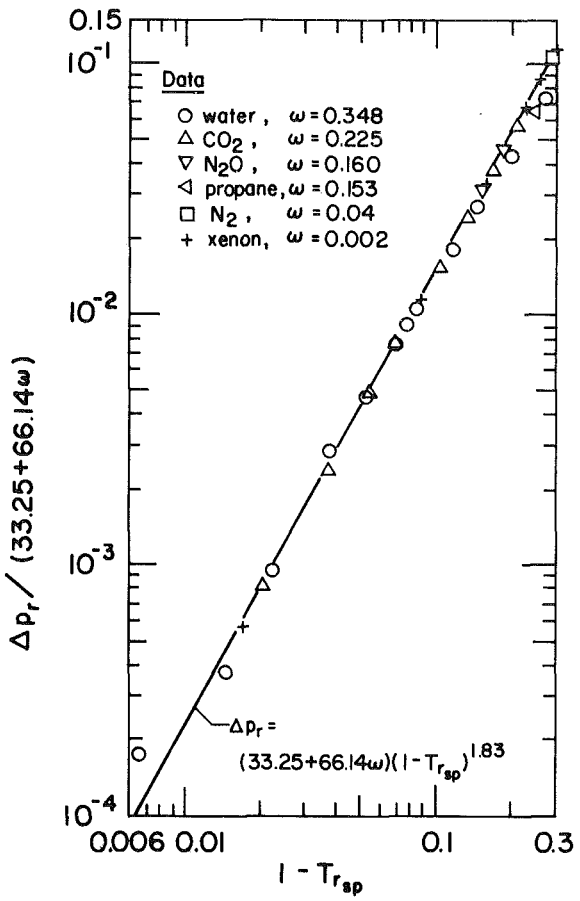

Fig. 4 Corresponding states correlation of the spinodal pressure undershoot

$$\Delta p_r = \frac{112.82 + 224.42\omega}{\sqrt{-ln(j)}}(1 - T_{r_{sp}})^{1.83} \qquad (7b)$$

which can be used to obtain Δp in real systems if j can be estimated.

Summary and Conclusions

The scarcity of high-pressure v_f, v_g, and σ data that appear in predictions of homogeneous nucleation (or of the spinodal limit) in liquids, often makes their evaluation difficult or impossible. We have shown how these predicted limits can easily be developed from corresponding states correlations. In particular we find that:

1 Equation (4) predicts spinodal points that are only slightly beyond the correlation of the highest homogeneous nucleation that has been achieved.

2 Equation (5) provides, *en passent*, a useful correlation of $1 - v_f/v_g$ in the range $0.98 \geqslant T_r \geqslant 0.7$. For lower temperatures, Fig. 3 should be used directly in place of equation (5), although in this range $1 - v_f/v_g \simeq 1$.

3 Equation (6) allows us to estimate the isothermal spinodal pressure depression with very limited physical data.

4 Equation (7) should be used in practical systems where $j << 10^{-5}$.

5 $\Delta T_r = 0.923 - T_{r_{sat}} + 0.077\ T_{r_{sat}}$ represents $T_{sp_{water}}$ better than equation (1) does. It also gives a better estimate of T_{sp} for other liquids, but it fails to include the role of ω, which *is* given by equation (4).

References

1 Lienhard, J. H. and Karimi, A., "Corresponding States Correlations of the Extreme Liquid Superheat and Vapor Subcooling," ASME JOURNAL OF HEAT TRANSFER, Vol. 100, No. 3, 1978, pp. 492–495.

2 Lienhard, J. H. and Karimi, A., "Homogeneous Nucleation and the Spinodal Line," ASME JOURNAL OF HEAT TRANSFER, Vol. 103, No. 1, 1981, pp. 61–64.

3 Blander, M. and Katz, J. L., "Bubble Nucleation in Liquids," *AICh.E Journal*, Vol. 21, No. 5, 1975, pp. 833–848.

4 Lienhard, J. H., "Correlation for the Limiting Liquid Superheat," *Chem. Engr. Sci.*, Vol. 31, 1976, pp. 847–849.

5 Skripov, V. P. and Paplov, P. A., "Explosive Boiling of Liquids and Fluctuation Nucleus Formation," *Teplofizika Vysokih Temp.*, Vol. 8, No. 4, 1970, pp. 833–839.

6 Pavlov, P. A. and Skripov, V. P., "Kinetics of Spontaneous Nucleation in Strongly Heated Liquids," *Teplofizika Vysokih Temp.*, Vol. 8, No. 3, 1970, pp. 579–585.

7 Pitzer, K. S., Lippman, D. Z., Curl, R. F., Huggins, C. M., Peterson, D. E., *Journal of the American Chemical Society*, Vol. 77, 1955, p. 3433.

8 Irvine, J. F. Jr., and Hamett, J. P., eds., *Steam and Air Tables in S.I. Units*, Hemisphere Pub. Co., Washington, D.C., 1976.

9 van Wylen, G. J. and Sonntag, R. E., *Fundamentals of Classical Thermodynamics 2nd ed.*, John Wiley and Sons, Inc., New York, 1973.

10 Lienhard, J. H., "Relation Between van der Waals' Fluid and Real Substances," *Iranian J. Sci. and Tech.*, Vol. 5, No. 3b, 1976, pp. 111–116.

11 Peck, R. E., "The Assimilation of van der Waals' Fluid in an Extended Law of Corresponding States," *Canadian Journal of Chemical Engineering*, (in press).

12 Brock, J. R. and Bird, R. B., "Surface Tension and the Principle of Corresponding States," *A.I.Ch.E. Jour.*, Vol. 1, No. 2, 1955, pp. 174–177.

13 Jasper, J. J., "The Surface Tension of Pure Liquid Compounds," *J. Phys. and Chem. Ref. Data.*, Vol. 1, No. 4, 1972, pp. 841–1010.

14 "Release of Surface Tension of Water Substance," The International Association for the Properties of Steam, Available from the Exec. Sec., IAPS, Office of Std. Ref. Data, Nat'l. Bur. of Stds., Dec. 1976.

15 Hijikata, K., Mori, Y., and Nagatan, T., "Experimental Study on Bubble Nucleation in the Oscillating Pressure Field," ASME Preprint 77-HT-22, ASME-AICHE Heat Transfer Conf., Salt Lake City, Utah, August 15–17, 1977.

On the Prediction of Pipe Freeze-Shut in Turbulent Flow

M. Epstein[1] and F. B. Cheung[2]

Introduction

Solidification in steady, turbulent pipe flow with a constant, uniform wall temperature has been analyzed as an entrance region problem both by Shibani and Ozisik [1] and by Thomason, Mulligan, and Everhart [2]. By ignoring the thermal entrance region, known to be short for highly turbulent flow and Prandtl numbers above ~ 0.5, we obtain a simple, asymptotic closed-form solution for the problem and use it to predict the conditions for the onset of freeze-shut in a pipe containing turbulent water flow. The observations of Gilpin [3] of the development of ice waves in internal solidification are used to fix the limitations on our results.

Analysis

Our model for internal solidification is identical with that of reference [2], viz. we consider a steady turbulent flow of a liquid with constant physical properties through a cold pipe of inside radius R_0. The flow is assumed to be axisymmetric, incompressible, hydrodynamically fully developed, and of uniform temperature T_0 greater than the freezing temperature T_f at the entrance $z = 0$ to the freeze section of the pipe. In the freeze section, the wall temperature T_w is taken to be uniform and below the freezing temperature of the liquid. We consider a small length, dz, of the freeze section of the pipe. The heat leaving through the frozen layer is equal to the decrease in enthalpy of the flowing liquid. Thus

$$\frac{1}{2}\rho C_p \left(\frac{R_0}{R}\right)^2 UR\frac{dT}{dz} = -h(T - T_f) \qquad (1)$$

[1]Fauske and Associates, Inc., Willowbrook, Ill. 60521. Mem. ASME

[2]Reactor Analysis and Safety Division, Argonne National Laboratory, Argonne, Ill. 60439. Mem. ASME

Contributed by the Heat Transfer Division for publication in the JOURNAL OF HEAT TRANSFER. Manuscript received by the Heat Transfer Division August 13, 1981.

where T is the bulk liquid temperature, ρ the liquid density, C_p the specific heat, R the crust radius, h the local heat-transfer coefficient, and where the local mean velocity u has been eliminated in favor of the mean velocity at the inlet to the freeze section, U, via the mass continuity relation $uR^2 = UR_0{}^2$. In terms of the local Nusselt number defined by $\mathrm{Nu} = 2Rh/k$, equation (1) becomes

$$\frac{1}{2} R_0 \mathrm{Re}\,\mathrm{Pr} \frac{dT}{dz} = -\mathrm{Nu}(T - T_f) \tag{2}$$

where $\mathrm{Re} = UD_0/\nu$ and $\mathrm{Pr} = \nu/\alpha$ are the Reynolds number and Prandtl number, respectively, and D_0 is the pipe diameter. At steady state, the local temperature distribution, T_s, in the frozen crust is given by

$$T_s = T_f - (T_f - T_w) \frac{\ln(r/R)}{\ln(R_0/R)} \tag{3}$$

where r is the radial coordinate. Invoking the definition of h, the condition for energy exchange at the solid-liquid interface is

$$-k_s \frac{\partial T_s}{\partial r}(R,z) = h(T - T_f) \tag{4}$$

or from equation (3),

$$\ln\left(\frac{R_0}{R}\right) = \frac{2T_w{}^*}{\mathrm{Nu}} \cdot \frac{T_0 - T_f}{T - T_f} \tag{5}$$

where $T_w{}^*$ is a dimensionless cooling temperature parameter defined by

$$T_w{}^* = \frac{k_s(T_f - T_w)}{k(T_0 - T_f)} \tag{6}$$

and where k, k_s are the thermal conductivities of liquid and solid, respectively. Clearly, the solid-liquid interface location as a function of axial distance, $R(z)$, can be determined from equations (2) and (5) once a relation for the local heat transfer is supplied.

Thomason et al. [2] employed the Sparrow-Hallman-Siegel solution [4] for the heat-transfer coefficient in turbulent, thermal entrance region flow. Implicit in the analysis of Thomason et al. is the assumption that the turbulent fluid motion and heat transport, when described in terms of the local parameter, R, are unaffected by the presence of the solidified layer. Hence the shear stress and heat-transfer rate are obtainable directly from experiments or from independent analyses of turbulent pipe flow in the absence of solidification. The expression for Nu given in [4] is an infinite series solution to a rather complex eigenvalue problem where the eigenvalues of the solution are functions of Reynolds number and Prandtl number. A short distance from the entrance to the freeze section (or thermal entrance), however, the temperature profile in the turbulent flow ceases to change its form and remains uniform down the pipe (see reference [2]). For this fully developed pipe flow region, the empirical equation recommended by Kays [5] may be used. When applied locally to the freezing liquid in turbulent flow, this equation takes the form

$$\mathrm{Nu} = 0.0155\,\mathrm{Re}^{0.83}\,\mathrm{Pr}^{0.5}\left(\frac{R_0}{R}\right)^{0.83} \tag{7}$$

Except for a short thermal entrance region of approximately 10 pipe diameters in length, the asymptotic Nusselt number given by the above equation holds with good accuracy in the entire freeze section. Over the range of small z values where the degree of tube closure is minimal and the bulk liquid temperature has decreased very little from its value at the inlet, we have from equations (5) and (7)

$$0.0078\,\mathrm{Re}^{0.83}\,\mathrm{Pr}^{0.5}\left(\frac{R_0}{R}\right)^{0.83} \ln\left(\frac{R_0}{R}\right) = T_w{}^* \tag{8}$$

for $z \to 0$. This expression gives the radial location of the solid-liquid interface, R, for values of z close to zero and thereby provides the necessary initial condition for calculating R at large z values where the frozen layer thickness is significant[3]. Eliminating the bulk liquid temperature, T, between equations (2) and (5), substituting equation (7) for Nu, and integrating the resultant equation in z, we find the inverted solution for the location of the solid-liquid interface:

$$\left[\left(\frac{R}{R_0}\right)^{0.83} + E_1\left(0.83 \ln\frac{R_0}{R}\right)\right]_{z\to 0} - \left[\left(\frac{R}{R_0}\right)^{0.83} + E_1\left(0.83 \ln\frac{R_0}{R}\right)\right] = 0.062\,\mathrm{Re}^{-0.17}\,\mathrm{Pr}^{-0.5}\left(\frac{z}{D_0}\right) \tag{9}$$

where the exponential integral $E_1(x) = \int_x^\infty (e^{-t}/t)\,dt$, and the subscript $z \to 0$ refers to values of R/R_0 obtained from equation (8).

Once $R(z)$ is determined, the axial pressure distribution, $P(z)$, may be calculated as follows. If the pressure drop between the inlet to the freeze section and position z is caused solely by frictional drag,[4] from a simple force balance we have

$$\left(P_0 + \frac{1}{2}\rho U^2\right) - \left(P + \frac{1}{2}\rho u^2\right) = \int_0^z (2\tau/R)\,dz \tag{10}$$

The frictional shear at the surface of the frozen layer, τ, is related to the mean axial velocity by

$$\tau = \frac{1}{2} f \rho u^2 \tag{11}$$

where f, the friction factor, is considered to be well-described by the Blasius formula:

$$f = 0.0791\left(\frac{2uR}{\nu}\right)^{-1/4} \tag{12}$$

Combining equations (10) to (12) and using the mass continuity relation to replace u with U, the pressure may be written as

$$\frac{2(P_0 - P)}{\rho U^2} = \frac{0.1582}{R_0 \mathrm{Re}^{1/4}} \int_0^z \left(\frac{R_0}{R}\right)^{19/4} dz + \left(\frac{R_0}{R}\right)^4 - 1 \tag{13}$$

Integrating the above expression using equation (9), we obtain

$$\frac{2(P_0 - P)}{\rho}\left(\frac{D_0}{\nu}\right)^2 = 5.1\,\mathrm{Re}^{1.92}\,\mathrm{Pr}^{0.5}\left\{\left[0.2117\left(\frac{R_0}{R}\right)^{3.92} + E_2\left(3.92 \ln\frac{R_0}{R}\right)\right] - \left[0.2117\left(\frac{R_0}{R}\right)^{3.92} + E_2\left(3.92 \ln\frac{R_0}{R}\right)\right]_{z\to 0}\right\} + \left(\frac{R_0}{R}\right)^4 - 1 \tag{14}$$

where the exponential integral $E_2(x) = \int_{-\infty}^x (e^t/t)\,dt$. Equations (8), (9), and (14) completely describe the shape of the cavity and the pressure drop along the freeze section under steady-state, turbulent flow conditions.

Results and Discussion

Inspection of equations (8) and (9) reveals the fact that the dimensionless cavity radius R/R_0, when plotted as a function of the dimensionless axial position variable $\mathrm{Re}^{-0.17}\,\mathrm{Pr}^{-0.5}$

[3] Of course, equation (8) does not apply to values of z equal to or very near zero where entrance region effects are important.

[4] Additional effects may be included in the force balance and do not represent the limitation of this analysis.

(z/D_0), depends only on a single dimensionless parameter, A, where

$$A = T_w^*/(0.001\ \mathrm{Re}^{0.83}\ \mathrm{Pr}^{0.5}) \tag{15}$$

The calculated crust profiles for various values of A are presented in Fig. 1. This result and the result for the pressure drop, equation (14), are practically identical to those obtained from the analysis of Thomason et al. [2], which incorporates entrance region effects.

In order to identify the conditions for blockage of a pipe by freezing with a turbulent flow in it, plots of the dimensionless pressure drop versus the flow Reynolds number are prepared in a manner similar to the graphical display of DesRuisseaux and Zerkle [6] for blockage of a laminar tube flow. Different sets of the cooling temperature parameter T_w^* and the freeze section-to-pipe diameter ratio z/D_0 are employed. For given values of T_w^*, z/D_0, and axial pressure drop, there exist either none, one, or two values of the liquid flow Reynolds number. Along the left-hand branch of these curves an increasing pressure drop results in a decreasing flow velocity which evidently signifies some unstable or imaginary state. Thus, only the right-hand branch of each curve represents the locus of physically possible steady-state conditions. For pressure drops less than the minimum system pressure, a steady-state condition does not exist and the pipe is predicted to freeze shut. Conditions of incipient pipe blockage may thus be established. Results are shown in Fig. 2 for the case of Pr = 10 (water). Clearly, the critical pressure drop below which freeze shut occurs may be increased by either increasing the value of the cooling temperature parameter T_w^* or increasing the value of the freeze section-to-pipe diameter ratio z/D_0. Physically, pipe blockage is more likely to occur in a longer pipe maintained at a lower wall temperature.

In the foregoing analysis, we have assumed that the steady-state crust profile always produces a uniformly tapered flow passage in the freeze section of the pipe. In reality, this "smooth crust structure" may not exist. Visual observations by Gilpin [3, 7] of the form of the ice growth in a pipe containing a laminar or turbulent flow show that under some circumstances a flow passage with a dramatic cyclic variation in cross section may occur in the freeze section of the pipe. This so-called "ice-band structure" is in fact found to be the more stable crust configuration for the case in which both T_w^* and z/D_0 are large. When a laminar flow entrance condition exists in the pipe, the ice-band structure occurs because of the sharp expansion of the flow at the exit of the freeze section. However, when the flow is turbulent, the ice bands appear to be independent of the exit condition but grow along the length of the freeze section from very small, naturally occurring undulations in the flow cavity. In contrast to the case of a smooth, uniformly tapered crust structure in which the major component of pressure drop is due to the viscous drag at the solid-liquid interface, in the case of an ice-band structure, the greatest pressure loss occurs in the sudden expansions downstream of each separation point of the ice-band structure [7]. Hence a more severe condition for pipe blockage may be expected when an ice-band structure exists in the pipe. It is therefore important to determine the form of the crust structure before the conditions for pipe freeze-shut be accurately predicted.

Based on the results of Gilpin's work, well-correlated by the relation $Z/D_0 = 80\,[k_s/(kT_w^*)]^2 + 6$, a dashed line is drawn in Fig. 2 to separate the smooth-crust regime from the ice-band regime. Physically, this dashed line represents the situation in which the dimension of the freeze section is identically equal to the steady-state, ice-band spacing [3, 7]. Note that the experiments in which ice band spacings have been measured were done for values of Z/D_0 of 40 and less, and, therefore, to construct the dashed line in Fig. 2, the correlation required extrapolation to the very large Z/D_0 values shown in the figure. The results of the present analysis are valid only in the region on the left-hand side of the dashed line. For large values of T_w^* and z/D_0, where ice-band structure is the favorable regime, the conditions under which a pipe will freeze shut have to be assessed by different methods such as the one outlined by Gilpin [7].

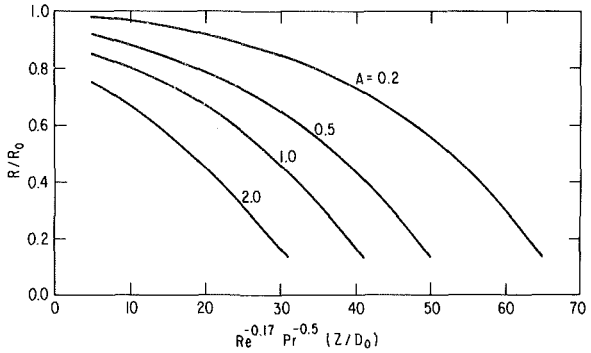

Fig. 1 The "concave" crust profiles for steady-state turbulent flow through a smooth, uniformly tapered, freeze section of a pipe

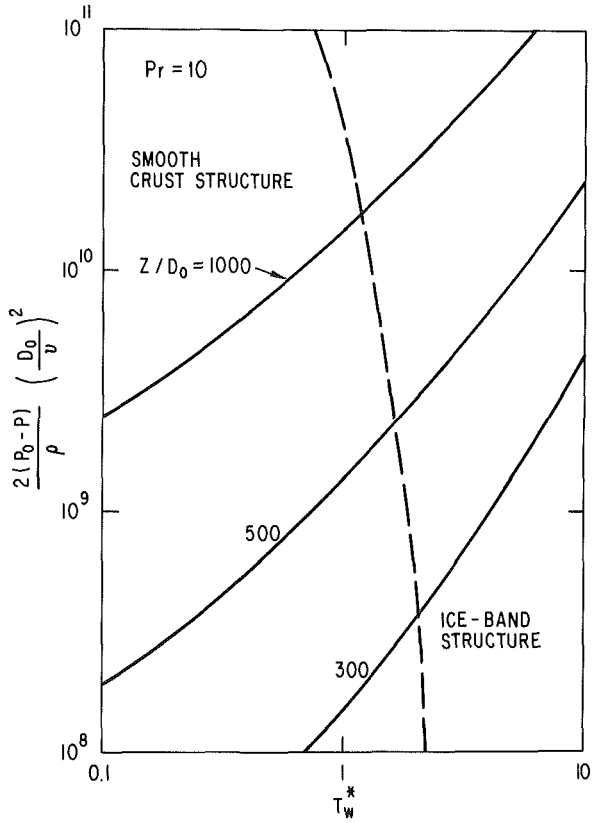

Fig. 2 Critical pressure drop versus the cooling parameter for solidification in turbulent pipe flow over various lengths of the freeze section

Finally, it should be stressed that the steady-state analysis presented in the foregoing is based on turbulent heat transfer and pressure drop characteristics for a constant diameter, smooth pipe. While the experimental results presented in [2] demonstrate the accuracy of both Kay's empirical formula and the Blasius formula for the solidification of ice in turbulent pipe flow when the ice layer is a small fraction of the tube radius, the analysis may not be valid when the flow cavity opening immediately upstream of the freeze section exit is predicted to be very small, owing to strong flow acceleration and laminarization effects. In many cases of practical interest, however, the limit of steady-state freezing is

reached under conditions in which the flow cavity radius is still a large fraction of the pipe radius. For example, taking Re = 1×10^4, we infer from Figs. 1 and 2 that, for freeze section length Z/D_0 and cooling temperature parameter T_w^* as large as 10^3 and 1.0, respectively, steady-state freezing is only possible for rather large cavity radii $R/R_0 > 0.5$. Note also that the flow passage in this example is sufficiently large to support heat transfer in turbulent flow along the entire length of the freeze section. Interestingly enough, in cases where the flow cavity is predicted to approach a near closure condition, $R/R_0 << 1$, the smooth, tapered flow passage assumption is predicted to break down as the critical points for freeze blockage move into the ice-band region in Fig. 2.

Acknowledgments

The authors wish to thank Marsha Reinke for typing the manuscript. The work by the second author was performed under the auspices of the U.S. Department of Energy.

References

1 Shibani, A. A. and Ozisik, M. N., "Freezing of Liquids in Turbulent Flow Inside Tubes," *Canadian Journal of Chemical Engineering*, Vol. 55, 1977, pp. 672-677.

2 Thomason, S. B., Mulligan, J. C., and Everhart, J., "The Effect of Internal Solidification on Turbulent Flow Heat Transfer and Pressure Drop in a Horizontal Tube," ASME JOURNAL OF HEAT TRANSFER, Vol. 100, 1978, pp. 387-394.

3 Gilpin, R. R., "The Morphology of Ice Structure in a Pipe at or Near Transition Reynolds Numbers," *AIChE Sym. Ser. 189*, Vol. 75, 1979, pp. 89-94.

4 Sparrow, E. M, Hallman, T. M., and Siegel, R., "Turbulent Heat Transfer in the Thermal Entrance Region of a Pipe with a Uniform Heat Flux," *Applied Science Reviews*, Vol.7, 1959, pp. 37-52.

5 Kays, W. M., *Convective Heat and Mass Transfer*, McGraw-Hill, New York, 1966.

6 DesRuisseaux, N. and Zerkle, R. D., "Freezing of Hydraulic Systems," *Canadian Journal of Chemical Engineering*, Vol. 47, 1969, pp. 223-237.

7 Gilpin, R. R., "Ice Formation in a Pipe Containing Flows in the Transition and Turbulent Regimes," ASME JOURNAL OF HEAT TRANSFER, Vol. 103, 1981, pp. 363-368.

View Factors in Radiation Between Two Parallel Oriented Cylinders of Finite Lengths

N. H. Juul[1]

A simple double-integral expression for the diffuse radiation view factor, F_{12}, between two parallel cylinders of finite lengths is derived. No closed-form solution appears possible except for the limiting case of infinite long cylinders for which an analytical expression for the view factor F_{12}^{∞} is derived by applying the crossed string method. The accuracies of the line source approximations are evaluated, and the regions for which they are accurate to one percentage or better are identified. The view factor F_{12} between two opposing cylinders of equal length is computed by numerical integration and normalized by F_{12}^{∞}. The results are presented. Analytical expressions, which approximate the view factors between two opposite cylinders of finite length, are derived and their accuracy is evaluated over a useful parameter range. The range of their applications corresponds approximately to that for the line source approximation. This result is expected, because the errors are caused in part by blockage of radiation which is similar.

[1] Department of Mechanical and Aerospace Engineering, State University of New York at Buffalo, Amherst, N.Y. 14260. Mem. ASME

Contributed by the Heat Transfer Division for publication in the JOURNAL OF HEAT TRANSFER. Manuscript received by the Heat Transfer Division April 24, 1981.

Introduction

The view factor between parallel cylinders is important in many industrial applications; for example, it is used to determine the radiant heat transfer between tubes in boilers, heat exchangers, etc.

Plamondon [1] has developed a quadruple integral expression with limits of integration for the view factor between two parallel cylinders of finite length for any radius ratio. However, no results of numerical integrations are presented.

The single integral equations derived by Stevenson and Grafton (2) for the view factor from a note on the surface of one cylinder to a note on the surface of a parallel cylinder are extended to the case of two opposing cylinders. The results for the length ratio $L/R = 50$ and the view factors F_{12}^{∞} for corresponding spacing and radius ratio show poor agreements. This result leaves in doubt the correctness of the equations presented in (2).

The view factors between two cylinders of finite length and equal radius have been investigated by Sparrow and Jonsson [3]. They determined the view factor from ring element located at $z = 0$ on cylinder 1 to cylinder 2 of length z, by first applying the contour integral method followed by two numerical integrations. The results of the view factor normalized by the view factor from the ring element to cylinder 2, which extends from $z = 0$ to $z = \infty$, are presented graphically. The view factor from cylinder 1 to cylinder 2, both of finite length, may be obtained by graphical integration, the accuracy of which is limited.

In this paper a new integration scheme is developed by which the quadruple integral for the view factor is reduced to a simple double integral the subsequent integration of which can only be carried out numerically.

The results are normalized by the view factor for the limiting case of infinite long cylinders. For this case an analytical expression for view factor is obtained by the crossed string method for cylinders of different radii. The only other expression available in the literature for this geometry is the special case where both cylinders are of equal radii [4]. The accuracies of the line source approximations for infinite long cylinders are investigated. Since closed-form integration of the integral expression for finite cylinders does not appear possible, analytical expressions which approximate the view factors between two parallel oriented cylinders of equal length and any radius ratio are developed. The accuracy of the approximations are evaluated in reference to the results of the numerical integration.

Analysis

Numerical method. Figure 1 shows the geometry and defines the variables for the view factor analysis. The view factor F_{12} is evaluated by

$$F_{12} = \frac{1}{A_1} \int_{A_1} \int_{A_2} \frac{\cos\theta_1 \cos\theta_2}{\pi l^2} \, dA_1 \, dA_2 \tag{1}$$

Expressions for $\cos\theta_1$, $\cos\theta_2$, l, dA_1 and dA_2 are obtained by Fig. 1 in terms of the lengths T and S, defined by Figs. 1(b) and 1(c), the latitude angles α_1 and α_2 for dA_1 and dA_2, respectively, radius r and R for cylinder 1 and 2, respectively, the spacing c and the coordinates ζ_1 and ζ_2. The above expressions are substituted into equation (1). Making use of symmetry, closed form integrations are carried out first in respect to ζ_2 and then in respect to ζ_1. After considerable manipulations we obtain

$$F_{12} = \frac{R}{\pi^2 (L_1 - 1_1)} \int_0^{\alpha_{1L}} d\alpha_1 \int_{\alpha_{2L1}}^{\alpha_{2L}}$$

$$\left((L_2 - 1_1) \tan^{-1} \frac{L_2 - 1_1}{\sqrt{a}} - (L_2 - L_1) \tan^{-1} \frac{L_2 - L_1}{\sqrt{a}} \right.$$

reached under conditions in which the flow cavity radius is still a large fraction of the pipe radius. For example, taking Re = 1×10^4, we infer from Figs. 1 and 2 that, for freeze section length Z/D_0 and cooling temperature parameter T_w^* as large as 10^3 and 1.0, respectively, steady-state freezing is only possible for rather large cavity radii $R/R_0 > 0.5$. Note also that the flow passage in this example is sufficiently large to support heat transfer in turbulent flow along the entire length of the freeze section. Interestingly enough, in cases where the flow cavity is predicted to approach a near closure condition, $R/R_0 << 1$, the smooth, tapered flow passage assumption is predicted to break down as the critical points for freeze blockage move into the ice-band region in Fig. 2.

Acknowledgments

The authors wish to thank Marsha Reinke for typing the manuscript. The work by the second author was performed under the auspices of the U.S. Department of Energy.

References

1 Shibani, A. A. and Ozisik, M. N., "Freezing of Liquids in Turbulent Flow Inside Tubes," *Canadian Journal of Chemical Engineering*, Vol. 55, 1977, pp. 672-677.

2 Thomason, S. B., Mulligan, J. C., and Everhart, J., "The Effect of Internal Solidification on Turbulent Flow Heat Transfer and Pressure Drop in a Horizontal Tube," ASME JOURNAL OF HEAT TRANSFER, Vol. 100, 1978, pp. 387-394.

3 Gilpin, R. R., "The Morphology of Ice Structure in a Pipe at or Near Transition Reynolds Numbers," *AIChE Sym. Ser. 189*, Vol. 75, 1979, pp. 89-94.

4 Sparrow, E. M, Hallman, T. M., and Siegel, R., "Turbulent Heat Transfer in the Thermal Entrance Region of a Pipe with a Uniform Heat Flux," *Applied Science Reviews*, Vol.7, 1959, pp. 37-52.

5 Kays, W. M., *Convective Heat and Mass Transfer*, McGraw-Hill, New York, 1966.

6 DesRuisseaux, N. and Zerkle, R. D., "Freezing of Hydraulic Systems," *Canadian Journal of Chemical Engineering*, Vol. 47, 1969, pp. 223-237.

7 Gilpin, R. R., "Ice Formation in a Pipe Containing Flows in the Transition and Turbulent Regimes," ASME JOURNAL OF HEAT TRANSFER, Vol. 103, 1981, pp. 363-368.

View Factors in Radiation Between Two Parallel Oriented Cylinders of Finite Lengths

N. H. Juul[1]

A simple double-integral expression for the diffuse radiation view factor, F_{12}, between two parallel cylinders of finite lengths is derived. No closed-form solution appears possible except for the limiting case of infinite long cylinders for which an analytical expression for the view factor F_{12}^{∞} is derived by applying the crossed string method. The accuracies of the line source approximations are evaluated, and the regions for which they are accurate to one percentage or better are identified. The view factor F_{12} between two opposing cylinders of equal length is computed by numerical integration and normalized by F_{12}^{∞}. The results are presented. Analytical expressions, which approximate the view factors between two opposite cylinders of finite length, are derived and their accuracy is evaluated over a useful parameter range. The range of their applications corresponds approximately to that for the line source approximation. This result is expected, because the errors are caused in part by blockage of radiation which is similar.

[1] Department of Mechanical and Aerospace Engineering, State University of New York at Buffalo, Amherst, N.Y. 14260. Mem. ASME

Contributed by the Heat Transfer Division for publication in the JOURNAL OF HEAT TRANSFER. Manuscript received by the Heat Transfer Division April 24, 1981.

Introduction

The view factor between parallel cylinders is important in many industrial applications; for example, it is used to determine the radiant heat transfer between tubes in boilers, heat exchangers, etc.

Plamondon [1] has developed a quadruple integral expression with limits of integration for the view factor between two parallel cylinders of finite length for any radius ratio. However, no results of numerical integrations are presented.

The single integral equations derived by Stevenson and Grafton (2) for the view factor from a note on the surface of one cylinder to a note on the surface of a parallel cylinder are extended to the case of two opposing cylinders. The results for the length ratio $L/R = 50$ and the view factors F_{12}^{∞} for corresponding spacing and radius ratio show poor agreements. This result leaves in doubt the correctness of the equations presented in (2).

The view factors between two cylinders of finite length and equal radius have been investigated by Sparrow and Jonsson [3]. They determined the view factor from ring element located at $z = 0$ on cylinder 1 to cylinder 2 of length z, by first applying the contour integral method followed by two numerical integrations. The results of the view factor normalized by the view factor from the ring element to cylinder 2, which extends from $z = 0$ to $z = \infty$, are presented graphically. The view factor from cylinder 1 to cylinder 2, both of finite length, may be obtained by graphical integration, the accuracy of which is limited.

In this paper a new integration scheme is developed by which the quadruple integral for the view factor is reduced to a simple double integral the subsequent integration of which can only be carried out numerically.

The results are normalized by the view factor for the limiting case of infinite long cylinders. For this case an analytical expression for view factor is obtained by the crossed string method for cylinders of different radii. The only other expression available in the literature for this geometry is the special case where both cylinders are of equal radii [4]. The accuracies of the line source approximations for infinite long cylinders are investigated. Since closed-form integration of the integral expression for finite cylinders does not appear possible, analytical expressions which approximate the view factors between two parallel oriented cylinders of equal length and any radius ratio are developed. The accuracy of the approximations are evaluated in reference to the results of the numerical integration.

Analysis

Numerical method. Figure 1 shows the geometry and defines the variables for the view factor analysis. The view factor F_{12} is evaluated by

$$F_{12} = \frac{1}{A_1} \int_{A_1} \int_{A_2} \frac{\cos\theta_1 \cos\theta_2}{\pi l^2} \, dA_1 \, dA_2 \tag{1}$$

Expressions for $\cos\theta_1$, $\cos\theta_2$, l, dA_1 and dA_2 are obtained by Fig. 1 in terms of the lengths T and S, defined by Figs. 1(b) and 1(c), the latitude angles α_1 and α_2 for dA_1 and dA_2, respectively, radius r and R for cylinder 1 and 2, respectively, the spacing c and the coordinates ζ_1 and ζ_2. The above expressions are substituted into equation (1). Making use of symmetry, closed form integrations are carried out first in respect to ζ_2 and then in respect to ζ_1. After considerable manipulations we obtain

$$F_{12} = \frac{R}{\pi^2 (L_1 - 1_1)} \int_0^{\alpha_{1L}} d\alpha_1 \int_{\alpha_{2L1}}^{\alpha_{2L}}$$

$$\left((L_2 - 1_1) \tan^{-1} \frac{L_2 - 1_1}{\sqrt{a}} - (L_2 - L_1) \tan^{-1} \frac{L_2 - L_1}{\sqrt{a}} \right.$$

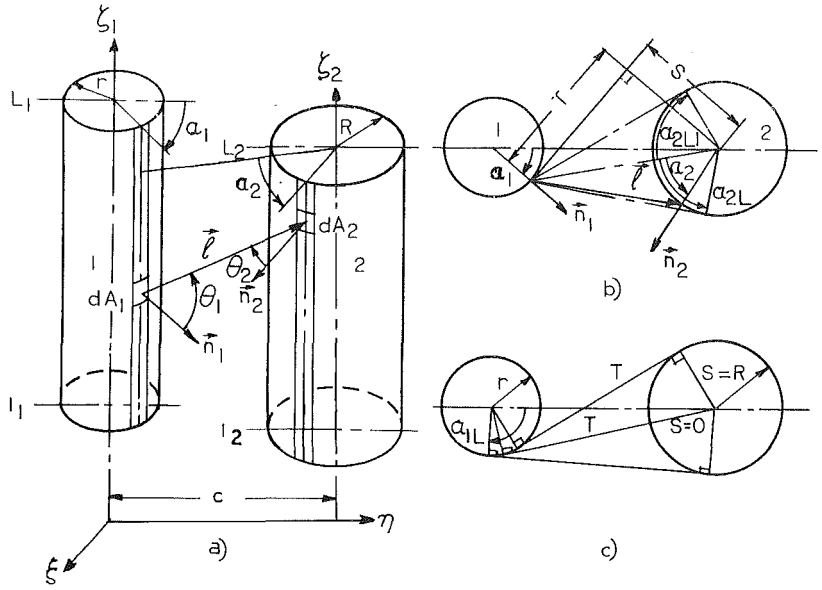

Fig. 1 Geometry for view factor analysis: (*a*) isometric view, (*b*) and (*c*) top view to define lengths, angles, limits of integration

$$+(1_2-L_1)\tan^{-1}\frac{1_2-L_1}{\sqrt{a}}-(1_2-1_1)\tan^{-1}\frac{1_2-1_1}{\sqrt{a}}\Bigg)$$
$$\frac{(S-R\cos\left(\alpha_2+\tan^{-1}\frac{T}{S}\right))(\sqrt{T^2+S^2}\cos\alpha_2-R)d\alpha_2}{(2a\sqrt{a})} \tag{2}$$

where $a = T^2 + S^2 + R^2 - 2R\sqrt{T^2+S^2}\cos\alpha_2$, $T = c\sin\alpha_1$ and $S = c\cos\alpha_1 - r$, and 1 and L are the ζ coordinates of the lower and upper cylinder ends, respectively.

The limits of integration are defined by

$$\alpha_{1L} = \sin^{-1}\frac{R-r}{c}+\frac{\pi}{2},\ \alpha_{2L} = \cos^{-1}\frac{R}{\sqrt{T^2+S^2}},$$

$$\alpha_{2L1} = -\alpha_{2L} \text{ when } S \geq R$$

$$\alpha_{2L1} = -\left(\tan^{-1}\frac{T}{S}-\cos^{-1}\frac{S}{R}\right) \text{ when}$$

$$\sin^{-1}\frac{r+R}{c} < \alpha_1 \leq \cos^{-1}\frac{r}{c} \text{ and } \alpha_{2L1} = \tan^{-1}\left|\frac{T}{S}\right|$$
$$-\cos^{-1}\left|\frac{S}{R}\right| \text{ when } \cos^{-1}\frac{r}{c} < \alpha_1 \leq \alpha_{1L}$$

By substituting a, $1_1 = 1_2 = 0$, and $L = L_1 = L_2$ into equation (2),

$$F_{12} = \frac{R}{\pi^2}\int_0^{\alpha_{1L}} d\alpha_1 \int_{\alpha_{2L1}}^{\alpha_{2L}} \frac{(S-R\cos\left(\alpha_2+\tan^{-1}\frac{T}{S}\right))(\sqrt{T^2+S^2}\cos\alpha_2-R)}{(T^2+S^2+R^2-2R\sqrt{T^2+S^2}\cos\alpha_2)^{1.5}} \times \tan^{-1}\frac{L}{\sqrt{T^2+S^2+R^2-2R\sqrt{T^2+S^2}\cos\alpha_2}}d\alpha_2 \tag{3}$$

which is the view factor for opposing cylinders of equal lengths.

The limiting case of infinite long parallel cylinders. An analytical expression for the exact view factor is derived by the crossed string method. The result is

$$F_{12}^{\infty} = 0.5/\pi(\sqrt{(c/r)^2-(R/r+1)^2}-\sqrt{(c/r)^2-(R/r-1)^2}$$
$$+\pi+(R/r-1)\cos^{-1}((R-r)/c)-(R/r+1)\cos^{-1}((R+r)/c)) \tag{4}$$

For $R = r$, equation (4) is in agreement with the expression derived in [4]. Letting $r \to 0$ the squared terms in equation (4) cancel since $R/r >> 1$ and the arc cosines become identical because $R = r$ and $R + r$ both become equal to R. Finally, we obtain,

$$F_{12}^{\infty} = 1/\pi \sin^{-1}(R/c) \tag{5}$$

which is identical to the well-known view factor from a cylindrical line source to cylinder 2.

Equation (5) is often used as an approximation for $r/R < 1$. Another approximation, which is useful for $r/R > 1$, is obtained by applying reciprocity using actual areas to the view factor from a line source, *ls*, which replaces cylinder 2, to cylinder 1. Thus we obtain

$$F_{12}^{\infty} = F_{ls1}A_2/A_1 = R/(\pi r)\sin^{-1}(r/c) \tag{6}$$

Approximate method. An analytical expression which approximates the view factor for opposing cylinders of equal lengths is developed. The arrangement which was first proposed by Glicksman [5] is shown in Fig. 4(*a*) where cylinder 1 is completely surrounded by cylinder 2 and $n-1$ hypothetical cylinder 2. The view factor from cylinder 1 to cylinder 2 is approximately by $F_{12} \sim F_{12n}/n$ where F_{12n} is the view factor from cylinder 1 to the n cylinders 2, the axis of which lie on a cylinder, which is concentric to cylinder 1 and has a radius equal to the spacing c. The approximation is good if the blockage of the rays from cylinder 1 to cylinder 2 by the cylinders adjacent to 2 is small. This is the case when $r << R$. When $r \to 0$, the expression becomes exact.

The view factor F_{12n} is evaluated by applying view factor algebra to the enclosure formed by the curved surface of cylinder 1, the curved surfaces of the n cylinders 2's facing cylinder 1, and the two identical end surfaces 3 and 4. Surface 3 is shown in Fig. 4(*a*). Thus we get:

$F_{12n} = 1 - F_{13} - F_{14} = 1 - 2F_{13}$, since $F_{14} = F_{13}$

F_{13} is difficult to evaluate since surface 3 has a complicated

geometry as shown in Fig. 4(*a*). Therefore, surface 3 is substituted with a ring surface 3′ of equal area. The outside radius R_0 of 3′ is evaluated by

$$\pi(R_0^2 - r^2) = A_3 = n\left(Rc\cos\beta - \pi R^2\,\frac{\pi - 2\beta}{2\pi}\right) - \pi r^2$$

where $\beta = \pi/n$.

The approximation assumes that the radiation from cylinder 1 through surface 3 and 3′ is identical. This requires that the energy escaping through the area of surface 3 which lies outside R_0, and the energy blocked by the surface of cylinder 2 inside R_0, are equal. The areas are shown hatch on Fig. 4(*a*). This requirement is approximately satisfied when n and R_0 are large.

Solving for R_0/R we get

$$R_0/R = \sqrt{\frac{n}{\pi}\sqrt{\frac{1}{\sin^2\frac{\pi}{n}} - 1} - \frac{n}{2} + 1}$$

where $n = 3,4,\infty$. However, only values of n for which

$$s/R = \frac{1}{\sin\frac{\pi}{n}} - \frac{r}{R}1 \geq 0$$

may be used. Applying view factor algebra on the enclosure formed by curved surfaces of cylinder 1 and cylinder 0 with radius R_0 and the two ring surfaces 3′ and 4′, we get $F_{12n} \sim 1 - 2F_{13'} = F_{10}$. Furthermore, $F_{12} \sim F_{10}/n$ and $nF_{12}^{\infty} \sim 1$ when the effect of blockage is small, which is the case for $r/R \leq 1$ and configurations for which the line source approximation is valid. By normalizing view factor F_{12} by F_{12}^{∞} and applying the above approximations we get:

$$F_{12}^N = \frac{F_{12}}{F_{12}^{\infty}} \sim F_{10}$$

F_{10} is obtained by applying the expression for the view factor between two concentric cylinders of equal length derived by Leuenberger and Person [6]. Finally we obtain

$$F_{12}^N = 1 - \frac{1}{\pi}\left\{\cos^{-1}\frac{C}{B} - \frac{R^2}{2rL}\left[\sqrt{(C + 2(R_0/R)^2)^2 - (2R_0/Rr/R)^2}\cos^{-1}\left(\frac{rC}{R_0 B}\right) + C\sin^{-1}\left(\frac{r}{R_0}\right) - \frac{\pi}{2}B\right]\right\} \quad (7)$$

where $C = (L/R)^2 - (R_0/R)^2 + (r/R)^2$, $B = (L/R)^2 + (R_0/R)^2 - (r/R)^2$ and

$$R_0/R = \sqrt{\frac{2\sqrt{c/R)^2 - 1} - \pi}{2\sin^{-1}\left(\frac{R}{c}\right)} + 1}$$ when n is eliminated.

In the limit for $r \to 0$, we obtain, by applying 1′, Hospital's rule to the squared bracket in equation (7),

$$F_{12}^N = 1 - \frac{1}{\pi}\cos^{-1}\left(\frac{(L/R)^2 - (R_0/R)^2}{(L/R)^2 + (R_0/R)^2}\right) \quad (8)$$

Furthermore, for $s/R = 0$ equation (8) becomes $F_{12}^N = 1$, since $R_0/R = 0$ for $c/R = 1$.

When $r > R$ the blockage is large. The errors caused by the blockage may be avoided by applying reciprocity. Since $F_{12} = R\,F_{21}/r$ and $F_{12}^{\infty} = R\,F_{21}^{\infty}/r$, we get that $F_{12}^N = F_{21}^N$. Thus, by using reciprocity, the normalized view factor is calculated by equation (7) after simply interchanging r and R.

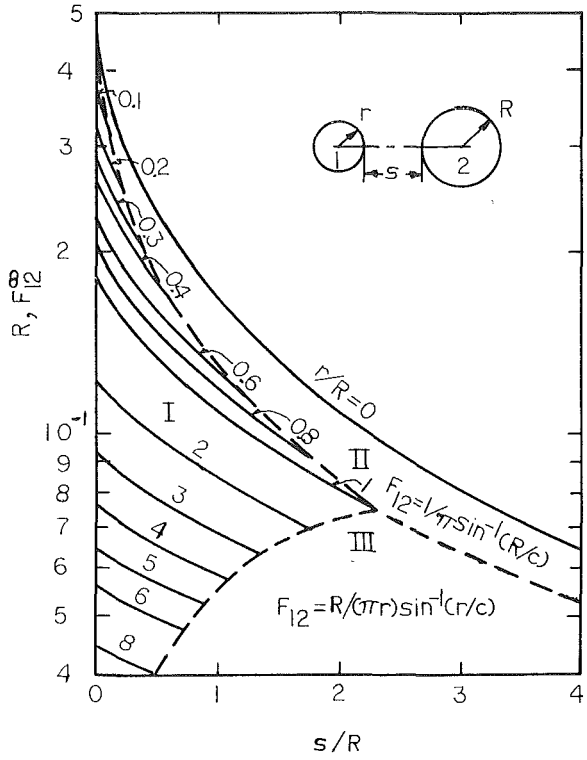

Fig. 2 The view factor is calculated by crossed-string method in region I and with an error of less than 1 percent by line source approximation in II and line source approximation with reciprocity in III.

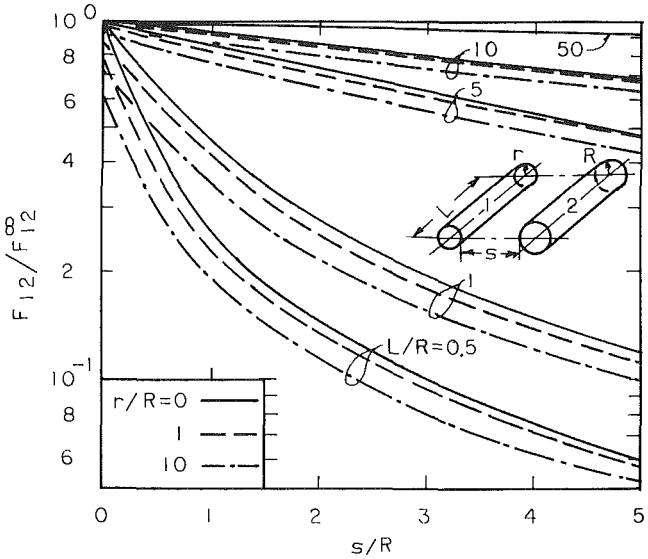

Fig. 3 Normalized view factor, F_{12}^N, as a function of separation ratios, s/R, for various length ratios L/R. F_{12} is obtained by numerical integration of equation (3) and F_{12}^{∞} by equation (4).

Results

Infinite long cylinder solution. The behavior of the view factor between two infinite long parallel cylinders is similar to the one found between two spheres [7], due to the similarity in symmetry. For example, if the view factors F_{12}^{∞} calculated by equation (4) are plotted as a function of spacing ratio, c/R for different radius ratios r/R then they would lie in a narrow band. The upper bound is defined by the locus of the view factors for zero separation ($s/R = 0$), and the lower bound by the cylindrical line source solution ($r/R = 0$). The two bounds converge into a point with the view factor of 0.5, as expected,

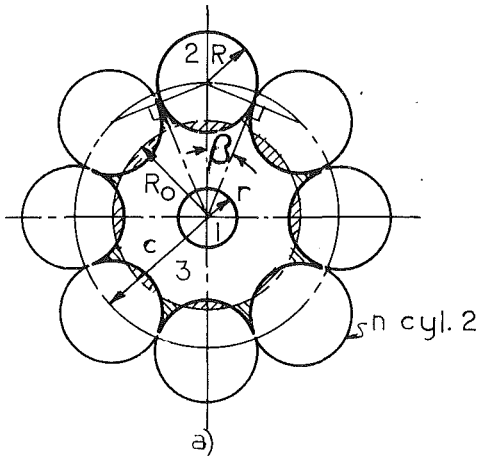

Fig. 4(*a*) Geometry for approximate method analysis

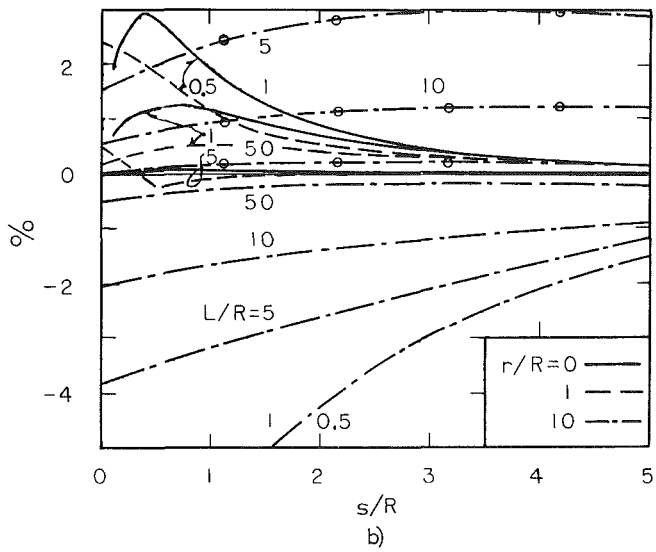

Fig. 4(*b*) Percent error for the approximate solutions is calculated by

$$100 \times \left(\frac{\text{equation (3)}}{\text{equation (4)}} - \text{equation (7)} \right) \frac{\text{equation (3)}}{\text{equation (4)}}.$$

The curves identified by dots are for the reciprocity case, for which r and R are interchanged in equation (7).

for $r = 0$ and $c/R = 1$. For the same radius ratio and spacing ratio the view factor between two cylinders is larger than the one between two spheres except for $c/R \to 1$ and $r \to 0$ when the view factor in both cases converge to 0.5. Since the line source approximations are only useful if the errors involved are known and the blockage errors for the approximate solutions for both cylinders of infinite and finite lengths are expected to be similar, an investigation of errors is carried out. The result is presented in Fig. 2 which shows the regions where equations (5) and (6) may be applied with an error of less than 1 percent.

Numerical Solution. The normalized view factor F_{12}^N is plotted in Fig. 3 as a function of the separation ration s/R for various values of length ratios L/R and radius ratio r/R. As expected $F_{12}^N = 1$ for any L/R when $r/R = 0$ and $s/R = 0$. The curves for r/R = constant shift down with increasing r/R for a given L/R. When $L/R = 50$, the curves for $r/R = 1$, and 1 and 10 merge into one curve. $F_{12}^N \geq .93$ for $L/R > 50$ and $0 < s/R < 5$ for all ratios of r/R.

Approximate solution. The accuracy of the approximate method is evaluated by the percent difference between F_{12}^N

Table 1 The tabulated view factors are obtained by numerical integration. The view factors in the blank regions may be calculated by the equations shown with an error less than 1 percent.

r/R	L/R	$S/R=0$	0.5	1.0	2.0
0	0.5	0.500	0.1037	0.0446	
	1.0		0.1526	0.0772	
	5.0				
	10.0		F_{12} = equations (8) × (5)		
	50.0				
.1	0.5	0.3453	0.0933	0.0415	
	1.0		0.1387	0.0721	
	5.0				
	10.0		F_{12} = equations (7) × (4)		
	50.0				
1.0	0.5	0.1440	0.0517	0.0264	
	1.0				
	5.0		F_{12} = equations (7) × (4)		
	10.0	0.1813			
	50.0	0.1834			
10.0	0.5	0.0233	0.0104	0.0062	0.0032
	1.0	0.0276	0.0167	0.0111	0.0062
	5.0	0.0344	0.0288	0.0246	0.0186
	10.0		F_{12} = equation (7) with		0.0229
	50.0		r and R interchanged × equation (4)		

calculated by the numerical method and the various approximate methods. The results are presented in Fig. 4(*b*) as a function of s/R for various values of L/R and r/R. Since the blockage is zero for $r/R = 0$, the curves for $r/R = 0$ in Fig. 4(*b*) show the error, introduced by the approximation $F_{12n} \sim F_{10}$, which is caused by replacing the complicated end surfaces with the ring surfaces. For $r/R = 0$ and s/R = constant, the error decreases with increasing L/R. This trend is due to the diminishing effect of the error on view factor, F_{13}', because the value of F_{13}' decreases with L/R. The errors due to blockage, which is neglected by the approximations, $F_{12} \sim F_{12n}/n$ and $nF_{12}^{\infty} \sim 1$, decrease as expected with increasing s/R. Figure 4(*b*) shows that the errors are positive for $r/R \leq 1$, smallest (less than 1 percent) for $r/R = 1$ and $L/R \geq 1$, and negative for $r/R = 10$. The curves, which are identified by circles, show the errors for $r/R = 10$ and $L/R = 5$, 10, and 50 when reciprocity is applied by interchanging r and R in equation (7). Comparison of the curves for $r/R = 10$ shows that for $s/R < 3$ the reciprocity method is best. Otherwise its performance is unexpectedly poor. It should be noted that the errors for $r/R > 1$ when reciprocity is applied, and the corresponding case with the reciprocate value of r/R, are identical, since r and R are simply interchanged if the numerical integrations satisfy reciprocity. Spot checks verify that this is the case. This point is illustrated by considering a configuration with $r/R = 10$, $L/R = 5$, and $s/R = 4$. Figure 4(*b*) shows that the error is -1.5 percent using equation (7) but 3 percent when reciprocity is applied by interchanging r and R in equation (7). By interchanging r and R for the given configuration, we obtain the reciprocate case with $r/R = 0.1$, $L/R = 0.5$ and $s/R = 0.4$. The error calculated by using equation (7) is 3 percent which is approximately the error shown by the curve for $r/R = 0$ and $L/R = 0.5$ at $s/R = 0.4$ in Fig. 4(*b*).

Table 1 presents the regions where the error on the view factor, calculated by the approximate methods, is less than 1 percent. The tabulated view factors are obtained by numerical integration of equation (3).

Conclusion

A simple double-integral equation for the view factor between parallel cylinders of finite lengths is derived. The numerical integration of this double integral requires significantly less computer time as compared to the integral

equations available in the literature. The cross-string method is used to derive the equation for the view factor as a function of radius ratio and separation ratios for the limiting case of infinitely long cylinders. The limits of application for the well-known cylindric line source approximation and the cylindric line source approximation with reciprocity are determined and presented for a useful range of parameters. The view factor for infinite long cylinders is used to normalize the view factor for opposed cylinders of finite length. The results of the numerical solution show that the normalized view factor goes to one when $L/R \geq 50$ for $0 \leq s/R \leq 5$ and $0 \leq r/R \leq 10$. Simple analytical expressions which approximate the normalizing view factors between two opposing cylinders of finite lengths are derived. The results of the approximate and numerical solutions are compared. The limits of applications for the approximate methods for cylinders of finite and infinite lengths are expected to be similar since the error depends to a large degree upon the blockage of radiation which is identical. The results show this is indeed the case. For $r/R \leq 1$, the approximation expressed by equation (7) is applicable in region II of Fig. 2 for any L/R, but when $L/R > 50$, then $F_{12}^N \sim 1$ and the view factor may be evaluated by the line source approximation equation (5). For $r/R \geq 1$, the application of reciprocity and equation (7) in region III of Fig. 2 is only satisfactorily for $L/R > 5$ or s/R large. When $L/R > 50$, then the normalized view factor is one, and equation (6) may be used. Table 1 gives the details of the regions for which the approximations for finite cylinders may be applied with an accuracy of 1 percent or better.

References

1 Plamondon, J. A., "Numerical Determination of Radiation Configuration Factors for Some Common Geometrical Situations," Tech. Report 32-127, Jet Propulsion Laboratory, California Institute of Technology, July 7, 1961, pp. 36, 37.

2 Stevenson, J. A. and Grafton, J. C., "Radiation Heat Transfer Analysis for Space Vehicles," North America Aviation Report SID-61-91 (AFASD TR61-119, Part 1), Sept. 9, 1961, pp. 173-175.

3 Sparrow, E. M. and Jonsson, V. K., "Angle Factors for Radiant Interchange Between Parallel-Oriented Tubes," ASME JOURNAL OF HEAT TRANSFER, Vol. 85, No. 4, Nov. 1963, pp. 382-384.

4 Siegel, R. and Howell, J. R., *Thermal Radiation Heat Transfer*, McGraw-Hill, New York, 1972, p. 207.

5 Glicksman, L. R., "Approximations for Configuration Factors Between Cylinders," Sept. 1972, unpublished paper.

6 Leuenberger, H. and Person, R. A., "Compilation of Radiation Shape Factors for Cylindrical Assemblies," ASME Paper No. 56-A-144, Nov. 1956.

7 Juul, N. H., "Investigation of Approximate Methods for Calculation of the Diffuse Radiation Configuration View Factor Between Two Spheres," *Letters in Heat and Mass Transfer Journal*, Vol. 3, No. 6, Nov./Dec. 1976, pp. 513-522.

Heat Transfer by Conduction and Radiation in One-Dimensional Planar Media Using the Differential Approximation[1]

A. C. Ratzel[2] and J. R. Howell[3]

Nomenclature

a = absorption coefficient
D = spacing between plates
e_{bi} = blackbody emissive power of wall, i
i' = radiative intensity distribution
I' = nondimensional radiative intensity $= i'/4e_{b1}$
I_b' = nondimensional blackbody intensity
I_0 = nondimensional zeroth moment of intensity
$I_{ij\ldots k}$ = nondimensional nth moment of intensity
K = thermal conductivity
$\hat{l}_i$ = direction cosine
N_1 = conduction-radiation parameter $= \alpha K T_1/4e_{b1}$
Q_C = nondimensional conduction heat-transfer rate
Q_R = nondimensional radiation heat-transfer rate
$\bar{r}$ = vector position in medium
T, T_i = temperature
x_i = position coordinate, i
α = extinction coefficient $= a + \sigma_s$
ϵ_i = diffuse emissivity of wall, i
θ = elevation angle $(0 \leq \theta \leq \pi)$
ρ_{di} = diffuse reflectivity of wall, i
σ_s = single scattering coefficient
τ = nondimensional position $= \alpha x_i$
τ_D = nondimensional optical thickness $= \alpha D$
ϕ = azimuthal angle $(0 \leq \phi \leq 2\pi)$
Ψ = nondimensional temperature $= T/T_i$
ω = solid angle
Ω_0 = single scattering albedo $= \sigma_s/(a + \sigma_s)$

Introduction

The combined conduction and radiation heat-transfer problem for a gray planar medium is considered using the differential approximation. Two governing energy equations which include isotropic scattering are developed incorporating the P-1 and P-3 approximations for the intensity distribution. The method of solution for the resulting nonlinear ordinary differential equations is summarized along with representative results.

Formulation

The problem considered is that of one-dimensional heat transfer between two isothermal parallel plates, where the intervening medium may absorb, emit, and isotropically scatter radiation. The medium is assumed to have a refractive index of one and is assumed to be gray and have uniform, temperature-independent properties. The enclosing plates diffusely emit energy, and may reflect incident energy both diffusely and specularly. Figure 1 presents the geometry and defines the nondimensional coordinate axes and boundary conditions. For this problem the energy equation reduces to:

$$\frac{dQ_R}{d\tau} = N_1 \frac{d^2\Psi}{d\tau^2} \tag{1}$$

The radiative flux, nondimensionalized by $4e_{b1}$, is obtained by integration of the radiative intensity distribution

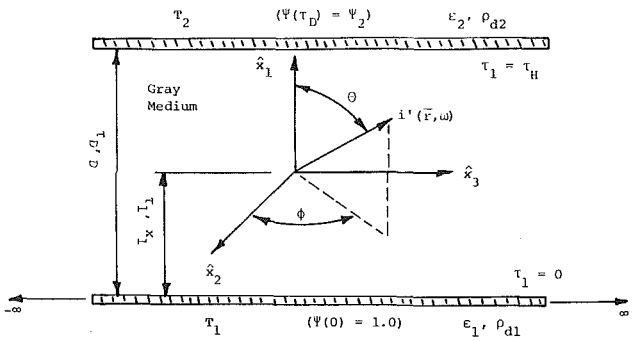

Fig. 1 Schematic of the planar geometry considered in the analysis

[1] This work performed at Sandia National Laboratories supported by the U.S. Department of Energy under contract DE-AC04-76DP00789.

[2] Sandia National Laboratories, Albuquerque, N.M. 87185

[3] Department of Mechanical Engineering, The University of Texas at Austin, Austin, Texas 78712. Mem. ASME

Contributed by the Heat Transfer Division for publication in the JOURNAL OF HEAT TRANSFER. Manuscript received by the Heat Transfer Division August 17, 1981.

equations available in the literature. The cross-string method is used to derive the equation for the view factor as a function of radius ratio and separation ratios for the limiting case of infinitely long cylinders. The limits of application for the well-known cylindric line source approximation and the cylindric line source approximation with reciprocity are determined and presented for a useful range of parameters. The view factor for infinite long cylinders is used to normalize the view factor for opposed cylinders of finite length. The results of the numerical solution show that the normalized view factor goes to one when $L/R \geq 50$ for $0 \leq s/R \leq 5$ and $0 \leq r/R \leq 10$. Simple analytical expressions which approximate the normalizing view factors between two opposing cylinders of finite lengths are derived. The results of the approximate and numerical solutions are compared. The limits of applications for the approximate methods for cylinders of finite and infinite lengths are expected to be similar since the error depends to a large degree upon the blockage of radiation which is identical. The results show this is indeed the case. For $r/R \leq 1$, the approximation expressed by equation (7) is applicable in region II of Fig. 2 for any L/R, but when $L/R > 50$, then $F_{12}^N \sim 1$ and the view factor may be evaluated by the line source approximation equation (5). For $r/R \geq 1$, the application of reciprocity and equation (7) in region III of Fig. 2 is only satisfactorily for $L/R > 5$ or s/R large. When $L/R > 50$, then the normalized view factor is one, and equation (6) may be used. Table 1 gives the details of the regions for which the approximations for finite cylinders may be applied with an accuracy of 1 percent or better.

References

1 Plamondon, J. A., "Numerical Determination of Radiation Configuration Factors for Some Common Geometrical Situations," Tech. Report 32-127, Jet Propulsion Laboratory, California Institute of Technology, July 7, 1961, pp. 36, 37.

2 Stevenson, J. A. and Grafton, J. C., "Radiation Heat Transfer Analysis for Space Vehicles," North America Aviation Report SID-61-91 (AFASD TR61-119, Part 1), Sept. 9, 1961, pp. 173-175.

3 Sparrow, E. M. and Jonsson, V. K., "Angle Factors for Radiant Interchange Between Parallel-Oriented Tubes," ASME JOURNAL OF HEAT TRANSFER, Vol. 85, No. 4, Nov. 1963, pp. 382-384.

4 Siegel, R. and Howell, J. R., *Thermal Radiation Heat Transfer*, McGraw-Hill, New York, 1972, p. 207.

5 Glicksman, L. R., "Approximations for Configuration Factors Between Cylinders," Sept. 1972, unpublished paper.

6 Leuenberger, H. and Person, R. A., "Compilation of Radiation Shape Factors for Cylindrical Assemblies," ASME Paper No. 56-A-144, Nov. 1956.

7 Juul, N. H., "Investigation of Approximate Methods for Calculation of the Diffuse Radiation Configuration View Factor Between Two Spheres," *Letters in Heat and Mass Transfer Journal*, Vol. 3, No. 6, Nov./Dec. 1976, pp. 513-522.

Heat Transfer by Conduction and Radiation in One-Dimensional Planar Media Using the Differential Approximation[1]

A. C. Ratzel[2] and J. R. Howell[3]

Nomenclature

a = absorption coefficient
D = spacing between plates
e_{bi} = blackbody emissive power of wall, i
i' = radiative intensity distribution
I' = nondimensional radiative intensity $= i'/4e_{b1}$
I'_b = nondimensional blackbody intensity
I_0 = nondimensional zeroth moment of intensity
$I_{ij\ldots k}$ = nondimensional nth moment of intensity
K = thermal conductivity
$\hat{l}_i$ = direction cosine
N_1 = conduction-radiation parameter $= \alpha K T_1/4e_{b1}$
Q_C = nondimensional conduction heat-transfer rate
Q_R = nondimensional radiation heat-transfer rate
$\bar{r}$ = vector position in medium
T, T_i = temperature
x_i = position coordinate, i
α = extinction coefficient $= a + \sigma_s$
ϵ_i = diffuse emissivity of wall, i
θ = elevation angle $(0 \leq \theta \leq \pi)$
ρ_{di} = diffuse reflectivity of wall, i
σ_s = single scattering coefficient
τ = nondimensional position $= \alpha x_i$
τ_D = nondimensional optical thickness $= \alpha D$
ϕ = azimuthal angle $(0 \leq \phi \leq 2\pi)$
Ψ = nondimensional temperature $= T/T_i$
ω = solid angle
Ω_0 = single scattering albedo $= \sigma_s/(a + \sigma_s)$

Introduction

The combined conduction and radiation heat-transfer problem for a gray planar medium is considered using the differential approximation. Two governing energy equations which include isotropic scattering are developed incorporating the P-1 and P-3 approximations for the intensity distribution. The method of solution for the resulting nonlinear ordinary differential equations is summarized along with representative results.

Formulation

The problem considered is that of one-dimensional heat transfer between two isothermal parallel plates, where the intervening medium may absorb, emit, and isotropically scatter radiation. The medium is assumed to have a refractive index of one and is assumed to be gray and have uniform, temperature-independent properties. The enclosing plates diffusely emit energy, and may reflect incident energy both diffusely and specularly. Figure 1 presents the geometry and defines the nondimensional coordinate axes and boundary conditions. For this problem the energy equation reduces to:

$$\frac{dQ_R}{d\tau} = N_1 \frac{d^2\Psi}{d\tau^2} \tag{1}$$

The radiative flux, nondimensionalized by $4e_{b1}$, is obtained by integration of the radiative intensity distribution

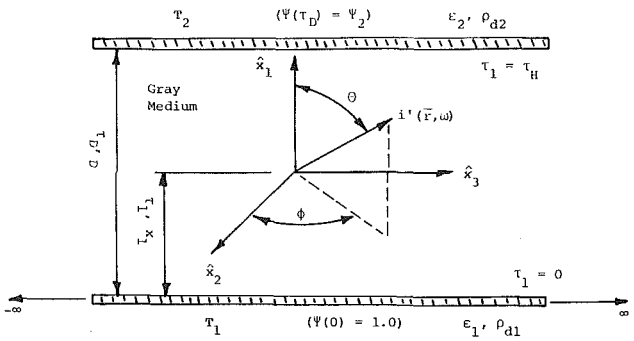

Fig. 1 Schematic of the planar geometry considered in the analysis

[1] This work performed at Sandia National Laboratories supported by the U.S. Department of Energy under contract DE-AC04-76DP00789.

[2] Sandia National Laboratories, Albuquerque, N.M. 87185
[3] Department of Mechanical Engineering, The University of Texas at Austin, Austin, Texas 78712. Mem. ASME

Contributed by the Heat Transfer Division for publication in the JOURNAL OF HEAT TRANSFER. Manuscript received by the Heat Transfer Division August 17, 1981.

(multiplied by the direction cosine) over 4π steradian solid angle,

$$Q_R(\tau) = \int_{\omega=4\pi} \hat{l}_l I'(\tau,\omega)\, d\omega \tag{2}$$

where $d\omega = \sin\theta d\phi d\theta$ and $\hat{l}_1 = \cos\theta$. The intensity is obtained from solution of the one-dimensional equation of transfer:

$$\hat{l}_1 \frac{dI'}{d\tau} = -I' + (1-\Omega_0) I'_b + \frac{\Omega_0}{4\pi} \int_{\omega=4\pi} I'(\tau,\omega)\, d\omega \tag{3}$$

Equations (2) and (3) are combined and substituted into equation (1) to yield a single integro-differential equation which may be solved subject to boundary conditions given in Fig. 1 [1, 2].

To simplify the analysis, the intensity distribution is represented by an infinite series of spherical harmonics, as given by equation (4) [3]:

$$I'(\bar{r},\omega) = \sum_{l=0}^{\infty} \sum_{m=-l}^{l} A_l^m(\bar{r})\, Y_l^m(\omega) \tag{4}$$

where $A_l^m(\bar{r})$ are position dependent coefficients and $Y_l^m(\omega)$ are the normalized spherical harmonics defined below:

$$Y_l^m(\omega) = \left[\frac{2l+1}{4\pi} \frac{(l-m)!}{(l+m)!}\right]^{1/2} e^{jm\phi} P_l^m(\cos\theta) \tag{5}$$

The intensity distribution is approximated by truncating the series after a finite set of terms, $l=1$ and $l=3$ for the P-1 and P-3 approximations, respectively. The intensity is recast in terms of moments of intensity (defined by equations (6)), by substituting equation (4) into equations (6), performing appropriate integrations, and then algebraically solving for the unknown coefficients $A_l^m(\bar{r})$ in terms of the moments [4, 5]. For the one-dimensional geometry considered, the resulting intensity distribution for the P-3 approximation is given by equation (7). The P-1 intensity distribution is comprised of the first two terms of equation (7).

Zeroth moment:

$$I_0(r) = \int_{\omega=4\pi} I'(\bar{r},\omega) d\omega \tag{6a}$$

Nth moment:

$$I_{ij\ldots k}(\bar{r}) = \int_{\omega=4\pi} \hat{l}_i \hat{l}_{j\ldots} \hat{l}_k I'(\bar{r},\omega)\, d\omega \tag{6b}$$

$$I'(\tau,\theta) = \frac{1}{4\pi}\left[I_0 + 3I_1\cos\theta + \frac{5}{4}(3I_{11} - I_0)(3\cos^2\theta - 1) + \frac{7}{4}(5I_{111} - 3I_1)(5\cos^3\theta - 3\cos\theta)\right] \tag{7}$$

The equation of transfer is transformed into a series of moment equations by multiplying equation (3) by appropriate direction cosines and integrating over 4π solid angle. Equations (8) are obtained for the P-3 approximation with the "closure" conditions for the P-1 and P-3 approximations given by equations (9*a*) and (9*b*), respectively. Note that equations (8*a*) and (8*b*) hold for the P-1 approximation.

Moment equations:

$$\frac{dI_1}{d\tau} = (1-\Omega_0)(4\pi I'_b - I_0) \tag{8a}$$

$$\frac{dI_{11}}{d\tau} = -I_1 \tag{8b}$$

$$\frac{dI_{111}}{d\tau} = -I_{11} + \frac{4\pi}{3}(1-\Omega_0) I'_b + \frac{\Omega_0}{3} I_0 \tag{8c}$$

$$\frac{dI_{1111}}{d\tau} = -I_{111} \tag{8d}$$

Closure conditions:

$$I_{11}(\tau) = \frac{I_0(\tau)}{3} \tag{9a}$$

$$I_{1111}(\tau) = \frac{6}{7} I_{11}(\tau) - \frac{3}{35} I_0(\tau) \tag{9b}$$

The radiative flux is equivalent to I_1 (equation (2)), and hence the energy conservation equation and moment of intensity relations are combined to yield temperature expressions by repeated backward substitutions and differentiations of equations (8), (9), and (1). The following fourth- and sixth-order nonlinear ordinary differential equations are obtained for the P-N approximations for $\Omega_0 < 1$.

P-1:

$$\frac{d^4\Psi}{d\tau^4} - \left[\frac{4(1-\Omega_0)}{N_1}\Psi^3 + 3(1-\Omega_0)\right]\frac{d^2\Psi}{d\tau^2} - \left[\frac{12(1-\Omega_0)}{N_1}\Psi^2 \frac{d\Psi}{d\tau}\right]\frac{d\Psi}{d\tau} = 0 \tag{10}$$

P-3:

$$\frac{d^6\Psi}{d\tau^6} - \frac{d^4\Psi}{d\tau^4}\left[(1-\Omega_0)\left(\frac{4}{N_1}\Psi^4 + 10\right) + \frac{35}{9}\Omega_0\right] - \frac{d^3\Psi}{d\tau^3}\left[\frac{48(1-\Omega_0)}{N_1}\Psi^2 \frac{d\Psi}{d\tau}\right] - \frac{d^2\Psi}{d\tau^2}\left[\frac{144(1-\Omega_0)}{N_1}\Psi\left(\frac{d\Psi}{d\tau}\right)^2 + \frac{36(1-\Omega_0)}{N_1}\Psi^2 \frac{d^2\Psi}{d\tau^2} - 35(1-\Omega_0) - \frac{140}{9}(1-\Omega_0)\Psi^3\right] - \frac{d\Psi}{d\tau}\left[\frac{24(1-\Omega_0)}{N_1}\left(\frac{d\Psi}{d\tau}\right)^3 - \frac{140}{3N_1}(1-\Omega_0)\Psi^2 \frac{d\Psi}{d\tau}\right] = 0 \tag{11}$$

For a purely scattering medium ($\Omega_0 = 1$), the radiative and conductive effects are decoupled and the radiative equation reduces to an ordinary differential equation [5].

In incorporating the spherical harmonics intensity approximations, two boundary conditions for the P-1 approximation and four boundary conditions for the P-3 approximation are required in addition to the boundary temperatures. These expressions are obtained by finding the intensity leaving the boundary surfaces and incorporating modified Marshak conditions [5, 6, 7]. The resulting boundary conditions for the P-1 and P-3 approximations are given by Bayazitoğlu and Higenyi [6] in moment notation and by Ratzel [7] in terms of nondimensional temperature.

Solution Method

The fourth- and sixth-order nonlinear boundary value ordinary differential equations were solved with a modified version of COLSYS [8], which uses collocation at Gaussian points implementing B-splines. Approximate solutions are computed in COLSYS until user-specified tolerances are satisfied. A damped Newton's method is used for the nonlinear iteration. Tolerances on nondimensional temperatures and corresponding derivatives for all results shown were fixed at 10^{-5}.

Rapid convergence was achieved by initially using the pure conduction solution to obtain results for $N_1 = 100$, and then reducing the conduction-radiation parameter by a factor of ten following convergence at each conduction-radiation

Table 1 Comparative results of nondimensional heat transfer: $\Psi_2 = 0.5$, $\epsilon_1 = \epsilon_2 = 1.0$, $\Omega_0 = 0$

Optical thickness (τ_D)	Conduction-radiation parameter (N_1)	Nondimensional heat transfer: Crosbie and Viskanta [2]	P-1 approx.	P-3 approx.
0.1	10.0	200.88	200.90	200.89
	1.0	20.88	20.90	20.89
	0.1	2.880	2.898	2.889
	0.01	1.080	1.098	1.088
	0.0	0.8535	0.8721	0.8641
1.0	10.0	20.57	20.62	20.58
	1.0	2.572	2.615	2.580
	0.1	0.7694	0.8085	0.7758
	0.01	0.5675	0.5948	0.5716
	0.0	0.5188	0.5357	0.5210
10.0	10.0	2.115	2.116	2.115
	1.0	0.3150	0.3166	0.3150
	0.1	0.1335	0.1349	0.1336
	0.01	0.1131	0.1144	0.1132
	0.0	0.1095	0.1103	0.1096

Table 2 Comparative results of nondimensional medium temperatures for $\tau_D = 1.0$: $\Psi_2 = 0.5$, $\epsilon_1 = \epsilon_2 = 1.0$, $\Omega_0 = 0$

Conduction-radiation parameter (N_1)	Optical depth position τ/τ_D	Nondimensional temperature: Crosbie [10]	P-1 approx.	P-3 approx.
1.0	0.1	0.9508	0.9506	0.9507
	0.2	0.9027	0.9028	0.9028
	0.4	0.8073	0.8084	0.8077
	0.6	0.7095	0.7114	0.7101
	0.8	0.6074	0.6091	0.6078
	0.9	0.5544	0.5554	0.5547
0.1	0.1	0.9504	0.9476	0.9497
	0.2	0.9105	0.9087	0.9107
	0.4	0.8407	0.8430	0.8416
	0.6	0.7611	0.7690	0.7633
	0.8	0.6538	0.6634	0.6562
	0.9	0.5838	0.5905	0.5855
0.01	0.1	0.9313	0.9239	0.9302
	0.2	0.9046	0.8987	0.9045
	0.4	0.8657	0.8641	0.8658
	0.6	0.8232	0.8266	0.8228
	0.8	0.7548	0.7676	0.7564
	0.9	0.6762	0.6921	0.6796

Table 3 Comparative results of nondimensional heat transfer for $\tau_D = 1.0$ and different single scattering albedos: $\Psi_2 = 0.5$, $\epsilon_1 = \epsilon_2 = 0.1$

Conduction-radiation parameter (N_1)	Isotropic scattering albedo (Ω_0)	Nondimensional heat transfer: Yuen Wong [9]	P-1 approx.	P-3 approx.
1.0	0.0	2.221	2.259	2.235
	0.5	2.154	2.167	2.159
	1.0	2.047	2.048	2.047
0.1	0.0	0.403	0.430	0.413
	0.5	0.346	0.357	0.350
	1.0	0.247	0.248	0.247
0.01	0.0	0.158	0.166	0.163
	0.5	0.130	0.135	0.132
	1.0	0.067	0.068	0.067

parameter value. After convergence, the nondimensional radiative heat-transfer rates were computed from the expressions for I_1 developed for the P-N approximations. The conductive heat-transfer rate was obtained from equation (12) and the total heat transfer was given by the sum of the radiative and conductive rates.

$$Q_C(\tau) = -4N_1 \frac{d\Psi}{d\tau} \tag{12}$$

Results

P-N approximation solutions for a range of conduction-radiation parameters, wall emissivities, and optical thicknesses were compared with results reported in the literature [1, 2, 9, 10]. Comparative results for non-dimensional heat-transfer rate and temperature are summarized in Tables 1 and 2, respectively. The agreement is excellent for both the P-1 and P-3 approximations. Maximum errors for the P-1 approximation rarely exceed 5 percent, while the maximum error for the P-3 approximation is below 1.0 percent. In all cases, the P-3 approximation results are superior to the P-1 results.

Additional nondimensional heat-transfer rates for the case of isotropic scattering are compared with results presented by Yuen and Wong [9] in Table 3. The P-3 approximation results for three isotropic scattering albedos and diffusely reflecting surfaces compare well with the Yuen and Wong published data, and the maximum error is below 2.5 percent. The P-1 approximation solution overestimates the nondimensional heat-transfer rates more than the P-3 method, but the maximum error measured when comparing the P-1 and Yuen-Wong work is still less than 7 percent. Overall, the greatest discrepancies between the two P-N methods occur for $N_1 \leq 0.1$. For such situations the P-3 approximation should be utilized wherever possible. For $N_1 > 1.0$, differences in nondimensional temperature and heat-transfer rate are negligible and the P-1 approximation would be preferred, since computational expenses are reduced.

Conclusions

The P-1 and P-3 methods yield results for combined conduction-radiation problems which are in close agreement with "exact" solutions for one-dimensional planar problems. Results for varied conditions have shown that the P-3 approximation method is superior to the P-1 method and that these results, when compared with work reported by Crosbie and Viskanta [2, 10], yield maximum errors below 2.5 percent. The P-N approximation methods work well for a variety of wall properties and scattering constraints and for all examined ranges of conduction-radiation parameters and optical thicknesses.

References

1 Viskanta, R. and Grosh, R. J., "Heat Transfer by Simultaneous Conduction and Radiation in an Absorbing Medium," ASME JOURNAL OF HEAT TRANSFER, Vol. 84, No. 1, 1962, pp. 63–72.

2 Crosbie, A. L. and Viskanta, R., "Interaction of Heat Transfer by Conduction and Radiation in a Nongray Planar Medium," *Warme-und Stoffubertragung*, Vol. 4, 1971, pp. 205–212.

3 Jeans, J. H., "The Equations of Radiative Transfer of Energy," *Monthly Notices of Royal Astronomical Society*, Vol. 78, Nov. 1917, pp. 28–36.

4 Cheng, P., "Dynamics of a Radiating Gas with Application to Flow Over a Wavy Wall," *AIAA Journal*, Vol. 4, No. 2, 1966, pp. 238–245.

5 Bayazitoğlu, Y. and Higenyi, J., "Higher Order Differential Equations of Radiative Transfer: P_3 Approximation," *AIAA Journal*, Vol. 17, No. 4, 1979, pp. 424–431.

6 Marshak, R. E., "Note on the Spherical Harmonic Method as Applied to the Milne Problem for a Sphere," *Phys. Rev.*, Vol. 71, 1947, pp. 443–446.

7 Ratzel, A. C., "P-N Differential Approximation for Solution of One- and Two-Dimensional Radiation and Conduction Energy Transfer in Gray Participating Media," Ph. D. dissertation, University of Texas at Austin, Dec. 1981.

8 Ascher, U., Christiansen, J. and Russell, R. D., "Collocation Software for Boundary Value ODE's," *Codes for Boundary Value Problems in Ordinary Differential Equations*, edited by B. Childs, et al., Berlin, Springer-Verlag, 1979, pp. 164–185.

9 Yuen, W. W. and Wong, L. W., "Heat Transfer by Conduction and Radiation in a One-Dimensional Absorbing, Emitting and Anisotropically Scattering Medium," ASME JOURNAL OF HEAT TRANSFER, Vol. 102, No. 2, 1980, pp. 303–307.

10 Crosbie, A. L., *Personal communication of results not given in reference* [3].

Vertical Fin Efficiency With Film Condensation

L. C. Burmeister[1]

Nomenclature

A = fin cross sectional area
F_1 = dimensionless parameter, $F_1 = [g(\rho_L - \rho_v)\,\mathrm{Pr}H^3/\rho_L \nu_L^2][h_{fg}/C_{p_L}(T_v - T_b)]$
F_2 = dimensionless parameter, $F_2 = tk/2Hk_L$
g = gravitational acceleration
H = fin height
h_{ave} = average heat transfer coefficient for fin everywhere at root temperature
h_{fg} = heat of vaporization
k = fin thermal conductivity
k_L = liquid thermal conductivity
M = parameter, $MH = (16\sqrt{2}/21)^{1/2}(F_1/F_2^4)^{1/8}$
m = parameter, $mH = (7/8)^{1/2}MH$
$\dot{m}$ = condensate mass flow rate per unit length
P = fin perimeter
Pr = liquid Prandtl number
Q = actual fin heat transfer, equation (15)
Q_{max} = maximum fin heat transfer, equation (16)
T = fin temperature
T_b = fin root temperature
T_v = vapor saturation temperature
t = fin total thickness
x = distance from fin tip
Δ = dimensionless liquid film thickness, $\Delta = \delta/H$
δ = liquid film thickness
η = fin efficiency
θ = dimensionless fin temperature, $\theta = (T_v - T)/(T_v - T_b)$
θ_0 = dimensionless fin tip temperature, $\theta_0 = \theta(\xi = 0)$
ν_L = liquid kinematic viscosity
ξ = dimensionless distance from fin tip, $\xi = x/H$
ρ_L = liquid density
ρ_v = vapor density

Introduction

Film condensation of a saturated vapor on a vertical rectangular fin whose lower end is maintained at a fixed temperature was recently analyzed by Nader [1] in an interesting study. Numerical methods were used to accurately determine the fin temperature distribution and efficiency, accounting for variable condensate thickness along the fin length, in terms of two dimensionless parameters F_1 and F_2. Although it was remarked that correlation required only a single dimensionless parameter $F_1/F_2{}^4$, the basis for this was not set forth. In an earlier study of broader scope, Lienhard and Dhir [2] gave this basis and numerically solved the same equations with slightly less accuracy but over a wider range of parameters.

The results of these prior studies were presented in tabular [1] and graphical [2] forms. In the following, a more convenient closed-form approximate solution is developed for fin efficiency.

Problem Formulation

In this problem the fin is of height, H, total thickness, t,

[1] Mechanical Engineering Department, University of Kansas, Lawrence, Kan. 66045. Mem. ASME

Contributed by the Heat Transfer Division for publication in the JOURNAL OF HEAT TRANSFER. Manuscript received by the Heat Transfer Division September 7, 1981.

Results

P-N approximation solutions for a range of conduction-radiation parameters, wall emissivities, and optical thicknesses were compared with results reported in the literature [1, 2, 9, 10]. Comparative results for non-dimensional heat-transfer rate and temperature are summarized in Tables 1 and 2, respectively. The agreement is excellent for both the P-1 and P-3 approximations. Maximum errors for the P-1 approximation rarely exceed 5 percent, while the maximum error for the P-3 approximation is below 1.0 percent. In all cases, the P-3 approximation results are superior to the P-1 results.

Additional nondimensional heat-transfer rates for the case of isotropic scattering are compared with results presented by Yuen and Wong [9] in Table 3. The P-3 approximation results for three isotropic scattering albedos and diffusely reflecting surfaces compare well with the Yuen and Wong published data, and the maximum error is below 2.5 percent. The P-1 approximation solution overestimates the nondimensional heat-transfer rates more than the P-3 method, but the maximum error measured when comparing the P-1 and Yuen-Wong work is still less than 7 percent. Overall, the greatest discrepancies between the two P-N methods occur for $N_1 \leq 0.1$. For such situations the P-3 approximation should be utilized wherever possible. For $N_1 > 1.0$, differences in nondimensional temperature and heat-transfer rate are negligible and the P-1 approximation would be preferred, since computational expenses are reduced.

Conclusions

The P-1 and P-3 methods yield results for combined conduction-radiation problems which are in close agreement with "exact" solutions for one-dimensional planar problems. Results for varied conditions have shown that the P-3 approximation method is superior to the P-1 method and that these results, when compared with work reported by Crosbie and Viskanta [2, 10], yield maximum errors below 2.5 percent. The P-N approximation methods work well for a variety of wall properties and scattering constraints and for all examined ranges of conduction-radiation parameters and optical thicknesses.

References

1 Viskanta, R. and Grosh, R. J., "Heat Transfer by Simultaneous Conduction and Radiation in an Absorbing Medium," ASME JOURNAL OF HEAT TRANSFER, Vol. 84, No. 1, 1962, pp. 63-72.

2 Crosbie, A. L. and Viskanta, R., "Interaction of Heat Transfer by Conduction and Radiation in a Nongray Planar Medium," *Warme-und Stoffubertragung*, Vol. 4, 1971, pp. 205-212.

3 Jeans, J. H., "The Equations of Radiative Transfer of Energy," *Monthly Notices of Royal Astronomical Society*, Vol. 78, Nov. 1917, pp. 28-36.

4 Cheng, P., "Dynamics of a Radiating Gas with Application to Flow Over a Wavy Wall," *AIAA Journal*, Vol. 4, No. 2, 1966, pp. 238-245.

5 Bayazitoğlu, Y. and Higenyi, J., "Higher Order Differential Equations of Radiative Transfer: P_3 Approximation," *AIAA Journal*, Vol. 17, No. 4, 1979, pp. 424-431.

6 Marshak, R. E., "Note on the Spherical Harmonic Method as Applied to the Milne Problem for a Sphere," *Phys. Rev.*, Vol. 71, 1947, pp. 443-446.

7 Ratzel, A. C., "P-N Differential Approximation for Solution of One- and Two-Dimensional Radiation and Conduction Energy Transfer in Gray Participating Media," Ph. D. dissertation, University of Texas at Austin, Dec. 1981.

8 Ascher, U., Christiansen, J. and Russell, R. D., "Collocation Software for Boundary Value ODE's," *Codes for Boundary Value Problems in Ordinary Differential Equations*, edited by B. Childs, et al., Berlin, Springer-Verlag, 1979, pp. 164-185.

9 Yuen, W. W. and Wong, L. W., "Heat Transfer by Conduction and Radiation in a One-Dimensional Absorbing, Emitting and Anisotropically Scattering Medium," ASME JOURNAL OF HEAT TRANSFER, Vol. 102, No. 2, 1980, pp. 303-307.

10 Crosbie, A. L., *Personal communication of results not given in reference* [3].

Vertical Fin Efficiency With Film Condensation

L. C. Burmeister[1]

Nomenclature

A = fin cross sectional area
F_1 = dimensionless parameter, $F_1 = [g(\rho_L - \rho_v)\,\mathrm{Pr}H^3/\rho_L \nu_L^2][h_{fg}/C_{p_L}(T_v - T_b)]$
F_2 = dimensionless parameter, $F_2 = tk/2Hk_L$
g = gravitational acceleration
H = fin height
h_{ave} = average heat transfer coefficient for fin everywhere at root temperature
h_{fg} = heat of vaporization
k = fin thermal conductivity
k_L = liquid thermal conductivity
M = parameter, $MH = (16\sqrt{2}/21)^{1/2}(F_1/F_2^4)^{1/8}$
m = parameter, $mH = (7/8)^{1/2}MH$
$\dot{m}$ = condensate mass flow rate per unit length
P = fin perimeter
Pr = liquid Prandtl number
Q = actual fin heat transfer, equation (15)
Q_{max} = maximum fin heat transfer, equation (16)
T = fin temperature
T_b = fin root temperature
T_v = vapor saturation temperature
t = fin total thickness
x = distance from fin tip
Δ = dimensionless liquid film thickness, $\Delta = \delta/H$
δ = liquid film thickness
η = fin efficiency
θ = dimensionless fin temperature, $\theta = (T_v - T)/(T_v - T_b)$
θ_0 = dimensionless fin tip temperature, $\theta_0 = \theta(\xi = 0)$
ν_L = liquid kinematic viscosity
ξ = dimensionless distance from fin tip, $\xi = x/H$
ρ_L = liquid density
ρ_v = vapor density

Introduction

Film condensation of a saturated vapor on a vertical rectangular fin whose lower end is maintained at a fixed temperature was recently analyzed by Nader [1] in an interesting study. Numerical methods were used to accurately determine the fin temperature distribution and efficiency, accounting for variable condensate thickness along the fin length, in terms of two dimensionless parameters F_1 and F_2. Although it was remarked that correlation required only a single dimensionless parameter $F_1/F_2{}^4$, the basis for this was not set forth. In an earlier study of broader scope, Lienhard and Dhir [2] gave this basis and numerically solved the same equations with slightly less accuracy but over a wider range of parameters.

The results of these prior studies were presented in tabular [1] and graphical [2] forms. In the following, a more convenient closed-form approximate solution is developed for fin efficiency.

Problem Formulation

In this problem the fin is of height, H, total thickness, t,

[1] Mechanical Engineering Department, University of Kansas, Lawrence, Kan. 66045. Mem. ASME

Contributed by the Heat Transfer Division for publication in the JOURNAL OF HEAT TRANSFER. Manuscript received by the Heat Transfer Division September 7, 1981.

Table 1 Vertical fin efficiency with film condensation

MH	Analytical, equation (17)	Numerical [1]	Average heat-transfer Coefficient, equation (18)
0.0	1.0000	---	1.0000
0.07784	0.9983	0.9988	0.9982
0.7784	0.8589	0.8745	0.8541
1.0380	0.8056	0.7989	0.7715
1.3842	0.6795	0.6969	0.6645
1.8459	0.5666	0.5776	0.5436
2.4616	0.4563	0.4603	0.4257
3.2825	0.3602	0.3612	0.3243
4.3773	0.2820	0.2823	0.2441

root temperature, T_b, and thermal conductivity, k. The saturated vapor at temperature $T_v > T_b$ condenses in a liquid film whose thickness δ increases from its initial zero value at the insulated tip. The condensate flow rate per unit length is given, as in common in such constant property situations [3], by

$$\dot{m} = g(\rho_L - \rho_v)\delta^3/3\nu_L$$

Assuming that the fin temperature varies solely with height, the change in conductive heat flow down the fin at a location x below the fin tip is made up by conductive heat flow across the condensate film. Thus,

$$d(-tkdT/dx)/dx = 2k_L(T_v - T)/\delta \tag{1}$$

Similarly, the change in condensate flow rate at a location x below the fin tip provides an energy flow due to the latent heat of vaporization given up which is conducted across the liquid film. Thus, neglecting convective contributions

$$h_{fg}d[g(\rho_L - \rho_v)\delta^3/3\nu_L]/dx = k_L(T_v - T)\delta \tag{2}$$

The boundary conditions imposed are

$$\delta(0) = 0 \tag{3}$$

$$dT(0)/dx = 0 \tag{4}$$

$$T(H) = T_b \tag{5}$$

The dimensionless forms of equations (1-5) are

$$d^2\theta/d\xi^2 = \theta/F_2\Delta \tag{6}$$

$$d\Delta^4/d\xi = 4\theta/F_1 \tag{7}$$

$$\Delta(0) = 0 \tag{8}$$

$$d\theta(0)/d\xi = 0 \tag{9}$$

$$\theta(1) = 1 \tag{10}$$

which were obtained earlier [1-2] in an equivalent form.

A single equation for temperature is obtained, solving equation (6) for Δ and substituting the result into equation (7), as

$$d(\theta/\theta'')^4/d\xi = (4F_2^4/F_1)\theta \tag{11}$$

where primes denote differentiation with respect to ξ. The single dimensionless parameter F_1/F_2^4 is seen to characterize the fin temperature distribution as was pointed out earlier [2].

Problem Solution

The solution of equation (11) proceeds by rewriting it as

$$(\theta/\theta'')^2 d(\theta/\theta'')/d\xi = (F_2^4/F_1)d\dot{\theta}/d\xi$$

Integration gives

$$(\theta/\theta'')^3 = (3F_2^4/F_1)(\dot{\theta} + C_1) \tag{12}$$

Noting that $\theta/\theta'' = F_2\,\Delta$ from equation (6) and considering equations (8) and (9), it is realized that $C_1 = 0$. Rearrangement of equation (12) as

$$(\dot{\theta})^{1/3} d\dot{\theta}/d\xi = (F_1/3F_2^4)^{1/3}\theta$$

and substitution of $\dot{\theta}d\,\dot{\theta}/d\theta$ for $d\dot{\theta}/d\xi$ enables a second integration with the result that

$$\dot{\theta} = (7/6)^{3/7}(F_1/3F_2^4)^{1/7}(\theta^2 - \theta_0^2)^{3/7} \tag{13}$$

taking equation (9) into account.

Equation (13) permits computation of the conductive heat flux at the fin root if the dimensionless tip temperature θ_0 is ascertained. The transformation $\theta = \theta_0\cosh(Z)$ followed by integration from $\xi = 0$ to $\xi = 1$ results in

$$\theta_0^{1/7}\int_0^{\operatorname{arccosh}(1/\theta_0)} \sinh^{1/7}(Z)\,dZ = (7/6)^{3/7}(F_1/3F_2^4)^{1/7} \tag{14}$$

Recognizing from equation (13) that accurate determination of θ_0 is only necessary when $\theta_0 \approx 1$, a satisfactory approximation is obtained from equation (14) by taking $\theta_0^{1/7} \simeq 1$ and $\sinh(Z) \simeq Z$ to obtain $\theta_0 = 1/\cosh(MH)$.

The conductive heat flow per unit length at the fin root is obtained by utilizing equations (13) and (14) in

$$Q = -ktdT(H)/dx$$

$$Q = 2k_L(T_v - T_b)(7/6)^{3/7}F_2(F_1/F_2^4)^{1/7}\tanh^{6/7}(MH) \tag{15}$$

Discussion

The results so far obtained enable computation of the fin efficiency, the ratio of the actual fin heat transfer to the fin heat transfer that would occur if the fin were everywhere at the root temperature. The latter quantity is [4]

$$Q_{\max} = 2k_L(T_v - T_b)2^{3/2}F_1^{1/4}/3 \tag{16}$$

The fin efficiency is found from equations (15) and (16) to be

$$\eta = [\tanh(MH)/MH]^{6/7} \tag{17}$$

The ability of equation (17) to represent the results numerically determined by Nader is illustrated in Table 1. Less than two percent deviation is observed. Lienhard and Dhir [2] reported slightly higher efficiencies-E in their equation (36), and Fig. 9 is related to the parameters of the present study by $E = 21(MH)^2/32$.

Equation (17) for the efficiency of a condensing fin is next compared to the efficiency of a fin with a constant heat-transfer coefficient. For a condensing fin everywhere at the root temperature, the average heat-transfer coefficient is available from equation (16) as

$$h_{\text{ave}} = 2^{3/2}k_L F_1^{1/4}/3H$$

Using this in the definition of MH reveals that

$$MH = (8/7)^{1/2}mH$$

Here $m^2 = h_{\text{ave}}\,P/kA$ is the parameter used to determine rectangular fin efficiency for a constant heat-transfer coefficient according to [4]

$$\eta = \tanh(mH)/mH \tag{18}$$

Table 1 shows that the simpler prediction of equation (18) is surprisingly accurate, although being increasingly low as efficiency decreases. The efficiency of the same condensing fin cooled along one vertical side reported elsewhere [3] is also predicted with surprising accuracy by the constant heat-transfer coefficient ideas underlying equation (18).

Heat-transfer coefficients for film condensation are high

enough that appreciable resistance to heat flow transverse to the fin height can occur within the fin. Thus, accurate efficiency prediction should account for temperature variation across the fin width.

References

1 Nader, W. K., "Extended Surface Heat Transfer With Condensation," Paper CS-5, *Sixth International Heat Transfer Conference*, Toronto, Canada, Aug. 1978.

2 Lienhard, J. H. and Dhir, V. K., "Laminar Film Condensation on Nonisothermal and Arbitrary-Heat-Flux Surfaces, and on Fins," ASME JOURNAL OF HEAT TRANSFER, Vol. 96, 1974, pp. 197-203.

3 Patankar, S. V. and Sparrow, E. M., "Condensation on an Extended Surface," ASME JOURNAL OF HEAT TRANSFER, Vol. 101, 1979, pp. 434-440.

4 Kreith, F. and Black, W. Z., *Basic Heat Transfer*, Harper & Row, 1980.

Steady Conduction in Three-Dimensional Shells

R. O. Warrington, Jr.[1], R. E. Powe[2] and R. L. Mussulman[3]

This note presents conduction heat-transfer shape factor results for three-dimensional shells. The inner and outer surfaces of the shells are isothermal. In such circumstances, the shape factor is defined as heat transfer divided by thermal conductivity and by temperature difference between the two surfaces. In addition to their usefulness in pure conduction problems, shape factors are useful is estimating natural convection heat transfer in enclosures that are geometrically similar to those of the conduction problems [1-3]. Geometries considered were cube-sphere (cubical inner surface and spherical outer surface), sphere-cube, cylinder-cube (cylinder with hemispherical end caps), and cube-cube. In all cases, the centroids of the inner and outer surface coincide.

The problem was formulated in Cartesian coordinates,

$$\frac{\partial^2 T}{\partial x^2}+\frac{\partial^2 T}{\partial y^2}+\frac{\partial^2 T}{\partial z^2}=0 \tag{1}$$

with the temperature prescribed along inner and outer boundaries:

$$T = T_i \text{ on inner surface,}$$
$$T = T_0 \text{ on outer surface} \tag{2}$$

The problem was converted to difference form using central differences. The curved surface was approximated by taking the closest mesh point, thus perturbing the actual region so that it coincides with the Cartesian grid. Figure 1 shows 1/4 of a cross section of the cube-sphere geometry (due to symmetry only 1/16th of the enclosed volume was used) and the points used to approximate the curved surface. Interpolation schemes at the boundary were not used since the slight increase in accuracy [4] would not outweigh the increased complexity in programming.

The extrapolated Leibmann or Successive Over-Relaxation (SOR) technique was used to solve the difference model. The basic equation took the form

$$T^{n+1}_{i,j,k}=\gamma(T^{n}_{i+1,j,k}+T^{n}_{i-1,j,k}+T^{n}_{i,j+1,k}+T^{n}_{i,j-1,k}+T^{n}_{i,j,k+1}+T^{n}_{i,j,k-1}+\left(6-\frac{1}{\gamma}\right)T^{n}_{i,j,k}) \tag{3}$$

where the superscripts show the order of iteration. The over-relaxation factor, γ, was set by trial and error at 0.31. This value of γ resulted in the most rapid rate of convergence. Convergence was checked by comparing the heat-transfer rates calculated at the inner and the outer surfaces. This heat balance established the criteria for convergence. The maximum difference between heat transfer calculated at the inner and outer surfaces was less than 0.8 percent for any of the geometries.

All shape factors S were normalized by the sphere-sphere shape factor S_s:

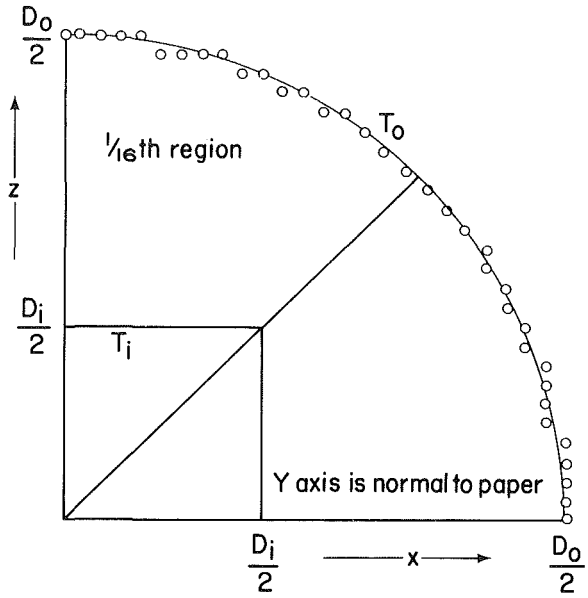

Fig. 1 Cube-sphere geometry in two dimensions

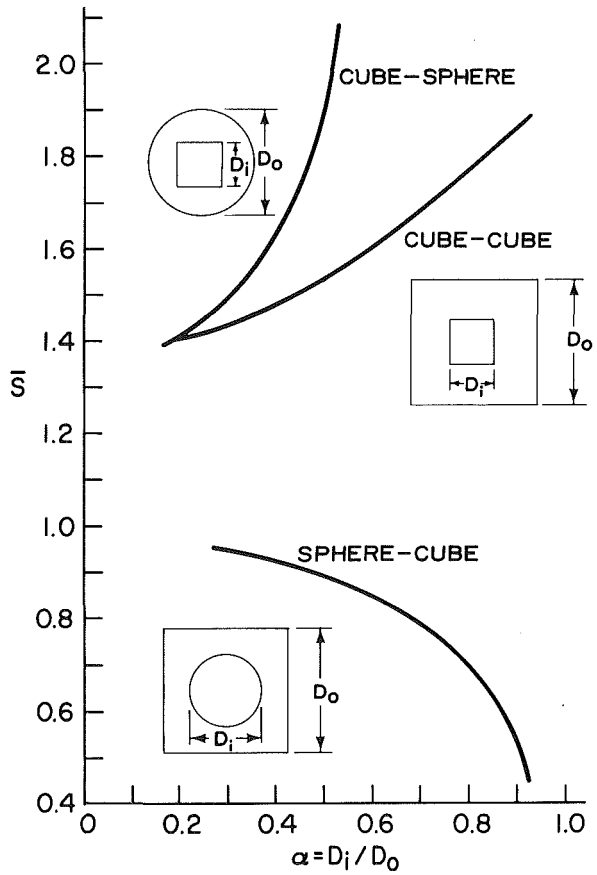

Fig. 2 Normalized heat transfer for various geometries

[1] Associate Professor, Mechanical Engineering Department, Montana State University, Bozeman, Mont. 59717. Mem. ASME

[2] Associate Vice President for Research, Mississippi State University, Mississippi State. Miss. Mem. ASME.

[3] Associate Professor, Mechanical Engineering Department, Montana State University, Bozeman. Mont. 59717

Contributed by the Heat Transfer Division for publication in the JOURNAL OF HEAT TRANSFER. Manuscript received by the Heat Transfer Division September 7, 1981.

enough that appreciable resistance to heat flow transverse to the fin height can occur within the fin. Thus, accurate efficiency prediction should account for temperature variation across the fin width.

References

1 Nader, W. K., "Extended Surface Heat Transfer With Condensation," Paper CS-5, *Sixth International Heat Transfer Conference*, Toronto, Canada, Aug. 1978.

2 Lienhard, J. H. and Dhir, V. K., "Laminar Film Condensation on Nonisothermal and Arbitrary-Heat-Flux Surfaces, and on Fins," ASME JOURNAL OF HEAT TRANSFER, Vol. 96, 1974, pp. 197-203.

3 Patankar, S. V. and Sparrow, E. M., "Condensation on an Extended Surface," ASME JOURNAL OF HEAT TRANSFER, Vol. 101, 1979, pp. 434-440.

4 Kreith, F. and Black, W. Z., *Basic Heat Transfer*, Harper & Row, 1980.

Steady Conduction in Three-Dimensional Shells

R. O. Warrington, Jr.[1], R. E. Powe[2] and R. L. Mussulman[3]

This note presents conduction heat-transfer shape factor results for three-dimensional shells. The inner and outer surfaces of the shells are isothermal. In such circumstances, the shape factor is defined as heat transfer divided by thermal conductivity and by temperature difference between the two surfaces. In addition to their usefulness in pure conduction problems, shape factors are useful is estimating natural convection heat transfer in enclosures that are geometrically similar to those of the conduction problems [1-3]. Geometries considered were cube-sphere (cubical inner surface and spherical outer surface), sphere-cube, cylinder-cube (cylinder with hemispherical end caps), and cube-cube. In all cases, the centroids of the inner and outer surface coincide.

The problem was formulated in Cartesian coordinates,

$$\frac{\partial^2 T}{\partial x^2}+\frac{\partial^2 T}{\partial y^2}+\frac{\partial^2 T}{\partial z^2}=0 \tag{1}$$

with the temperature prescribed along inner and outer boundaries:

$$T = T_i \text{ on inner surface,}$$
$$T = T_0 \text{ on outer surface} \tag{2}$$

The problem was converted to difference form using central differences. The curved surface was approximated by taking the closest mesh point, thus perturbing the actual region so that it coincides with the Cartesian grid. Figure 1 shows 1/4 of a cross section of the cube-sphere geometry (due to symmetry only 1/16th of the enclosed volume was used) and the points used to approximate the curved surface. Interpolation schemes at the boundary were not used since the slight increase in accuracy [4] would not outweigh the increased complexity in programming.

The extrapolated Leibmann or Successive Over-Relaxation (SOR) technique was used to solve the difference model. The basic equation took the form

$$T^{n+1}_{i,j,k}=\gamma(T^{n}_{i+1,j,k}+T^{n}_{i-1,j,k}+T^{n}_{i,j+1,k}+T^{n}_{i,j-1,k}+T^{n}_{i,j,k+1}+T^{n}_{i,j,k-1}+\left(6-\frac{1}{\gamma}\right)T^{n}_{i,j,k}) \tag{3}$$

where the superscripts show the order of iteration. The over-relaxation factor, γ, was set by trial and error at 0.31. This value of γ resulted in the most rapid rate of convergence. Convergence was checked by comparing the heat-transfer rates calculated at the inner and the outer surfaces. This heat balance established the criteria for convergence. The maximum difference between heat transfer calculated at the inner and outer surfaces was less than 0.8 percent for any of the geometries.

All shape factors S were normalized by the sphere-sphere shape factor S_s:

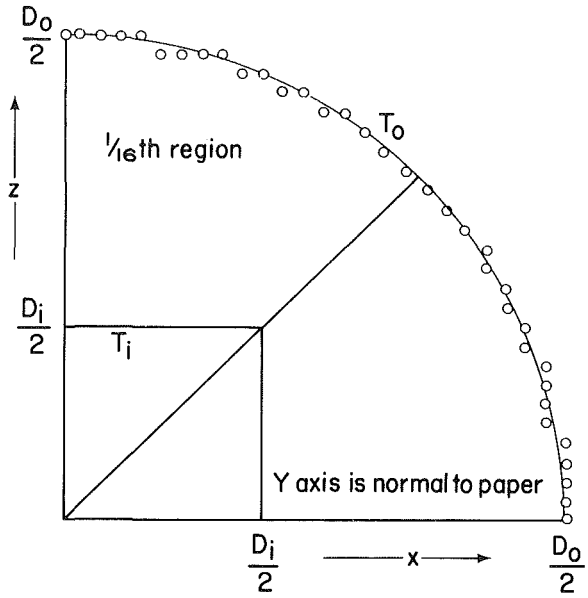

Fig. 1 Cube-sphere geometry in two dimensions

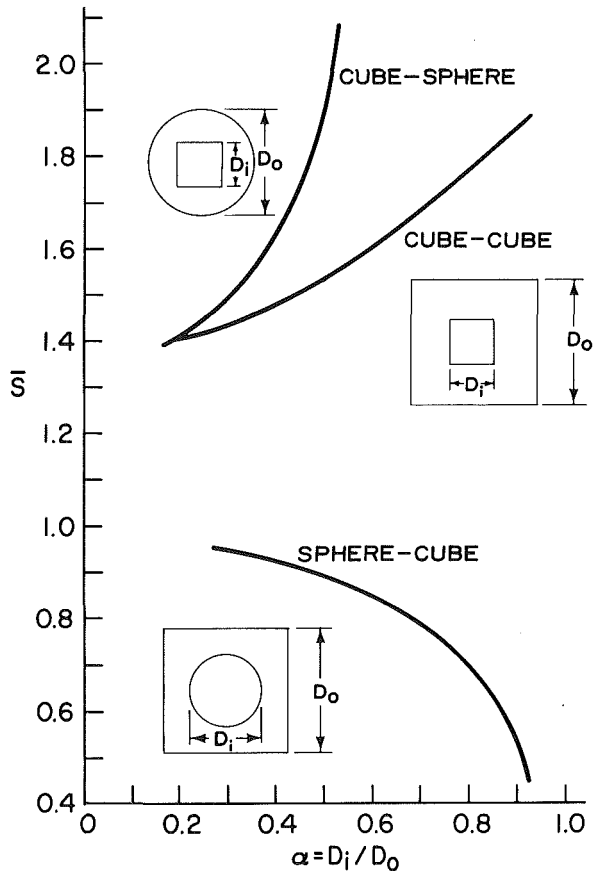

Fig. 2 Normalized heat transfer for various geometries

[1] Associate Professor, Mechanical Engineering Department, Montana State University, Bozeman, Mont. 59717. Mem. ASME

[2] Associate Vice President for Research, Mississippi State University, Mississippi State. Miss. Mem. ASME.

[3] Associate Professor, Mechanical Engineering Department, Montana State University, Bozeman. Mont. 59717

Contributed by the Heat Transfer Division for publication in the JOURNAL OF HEAT TRANSFER. Manuscript received by the Heat Transfer Division September 7, 1981.

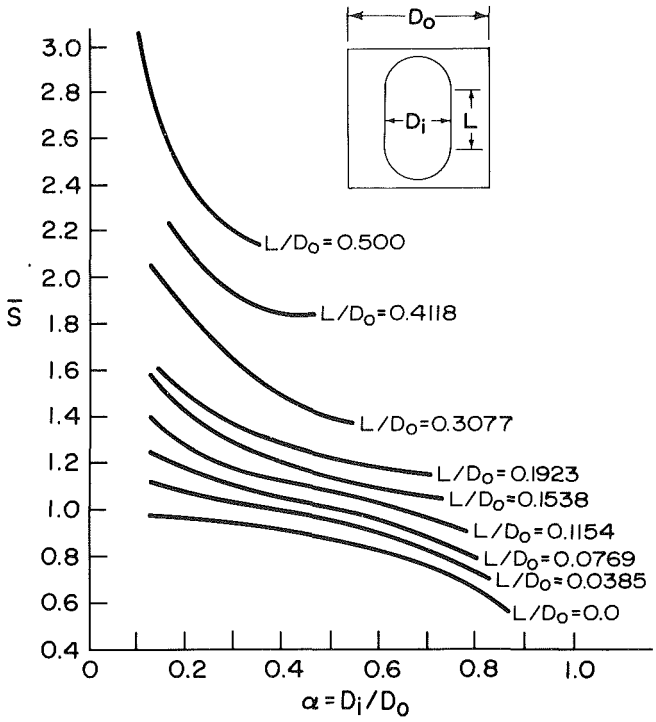

Fig. 3 Normalized heat transfer for cylinder-cube geometry

$$\bar{S} = S/S_s, S_s = 2\pi D_i D_0/(D_0 - D_i) \tag{4}$$

D_0 and D_i are equivalent diameters of the outer and inner surfaces, respectively. The equivalent diameter of a cube is its edge length, the equivalent diameter of a cylinder is its diameter, and the equivalent diameter of a sphere is its diameter.For the cube-sphere, sphere-cube, and cube-cube geometries a 35 × 35 × 35 grid was used. Results are shown in Fig. 2.

For the sphere-cube geometry, $\bar{S} \to 1$ as $\alpha = D_i/D_0 \to 0$. This limit is equivalent to conduction from the sphere to infinite surroundings. That is, for this limit, the outer surface geometry is irrelevant. At the other extreme $\bar{S} \to 0$ as $\alpha \to 1$. The inner and outer surfaces approach contact in this limit. But the surface contact causes heat transfer in the denominator of $\bar{S}$ to dominate the point contact heat transfer in the numerator.

For the cube-cube geometry, heat transfer approaches the one dimensional limit as the aspect ratio α approaches unity. Thus,

$$\lim_{\alpha \to 1} \bar{S} = \frac{\text{Inner cube surface area}}{\text{Equivalent sphere surface area}} = \frac{6}{\pi} \tag{5}$$

Results for the cube-sphere and cube-cube approach the same limit as the aspect ratio approaches zero, because the outer surface geometry is irrelevant in this limit. For the cube-sphere geometry, $\bar{S} \to \infty$ as $\alpha \to 3^{-1/2}$, because the cube corners contact the sphere in this limit.

For the cylinder-cube geometry, a 27 × 27 × 27 grid was used. The results are shown in Fig. 3, where L represents the length of the straight section of the cylinder. All the curves (except the bottom one in which the inner surface is spherical) have the limit $\bar{S} \to \infty$ as $\alpha \to 0$, because the inner body surface area is much larger than the surface area of a sphere of the same diameter in that limit.

The cube-cube results can be compared with the experimental work of Langmiur et al. [5] which give

$$\bar{S} = 0.9740\alpha + 0.8403 + 0.09549/\alpha, \text{ for } \alpha < \frac{1}{11} \tag{6}$$

These results deviated by an average of 1.0 percent from the present results over the range $0.3846 \le \alpha \le 1.0$. This is remarkable agreement for experimental work which was performed in 1912 and which is still difficult to accurately accomplish. The results of reference [5] deviate more at small α (8.2 percent at $\alpha = 0.2$) where the experiments were undoubtedly quite difficult to perform and were subject to considerable controversy.

The results presented here for conduction shape factors are useful both for conduction problems and employment of natural convection correlations.

Acknowledgments

This work was supported in part by the National Science Foundation under grant number GK-31908.

References

1 Raithby, G. D. and Hollands, K. G. T., "A General Method of Obtaining Approximate Solutions to Laminar and Turbulent Free Convection Problems," *Advances in Heat Transfer*, Vol. 11, Academic Press, 1975, pp. 265-315.

2 Powe, R. E., Warrington, R. O., and Scalan, J. S., "Natural Convection Heat Transfer Between Bodies and Their Spherical Enclosure," ASME Publication HTD Vol. 8, 19th National Heat Transfer Conference, Orlando, Fla., July 1980, pp. 79-87.

3 Warrington, R. O. and Powe R. E., "Natural Convection Between Bodies and Their Enclosures," ASME Publication HTD Vol. 16, 20th National Heat Transfer Conference, Milwaukee, Wis., Aug. 1981, pp. 111-125.

4 Warrington, R. O., Reihman, T. C., Stotts, R., and Brown, P., "A Comparative Study of Numerical Solutions of Steady-State Heat Transfer Problems with Irregular Boundaries," *Proceedings of the First National Conference on Numerical Methods in Heat Transfer*, College Park, M.D., Sept. 1979, pp. 425-435.

5 Langmuir, I., Adams, E. Q., and Meikle, G. S., "Flow of Heat Thru Furnace Walls: The Shape Factor," *Transactions of the American Electrochemical Society*, Vol. 24, 1913, pp. 53-84.

ERRATA

Corrections to Author's Closure by D. W. Pepper and R. E. Copper, published in the February 1982 issue of the ASME JOURNAL OF HEAT TRANSFER, pp. 218–219.

Author's Closure

Dr. Beckett's observations on the use of a vector potential in solving three-dimensional flows are well-taken. The formulation of boundary conditions for the vector potential can be troublesome, and is certainly more involved than the constraints imposed when using the primitive equations. It is particularly important that the boundary conditions be well-posed, and care must be taken to properly ensure that the tangential velocities vanish at the surfaces. We agree with Dr. Beckett that ψ must be everywhere solenoidal; likewise, the flow should be divergence free, i.e. $\nabla \cdot \bar{u} = 0$. This condition is not readily guaranteed when using numerical methods, irrespective of the accuracy of the method. Even the use of variational methods (e.g., Lagrangian multipliers) to correct the velocity field is not always satisfactory. However, a good indication of the effectiveness of the numerical solution to obtain a converged solution is to check for divergence. Our computation of the size of $\nabla \cdot \bar{u}$ was obtained by first expressing the velocity components as the gradients of ψ, then computing the gradients of $\bar{u}$. The reason for this is that only ψ and ω values need to be solved in the solution sequence, avoiding the solution of the primitive equations and the troublesome Poisson equation for pressure. Hence, our test for $\nabla \cdot \bar{u}$ (although in terms of ψ) does not necessarily ensure that $\nabla \cdot \psi$ is conserved within the solution domain. It is easy to include a test for $\nabla \cdot \psi$ along with $\nabla \cdot \bar{u}$; testing for $\nabla \cdot \bar{u}$ provides an overall perspective of the solution accuracy of the "numerical" governing equations.